Advances in Polymer Science 273

Martin D. Hager
Sybrand van der Zwaag
Ulrich S. Schubert *Editors*

Self-healing Materials

Springer

273
Advances in Polymer Science

Aims and Scope

The series Advances in Polymer Science presents critical reviews of the present and future trends in polymer and biopolymer science. It covers all areas of research in polymer and biopolymer science including chemistry, physical chemistry, physics, material science.

The thematic volumes are addressed to scientists, whether at universities or in industry, who wish to keep abreast of the important advances in the covered topics.

Advances in Polymer Science enjoys a longstanding tradition and good reputation in its community. Each volume is dedicated to a current topic, and each review critically surveys one aspect of that topic, to place it within the context of the volume. The volumes typically summarize the significant developments of the last 5 to 10 years and discuss them critically, presenting selected examples, explaining and illustrating the important principles, and bringing together many important references of primary literature. On that basis, future research directions in the area can be discussed. Advances in Polymer Science volumes thus are important references for every polymer scientist, as well as for other scientists interested in polymer science - as an introduction to a neighboring field, or as a compilation of detailed information for the specialist.

Review articles for the individual volumes are invited by the volume editors. Single contributions can be specially commissioned.

Readership: Polymer scientists, or scientists in related fields interested in polymer and biopolymer science, at universities or in industry, graduate students.

Special offer:
For all clients with a standing order we offer the electronic form of Advances in Polymer Science free of charge.

More information about this series at http://www.springer.com/series/12

Martin D. Hager • Sybrand van der Zwaag •
Ulrich S. Schubert
Editors

Self-healing Materials

With contributions by

M. AbdolahZadeh · J. Ahner · N. De Belie · W.H. Binder · S. Bode · R.K. Bose · J. Bluhm · D. Crespy · B. Dietzek · D. Döhler · M. Enke · Y.Ç. Erşan · J. Fickert · S.J. Garcia · B. Grabowski · A.M. Grande · M.D. Hager · M.J. Harrington · M. Hernandez · H.M. Jonkers · N. Kuhl · K. Landfester · M. Micheel · R. Mors · D. Palin · M. Rohwerder · E. Schlangen · J. Schröder · U.S. Schubert · M.G. Sierra-Beltrán · S. Specht · O. Speck · T. Speck · A. Tabaković · C.C. Tasan · K. Van Tittelboom · E. Tziviloglou · S. Wagner · J. Wang · R. Weinkamer · V. Wiktor · S. van der Zwaag

Springer

Editors
Martin D. Hager
Laboratory for Organic and
Macromolecular Chemistry (IOMC)
& Jena Center for Soft Matter (JCSM)
Friedrich Schiller University Jena
Jena
Germany

Ulrich S. Schubert
Laboratory for Organic and
Macromolecular Chemistry (IOMC)
& Jena Center for Soft Matter (JCSM)
Friedrich Schiller University Jena
Jena
Germany

Sybrand van der Zwaag
Faculty of Aerospace Engineering
Delft University of Technology
Delft
The Netherlands

ISSN 0065-3195 ISSN 1436-5030 (electronic)
Advances in Polymer Science
ISBN 978-3-319-32776-1 ISBN 978-3-319-32778-5 (eBook)
DOI 10.1007/978-3-319-32778-5

Library of Congress Control Number: 2016941459

Printed on acid-free paper

This Springer imprint is published by Springer Nature
The registered company is Springer International Publishing AG Switzerland

Preface

Self-healing materials, and in particular self-healing polymers, have been intensively investigated over the past 15 years. Several approaches and material systems have been developed, resulting in materials capable of dealing with damage events. In contrast to "classical" materials, the original properties and functionalities of self-healing materials are (partially) restored without significant human intervention. These materials – reminiscent of a science fiction dream – promise high potential for the future, enabling longer life times, reduced maintenance (time and costs), and increased safety.

This volume "Self-healing materials" covers the present state-of-the-art knowledge about different classes of self-healing materials. The first part is devoted to self-healing polymers and presents the main approaches for achieving self-healing: reversible covalent bonds and supramolecular interactions. Two chapters are dedicated to the characterization of these materials and to the modeling of their behavior and properties. The next four chapters deal with applications of self-healing polymers: self-healing sol–gel coatings, encapsulated healing agents for anticorrosion, functional polymeric materials, and self-healing asphalt motorways. Chapters on the relationship between polymer architecture and healing are followed by a chapter on characterization and quantification methods for healing in polymers. Quite unusual for *Advances in Polymer Science*, the final three chapters are not devoted to polymeric materials but could serve as a source of inspiration for the development of novel self-healing polymers. Besides the biological archetypes, bacterially based self-healing concrete and self-healing in metals are discussed.

This special volume on self-healing materials would not have been possible without the excellent contributions from many scientists. We want to express our gratitude to them for sharing their scientific point of view on different aspects of self-healing materials.

We hope that this volume will contribute to the further development not only of self-healing polymers, but also of other material classes that can help to bridge borders between the different disciplines. We are curious to see what novel materials, characterization techniques, and applications will open up in the future.

Jena, Germany — Martin D. Hager
Delft, The Netherlands — Sybrand van der Zwaag
Jena, Germany — Ulrich S. Schubert

Contents

Adv Polym Sci (2016) 273: 1–58
DOI: 10.1007/12_2015_336

Published online: 7 November 2015

Self-Healing Polymers Based on Reversible Covalent Bonds

Natascha Kuhl, Stefan Bode, Martin D. Hager, and Ulrich S. Schubert

Abstract Starting with reversible polymer networks based on the Diels–Alder reaction of furan and maleimide, a large variety of different self-healing polymers based on reversible covalent interactions have been developed in the last decade. These intrinsic self-healing polymers are mainly based on reversible addition reactions, exchange reactions, and condensations. The most prominent examples of such materials are based on Diels–Alder chemistry, photocycloadditions, disulfide reactions, acylhydrazones, and reversible radical reactions.

Keywords Diels–Alder reaction • Disulfide bonds • Intrinsic self-healing polymers • Radicals • Reversible addition reactions • Reversible covalent bonds • Self-healing polymers

Contents

N. Kuhl, S. Bode, M.D. Hager (✉), and U.S. Schubert (✉)
Laboratory of Organic and Macromolecular Chemistry (IOMC), Friedrich Schiller University Jena, Humboldtstrasse 10, 07743 Jena, Germany

Jena Center of Soft Mater (JCSM), Friedrich Schiller University Jena, Philosophenweg 7, 07743 Jena, Germany
e-mail: martin.hager@uni-jena.de; ulrich.schubert@uni-jena.de

1 Introduction

Self-healing materials are currently of great interest because of the possibility of improving the reliability, durability, and lifetime of materials [1–4]. Polymers in particular have gained significant attention because of their wide field of application and the large variety of different healing mechanisms available for polymers compared with other material classes. However, conventional polymers do not generally possess healing ability; specific groups have to be introduced into polymeric materials to impart self-healing ability.

Generally, self-healing materials can be classified into extrinsic and intrinsic materials. In extrinsic self-healing materials, a healing agent is encapsulated into a matrix and is released in response to damage. One of the most prominent examples of extrinsic self-healing materials was reported by White et al. in 2001 [5]. The system consists of microencapsulated dicyclopentadiene embedded in an epoxy matrix containing Grubbs' catalyst. Upon crack formation, dicyclopentadiene is released and the catalyst initiates ring-opening metathesis polymerization (ROMP) to form a tough and highly crosslinked network, which subsequently leads to crack closure (Scheme 1). This concept can be further improved by utilization of WCl_6 as catalyst, which is more cost-effective and tolerates higher temperatures [6].

Such a system only allows one-time healing at a specific position, whereas Toohey et al. developed a system that is able to heal repeated damage by the utilization of a three-dimensional (3D) microvascular network [7]. However, the healing ability is limited to a certain number of healing cycles. This drawback can be overcome by the design of intrinsic self-healing materials, which can theoretically heal endlessly. In most extrinsic systems the healing process occurs

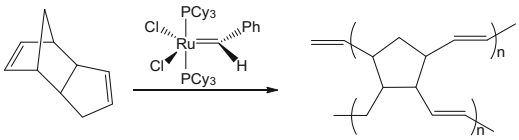

Scheme 1 Ring-opening metathesis polymerization (ROMP) of dicyclopentadiene. Adopted from [5]

autonomously, but intrinsic self-healing materials usually require an external trigger such as light or heat. To develop intrinsic self-healing polymers the incorporation of, for example, noncovalent bonds (e.g., hydrogen bonding [8, 9], ionic interactions [10, 11], or metal–ligand interactions [12–14]) into the polymeric matrix is required. For this purpose, Leibler and coworkers prepared a reversibly crosslinked rubber that could restore its properties after damage as a result of the high reversibility of the hydrogen bonds [8]. Metal–ligand interactions have also been used in the design of self-healing polymers. Burnworth et al. prepared an optically healable metal-containing polymer based on poly(ethylene-*co*-butylene) end-functionalized with 2,6-bis(1′-methylbenzimidazolyl)pyridine, which was complexed by addition of zinc or lanthanum salts [15]. Self-healing of the damaged surface could be achieved through ultraviolet (UV) radiation with a wavelength of 320–390 nm. Moreover, Bode et al. developed a crosslinked metallopolymer based on the complexation of a terpyridine-containing polymer and iron(II) sulfate heptahydrate, which was able to self-heal upon heat treatment at 100 °C [13]. This system was further improved by the use of cadmium(II) salts [14].

In addition, polymers with certain ionic groups (so-called ionomers) can also be used to create self-healing polymers. For this purpose, Kalista et al. investigated poly(ethylene-*co*-methacrylic acid) copolymer films and demonstrated healing ability following high-energy impact (i.e., ballistic impact) [10, 16].

Another opportunity is the incorporation of reversible covalent bonds (e.g., based on the Diels–Alder reaction [17–19], disulfides [20–22] or acylhydrazones [23, 24]) into the polymer matrix to introduce self-healing properties. The strength of the materials is improved compared with incorporation of weaker noncovalent bonds. This effect could be beneficial for several industrial applications. Therefore, scientists have designed a variety of reversible covalent polymers with self-healing ability.

This chapter highlights developments in the field of self-healing polymers based on reversible covalent bonds. For this purpose, reversible cycloadditions such as the [2+2], [4+4] and (the most prominent example of reversible covalent bonds in self-healing materials) [4+2] cycloadditions (Diels–Alder) are described. Thereby, the versatility of feasible monomers as well as the different healing conditions are presented. Furthermore, reversible covalent systems based on acylhydrazone bonds are discussed, followed by disulfides, which show many different possible exchange mechanisms, including radical reactions. Furthermore, self-healing polymers based on radical reactions are discussed. Self-healing mechanisms based on highly reversible transesterifications complete this chapter.

2 Cycloadditions

2.1 [4+2] Cycloaddition (Diels–Alder Reaction)

The most prominent reaction employed to introduce reversible covalent bonds into polymeric materials is the Diels–Alder (DA) reaction [25–27]. The DA reaction is a [4+2] cycloaddition between an electron-rich diene and an electron-poor dienophile

(or vice versa), resulting in a stable cyclohexene adduct (Scheme 2). Several compounds can be used to build up such a reversible system, but the most prominent examples are furan and maleimide derivatives. Table 1 lists some selected dienes and dienophiles as well as the resulting DA adducts. Furthermore, the DA reaction is thermally reversible, thus enabling design of new self-healing polymers. Upon

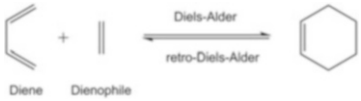

Scheme 2 General mechanism of Diels–Alder/retro-Diels–Alder reactions of a diene and a dienophile

Table 1 Selected examples of dienes/dienophiles and their DA-adduct

Diene	Dienophile	DA-adduct
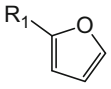 Furan	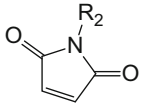 Maleimide	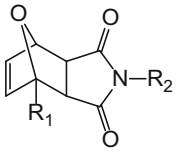
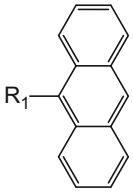 Anthracene	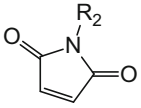 Maleimide	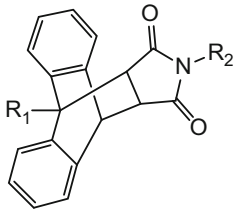
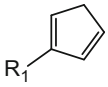 Cyclopentadiene	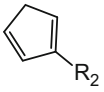 Cyclopentadiene	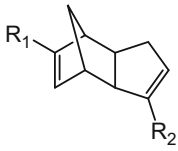
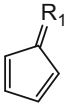 Fulvene	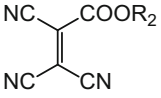 Cyanoolefine	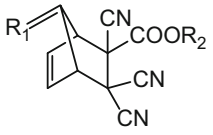
	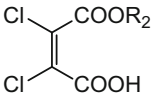 Dichloromaleic acid	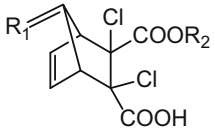

thermal treatment the DA adduct undergoes the reverse reaction (retro-DA), breaking the previously formed covalent bonds. Cooling to lower temperatures allows the cycloaddition to take place again and, therefore, to re-form the covalent bonds.

2.1.1 Systems Based on the Furan–Maleimide Pair

The first self-healing polymer based on the thermoreversible DA reaction was reported by Wudl and coworkers [17]. Their system was based on the cycloaddition of a multifuran monomer containing four furan groups (4F) and a multimaleimide monomer consisting of three maleimide functionalities (3M) (Scheme 3). The resulting covalent crosslinked network (3M4F) displayed reversibility upon heating to 150 °C for 15 min, leading to a cleavage of about 25% of the DA adduct (retro-DA). Upon cooling to 80 °C and subsequent curing at this temperature, the broken bonds were allowed to fully reconnect. By virtue of this special behavior, self-healing experiments were performed by cutting the sample into two pieces. After damage, the two cut surfaces were brought closely into contact, heated to 150 °C to allow the retro-DA reaction and, finally, cooled to room temperature (Fig. 1b, c). The restoration of mechanical integrity across the healed fracture surface was studied by scanning electron microscopy (SEM), which indicated almost complete recovery (Fig. 1d, e). The average healing efficiency was found to be about 50% of the original fracture energy (Fig. 1a). This first example reveals the most significant difference between these systems and extrinsic capsule-based self-healing systems. Instead of "modification" of a given polymer matrix with an additional healing agent, these systems require the design and synthesis of new monomers, polymers, crosslinkers, etc.. This fact remains throughout all other examples. A year later the same authors improved their work by the utilization of low-melting point monomers, which feature a higher mobility in the resulting crosslinked network [18]. Thereby, the self-healing efficiency could be increased to about 80%. In 2007, Nemat-Nasser and coworkers used the same system to study the repeated fracture–healing characteristics more quantitatively [28]. For this purpose, the authors used a double cleavage drilled compression (DCDC) sample geometry,

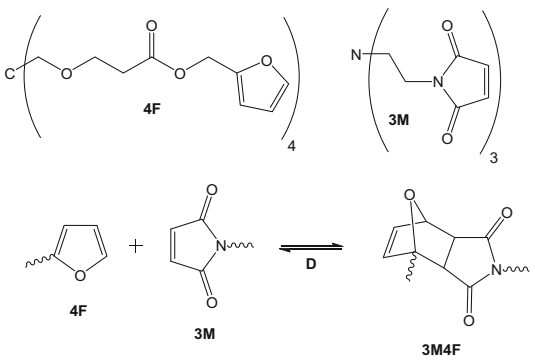

Scheme 3 Schematic representation of the reaction of the monomers containing four furan groups (*4F*) and three maleimide functionalities (*3M*). Adopted from [17]

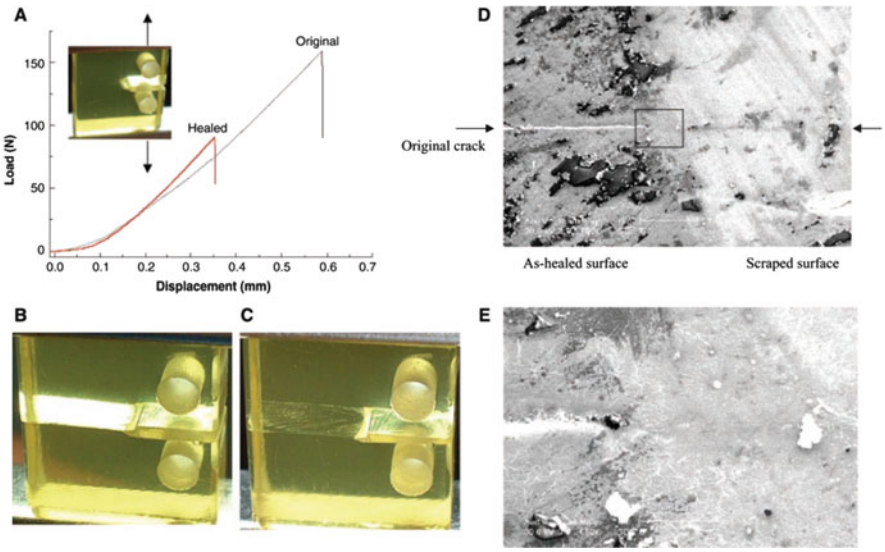

Fig. 1 (**a**) Healing efficiencies obtained by compact tension tests. (**b**) Image of the broken specimen before thermal treatment. (**c**) Image of the healed specimen. (**d**) SEM image of the healed specimen: *left* as-healed sample, *right* scraped surface. (**e**) Enlarged image of the boxed area in (**d**) (Reproduced with permission from [17] Copyright 2015 The American Association for the Advancement of Science)

which allowed controlled crack growth, and ran several fracture–healing cycles. The authors demonstrated that a very fast and repeated healing took place that was largely independent of time. Therefore, the healing process is more probably controlled by the kinetics of the DA reaction than a diffusion-controlled process. Park et al. prepared some composite materials based on the described system and carbon fibers using a vacuum transfer molding method [29]. One attractive feature of this new system was that an applied electrical current increased the sample temperature and, therefore, stimulated the self-healing process. Three-point flexural tests revealed a high recovery of about 90% when the sample was heated to 100 °C for 3 h.

Broekhuis and coworkers designed thermally self-healing polymeric materials based on furan-functionalized, alternating thermosetting polyketones and bismaleimides [30]. The reversibility of the reaction was studied by NMR and Fourier transform infrared spectroscopy (FTIR) spectroscopy as well as by measurement of the gelation time and the gel content (in DMSO). The DA reaction proceeded in 2 h at 50 °C (gel formation) whereas the retro-DA reaction was achieved by heating the polymer to 150 °C for 5 min, resulting in a solution. As a result of cleavage of the DA adducts upon thermal treatment and their reconnection during the cooling process, this polymer displayed some important properties with respect to reprocessability, remeltability, and recyclability. Additionally, self-healing ability was studied by dynamic mechanical analysis (DMA) and

three-point bending tests. Under thermal treatment, the DA/retro-DA cycles could be repeated up to seven times with no significant changes in the dynamic mechanical properties. The self-healing efficiency was found to be approximately 100%. The same authors further investigated this system by varying the number of furan groups and using different molar ratios of furan to maleimide [31].

Yoshie et al. prepared a polymeric network crosslinked by thermally reversible DA bonds with re-mending properties [32]. For this purpose, furfuryl-telechelic poly(ethylene adipate) ($PEAF_2$) was reacted with a tris-maleimide (M_3) to form the crosslinked network $PEAF_2M_3$ after keeping the bulk mixture at 60 °C for 15 h. The retro-DA was found to occur at 145 °C within 20 min. To investigate the self-healing properties, strips of $PEAF_2M_3$ were cut into two pieces and, subsequently, the two cut surfaces were placed in contact with each other and kept at 60 °C for 5 days. After this procedure, the two cut pieces were rejoined. Tensile tests revealed a recovery of 68%, when the sample was mended for 1 week at 60 °C. The expected mechanism is based on the dissociation of DA-adducts at the damaged surfaces, resulting in free furan and maleimide. Bringing the cut surfaces back into contact and keeping the temperature at 60 °C initiates the DA reaction to rejoin the cut surfaces. Moreover, exchange reactions might also contribute to the mending process.

Weizman et al. synthesized a self-healing polymeric network on the basis of a tetrafuran monomer derived from pentaerythrithol (4FS) and diphenyl bismaleimide [33]. Differential scanning calorimetry (DSC) measurements revealed an exothermic peak at 79 °C attributed to the DA cycloaddition, a glass transition temperature of 97 °C, and an endothermic peak ranging from 110 °C to 130 °C belonging to the retro-DA reaction. For the self-healing experiment, a thin film was prepared, slit, and then heated for 2 h at 120 °C. The fracture could be virtually healed, as demonstrated by optical microscopy.

Postiglione and coworkers designed a self-healing polymer network based on the reaction of trifunctional and difunctional furanized resins with a bismaleimide [34]. The reversible nature of the network was characterized by means of FTIR, DSC, and DMA investigations. Whereas the DA reaction was found to occur at a temperature above 50 °C, the retro-DA reaction took place at about 120 °C. Because the polymer network was very brittle and, thus, the mobility was too low to obtain good self-healing properties, 10% benzyl alcohol was intermixed as a plasticizer. Optical microscopy was used to investigate the self-healing behavior of this system. The sample surface was damaged by a razor blade and heated to 120 °C for 10 min to allow self-healing. In the case of small scratches, a full recovery could be obtained. Gloss measurements revealed an "aesthetic healing" of about 95%, but recovery of tensile strength was only 48%.

Another system based on a crosslinked epoxy resin-like material was prepared by Liu and coworkers [35]. For this purpose, a trifunctional maleimide (TMI) was reacted with a trifunctional furan (TF) to form a crosslinked network by the DA reaction (Fig. 2). The thermal reversibility was studied by DSC and FTIR, indicating the repeated bonding and de-bonding ability of the DA adduct. The self-healing process was monitored by SEM (Fig. 3). For this purpose, the sample was cut with a

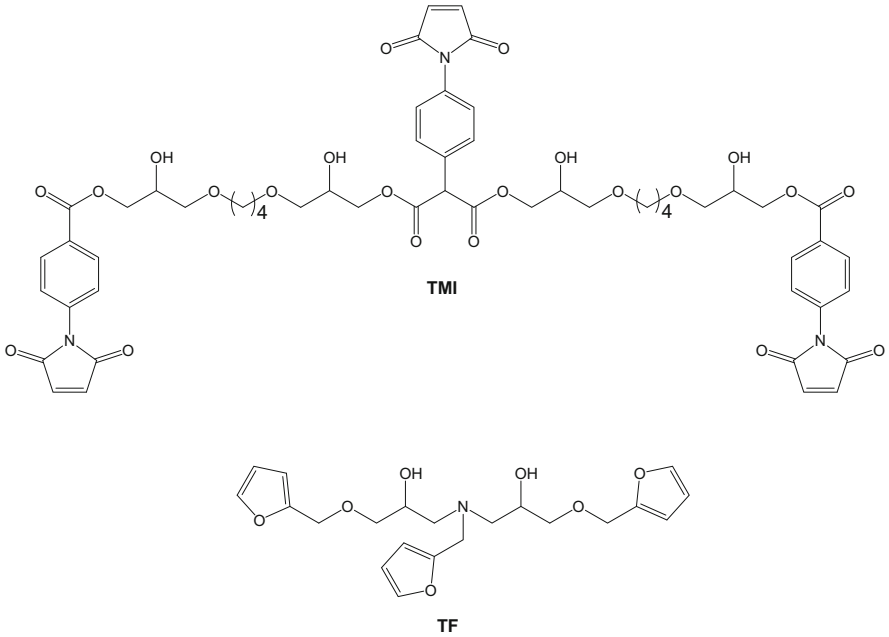

Fig. 2 Monomers trifunctional maleimide (*TMI*) and trifunctional furan (*TF*). Adopted from [35]

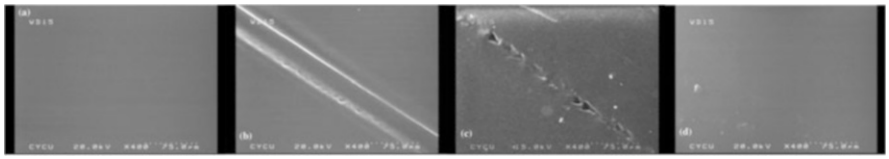

Fig. 3 Self-healing process monitored by SEM: (**a**) Crosslinked sample, (**b**) knife-cut sample, (**c**) partially healed cut after 12 h at 50 °C, and (**d**) healed sample after 24 h at 50 °C (Reproduced with permission from [35]. Copyright 2015 Wiley Periodicals, Inc.)

knife, heated to 120 °C for 20 min to allow debonding and, finally, cured at 50 °C for 24 h. This procedure resulted in complete recovery of properties. The same authors also reported a reversible DA system based on crosslinked polyamides [36]. For this purpose, they synthesized maleimide- and furan-containing polyamides (PA-MI and PA-F) and reacted them with each other via a DA reaction. The resulting polymeric networks of PA-MI/PA-F with different crosslinking densities exhibited strong mechanical properties, high glass transition temperatures, and high toughness, as evaluated by DMA. Related to these properties, the damaged surface of the sample could only be partially healed after treating the sample at 120 °C for 3 h followed by curing at 50 °C for 5 days.

In 2009, Tian et al. developed a thermally re-mendable epoxy resin consisting of *N*,*N*-diglycidyl-furfurylamine (DGFA) and *N*,*N*′-(4,4′-diphenylmethane)

bismaleimide. Thermally stable bonds were formed by the reaction of epoxy and anhydride [37]. Given the nature of these two different kinds of chemical bonds, the resulting crosslinked network displayed similar mechanical properties to commercial epoxy resins. However, thermally induced self-healing properties were also obtained. The self-healing process was monitored optically. To this aim, a polymer plate was cracked, heated to 125 °C for 20 min and subsequently annealed at 80 °C. Using this procedure, the damage was healed to 66% through the successive retro-DA and DA reactions. One year later, the same authors prepared a similar epoxy resin utilizing furfuryl glycidyl ether (FGE) instead of DGFA [38]. By the replacement of DGFA by FGE it was possible to perform the DA reaction with a lower activation energy. For this reason, the healing efficiency could be increased from 66% (DFGA) to 96% (FGE) using the same healing conditions.

In contrast to the above described approaches using functional (oligomeric/polymeric) monomers (i.e., maleimides and furans), Wouters et al. prepared functional copolymers with furfuryl methacrylate (FMA) and butyl methacrylate (BMA) and crosslinked them with different bismaleimides (aromatic and aliphatic) [39]. The authors fabricated polymer films and demonstrated the re-mendability of the crosslinked materials. Moreover, reversible covalent bonds were incorporated into an epoxy-amine network structure. For this purpose, an epoxy-modified furan was crosslinked with different bismaleimides, followed by the addition of different commercially available amines (Jeffamine D-230 and D-400, Euredur 76). Rheological measurements were performed to confirm the thermal reversibility of the network, which could be applied as a potential coating material. Related to the work of Wouters, Scheltjens et al. reported a reversible crosslinked polymer network formed by reaction of FGE-functionalized Jeffamine D-400 and 1,1′-(methylenedi-4,1-phenylene)bismaleimide (DPBM) (Fig. 4) [40]. For investigation of the self-

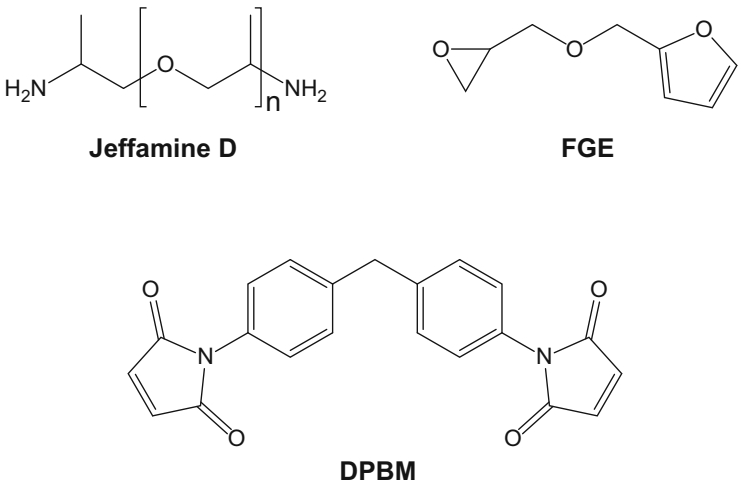

Fig. 4 Components used for the synthesis of the reversible crosslinked network; *FGE* furfuryl glycidyl ether, *DPBM* 1,1′-(methylenedi-4,1-phenylene)bismaleimide. Adopted from [40]

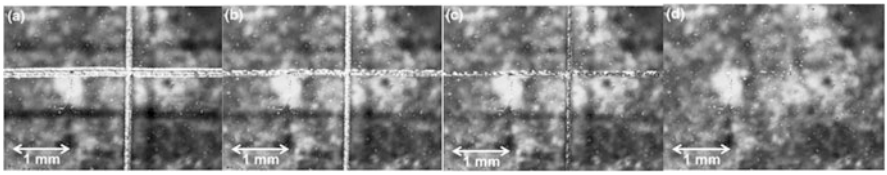

Fig. 5 Self-healing process: (**a**) Scratched surface before thermal treatment, (**b**) at 90 °C, (**c**) at 110 °C, and (**d**) after 2 min at 130 °C (Reproduced from [40] Copyright 2015 Springer)

healing behavior, a solvent-cast coating was prepared and scratched using a microscalpel. Heating to 130 °C for 2 min fully healed the damage (Fig. 5). Further self-healing studies on this epoxy-amine based network were performed by the same authors using atomic force microscopy (AFM) [41]. The influence of amines (aliphatic and aromatic) on the self-healing properties was also investigated. The authors could demonstrate that with increasing crosslinking density, as well as by replacement of aliphatic amines by aromatic amines, the thermoreversibility (i.e., healing) was shifted toward higher temperatures. Thus, the properties of the coating could be fine-tuned by the choice of different amines, varying the spacer length in the furan functional compound. Hence, the polymer network with Jeffamine D-400 resulted in a glassy system, which required a healing temperature of 100 °C for 15 min, whereas the Jeffamine D-4000 network resulted in an elastomer for which the required healing temperature decreased to 80 °C for 7 min. Furthermore, kinetic studies and rheological experiments were performed on two elastomeric model systems using Jeffamine D-2000 and Jeffamine D-4000 [42].

Another approach to the synthesis of a self-healing epoxy polymer based on the DA reaction was reported by Bai et al. in 2013 [43]. A new diamine crosslinker composed of two DA adducts at each end was synthesized and mixed with the diglycidyl ether of bisphenol A (DGEBA). The resulting crosslinked epoxy polymer was characterized by DSC, FTIR, and thermogravimetric analysis (TGA). Cracks were introduced into the material using a razor blade and the self-healing behavior was investigated. The scratches fully disappeared after thermal treatment for 30 min at 140 °C. The effect of the curing conditions and the self-healing mechanism of this system are reported elsewhere [44].

Further work in field of self-healing polymers based on the DA reaction between furan and maleimide derivatives was performed by the group of Palmese [45]. In 2009, the authors designed a reversibly crosslinked gel by the reaction of furfuryl amine with DGEBA in *N*,*N*′-dimethylformamide (DMF) and subsequent crosslinking with DPBM. The resulting DMF-swollen gel could be converted to a polymer-bismaleimide solution by heating for 20 min at 90 °C. After cooling back to ambient temperature, gelation occurred after approximately 13 h. This system was employed as a healing agent for conventional epoxy resins. The gel was transferred to a solid material and mixed with an epoxy-amine resin. Healing studies revealed that cracks in the material could be removed by heating to 90 °C as a result of flow of the liquefied healing agent. However, only 21% of the initial strength could be restored after the first healing cycle. Consequently, a modified

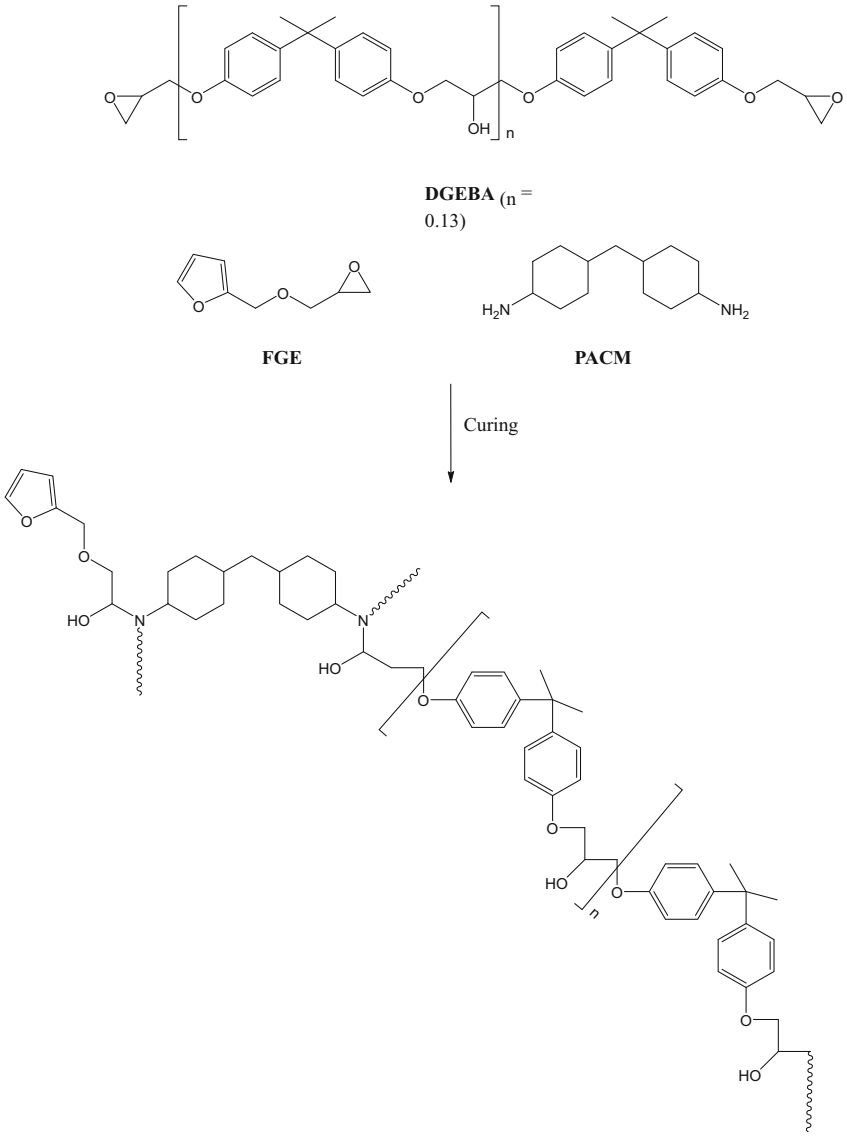

Scheme 4 Formation of the epoxy network (see text for details) [46]

system was prepared in which a bismaleimide solution promoted the self-healing process by solvent-induced swelling and softening of the crack surfaces [46]. For this purpose, furan-functionalized polymers were synthesized by adding stoichiometric amounts of DGEBA and FGE to 4,4′-methylene biscyclohexanamine (PACM) (Scheme 4). Treatment of a crack surface with a DMF-based DPBM solution resulted in average healing efficiencies of approximately 70%. A

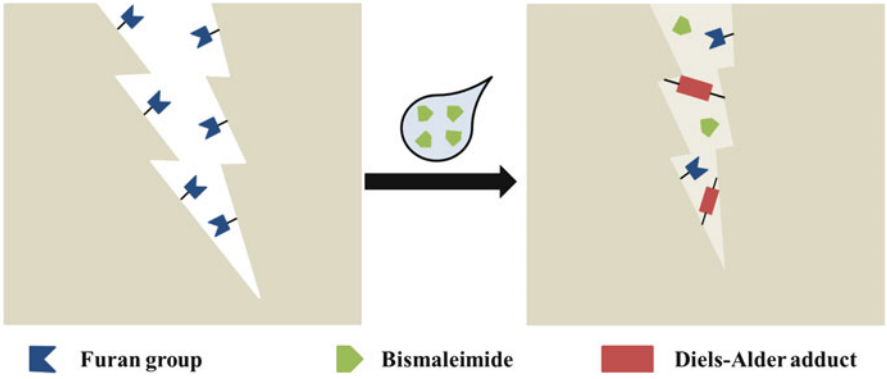

Fig. 6 Concept of the solution-triggered healing process

schematic representation of the healing procedure is depicted in Fig. 6. The healing efficiency was found to depend on the amount of solvent as well as on the maleimide concentration. Two years later the self-healing mechanism was studied and found to be a combination of diffusion and DA reaction [47]. The system was further investigated to study the effect of the solvent, healing time, healing agent concentration, and structure on the healing efficiency [48, 49]. Healing times of 12 h, 24 h, and 20 days were used to distinguish between the effects of three different maleimides (two aromatic and one aliphatic). Healing efficiencies of about 90% were achieved for all maleimides after 20 days. However, the healing efficiency was also dependent on the maleimide concentration and was found to be best for the aliphatic bismaleimide with the highest possible concentration of 1.16 M. Furthermore, Palmese and coworkers showed that the use of phenyl acetate instead of DMF in combination with the use of an aliphatic bismaleimide resulted in higher healing efficiencies. Microcapsules were prepared containing this bismaleimide-phenyl acetate solution and were dispersed in a furan-functionalized epoxy-amine thermoset. The addition of fumed silica as a viscosity modifier improved the capsule dispersion, giving rise to an average healing efficiency of 71% (after 2 days with a bismaleimide concentration of 0.3 M).

Another approach based on the self-healing system described above was the fabrication of a fiber-reinforced composite with re-mendable interfaces [50]. For this purpose, the same furan-functionalized polymer was used as well as water-sized E-glass fibers, which were functionalized with maleimide groups using a two-step process. The healing ability was investigated via microdroplet single fiber pull-out tests, demonstrating an average healing efficiency of 41%. After interfacial failure, the tested specimens were healed for 1 h at 90 °C and for 12 h at 22 °C. Multiple healing was also possible (up to five cycles) but reduced the healing efficiency step-by-step until a plateau of about 10% was reached after the third cycle. Further studies with respect to kinetic and physical parameters were reported later [51]. The healing efficiency was found to be independent of the furan content as long as furan was present in the network at a level $> 20\%$. DA bond formation

was suggested to be very important for strength recovery at the fiber–polymer interface and was influenced by the glass transition temperature and the healing temperature.

In addition, Duchet and coworkers examined the self-healing ability in carbon fiber-reinforced composites [52]. For this purpose, a furan-functionalized polymer similar to that investigated by the group of Palmese was used. The carbon fibers were first oxidized, followed by grafting of amino groups, which were required to allow subsequent introduction of maleimide groups via Michael addition. The healing ability was studied via a microdroplet single fiber pull-out test following the same healing procedure as described above, with the sole difference that the sample was left for 24 h at room temperature instead of 12 h. Healing efficiencies of up to 82% could be achieved, which decreased to 58% after the fourth healing cycle.

Singha and coworkers developed a system on the basis of the homo- and copolymers of FMA crosslinked with a bismaleimide [53]. The FMA homopolymer as well as the copolymer with methyl methacrylate (MMA) were synthesized via atom-transfer radical polymerization (ATRP). Well-defined crosslinked polymers could be obtained upon addition of DPBM, resulting in the formation of DA adducts. Heating the crosslinked polymer above 100 °C led to de-crosslinking of the network as a result of the retro-DA reaction. The self-healing ability of the networks was investigated by SEM. For this purpose, the sample was damaged with a knife and heated at 120 °C for 4 h, resulting in full recovery. DMA studies underlined the reversible character of this system, resulting from decreases in the storage and loss moduli and in the dynamic viscosity upon heating. Moreover, Shinga and coworkers prepared a similar network via synthesis of a copolymer based on FMA and BMA (PFMA-*b*-PBMA) and subsequent crosslinking with DPBM [54]. This time, the authors utilized the reversible addition fragmentation chain transfer (RAFT) polymerization technique to prepare the copolymers. Self-healing of damaged films was achieved after heating the material to 130 °C for 4 h and further treatment at 50 °C for 24 h to allow reconnection of the broken DA bonds. The same authors expanded their work by the preparation of a tailor-made thermoreversible ABA triblock copolymer bearing reactive furfuryl functionalities [55]. The ABA triblock copolymer poly(furfuryl methacrylate)-*b*-poly (2-ethylhexyl acrylate)-*b*-poly(furfuryl methacrylate) (PFMA-*b*-PEHA-*b*-PFMA) was crosslinked by the addition of DPBM. DSC studies of the triblock copolymer revealed two glass transition temperatures, one for the hard segment at 65 °C (PFMA) and one for the soft segment at −50 °C (PEHA). For the crosslinked network, an endothermic peak at 150 °C related to the retro-DA was obtained. Furthermore, the glass transitions of the triblock copolymer were shifted to higher temperatures (−44 °C and 114 °C) as a result of crosslinking. In order to investigate the self-healing ability, a scratch was inflicted on the material and the healing process monitored using SEM. After heating the sample to 120 °C for 4 h the sample was kept at 25 °C for 24 h, resulting in complete recovery from the damage.

The previous examples are all based on the utilization of different monomers (i.e., multifunctional maleimides and furans), low molar mass crosslinkers, and

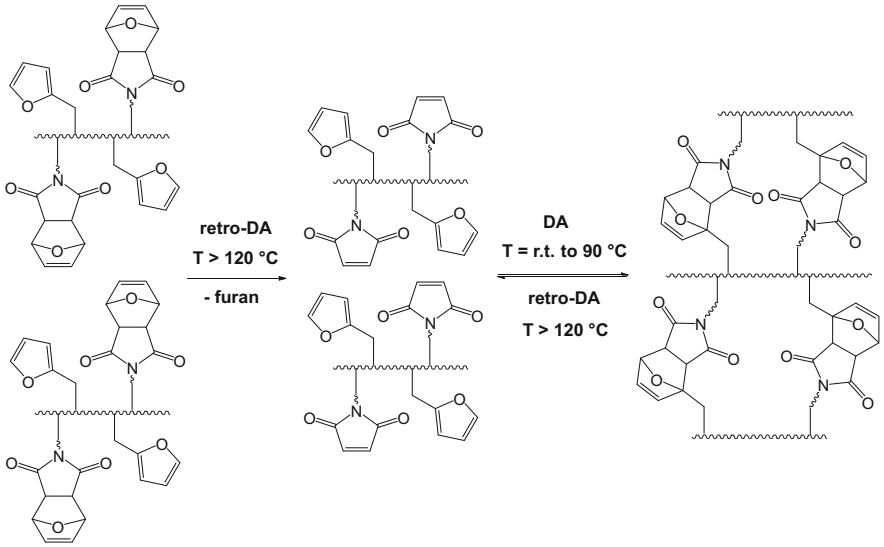

Scheme 5 Self-healing concept of a one-component Diels–Alder system. Adopted from [19]

polymers as well as two polymeric (oligomeric) compounds bearing the respective binding units. In contrast to this approach, Kötteritzsch et al. developed a one-component intrinsic self-healing system [19]. Linear self-healing polymers with a methacrylate-based backbone bearing furan and maleimide moieties in the side chain within the same polymer chain were synthesized (Scheme 5). The advantage of this one-component system is that networks can be formed without the need for a separate crosslinker or a second homo- or copolymer. The reversible crosslinked polymers could be obtained by copolymerization of different alkyl methacrylates (MMA, BMA, and lauryl methacrylate) with FMA and furan-protected maleimide methacrylate (MIMA) via ATRP. Different alkyl methacrylates were used to improve the mobility and flexibility of the comonomers. Moreover, the degree of functionalization was varied from 10% to 67% to investigate its influence on self-healing behavior. The self-healing ability was studied using AFM and SEM. For this purpose, scratches were inflicted on spin-coated films, which were subsequently heated to 160 °C to induce the retro-DA reaction and, thus, healing (Fig. 7). The best self-healing could be obtained using lauryl methacrylate as comonomer and a degree of functionalization of 20%; after 2 min at 160 °C the scratches were completely removed. The reversibility and healing ability of this system was further studied by Bose et al. using a combination of FTIR spectroscopy and oscillatory shear rheological measurements [56]. In addition, Geitner et al. performed the first Raman spectroscopic 2D correlation analysis on self-healing polymers utilizing this system [57]. Kötteritzsch et al. expanded their research on the one-component system by using maleimides with three different linker units as well as by the use of polar and nonpolar comonomers for the synthesis of their copolymers [58]. Thereby, they could obtain copolymers with

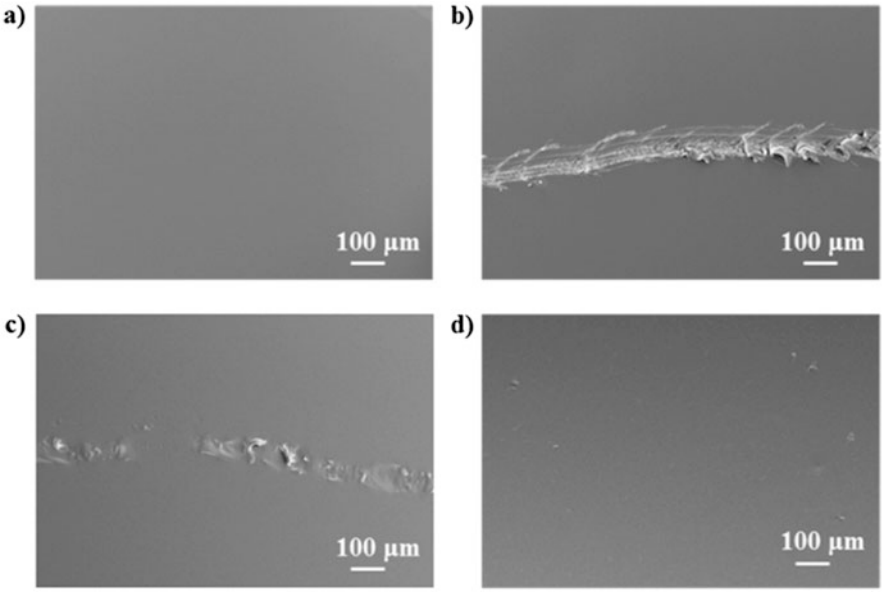

Fig. 7 Self-healing process monitored by SEM: (**a**) cross-linked film, (**b**) scratch before thermal treatment, (**c**) scratch after 1 min at 160 °C, and (**d**) healed polymer film after 3 min at 160 °C (Reproduced from [19]. Copyright 2015 Wiley-VCH Verlag GmbH & Co KGaA)

improved self-healing properties. In particular, a decreased healing temperature was observed and scratches, even at the millimeter scale, could be healed by introducing a longer linker for the maleimide.

A self-healing nanocomposite based on the combination of a methacrylate-containing copolymer and silica nanoparticles was reported by Kickelbick and Engel [59]. A linear polymer was synthesized by the copolymerization of BMA with furan-protected maleimidopropyl methacrylate in a 10:1 ratio using the ATRP technique. Silica–polymer core–shell particles with pendant furfuryl groups were prepared by surface-initiated ATRP of the nanoparticles (tetraethyl orthosilicate) with BMA and FMA. Afterwards, the linear maleimide-containing polymer was mixed with a suspension of the furan-functionalized nanoparticles and cured for 24 h at 80 °C to obtain a nanocomposite healable by means of the DA reaction. The self-healing ability was investigated on drop-cast composite films, which were damaged by a diamond scratching pen. The self-healing process was monitored by an optical microscope. After heating the material for 15 min at 150 °C the scratch was completely absent.

In addition, Xu et al. prepared a self-healing polyhedral oligomeric silsesquioxane (POSS) nanocomposite material through a thermally reversible DA reaction [60]. The POSS nanocomposite was obtained by the reaction of furan-functionalized POSS (eight furan units) with DPBM, resulting in a highly crosslinked network. The self-healing properties were investigated through visual

inspection of the healing process during thermal treatment. For this purpose, the POSS nanocomposite was scratched and subsequently heated to 135 °C for 30 min to induce the retro-DA reaction. After that, the material was cooled slowly in an oven to allow reconnection of the furan and maleimide units by the DA reaction. After this procedure, the cracks were completely healed.

Furthermore, Li et al. reported a thermally healable graphene oxide/polyurethane composite based on the DA reaction [61]. Graphene oxide was prepared by Hummers' method followed by in situ polymerization of 4,4-diphenylmethane diisocyanate, poly(tetramethylene glycol), and furfuryl alcohol to obtain a graphene oxide/polyurethane composite. Upon addition of *N*,*N*′-(4,4′-diphenylmethane)-bismaleimide the DA reaction occurred, resulting in a covalently crosslinked network. The self-healing properties of the material were investigated by AFM. For this purpose, a spatula was used to introduce surface defects on the material. The material was heated to 150 °C for 4 h to induce de-crosslinking by means of the retro-DA reaction, followed by slow cooling to 65 °C and curing at this temperature for 24 h to allow re-crosslinking. Profilometry measurements revealed that the scratches were almost completely removed, with an average healing efficiency of 78%.

Du et al. prepared a linear self-healing polyurethane (PU)-based on the thermally reversible DA reaction (Scheme 6) [62]. First, 4,4-diphenylmethane diisocyanate (MDI) was reacted with poly(1,4-butylene adipate glycol) (PBA1000) followed by the addition of furfuryl amine, resulting in a polyurethane prepolymer bearing two furan groups (MPF). Next, the DA reaction was carried out by mixing MPF with DPBM to obtain linear polyurethanes with thermally reversible DA units (PU-DA). The self-healing ability of this system was studied using AFM and polarizing optical microscopy (POM) (Fig. 8). The PU-DA film was cut with a surgical blade and heated to 120 °C. After approximately 300 s the crack was no longer visible. Recovery tests were performed to determine the healing efficiency, which was found to be 80% for the first healing cycle and 66% for the second. The same authors expanded their work by the utilization of a polymeric MDI to prepare a multiple-furan monomer [63]. Upon addition of DPBM the DA reaction proceeded to form a polyurethane network. Self-healing experiments revealed that a damaged sample could be self-healed by heating the material for 5 min at 130 °C, with a healing efficiency of 92.4%.

Another system based on a crosslinked polyurethane was developed by Zhang et al. [64]. For this purpose, a co-network comprising a 1:1 mixture of linear bisfuranic-terminated poly(tetramethylene oxide) (PTMEG-BF) and poly(*p*-dioxanone) (PPDO-BF) was crosslinked by the addition of tris(2-maleimide ethyl)amine. DMA studies revealed the existence of two separate melting points (25 °C and 103 °C), which correspond to the "melting" of the PPDO-BF and the PTMEG-BF segments, respectively. These two melting points allowed the DA co-network to undergo triple-shape memory effects. Moreover, the self-healing ability was tested by the introduction of damage using a razor blade and monitoring the healing process with an optical microscope. The fracture disappeared almost completely under thermal treatment, with a healing efficiency of 75%, as

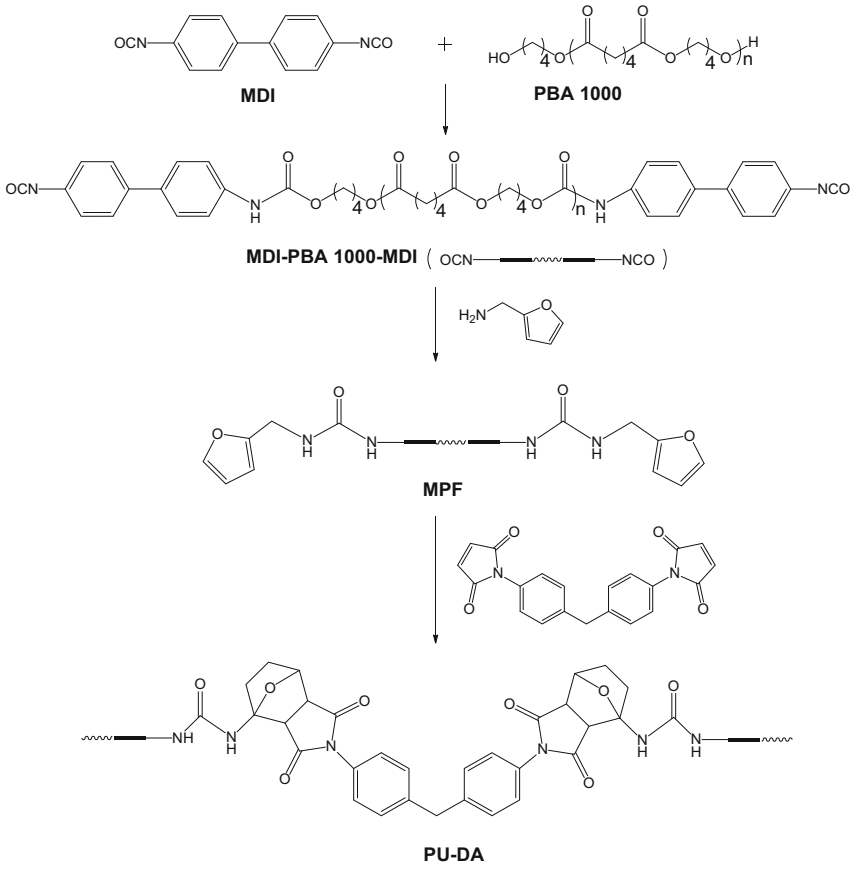

Scheme 6 Synthesis of the linear polyurethane PU-DA (see text for details). Adopted from [62]

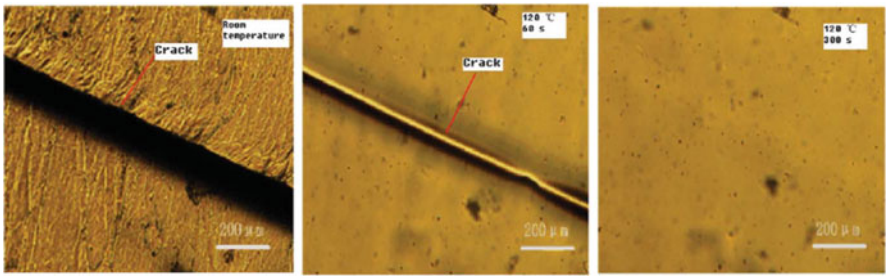

Fig. 8 Self-healing process monitored by polarizing optical microscopy (Reproduced from [62]. Copyright 2015 The Royal Society of Chemistry)

determined by tension tests. Two years later, the group of Sodano and coworkers investigated self-healing polyurethanes with shape recovery properties [65]. First, a pre-crosslinked DA monomer was prepared by the reaction of furfuryl alcohol with

N-(2-hydroxyethyl)-maleimide. Thereafter, this DA monomer was reacted with triethanolamine (TEA) and hexamethylene diisocyante (HDI) to obtain polyurethanes. Fracture testing experiments revealed healing efficiencies in the range of 80–85%, whereas cycling tensile tests indicated a shape memory effect, which could replace the need for external forces to close the crack. Likewise, Rivero et al. synthesized thermo-re-mendable shape memory polyurethanes [66]. Preparation of the polyurethanes was based on a two-step strategy. First, a DA monomer was synthesized by the reaction of a furan diol with a bismaleimide. After that, different amounts of polycaprolactone (PCL) and HDI were added to produce covalently crosslinked polyurethanes. By the application of three consecutive cycles of large tensile deformations, all polyurethanes featured excellent shape memory recoveries. In addition, the self-healing ability was investigated using optical microscopy. The authors discovered that healing was only effective if a high content of hard segment was incorporated into the network. Nevertheless, self-healing could be obtained at mild temperatures of 50 °C (after 24 h), being the result of the DA shape memory assisted self-healing.

Lu et al. developed covalently crosslinked polyurethanes and used ultrasound to trigger shape memory assisted self-healing [67]. The polyurethane network could be obtained by the reaction of a DA monomer containing two reactive hydroxyl groups with NCO-terminated PCL prepolymer and hexamethylene diisocyanate trimer (tri-HDI) (Fig. 9a). Upon treatment of PU-FM with high-intensity focused ultrasound (HIFU) the temperature of the sample rose quickly, resulting in shape recovery of the material (Fig. 9b). One advantage of HIFU is that the heat treatment can be localized in a small area, so that the shape memory process can be induced only in a selected part of the polymer. Consequently, damaged surfaces of the polyurethane network could be brought back into contact by HIFU treatment, thus initiating the self-healing process through reconnection of DA bonds. Self-healing efficiencies of ~92%, ~84%, and ~70%, for the first three healing cycles could be obtained.

Another approach based on the use of furan and maleimide derivative was described by Mallek et al. in 2013 [68]. For this purpose, a series of PCL-based multifurane prepolymers were prepared by the catalytic ring-opening copolymerization of ε-caprolactone with furfuryl glycidyl ether (FGE) using furfuryl alcohol as chain limiting agent. In the next step, these furan-functionalized copolymers were crosslinked by the addition of bis- or tris-maleimide to form a thermally reversible network. The thermal and mechanical properties were characterized by DSC, TGA, and DMA. Self-healing experiments after knife-cutting the sample surface revealed a fully restored material after thermal treatment at 140 °C for 20 min, followed by curing for 12 h at 40 °C.

In addition, Barthel et al. prepared various well-defined poly(ethylene oxide)-*b*-(furfuryl glycidyl ether) (PEO-*b*-PFGE) block copolymers and crosslinked them by the addition of 1,1-diphenylmethyl bismaleimide to form a thermoreversible network in means of retro-DA chemistry (Fig. 10) [69]. DSC and depth sensing indentation (DSI) measurements revealed that PEO_{330}-*b*-$PFGE_{20}$ featured the best properties for creating a self-healing material upon crosslinking with

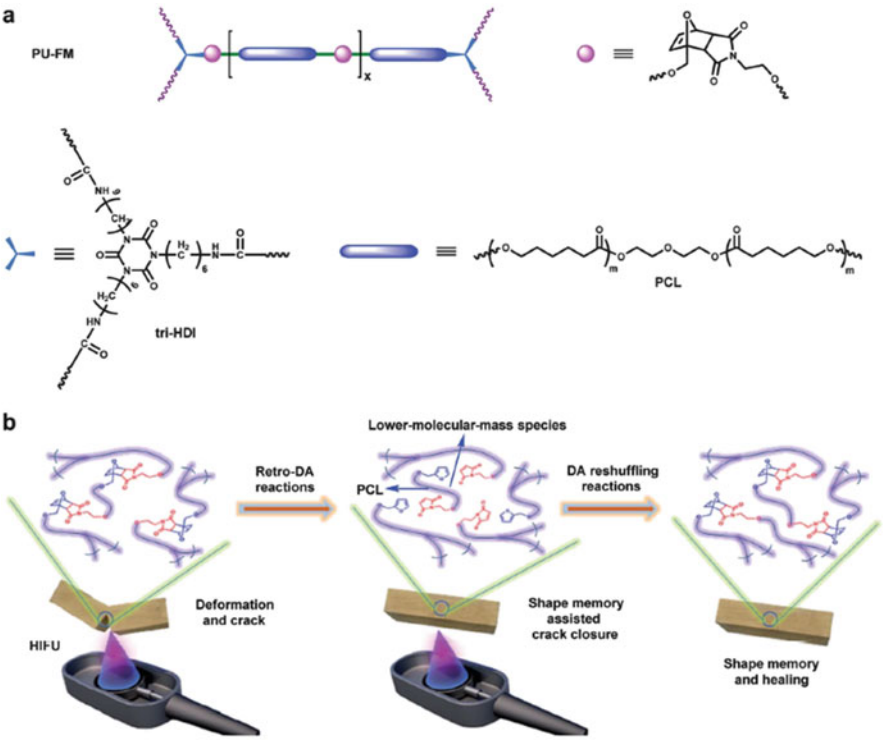

Fig. 9 (**a**) Characteristic structure elements of the monomers (see text for details). (**b**) The concept of self-healing by treatment with high-intensity focused ultrasound (*HIFU*) (Reproduced from [67]. Copyright 2015 The Royal Society of Chemistry)

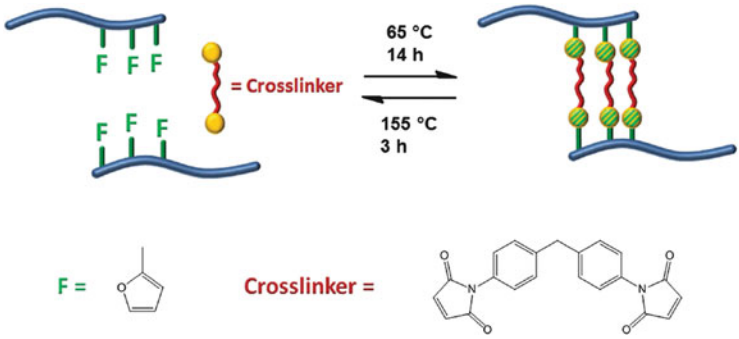

Fig. 10 Crosslinking reaction for block copolymers of PEO-*b*-PFGE (Reproduced from [69]. Copyright 2015 Wiley-VCH Verlag GmbH & Co. KGaA)

1,1-diphenylmethyl bismaleimide. Profilometry measurements were used to study the self-healing ability of this reversible network. The surface of drop-casted films was damaged using a spatula. Heating the damaged material to 155 °C for 3 h to

induce retro-DA (de-crosslinking), and subsequent re-crosslinking by slowly cooling to 65 °C and keeping the material for 14 h at this temperature led to the complete disappearance of small scratches (up to 6 μm depth and 1.7 mm width). Multiple healing of small scratches was also possible (up to four cycles were tested).

Further work in the synthesis of self-healing polymers by DA chemistry was performed by Zeng et al. in 2013 [70]. The authors prepared biobased furan polymers such as poly(2,5-furandimethylene succinate) (PFS), obtained by the polycondensation of 2,5-bis(hydroxymethyl)furan (BHS) with succinic acid. Addition of different amounts of 1,8-bis(maleimido)triethylene glycol (M_2) to crosslink the linear furan-functionalized polymers resulted in biobased networks. The self-healing behavior was studied in detail with respect to the varied compositions of the networks. The healing efficiency was found to be dependent on the M_2 content and thus the furan/maleimide ratio. The best healing efficiency of 75% could be achieved for a PFS/M_2 ratio of 6:1. The efficiency could be further improved to above 90% by treatment with chloroform or 70 mg mL^{-1} M_2 solution. Furthermore, the influence of different maleimides on the self-healing ability was investigated by the same authors [71]. They could show that maleimides with a long flexible chain displayed better healing efficiencies than those with rigid phenylene linkers or shorter chains. Moreover, Ikezaki et al. synthesized a series of poly(2,5-furandimethylene succinate-*co*-butylene succinate) copolymers by the polycondensation of BHS, 1,4-butandiol, and succinic acid followed by crosslinking with bismaleimide M_2 [72]. The thermal and mechanical properties of the networks were investigated by DSC and tensile test measurements. The self-healing ability of the materials was tested by cutting dumbbell-shaped specimens into two pieces and bringing them back into contact to allow reconnection of the broken bonds. Some of the specimens featured a healing ability even at room temperature, which could be increased by heating or treatment with a solvent. However, the healing efficiency was found to be dependent on the FS content and the furan/maleimide/furan ratio.

In conclusion, the DA furan and maleimide system is a prime example of self-healing polymers based on reversible covalent bonds. Because of the ready availability of the monomers, in particular bismaleimides, and the straightforward synthesis and functionalization of polymers with the binding units, such systems have been introduced into many different polymeric materials. Generally, all the systems require heating to initiate the healing process. Typically, temperatures around 80 °C are required for the healing of bulk materials, although scratch healing often needs higher temperatures (ca. 120 °C). The possible hydrolytic instability of furan (promoted by acids and high temperatures) is the sword of Damocles. Driven by these disadvantages and the high temperatures needed, other systems have been investigated.

2.1.2 Systems Based on Anthracene–Maleimide

Besides the use of furan derivatives as diene in the thermoreversible DA reaction, there is also the possibility to use anthracene derivatives. Syrett et al. developed a system based on the DA reaction between anthracene and maleimide [73]. For this purpose, a difunctional initiator (DA2) comprising a DA adduct was prepared by the treatment of *N*-(2-hydroxyethyl)maleimide with 9-anthracenemethanol followed by esterification of the resulting diol with 2-bromoisobutyryl bromide. With the help of DA2, a linear poly(methyl methacrylate) (PMMA) was synthesized. Furthermore, a similar DA adduct based on furan/maleimide was used to prepare a polymer for comparison. The polymer with the anthracene–maleimide linker displayed a higher thermal stability than that with the furan–maleimide linker. The DA bonds of the anthracene–maleimide polymer, which could be cleaved by heating to 200 °C (retro-DA reaction), were reconnected by means of the DA reaction by slowly cooling back to room temperature. However, the self-healing ability of the polymers has not been studied. In a further study of this system, mechanical force was utilized to trigger the retro-DA reaction in a mechanochemical approach [74].

Yoshie and coworkers reported a self-mending polymer network ($PEAA_2M_3$), which was prepared by the reaction of anthryl-telechelic poly(ethylene adipate) ($PEAA_2$) and a tris-maleimide (M_3) (see Scheme 7) [75]. In comparison to the network prepared from furfuryl-telechelic poly(ethylene adipate) ($PEAF_2$), the network with anthracene groups displayed a greater thermal stability as a result of higher crosslinking density. Tensile tests of the original uncut and mended samples demonstrated that the best recovery rates were about 55% in tensile strength and about 90% in elongation at break (mending at 100 °C for 7 days) (Fig. 11). The mending process is thought to be the result of reconnection of free anthracene and maleimide groups, generated when the sample was cut.

2.1.3 Systems Based on Cyclopentadiene

A further approach is based on the use of cyclopentadienes (CPDs), which could act as both the diene and the dienophile. Consequently, only one functional monomer is required. Upon dimerization of CPDs dicyclopentadiene (DCPD) is formed, which could re-form CPDs under thermal treatment via the retro-DA reaction [25]. Murphy et al. developed a single-component system consisting of DCPDs to create a thermally re-mendable polymer network [76]. The DCPD monomers (monomer 400 and monomer 401) were prepared by the reaction of DCPD dicarboxylic acid with oxalyl chloride and the subsequent bislactonization with a diol (Scheme 8). 1,4-Butandiol was used to form monomer 400, whereas monomer 401 was obtained using diethylene glycol. Upon heating to 120 °C, the retro-DA reaction occurred producing two reactive CPDs. Polymerization by the DA reaction of the two monomers was carried out by heating the monomer to 150 °C

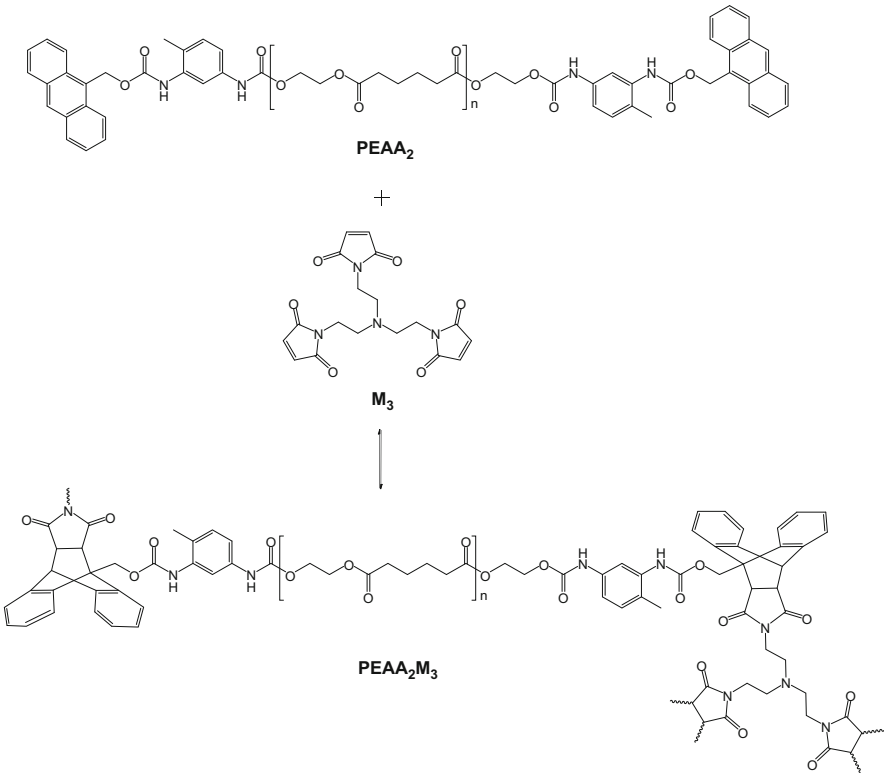

Scheme 7 Diels–Alder reaction between $PEAA_2$ and M_3 (see text for details). Adopted from [75]

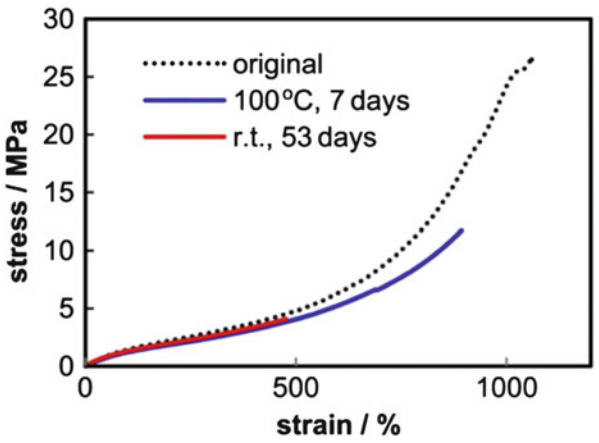

Fig. 11 Tensile test measurements of the original and mended $PEAA_2M_3$ (Reproduced from [75]. Copyright 2015 Elsevier Ltd.)

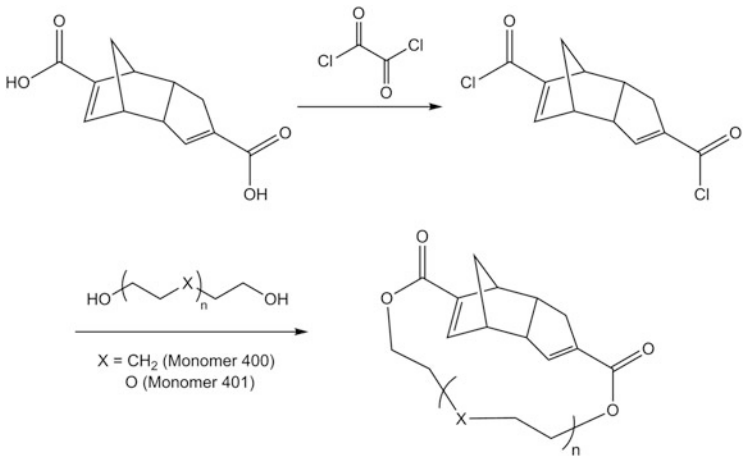

Scheme 8 Dicyclopentadiene-based monomers. Adopted from [76]

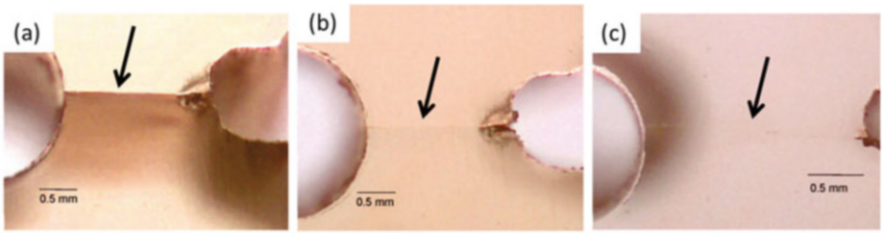

Fig. 12 Polymer 400 (**a**) after fracture, (**b**) after healing, and (**c**) after surface polishing (Reproduced from [76]. Copyright 2015 The American Chemical Society)

for about 10 h followed by slow cooling to room temperature. The resulting polymers were characterized by DSC, three-point flexural tests, compression tests, and DMA. Thereby, polymer 401 was found to be stronger, stiffer, and more brittle than polymer 400. These properties were also reflected in the fracture tests, which revealed an average recovered strength of 46% for polymer 400 and 23% for polymer 401. However, visual inspection of the self-healing process by optical images displayed complete crack recovery after surface polishing (Fig. 12). In further work, monomer 401 was cured on a graphite/epoxy laminate coupon to investigate the healing ability induced by electrical resistive heating [77]. Self-healing of microcracks could be obtained at relatively low temperatures of 70–100 °C within a few minutes.

2.1.4 Systems Based on Fulvene and Cyanoolefin/Dichloromaleic Acid

Reutenauer et al. developed a DA system on the basis of a fulvene (diene) and a cyanoolefin (dienophile) as polymers with self-healing properties [78]. For this purpose, a bis(fulvene) was prepared by the reaction of 4-cyclopenta-2,4-dienylidenpentanoic acid and poly(ethylene glycol) (PEG 400). Highly flexible DA dynamers were formed by mixing the bis(fulvene) with bis(tricyanoethylene-carboxylate). This dynamic system featured a very high reversibility, even at room temperature. Self-healing experiments were performed by cutting a thin film and bringing the two cut surfaces back into contact by gently pressing. After only 10 s the two pieces were recombined and could withstand mechanical elongation stress.

Furthermore, Wei et al. synthesized a dextran-based self-healing hydrogel via the DA reaction of a cytocompatible fulvene-modified dextran (DEX-FE) and dichloromaleic-acid-modified poly(ethylene glycol) (PEG-DICMA) (Scheme 9) [79]. To investigate the self-healing behavior, hydrogel disks were prepared and cut into two pieces using a razor blade. Subsequently, the two pieces were closely brought into contact and incubated at 37 °C for 12 h. After this procedure, the two pieces were reconnected to a single hydrogel disk. The self-healing process was studied using scanning electrochemical microscopy (SECM) and optical microscopy (Fig. 13). Thereby, it could be shown that after 7 h of incubation at 37 °C the scratches on the hydrogel film had nearly completely disappeared. Comparison of the scratch depth at different healing times demonstrated a healing efficiency of 99%.

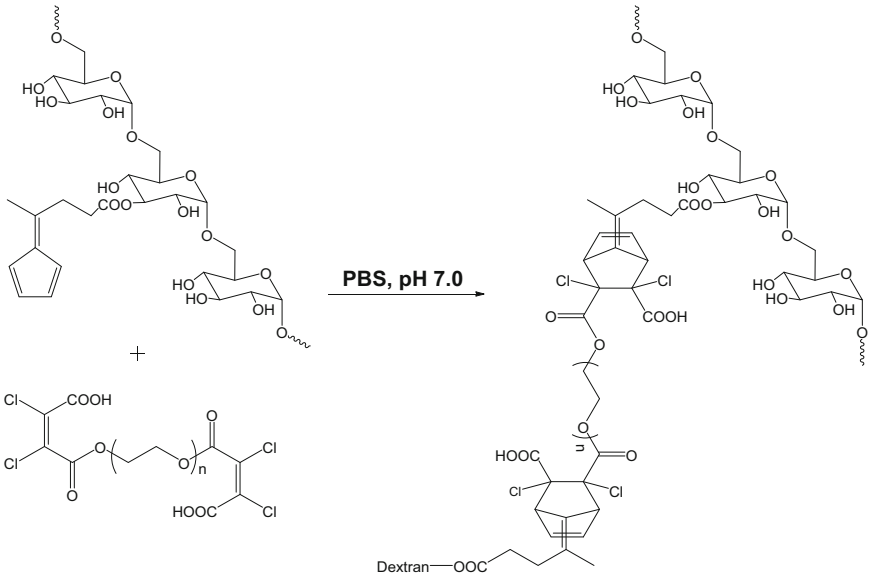

Scheme 9 Synthesis of dextran-based hydrogel crosslinked by the reversible Diels–Alder reaction. Adopted from [79]

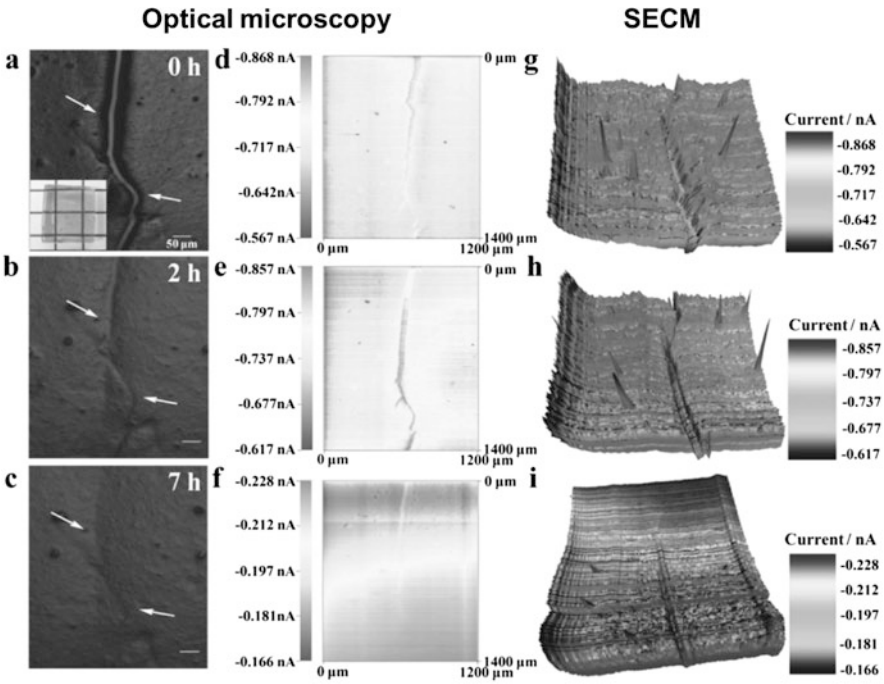

Fig. 13 Optical microscope images (*left* and *middle*) and corresponding SECM images (*right*) of the self-healing process: (**a**, **d**, **g**) Fractured surface before healing; (**b**, **e**, **h**) after 2 h, and (**c**, **f**, **i**) after 7 h of healing (Reproduced from [79]. Copyright 2015 Wiley-VCH Verlag GmbH & Co. KgaA)

In contrast to the classical DA systems, fulvene and electron-poor dienophiles feature a much higher reversibility, resulting in exchange even at room temperature. As a result, these systems could also be applied in temperature-sensitive systems (e.g., hydrogels), despite their more complicated synthesis route.

2.1.5 Systems Based on Acid-Activated Dithioesters–Cyclopentadiene (Hetero-Diels–Alder Reaction)

The hetero-DA reaction of electron-deficient dithioesters and cyclopentadiene was intensively used for the efficient functionalization of RAFT polymers [80–83].

Oehlenschlaeger et al. transferred this system to novel self-healing systems based on a new cyanodithioester (CDTE) compound and cyclopentadiene (Cp) [84]. For this purpose, the authors synthesized a tetrafunctionalized CDTE linker on the basis of pentaerythritol, which was protected by Cp moieties. By heating to 125 °C, this linker was deprotected and, subsequently, Cp_2-polymer P(*i*BoA-*n*BA) was added. Upon cooling to room temperature, the crosslinked network was formed by the hetero-DA reaction of the unprotected CDTE linker with the Cp end groups of the polymer. Repetitive tensile tests of a rod-shaped

sample revealed that the damage could be removed completely after treatment in a heat press for 10 min at 120 °C and 1 kN. These systems require still higher healing temperatures, although the retro-hetero-DA in solution was achieved at lower temperatures.

2.2 [2+2] Cycloaddition

The [2+2] cycloaddition is well known as a reversible photocrosslinking reaction in the field of self-healing polymers [85–87]. Thereby, two unsaturated compounds react with each other to form a cyclobutane ring or derivative. This reaction can only proceed photochemically and not thermally according to the Woodward–Hoffmann rules, allowing the utilization of light as the trigger for healing. The most used monomers in the field of self-healing are based on cinnamate [88–91] or coumarin [92, 93] derivatives. Irradiation with light of $\lambda \geq 280$ nm causes photodimerization, whereas light of $\lambda < 280$ nm induces photocleavage. The reversible photodimerization and photocleavage of these two monomers is depicted in Scheme 10.

The first photochemical crack healing in polymers was described by Chung et al. [88]. The authors synthesized a photocrosslinkable 1,1,1-tris (cinnamoyloxymethyl)ethane (TCE) monomer, which was copolymerized with two different methacrylates, 1,6-bis(2′-methacryloyloxyethoxy-carbonylamino)-2,4,4-trimethylhexane (UDMA) and tri(ethylene glycol) dimethacrylate (TEGDMA). Upon irradiation for 10 min with light of $\lambda > 280$ nm the copolymers were crosslinked, resulting in very hard and transparent specimens. After that, the material was damaged using a small hammer and irradiated for 10 min with light of $\lambda > 280$ nm, resulting in crack healing. This was proven by flexural strength measurements of the original, cracked, and healed samples. The healing ability could be further improved by increasing the TCE content and by heating the samples to 100 °C during photoirradiation. Furthermore, a sample synthesized without any TCE did not show any crack recovery.

Scheme 10
Photodimerization and photocleavage of (**a**) coumarin and (**b**) cinnamate

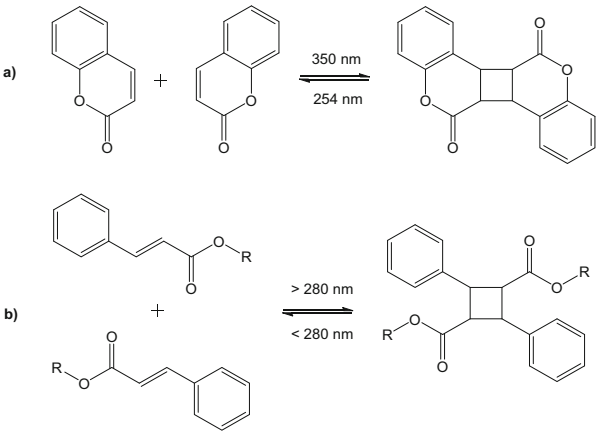

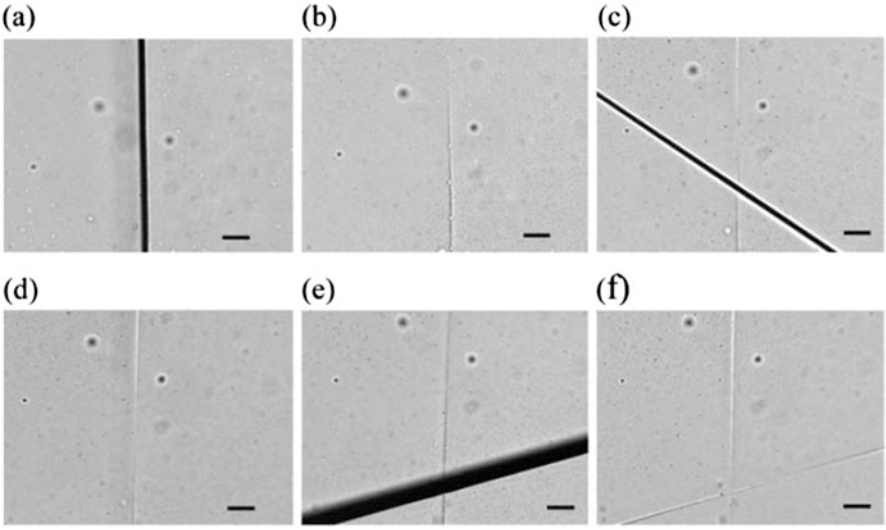

Fig. 14 Multiple healing of razor wounds via irradiation with 254 nm UV light for 1 min followed by irradiation of 350 nm for 90 min: (**a**) First cut, (**b**) after first repair, (**c**) second cut, (**d**) after second repair, (**e**) third cut, and (**f**) after third repair (Reproduced from [92]. Copyright 2015 The Royal Society of Chemistry)

Ling et al. used coumarin derivatives to achieve self-healing systems based on the reversible [2+2] cycloaddition [92, 93]. For this purpose, the authors synthesized polymer films based on polyurethane networks, which consisted of tri-HDI, PEG400, and the photoreversible unit 7-(hydroxyethoxy)-4-methylcoumarin (HEOMC). These films were crosslinked via photodimerization by UV irradiation at a wavelength of 350 nm. To investigate the self-healing ability, the films were cut using a razor blade. The damage could be healed by exposure to UV light (254 nm) for 1 min followed by UV light (350 nm) for 90 min (Fig. 14). This process could be repeated multiple times. Furthermore, the authors demonstrated that HEOMC is required for the healing process by performing control experiments without the coumarin moiety. Related to this, the same authors prepared another system using a dihydroxyl coumarin derivate, namely 5,7-bis(2-hydroxyethoxy)-4-methylcoumarin (DHEOMC).

The self-healing of thin hydrogel films based on the [2+2] cycloaddition was shown by Froimowicz et al. [91]. The authors synthesized nanoparticles by a miniemulsion copolymerization and functionalized these particles with cinnamate groups. Subsequently, films were prepared by drop-casting. The reversible photocrosslinking ability of the cinnamoyl groups using UV-Vis and infrared spectroscopy could be demonstrated. Irradiation with light of 280 nm caused dimerization, whereas light of 254 nm induced photocleavage. Furthermore, the self-healing ability of these films was investigated using SEM and step profilometry. Complete healing of the films was obtained by addition of water and its subsequent slow evaporation. However, the self-healing properties of this

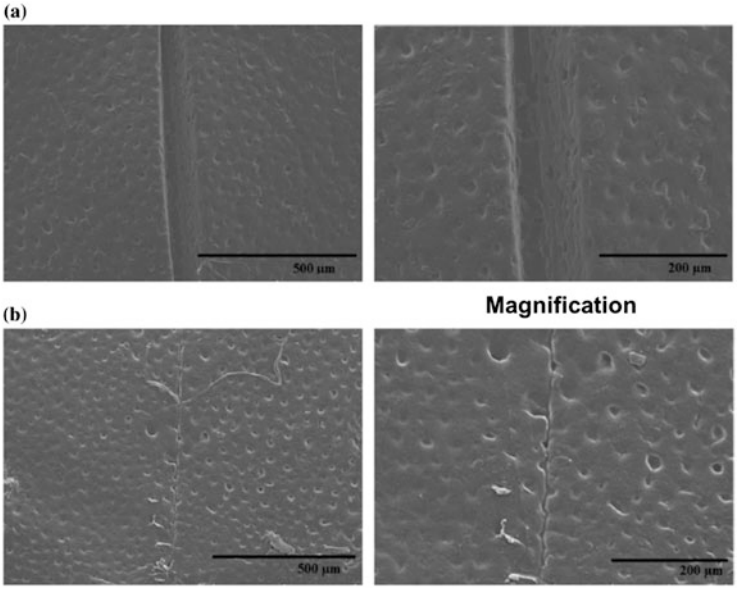

Fig. 15 SEM images of the healing process: (**a**) knife-cut surface, and (**b**) scar on the self-repaired film surface (Scalebar: *left*: 500 µm *right*: 200 µm) (Reproduced from [90]; Copyright 2015 Springer)

system are mainly related to swelling in the azeotropic solvent and not to its photochemistry.

Oya et al. synthesized a photo-induced mendable polymer network by the reaction of a cinnamoyl-telechelic poly(butylene adipate) ($PBAC_2$) and a tetra-cinnamoyl linker (C_4) [89]. The network was formed upon UV irradiation ($\lambda = 300$–400 nm) by the [2+2] cycloaddition of the cinnamoyl functionalities of the educts. The self-healing properties of the crosslinked films were analyzed by UV-Vis spectroscopy. The absorbance at 280 nm, which belongs to the cinnamoyl group, was monitored during the whole process (polymerization, damage, and re-dimerization). Upon polymerization, the characteristic peak at 280 nm significantly decreased. After that, the induced damage resulted in a slight increase in absorbance, whereas the re-dimerization process led to a decrease in the peak (to the original intensity before damage), indicating complete recovery of the chemical structure of the polymer.

One recent example in this field was explored by Hu et al. in 2015 [90]. The authors prepared UV-triggered self-healing polyphosphazenes by the introduction of ethyl-4-aminocinnamate into linear polyphosphazenes. Upon UV irradiation at 365 nm the [2+2] cycloadditon occurred, resulting in a crosslinked network. The self-healing ability of crosslinked polyphosphazene was examined by cutting the surface of the membranes with a blade. The resulting broken polyphosphazenes could be healed by irradiation with UV light at 365 nm for about 30 min. This process was studied in detail by UV-Vis spectroscopy and SEM. Figure 15 shows SEM images of the self-healing process.

Photochemically triggered [2+2] cycloadditions have been successfully used for the fabrication of self-healing polymers. Investigations have particularly focused on the scratch healing of these materials, which is related to the use of light as a trigger. The penetration depth is always limited, essentially complicating the healing of bulk materials.

2.3 [4+4] Cycloaddition

Photoreversible [4+4] cycloaddition [85, 86] offers another opportunity to introduce self-healing into polymeric materials. Similarly to the [2+2] cycloaddition, the [4+4] cycloaddition proceeds photochemically; however, in this case, two four-carbon fragments form an eight-membered ring. Representative functionalities that undergo this photodimerization are anthracene and its derivatives [94]. This photoreversible process is depicted in Scheme 11. In contrast to the [2+2] cycloaddition of coumarin and cinnamate, the [4+4] cycloaddition of anthracene is a more reliable phototriggered reaction because of its stability against hydrolysis and isomerization reactions. Furthermore, by the introduction of different substituents at position 9 and 10, radical polymerization can be prevented.

One reversible system based on [4+4] cycloaddition was reported by Chujo et al. in 1993 [95]. The authors used polyoxazolines with both anthracene and disulfide groups to prepare a hydrogel that was redox-sensitive and photosensitive. The hydrogel was formed by dimerization of the anthracene groups via irradiation with a 450-W high-pressure Hg lamp ($\lambda > 300$ nm). Incorporated disulfide bridges allowed the system to become soluble again by reductive cleavage with sodium borohydride. Thus, Chujo et al. demonstrated a multiresponsive hydrogel that could be applied as a functional polymeric material.

Connal et al. prepared an anthracene-functionalized poly(methyl acrylate) core crosslinked star polymer with a low glass transition temperature [96]. This system exhibited a highly photo-induced reversibility as a result of dimerization of the anthracene groups. Self-healing studies were not performed, but these films could be potential candidates as self-healing polymers because of their mechanical and thermal properties as well as the photoreversibility.

Another interesting system was described by Xu et al. in 2013 [97]. The authors prepared double-dynamic polymers by the combination of reversible covalent

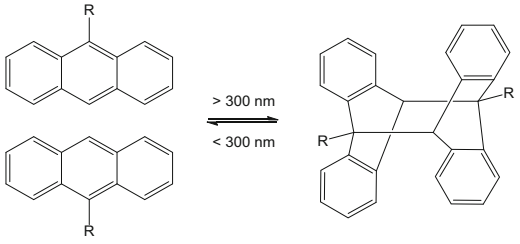

Scheme 11 Reversible photodimerization of anthracene via the [4+4] cycloaddition

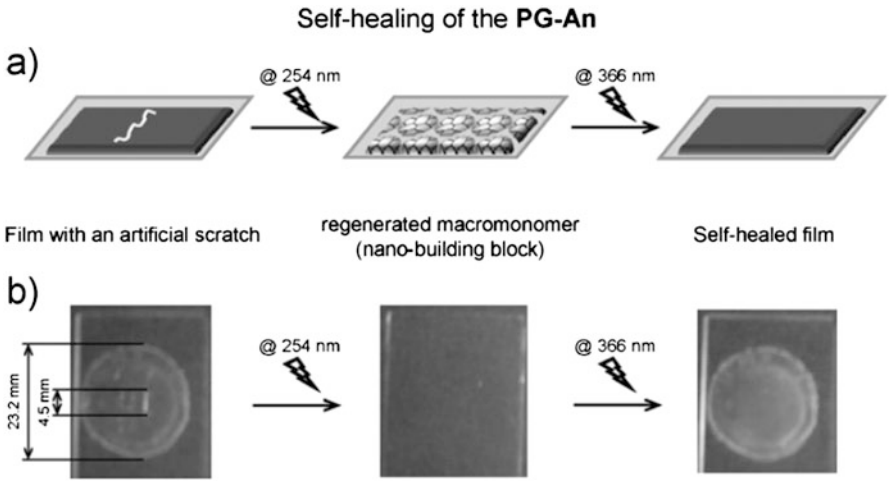

Fig. 16 (**a**) Self-healing procedure for anthracene-containing hyperbranched polyglyceol (*PG-An*). (**b**) Self-healing of a damaged sample for a system based on the reversible [4+4] cycloaddition (Reproduced from [98]. Copyright 2015 Wiley-VCH Verlag GmbH & Co. KGaA)

anthracene dimerization with reversible noncovalent pillar[5]arene/imidazole host–guest interactions. The authors mixed anthracene-derivatized pillararene with bisimidazole alkane (2:1 molar ratio). The resulting double-dynamic polymers could be depolymerized by heating through dissociation of either the host–guest complexes alone or the combination of both (i.e., cleavage of anthracene dimers and host–guest interaction). The polymers could be reformed by irradiation or cooling. Therefore, this system seems to be quite promising for the construction of smart materials.

Froimowicz et al. demonstrated the first self-healing polymer on the basis of photoreversible [4+4] cycloaddition by the utilization of an anthracene-containing hyperbranched polyglycerol (PG-An) [98]. After scratching a crosslinked film, the material was irradiated for 15 min with 254 nm light (de-crosslinking condition) to regenerate the macromonomer. Subsequently, the material was kept overnight at room temperature and in the darkness. The PG-An could reorganize itself and refill the damaged area as a result of its low T_g of −46 °C. Finally, the film was irradiated with 366 nm light (crosslinking condition) to regenerate the self-healing network. The self-healing process is depicted in Fig. 16.

In conclusion, photochemically triggered [4+4] cycloaddition was used in a similar manner to the [2+2] cycloadditions, mainly for scratch healing. The applied systems still require the application of light, with short wavelengths limiting the wider applicability of this approach.

3 Reversible Acylhydrazones

Another important functionality for the design of self-healing polymers are acylhydrazones. Acylhydrazones are formed by the condensation reaction of an aldehyde with a hydrazide (Scheme 12). This reaction displays reversibility under mild conditions, with acid catalysis regenerating the starting materials. On the one hand, the acylhydrazone functionality provides dynamic character through the reversibility of the imino bond and, on the other hand, additional hydrogen bonding through the amide group (Fig. 17). These two specific structural features are of great importance for the design of new self-healing polymers. It is noteworthy that the hydrogen bonds of the acylhydrazones do not show the pronounced effects found in supramolecular self-healing polymers. Furthermore, acylhydrazones are able to reversibly exchange their components by adding either an aldehyde or a hydrazide (Scheme 12). Therefore, the physical properties of the polymers can be influenced [99–101].

Deng et al. reported the first crosslinked self-healing polymer gel based on reversible acylhydrazones [23, 102]. The authors synthesized a network with acylhydrazone crosslinks by the condensation of a poly(ethylene oxide) (PEO) containing two acylhydrazines as end groups with the aldehyde groups of tris [(4-formylphenoxy)methyl]ethane (Scheme 13). A strong polymer gel with covalent crosslinked networks could be obtained by swelling in DMF in the presence of

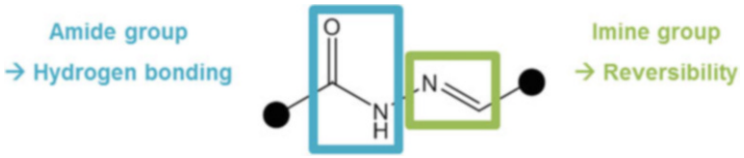

Fig. 17 Representation of the acylhydrazone functionality. Adopted from [99]

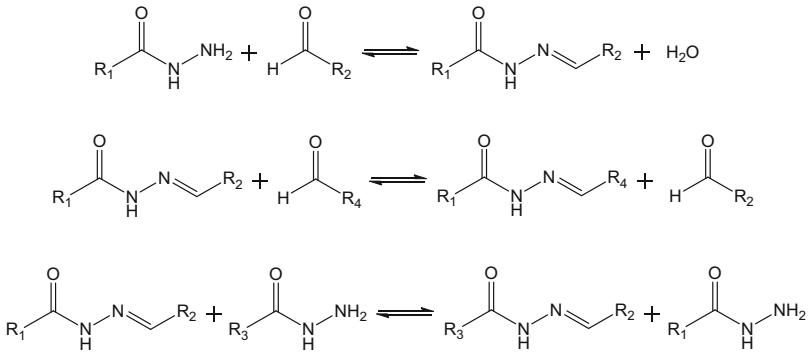

Scheme 12 Synthesis of acylhydrazones and the reversible exchange reactions. Adopted from [99]

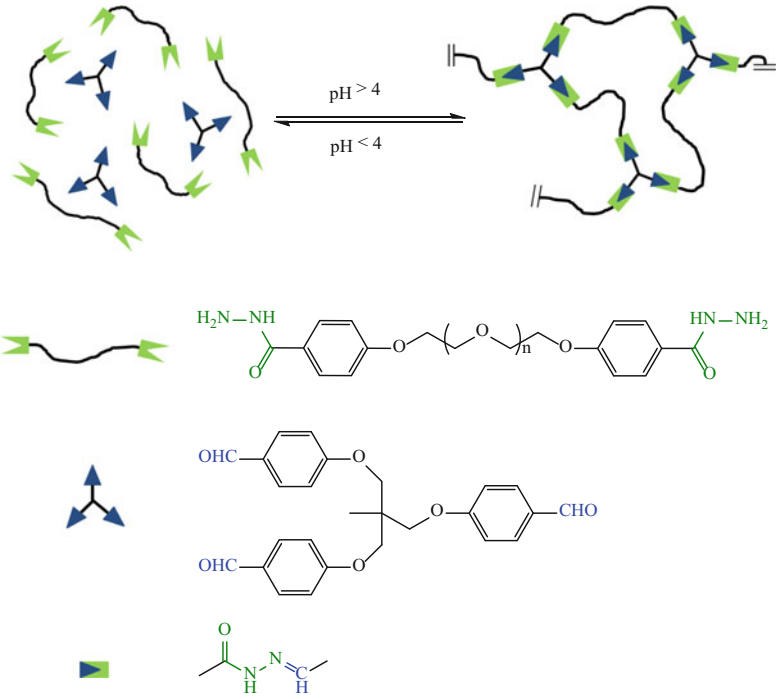

Scheme 13 Synthesis of covalent crosslinked polymer gels based on reversible acylhydrazone bonds. Adopted from [23]

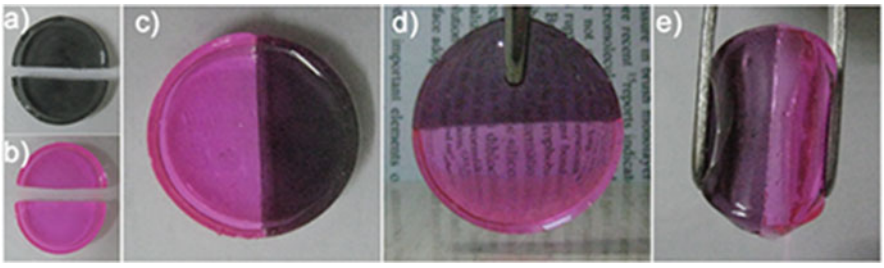

Fig. 18 Self-healing process and properties of acylhydrazone gel: (**a**) cracked gel containing carbon black, (**b**) cracked gel containing rhodamine B, (**c**) bicolor gel merged by simply putting half **a** and half **b** together for 7 h, (**d**) merged bicolor gel lifted by tweezers, and (**e**) merged bicolor gel squeezed by tweezers (Reproduced from [23]. Copyright 2015 The American Chemical Society)

some small pieces of acid catalyst, which was confirmed by dynamic rheological measurements. Besides sol–gel phase transition ability in response to acidity changes, the gel revealed interesting self-healing properties (Fig. 18). Two pieces of cracked gel plate were brought into contact for 7 h. After that time, the autonomous self-healing process was complete and could also be repeated.

In 2011, the same authors synthesized double-dynamic polymer hydrogels by the introduction of acylhydrazone and disulfide bonds into the same system [24]. For this purpose, they utilized aldehyde-terminated three-armed PEO and dithiodipropionic acid dihydrazide to obtain both functionalities. This combination allowed self-healing through a wide range of pH conditions (acidic, neutral, and basic). Thus, in an acidic environment the hydrogel undergoes acylhydrazone exchange, whereas at higher pH values the disulfide exchange takes place. At neutral pH, both dynamic bonds are kinetically locked. Nevertheless, self-healing is possible by adding aniline as catalyst, which accelerates the acylhydrazone exchange. For comparison, they prepared a hydrogel with only acylhydrazone bonds by the use of hexanedioic acid dihydrazide. This gel could only self-heal at acidic and neutral conditions (with aniline), but not under basic conditions.

Zhang et al. also used this combination of acylhydrazones and disulfides for the design of polymer gels with self-healing properties [103]. Their system was prepared by the crosslinking of benzhydrazide-containing poly(triazole) with a novel disulfide-containing dialdehyde. Self-healing experiments were carried out in acidic and neutral (with and without catalytic aniline) conditions. The best healing efficiency of 85% was observed for the aniline-catalyzed gel, because in this case both acylhydrazone and disulfide exchange reactions are responsible for the self-healing process.

A further double-dynamic self-healing polymer was investigated by Lehn and coworkers [104]. The dynamic polymer with bisacylhydrazone moieties was obtained by polycondensation of a siloxane-based dialdehyde and carbohydrazide. A soft stretchy film was prepared, providing both reversibility and lateral hydrogen bonding interactions through the acylhydrazone units. Self-healing experiments were performed by cutting the film with scissors, bringing the two cut surfaces back into contact for a few minutes, followed by gentle pressing of the overlapped surfaces. After a few hours the film was completely healed without additional pressure or load. Stress–strain curves of the native and the self-healed polymer revealed 90% recovery of the original strain.

Apostolides et al. synthesized a self-healing gel by the reaction of pentaerythritol tetra(benzohydrazide) and 1,10-decanediol dibenzaldehyde [105]. In addition to gel reversibility and exchange reaction studies, the self-healing of such networks was also investigated. A disk of a DMF-swollen gel was cut into two pieces, which were then brought back into contact. Five drops of acetic acid were added to accelerate the acylhydrazone bond exchange process. After 24 h the two cut pieces were reconnected and this process could be repeated three times.

A new biocompatible polysaccharide-based self-healing hydrogel was reported by Wei et al. [106]. The reversible imine and acylhydrazone bonds were introduced into the hydrogel networks by the reaction of *N*-carboxyethyl chitosan and adipic acid dihydrazide with oxidized sodium alignate. The self-healing ability was investigated by rheological recovery tests, macroscopic self-healing experiments, and beam-shaped strain compression measurements. The healing efficiency was found to be 95% under physiological conditions without any external stimulus.

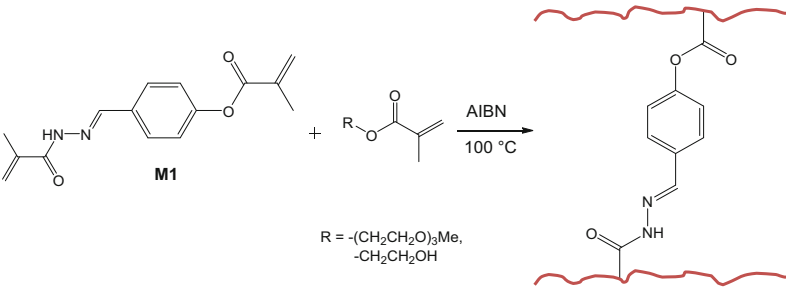

Scheme 14 Synthesis of acylhydrazone-crosslinked polymers. Adopted from [107]

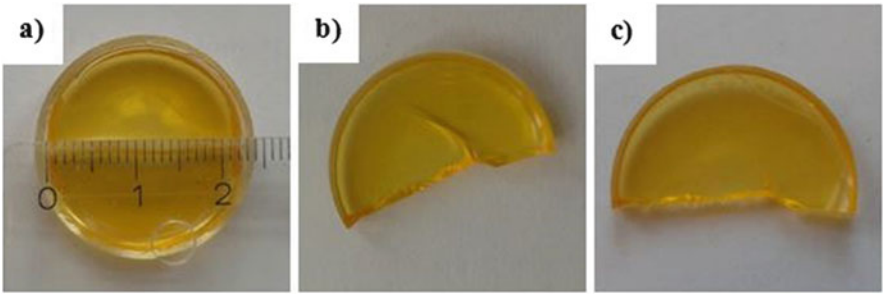

Fig. 19 Self-healing of an acylhydrazone-crosslinked polymer: (**a**) Polymer film, (**b**) scratch before thermal treatment, and (**c**) scratch after 64 h at 100 °C (Reproduced from [107]. Copyright 2015 Wiley-VCH Verlag GmbH & Co. KGaA)

Kuhl et al. reported the first covalently crosslinked polymer based on reversible acylhydrazones, which was able to self-heal in the solid state [107]. The authors synthesized an acylhydrazone crosslinker (M1) by the condensation of 4-formylphenyl methacrylate with methacryloyl hydrazide. Then, polymer films were prepared by the copolymerization of 10 mol% of M1 with a monomer mixture of triethylene glycol methylether methacrylate (TEGMEMA) and 2-hydroxyethyl methacrylate (HEMA) in bulk by a free radical polymerization process (Scheme 14). The self-healing ability was studied by scratch test experiments and profilometry measurements. In this manner, Kuhl et al. could show that deep scratches of up to 1 cm in length could be healed by heating the samples for 64 h at 100 °C (see Fig. 19).

The rich chemistry of acylhydrazone, (i.e., water (acid)-induced cleavage to aldehyde and hydrazide, and exchange reactions) has mainly been investigated in solution and gel-like materials, providing more mobility and the presence of a catalyst (acid) for the reversible reactions. As a consequence, healing at low temperatures could be achieved. Transferring this reaction to bulk materials (reducing the "degrees of freedom") required higher temperatures to enable exchange between the different reversible crosslinkers.

4 Disulfides

A further opportunity to obtain self-healing based on reversible covalent bonds is the introduction of dynamic disulfide groups into polymers [108]. Disulfide groups are a versatile tool for the design of self-healing polymers because they can undergo different reversible reactions such as disulfide exchange [21], thiol–disulfide exchange [109], reduction–oxidation [110], and radical-mediated disulfide fragmentation [111] to obtain self-healing properties (Scheme 15). The disulfide moiety can be incorporated into the main chain [112] of polymers or can act as a crosslinker in the side chain [113]. But, the main approach for incorporation of disulfides into self-healing polymers is the preparation of networks out of multifunctional thiols [22].

4.1 Disulfide Exchange Reactions

Otsuka et al. reported a disulfide-containing polyester (DSPES) that was able to undergo a disulfide metathesis reaction upon photoirradiation [112]. This dynamic

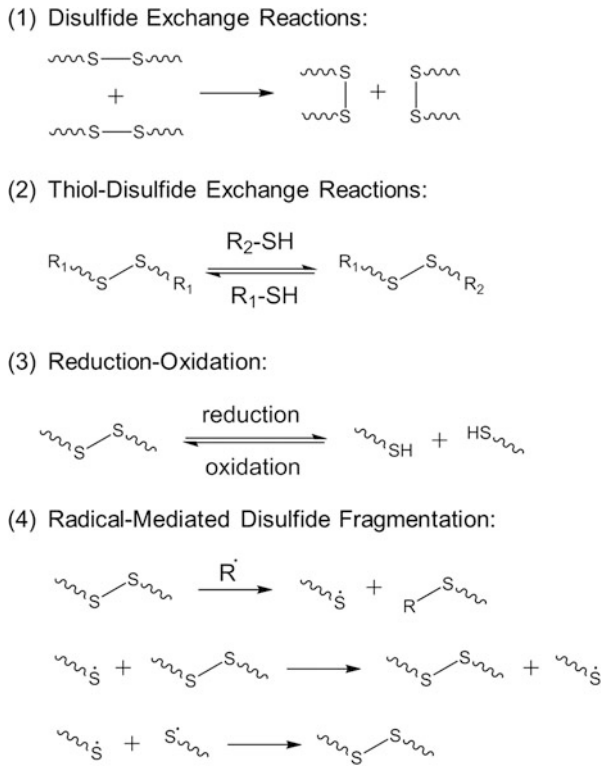

Scheme 15 Possible healing mechanisms for disulfide-crosslinked polymers

DSPES was prepared by polycondensation of bis(2-hydroxyethyl) disulfide and adipoyl chloride. Size-exclusion chromatography (SEC) studies revealed that the molar mass distribution broadened after photoirradiation for 60 min but that there was no significant change in the peak maxima compared with the initial profile. This observation was not observed when the reaction was performed in the dark and could, therefore, be attributed to the exchange reaction of the disulfide bond units between the main chains of DSPES.

Canadell et al. used disulfide moieties to introduce a self-healing ability into a covalently crosslinked rubber [21]. For this purpose, epoxy resins (EPS25 and DER732) were crosslinked with pentaerythritol tetrakis(3-mercaptopropionate). The thermal and mechanical properties of this crosslinked rubber were investigated by DMA, creep measurements, and tensile testing experiments. Moreover, the self-healing ability was studied by optical microscopy. The material was cut and after 1 h at 60 °C the sample was almost completely healed. This process could be repeated efficiently multiple times, with full restoration of the mechanical properties. The proposed healing mechanism is based on the exchange of disulfide units, leading to renewal of crosslinks across the damaged surfaces.

Lafont and coworkers studied the influence of crosslinker and chain rigidity on the healing ability of thermoset rubber materials containing disulfide bonds [22]. For this purpose, several polysulfide-containing materials were prepared by mixing different amounts of resins (EPS25, EPS70) and crosslinkers [pentaerythritol tetrakis(3-mercaptopropionate) (4-SH) and Capcure 3-800 (3-SH)] followed by a curing step for 2 h at 65 °C (Fig. 20). The cohesive and adhesive self-healing was investigated by cohesion recovery tests and lap-shear experiments. The results showed a dependency on the network crosslink density as well as on the chain rigidity. However, all samples could be healed within 20–300 min at 65 °C, and multiple healing was possible. Figure 21a depicts the self-healing process, which was monitored by optical microscopy, and Fig. 21b illustrates the cohesion recovery. Disulfide exchange reactions seem to be responsible for the self-healing ability, as described for the systems of Canadell et al. [21].

Lei et al. reported a crosslinked polymer that was self-healable at room temperature as a result of the dynamic exchange of disulfide bonds [114]. The authors synthesized a disulfide-crosslinked polymer by mixing polysulfide diglycidyl ether (EPS25) and diethylenetriamine as hardener. Tri-*n*-butylphosphine was used to catalyze the air-insensitive metathesis reaction under alkaline conditions. The self-healing ability was studied using tensile tests, whereby a maximum healing of 91% was observed after 24 h at room temperature. The healing process could also be repeated multiple times. At higher temperatures of about 60 °C a similar healing effect could be obtained even after 2 h. Moreover, this polymer was able to reform its shape through rearrangement of the crosslinked network upon compression at room temperature.

Another system of self-healing polymers based on disulfide exchange reactions was studied by Odriozola and coworkers [115, 116]. For this purpose, the authors prepared two different poly(urea-urethanes) and mixed them in a certain ratio to obtain a material with good elastomeric properties. This material, which contained

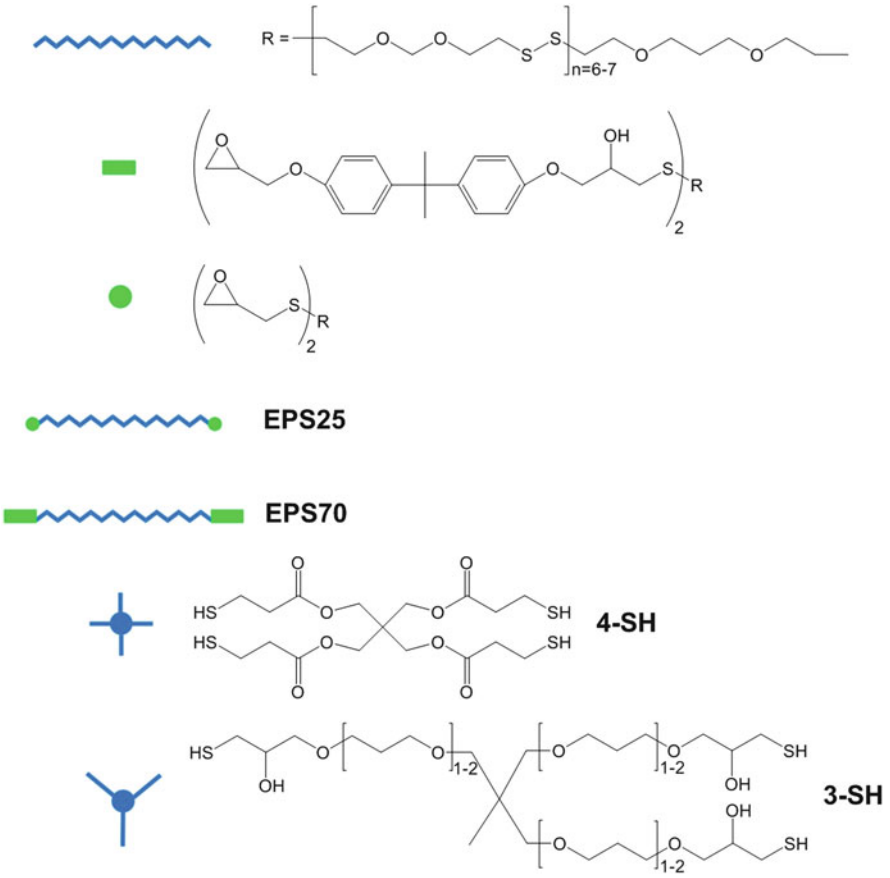

Fig. 20 Monomer structure of epoxy resins EPS25 and EPS70 and crosslinkers 4-SH and 3-SH; see text for details. Adopted from [22]

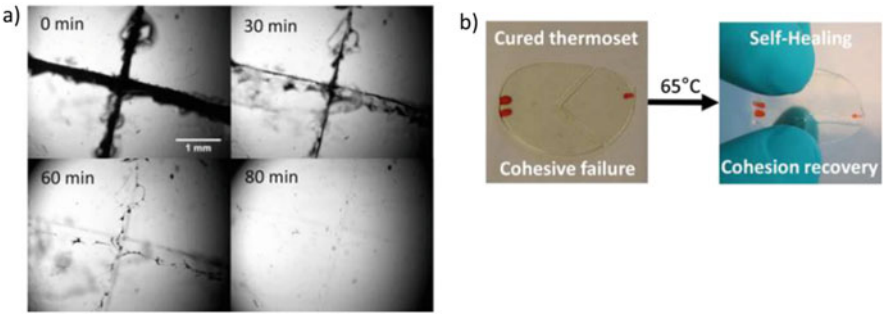

Fig. 21 (**a**) Self-healing of a polymer, based on disulfide exchange reactions monitored by an optical microscope. (**b**) Example of macroscopic cohesion recovery (Reproduced from [22]. Copyright 2015 The American Chemical Society)

residual isocyanate end groups, was then crosslinked by the addition of bis (4-aminophenyl) disulfide. Self-healing experiments demonstrated that two cut pieces of these poly(urea-urethane) elastomers with aromatic disulfide crosslinks are able to self-mend at room temperature without the use of any external stimulus or catalyst. Tensile strength measurements demonstrated that after 24 h of contact 97% of the initial mechanical properties could be recovered. As described for the system of Lei et al. [114], these poly(urea-urethane) elastomers could be reshaped by putting them in a hot press at 150 °C and 30 bar for 20 min; the mechanical properties after this procedure remained unchanged.

4.2 Thiol–Disulfide Exchange Reactions

Pepels et al. studied a number of thermoset systems based on disulfide bonds that exhibit self-healing properties as a result of disulfide–thiol exchange reactions [109]. The best system was prepared by mixing polysulfide diglycidyl ether T25 with pentaerythritol tetrakis(2-mercaptopropionate) (PTM2); dimethylaminopropylamine (DMAPA) was added as a base. Stress relaxation tests revealed a fast and almost complete stress relaxation as a result of the ability to rearrange caused by thiol–disulfide exchange reactions. Self-healing experiments were performed by cutting a dumbbell-shaped tensile bar into two pieces and subsequently bringing the two cut surfaces back into contact. After 24 h, almost complete healing could be observed. However, when the samples were stored for a longer time under atmospheric conditions, the stress relaxation and healing efficiency decreased, probably because the oxidative coupling reactions of the thiol groups limits the long-term stability of these materials.

Another system related to disulfide-crosslinked redox-responsive stars with the potential to act as self-healing materials was described by Yoon et al. [113]. The authors prepared a star polymer based on poly(ethylene glycol diacrylate)-[poly(*n*-butyl acrylate)], which was crosslinked with bis(2-methacryloyloxyethyl) disulfide (DSDMA). Upon addition of a reducing agent, the disulfide bonds could be cleaved to form thiol-functionalized soluble stars. Reoxidation resulted in reformation of the S–S bonds to form an insoluble network. Self-healing studies of the re-crosslinked film revealed good self-healing ability without any external trigger, probably as a result of thiol–disulfide exchange reactions. AFM measurements illustrated that the extent of healing was dependent on the initial film thickness and the width of the cut.

AbdolahZadeh et al. reported the synthesis of a self-healable dual organic–inorganic crosslinked sol–gel-based polymer containing nonreversible crosslinks and reversible tetrasulfide groups [117]. For this purpose, the authors used a pre-mixture of organically modified silicone alkoxides (OMSAs) with bis[3-(triethoxysilyl)propyl]tetrasulfide (BS) and (3-aminopropyl) trimethoxysilane. These OMSAs were added to the epoxy resin Epikote828. Finally, the organic crosslinker Ancamine2500 and the tetrathiol were added, resulting in an organic–inorganic hybrid network (Fig. 22). The thermal and mechanical properties of the network were studied by different

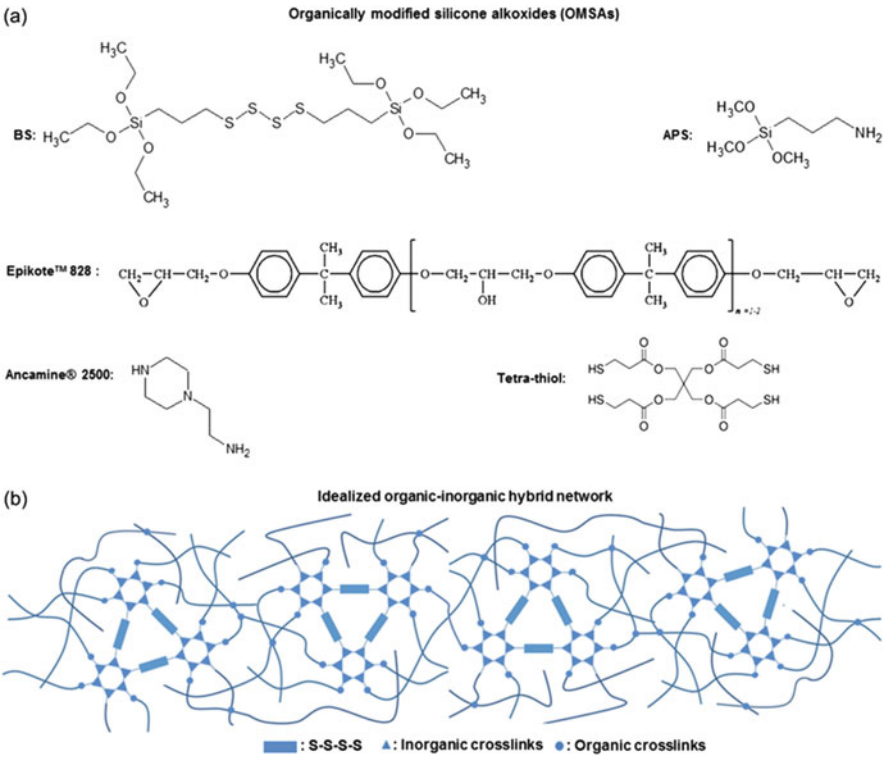

Fig. 22 (**a**) Chemical structure of components used for synthesis of a self-healable organic–inorganic hybrid polymer. (**b**) Idealized structure of hybrid sol–gel polymer (Reproduced from [117]. Copyright 2015 Wiley Periodicals)

methods (e.g., TGA, DSC, and dynamic mechanical thermal analysis). Gap closure kinetic curves revealed the possibility of multiple healing as a result of the reversible nature of the S–S bonds (Fig. 23). The healing process was found to be strongly influenced by temperature, tetrasulfide content, and crosslinking density.

4.3 Reduction–Oxidation

Bapat et al. reported the synthesis of disulfide core-crosslinked stars and miktoarm stars that could undergo dynamic covalent disassembly and reassembly upon exposure to reducing and oxidizing conditions [110]. The core-crosslinked stars could be obtained by the reaction of well-defined block copolymers, containing a reactive poly(styrene-*alt*-maleic anhydride) segment, with cystamine dihydrochloride as a diamine crosslinker. In the presence of a suitable reducing

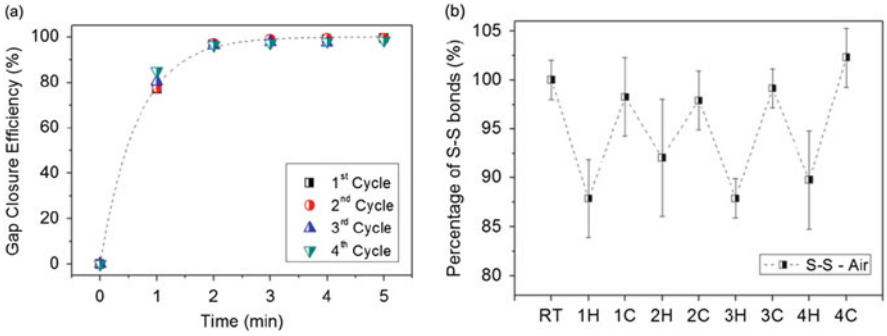

Fig. 23 Raman experiments: (**a**) Gap closure kinetics for multiple healing cycles and (**b**) percentage of S–S bonds in the sample during four consecutive cycles of heating (*H*) and cooling (*C*) (Reproduced from [117]. Copyright 2015 Wiley Periodicals)

agent (e.g., tributylphosphine) the disulfides linkages were cleaved, resulting in star dissociation into linear arms with pendant thiol groups. The reassembly or self-healing of the stars could be obtained by oxidation of these thiols in the presence of air and at room temperature. This process of star formation/dissociation could be repeated over at least four cycles. However, addition of the respective reducing agent or oxidizing agent (alternatively by air) is required, hindering a more autonomous approach.

4.4 Radical-Mediated Disulfide Fragmentation

Fairbanks et al. made use of a disulfide-crosslinked hydrogel that could undergo a radical-mediated disulfide fragmentation reaction and disulfide exchange reactions to obtain self-healing properties [111]. For this purpose, disulfide-crosslinked hydrogel networks were synthesized by the oxidation of thiol-functionalized four-armed PEG macromolecules, followed by swelling in a photoinitiator solution. Self-healing experiments were performed by pressing two swollen gels together with a force of 50 g/cm^2. Upon exposure to 365 nm light, radicals were formed by scission of the photoinitiator resulting in the cleavage of the disulfides. This process led to formation of thiyl radicals, which could subsequently undergo fragmentation and exchange with other disulfides. The two gels were brought into contact and annealed to form a single gel of combined dimensions.

Another important system, based on covalently crosslinked polymers that were able to self-heal by reshuffling thiuram disulfide (TDS) moieties, was reported by Amamoto et al. in 2012 [20]. The authors synthesized TDS-containing crosslinked polyurethanes with low glass transition temperatures to obtain self-healing at ambient temperatures in a bulk material. For this purpose, they performed a simple polyaddition between a TDS diol, the reactive reshuffling unit, a tetra(ethylene glycol) (TEG) chain extender, TEA crosslinker, and HDI (Scheme 16). To test the

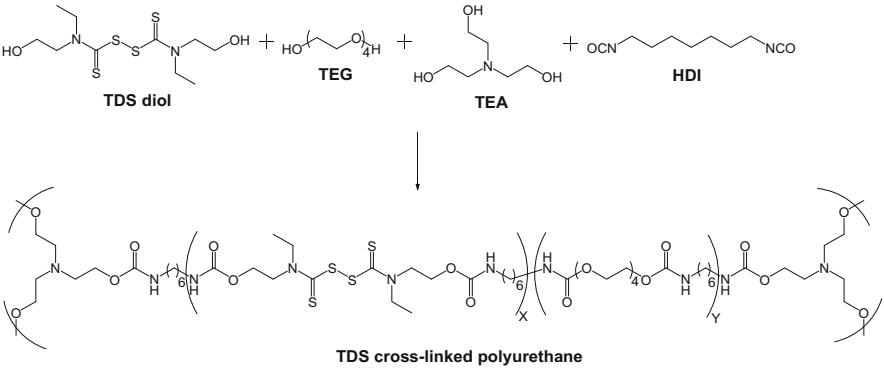

Scheme 16 Preparation of thiuram disulfide (TDS)-crosslinked polyurethane. Adopted from [20]

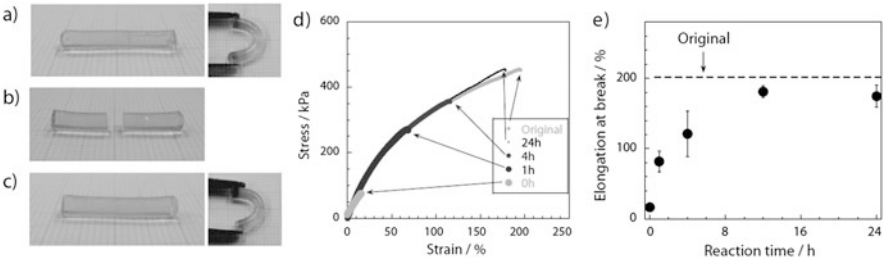

Fig. 24 Self-healing of thiuram disulfide (TDS)-crosslinked polyurethane: (**a**) Sample before damage, (**b**) after cutting, (**c**) after self-healing for 24 h, (**d**) stress–strain curve, and (**e**) elongation value at break (Reproduced from [20]. Copyright 2015 Wiley-VCH Verlag GmbH& Co. KGaA)

self-healing ability, a cylindrical sample was cut with a blade and the two pieces were brought into close contact for 1 min (Fig. 24a, b). After that, the sample was exposed to visible light (commercial tabletop lamp) under air and at room temperature, resulting in a completely self-healed sample after 24 h (Fig. 24c). Regeneration via the reshuffling reactions was supported by tensile tests, DMA, and creep measurements (Fig. 24d, e).

In addition, there are also some systems reported that utilize a combination of disulfides and acylhydrazones [24, 103].

In conclusion, self-healing polymeric materials based on disulfides represent a straightforward approach because of the good availability of the required monomers and crosslinkers. Self-healing was achieved under different conditions (triggered by heat or light). However, the potential sensitivity of most of these materials to oxygen is a major drawback. Thiols present in the material oxidize over time, which results in loss of the self-healing capability of these materials.

5 Radicals

Among the large variety of self-healing systems based on dynamic covalent bonds, the reversible nature of C–ON bonds in alkoxyamine units seems to be promising for the design of new self-healing materials. Before becoming attractive in the field of self-healing, the reversible C–ON bond in alkoxyamines was extensively utilized in nitroxide-mediated radical polymerization (NMP) [118]. Under the polymerization conditions in the NMP process, the C–ON bonds in alkoxyamine moieties are homolytically unstable. Thus, they cleave to produce transient carbon-centered radicals and persistent nitroxide radicals, which can immediately recombine or perform crossover reactions. By virtue of these special properties, alkoxyamines units are also used as reversible crosslinkers in polymeric networks.

5.1 Systems Based on Alkoxyamine Units as Crosslinks

Takahara and coworkers described the dynamic formation of graft polymers via radical crossover reaction of alkoxyamines [119]. For this purpose, a methacrylic ester-containing 2,2,6,6-tetramethylpiperidinyl-1-oxy (TEMPO)-based alkoxyamine was prepared and copolymerized with MMA using the ATRP technique to synthesize a polymer with alkoxyamine units in the side chain. Furthermore, a TEMPO-based alkoxyamine-terminated polystyrene was synthesized via NMP. Mixing these two alkoxyamine-containing polymers and heating to 100 °C under an argon atmosphere produced graft polymers through the radical crossover reaction between the alkoxyamine units in the side chain and the chain end. Moreover, this reaction was found to be reversible by heating the graft polymer to 100 °C with an excess of alkoxyamine derivative. Two years later, the same authors expanded their work by the preparation of a novel reversible crosslinked system with radically exchangeable covalent bonds [120]. This time, two different copolymers with alkoxyamine units in the side chain were used as starting materials. In addition, Otsuka et al. synthesized various poly(alkoxyamine)s by the polycondensation of an alkoxyamine-based diol and adipoyl chloride [121]. As described above, heating to 100 °C caused the radical crossover reaction of the alkoxyamine units between the main chains. The addition of an excess of nitroxide stable free radical resulted in scission of the main chain through a chain transfer reaction. However, the self-healing ability of all these systems has not yet been studied.

The first self-healing system related to the reversible C–ON bond of alkoxyamine units was described by Yuan et al. [122]. For this purpose, a TEMPO-based diol was reacted with methacryloyl chloride resulting in a dimethacrylic ester, which was subsequently copolymerized with polystyrene in bulk to produce a crosslinked polystyrene with reversible alkoxyamine functionalities. Temperature-dependent electron spin resonance (ESR) spectroscopy

indicated homolytic cleavage of the alkoxyamine unit at about 125 °C, which is the glass transition temperature of the polymer. Therefore, a healing temperature of 130 °C was chosen for the investigation of the self-healing behavior. To evaluate the healing efficiency, double cleavage drilled compression (DCDC) tests were performed. Thereby, a healing efficiency of 76% could be obtained after 2.5 h at 130 °C. However, the healing efficiency slightly decreased with healing/re-fracture cycles. Moreover, the amount of crosslinker and the healing temperature were found to influence the healing efficiency. Zhang and coworkers further analyzed the reversibility of solid state radical reactions in thermally re-mendable polymers with C–ON bonds [123]. For this purpose, the authors synthesized two similar copolymers on the basis of poly(4-vinylbenzyl chloride) (PCMS) with two different alkoxyamine units [2,2,6,6-tetramethylpiperidinyl-1-oxy (TEMPO) and 1-(1-phenylethoxy)-2,2,6,6-tetramethylpiperidin (TEMPO-EOPh)] as pendent groups (Fig. 25). After that, PCMS-TEMPO/PCMS-TEMPO-EOPh blends were prepared to check the self-healing ability through radical crossover reactions. First, a solution of PCMS-TEMPO/PCMS-TEMPO-EOPh was heated to 125 °C for 20 min, resulting in the formation of a gel and, thus, proving the occurrence of cross-reactions. This could also be confirmed by DSC measurements. For investigation of the self-healing behavior, a cross-shaped razor cut was induced on a film-specimen of the blend. Heating for 30 min at 125 °C healed the damage and multiple healing was possible (Fig. 26).

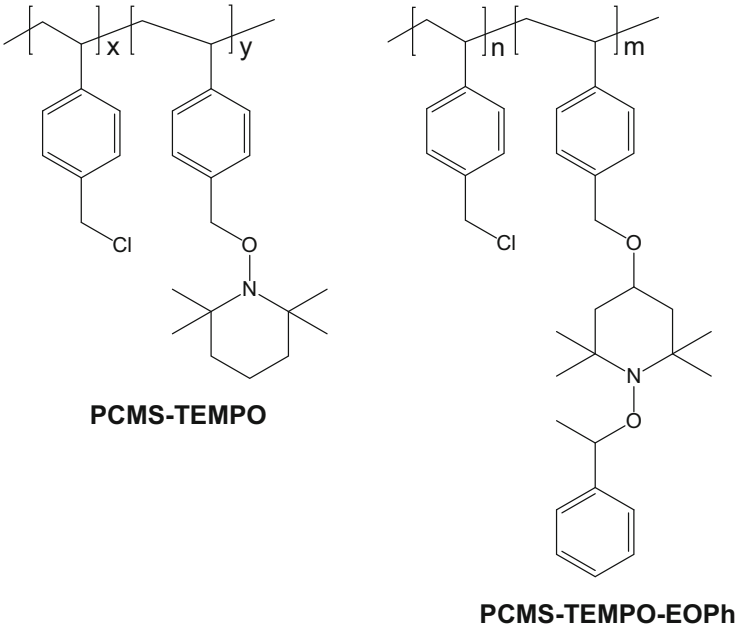

Fig. 25 Poly(4-vinylbenzyl chloride) (*PCMS*)-based polymers with two different alkoxyamine moieties as side groups. Adopted from [123]

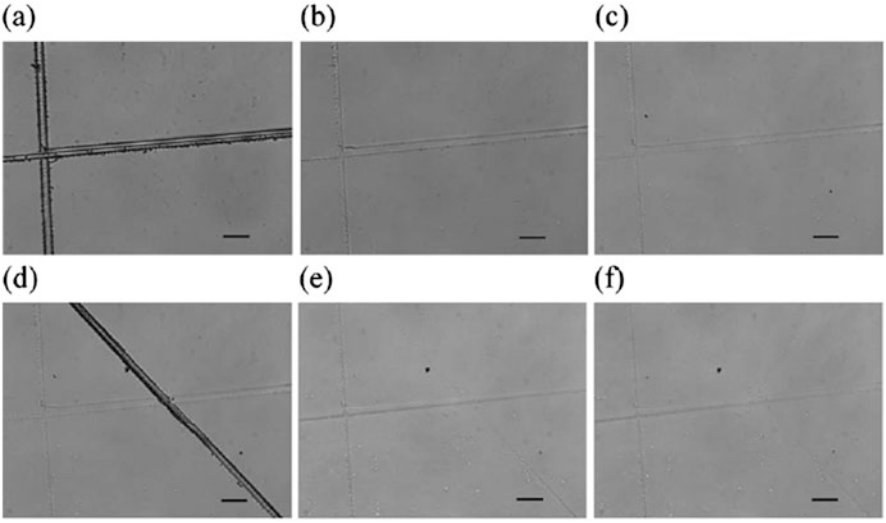

Fig. 26 Multiple self-healing of the network obtained from the crossover of PCMS-TEMPO and PCMS-TEMPO-EOPh: (**a**) First cut, (**b**) first cut after healing for 15 min, (**c**) first cut after healing for 30 min, (**d**) second cut, (**e**) second cut after healing for 15 min, and (**f**) second cut after 30 min of healing. The *Scale bars* represent 20 μm (Reproduced from [123]. Copyright 2015 The American Chemical Society)

A further self-healing system based on a polyurethane elastomer with thermally reversible alkoxyamines was studied by Yuan et al. [124]. First, an alkoxyamine-based diol [4-hydroxy-1-(20-hydroxy-10-phenyl-10-methyl) ethyl-TEMPO] was prepared, which was subsequently converted with tri-HDI and different poly(ethylene glycol)s (PEG200, PEG400, and PEG600) to result in crosslinked polyurethanes. ESR measurements revealed homolytic cleavage at temperatures above 40 °C and dynamic equilibrium could be reached at 80 °C. Thus, the self-healing experiments were performed at 80 °C using impact tests. The specimens were cut into two pieces, subsequently brought back into contact, and heated to 80 °C for 2.5 h under an argon atmosphere. The best self-healing efficiency of about 70% could be obtained with the system using PEG400 as chain extender. Multiple healing was possible and is depicted in Fig. 27. The same authors expanded their work to the synthesis of thermally re-mendable epoxy-containing alkoxyamines [125]. For this purpose, the previously synthesized alkoxyamine-based diol was reacted with chlorodimethylsilane and, finally, with allyl glycidyl ether resulting in the alkoxyamine-containing epoxy (diEP). The diEP was then blended with bisphenol A diglycidyl ether to provide the system with a certain mechanical strength. Impact tests were performed to evaluate the self-healing ability. Upon heating to 90 °C for 1.5 h, an average healing efficiency of 62% for the first healing could be obtained. The system was also able to heal multiple times with a slight decrease in the healing efficiency during several healing/re-fracture cycles.

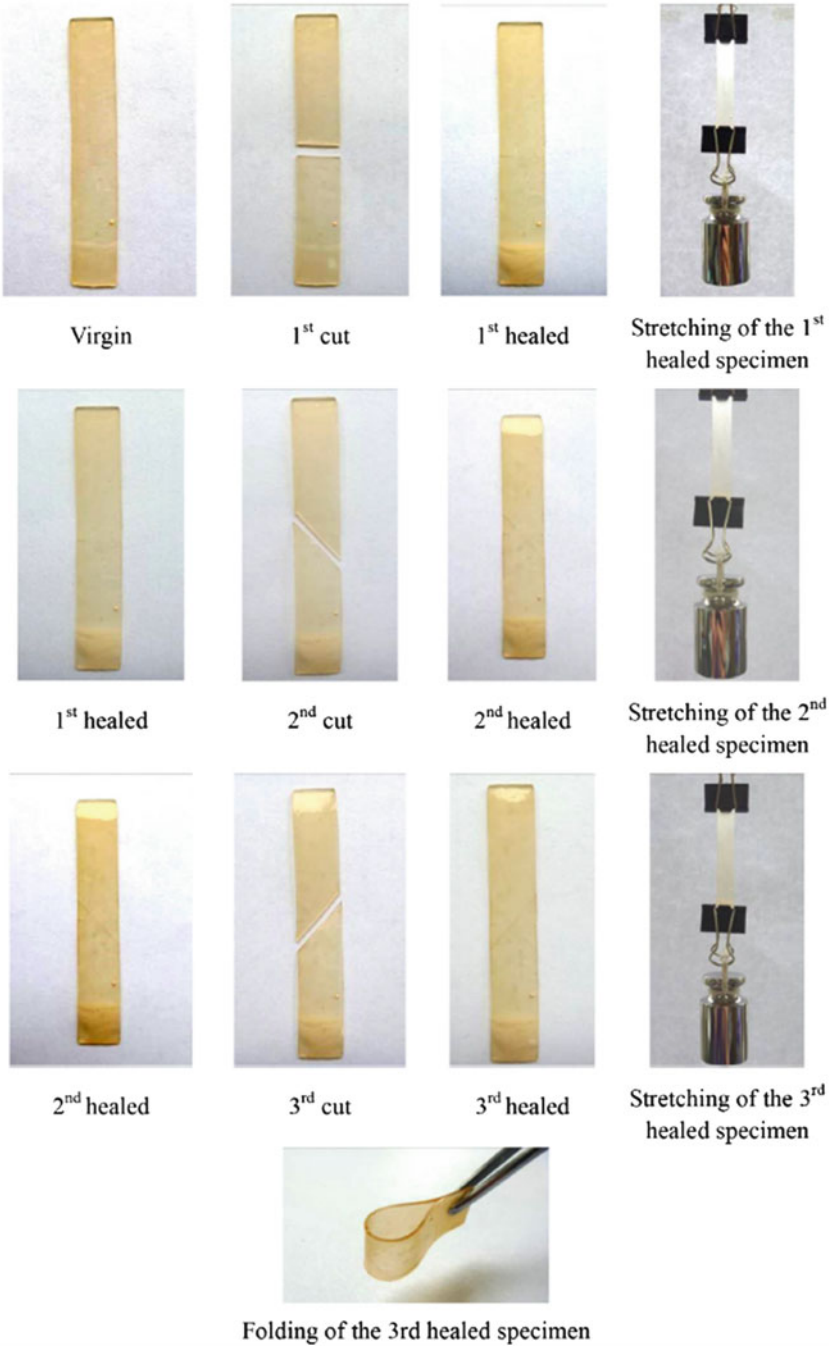

Fig. 27 Repeated self-healing of crossed ruptured specimen of a polyurethane with reversible alkoxyamine units (Reproduced from [124]. Copyright 2015 Elsevier)

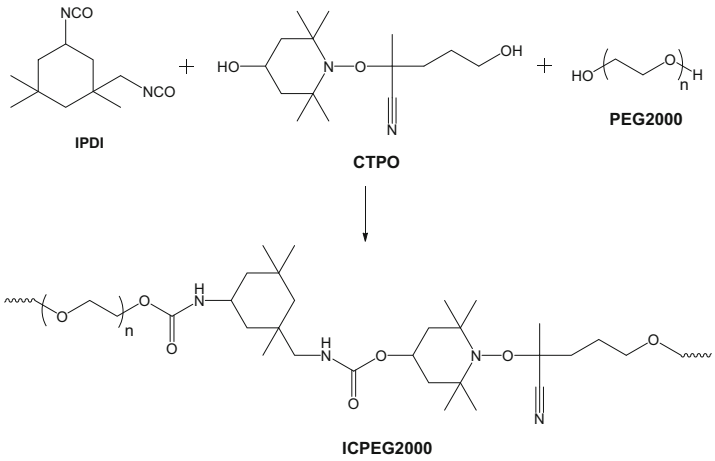

Scheme 17 Synthesis of the reversible polyurethane ICPEG2000 (see text for details). Adopted from [126]

Zhang et al. reported an alkoxyamine-crosslinked polyurethane that was capable of autonomous healing at ambient temperatures [126]. Therefore, an alkoxyamine derivative, 5-hydroxy-2-(4-hydroxy-2,2,6,6-tetramethylpiperidin-1-yloxy)-2-methyl pentane-nitrile (CTPO), was synthesized. A stiff crosslinked polyurethane (ICPEG2000) was obtained by the bulk polymerization of the CTPO monomer with 3-isocyanatomethyl-3,5,5-trimethyl-cyclohexylisocyanate (IPDI) and PEG2000 (Scheme 17). ESR spectroscopy measurements revealed a homolysis temperature for ICPEG2000 above 10 °C. Thus, the self-healing experiments carried out through impact tests were performed at 15 °C and 25 °C. Average healing efficiencies of 90–95% could be obtained for both temperatures and decreased slightly over several healing/re-fracture cycles. The healing mechanism was proposed to be a combination of interdiffusion of broken chain fragments across the fractured material and the dynamic reaction of reversible C–ON bonds in the alkoxyamine units. Zhang et al. synthesized a similar self-healing polyurethane using PCL diol instead of PEG2000. With this system, the healing efficiencies could be further improved (95–98%). One year later, the same authors prepared a novel glycidyl-terminated alkoxyamine, which was incorporated into crosslinked epoxy elastomer by reacting with the hardener polythiol [127]. As with their previous reported system, multiple self-healing at room temperature was possible.

Another approach related to self-healing alkoxyamine-crosslinked polymer networks was reported by Telitel et al. [128]. In contrast to the previous described systems, UV irradiation was employed to trigger the dissociation of alkoxyamine units and, thus, the self-healing process. For this purpose, two four-armed star-like poly(*n*-butyl acrylate) oligomers (degree of polymerization (DP): 10 and 15) with azide terminal groups were prepared and reacted with alkyne-difunctionalized alkoxyamine by means of copper-catalyzed click chemistry. The dissociation behavior under UV irradiation of the resulted covalent networks was studied via

ESR measurements. Self-healing experiments were performed by the introduction of scratches using an AFM tip in tapping mode. After UV light irradiation for 24 h the crosslinked polymer with DP of 15 revealed complete scratch recovery whereas the polymer with DP of 10 featured no noticeable healing.

All these examples have the same crucial issue: The stability of the persistent carbon radical. Combination of these radicals leads to the formation of covalent (non-reversible) crosslinks, limiting a second self-healing procedure. Moreover, these systems also require relatively high temperatures.

5.2 *Diarylbibenzofuranone*

Imato et al. reported the self-healing of a chemical gel crosslinked by diarylbibenzofuranone (DABBF) units [129]. First, the covalent crosslinker DABBF (see Scheme 18) was synthesized through the reaction of 4-hydroxymandelic acid and 2,4-di-*tert*-butylphenol. After that, polyaddition of DABBF and a toluene-2,4-diisocyanate-terminated poly(propylene glycol) (PPG) was performed to obtain the final crosslinked network. According to SEC and NMR measurements, the covalent DABBF units were found to autonomously exchange in DMF at room temperature. The formed radicals can only combine with each other. There are no other side reactions possible (unlike the case of NO radicals). The self-healing ability of this polymer gel was studied. For this purpose, the samples were cut into two pieces using a razor blade, wet with a small piece of DMF and, subsequently, brought back into contact. After 24 h at room temperature the cut samples were reconnected and could withstand manually stretching (Fig. 28). Tensile tests revealed that the cut sample recovered 98% of the original elongation at break. Moreover, the influence of the freshness of the cut surface was investigated. It was shown that, even after 5 days of being separated, a recovery of 70–90% could be obtained.

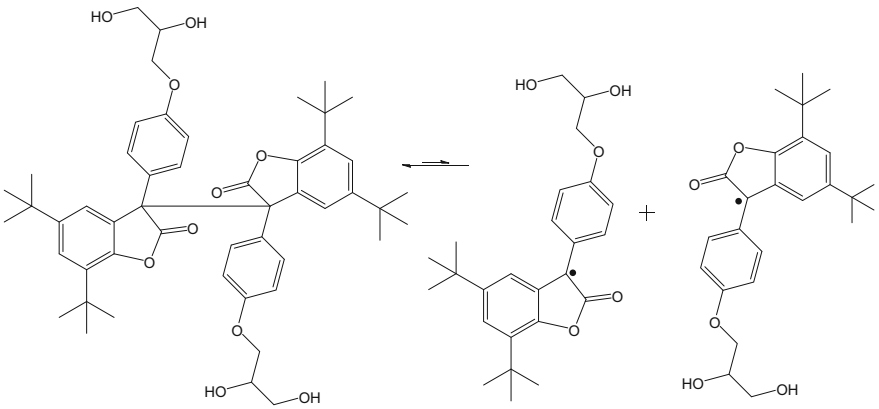

Scheme 18 Structure of diarylbibenzofuranone (DABBF) and its reversible scission into radicals. Adopted from [129]

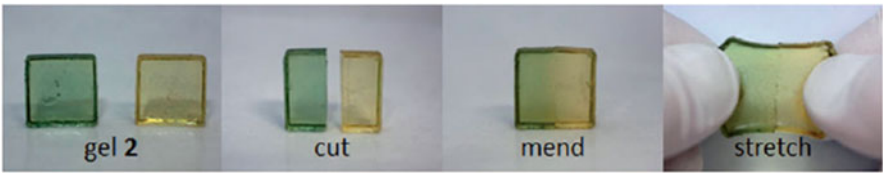

Fig. 28 Photographs of the self-healing behavior of crosslinked polymer gels based on diarylbibenzofuranone crosslinks (Reproduced from [129]. Copyright 2015 Wiley-VCH Verlag GmbH & Co. KGaA)

6 Transesterification

This section presents the highly reversible transesterification reactions of carboxylic and boronic acids. These reactions enable the fabrication of reversible networks based on exchange reactions.

6.1 Carboxylic Acids

The group of Leibler and coworkers reported an epoxy-acid network with the ability to heal and assemble through metal-catalyzed transesterification [130, 131]. The diglycidyl ether of bisphenol A (DGEBA) was reacted with a mixture of dicarboxylic and tricarboxylic fatty acids in the presence of zinc acetate as catalyst. The resulting soft epoxy network featured good elastomeric properties with a glass transition temperature of about 15 °C. Previously, the authors could demonstrate that epoxy-acid and epoxy-anhydride networks can be rearranged by transesterification exchange reactions without modification of the numbers of links and average functionality [130]. Thereby, at lower temperatures the networks behave like classical epoxy thermosets expressed through very sluggish exchange reactions. However, at higher temperatures the polymers showed viscoelastic behavior. Lap-shear tests indicated that the epoxy-acid network can be welded after 1 h at 150 °C, and after several hours a full recovery of the mechanical property could be obtained. The welding process was found to be dependent on the concentration and nature of the transesterification catalyst, as well as on the concentration of residual hydroxyl groups present in the network. A schematic representation of the welding process is depicted in Fig. 29.

6.2 Boronic Acids

The complexation between boronic acids and 1,2- or 1,3-diols is a further possibility for the production of reversible covalent polymers with the ability to self-heal

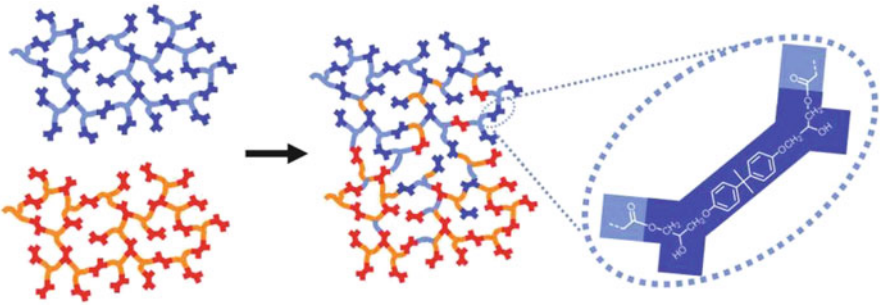

Fig. 29 Welding of two pieces of epoxy resin via transesterification exchange reactions (Reproduced from [131]. Copyright 2015 The American Chemical Society)

[132, 133]. Until now, most of the approaches related to self-healing based on boronate ester crosslinks involve formation of hydrogels [134–137]. The stability of the boronate ester bonds in aqueous media is strongly dependent on the pH value and the pK_a value of the boronic acid [133]. At pH values above the pK_a of the boronic acid, the boronate ester bond is stabilized, whereas the equilibrium is shifted towards free boronic acid and diol at pH values below the pK_a. However, the pK_a of the boronic acid can be tuned by the addition of various substituents, so that this reversible covalent bond can be applied over a large range of pH values.

Jay et al. reported a pH-responsive polymeric network crosslinked through boronate–diol complexes with self-healing properties [134]. For this purpose, a 10 mol% phenyl boronic acid (PBA)-functionalized poly(2-hydroxypropylmethacrylamide) [poly(HPMAm)] and a 1 mol% salicylhydroxamic acid (SHA)-functionalized poly(HPMAm) were synthesized and mixed with each other, resulting in a covalent crosslinked network across the entire pH range. However, at neutral pH (7.5) the boronate–diol complexes were stabilized, resulting in a higher crosslinking density than that at low pH value (4.5). For the investigation of the self-healing properties, dynamic rheology measurements were performed at both neutral and acidic pH values. The material was exposed to high oscillatory stress for 2 min, resulting in an approximately 50% decrease in the elastic modulus. After 60 min, the network displayed recovery at both pH values and was able to heal multiple times (up to five cycles tested).

He et al. synthesized a pH-responsive self-healing hydrogel formed by boronate–catechol complexation [135]. The covalent hydrogels could be obtained by mixing a four-arm PEG end-functionalized with catechol (cPEG) together with 1,3-benzenediboronic acid (BDBA) at pH 9 (Scheme 19). At alkaline pH, a covalent gel was formed and a gel-to-sol transition was observed at neutral and acid pH values. Furthermore, hydrogel formation was dependent on the polymer concentration and was found to be best with 15 wt%. The self-healing ability was studied by cutting a cube of 15 wt% hydrogel into two pieces and subsequently rejoining the fractured surfaces (Fig. 30). The hydrogel was able to heal autonomously, rapidly, and multiple times and could also withstand mechanical stress.

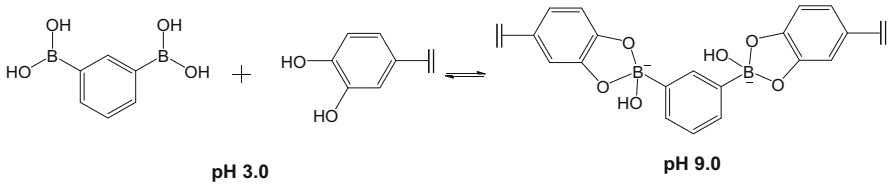

Scheme 19 pH-responsive hydrogel based on cPEG and 1,3-benzenediboronic acid. Adopted from [135]

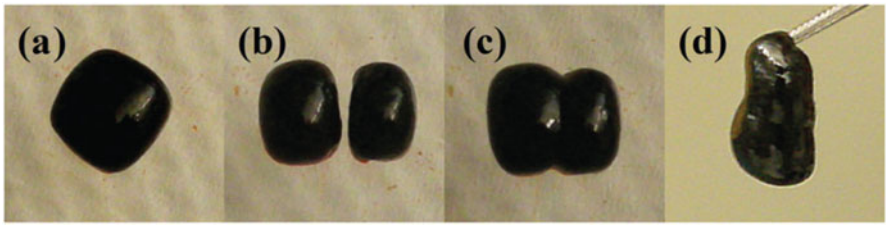

Fig. 30 Self-healing behavior of a boronic acid-based hydrogel: (**a**) Cube of the hydrogel, (**b**) cut into two pieces, (**c**) fused together, and (**d**) stretched without fracture after 30 s of fusion (Reproduced from [135]. Copyright 2015 The Royal Society of Chemistry)

Oscillatory rheology measurements were performed to prove these self-healing properties.

Another approach related to self-healing hydrogels based on reversible boronic ester crosslinks was demonstrated by Tarus et al. [136]. For this purpose, two polymers were synthesized by grafting phenyl boronic acid (PBA) moieties and maltose derivatives onto hyaluronic acid (HA). The resulting functionalized polymers (HA-PBA and HA-maltose) were mixed with each other to form a transparent gel on the basis of boronate ester bonds (total polymer concentration 15 g L^{-1}, [PBA]/[maltose] = 1). Dynamic rheological measurements were consistent with typical covalent crosslinked hydrogels, exhibiting storage moduli (G') greater than loss moduli (G''). This was also the case when the pH value was varied in the range of 6.5–9.5. The self-healing ability of this hydrogel was studied. The gel displayed complete recovery of mechanical properties after five cycles of high oscillatory stress. Moreover, freshly prepared gel pieces were cut in half and self-healed within a few minutes simply by bringing the two cut surfaces into contact.

In addition, Deng et al. prepared hydrogels based on boronic acid that were able to self-heal under neutral and acidic conditions [137]. The pinacol-protected ester of 2-acrylamido-phenylboronic acid (2APBA) was copolymerized with *N*,*N*-dimethylacrylamide (DMA), resulting in poly(2APBA-*co*-DMA) with 10 and 15 mol% of 2APBA. Furthermore, two different diol-containing polymers were synthesized, one copolymer consisting of dopamine acrylamide (DOPAAm) and DMA and the other being poly(vinyl alcohol) (PVOH). Hydrogels were prepared by mixing poly(2APBA-*co*-DMA) copolymers and poly(DOPAAm-*co*-DMA) or PVOH at pH 4. In the case of poly(DOPAAm-*co*-DMA) for hydrogel preparation,

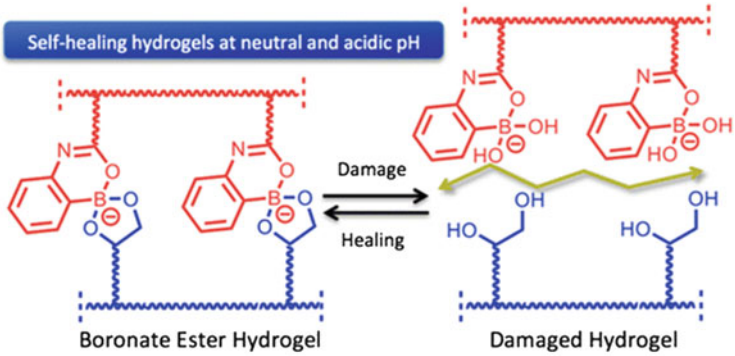

Scheme 20 Healing process for boronate ester-crosslinked hydrogels (Reproduced from [137]. Copyright 2015 The American Chemical Society)

reducing conditions were required to prevent catechol oxidation. The self-healing behavior was studied by cutting hydrogel disks in half and subsequently placing them next to each other. After 60 min the disks completely recovered from the damage. A schematic representation of the healing process is depicted in Scheme 20. Strain-sweep experiments revealed possible self-healing at neutral and acidic pH values. However, the PVOH-crosslinked hydrogels featured greater strength than those with DOPAAm because of an increased crosslinking density. The strength of the hydrogels seemed to be little affected by varying the pH value.

Cash et al. reported polymers crosslinked through reversible covalent boronic esters with the ability to self-heal in the bulk at room temperature [138]. For this purpose, they prepared a boronic ester diene (VPBE), which was reacted with commercially available thiols such as 3,6-dioxa-1,8-octanedithiol (DODT) and pentaerythritol tetrakis(3-mercaptopropionate) (PTMP) via a photo-initiated thiol–ene click-reaction to result in boronic ester networks. The addition of some drops of water to induce boronic acid hydrolysis and reformation was found to facilitate the exchange reactions and, thus, the healing process (Fig. 31a). Self-healing experiments were performed by completely cutting the sample, adding two or three drops of water and bringing the cut surfaces back into contact (Fig. 31b). After 3.5 days, the damage was nearly complete recovered and the healed sample could also withstand tensile stress without fracturing (tested after 4 days) (Fig. 31b). Additionally, the cut samples were also able to heal without the addition of water in high humidity environments (85%). Three cut–repair cycles were conducted and resulted in nearly complete recovery of the material after each cycle.

Recently, Guan and coworkers also designed self-healing bulk materials through dynamic boronic ester linkages [139]. In order to study the kinetics of exchange reactions and the self-healing ability of such polymeric networks two different diboronic acids crosslinkers (“slow” crosslinker **3**, “fast” crosslinker **4**) were synthesized (Fig. 32). Furthermore, a 1,2-diol-containing polycyclooctene polymer (20%-diol PCO) was prepared through the ring opening metathesis polymerization (ROMP) of cyclooctene-based monomers (Fig. 32). Next, polymer films were

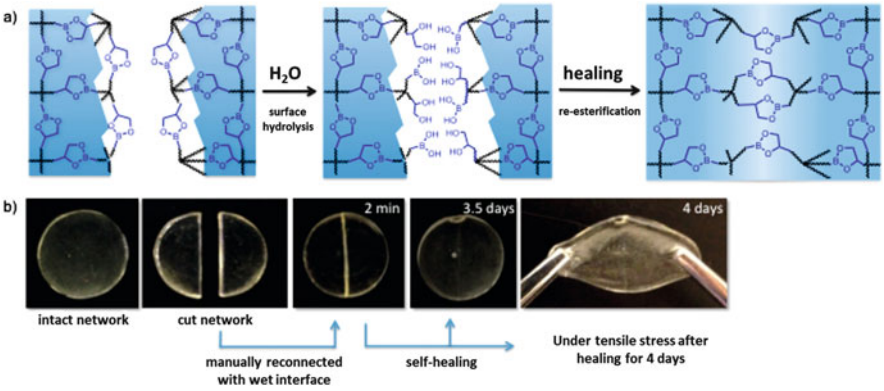

Fig. 31 Self-healing of boronic ester network materials: (**a**) Proposed healing mechanism and (**b**) images of the healing process of a sample (Reproduced from [138]. Copyright 2015 The American Chemical Society)

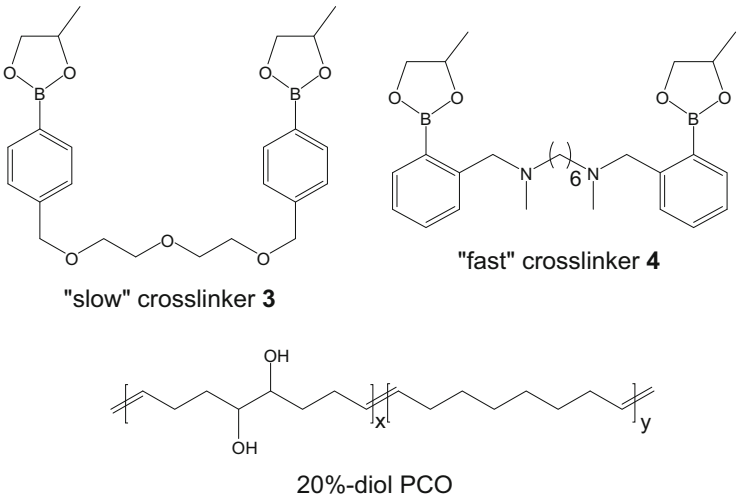

Fig. 32 Structures of the "slow" and "fast" crosslinkers and the 1,2-diol-containing cyclooctene (20%-diol PCO) used for the synthesis of a network containing reversible boronic acid linkages. Adopted from [139]

prepared by the reaction of 0.5% and 1% of each diboronic acid crosslinker with the 20%-diol PCO polymer. After that, the films were completely cut through using a razor blade, brought back into contact for 1 min, and allowed to self-heal for 16 h at a slightly elevated temperature of 50 °C. Only the film with crosslinker **4**, which was found to be the one with faster exchange kinetics, displayed almost quantitatively self-healing. Moreover, the samples could be reprocessed multiple times without significant loss of their mechanical properties.

Transesterification reactions, in particular of boronic acids, have been utilized often for self-healing polymers. Because of the possible contribution of water (depending on the pH value), these systems are particularly interesting for hydrogels. The carboxy-epoxy systems (the so-called vitrimers) are interesting polymer systems and represent a "reversible duromer."

7 Conclusion and Outlook

In the past decade, a large variety of different self-healing polymers based on reversible covalent interactions have been developed. Starting with the reversible DA reaction of furan and maleimide, many other reversible covalent chemistries have been explored. The [2+2] and [4+4] cycloadditions allow the use of light as trigger for the healing process. Moreover, acylhydrazones, reversible radical reactions, and disulfide-based systems have been explored.

In principle, every other reversible organic reaction could also be applied as a reversible binding motif for such polymers (for an overview on covalent adaptable networks see [140–142]). Noteworthy, the reversibility of these reactions can also strongly depend on the surrounding environment (i.e., solution, hydrogel, organogel, or polymer). A reaction that is highly reversible in solution might be hampered in the bulk polymeric material as a result of steric effects, availability of the respective binding partners, concentration effects, or changed polarity. The reactions presented in this review can be divided into three main types: (1) Reversible addition/cycloaddition reactions, (2) reversible exchange reactions, and (3) reversible condensation reactions. The investigated self-healing polymers (from elastomers to highly crosslinked networks) are mainly based on reversible DA reactions (i.e., type 1). A reversible linker moiety is cleaved, resulting in two reactive groups that subsequently react. The main drawback of DA systems is, in most cases, the high temperatures (80–130 °C) required. Investigations on decreasing this temperature (e.g., hetero-DA reactions, different polarity) have not been successful. Only the highly reversible fulvene systems have been used for room temperature healing of soft materials. The other two approaches have been studied less frequently, but reversible condensation reactions (e.g., aldehyde and acylhydrazide) offer additional possibilities. Water, which can be present in the case of damage (e.g., scratch in a coating), can start the healing process of acylhydrazone-based polymeric materials. Here, gel-like polymers have been investigated, but the transfer to more rigid materials is in this case more difficult. Self-healing polymeric materials have been successfully fabricated using disulfides, which feature different possible healing mechanisms (exchange, reductive cleavage, and oxidative coupling). Despite stability issues for some species, these systems are interesting candidates for other materials. Disulfides (and higher homologs) are present in all sulfur-vulcanized rubbers. Moreover, radicals have been utilized for self-healing polymers. However, integration into these materials as well as the possible side reactions are unfavorable. In contrast, transesterification

reactions offer greater potential for the design of self-healing polymers. Considering the above described examples, it is difficult to decide which system/which reversible chemistry and which crosslinker/reversible moiety to choose. Depending on the application, different systems might be preferable. The required healing temperature is one of the most crucial points. Depending on the application, different temperature profiles are available or possible. Most systems (e.g., DA) require elevated temperatures (80–100 °C). Healing at lower temperatures was often only achieved for softer materials or gels.

The existing toolbox of different reversible interactions will be expanded in future research on intrinsic self-healing polymers. One of the main challenges of this research is the stability of the involved species. For self-healing based on radical species, only persistent radicals cannot combine. All C-centered radicals involved could potentially result in non-reversible covalent C–C bonds. Another challenge is the lower mobility of bulk materials. The transfer of reversible reactions from solution (or hydrogels/organogels) requires additional investigation. Equilibrium constants are available for solutions; however, bulk materials still represent a blank spot. One major challenge is expansion of potential triggers for the healing process. The Achilles' heel of most systems described is the required heating. However, the general applicability of such systems is limited. In an ideal case, the damage itself would be the trigger. This approach requires the combination of intrinsic self-healing polymers with mechanochemistry [143–145]. The mechanical damage could either lead to cleavage of the reversible bond or to generation of active species that catalyze an exchange reaction [146].

In contrast to extrinsic self-healing polymers (e.g., capsule-based healing), intrinsic self-healing polymers based on reversible covalent interactions are still a long way from commercial application. The required trigger and design of new materials seem to be the main impediments. Consequently, future research should be devoted to the transfer of reversible interactions into commercial polymer systems (e.g., utilization of a reversible crosslinker instead of a covalent crosslinker). Additionally, the cost of these systems needs to be decreased and easy access made possible.

Acknowledgement The authors thank the Deutsche Forschungsgemeinschaft (DFG, SPP 1568) for financial support.

References

1. Hager MD, Greil P, Leyens C, van der Zwaag S, Schubert US (2010) Adv Mater 22:5424–5430
2. Wu DY, Meure S, Solomon D (2008) Prog Polym Sci 33:479–522
3. Guimard NK, Oehlenschlaeger KK, Zhou J, Hilf S, Schmidt FG, Barner-Kowollik C (2012) Macromol Chem Phys 213:131–143
4. Billiet S, Hillewaere XKD, Teixeira RFA, Prez FED (2013) Macromol Rapid Commun 34:290–309

5. White SR, Sottos NR, Geubelle PH, Moore JS, Kessler MR, Sriram SR, Brown EN, Viswanathan S (2001) Nature 409:794–797
6. Kamphaus JM, Rule JD, Moore JS, Sottos NR, White SR (2008) J R Soc Interface 5:95–103
7. Toohey KS, Sottos NR, Lewis JA, Moore JS, White SR (2007) Nat Mater 6:581–585
8. Cordier P, Tournilhac F, Soulie-Ziakovic C, Leibler L (2008) Nature 451:977–980
9. Herbst F, Döhler D, Michael P, Binder WH (2013) Macromol Rapid Commun 34:203–220
10. Kalista SJ Jr, Ward TC (2007) J R Soc Interface 4:405–411
11. Varley RJ, Shen S, van der Zwaag S (2010) Polymer 51:679–686
12. Varghese S, Lele A, Mashelkar R (2006) J Polym Sci A Polym Chem 44:666–670
13. Bode S, Zedler L, Schacher FH, Dietzek B, Schmitt M, Popp J, Hager MD, Schubert US (2013) Adv Mater 25:1634–1638
14. Bode S, Bose RK, Matthes S, Ehrhardt M, Seifert A, Schacher FH, Paulus RM, Stumpf S, Sandmann B, Vitz J, Winter A, Hoeppener S, Garcia SJ, Spange S, van der Zwaag S, Hager MD, Schubert US (2013) Polym Chem 4:4966–4973
15. Burnworth M, Tang L, Kumpfer JR, Duncan AJ, Beyer FL, Fiore GL, Rowan SJ, Weder C (2011) Nature 472:334–337
16. Kalista SJ, Pflug JR, Varley RJ (2013) Polym Chem 4:4910–4926
17. Chen X, Dam MA, Ono K, Mal A, Shen H, Nut SR, Sheran K, Wudl F (2002) Science 295:1698–1702
18. Chen X, Wudl F, Mal AK, Shen H, Nutt SR (2003) Macromolecules 36:1802–1807
19. Kötteritzsch J, Stumpf S, Hoeppener S, Vitz J, Hager MD, Schubert US (2013) Macromol Chem Phys 214:1636–1649
20. Amamoto Y, Otsuka H, Takahara A, Matyjaszewski K (2012) Adv Mater 24:3975–3980
21. Canadell J, Goossens H, Klumperman B (2011) Macromolecules 44:2536–2541
22. Lafont U, van Zeijl H, van der Zwaag S (2012) ACS Appl Mater Interfaces 4:6280–6288
23. Deng G, Tang C, Li F, Jiang H, Chen Y (2010) Macromolecules 43:1191–1194
24. Deng G, Li F, Yu H, Liu F, Liu C, Sun W, Jiang H, Chen Y (2012) ACS Macro Lett 1:275–279
25. Liu Y-L, Chuo T-W (2013) Polym Chem 4:2194–2205
26. Sanyal A (2010) Macromol Chem Phys 211:1417–1425
27. Tasdelen MA (2011) Polym Chem 2:2133–2145
28. Plaisted TA, Nemat-Nasser S (2007) Acta Mater 55:5684–5696
29. Park JS, Darlington T, Starr AF, Takahashi K, Riendeau J, Hahn HT (2010) Compos Sci Technol 70:2154–2159
30. Zhang Y, Broekhuis AA, Picchioni F (2009) Macromolecules 42:1906–1912
31. Toncelli C, De Reus DC, Picchioni F, Broekhuis AA (2012) Macromol Chem Phys 213:157–165
32. Yoshie N, Watanabe M, Araki H, Ishida K (2010) Polym Degrad Stab 95:826–829
33. Weizman H, Nielsen C, Weizman OS, Nemat-Nasser S (2011) J Chem Educ 88:1137–1140
34. Postiglione G, Turri S, Levi M (2015) Prog Org Coat 78:526–531
35. Liu Y-L, Hsieh C-Y (2006) J Polym Sci A Polym Chem 44:905–913
36. Liu Y-L, Chen Y-W (2007) Macromol Chem Phys 208:224–232
37. Tian Q, Yuan YC, Rong MZ, Zhang MQ (2009) J Mater Chem 19:1289–1296
38. Tian QA, Rong MZ, Zhang MQ, Yuan YC (2010) Polym Int 59:1339–1345
39. Wouters M, Craenmehr E, Tempelaars K, Fischer H, Stroeks N, van Zanten J (2009) Prog Org Coat 64:156–162
40. Scheltjens G, Brancart J, De Graeve I, Van Mele B, Terryn H, Van Assche G (2011) J Therm Anal Calorim 105:805–809
41. Brancart J, Scheltjens G, Muselle T, Van Mele B, Terryn H, Van Assche G (2014) J Intell Mater Syst Struct 25:40–46
42. Scheltjens G, Diaz MM, Brancart J, Van Assche G, Van Mele B (2013) React Funct Polym 73:413–420
43. Bai N, Saito K, Simon GP (2013) Polym Chem 4:724–730

44. Bai N, Simon GP, Saito K (2013) RSC Adv 3:20699–20707
45. Peterson AM, Jensen RE, Palmese GR (2009) ACS Appl Mater Interfaces 1:992–995
46. Peterson AM, Jensen RE, Palmese GR (2010) ACS Appl Mater Interfaces 2:1141–1149
47. Pratama PA, Peterson AM, Palmese GR (2012) Macromol Chem Phys 213:173–181
48. Pratama PA, Sharifi M, Peterson AM, Palmese GR (2013) ACS Appl Mater Interfaces 5:12425–12431
49. Pratama PA, Peterson AM, Palmese GR (2013) Polym Chem 4:5000–5006
50. Peterson AM, Jensen RE, Palmese GR (2011) Compos Sci Technol 71:586–592
51. Peterson AM, Jensen RE, Palmese GR (2013) ACS Appl Mater Interfaces 5:815–821
52. Zhang W, Duchet J, Gerard JF (2014) J Colloid Interface Sci 430:61–68
53. Kavitha AA, Singha NK (2009) ACS Appl Mater Interfaces 1:1427–1436
54. Pramanik NB, Nando GB, Singha NK (2015) Polymer 69:349–356
55. Kavitha AA, Singha NK (2010) Macromolecules 43:3193–3205
56. Bose RK, Kotteritzsch J, Garcia SJ, Hager MD, Schubert US, van der Zwaag S (2014) J Polym Sci A Polym Chem 52:1669–1675
57. Geitner R, Kötteritzsch J, Siegmann M, Bocklitz TW, Hager MD, Schubert US, Grafe S, Dietzek B, Schmitt M, Popp J (2015) Phys. Chem. Chem. Phys 17:22587–22595
58. Kötteritzsch J, Hager MD, Schubert US (2015) Polymer 69:321–329
59. Engel T, Kickelbick G (2014) Polym Int 63:915–923
60. Xu ZG, Zhao Y, Wang XG, Lin T (2013) Chem Commun 49:6755–6757
61. Li JH, Zhang GP, Deng LB, Zhao SF, Gao YJ, Jiang K, Sun R, Wong CP (2014) J Mater Chem A 2:20642–20649
62. Du PF, Liu XX, Zheng Z, Wang XL, Joncheray T, Zhang YF (2013) RSC Adv 3:15475–15482
63. Du PF, Wu MY, Liu XX, Zheng Z, Wang XL, Joncheray T, Zhang YF (2014) J Appl Polym Sci 131(9):40234
64. Zhang J, Niu Y, Huang C, Xiao L, Chen Z, Yang K, Wang Y (2012) Polym Chem 3:1390–1393
65. Heo Y, Sodano HA (2014) Adv Funct Mater 24:5261–5268
66. Rivero G, Nguyen LTT, Hillewaere XKD, Du Prez FE (2014) Macromolecules 47:2010–2018
67. Lu XL, Fei GX, Xia HS, Zhao Y (2014) J Mater Chem A 2:16051–16060
68. Mallek H, Jegat C, Mignard N, Abid M, Abid S, Taha M (2013) J Appl Polym Sci 129:954–964
69. Barthel MJ, Rudolph T, Teichler A, Paulus RM, Vitz J, Hoeppener S, Hager MD, Schacher FH, Schubert US (2013) Adv Funct Mater 23:4921–4932
70. Zeng C, Seino H, Ren J, Hatanaka K, Yoshie N (2013) Macromolecules 46:1794–1802
71. Zeng C, Seino H, Ren J, Hatanaka K, Yoshie N (2013) Polymer 54:5351–5357
72. Ikezaki T, Matsuoka R, Hatanaka K, Yoshie N (2014) J Polym Sci A Polym Chem 52:216–222
73. Syrett JA, Mantovani G, Barton WRS, Price D, Haddleton DM (2010) Polym Chem 1:102–106
74. Wiggins KM, Syrett JA, Haddleton DM, Bielawski CW (2011) J Am Chem Soc 133:7180–7189
75. Yoshie N, Saito S, Oya N (2011) Polymer 52:6074–6079
76. Murphy EB, Bolanos E, Schaffner-Hamann C, Wudl F, Nutt SR, Auad ML (2008) Macromolecules 41:5203–5209
77. Park JS, Takahashi K, Guo ZH, Wang Y, Bolanos E, Hamann-Schaffner C, Murphy E, Wudl F, Hahn HT (2008) J Compos Mater 42:2869–2881
78. Reutenauer P, Buhler E, Boul PJ, Candau SJ, Lehn JM (2009) Chem Eur J 15:1893–1900
79. Wei Z, Yang JH, Du XJ, Xu F, Zrinyi M, Osada Y, Li F, Chen YM (2013) Macromol Rapid Commun 34:1464–1470

80. Inglis AJ, Nebhani L, Altintas O, Schmidt FG, Barner-Kowollik C (2010) Macromolecules 43:5515–5520
81. Zhou J, Guimard NK, Inglis AJ, Namazian M, Lin CY, Coote ML, Spyrou E, Hilf S, Schmidt FG, Barner-Kowollik C (2012) Polym Chem 3:628–639
82. Guimard NK, Ho J, Brandt J, Lin CY, Namazian M, Mueller JO, Oehlenschlaeger KK, Hilf S, Lederer A, Schmidt FG, Coote ML, Barner-Kowollik C (2013) Chem Sci 4:2752–2759
83. Oehlenschlaeger KK, Guimard NK, Brandt J, Mueller JO, Lin CY, Hilf S, Lederer A, Coote ML, Schmidt FG, Barner-Kowollik C (2013) Polym Chem 4:4348–4355
84. Oehlenschlaeger KK, Mueller JO, Brandt J, Hilf S, Lederer A, Wilhelm M, Graf R, Coote ML, Schmidt FG, Barner-Kowollik C (2014) Adv Mater 26:3561–3566
85. Dilling WL (1983) Chem Rev 83:1–47
86. Cardenas-Daw C, Kroeger A, Schaertl W, Froimowicz P, Landfester K (2012) Macromol Chem Phys 213:144–156
87. Trenor SR, Shultz AR, Love BJ, Long TE (2004) Chem Rev 104:3059–3077
88. Chung C-M, Roh Y-S, Cho S-Y, Kim J-G (2004) Chem Mater 16:3982–3984
89. Oya N, Sukarsaatmadja P, Ishida K, Yoshie N (2012) Polym J 44:724–729
90. Hu L, Cheng X, Zhang A (2015) J Mater Sci 50:2239–2246
91. Froimowicz P, Klinger D, Landfester K (2011) Chem Eur J 17:12465–12475
92. Ling J, Rong MZ, Zhang MQ (2011) J Mater Chem 21:18373–18380
93. Ling J, Rong MZ, Zhang MQ (2012) Polymer 53:2691–2698
94. Zheng Y, Micic M, Mello SV, Mabrouki M, Andreopoulos FM, Konka V, Pham SM, Leblanc RM (2002) Macromolecules 35:5228–5234
95. Chujo Y, Sada K, Nomura R, Naka A, Saegusa T (1993) Macromolecules 26:5611–5614
96. Connal LA, Vestberg R, Hawker CJ, Qiao GG (2008) Adv Funct Mater 18:3315–3322
97. Xu J-F, Chen Y-Z, Wu L-Z, Tung C-H, Yang Q-Z (2013) Org Lett 15:6148–6151
98. Froimowicz P, Frey H, Landfester K (2011) Macromol Rapid Commun 32:468–473
99. Skene WG, Lehn J-MP (2004) Proc Natl Acad Sci USA 101:8270–8275
100. Lehn J-M (2005) Prog Polym Sci 30:814–831
101. Lehn J-M (2010) Aust J Chem 63:611–623
102. Liu F, Li F, Deng G, Chen Y, Zhang B, Zhang J, Liu C-Y (2012) Macromolecules 45:1636–1645
103. Zhang P, Deng FY, Peng Y, Chen HB, Gao Y, Li HM (2014) RSC Adv 4:47361–47367
104. Roy N, Buhler E, Lehn J-M (2014) Polym Int 63:1400–1405
105. Apostolides DE, Patrickios CS, Leontidis E, Kushnir M, Wesdemiotis C (2014) Polym Int 63:1558–1565
106. Wei Z, Yang JH, Liu ZQ, Xu F, Zhou JX, Zrínyi M, Osada Y, Chen YM (2015) Adv Funct Mater 25:1352–1359
107. Kuhl N, Bode S, Bose RK, Vitz J, Seifert A, Hoeppener S, Garcia SJ, Spange S, van der Zwaag S, Hager MD, Schubert US (2015) Adv Funct Mater 25(22):3295–3301
108. Gyarmati B, Nemethy A, Szilagyi A (2013) Eur Polym J 49:1268–1286
109. Pepels M, Filot I, Klumperman B, Goossens H (2013) Polym Chem 4:4955–4965
110. Bapat AP, Ray JG, Savin DA, Sumerlin BS (2013) Macromolecules 46:2188–2198
111. Fairbanks BD, Singh SP, Bowman CN, Anseth KS (2011) Macromolecules 44:2444–2450
112. Otsuka H, Nagano S, Kobashi Y, Maeda T, Takahara A (2010) Chem Commun 46:1150–1152
113. Yoon JA, Kamada J, Koynov K, Mohin J, Nicolaÿ R, Zhang Y, Balazs AC, Kowalewski T, Matyjaszewski K (2011) Macromolecules 45:142–149
114. Lei ZQ, Xiang HP, Yuan YJ, Rong MZ, Zhang MQ (2014) Chem Mater 26:2038–2046
115. Rekondo A, Martin R, Ruiz de Luzuriaga A, Cabanero G, Grande HJ, Odriozola I (2014) Mater Horiz 1:237–240
116. Martin R, Rekondo A, Ruiz de Luzuriaga A, Cabanero G, Grande HJ, Odriozola I (2014) J Mater Chem A 2:5710–5715

117. AbdolahZadeh M, Esteves ACC, van der Zwaag S, Garcia SJ (2014) J Polym Sci A Polym Chem 52:1953–1961
118. Hawker CJ, Barclay GG, Dao J (1996) J Am Chem Soc 118:11467–11471
119. Higaki Y, Otsuka H, Takahara A (2004) Macromolecules 37:1696–1701
120. Higaki Y, Otsuka H, Takahara A (2006) Macromolecules 39:2121–2125
121. Otsuka H, Aotani K, Higaki Y, Amamoto Y, Takahara A (2007) Macromolecules 40:1429–1434
122. Yuan C, Rong MZ, Zhang MQ, Zhang ZP, Yuan YC (2011) Chem Mater 23:5076–5081
123. Wang F, Rong MZ, Zhang MQ (2012) J Mater Chem 22:13076–13084
124. Yuan C, Rong MZ, Zhang MQ (2014) Polymer 55:1782–1791
125. Yuan C, Zhang MQ, Rong MZ (2014) J Mater Chem A 2:6558–6566
126. Zhang ZP, Rong MZ, Zhang MQ, Yuan C (2013) Polym Chem 4:4648–4654
127. Zhang ZP, Rong MZ, Zhang MQ (2014) Polymer 55:3936–3943
128. Telitel S, Amamoto Y, Poly J, Morlet-Savary F, Soppera O, Lalevee J, Matyjaszewski K (2014) Polym Chem 5:921–930
129. Imato K, Nishihara M, Kanehara T, Amamoto Y, Takahara A, Otsuka H (2012) Angew Chem Int Ed 51:1138–1142
130. Montarnal D, Capelot M, Tournilhac F, Leibler L (2011) Science 334:965–968
131. Capelot M, Montarnal D, Tournilhac F, Leibler L (2012) J Am Chem Soc 134:7664–7667
132. Guan Y, Zhang Y (2013) Chem Soc Rev 42:8106–8121
133. Cambre JN, Sumerlin BS (2011) Polymer 52:4631–4643
134. Jay JI, Langheinrich K, Hanson MC, Mahalingam A, Kiser PF (2011) Soft Matter 7:5826–5835
135. He L, Fullenkamp DE, Rivera JG, Messersmith PB (2011) Chem Commun 47:7497–7499
136. Tarus D, Hachet E, Messager L, Catargi B, Ravaine V, Auzély-Velty R (2014) Macromol Rapid Commun 35:2089–2095
137. Deng CC, Brooks WLA, Abboud KA, Sumerlin BS (2015) ACS Macro Lett 4:220–224
138. Cash JJ, Kubo T, Bapat AP, Sumerlin BS (2015) Macromolecules 48:2098–2106
139. Cromwell OR, Chung J, Guan Z (2015) J Am Chem Soc 137(20):6492-6495
140. Kloxin CJ, Scott TF, Adzima BJ, Bowman CN (2010) Macromolecules 43:2643–2653
141. Kloxin CJ, Bowman CN (2013) Chem Soc Rev 42:7161–7173
142. Bowman CN, Kloxin CJ (2012) Angew Chem Int Ed 51:4272–4274
143. May PA, Moore JS (2013) Chem Soc Rev 42:7497–7506
144. Ribas-Arino J, Marx D (2012) Chem Rev 112:5412–5487
145. Craig SL (2012) Nature 487:176–177
146. Groote R, Jakobs RTM, Sijbesma RP (2013) Polym Chem 4:4846–4859

Adv Polym Sci (2016) 273: 59–112
DOI: 10.1007/12_2015_345

Published online: 17 December 2015

Intrinsic Self-Healing Polymers Based on Supramolecular Interactions: State of the Art and Future Directions

Marcel Enke, Diana Döhler, Stefan Bode, Wolfgang H. Binder, Martin D. Hager, and Ulrich S. Schubert

Abstract Supramolecular polymers are an intriguing class of materials with dynamic behavior as a result of the presence of non-covalent bonds. These bonds include hydrogen bonds, metallopolymers, ionomers, host–guest as well as π–π interactions. The strength of these supramolecular bonds can be tuned by varying the binding motifs. Their reversible and dynamic character can be utilized to engineer self-healing polymers. This review briefly presents the preconditions for design of self-healing polymers and summarizes the development of supramolecular self-healing polymers based on various non-covalent interactions. Furthermore, challenges and perspectives for the understanding of self-healing mechanisms and the preparation of novel materials with enhanced properties are discussed.

Keywords Host–guest interactions • Hydrogen bonding • Metallopolymers • Self-healing • Supramolecular polymers

---

Marcel Enke and Diana Döhler are equally contributed.

M. Enke, S. Bode, M.D. Hager (✉), and U.S. Schubert (✉)
Laboratory of Organic and Macromolecular Chemistry (IOMC), Friedrich Schiller University Jena, Humboldtstrasse 10, 07743 Jena, Germany

Jena Center for Soft Matter (JCSM), Friedrich Schiller University Jena, Philosophenweg 7, 07743 Jena, Germany
e-mail: martin.hager@uni-jena.de; ulrich.schubert@uni-jena.de

D. Döhler and W.H. Binder (✉)
Chair of Macromolecular Chemistry, Faculty of Natural Science II (Chemistry, Physics and Mathematics), Martin Luther University Halle-Wittenberg, Von-Danckelmann-Platz 4, 06120 Halle (Saale), Germany
e-mail: wolfgang.binder@chemie.uni-halle.de

Contents

1 Introduction

Inspired by nature – more precisely by the greater burdock – the Swiss electrical engineer de Mestral invented Velcro and enabled the reversible connection of two textile components. This function is based on the interconnection of many hooks with the corresponding loops, leading to an effective "binding." Supramolecular polymers feature a kind of molecular hook-and-loop fastener because of their reversible supramolecular interactions (e.g., hydrogen bonds, metal–ligand interactions, and host–guest interactions). These materials offer great opportunities for the design of smart materials (e.g., stimuli-responsive materials) [1–4] or even self-healing materials, as a result of their non-covalent secondary interactions within the polymeric structure [5, 6].

All those interactions feature a dynamic character, which is essential in the design of self-healing materials [7, 8]. The self-healing mechanism of supramolecular polymers is based on the re-association of non-covalent interactions and clusters, or on the stimuli-responsive opening and closing of the supramolecular binding unit, depending on the binding strength of the utilized interaction (Fig. 1).

To achieve a healing response, a sufficient level of chain dynamics is required to enable mobility of the supramolecular motifs within the bulk material [9], which is related to the time required to renew the chain conformation under unstrained conditions and to reestablish the equilibrium [10, 11]. Thus, motion of the whole polymer chain is controlled by the lifetime and concentration of supramolecular tie points. However, the polymer chains can also diffuse at timescales longer than the lifetime of the supramolecular interactions [12, 13].

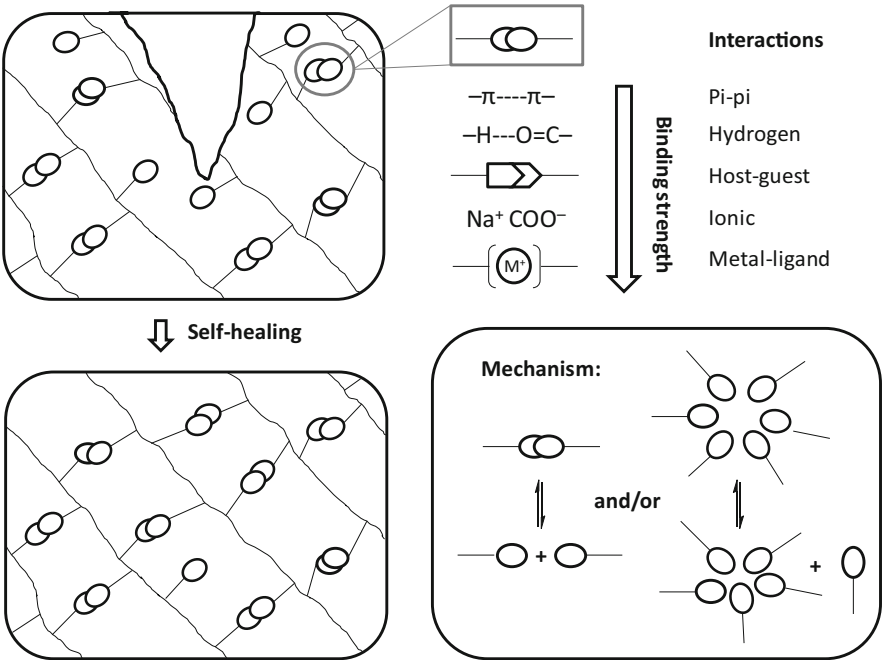

Fig. 1 *Left*: Scheme of the self-healing process. *Top right*: Supramolecular interactions ordered by their binding strength. *Bottom right*: Proposed self-healing mechanism of supramolecular polymers based on either cluster formation and/or stimuli-responsive opening of the non-covalent binding unit

Strong supramolecular interactions are associated with a high binding constant and are comparable to covalent bonds. In analogy to dynamic covalent bonds (e.g., Diels–Alder units) [14–16], the self-healing mechanism is not solely based on the presence of residual supramolecular binding after mechanical damage.

The first accidental approach towards self-healing of supramolecular polymers is already over 25 years old [17–20] and relies on the use of weak stickers (urazole moieties) affixed onto butadiene polymers, leading to reversible, sticky moieties within a thermoplastic material. Without being intentional, such supramolecular polymers display intrinsic self-healing properties, as demonstrated by their viscoelastic properties [18] and the resulting chain dynamics – an idea taken up later in the intentional design of rubbers with self-healing properties [21]. A second (old) concept is based on ionic clusters embedded in the polymeric matrix to achieve dynamic properties via ionic clusters formed according to the Eisenberg–Moore–Hird model [22], resulting in self-healing ionomers. In a similar manner, ureidopyrimidone (UPy) units affixed onto terminal functionalized monomers and bound by strong self-dimerization with four cooperative hydrogen bonds, lead to significant improvement in material properties as a result of the additional non-covalent crosslinks and, thus, can introduce dynamic properties into a thermoplastic material [23].

This chapter presents different supramolecular polymer classes, set apart by the nature of their non-covalent interactions, that have been used for the design of self-

healing materials. We focus on the following supramolecular interactions: Hydrogen bonds, π–π interactions, ionic interactions, metal–ligand interactions, and host–guest recognition. In this context, the state of the art for each class of polymers is summarized in detail.

2 Hydrogen-Bonded Supramolecular Self-Healing

2.1 Hydrogen Bonding Interactions and Their Principal Role in Self-Healing Polymers

Supramolecular self-healing concepts offer the possibility to create self-healing materials that can heal local damage multiple times. Hydrogen bonding interactions in particular play a key role because of their highly dynamic nature and responsiveness to external stimuli, in combination with a tunable and directed association strength [24]. Accordingly, supramolecular polymers with incorporated hydrogen bonding moieties are at the front line for industrial applications. A selection of different hydrogen bonding moieties used to induce self-healing are highlighted in Fig. 2.

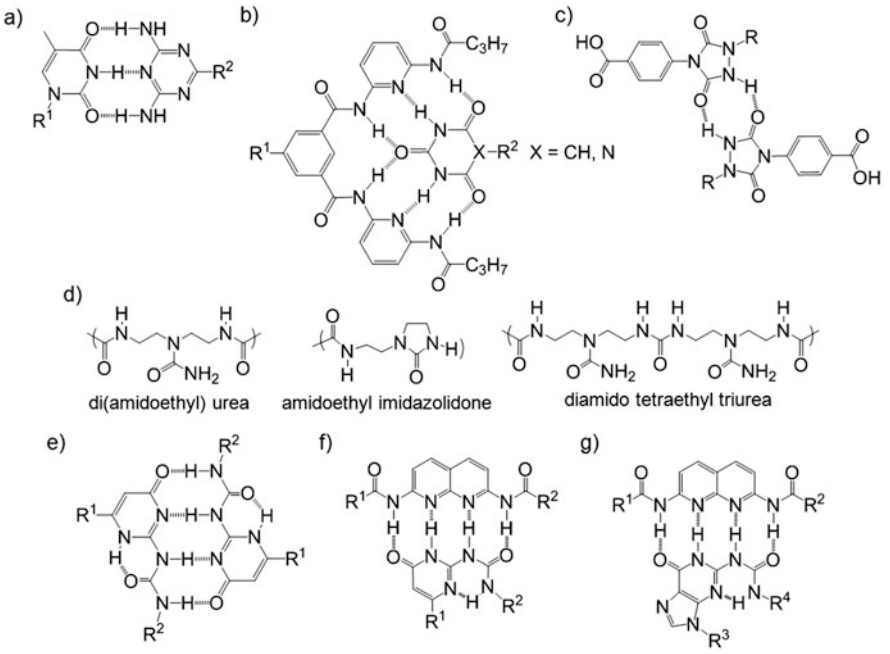

Fig. 2 Hydrogen bonding moieties useful for incorporating of self-healing properties into polymers: (**a**) Thymine (THY) and diaminotriazine (DAT), (**b**) Hamilton wedge and cyanuric/barbituric acid wedge, (**c**) two phenyl urazole acids, (**d**) components forming a self-healing rubber, (**e**) ureidopyrimidones (UPy), (**f**) UPy and 2,7-diamido-1,8-naphthyridine (DAN), and (**g**) DAN and ureido-7-deazaguanine (DeUG)

Thus, a large structural variety of hydrogen bonding moieties exists, which allows tuning of the stability/lability and, therefore, of the inherent dynamics of hydrogen-bonded polymers. However, self-healing is not only determined by the absolute strength of the applied hydrogen bonds [25], but also by phase segregation effects between the polymeric interphases [26, 27]. The strength of hydrogen bonds in the solid and melt states of polymers is generally not known and is certainly different from the values known from polymer solutions. Even "weak" bonds in solution can exert a significant effect on self-healing, whereas "strong" bonds often display no or retarded self-healing effects. Thus, nanophase separation between hard and soft domains within a copolymer or composite material, or the crystallization or clustering of introduced supramolecular moieties, can introduce a self-healing response based on the autonomous rearrangement between hard and soft phases after a damage event.

A representative example of these effects can be seen by comparing association constants within the well-investigated THY–DAT trivalent hydrogen bonding system (Fig. 2a). The possible modes of aggregation for the supramolecular groups A (DAT) and B (THY) in solution and in the melt are schematically illustrated in Fig. 3.

In solution, the THY–DAT interaction is usually stronger than the self-association of each building unit with itself (i.e. dimerization), resulting in specific a interaction according to the lock-and-key model [$K_{\mathrm{dim1}} \approx K_{\mathrm{dim2}} \ll K_{\mathrm{assn.}}$, K_{dim1}

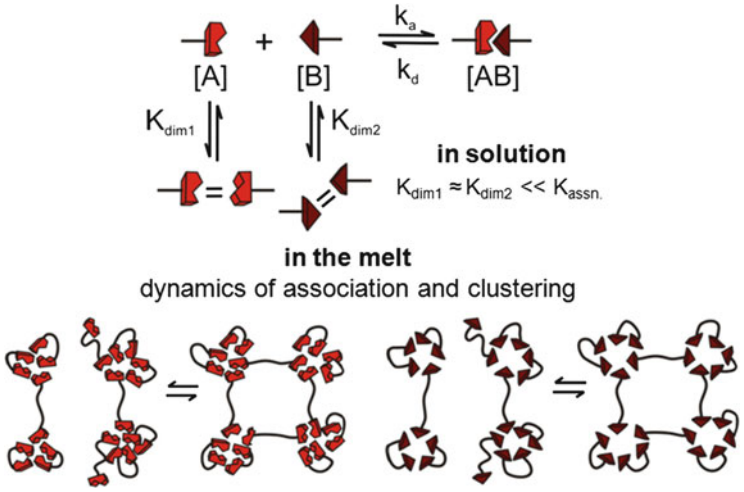

Fig. 3 Possible modes of aggregation for supramolecular groups *A* and *B* in solution and in the melt. Figure reprinted and adopted from [28] with permission from The Royal Society of Chemistry (Copyright 2012)

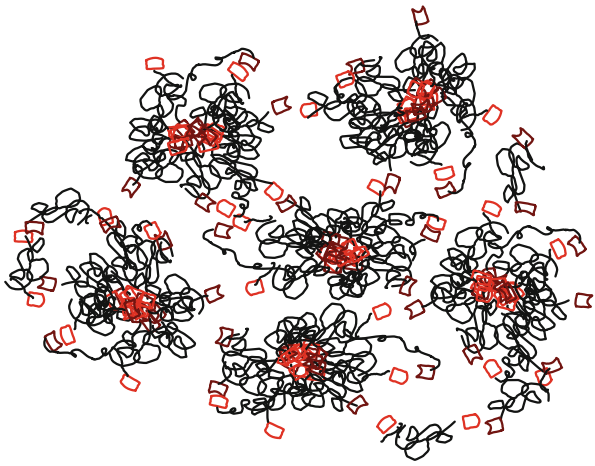

Fig. 4 Crosslinked supramolecular micelles composed of bivalent THY- and DAT-telechelic PIBs. Figure reprinted and adopted with permission from [26] (Copyright (2014) American Chemical Society)

(THY–THY) = 70 ± 14 M^{-1}, K_{dim2} (DAT–DAT) = 22 ± 7 M^{-1}, $K_{assn.}$ (THY–DAT) = 2.6 ± 1.3 × 10^3 M^{-1}]. In contrast, in the molten state (e.g., the same polymer system without any solvent) the dynamics of association and, therefore, the clustering of complementary hydrogen bonding units, often overrides a simple AB interaction, resulting in self-aggregation of DAT–DAT units or THY–THY units comparable to that of the THY–DAT system in solution [25].

Thus, combined and detailed rheology and small-angle X-ray scattering (SAXS) investigations of polymer blends composed of bivalent THY- and DAT-telechelic poly(isobutylene)s (PIBs) revealed the formation of a supramolecular network of supramolecular crosslinked disordered micelles (Fig. 4). The formation of linear supramolecular chains followed by entanglement or the presence of ordered micellar structures could be clearly excluded [26].

Inspired by the design of self-healing polymers with exchangeable and therefore weak covalent bonds [29, 30], hybrid computational models [31–33] have been applied to predict the influence of the fraction of permanent and labile bonds, in turn simulating the mechanism of strain recovery. Thus, a competitive effect between the extent and the rate of strain recovery was proven via calculations. For an increasing labile bond energy, related to the increased time scale required for strain recovery, a tougher material with improved mechanical properties was obtained. In contrast, an increasing amount of permanent bonds provided better and faster strain recovery after exposure to several stretch–relaxation cycles. The incorporation of a small fraction of labile bonds (20–30%) resulted in a significant improvement in tensile strength, while at the same time creating an additional self-healing response after tensile deformation. Thus, labile bonds acted as sacrificial species while dissipating the energy emerging from a rupture event by structural rearrangements and preserving the overall mechanical integrity [30, 34].

2.2 Fatty Acid-Based Formation of Thermoplastic Elastomers

Thermoreversible supramolecular polymers with a low glass transition temperature (T_g) have been formed by hydrogen bonding interactions between polyamide oligomers prepared from fatty diacids treated with sulfonyl isocyanate and ethylenediamine [35]. The obtained thermoplastic elastomers (s) exhibited a high rubbery plateau and the introduced rubber elasticity resulted in 88% recovery of the tensile strength after keeping reassembled samples at 50 °C for 18 h [35].

In a very similar manner, poly(dimethyl siloxane) (PDMS)-based supramolecular elastomers associated via multiple hydrogen bonding interactions and therefore showing a low temperature self-healing response have been prepared. The rubber-like elastic behavior allowed imposed formations to recover within seconds after releasing the stress [36]. The preparation of a soft supramolecular rubber [37–40] by condensing diethylene triamine and urea with a mixture of multiply functionalized fatty acids (Fig. 2d) has also been reported. The degree of branching was controlled by the choice of fatty acids and by adjusting their ratio. Thus, complementary hydrogen bonding units were incorporated in the resulting oligomeric material, plasticized with dodecane (11 wt%) to lower its (T_g) to 8 °C. Complete self-healing of cut pieces was observed within 3 h at room temperature. The maximum waiting time for keeping cut samples apart from each other before allowing self-healing was 48 h at 48 °C [37], but healing was completely suppressed by annealing at 90 °C as a result of equilibrating hydrogen bonding moieties [41]. Consequently, the required healing time related to the re-association of hydrogen bonding interactions strongly depends on the mobility of the whole polymer backbone, as reorganization over a larger length scale within the bulk material is required [41]. Furthermore, the strength required to separate a formerly cracked and subsequently healed surface was significantly higher than for a purely melt-pressed sample, presumably because of its enhanced self-adhesive strength [41]. Various rheological and NMR investigations proved that this rubber behaves like a nanophase-separated system consisting of a less mobile part (85%) with a T_g just below room temperature (corresponding to ongoing mechanical relaxation) and a more mobile part (15%). It was found that irreversible (chemical) crosslinking occurred above 110 °C, resulting in an aging effect and, therefore, in weakening of the self-healing ability [42].

2.3 Hydrogen Bonding Interactions Between Nucleobase Analogs and Tailor-Made Hydrogen Bonding Wedges

Several supramolecular polymers based on hydrogen bonding interactions between nucleobases and their analogs and tailor-made hydrogen bonding wedges have been described [25, 43–51]. The self-healing mechanism is often supported by a second

principle such as phase segregation phenomena or a second supramolecular interaction (e.g., π–π interactions) [26, 28, 52–56].

Self-healing polymers based on weak hydrogen bonding interactions were accomplished by the synthesis of bivalent PIBs functionalized with barbituric acid moieties and a Hamilton wedge [28] (Fig. 2b) and investigated via temperature-dependent melt rheology. The formation of dynamic supramolecular junction points was confirmed by rheological investigations showing terminal flow at low frequencies but a rubbery plateau zone at high frequencies. The occurrence of aggregation could be confirmed by small angle X-ray scattering (SAXS) measurements [26, 28]. Thus, strong and tough self-healing supramolecular polymers with an increased thermal stability were observed for barbituric acid telechelic PIBs, although their dimerization is very weak in solution (Fig. 5a). The self-healing behavior was related to thermoreversible formation of larger aggregates enhanced by microphase separation between the polar hydrogen bonding synthons and the nonpolar PIB backbone. Interestingly, the molar mass of the investigated polymers barely had an effect on the supramolecular bond lifetime or on the temperature-dependent viscosity behavior. Consequently, freshly cut pieces of PIBs modified with barbituric acid groups were completely healed within 48 h, suggesting application as a room temperature self-healing material (Fig. 5b). In contrast, PIBs bearing Hamilton wedges and barbituric acid moieties behaved like brittle rubbers. Consequently, terminal flow was only observed at temperatures above 100 °C [28].

This approach was extended to four-arm star-shaped polymers functionalized with thymine moieties to investigate the influence of polymer architecture on the strength of the supramolecular interaction and the subsequent self-healing performance, while keeping the density of supramolecular moieties approximately constant (Fig. 6) [56]. Although thymine motifs display an even lower dimerization tendency than barbiturate moieties in solution, neat four-arm star thymine-telechelic PIB behaved like a tough rubber with a prominent rubbery plateau at room temperature. In comparison with bivalent barbiturate-telechelic PIB, the observed plateau modulus (1.1×10^6 Pa) was higher, which was attributed to supramolecular cluster formation consisting of up to ten hydrogen bonding moieties, as demonstrated via SAXS investigations. Consequently, an increased supramolecular bond lifetime of $\tau_B = 67$ s was also observed. Self-healing occurred within 72 h at room temperature [56].

Four-arm star-shaped polymers have also been utilized for the preparation of interwoven network-structured self-healing materials, where the self-healing behavior is related to supramolecular clustering of hydrogen bonding moieties. These polymers are additionally reinforced by a covalent network formed via a CuAAC click reaction (Fig. 7). Hence, four-arm star-shaped polymers containing both thymine moieties and azide end groups have been prepared and crosslinked with a multivalent star-shaped alkyne-functionalized polymer [56].

Furthermore, the influence of the architecture on the dynamics of association and clustering, and therefore on the self-healing of supramolecular hydrogen-bonded polymers, was also investigated by preparing structurally simple supramolecular

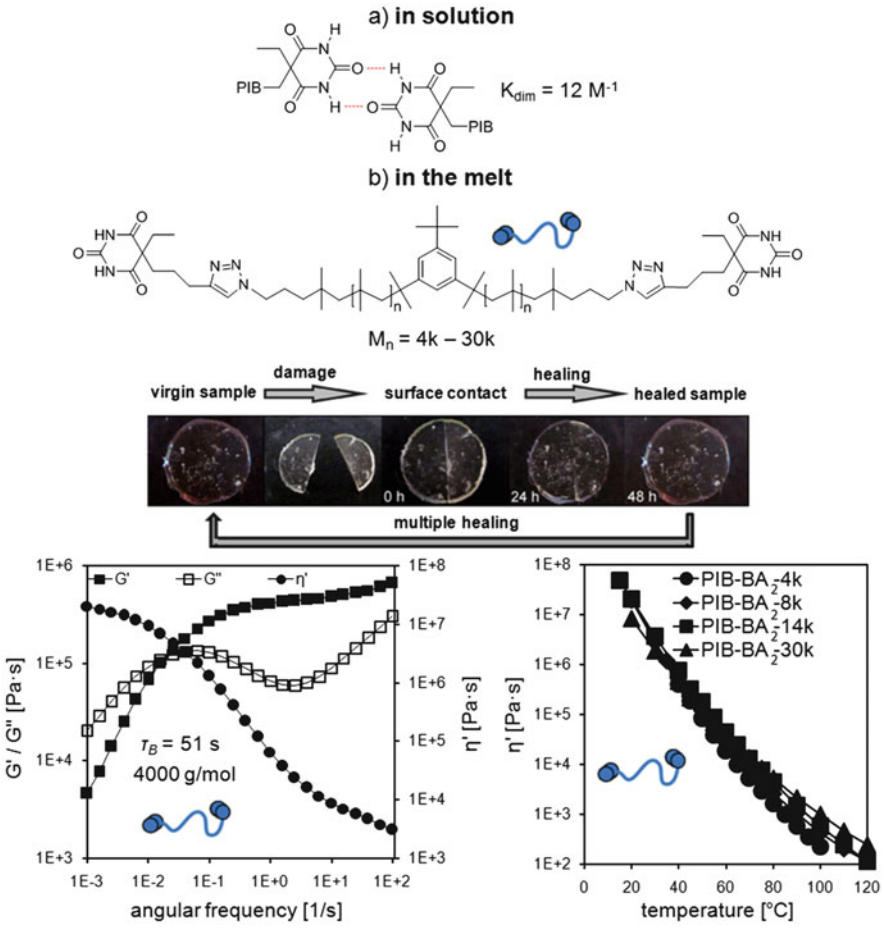

Fig. 5 (**a**) Dimerization of two PIB chains functionalized with barbiturate moieties (in solution: $K_{dim} = 12\ M^{-1}$). (**b**) Bivalent barbiturate-telechelic PIBs with molar masses of 4,000 – 30,000 g/mol show a self-healing response at room temperature as a result of formation of supramolecular clusters containing polar barbiturate moieties. The supramolecular bond lifetime for a bivalent barbiturate-telechelic PIB with a molar mass of 4,000 g/mol is $\tau_B = 51$ s (*bottom left*). The viscosity is unaffected by an increase in molar mass from 4,000 – 30,000 g/mol (*bottom right*). Figure reprinted and adopted from [28] with permission from The Royal Society of Chemistry (Copyright 2012)

PIB "graft" polymers with 1 mol% of a 4-pyridine substituted styrene monomer **1** (Fig. 8) [54]. Although, on average, less than one crosslinker per chain is present in PIB-**1** (2,800 g/mol), approximately two crosslinkers per chain were found in PIB-**1** (9,000 g/mol). Accordingly, only for polymers with a molar mass higher than 9,900 g/mol a formation of a rubbery plateau was observed related to weak supramolecular network formation as a result of the pyridine-N–H–N-pyridine bonds present (Fig. 8d). This was further proven by comparing the theoretical

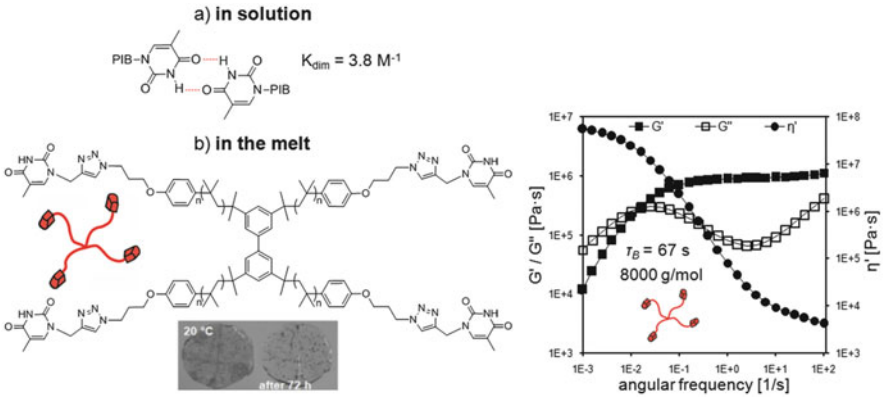

Fig. 6 (**a**) Dimerization of two PIB chains functionalized with thymine moieties (in solution: $K_{dim} = 3.8\ M^{-1}$). (**b**) Rheology of tetravalent star-shaped thymine-telechelic PIB with a molar mass of 8,000 g/mol and supramolecular bond lifetime of $\tau_B = 67$ s (right diagram) shows self-healing at room temperature. Figure reprinted and adopted with permission from [56] with permission from Elsevier Ltd. (Copyright 2015)

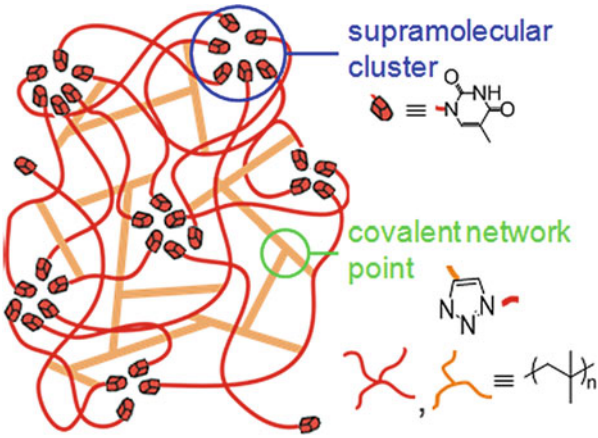

Fig. 7 Interwoven network structure composed of supramolecular clusters of thymine moieties and a covalent network created via a CuAAC click reaction between multivalent azide- and alkyne-functionalized star-shaped polymers. Figure reprinted and adopted from [9] with permission from Elsevier Ltd. (Copyright 2015)

segment length between two supramolecular crosslinking points ($M_{c\ theo}$) with the segment length determined via rheology measurements ($M_{c\ plat}$) [54].

The influence of molecular architecture on the self-healing behavior was probed by investigating V- and H-shaped supramolecular copolymers. For this purpose, a molecular design reminiscent of thermoplastic elastomers (TPEs) was utilized. Furthermore, the influence of the position of the hydrogen bonding moiety on the self-healing ability was investigated in detail (Fig. 9) [55]. Thus, a V-shaped

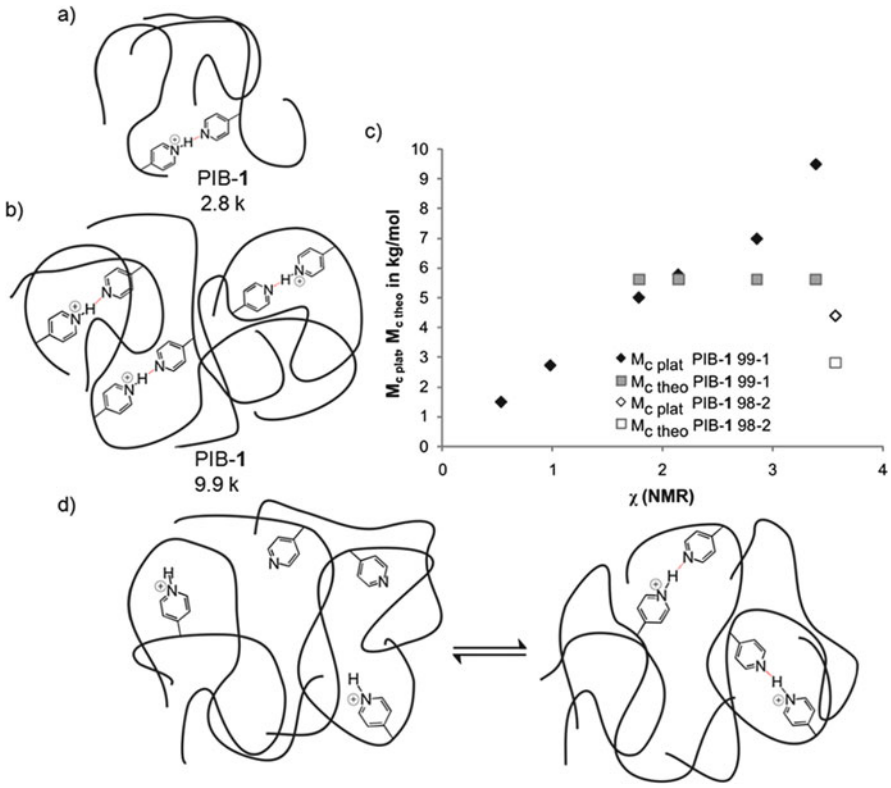

Fig. 8 PIB copolymers with 1 mol% of a 4-pyridine-substituted styrene monomer **1** with (**a**) molar mass of 2,800 g/mol (1.0% incorporation) or (**b**) molar mass of 9,900 g/mol (1.1% incorporation). (**c**) Comparison of the molar mass ($M_{c\ plat}$) between the incorporated supramolecular units **1** (determined via rheology measurements) and the theoretical segment length ($M_{c\ theo}$) between incorporated units **1** (determined via NMR investigations). χ is the number of comonomer **1** units per chain. (**d**) Equilibrium between aggregated/de-aggregated polymer chains. Figure reprinted and adopted from [54] with permission from John Wiley and Sons (Copyright 2012)

barbiturate-functionalized soft–hard–soft triblock copolymer, with the hydrogen bonding moiety located in the hard block to introduce an additional shape-persistence, was synthesized via reversible addition-fragmentation chain-transfer (RAFT) polymerization. The copolymer was blended with a complementary α,ω-Hamilton wedge telechelic isoprene to obtain an even more sophisticated polymer architecture. Both, the pure barbiturate-functionalized copolymer and the polymer blend showed a self-healing response at 30 °C, resulting in a 95% or 91% recovery of the original strain at break within 24 h, respectively. The V-shaped copolymer provided better mechanical properties as a result of the higher fraction of the hard block. These results demonstrate that polymer blends, fixed by matching hydrogen bonding moieties, can exert self-healing properties, which indicates a useful approach for tailoring material properties within a self-healing polymer [55].

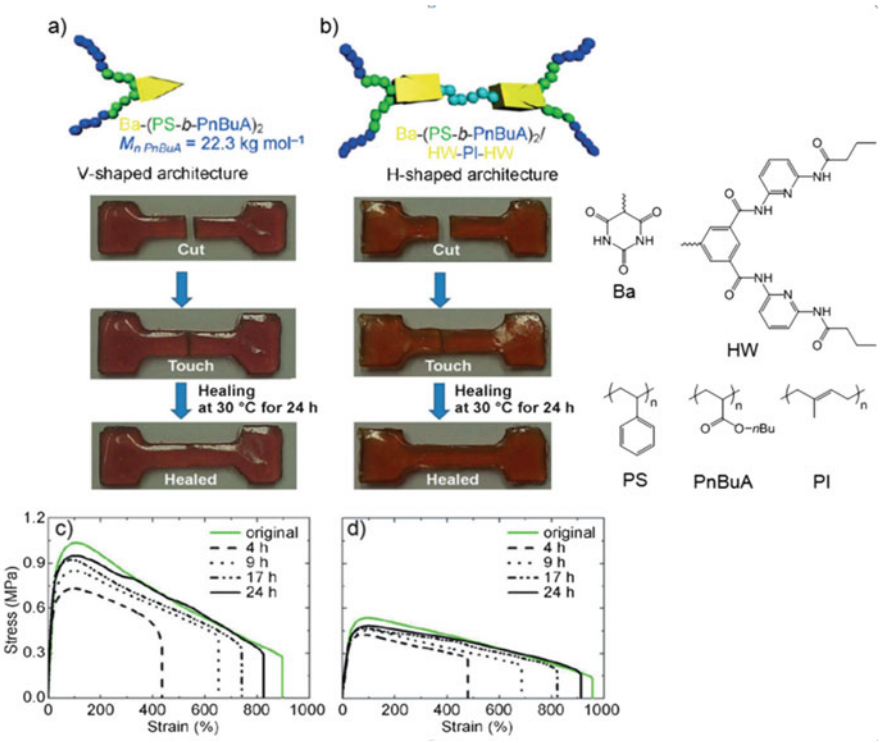

Fig. 9 (**a**) V-shaped barbiturate (Ba)-functionalized polymer blend (PS-*b*-PnBuA)$_2$ and (**b**) H-shaped polymer blends consisting of Ba-functionalized (PS-*b*-PnBuA)$_2$ and bivalent Hamilton-wedge (HW)-functionalized PI (2:1 blend) prepared via RAFT polymerization show self-healing at 30 °C within 24 h. (**c, d**) Tensile tests of pristine V-shaped Ba-functionalized (PS-*b*-PnBuA)$_2$ (**c**) and pristine H-shaped polymer blends consisting of Ba-functionalized (PS-*b*-PnBuA)$_2$ and bivalent HW-functionalized PI (**d**) after 4, 9, 17, and 24 h of self-healing. Figure reprinted and adopted from [55] with permission from John Wiley and Sons (Copyright 2015)

By investigating adenine-, thymine- and cytosine-modified low molar mass polyTHFs [52, 53] it was found that only the adenine- and the cytosine-terminated polymers demonstrated film- and fiber-forming capabilities as a result of hydrogen bonding interactions. As the supramolecular interactions presented are generally weak, it was assumed that a second driving force, namely π–π-stacking interactions of hard crystalline nucleobase chain ends in combination with phase segregation between the soft polymer backbone and the hard hydrogen bonding moieties, must have contributed to this self-assembly behavior [52, 53]. Applications of self-healing adenine-modified polyTHFs were reported, utilizing the temperature stability of the resulting supramolecular network structures up to 90–120 °C [53].

2.4 *Hydrogen Bonding Interactions Between Ureidopyrimidone Synthons*

Supramolecular polymers functionalized with ureidopyrimidone (UPy) moieties and their dynamic properties in solution have been intensely studied because of their high dimerization constant ($CHCl_3$, $K_{dim} = 10^6\ M^{-1}$) [57, 58]. Consequently, the generation of supramolecular polymers, polymer networks, or polymeric nanoparticles have been investigated in the bulk phase [59]. Furthermore, self-healable polymers as well as supramolecular rubbers based on UPy hydrogen bonding interactions have been commercialized under the trade names SupraB™ and Kraton® by SupraPolixBV [24, 60].

Thus, the phase separation of bivalent UPy-telechelic PEG (Fig. 10) in hydrophobic hydrogen bonding domains consisting of UPy moieties and the PEG backbone resulted in the formation of solid-like hydrogels. Self-healing of these materials was observed at 50 °C when the initial properties switched to those of a viscous liquid [61, 62].

The formation of supramolecular hydrogen-bonded polymer networks between trivalent UPy-functionalized PPE-PEO block copolymers and bivalent UPy-modified PDMS has been reported [23]. The resulting supramolecular crosslinked materials behaved similarly to entangled linear polymers. Both, gel formation in solution and crystallization in the bulk phase were observed as a result of the directionality of the supramolecular interactions [23]. Thus, UPy-telechelic PDMS formed TPEs with a rubbery plateau and a high activation enthalpy for stress relaxation [63, 64] caused by lateral stacking of UPy dimers additionally reinforced by π–π interactions. The observed aggregation behavior leading to assembly of spherical aggregates or fibers was attributed to the incompatibility of the hard block consisting of microcrystalline domains of associated UPy dimers and the soft

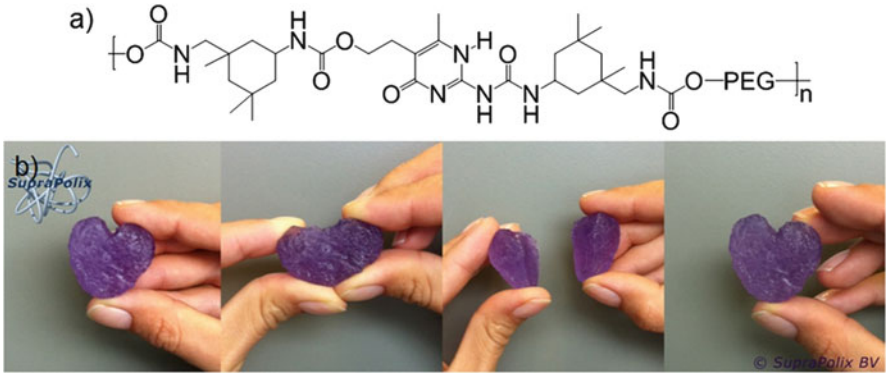

Fig. 10 (**a**) UPy-functionalized PEG. (**b**) Self-healing of an UPy-functionalized PEG heart (colored by adding a purple dye, 15 wt% in water): Initial heart shape was reestablished after pressing cut halves together. Figure reprinted and adopted from [61] with permission from SupraPolix BV and John Wiley and Sons (Copyright 2011)

PDMS backbone, leading to microphase separation [63, 64]. Similarly, UPy-telechelic poly(*n*-butyl acrylate) (P*n*BA), polystyrene (PS), and poly(butadiene) form micellar clusters of UPy aggregates in the solid state [65], comparable with observations for DAT/THY systems [25–27].

Investigations of crystalline UPy-modified poly(ethylene adipate) [66] showed that the self-healing performance depended on the junction unit between the polymer backbone and the hydrogen bonding moiety, proving the strong influence of even remote functional groups on the assembly of hydrogen bonds. Thus, self-healing at room temperature was observed for polymers containing hexamethylene linkers, related to slower recovery in crystallinity. In contrast, tolyl linkers allowed a faster recovery of crystallinity, while shifting the healing temperature above the melt temperature [66].

Bivalent UPy-telechelic perfluoropolyethers (PFPEs) [67] recovered their storage modulus within 2 min of shearing at 130 °C as a result of formation of hard crystalline UPy domains based on phase separation between the soft polymer backbone and the hydrogen bonding moieties. In contrast, PFPEs functionalized with alkylated UPy groups showed suppressed crystallization, resulting in an increased recovery time of the storage modulus of 18 min after shearing at 110 °C [67] (Fig. 11).

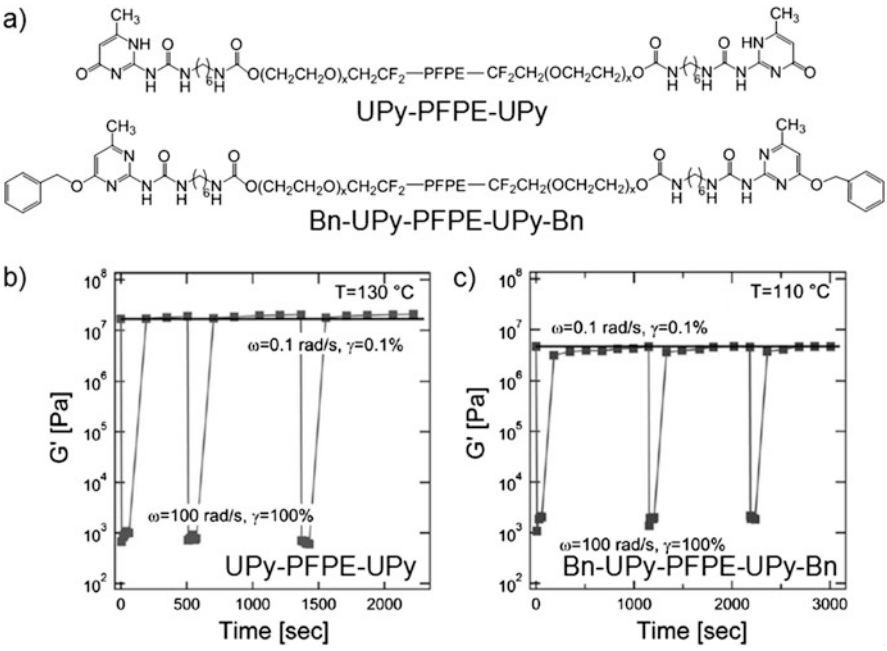

Fig. 11 (**a**) Structures of bivalent UPy-telechelic PFPE and bivalent Bn-UPy-telechelic PFPE. (**b**, **c**) Multiple deformation-recovery cycles of bivalent UPy-telechelic PFPE (**b**) and bivalent Bn-UPy-telechelic PFPE (**c**). Figure reprinted from [67] with permission from John Wiley and Sons (Copyright 2013)

In bivalent UPy-modified polycaprolactone (PCL), stacking of UPy dimers supported by hydrogen bonding interactions between urethane linker groups was observed, however, chain scission proceeded faster than reptation. The materials obtained showed a rubber plateau zone even at low frequencies and viscous flow as a result of supramolecular network formation [68]. In contrast, no rubbery plateau was observed for tri- and tetravalent UPy-urethane modified PCLs because the crystallization and stacking of UPy dimers was prevented by the polymer architecture, resulting in a too-short lifetime of the supramolecular network [69]. Similarly, large and bulky substituents interfered with supramolecular assembly due to steric hindrance [68].

By comparing copolymers composed of *n*-butyl acrylate (*n*BA) and an UPy-functionalized acrylate, acrylamidopyridine, acrylic acid, or carboxyethylacrylate [70], it was found that copolymers containing weak hydrogen bonding interactions behaved like un-entangled melts, with hydrogen bonding dynamics faster than rheological chain relaxation. In contrast, copolymers with strong hydrogen bonding interactions behaved like entangled polymer networks, resulting in soft and elastic solids. Flow activation energies increased linearly with increasing amount of hydrogen bonding moieties showing a dimer lifetime longer than 10 s [70]. Thus, copolymers prepared from poly(2-ethylhexyl methacrylate) and an UPy-modified methacrylate revealed an increase in complex viscosity as well as an increase and a lengthening of the plateau modulus with increasing UPy content [71]. Similar copolymers composed of *n*BA and UPy-functionalized acrylate (UPy content of 7.2%) showed a recovery of the self-adhesion strength of fractured surfaces up to 100% after a healing time of 50 h [72].

TPEs with a prominent plateau modulus and with bulk properties depending on the distance between stacked aggregates of UPy dimers were obtained by copolymerizing UPy-modified *n*BA with a Boc-protected amine-functionalized monomer [73]. With increasing UPy content, a linear increase in the plateau modulus was observed. The effective bond lifetime of hydrogen-bonded aggregates increased, proving that every UPy side group was active within the network for UPy contents of 7 mol% or higher [73]. Similarly, the formation of soft rubbers or TPEs was observed for bivalent UPy-modified poly(ethylene butylene)s [74]; multifunctionalized poly(ethylene butylene)s carrying urethane, urea, and UPy groups [75, 76]; and UPy-functionalized amorphous polyesters [77].

UPy-functionalized poly(urethane)s [78] also found application as stress-sensing systems by incorporating spiropyran units into the polymer backbone, enabling stress-induced ring-opening that resulted in the merocyanine form, visualized by a color change. Furthermore, UPy-modified polymers able to dissipate strain energy were used to mimic the modular structure within titin, as the dissociation of hard UPy domains consisting of stacked dimers is similar to the unfolding process of sacrificial bonds in modular biomacromolecules [78]. Thus, a titin-mimicking modular polymer with high toughness and adaptive behavior, including self-healing ability, demonstrated full recovery of toughness and strength at 80 °C within 30 s [79].

2.5 Hydrogen Bonding Interactions Between Acid-, Phenyl Urazole Acid- or Phenyl Urazole-Functionalized Polymers

Urazole moieties belong to the first generation of investigated supramolecular moieties incorporating dynamic (thermoreversible) properties into bulk butadiene polymers [17–20, 80], thereby guiding the later design of self-healing rubbers [21, 81, 82]. Viscoelastic properties [80] and a self-healing response were introduced into a thermoplastic material by reversible association of weak urazole motifs, resulting in multiphased structures as a result of phase separation effects [83, 84]. As a consequence, time–temperature superposition of rheological data was impossible even for low concentrations of hydrogen bonding synthons [84], which was indicative of the strong effect of the few "weak" hydrogen bonds on the recovery of material properties after applied stress [85, 86]. As a result of the formation of hydrogen bonding interactions, related to hindrance of local flow processes, a broadening of the relaxation time up to seconds was observed. Furthermore, an increase in the activation enthalpy was attributed to an increasing degree of functionalization and, thus, to the formation of supramolecular clusters with higher stability [85–87].

4-Urazoylbenzoic acid-modified bivalent PIBs [19, 88] able to form hydrogen-bonded dimers revealed melting of ordered hydrogen bonding clusters at 110–120 °C. Within this temperature range a transition from elastic to viscous behavior was observed, related to the reorientation and breaking of ordered supramolecular clusters into disordered multiplets of associated hydrogen bonding chains. As expected, the time–temperature superposition failed and stress relaxation within the polymer was attributed to the relaxation of multiplets and deformation of supramolecular clusters [19, 88].

2.6 Bis(urea)-Based Hydrogen Bonding Interactions

Urea-based hydrogen bonds are one of the simplest systems for introducing dynamic properties into a polymer, as the synthesis only requires a reaction between isocyanate and amine building blocks, which are widely available in polymer technology.

Thus, P*n*BAs functionalized with a bis(urea) group in the middle showed viscoelastic properties. The viscosity increased with decreasing molar mass up to 20,000 g/mol, which was attributed to hydrogen bonding interactions completely determining the rheological properties. In contrast, for functionalized P*n*BAs with a molar mass higher than 20,000 g/mol, the polymers behaved almost like unfunctionalized high molar mass P*n*BAs. Their rheology was controlled by polymer dynamics, while incorporated supramolecular binding motifs simply increased the terminal relaxation time as a result of hydrogen bonding interactions [89].

Similarly, PDMS grafted with bis(urea) moieties formed TPEs as a result of supramolecular crosslinking related to (partial) self-organization of incorporated bis(urea) units in crystal-like domains [90]. Investigations of poly(urethane)-based TPEs containing a soft poly(ethylene-*co*-butylene) middle block [91] showed that an increase in microphase separation in the bulk led to an increased hydrogen bonding potential. Thus, an increase in the scattering intensity in SAXS experiments and an increase in the storage modulus were observed when the end group changed in the order dibutyl < morpholine < diol [91]. Polyurea-urethanes with triuret blocks displayed a crosslinked structure at room temperature as a result of hydrogen bonding interactions, whereas de-crosslinking was observed between 105 and 135 °C [92]. In contrast, tetrauret block-containing polyurea-urethanes resulted in a folded structure as a result of the zigzag conformation, with a higher thermal stability up to 170–190 °C [92].

Single- or double-stranded structures were also observed for self-healing supramolecular silicones prepared by crosslinking of tris(urea)-modified PDMS with hydrazine units [93] via sextuple hydrogen bonding interactions. These materials revealed a self-healing ability when cut films were reassembled immediately, whereas no self-healing behavior was observed after keeping cut surfaces apart for more than 10 min as a result of equilibrating and reassembling of hydrogen bonding moieties [93].

Low molar mass bis(urea) moieties as well as PIBs containing bis(urea) functionalities within the polymer backbone formed comb-shaped supramolecular assemblies at room temperature, resulting in the formation of filaments or tubes. The length of the tubes could be tuned by varying the concentration and/or the solvent [94, 95]. The supramolecular association present strongly influences the bulk properties and, therefore, the self-healing ability within the bulk material could be estimated as a result of the dissipative nature upon deformation [95, 96]. The investigated polymers showed a self-organization behavior over a timescale of days, resulting in viscoelastic soft gels at room temperature, which disrupted at 80 °C but retrieved their structure after 20 h of annealing, highlighting their potential as dissipative soft adhesives and self-healing materials [96].

Similarly, low molar mass *N*,*N*′-disubstituted ureas formed supramolecular polymers comparable to high molar mass poly(urethane)s and behaved like organogels, showing viscoelastic properties and a relaxation time of several seconds [97–99].

2.7 *Hydrogen Bonding Interactions Between 2,7-Diamido-1,8-naphthyridine Synthons and Ureidopyrimidone, Ureido-7-deazaguanine, or the Butylurea of Guanosine*

By investigating 2,7-diamido-1,8-naphthyridine (DAN) and UPy end-functionalized P*n*BAs and poly(benzyl methacrylate)s it was found that the phase behavior and microstructure in the bulk were controlled by hydrogen bonding interactions [100]

as well as by temperature changes, directly influencing the compatibility of the phases [101]. Thus, UPy dimerization led to compatibilization, whereas complementary hydrogen bonding interactions resulted in significant reduction in macroscopic phase separation [100] and in the formation of supramolecular diblock copolymers [101] or graft polymers [102].

Supramolecular alternating copolymers were formed by hydrogen bonding interactions between a 1:1 mixture of a bis-UPy-functionalized polyTHF and a bis-DAN-functionalized low molar mass linker [103]. By increasing the bis-DAN linker content, the virtual degree of polymerization decreased because the bis-DAN linker acted as a chain stopper [103]. Accordingly, the concentration dependence of the virtual degree of polymerization and, thus, the chain length can be blocked in a defined concentration range by the use of chain stoppers, which enables conclusions to be drawn about the hydrogen bonding interaction corrected for concentration effects [104–106]. In contrast, in the case of weaker hydrogen bonding interactions in urea-modified polyether polyols, no break-up of the supramolecular assembly was observed because the polymer ends were incorporated in the microphase-separated hydrogen bonding arrays, resulting in the formation of phase-separated TPEs [107].

The hydrogen bonding interactions between ureido-7-deazaguanine (DeUG) and DAN as well as between the butylurea of guanosine (UG) and DAN have been intensely studied in solution [108–112]. It was found that DAN revealed a redox-responsive behavior and, therefore, a chemically and electrochemically switchable high affinity for DeUG in its reduced form and a low affinity for the oxidized form of DeUG. This characteristic might be interesting and applicable for tailoring self-healing applications, because the on–off switch ability has already found use in the control of supramolecular network formation [113].

3 Self-Healing by π–π Stacking Interactions

π–π stacking interactions in non-hydrophilic environments are among the most important supramolecular interactions, although rated significantly weaker in strength than hydrogen bonds or ionic interactions [114]. Usually, association constants for simple π–π systems are ~10^2 M^{-1}, with some values just exceeding 10^3 M^{-1} [115]. Basically, the conventional π–π stacking systems of, for example, pure aromatic rings are too weak to enable a significant healing effect and, thus, are not suitable (e.g., PS is not a self-healing polymer below its T_g). A literature study revealed the use of multivalent "stacked" or chain-folded π-systems (Fig. 12) as significantly more stable supramolecular systems. Thus, careful molecular design of π–π-stacking [117] (Table 1, entry 1), mostly induced via the formation of stacked charge-transfer structures, can lead to significantly enhanced association constants, even reaching association constants ranging from ~11,000 M^{-1} [118] to ~100,000 M^{-1} (Fig. 12c) [116, 119]. Thus, the use of multivalent electron-deficient naphthalene diimide units in a polymer chain, together with suitably planned

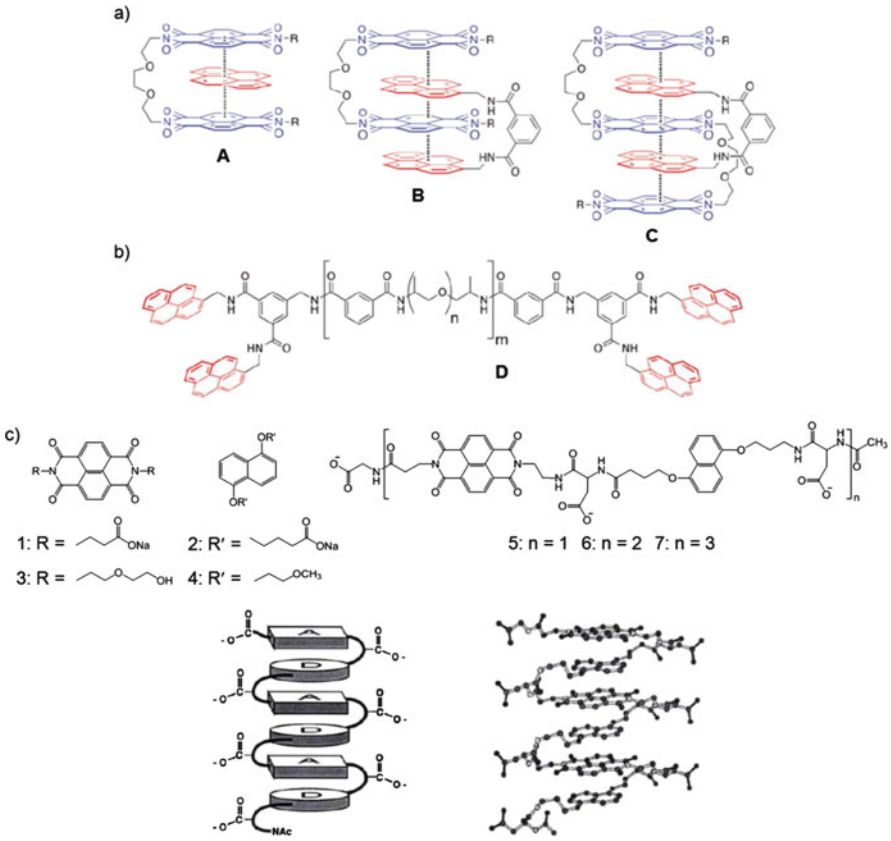

Fig. 12 (**a**) Examples of π–π complexes *A*–*C* formed between naphthalene diimide oligomers (*blue*) and pyrene or a tweezer-type pyrene-derivative (*red*) containing two to four face-to-face π–π stacking interactions. K_a values are 130, 3.50×10^3, and 11.0×10^3 M^{-1} for π–π complexes A, B, and C, respectively. (**b**) Structure of a bis-tweezer-type pyrene-end-capped polyamide D. (**c**) 1,5-Dialkoxynaphthalenes and 1,4,5,8-naphthalenetetracarboxylic diimides as aromatic donor and acceptor units. A pleated secondary structural element based on donor–acceptor interactions is formed: schematic representation (*bottom left*) and computer-generated representation (*bottom right*). Figure reprinted and adopted with permission from [116] (Copyright (2011) American Chemical Society) and from [117] (Copyright 1995, Rights Managed by Nature Publishing Group)

tweezer-like electron-rich bipyrenyl end groups (Table 1, entries 2, 3, and 5–9) can lead to strongly enhanced binding constants, additionally supported by the formation of hydrogen bonding interactions between the amide groups of the naphthalene diimide-modified acceptors and the carbonyl groups of the pyrenyl-functionalized donors (Fig. 12a, b) [118–125, 127].

The reversibility [134] of such supramolecular bonds can enable the design of a reversible healing system that is able to heal after overcoming the required activation energies, in turn achieving reorganization of (polymer) chains and resulting in healing. A significant number of different self-healing systems at elevated

Table 1 Summary of π–π stacking interactions utilized for the design of self-healing

Entry number	Donor (D) moiety	Acceptor (A) moiety	Polymer	Healing temperature/ °C	References
1	Dialkoxynaphthalenes	Naphthalene tetracarboxylic diimides	–	–[a]	[117]
2	Pyrenyl/tweezer-type pyrenyl units	Naphthalene tetracarboxylic diimide units	–	–[a]	[118]
3	Pyrene-end-capped/bis-tweezer-type pyrene-end-capped	Naphthalene diimide units	D: polyamide A: PEO-PPO copolymer	140	[116]
4	Pyrenyl units	Naphthalene tetracarboxylic diimide units	PEO (all-in-one system)	–[a]	[119]
5	Tweezer-type pyrenyl units	Pyromellitimide units /4,4′-bi-phenylenedisulfone units/naphthalene tetracarboxylic diimide units	D: – A: macrocyclic ether-imide-sulfones	–[a]	[120]
6	Tweezer-type pyrenyl units	Pyromellitimide units/4,4′-bi-phenylenedisulfone units	D: – A: macrocyclic ether-imide-sulfones/poly (imide)s	–[a]	[121]
7	Tweezer-type pyrenyl units	Pyromellitimide units/4,4′-bi-phenylenedisulfone units	D: – A: poly(imide)s-	–[a]	[122]
8	Tweezer-type pyrenyl units	Pyromellitimide units/4,4′-bi-phenylenedisulfone units/naphthalene tetracarboxylic diimide units	D: – A: poly(imide)s	–[a]	[123]
9	Tweezer-type pyrenyl units	Pyromellitimide units/4,4′-bi-phenylenedisulfone units/naphthalene tetracarboxylic diimide units	D: – A: macrocyclic ether-imide-sulfones/poly (imide)s	–[a]	[124]
10	Pyrene-end-capped	Naphthalene tetracarboxylic diimide units	D: polysiloxane A: PEO	≈100	[125]
11	Pyrene-end-capped	Naphthalene tetracarboxylic diimide units	D: polyamide A: PEO-PPO copolymer	≥50	[126]

12	Pyrene-end-capped	Naphthalene tetracarboxylic diimide units	D: polybutadiene A: PEO-PPO copolymer	≈100	[127]
13	Pyrene-end-capped	Naphthalene tetracarboxylic diimide units	D: PEO A: PEO-PPO copolymer	75–100	[128, 129]
14	Pyrene-end-capped/perylene-end-capped	Naphthalene tetracarboxylic diimide units	D: PEO A: PEO-PPO copolymer	≥75	[130]
15	Pyrene-end-capped	Naphthalene diimide units	D: polyamide A: PEO-PPO copolymer + cellulose nanocrystalls	≥65	[131]
16	Pyrene-functionalized gold nanoparticles	Naphthalene diimide units	D: – A: PEO	–[a]	[132]
17	Pyrene-end-capped + pyrene-functionalized gold nanoparticles	Naphthalene diimide units	D: polyamide A: PEO-PPO copolymer	≈75	[133]

[a]No healing temperature reported

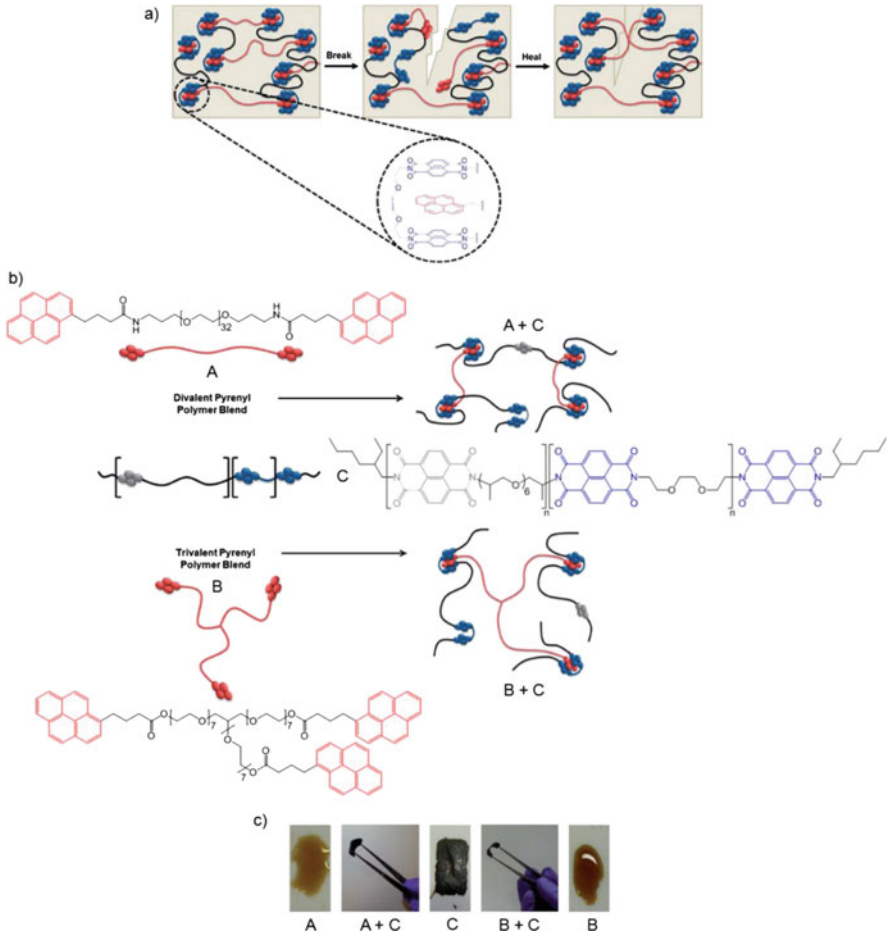

Fig. 13 (**a**) Complementary π–π stacking in polymer blends based on a π-electron-deficient naphthalene diimide unit (*blue*) and a π-electron-rich pyrenyl unit (*red*). In the case of a damage event, the π–π complex is disrupted and shows a self-healing response upon heating. (**b**) Formation of supramolecular polymer blends based on π–π stacking interactions between a π-electron-rich divalent or trivalent pyrenyl-terminated PEG (*red*, A or B) and a chain-folding naphthalene diimide-containing copolymer (*grey*/*blue*, C). (**c**) Polymer films of A, B and C and polymer blends of A + C and B + C cast from 2,2,2-trichlorethanol (dried at room temperature for 24 h, at 40 °C for 24 h and subsequently heated to 80 °C for 24 h). Figure reprinted from [128] with permission from The Royal Society of Chemistry (Copyright 2014)

temperatures (75 °C or above) have been designed, leading to reversible healing of polymer systems [116, 118–133, 135–140] (Fig. 13 and Table 1). Based on the suitable placement of the (multi)aromatic rings as well as on additional clustering effects of the aromatic units (segregating from the incompatible polymer chains) and the usually high activation barrier of (multi)aromatic interactions, healing of a polymeric material under high thermal loads can be achieved.

One of the first systems displaying self-healing via purely π–π stacking interactions was reported by the group of Hayes, relying on a relatively simple supramolecular blend containing naphthalene tetracarboxylic diimides and a pyrene molecule [125] (Table 1). PDMS polymers were utilized in these blends, which showed self-healing behavior at temperatures of ~115 °C (Table 1, entry 10). The concept was further extended to mixtures of two different polymers (Fig. 13 and Table 1, entries 11–13), where a multivalent poly(naphthalene tetracarboxylic diimide) polymer was mixed with bi- and trivalent pyrenyl-functionalized polymers [126–128], again displaying healing effects at elevated temperatures (200 °C, some starting at ~50 °C) [128]. In many of these examples, the tensile modulus recovered up to 95% of the initial value [127], also indicating the contribution of multivalency effects [128], leading to a higher tensile strength of the final material [130].

A significant contribution to self-healing using these naphthalene tetracarboxylic diimide/pyrene systems is also given by cluster formation. Clusters with a size of ~10 nm were detected via SAXS [128]. Presumably, self-healing is based on the cluster formation, because there is no direct linear correlation between the strength of the supramolecular interaction and the healing temperature or efficiency.

An extension of these systems towards self-healing nanocomposites was enabled by embedding cellulose nanocrystals with an aspect ratio of ~80 (Table 1, entry 15) [131] or Au nanoparticles (Table 1, entries 16 and 17) [132, 133] bearing pyrene functionalities on their surface. Whereas the cellulose whiskers served as a pure reinforcing element, the Au nanoparticles acted as an additional thermoresponsive element, facilitating healing by thermal activation. In both cases, percolating networks of the embedded filler systems were observed (cellulose whiskers at more than 10%) [131], together with the clustering effects of the Au nanoparticles (added amount 10–15%) [132, 133]. Although the addition of such large amounts of fillers led to a strongly reduced healing efficiency at the same temperature, presumably as a result of formation of percolated nanoparticle networks, which strongly reduced polymer dynamics and, thus, healing. Overall, despite the relatively simple concept, self-healing within π–π based systems takes place at comparable high temperatures (often more than 100 °C), placing the quest for still lower healing temperatures within the future prospects of development.

4 Self-Healing Ionomers

Compared with the relatively weak π–π-interactions and hydrogen bonds, ionic interactions show a higher aggregation strength. In general, ionomers are a subgroup of polymeric material that bear up to 15 mol% of ionic groups within the polymer. These groups can be distributed randomly as pendant groups or well-ordered in block copolymer-like architectures. They can also be located in the side chains or act as end groups [141]. The most common pendant ionic group for self-healing applications is a carboxylate group neutralized with sodium or zinc ions [142–145]. Unsaturated monomers containing carboxylate groups can be

polymerized via radical polymerization techniques. Afterwards, the unsaturated anions require neutralization with the desired metal counterion to provide the ionic character of the ionomers [146].

Compared with nonionic polymers, the introduction of ionic groups leads to significant changes in polymer properties (i.e. thermal and mechanical characteristics) as a result of new inter- and intramolecular interactions [147]. To explain these unique changes, several models of the inner structure of ionomers have been suggested. The multiplet-cluster model (Eisenberg–Hird–Moore or EHM model), which is briefly explained next, is one of the most accepted and reported models for how ionic groups influence the morphology of these materials [22]. In general, ionic groups (hydrophilic) show phase separation from the surrounding polymer matrix (hydrophobic) because of the low dielectric constant and the low T_g of the matrix [141, 148]. This phase separation leads to aggregation of a certain number of ion pairs, called multiplets, in which the ion pairs closely interact. On the one hand, electrostatic interactions of the ion pairs and, on the other hand, elastic forces of the attached polymer chains affect the formation of these multiplets as well as their size [22, 149]. A schematic representation of such a multiplet is depicted in Fig. 14 for a poly(styrene-*co*-sodium methacrylate) ionomer. The multiplet in the inner dashed

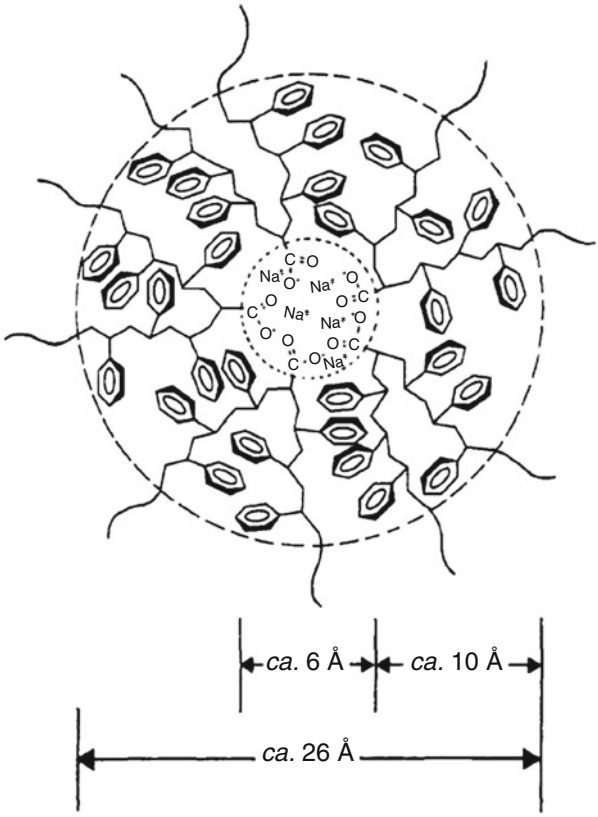

Fig. 14 Multiplet (*inner dashed circle*) surrounded by the region of restricted mobility (between *inner* and *outer dashed circles*), according to the multiplet-cluster model (reprinted with permission from [22])

circle is completely surrounded by the polymer matrix. These fixed points influence the region between the two dashed circles. Here, the polymer chains have reduced mobility compared with the outside, where the undisturbed polymer mobility is present. Furthermore, the multiplets can form clusters beyond a minimum ion concentration. Thereby, only the regions of restricted mobility overlap and, if the overlap is large enough, a phase-separated region is generated, which leads to an additional (higher) T_g of the material [22].

Besides this well-established concept, there are also publications that describe the behavior of ionomers in a different fashion [150–152]. Han and Williams used Fourier transform infrared (FTIR) spectroscopy to investigate poly(ethylene-*co*-methacrylic acid) copolymers (EMAA) containing several metal ions [153]. The authors proposed two different mechanisms for the formation of ionomers. The first mechanism is described by the existing multiplet-cluster model, which is only applicable for ionomers based on alkali and alkaline earth metals. Ionomers with transition metal ions can be described with the specific coordinated complex model. In this model the different coordination structures are considered.

As mentioned above, the ionic content significantly influences the properties of the polymer and also plays a key role in later self-healing applications. Tadano et al. investigated the thermal properties of ionomers (EMAA) and demonstrated that the ionic clusters undergo an order–disorder transition [148]. At room temperature three phases are present: ionic clusters, a crystalline domain (i.e. polyethylene), and an amorphous domain (Fig. 15). By increasing the temperature, the ordered character of the ionic cluster disappears at a certain temperature T_i. At this point, the disordered state is present. During further heating, the polyethylene crystals melt at the melting point T_m. After cooling from above T_m, the molten polyethylene recrystallizes at T_c. Further cooling to room temperature does not

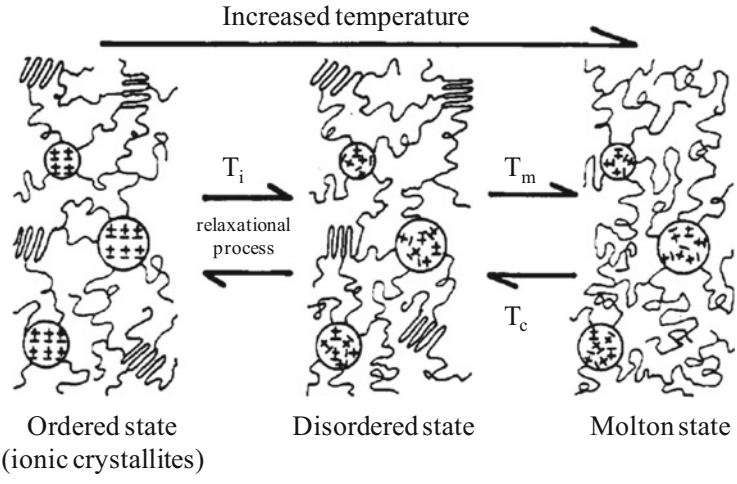

Fig. 15 Model of the order–disorder transition of clusters in ionomers and melting of the polyethylene domain during heating (reprinted with permission from [148])

result in any spontaneous transition of the ionic cluster. However, it was shown that re-formation of the ionic cluster takes approximately 38 days.

4.1 Self-Healing Under Ballistic Impact

Compared with nonionic polymers, ionomers have improved tensile strength, fracture resistance, toughness, and flexibility [8, 154]. The properties of the ionomers depend on their material structure, which is strongly influenced by the utilized ion pairs, the ion content (neutralization level), and the elastic behavior of the main chain [148, 153, 155].

Thermoplastic EMAA copolymers (Scheme 1) have been widely investigated for self-healing under ballistic impact [144, 145, 156–159]. Commercially available nonionic copolymers (Nucrel®) (http://www.dupont.com/products-and-services/plastics-polymers-resins/ethylene-copolymers/brands/nucrel-ethylene-acrylic-acid.html) and ionomers (Surlyn®) [26, 160] have mainly been investigated. The sodium ionomers differ in their neutralization levels (Surlyn 8940 with 30% and Surlyn 8920 with 60% neutralized acid groups). The ionomers provide excellent clarity, high toughness, and high stiffness, enabling a variety of different applications (e.g., food, cosmetics and medical device packaging, coatings for golf balls or ski boots) [161]. The self-healing behavior of these commercial materials has been tested in detail over the last two decades, equipped with the range of properties, knowledge about the materials, and their easy availability.

Fundamental work from both Fall and Kalista have shown the potential for self-healing after damage by high impact (i.e. ballistic penetration) [162, 163]. Thin films of EMAA materials were bombarded with projectiles, which completely passed through the material. After damage, the resulting hole closed very fast and only a small scar at the puncture site remained. These findings started several investigations on utilizing this unique self-healing capacity for healing layers in space vessels and navy aircraft fuel tanks or in medical applications [162, 164–166]. To optimize the self-healing ability, an understanding of the healing process including the mechanism is required. In the early state, the basic model describes the reversibility of the ionic interactions (i.e., physical crosslinks) as playing a key role in the ability to self-repair after a damage event. In addition, the free acid functions can form hydrogen bonds as a second form of reversible crosslink

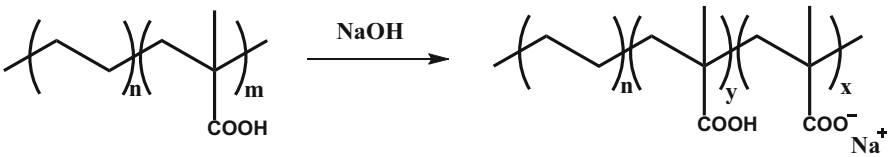

Scheme 1 Synthesis of the sodium ionomers of poly(ethylene-*co*-methacrylate acid) (EMAA) ($x + y = m$)

[146, 154, 167]. Kalista et al. investigated several ionomers and non-ionomers of EMAA and demonstrated that the ionic content does not correlate with the self-healing efficiency [168]. Nonionic EMAA polymers also showed self-healing behavior, whereas higher neutralized ionomers (e.g., Surlyn 8920) featured decreased self-healing capacity. Consequently, an alternative mechanism was proposed: hydrogen bonds present in nonionic Nucrel act as reversible crosslinks and enable self-healing properties [144, 146].

It has been proposed that a two-stage mechanism/healing process takes place after the projectile goes through the material [165, 168]. During impact, the material close to the bullet hole is heated to temperatures of approximately 92 °C (above the melting temperature) as a result of viscous dissipation [162]. This effect was also recently proven by Haase et al. using dynamic puncture tests [169]. After the projectile has passed through the material, the elastic properties of the materials cause a "flip back" of the polymer to the pre-impact position during the first stage. The molten polymer in the impact zone now has the possibility to rebound and close the hole. The subsequent slow second stage results in a completely sealed film through reorganization of the polymer chains (Fig. 16). Consequently, the unique combination of elastic rebound and viscous reflow of EMAA copolymers and other ionomers enables the self-healing response [159, 165, 168].

Further studies investigated different parameters of the ballistic and environmental conditions to learn more about the self-healing process and gain a deeper understanding of the underlying mechanism. Kalista et al. investigated the self-healing behavior after different damage types, including sawing, cutting, and nail puncture [165]. Cutting does not enable a later rebound of the two fragments. In contrast, the sawed samples featured self-healing properties as a result of the higher energy impact generated by frictional processes during sawing. Nevertheless, a higher energy impact is required to achieve effective self-healing behavior. Therefore, ballistic conditions were further investigated with respect to their thermal response and the so-initiated self-healing process. The self-healing capacities of ionomer films were tested over a range of temperatures. Heating the film reduced its

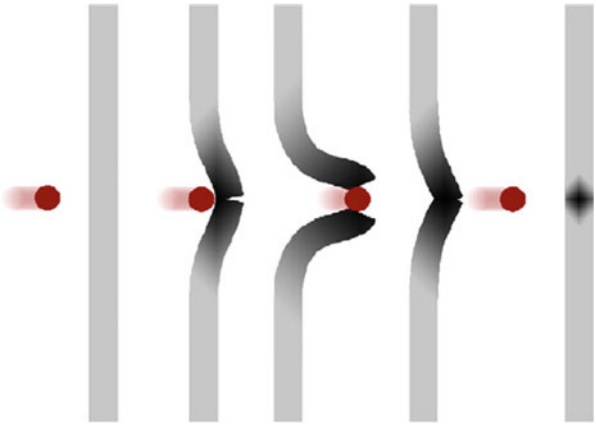

Fig. 16 Self-healing of ionomers after high-energy impact during ballistic penetration (reprinted with permission from [159])

elastic ability to return to its initial position after ballistic puncture. Thus, temperatures above 60 °C resulted in obstruction of the healing [144, 165]. To investigate the behavior of EMAA films at room temperature, Kalista et al. cooled the samples to 10, −10, and −30 °C, respectively. The authors found that self-healing is possible even at low temperatures. As a result of the two-stage mechanism, the local area around the puncture zone has to melt to achieve complete hole closure. Hence, a larger temperature rise is required for samples starting at −30 °C. Nucrel 925 was the only sample that did not heal at −30 °C, because of the formation of a brittle puncture zone resulting in a nonelastic behavior after ballistic penetration [165].

In 2008, Varley and van der Zwaag reported a new method for investigating the self-healing behavior of EMAA ionomers after ballistic treatment [159]. The method imitates the bombardment of a projectile by the utilization of a modified hydraulic tensile testing apparatus. Hereby, a disk-shaped object attached to a rod was pulled in a controlled manner out of the probe. Furthermore, the tool enabled quantitative information to be obtained about the healing process, because the damaging object is heatable and can be pulled at different velocities. The findings correlate with the proposed two-stage mechanism. Later, Varley and van der Zwaag intensively studied the ionomer Surlyn 8940 with this method [156, 167, 170]. In addition, the authors investigated the influence on the self-healing process of using different projectiles of varying size, weight, shape, and velocity. Self-healing behavior was achieved for all tested parameters. Although the impact morphologies showed differences depending on the projectile parameters, a similar healing mechanism was proven. Furthermore, the importance of the presence of ionic clusters and the resulting unique properties was demonstrated by comparison with other polymers such as linear low-density polyethylene and polypropylene. In addition, certain amounts of zinc stearate (a plasticizer) were added to the ionomers, which reduced the self-healing response after several healing cycles [156]. Additionally, aliphatic di- and tricarboxylic acid-based modifiers (oxalic acid, succinic acid, adipic acid, citric acid, and sebacic acid) and the corresponding amides of sodium-neutralized analogs were added to the ionomer blend (10 wt%). In situ mechanical evaluation illustrated that only the carboxylic acid derivates reduced the elastic properties and improved the elastomeric behavior, resulting in better healing [170]. Further work from Varley and van der Zwaag pointed out that the penetration of a bullet triggers three contiguous events in the ionomer: an initial elastic response, an inelastic response, and then pseudo-brittle failure [167].

Di Landro and coworkers analyzed the self-healing behavior of ionomers blended with semicrystalline poly(vinyl alcohol-*co*-ethylene) (EVA) or epoxidized natural rubber (ENR) (15–50 wt%) [171]. In general, the addition of EVA increases the stiffness whereas ENR reduces it. Ballistic puncture tests demonstrated that addition of up to 30% EVA still results in self-healing behavior. By increasing the amount to 50% EVA, the self-healing properties are reduced, resulting in incomplete repair of the damage as a result of the higher stiffness of the film. In contrast, the ENR blends in all investigated compositions show complete self-healing behavior. The authors assigned this finding to the same or improved crystallinity of the ionomer phase [171, 172]. It was further demonstrated that EMAA ionomers

neutralized with zinc ions (10%) and afterwards mixed with ENR did not show any self-healing property as a result of several crosslinks between the epoxy group of ENR and the EMAA ionomer, which reduced the molecular mobility [173]. Recently, different epoxidation levels of ENR (25 mol% and 50 mol% ENR) were investigated in blends with EMAA ionomers in different compositions. The studies revealed that the level of epoxidation in ENR has a significant influence on the self-healing properties of the resulting blends. Only blends with 50 mol% ENR achieved self-healing [145].

Recently, Kalista et al. tested a large number of nonionic copolymers of EMAA (Nucrel 925 and Nucrel 960) and ionomers (Surlyn 8940 and Surlyn 8920) using differential scanning calorimetry (DSC), dynamic mechanical analysis (DMA), FTIR, and rheological tests [144]. The ballistic puncture was tested at temperatures ranging from −50 to 140 °C. On the basis of these data, a comprehensive self-healing "phase diagram" was created showing the healing ability as a function of the degree of neutralization and of temperature. In general, 30% neutralized EMAA provided good healing up to the order–disorder transition ($T_i = 40$ °C); 60% neutralized EMAA showed improved healing above the melting temperature ($T_m = 90$ °C). A higher amount of crosslinks, resulting from a higher amount of ionic groups, resulted in stiffer materials and thus further decreased the self-healing ability. Increasing the temperature induced mobility and, thus, self-healing was possible. A higher ionic content was suitable for healing at higher temperatures, whereas a lower ionic content was beneficial for self-healing at lower temperatures. These findings suggest that hydrogen bonds additionally act as reversible crosslinks at low temperatures, whereas ionic clusters are the responsible reversible crosslinks at elevated temperatures.

Furthermore, the two-stage mechanism was extended by a subsequent third stage: the long-term reorganization of polymer chains, resulting in a stable polymer structure [144, 146]. To learn more about the last two stages of the mechanism, acoustic and ultrasonic time-dependent resonant spectroscopy (TSRS) was performed by Ricci and coworkers [174]. Two ionomers based on EMAA were measured from 1 kHz to 2 MHz before and after damage. This method facilitates the investigation of energy dissipation, relaxation, and morphology of self-healing ionomers. After the damage occurred, the self-healing process began immediately. During the second stage, the material is welded and finally sealed. Long after these visible events, TSRS proved the presence of quality factor variations in the resonance spectra resulting from energy dissipation instability (Surlyn 9840 7 h; Surlyn 9820 >18 h), which were ascribed to long-term reorganization within the polymer.

To evaluate ionomers for application in astronautics, hypervelocity ballistic tests of Surlyn 9840 were performed [175]. It was demonstrated that complete healing of 5-mm thick ionomer films damaged by impact at velocities of 2–4 km/s is possible. Furthermore, the self-healing ionomer was compared with thin-wall aluminum-alloy bumpers (AL-7075-T6) [176]. In general, the ionomers showed lower primary damage than aluminum. However, it was found that aluminum bumpers have better debris fragmentation abilities than ionomers. Furthermore, Sundaresan et al. demonstrated the healing ability of a composite material based on EMAA

and carbon fibers after medium-velocity impact and proposed their utilization for aerospace applications [177].

4.2 Self-Healing of Ionomers After Nonballistic Impact

As an alternative to ballistic high-energy impact puncture and instantaneous starting of the self-healing process, a handful of studies have reported self-healing based on different polymer structures or different testing procedures. Maure et al. generated a two-component system that included particles or fibers of an EMAA copolymer (Nucrel 2940) and carbon fiber laminates [178]. The melt of EMAA generated after heating to 150 °C for 30 min is able to flow into the damage zone and can act as the healing agent. Therefore, fractured surfaces were re-bound and initial properties were almost completely restored after heating. The same phenomenon was observed in systems made by adding EMAA to epoxy resins [179]. Furthermore, Pingkarawat et al. added EMAA copolymers to carbon fiber-epoxy laminates to investigate their influence on the material properties and self-repair capacity [180, 181]. On the one hand, the addition of EMAA improved the ability to heal delamination cracks after thermal treatment. On the other hand, the original toughness of the laminates was optimized.

James et al. designed a system (EMAA neutralized with zinc) in which the ionomer was utilized to restore piezoelectric properties [143]. For this purpose, zirconium titanate powder was dispersed within the ionomer. After the damage event, the mechanical properties and the lost piezoelectric properties could be repaired by thermal healing. Magnetically activated healing of ionomeric elastomers was recently investigated [182]. The self-healing effect was achieved by heat dissipation of the introduced magnetic nanoparticles and was studied with the help of tensile experiments. Almost full repair of the tensile strength after 10 min was possible using electromagnetic treatment. The material is potentially utilizable in hard-to-reach areas, because of the fast response and the non-contact healing properties of the system.

Mecerreyes and coworkers reported a new class of supramolecular ionic polymers based on compounds with multiple carboxyl or amine functions [183]. Rheological tests demonstrated a transition of the formed gel into a viscous liquid between 30 °C and 80 °C. Initial self-healing tests showed the ability of this material class to self-heal scratches on the surface or to re-bind two separated pieces during low energy impact. Furthermore, an ionic network formed by the combination of citric acid and different aliphatic diamines provided a network with unique rheological properties, which featured good self-healing potential [184]. Recently, the authors also expanded the new polymer class with various chemicals from renewable sources [185].

Bose et al. investigated an ionomeric elastomer with respect to the content of ionic groups and the influence of the utilized counterion [142]. The authors synthesized poly(butyl acrylate-*co*-acrylic acid)s with different compositions.

Neutralization with sodium, zinc, and cobalt resulted in a range of different ionomers. These materials were studied with temperature-dependent dynamic rheology combined with simultaneous FTIR analysis. An important parameter, supramolecular bond life (τ_b) (i.e. the time required for cleavage and re-bonding of reversible bonds), was thought to enclose the required parameters (i.e. dynamic character of the reversible interactions) for scratch healing, leading to a correlation between these two factors. A supramolecular bond life of 10–100 s is ideal to enable enough mobility of the polymer chains for ideal macroscopic healing. Recently, the same polymer architecture was utilized to investigate the influence of different amounts of cobalt salts (3, 5, and 7% cobalt) [186]. In this context, chain dynamics and relaxation lifetimes were calculated and compared with the macroscopic self-healing behavior of the cobalt ionomers. It was pointed out that the cluster activation determines the healing kinetics.

Although the EMAA copolymer and its ionomers have been well investigated, other ionomeric polymer classes receive less interest. New methods, such as ^{1}H low-field NMR measurements [187], for investigating self-healing ionomers with respect to their mechanical and self-healing behavior should yield a more detailed understanding of the mechanism. These results could provide evidence for structural changes in the polymer itself, which result in improved properties of the resulting material. Another strategy is to mimic processes found in nature, such as the self-healing achieved in human bones [188].

5 Self-Healing Metallopolymers

Compared with ionomers, which exhibit cluster formation of the ionic groups, the reversible character of metallopolymers can have a different origin. Besides the reversible non-covalent metal–ligand interactions, metallopolymers can also benefit from clusters generated from the metal ions and the corresponding counterion or simply as a result of phase separation [189]. Thus, metal–ligand interactions as crosslinks can imbue polymers with tunable mechanical and self-healing properties. An overview of the state of the art in metallopolymers is presented in Table 2.

In 2005, Varghese et al. demonstrated a self-healing hydrogel based on acryloyl-6-amino caproic acid (A6ACA) after treatment with a copper(II) chloride solution at ambient temperature [208]. After 12 h, 75% of the tensile strength was recovered. If the gel was added to an aqueous solution without the metal salt, no self-healing behavior was observed. This indicates that the self-healing process was mediated by the metal ions. Another metallogel was presented by Chen and coworkers [196]. The authors synthesized 2,6-bis(1,2,3-triazole-4-yl)pyridine (BTP)-containing polyurethanes via the copper(I)-catalyzed azide–alkyne 1,3-dipolar cycloaddition (CuAAC). The ligand BTP is incorporated in the polymer backbone and can be crosslinked with Zn^{2+}, Ni^{2+}, Fe^{2+}, and Ru^{2+} in a stoichiometry of 1:2 (metal to ligand). Furthermore, crosslinking with Eu^{3+} leads to 1:3 complexes. Gels

Table 2 Summary of ligand–metal systems utilized for the design of self-healing metallopolymer networks

Ligand system	Metal	References
Catechol	Fe^{3+}	[190, 191]
Histidine	Zn^{2+}	[192, 193]
	Ni^{2+}, Co^{2+}, Cu^{2+}	[192]
Imidazole	Zn^{2+}	[194]
Poly(ethyleneimine)	Cu^{2+}	[195]
Pyridine		
2,6-Bis(1,2,3-triazole-4-yl)pyridine (BTP)	Zn^{2+}, Eu^{3+}	[196–198]
	Tb^{3+}	[198]
2,6-Bis(1′-methylbenzimidazolyl)pyridine (Mebip)	Zn^{2+}, La^{3+}	[199]
4,4′-{[(Pyridine-2,6-dicarbonyl)bis-(azanediyl)]bis(methylene)}-dibenzoic acid	Eu^{3+}, Tb^{3+}	[200]
4-(Pyridin-2-yl)-1*H*-1,2,3-triazole	Fe^{2+}, Co^{2+}	[201]
Terpyridine	Ni^{2+}	[202]
	Fe^{2+}	[203, 204]
	Cd^{2+}	[205]
Tyrosine	Ni^{2+}	[206]
L-Valine	Zn^{2+}	[207]

swollen in acetonitrile or THF and crosslinked with $Zn(OTf)_2$ or $Eu(OTf)_3$ demonstrated excellent self-healing behavior. Another approach using CuAAC to copolymerize BIP and spiropyran (SP) in a polyurethane backbone was shown [197]. The addition of Zn^{2+} or Eu^{3+} leads to the formation of supramolecular gels revealing a hard/soft morphology. Zinc-containing gels showed better self-healing properties compared with Eu^{3+}. Recovery of the original mechanical properties after treatment with solvent was achieved. Recently, Yang et al. synthesized BIP-containing polymers via thiol–ene "click" reactions [198]. The corresponding gel was formed by mixing with Zn^{2+}, Eu^{3+}, or Tb^{3+} salts. Rheological analyses of the three gels demonstrated that the storage modulus G' fully recovers after damage within 20 min. Terech et al. utilized bis-terpyridine cyclam as tritopic ligand for nickel ions, resulting in a supramolecular gel [202]. In addition, a fatty acid organogel based on 12-hydroxy stearic acid (HSA) with similar elasticity was utilized to compare the self-healing properties. First, the different gels were damaged with a spatula in a test tube, which was then placed upside down. In contrast to the HSA gel, the metallogel revealed a recovery of the strain after 48 h. The metallo-supramolecular gel showed a recovery capability of up to 72%, whereas the HSA gel exhibited only 32%.

Multistimuli-responsive healable hydrogels based on nickel–tyrosine interactions were described by Banerjee and coworkers [206]. Interestingly, TEM studies indicated nanofibers in the range of 60–150 nm. All hydrogels healed within 30 min of putting the cut pieces together. Rheological experiments also showed the recovery of up to 83% of their original stiffness. The variation in chain length of the

tyrosine derivates influences the self-healing ability (i.e., longer chain length correlates with faster self-healing). Additionally, the same group investigated the self-healing properties of a non-polymeric supramolecular hydrogel based on an L-valine-functionalized ligand and Zn^{2+} ions [207]. In addition to interesting multiresponsive gel-to-sol and sol-to-gel transitions, the hydrogel can bear 60-fold its own weight without any change in shape. Furthermore, it exhibits rapid self-healing behavior at room temperature. Recently, a pyridine-2,6-dicarboxylic acid derivate was utilized to design self-healing luminescent supramolecular metallogels [200]. For this purpose, lanthanides (i.e., Eu^{3+} and Tb^{3+}) were added in different stoichiometric ratios. The nature of the metal salt influences the resulting color. The metallogels were further swollen in methanol to enable self-healing of these materials. Gels with only one metal ion show instantaneous self-healing after cutting the material. Rheological studies showed that the gel containing both Eu^{3+} and Tb^{3+} is softer than gels with only Eu^{3+} or Tb^{3+}. However, all gels provide fast recovery of the initial G' after damage.

The first photoinduced self-healing of a metallopolymer was reported in 2011 [199]. Here, Burnworth et al. end-functionalized poly(ethylene-*co*-butylene) with two 2,6-bis(1′-methylbenzimidazolyl)pyridine (Mebip) ligands. The addition of $Zn(NTf_2)_2$ or $La(NTf_2)_3$ leads to linear metallopolymers that showed self-healing under irradiation with UV light (320–390 nm, 950 mW/cm^2). The irradiation induced two different phenomena: Cleavage of the metal–ligand complex and heating of the polymer (approximately 220 °C). Consequently, the flexibility of the polymer increased, which enabled healing. After irradiation, both metallopolymers can rapidly recover their initial mechanical properties (~1 min). Wang et al. copolymerized *n*BA and methyl methacrylate with a Mebip-containing acrylate via RAFT polymerization (approx. 3, 5, or 8% Mebip) [209]. Subsequent crosslinking with $Zn(OTf)_2$ led to a gel, whereas crosslinking with $Eu(OTf)_3$ resulted in a highly viscous material. This fact indicated that Eu^{3+} binds more weakly than Zn^{2+} to Mebip. Rheological measurements further revealed that the amount of crosslinks influenced the storage modulus (G'). Thus, a higher Mebip content, corresponding to a higher crosslinking density, led to higher G'. Furthermore, T_g increased with a higher content of Zn^{2+} and, similarly, the viscous flow temperature (T_f) increased. The material showed both shape-memory and healing properties. For self-healing tests, a copolymer containing 5% of Mebip was used because of its good mechanical properties. First, a rectangular plate of this material was damaged with a razor blade and then the plate was bent at an angle of 90° to separate the crack surfaces. Heating to 140 °C initiated a shape-memory-assisted self-healing process (SMASH) and healing was obtained within 25 min. Furthermore, the healing ability during irradiation with UV light (300–400 nm, 127 mW/cm^2) was investigated. Here, the polymer was heated to 185 °C, which enabled healing within 4 min.

Recently, Wang and Urban presented a supramolecular network based on copper–poly(ethyleneimine) (PEI) interactions. The resulting metallopolymer was capable of healing under irradiation with UV light [195]. The key step for the healing process is not the heating of the polymer network during UV irradiation, but

the UV-induced re-formation of the Cu-amine complexes. UV absorption induces a square-planar-to-tetrahedral transition of the Cu-PEI complex. The ground state of the Cu-amine complex has a square-planar geometry as a result of the high energy difference between $d_{x2-y2}$and $d_{xz/yz}$ orbitals. After UV irradiation, the energy difference between these two orbitals is decreased, which leads to transition to the tetrahedral structure. In the self-healing experiments, the material was completely cut into different pieces. The combined pieces healed multiple times under UV light. Furthermore, films of this network were coated onto a glass substrate and mechanically damaged. Surprisingly, the self-healing process was only possible two to three times.

Bode et al. synthesized terpyridine-functionalized poly(alkyl methacrylates) via the RAFT polymerization technique [203]. The polymers containing approximately 10% terpyridine units were crosslinked by the addition of iron(II) sulfate. The authors utilized methyl-, butyl-, and lauryl methacrylate as comonomers for the copolymerization. Thus, different T_g values were observed, decreasing with longer side chains. Therefore, no self-healing behavior of the poly(methyl methacrylate)-based polymer was observed as a result of the high T_g of 74 °C. In the other two cases, self-healing was achieved at 100 °C. Films based on butyl methacrylate revealed the healing of small cracks (length 180 μm, width 10 μm) within 40 min of damaging the film with a scalpel. However, reducing the temperature to 80 °C led to a significantly longer healing time (i.e. 30 h). Changing the comonomer to lauryl methacrylate resulted in a more flexible network. Consequently, the polymer film healed larger and wider scratches. Moreover, SAXS measurements of the metallopolymer suggested the presence of (ionic) clusters. Temperature-dependent Raman spectroscopy indicated that free terpyridine moieties are present during healing as a result of partial thermal decomplexation. In addition, quantum mechanical/molecular mechanical (QM/MM) simulations were performed to investige two possible healing mechanisms: (1) Thermal decomplexation of the metal–ligand interaction and the formation of new crosslinks upon cooling and (2) thermal dissociation of the ionic clusters (Fig. 17). The possibility of thermal decomplexation was confirmed by QM/MM simulations. In contrast, these simulations revealed that neither complete thermal cleavage of the relatively stable ionic cluster nor formation of new crosslinks are possible at the applied temperature (100 °C) [204].

Further investigations revealed that the self-healing behavior is connected with the strength of the metal–ligand interaction. As a consequence, variation of ligands and metal salts are key factors in tuning these intrinsic properties [189]. In the same manner, the self-healing behavior of terpyridine-containing polymers was improved by changing the metal ion as well as the counterion. Cadmium acetate was utilized as the crosslinker, because of weaker metal–ligand interactions (compared with iron). The resulting materials showed multiple healing cycles at 80 °C [205]. Furthermore, the formation of monoterpyridine complexes was verified, which are crosslinked via acetate bridges. Recently, an alternative ligand system was utilized to design self-healing materials [201]. A bidentate triazole-pyridine was copolymerized with lauryl methacrylate via RAFT. Crosslinking with iron

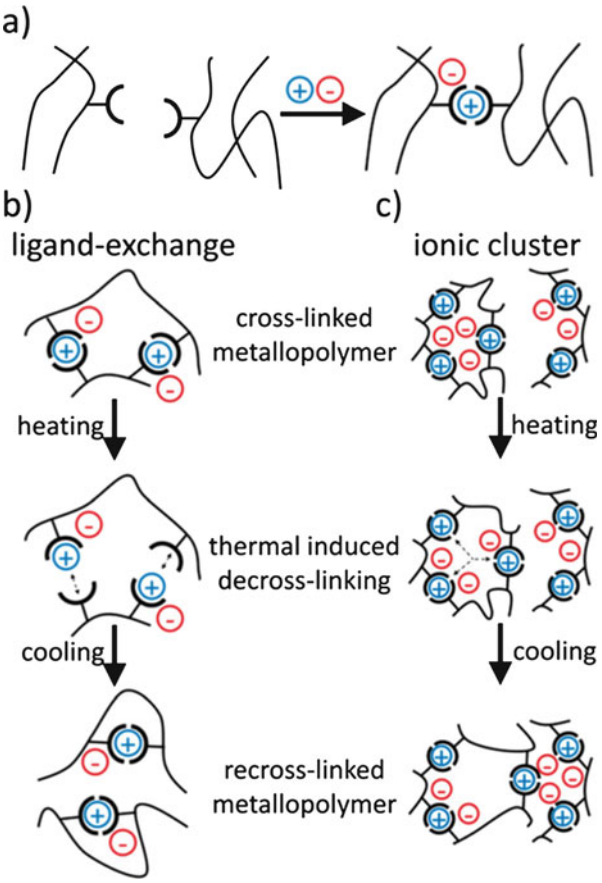

Fig. 17 Proposed healing mechanism of metallopolymers: (**a**) crosslinking by the addition of a metal salt, (**b**) reversibility based on ligand-exchange, and (**c**) reversibility based on ionic cluster (reprinted with permission from [204])

(II) and cobalt(II) salts led to self-healing polymers that could heal at temperatures between 50 and 100 °C.

Further investigation of this system also revealed a correlation between the supramolecular bond lifetime and the healing behavior of metallopolymers [210]. For this purpose, a terpyridine-containing poly(butyl methacrylate) was crosslinked by the addition of 12 different metal salts. Manganese(II), cobalt(II), zinc(II), and nickel(II) were chosen as cations and chloride, nitrate, and acetate as the corresponding anions. The healing behavior of these 12 metallopolymers was investigated. The polymer network crosslinked by manganese(II) chloride featured the best self-healing behavior. The mechanical properties were studied by rheology and a crossover of G' and G'' was demonstrated, which is related to the self-healing behavior of the metallopolymer.

Guan and coworkers designed a multiphase network consisting of zinc–imidazole interactions in a hard/soft brush copolymer structure [194]. First, they copolymerized styrene and 4-vinylbenzyl chloride (5 and 10%) via free radical polymerization (approximately 140 repeating units). Post-polymerization

functionalization of the benzyl chloride with potassium ethyl trithiocarbonate enabled selective introduction of a RAFT chain transfer agent. Subsequently, the trithiocarbonate was utilized for the RAFT polymerization of *n*BA with an imidazole-containing acrylate (approximately 180 repeating units). The imidazole content was adjusted to 25 or 35 mol%. SAXS measurements revealed the presence of a broad reflection corresponding to a domain size of 7–20 nm. Furthermore, the mechanical properties were tuned by varying several polymer parameters (e.g., the content of imidazole and the ratio between ligand and zinc salt). Self-healing tests were performed by cutting the material to a depth of 70–90% of the material thickness. Afterwards, the material was reconnected for 1 min at room temperature. Recovery of the original mechanical properties was analyzed in a tensile test, which revealed full recovery of the toughness after 3 h. Interestingly, the Young's modulus and the yield stress recovered rapidly.

Scientists are often inspired by nature. On the one hand, macroscopic self-healing in nature can rehabilitate broken bones or injured skin and, on the other hand, it can occur on a molecular scale. Repair of DNA through various processes after self-replication [211], regeneration of hydra (fresh-water polyps) [212], recovery of egg capsules of marine whelks [213], and the self-healing behavior of mussel byssal threads after stress [214] are just a few of thousands of natural examples. However, the latter example has been widely discussed in recent years [215–220]. The material exhibits both the interaction between 3,4-hydroxy-phenylalanine (DOPA) and iron ions [190, 221] and histidine–metal interactions [217, 222]. In detail, mussel byssus consists of several threads and acts as a shock-absorbing line for mussels in marine environments. Secreted by the mussel foot, the threads attach the organism to rocks with an adhesive plaque built-up from several DOPA-containing proteins. Furthermore, the mussel thread consists of a distal and a proximal region. It was found that the self-healing behavior might be based on histidine–zinc interactions in a block copolymer-like protein structure [214, 218, 220, 223].

The first study by Holten-Andersen et al. utilized catechol-Fe^{3+} and its pH dependency to form self-healing polymer gels [190]. DOPA-containing star-shaped branched poly(ethylene glycol) (PEG) chains were synthesized and further crosslinked with iron(III) chloride. Deprotonation of the hydroxyl groups of DOPA leads to a variation in the stoichiometry of the DOPA-Fe^{3+} complexes (Scheme 2). The changes in the complex structure can be monitored by UV–vis spectroscopy, which verified the pH values of ~5, ~8, and ~12 for the mono-, di- and tris-complexes, respectively. Furthermore, resonance Raman spectroscopy of the hydrogel at high pH values corresponds to results obtained from native mussel thread cuticles. Self-healing tests demonstrate almost full recovery of stiffness and cohesiveness after damage.

This system was recently investigated with respect to tenability via control of crosslinking by variation of the metal ions [191]. For this propose, chloride salts of iron(III), vanadium(III), and aluminum(III) were added in a ratio of 1:3 (metal to catechol). The pH was adjusted to 8 to mimic typical oceanic conditions. UV–vis spectroscopy showed that the vanadium-based gels exhibit tris-catechol complexes

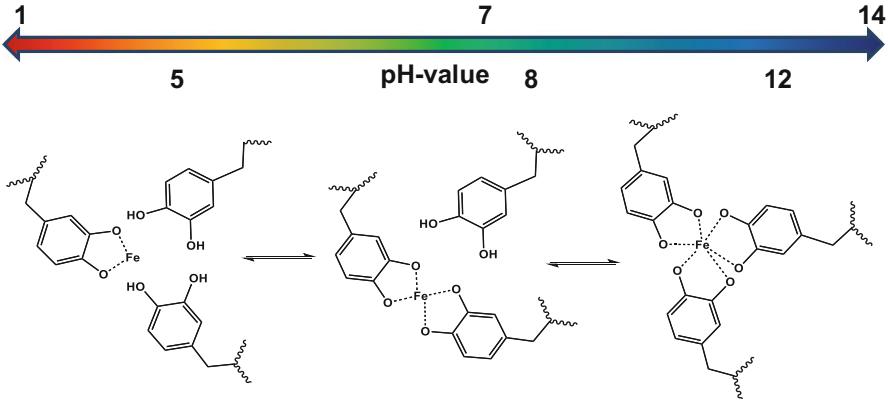

Scheme 2 Complexes of iron(III) ions with catechol and their pH-induced crosslinking character

and that di-catechol complexes were obtained using iron-based gels. In contrast, the aluminum–catechol interactions were thought to be the weakest, because of the low UV–vis-absorption of the polymer gel. Resonance Raman spectroscopy measurements supported these results. Therefore, vanadium is an optimal coordination partner for DOPA-based polymer gels at pH 8. Results showed a tenfold higher stability of the gel containing vanadium compared with the iron-based system. These findings illustrate the dependency of the complex structure on both pH and metal salt. This study provides excellent inspiration for new self-healing materials. In addition, Krogsgaard et al. utilized DOPA-containing polyallylamine, crosslinked with $FeCl_3$, to further optimize the self-healing behavior of such hydrogels [224]. After damaging this hydrogel with a spatula at pH 8, full recovery of the original shape and mechanical strength was achieved. Tensile tests also confirmed a fast recovery of the storage modulus G' of 4,700 Pa.

Another mussel-inspired approach is the utilization of metal–histidine interactions for formation of self-healing materials. Fullenkamp et al. studied a four-arm star polymer based on terminal-functional histidine-modified PEG [192]. This polymer was subsequently crosslinked with zinc(II), copper(II), nickel(II), and cobalt(II) ions in a ratio of 1:2 and 1:4 (metal to histidine). The resulting hydrogels were investigated via rheology. The authors reported that the rate of self-repair follows the order $Zn^{2+} > Cu^{2+} > Co^{2+} > Ni^{2+}$. Recently, Enke et al. developed for the first time self-healable coatings based on zinc–histidine interactions [193]. For this purpose, two novel histidine monomers were synthesized. Both histidine moieties were protected with a triphenylmethyl group (Trt) on the N^{τ}-position to optimize their solubility in organic solvents. In the case of the first monomer (Trt-His-OMe, **1**), the acid function is blocked with a methyl ester, whereas the second monomer (Trt-His-OH, **2**) bears free carboxylic acid (Fig. 18).

Afterwards, butyl methacrylate (BMA) and lauryl methacrylate (LMA) were copolymerized with those histidine monomers via RAFT polymerization. In a further step, the Trt group was cleaved off in order to visualize the influence of

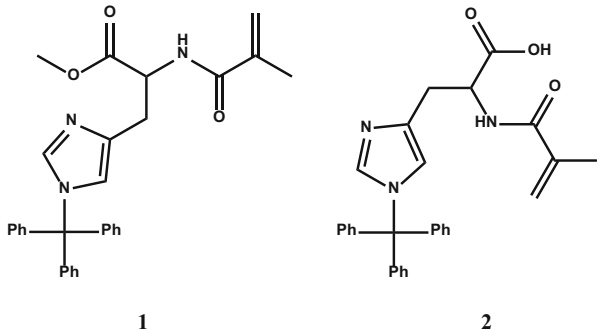

Fig. 18 Novel histidine monomers **1** and **2**

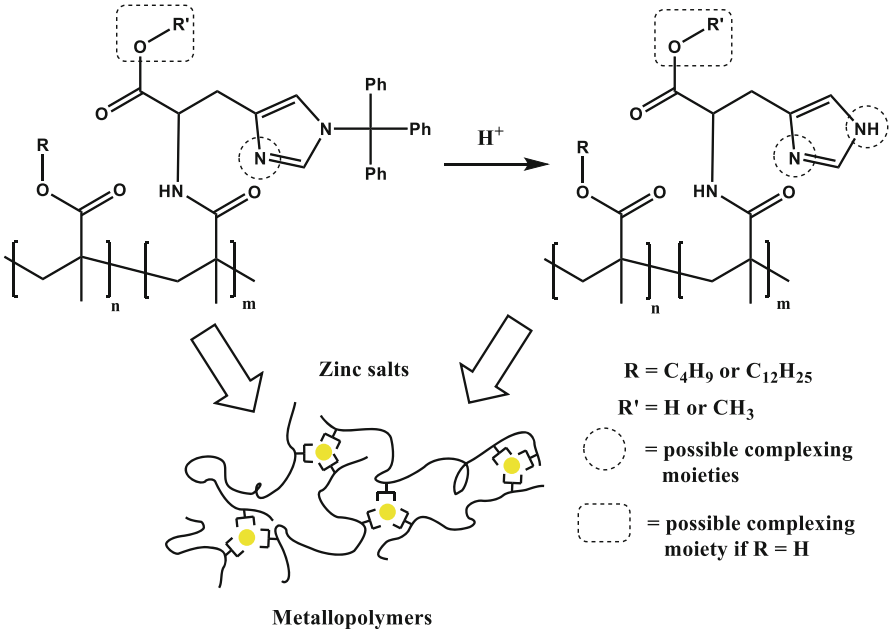

Scheme 3 Histidine monomers and synthesis of the corresponding copolymers, which were further crosslinked with several zinc salts (reproduced with permission from [193])

the protecting group (Scheme 3). Finally, the different copolymers were crosslinked with several zinc salts in the ratio 1:3 (zinc to histidine) and drop-coated onto microscope slides. The resulting films were investigated with respect to their crack-healing behavior. Best self-healing results were found for LMA/**1**-containing metallopolymers (40–60 °C within 20 min). In general, LMA copolymers demonstrate better self-healing as a result of their longer side chain, which mediates higher flexibility. Furthermore, the counterion is found to have a considerable influence on the self-healing capacity. Thus, the utilization of zinc(II) nitrate results in the best

self-healing properties compared with zinc(II) chloride and zinc(II) acetate. This fact leads to the suggestion that the binding strength of the counterion is responsible for this behavior. Cleavage of the Trt group of Trt-His-OMe-containing metallopolymers leads to an increase in the temperature required for the self-healing process. The higher binding strength of the formed complexes as a result of the higher coordination possibilities might require more energy to show reversibility. Another trend was found in the case of Trt-His-OH-containing copolymers. Here, the self-healing temperature significantly decreased after cleavage of the Trt group. The authors supposed that the free carboxylic acid function plays a key role in the structure of the histidine–zinc complexes, which influences the self-healing behavior extensively. However, this effect should be further investigated in detail to obtain the required information for enhancing self-healing behavior in a controlled manner.

In recent years, promising strategies for self-healing metallopolymers have been developed and further improved. A deeper understanding of the self-healing mechanism for each metal–ligand system is a key factor in designing well-defined future self-healing materials. Furthermore, the processability of the metallopolymers, in particular of the networks, has to be improved to enable broader applications.

6 Self-Healing Polymers Based on Reversible Host–Guest Interactions

Compared with metal–ligand interactions, the non-covalent binding between a host and a guest (i.e. molecular recognition) can be based on several interactions, such as van der Waals, charge-transfer, ion-dipole, and hydrophobic interactions [225]. A typical example of a host–guest interaction is the human immune system with its antibodies, which selectively bind on antigens and finally eliminate pathogens. Furthermore, enzymes are known for their catalytic influence via selective reactions (i.e. key and lock model) [226].

Self-healing supramolecular networks based on host–guest interactions are a relatively new topic, begun with the pioneering work of Harada and coworkers in 2011 [227]. Since then, several macrocyclic hosts (cyclodextrins, crown ethers, and cucurbit[*n*]urils) have been used for the preparation of self-healing supramolecular networks (Fig. 19).

Cyclodextrins (CDs) are water-soluble macrocycles consisting of six, seven, or eight to 16 glucose units linked by α-1,4-glycosidic bonds. Most utilized cyclodextrins are α-, β- and γ-CDs consisting of six, seven, or eight linked units [228, 229]. Moreover, the possibility of synthesizing polymers containing CDs via controlled radical polymerizations (e.g., RAFT) or post-polymerization functionalization offers easy synthetic pathways [230]. The CDs can form inclusion complexes with a large number of guests through hydrophobic interactions.

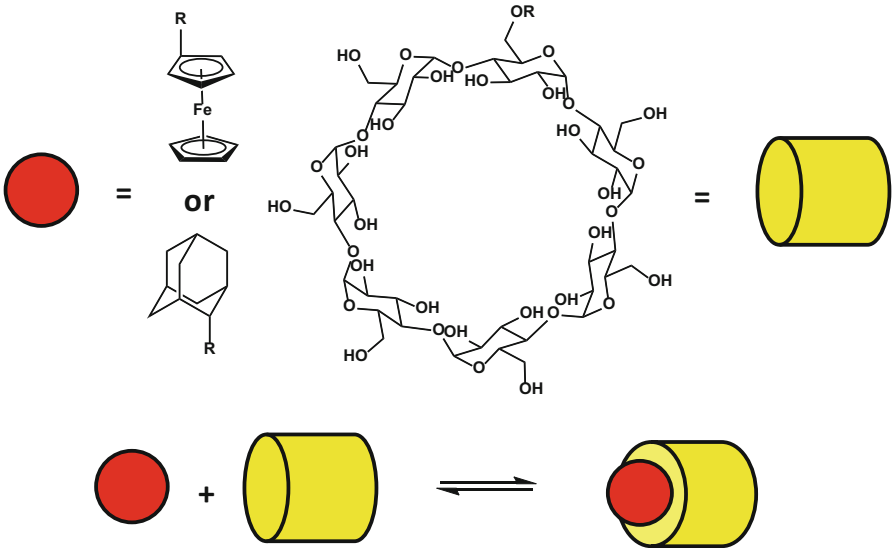

Fig. 19 Host β-cyclodextrin with ferrocene and adamantane as guest molecules with a binding stoichiometry of 1:1

Important guests for self-healing materials are ferrocene and adamantane units (Fig. 19) [231].

The unique reversibility of the host–guest interaction between β-CD and ferrocene (Fc) was utilized by Harada and coworkers to design the first example of those materials [227]. For this purpose, poly(acrylic acid) was functionalized with either β-CD or Fc. The two functionalized polymers were mixed together to form a supramolecular hydrogel. The authors utilized the redox-responsive host–guest interaction to induce a sol–gel phase transition of the hydrogel. β-CD has a high affinity for the neutral Fc; however, the complex rapidly dissociates when Fc is oxidized (Fc^+) [232]. The self-healing properties were also investigated. When the material was cut into two pieces and, subsequently, brought into close contact, the two halves reconnected within 24 h. The adhesive strength of the material was recovered up to 84% of the initial strength. To demonstrate the dependency of the self-healing process on the reversible host–guest interactions, the freshly cut surface was treated with competitive guest and host molecules. After 24 h, the connected pieces showed no self-healing. In addition, the influence of an oxidizing reagent was studied with respect to control of the self-healing ability. The addition of an aqueous solution of sodium hypochlorite to the freshly cut surface resulted in oxidation of Fc to Fc^+, which led to no complex formation with β-CD. Hence, self-healing was not obtained. The authors discussed the potential utilization of these materials for drug delivery because of their excellent properties and the biocompatibility of cyclodextrin.

Yan et al. synthesized a water-soluble oligo(ethylene glycol) (OEG) functionalized with ferrocene (Fc-OEG-Fc) and cyclodextrin (β-CD-OEG-β-CD) units [233]. By mixing these monomers together an AA–BB-type supramolecular polymerization was achieved. Furthermore, these polymers showed hierarchical assembly into nanofibers and self-degradable and self-healing properties under electrochemical conditions.

Self-healing polymers triggered by electrochemical stimuli, based on poly (glycidyl methacrylate) modified with Fc and difunctional β-CD, were fabricated [234]. The self-healing properties of the coated polymer films were investigated with scanning electron microscopy (SEM). The best self-healing behavior was obtained by electrical treatment with a 9-V cell for 24 h and subsequent heating to 85 °C for 24 h. In addition, utilization of the polymer as a self-healing agent in commercial painting products was tested successfully.

Wang et al. utilized fatty acids modified with β-CD and poly(ethylenimine) oligomer-grafted Fc, in the design of a supramolecular network with self-healing properties [235]. After cutting this material into pieces and then bringing the pieces together, the material healed within 5 min (the presence of absorbed water is required for self-healing). To determine the importance of the host–guest interaction on the healing process, competitive hosts were added onto the freshly cut surfaces and resulted in no self-healing even after 24 h. Therefore, the interaction between the host and the guest plays a key role in the self-healing mechanism. The authors address the possibility of utilizing the presented system as an efficient cushioning material. Recently, β-CD and Fc were separately introduced as pendant groups in a poly(*N*,*N*′-dimethylacrylamide) backbone. The resulting hydrogel was formed by simple mixing of the two polymers in an aqueous solution. Self-healing was proven by rheological tests; damaged hydrogels could rapidly restore their initial level. In addition, cytotoxicity measurements demonstrated the biocompatibility of these materials, enabling biological applications such as tissue engineering and drug delivery [236].

Another important guest for cyclodextrin-based self-healing systems is adamantane (Ad). Harada and coworkers presented the formation of a hydrogel by copolymerization of acrylamide and the inclusion complex of a CD monomer with the guest monomers *n*BA or *N*-adamantane-1-yl-acrylamide in water [237]. After cutting the β-CD-Ad hydrogel into half and then putting the surfaces together, the surfaces more or less immediately formed one piece again. In contrast, the rejoined two pieces of the α-CD-*n*BA hydrogel required several hours to achieve reattached material. Complete recovery of the gel strength of β-CD-Ad hydrogel took 24 h, whereas the α-CD-*n*BA hydrogel restored only 74% of the initial strength after the same time. The different behavior of the hydrogels is associated with the higher binding constant of β-CD with an Ad group ($K_a = 1{,}500\ M^{-1}$) than α-CD with *n*BA ($K_a = 57\ M^{-1}$). In addition, self-healing of the β-CD-Ad hydrogel was achieved even if the two halves were separately stored for 20 h and brought together afterwards. Recently, Harada and coworkers demonstrated a hard self-healing xerogel based on host–guest interactions of β-CD and Ad [238]. For self-healing tests, the β-CD xerogel and the Ad xerogel were

mixed together. The molar ratio (mol%) of the host and the guest was varied. The self-healing capacity of β-CD-Ad xerogels was investigated by tensile tests. The xerogel containing 0.3 mol% of β-CD and 0.4 mol% of Ad showed an adhesive strength of 2.8 MPa. After damage, the reattached xerogel demonstrated a recovery stress ratio of 40% after 1 h and 88% after 48 h.

Himmelein et al. prepared an Ad-modified cellulose polymer that was crosslinked with cyclodextrin-containing vesicles [239]. This material revealed shear-thinning and self-healing properties. Recently, Zhang et al. presented a self-healing conductive network based on small molecules and nanotubes [240]. The authors utilized single-walled carbon nanotubes containing β-CD and Ad-modified PEI to fabricate a recyclable supramolecular composite. The material restored its initial electrical and mechanical properties to over 90% after damage (tensile tests). Nevertheless, the addition of water is required for the self-healing process. The authors proposed that the self-healing is based on host–guest interactions as well as on hydrogen bonds. Rodell et al. modified hyaluronic acid separately with β-CD and Ad [241]. The Ad unit is bound to the polymer backbone via a peptide chain, which offers the possibility of proteolytic degradation of the network. After mixing these polymers, a hydrogel with self-healing behavior is formed. The authors highlighted the injectability and the biodegradability of the presented material with the potential for medical applications such as drug or cell delivery.

Zhu and coworkers synthesized a photoresponsive supramolecular hyperbranched polymer based on the non-covalent interactions between an azobenzene dimer and a β-CD trimer [242]. The authors suggested further investigation of its self-healing properties because of the photocontrolled reversible complexation of the host by the guest by alternating UV–vis irradiation. This principle is based on the different aggregation constant between β-CD and either the *trans*- or the *cis*-isomer. Selective irradiation with 365 nm led to the *cis*-conformation, which has a much lower association constant with β-CD than the *trans*-isomer, resulting in dissociation of the polymer. This effect generated mobility in the material and enabled healing (e.g., crack healing in a coated polymer film). Chen et al. investigated the host–guest interactions between β-CD and α-bromonaphthalene (α-BrNp) in a hydrogel based on a polyacrylamide backbone [243]. After cutting the material into pieces and placing the surfaces together, rapid self-healing behavior was observed (1 min). The rheological properties were restored after 1 h. The authors pointed out that the self-healing behavior is influenced by both host–guest interactions as well as hydrogen bonds. In addition to the self-healing properties, the hydrogel showed the ability to produce room-temperature phosphorescence.

Yu et al. utilized a new method for radical polymerization (magnetically induced frontal polymerization, MIFP) to synthesize Fe_3O_4-doped supramolecular gels based on the host–guest recognition of β-CD and *N*-vinyl imidazole (VI) copolymerized with 2-hydroxypropyl acrylate [244]. Thus, the β-CD moiety is not included in the polymer chain. The ability of VI to form dimer inclusion complexes with β-CD enables reversible crosslinks in the polymer matrix. Increasing the amount of β-CD and introduction of Fe_3O_4 nanoparticles significantly

improved the mechanical properties. However, increasing the β-CD concentration can block the imidazole groups, resulting in a decreased self-healing capacity. A β-CD to VI ratio of 1:5 (w/w) was found to represent an optimum between mechanical and self-healing properties. Furthermore, the healing time was significantly decreased when the damaged gels were treated with an external magnetic field of 450 kHz.

Compared with cyclodextrin, which mainly forms host–guest interactions in aqueous solutions, organic solvents are utilized for crown ether-based supramolecular polymers [245]. Crown ethers have a long history, beginning with the discovery of these cyclic polyethers in 1967 [246]. They can be utilized for the complexation of metals or organic ions. Moreover, the host–guest recognition is responsive to temperature, pH, and competing ions. These properties can be utilized to introduce self-healing behavior in crown ether-based polymers [231]. In 2012, Huang and coworkers presented the first self-healing supramolecular gel with crown ether moieties [247]. For this purpose, poly(methyl methacrylate) containing dibenzo[24]crown-8 (DB24C8) was synthesized and crosslinked with two bis-(ammonium salts) having different end-group sizes (Fig. 20). Gel **1** was immediately prepared by simple mixing of the two compounds in organic solvents. Gel **2** was formed by heating for 30 days and stirring for further 45 days after mixing. The longer time for recognition is explained by the larger size of the end group (cyclohexyl unit). The host–guest interactions were proven by ^{1}H NMR

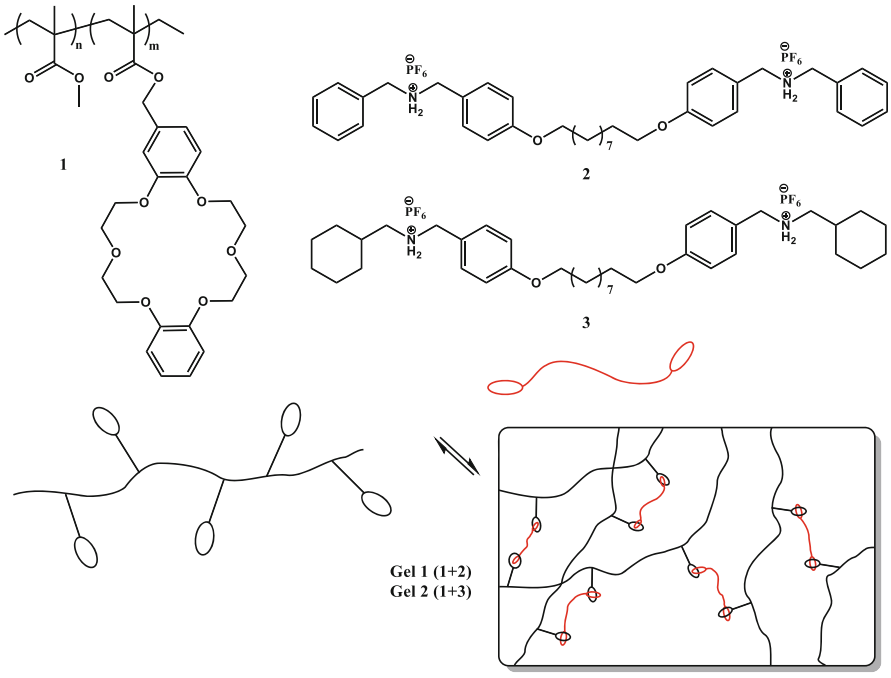

Fig. 20 Supramolecular gels based on crown ether interactions [247]

spectroscopy, indicating a chemical shift for the aromatic protons after complexation. Moreover, the gels are degradable, triggered by pH stimuli; for example, addition of a base causes deprotonation of the amines, resulting in disintegration of host and guest. Self-healing studies pointed out that the self-healing mechanism of gel **1** is based on host–guest interactions, whereas gel **2** can heal mainly through electrostatic interactions and hydrogen bonds, resulting in faster self-healing behavior. Furthermore Chen and coworkers investigated the host–guest interactions of DB24C8 and dibenzylammonium (DBA) [248]. The supramolecular network was based on a triptycene-based bis(crown ether) and a copolymer containing DBA. The resulting gel showed thermo-, acid/base- and chemo-induced gel–sol transitions. Furthermore, self-healing behavior was demonstrated after damaging the gel with a knife. The copolymerization of ethyl acrylate and a guest monomer containing DBA led to another supramolecular network if a DB24C8-containing bis(crown ether) was utilized for crosslinking [249]. The gel showed pH- and thermoresponsive behavior. Moreover, a mechanical strength of 14.8 kPa and fast self-healing properties distinguished the material.

A self-healing supramolecular organogel based on the crosslinks of DB24C8 and DBA, which were separately incorporated in a glycidyl triazole polymer backbone, was described by Ikeda and coworkers [250]. The advantage of this gel is the high elasticity under large deformation as a result of the mobile polymer chains with higher molar masses.

Huang and coworkers prepared novel crosslinked supramolecular networks based on a linear polymer: AA monomer bis(benzo-21-crown-7) (B21C7) and BB monomer bis(dialkylammonium salt) [251]. Additional 1,2,3-triazole groups were crosslinked with $PdCl_2(PhCN)_2$, resulting in a highly crosslinked, transparent self-healable gel, which also showed quadruple-stimuli responsive gel–sol transitions. The combination of two reversible non-covalent bonds led to a supramolecular polymer network with unique properties. In this way, good mechanical properties were introduced with the formation of relatively strong metal–ligand interactions. In contrast, weaker host–guest interactions facilitated self-healing. With the same concept, Zhan et al. prepared a gel based on multiple orthogonal interactions [252]. The authors utilized the same interactions as Huang and coworkers [251], but they added another metal–ligand interaction between terpyridine and $Zn(OTf)_2$. The resulting multiresponsive supramolecular gel showed fast self-healing behavior, with broken films showing full recovery after 300 s.

Besides cyclodextrins and crown ethers, cucurbit[*n*]urils (CB[*n*]s) can be utilized to fabricate self-healing materials. CB[*n*]s are cyclic oligomers of glycoluril that can bind single guests such as metals or imidazolium ions ($n = 5$–7). Large guests or even two guests can find space in one CB unit [8] because of the large cavity volume [253]. One example of a healable hydrogel based on CB [8] recognition was published recently by Ikkala and coworkers [254]. The authors synthesized naphthyl-functionalized cellulose nanocrystals and poly(vinyl alcohol) containing methyl viologen to enable host–guest interaction with CB [8] after mixing the compounds together in water. Here, the host acts as dynamic crosslinker

Table 3 Summary of host–guest interactions utilized for self-healing materials

Host	Guest	Literature
Cyclodextrin (CD)		
β-CD	Ferrocene (Fc)	[227, 233–236]
	Adamantane (Ad)	[237–241]
	Azobenzene	[242]
	α-Bromonaphthalene	[243]
	N-Vinylimidazole	[244]
α-CD	*n*-Butane	[237]
Crown ether		
Dibenzo[24]crown-8	Dibenzylammonium	[247–250]
	Cyclohexyl-benzylammonium	[247]
Benzo-21-crown-7	Alkylammonium salt	[251, 252]
Cucurbit[8]urils	Naphthyl/methyl viologen	[254]

of the two different guests. The self-healing properties were investigated with the help of step–strain experiments, demonstrating full recovery of their initial mechanical behavior within a few seconds of damage. Two cut pieces of this hydrogel heal within 30 s. Moreover, calix[*n*]arenes [255, 256] and pillar[*n*]arenes [257, 258] have high potential to be used in self-healing materials because of their cavity size and specific reversible host–guest interactions. Thus, new supramolecular structures should be investigated in order to improve the material properties (i.e. mechanical and self-healing properties) and eventually enable engineering and medical applications [231]. A summary of the host–guest interactions used is given in Table 3.

7 Conclusions and Outlook

Nature itself, as an outstanding demonstrator of self-healing materials, can be a great source of inspiration for the design of novel synthetic smart materials. The interplay of different supramolecular interactions provides the basis for the unique properties of natural materials (systems). Consequently, synthetic supramolecular polymers have been intensively investigated in recent years, because these materials feature interesting properties such as reversibility, stimuli-responsiveness, and tunability of their mechanical properties. Generally, these properties are ideal preconditions for the design of self-healing materials and a variety of different examples have been presented over the last few years.

The properties of these polymers as well as their ability to close cracks can be easily tuned by changing the supramolecular binding motif. Hydrogen bonds feature weak interactions, resulting in rubber-like materials with self-healing properties at room temperature, but metallopolymers reveal much stronger supramolecular bonds. This increase in the binding energy can lead to "stronger" materials,

although external stimuli are often required for such materials to achieve self-healing.

In recent years, a wide range of different systems have been investigated and the underlying healing mechanisms were studied in detail. Nevertheless, there are still many future challenges, such as a complete understanding of the healing mechanism for all supramolecular polymers. Bulk properties and the behavior of the supramolecular unit within the polymer are still poorly understood. The behavior of these moieties and their responsiveness in solution and in the melt are often strongly different; thus, the behavior in bulk still requires other types of investigation. A first study regarding this analysis was performed by Bose et al. [142, 186], who analyzed the behavior of ionomers using rheological measurements. The authors found a crossover of G' and G'' and could correlate this behavior to a supramolecular bond lifetime (τ). This bond lifetime could be used to predict the mechanical and healing properties.

Furthermore, supramolecular systems are also ideal candidates for the commercialization of self-healing materials. Arkema commercialized the polymers investigated by Leibler and coworkers [37], which are similar to the commercially available Surlyn® (http://www.dupont.com/products-and-services/plastics-polymers-resins/ethylene-copolymers/brands/nucrel-ethylene-acrylic-acid.html) or materials from Suprapolix (http://www.suprapolix.com/pages/polymers) which also feature self-healing properties. Nevertheless, more supramolecular systems will appear on the market in the future. Preconditions are the scale-up of the synthesis and, importantly, an improvement in the accessibility of these polymers because many current systems are too expensive for industrial application. Consequently, the basic healing mechanism should be transferred to cheaper systems. Moreover, an intrinsic problem – the creep – of most supramolecular systems has to be solved. The high reversibility of the supramolecular bonds results in a time-dependent response to constant external forces. Introducing additional covalent bonds could remedy this problem but might also reduce the self-healing ability. Alternatively, inclusion of inert rigid particles could lead to a yield point solving the problem without destroying the self-healing characteristics.

The processability of supramolecular self-healing systems also requires more research. Some systems, in particular metallopolymers, were often utilized as networks and synthesized from two compounds, resulting in weakly soluble systems. Thus, the manufacturing of these systems needs to be improved [259–261]. A further challenge is the improvement in the mechanical properties of very good self-healing systems. In general, the supramolecular unit defines the properties of the final polymer. Very weak interactions lead to polymers that are rubber-like, but have a high self-healing capacity. On the other hand, strong supramolecular interactions yield high mechanical properties, but the self-healing ability is reduced and an external stimulus is often required. In recent years, two strategies have been investigated in order to overcome this problem: The first method is to utilize a double network structure with incorporation of covalent crosslinks, which enhance the mechanical properties [56]. Another possibility is a multiphase design in which

both hard and soft segments are utilized to feature both high mechanical properties and self-healing behavior at room temperature [55, 194, 262].

In conclusion, supramolecular systems are well established for the design of self-healing polymers and feature the advantage that their strength is tuneable. Several interactions have been utilized for their preparation, and healing at different temperatures is possible. Thus, an on-demand synthesis of a supramolecular self-healing polymer is possible and the next step towards industrial application is heralded.

Acknowledgements WHB and DD thank the following funding institutions for financial support: funding from the European Union's Seventh Framework Program for research, technological development and demonstration under grant agreement no. 313978 as well as the Deutsche Forschungsgemeinschaft, grant DFG-BI 1337/8–1 and DFG-BI1337/8-2 within the SPP 1568 ("Design and Generic Principles of Self-Healing Materials") and the SFB TRR 102 (project A3).

USS, MDH, ME, and SB thank the Deutsche Forschungsgemeinschaft (DFG, SPP 1568) for financial support.

References

1. Whittell GR, Hager MD, Schubert US, Manners I (2011) Nat Mater 10:176–188
2. Roy D, Cambre JN, Sumerlin BS (2010) Prog Polym Sci 35:278–301
3. Stuart MAC, Huck WTS, Genzer J, Muller M, Ober C, Stamm M, Sukhorukov GB, Szleifer I, Tsukruk VV, Urban M, Winnik F, Zauscher S, Luzinov I, Minko S (2010) Nat Mater 9:101–113
4. Yan X, Wang F, Zheng B, Huang F (2012) Chem Soc Rev 41:6042–6065
5. Lehn J-M (2002) Polym Int 51:825–839
6. Binder W, Zirbs R (2007) Supramolecular polymers and networks with hydrogen bonds in the main- and side-chain. In: Binder WH (ed) Hydrogen bonded polymers, Advances in polymer science. Springer, Berlin, pp 1–78
7. Brunsveld L, Folmer B, Meijer E, Sijbesma R (2001) Chem Rev 101:4071–4098
8. Herbst F, Döhler D, Michael P, Binder WH (2013) Macromol Rapid Commun 34:203–220
9. Michael P, Döhler D, Binder WH (2015) Polymer 69:216–227
10. Green MS, Tobolsky AV (1946) J Chem Phys 14:80–92
11. De Gennes PG (1971) J Chem Phys 55:572–579
12. Leibler L, Rubinstein M, Colby RH (1991) Macromolecules 24:4701–4707
13. Hackelbusch S, Rossow T, van Assenbergh P, Seiffert S (2013) Macromolecules 46:6273–6286
14. Chen X, Dam MA, Ono K, Mal A, Shen H, Nutt SR, Sheran K, Wudl F (2002) Science 295:1698–1702
15. Chen X, Wudl F, Mal AK, Shen H, Nutt SR (2003) Macromolecules 36:1802–1807
16. Kötteritzsch J, Stumpf S, Hoeppener S, Vitz J, Hager MD, Schubert US (2013) Macromol Chem Phys 214:1636–1649
17. de Lucca Freitas L, Stadler R (1988) Colloid Polym Sci 266:1095–1101
18. Stadler R (1993) Kautsch Gummi Kunstst 46:619–628
19. Müller M, Dardin A, Seidel U, Balsamo V, Iván B, Spiess HW, Stadler R (1996) Macromolecules 29:2577–2583
20. Stadler FJ, Pyckhout-Hintzen W, Bailly C (2008) AIP Conf Proc 1027:552–554
21. Subramaniam K, Das A, Simon F, Heinrich G (2013) Eur Polym J 49:345–352

22. Eisenberg A, Hird B, Moore RB (1990) Macromolecules 23:4098–4107
23. Sijbesma RP, Beijer FH, Brunsveld L, Folmer BJB, Hirschberg JHKK, Lange RFM, Lowe JKL, Meijer EW (1997) Science 278:1601–1604
24. Bosman AW, Brunsveld L, Folmer BJB, Sijbesma RP, Meijer EW (2003) Macromol Symp 201:143–154
25. Herbst F, Binder WH (2013) Polym Chem 4:3602–3609
26. Yan T, Schröter K, Herbst F, Binder WH, Thurn-Albrecht T (2014) Macromolecules 47:2122–2130
27. Zare P, Stojanovic A, Herbst F, Akbarzadeh J, Peterlik H, Binder WH (2012) Macromolecules 45:2074–2084
28. Herbst F, Seiffert S, Binder WH (2012) Polym Chem 3:3084–3092
29. Yoon JA, Kamada J, Koynov K, Mohin J, Nicolaÿ R, Zhang Y, Balazs AC, Kowalewski T, Matyjaszewski K (2011) Macromolecules 45:142–149
30. Kolmakov GV, Matyjaszewski K, Balazs AC (2009) ACS Nano 3:885–892
31. Iyer BVS, Salib IG, Yashin VV, Kowalewski T, Matyjaszewski K, Balazs AC (2013) Soft Matter 9:109–121
32. Iyer BVS, Yashin VV, Hamer MJ, Kowalewski T, Matyjaszewski K, Balazs AC (2015) Prog Polym Sci 40:121–137
33. Iyer BVS, Yashin VV, Kowalewski T, Matyjaszewski K, Balazs AC (2013) Polym Chem 4:4927–4939
34. Salib IG, Kolmakov GV, Gnegy CN, Matyjaszewski K, Balazs AC (2011) Langmuir 27:3991–4003
35. Chen Y, Wu W, Himmel T, Wagner MH (2013) Macromol Mater Eng 298:876–887
36. Zhang A, Yang L, Lin Y, Yan L, Lu H, Wang L (2013) J Appl Polym Sci 129:2435–2442
37. Cordier P, Tournilhac F, Soulie-Ziakovic C, Leibler L (2008) Nature 451:977–980
38. Montarnal D, Cordier P, Soulié-Ziakovic C, Tournilhac F, Leibler L (2008) J Polym Sci A Polym Chem 46:7925–7936
39. Montarnal D, Tournilhac F, Hidalgo M, Couturier J-L, Leibler L (2009) J Am Chem Soc 131:7966–7967
40. Tournilhac F, Cordier P, Montarnal D, Soulié-Ziakovic C, Leibler L (2010) Macromol Symp 291–292:84–88
41. Maes F, Montarnal D, Cantournet S, Tournilhac F, Corte L, Leibler L (2012) Soft Matter 8:1681–1687
42. Zhang R, Yan T, Lechner B-D, Schröter K, Liang Y, Li B, Furtado F, Sun P, Saalwächter K (2013) Macromolecules 46:1841–1850
43. Berl V, Schmutz M, Krische MJ, Khoury RG, Lehn J-M (2002) Chem Eur J 8:1227–1244
44. Kolomiets E, Buhler E, Candau SJ, Lehn JM (2006) Macromolecules 39:1173–1181
45. Nair KP, Breedveld V, Weck M (2008) Macromolecules 41:3429–3438
46. Binder WH, Kunz MJ, Ingolic E (2004) J Polym Sci A Polym Chem 42:162–172
47. Binder WH, Kunz MJ, Kluger C, Hayn G, Saf R (2004) Macromolecules 37:1749–1759
48. Kunz MJ, Hayn G, Saf R, Binder WH (2004) J Polym Sci A Polym Chem 42:661–674
49. Binder WH, Bernstorff S, Kluger C, Petraru L, Kunz MJ (2005) Adv Mater 17:2824–2828
50. Binder WH, Machl D (2005) J Polym Sci A Polym Chem 43:188–202
51. Ostas E, Schröter K, Beiner M, Yan T, Thurn-Albrecht T, Binder WH (2011) J Polym Sci A Polym Chem 49:3404–3416
52. Rowan SJ, Suwanmala P, Sivakova S (2003) J Polym Sci A Polym Chem 41:3589–3596
53. Sivakova S, Bohnsack DA, Mackay ME, Suwanmala P, Rowan SJ (2005) J Am Chem Soc 127:18202–18211
54. Hackethal K, Herbst F, Binder WH (2012) J Polym Sci A Polym Chem 50:4494–4506
55. Chen S, Mahmood N, Beiner M, Binder WH (2015) Angew Chem Int Ed 54:10188–10192
56. Döhler D, Peterlik H, Binder WH (2015) Polymer 69:264–273
57. Beijer FH, Kooijman H, Spek AL, Sijbesma RP, Meijer EW (1998) Angew Chem Int Ed 37:75–78

58. Beijer FH, Sijbesma RP, Kooijman H, Spek AL, Meijer EW (1998) J Am Chem Soc 120:6761–6769
59. Kaitz JA, Possanza CM, Song Y, Diesendruck CE, Spiering AJH, Meijer EW, Moore JS (2014) Polym Chem 5:3788–3794
60. Bosman AW, Sijbesma RP, Meijer EW (2004) Mater Today 7:34–39
61. van Gemert GML, Peeters JW, Söntjens SHM, Janssen HM, Bosman AW (2012) Macromol Chem Phys 213:234–242
62. Dankers PYW, Hermans TM, Baughman TW, Kamikawa Y, Kieltyka RE, Bastings MMC, Janssen HM, Sommerdijk NAJM, Larsen A, van Luyn MJA, Bosman AW, Popa ER, Fytas G, Meijer EW (2012) Adv Mater 24:2703–2709
63. Botterhuis NE, van Beek DJM, van Gemert GML, Bosman AW, Sijbesma RP (2008) J Polym Sci A Polym Chem 46:3877–3885
64. Hirschberg JHKK, Beijer FH, van Aert HA, Magusin PCMM, Sijbesma RP, Meijer EW (1999) Macromolecules 32:2696–2705
65. Bobade S, Wang Y, Mays J, Baskaran D (2014) Macromolecules 47:5040–5050
66. Oya N, Ikezaki T, Yoshie N (2013) Polym J 45:955–961
67. Li G, Wie JJ, Nguyen NA, Chung WJ, Kim ET, Char K, Mackay ME, Pyun J (2013) J Polym Sci A Polym Chem 51:3598–3606
68. van Beek DJM, Spiering AJH, Peters GWM, te Nijenhuis K, Sijbesma RP (2007) Macromolecules 40:8464–8475
69. Wietor J-L, van Beek DJM, Peters GW, Mendes E, Sijbesma RP (2011) Macromolecules 44:1211–1219
70. Lewis CL, Stewart K, Anthamatten M (2014) Macromolecules 47:729–740
71. Elkins CL, Park T, McKee MG, Long TE (2005) J Polym Sci A Polym Chem 43:4618–4631
72. Faghihnejad A, Feldman KE, Yu J, Tirrell MV, Israelachvili JN, Hawker CJ, Kramer EJ, Zeng H (2014) Adv Funct Mater 24:2322–2333
73. Feldman KE, Kade MJ, Meijer EW, Hawker CJ, Kramer EJ (2009) Macromolecules 42:9072–9081
74. Folmer BJB, Sijbesma RP, Versteegen RM, van der Rijt JAJ, Meijer EW (2000) Adv Mater 12:874–878
75. Kautz H, van Beek DJM, Sijbesma RP, Meijer EW (2006) Macromolecules 39:4265–4267
76. Keizer HM, van Kessel R, Sijbesma RP, Meijer EW (2003) Polymer 44:5505–5511
77. Sontjens SHM, Renken RAE, van Gemert GML, Engels TAP, Bosman AW, Janssen HM, Govaert LE, Baaijens FPT (2008) Macromolecules 41:5703–5708
78. Fang X, Zhang H, Chen Y, Lin Y, Xu Y, Weng W (2013) Macromolecules 46:6566–6574
79. Kushner AM, Vossler JD, Williams GA, Guan Z (2009) J Am Chem Soc 131:8766–8768
80. Stadler R (1993) Kautsch Gummi Kunstst 46:619–628
81. Peng C-C, Abetz V (2005) Macromolecules 38:5575–5580
82. Chino K, Ashiura M (2001) Macromolecules 34:9201–9204
83. Hilger C, Stadler R (1991) Polymer 32:3244–3249
84. Hilger C, Stadler R, Liane L, Freitas DL (1990) Polymer 31:818–823
85. Müller M, Seidel U, Stadler R (1995) Polymer 36:3143–3150
86. Stadler R, de Lucca Freitas L (1986) Colloid Polym Sci 264:773–778
87. Stadler R, de Araujo MA, Kuhrau M, Rösch J (1989) Makromol Chem 190:1433–1443
88. Schirle M, Hoffmann I, Pieper T, Kilian H-G, Stadler R (1996) Polym Bull 36:95–102
89. Callies X, Fonteneau C, Véchambre C, Pensec S, Chenal JM, Chazeau L, Bouteiller L, Ducouret G, Creton C (2015) Polymer 69:233–240
90. Colombani O, Barioz C, Bouteiller L, Chanéac C, Fompérie L, Lortie F, Montès H (2005) Macromolecules 38:1752–1759
91. Woodward PJ, Hermida Merino D, Greenland BW, Hamley IW, Light Z, Slark AT, Hayes W (2010) Macromolecules 43:2512–2517
92. Ni Y, Becquart F, Chen J, Taha M (2013) Macromolecules 46:1066–1074
93. Roy N, Buhler E, Lehn J-M (2013) Chem Eur J 19:8814–8820

94. Ribagnac P, Cannizzo C, Meallet-Renault R, Clavier G, Audebert P, Pansu RB, Bouteiller L (2013) J Phys Chem B 117:1958–1966
95. Pensec S, Nouvel N, Guilleman A, Creton C, Boué F, Bouteiller L (2010) Macromolecules 43:2529–2534
96. Courtois J, Baroudi I, Nouvel N, Degrandi E, Pensec S, Ducouret G, Chanéac C, Bouteiller L, Creton C (2010) Adv Funct Mater 20:1803–1811
97. Shikata T, Nishida T, Isare B, Linares M, Lazzaroni R, Bouteiller L (2008) J Phys Chem B 112:8459–8465
98. Woodward P, Clarke A, Greenland BW, Hermida Merino D, Yates L, Slark AT, Miravet JF, Hayes W (2009) Soft Matter 5:2000–2010
99. Lortie F, Boileau S, Bouteiller L (2003) Chem Eur J 9:3008–3014
100. Feldman KE, Kade MJ, de Greef TFA, Meijer EW, Kramer EJ, Hawker CJ (2008) Macromolecules 41:4694–4700
101. Feldman KE, Kade MJ, Meijer EW, Hawker CJ, Kramer EJ (2010) Macromolecules 43:5121–5127
102. Ohkawa H, Ligthart GBWL, Sijbesma RP, Meijer EW (2007) Macromolecules 40:1453–1459
103. Ligthart GBWL, Ohkawa H, Sijbesma RP, Meijer EW (2004) J Am Chem Soc 127:810–811
104. Bouteiller L (2007) Assembly via hydrogen bonds of low molar mass compounds into supramolecular polymers. In: Binder W (ed) Hydrogen bonded polymers, vol 207, Advances in polymer science. Springer, Berlin, pp 79–112
105. Knoben W, Besseling NAM, Bouteiller L, Cohen-Stuart MA (2005) Phys Chem Chem Phys 7:2390–2398
106. Lortie F, Boileau S, Bouteiller L, Chassenieux C, Lauprêtre F (2005) Macromolecules 38:5283–5287
107. Lange RFM, Van Gurp M, Meijer EW (1999) J Polym Sci A Polym Chem 37:3657–3670
108. Kuykendall DW, Anderson CA, Zimmerman SC (2008) Org Lett 11:61–64
109. Park T, Todd EM, Nakashima S, Zimmerman SC (2005) J Am Chem Soc 127:18133–18142
110. Park T, Zimmerman SC (2006) J Am Chem Soc 128:13986–13987
111. Park T, Zimmerman SC (2006) J Am Chem Soc 128:11582–11590
112. Park T, Zimmerman SC, Nakashima S (2005) J Am Chem Soc 127:6520–6521
113. Li Y, Park T, Quansah JK, Zimmerman SC (2011) J Am Chem Soc 133:17118–17121
114. Meyer EA, Castellano RK, Diederich F (2003) Angew Chem Int Ed 42:1210–1250
115. Varshey DB, Sander JRG, Friščić T, MacGillivray LR (2012) Supramolecular interactions. In: Steed JW, Gale PA (eds) Supramolecular chemistry. Wiley, Hoboken, pp 9–24
116. Burattini S, Greenland BW, Hayes W, Mackay ME, Rowan SJ, Colquhoun HM (2011) Chem Mater 23:6–8
117. Scott Lokey R, Iverson BL (1995) Nature 375:303–305
118. Greenland BW, Burattini S, Hayes W, Colquhoun HM (2008) Tetrahedron 64:8346–8354
119. Greenland BW, Bird MB, Burattini S, Cramer R, O'Reilly RK, Patterson JP, Hayes W, Cardin CJ, Colquhoun HM (2013) Chem Commun 49:454–456
120. Colquhoun HM, Zhu Z, Williams DJ (2003) Org Lett 5:4353–4356
121. Colquhoun HM, Zhu Z (2004) Angew Chem Int Ed 43:5040–5045
122. Colquhoun HM, Zhu Z, Cardin CJ, Gan Y (2004) Chem Commun 2004(23): 2650–2652
123. Colquhoun HM, Zhu Z, Cardin CJ, Gan Y, Drew MGB (2007) J Am Chem Soc 129:16163–16174
124. Zhu Z, Cardin CJ, Gan Y, Murray CA, White AJP, Williams DJ, Colquhoun HM (2011) J Am Chem Soc 133:19442–19447
125. Burattini S, Colquhoun HM, Greenland BW, Hayes W (2009) Faraday Discuss 143:251–264
126. Burattini S, Colquhoun HM, Fox JD, Friedmann D, Greenland BW, Harris PJF, Hayes W, Mackay ME, Rowan SJ (2009) Chem Commun 2009(44): 6717–6719
127. Burattini S, Greenland BW, Hermida Merino D, Weng W, Seppala J, Colquhoun HM, Hayes W, Mackay ME, Hamley IW, Rowan SJ (2010) J Am Chem Soc 132:12051–12058

128. Hart LR, Hunter JH, Nguyen NA, Harries JL, Greenland BW, Mackay ME, Colquhoun HM, Hayes W (2014) Polym Chem 5:3680–3688
129. Hart LR, Harries JL, Greenland BW, Colquhoun HM, Hayes W (2015) ACS Appl Mater Interfaces 7:8906–8914
130. Hart LR, Nguyen NA, Harries JL, Mackay ME, Colquhoun HM, Hayes W (2015) Polymer 69:293–300
131. Fox J, Wie JJ, Greenland BW, Burattini S, Hayes W, Colquhoun HM, Mackay ME, Rowan SJ (2012) J Am Chem Soc 134:5362–5368
132. Vaiyapuri R, Greenland BW, Rowan SJ, Colquhoun HM, Elliott JM, Hayes W (2012) Macromolecules 45:5567–5574
133. Vaiyapuri R, Greenland BW, Colquhoun HM, Elliott JM, Hayes W (2013) Polym Chem 4:4902–4909
134. Claessens CG, Stoddart JF (1997) J Phys Org Chem 10:254–272
135. Burattini S, Greenland BW, Chappell D, Colquhoun HM, Hayes W (2010) Chem Soc Rev 39:1973–1985
136. Burattini S, Colquhoun HM, Greenland BW, Hayes W (2012) Self-healing and mendable supramolecular polymers. In: Steed JW, Gale PA (eds) Supramolecular chemistry. Wiley, Hoboken, pp 3221–3234
137. Colquhoun HM (2012) Nat Chem 4:435–436
138. Colquhoun H, Klumperman B (2013) Polym Chem 4:4832–4833
139. Hart LR, Harries JL, Greenland BW, Colquhoun HM, Hayes W (2013) Polym Chem 4:4860–4870
140. Vaiyapuri R, Greenland BW, Colquhoun HM, Elliott JM, Hayes W (2014) Polym Int 63:933–942
141. Capek I (2005) Adv Colloid Interf Sci 118:73–112
142. Bose RK, Hohlbein N, Garcia SJ, Schmidt AM, van der Zwaag S (2015) Phys Chem Chem Phys 17:1697–1704
143. James NK, Lafont U, van der Zwaag S, Groen WA (2014) Smart Mater Struct 23:055001
144. Kalista SJ, Pflug JR, Varley RJ (2013) Polym Chem 4:4910–4926
145. Rahman MA, Spagnoli G, Grande AM, Di Landro L (2013) Macromol Mater Eng 298:1350–1364
146. Kalista SJ (2009) Self-healing ionomers. In: Ghosh SK (ed) Self-healing materials: fundamentals, design strategies, and applications. Wiley-VCH, Weinheim, pp 73–100
147. Ma X, Sauer JA, Hara M (1995) Macromolecules 28:3953–3962
148. Tadano K, Hirasawa E, Yamamoto H, Yano S (1989) Macromolecules 22:226–233
149. Eisenberg A (1970) Macromolecules 3:147–154
150. Williams CE, Russell TP, Jerome R, Horrion J (1986) Macromolecules 19:2877–2884
151. Tsujita Y, Hsu SL, MacKnight WJ (1981) Macromolecules 14:1824–1826
152. Squires E, Painter P, Howe S (1987) Macromolecules 20:1740–1744
153. Han K, Williams HL (1991) J Appl Polym Sci 42:1845–1859
154. Zhang L, Brostowitz NR, Cavicchi KA, Weiss RA (2014) Macromol React Eng 8:81–99
155. Hohlbein N, von Tapavicza M, Nellesen A, Schmidt AM (2013) Self-healing ionomers. In: Binder WH (ed) Self-healing polymers: from principles to applications. Wiley-VCH, Weinheim, pp 315–334
156. Varley RJ, van der Zwaag S (2008) Acta Mater 56:5737–5750
157. Pestka KA II, Kalista SJ, Ricci A (2013) AIP Adv 3:082113/082111–082113/082115
158. Bergman SD, Wudl F (2008) J Mater Chem 18:41–62
159. Varley RJ, van der Zwaag S (2008) Polym Test 27:11–19
160. Chen S, Deng Y, Chang X, Barqawi H, Schulz M, Binder WH (2014) Polym Chem 5:2891–2900
161. Malke M, Barqawi H, Binder WH (2014) ACS Macro Lett 3:393–397
162. Fall R (2001) Puncture reversal of ethylene ionomers—mechanistic studies. MSc dissertation. Virginia Polytechnic Institute and State University, Blacksburg

163. Kalista Jr. SJ (2003) Self-healing of thermoplastic poly(ethylene-co-methacrylic acid) copolymers following projectile puncture. MSc dissertation. Virginia Polytechnic Institute and State University, Blacksburg
164. Coughlin CS, Martinelli AA, Boswell RF (2004) Abstr Papers Am Chem Soc 228:261-PMSE. http://oasys2.confex.com/acs/228nm/techprogram/P779385.HTM
165. Kalista SJ Jr, Ward TC, Soc JR (2007) Interface 4:405–411
166. Huber A, Hinkley J (2005) Impression testing of self-healing polymers. NASA technical memorandum, NASA/TM-2005-213532. NASA, Hampton. http://ntrs.nasa.gov/archive/nasa/casi.ntrs.nasa.gov/20050082215.pdf
167. Varley RJ, van der Zwaag S (2010) Polym Int 59:1031–1038
168. Kalista SJ, Ward TC, Oyetunji Z (2007) Mech Adv Mater Struct 14:391–397
169. Haase T, Rohr I, Thoma K (2014) J Intell Mater Syst Struct 25:25–30, 26
170. Varley RJ, Shen S, van der Zwaag S (2010) Polymer 51:679–686
171. Rhaman MA, Penco M, Spagnoli G, Grande AM, Di Landro L (2011) Macromol Mater Eng 296:1119–1127
172. Penco M, Rhaman A, Spagnoli G, Janszen G, Di Landro L (2011) Mater Lett 65:2107–2110
173. Rahman MA, Penco M, Peroni I, Ramorino G, Grande AM, Di Landro L (2011) ACS Appl Mater Interfaces 3:4865–4874
174. Pestka KA, Kalista SJ, Ricci A (2013) AIP Adv 3:082113
175. Grande AM, Castelnovo L, Di Landro L, Giacomuzzo C, Francesconi A, Rahman MA (2013) J Appl Polym Sci 130:1949–1958
176. Francesconi A, Giacomuzzo C, Grande AM, Mudric T, Zaccariotto M, Etemadi E, Di Landro L, Galvanetto U (2013) Adv Space Res 51:930–940
177. Sundaresan VB, Morgan A, Castellucci M (2013) Smart Mater Res 2013:271546
178. Maure S, Furman S, Khor S (2010) Macromol Mater Eng 295:420–424
179. Maure S, Wu DY, Furman S (2009) Acta Mater 57:4312–4320
180. Pingkarawat K, Wang CH, Varley RJ, Mouritz AP (2012) Compos Part A 43:1301–1307
181. Pingkarawat K, Wang CH, Varley RJ, Mouritz AP (2012) J Mater Sci 47:4449–4456
182. Hohlbein N, Shaaban A, Schmidt AM (2015) Polymer 69:301–309
183. Aboudzadeh MA, Munoz ME, Santamaria A, Marcilla R, Mecerreyes D (2012) Macromol Rapid Commun 33:314–318
184. Aboudzadeh MA, Muñoz ME, Santamaría A, Fernández-Berridi MJ, Irusta L, Mecerreyes D (2012) Macromolecules 45:7599–7606
185. Aboudzadeh A, Fernandez M, Munoz ME, Santamaria A, Mecerreyes D (2014) Macromol Rapid Commun 35:460–465
186. Bose RK, Hohlbein N, Garcia SJ, Schmidt AM, van der Zwaag S (2015) Polymer 69:228–232
187. Malmierca MA, González-Jiménez A, Mora-Barrantes I, Posadas P, Rodríguez A, Ibarra L, Nogales A, Saalwächter K, Valentín JL (2014) Macromolecules 47:5655–5667
188. Akbarzadeh J, Puchegger S, Stojanovic A, Kirchner HOK, Binder WH, Bernstorff S, Zioupos P, Peterlik H (2014) Bioinspir Biomime Nanobiomater 3:123–130
189. Sandmann B, Bode S, Hager MD, Schubert US (2013) Adv Polym Sci 262:239–258
190. Holten-Andersen N, Harrington MJ, Birkedal H, Lee BP, Messersmith PB, Lee KYC, Waite JH (2011) Proc Natl Acad Sci USA 108:2651–2655
191. Holten-Andersen N, Jaishankar A, Harrington MJ, Fullenkamp DE, DiMarco G, He L, McKinley GH, Messersmith PB, Lee KYC (2014) J Mater Chem B 2:2467–2472
192. Fullenkamp DE, He L, Barrett DG, Burghardt WR, Messersmith PB (2013) Macromolecules 46:1167–1174
193. Enke M, Bode S, Vitz J, Schacher FH, Harrington MJ, Hager MD, Schubert US (2015) Polymer 69:274–282
194. Mozhdehi D, Ayala S, Cromwell OR, Guan Z (2014) J Am Chem Soc 136:16128–16131
195. Wang Z, Urban MW (2013) Polym Chem 4:4897–4901
196. Yuan J, Fang X, Zhang L, Hong G, Lin Y, Zheng Q, Xu Y, Ruan Y, Weng W, Xia H, Chen G (2012) J Mater Chem 22:11515–11522

197. Hong G, Zhang H, Lin Y, Chen Y, Xu Y, Weng W, Xia H (2013) Macromolecules 46:8649–8656
198. Yang B, Zhang H, Peng H, Xu Y, Wu B, Weng W, Li L (2014) Polym Chem 5:1945–1953
199. Burnworth M, Tang L, Kumpfer JR, Duncan AJ, Beyer FL, Fiore GL, Rowan SJ, Weder C (2011) Nature 472:334–337
200. Martínez-Calvo M, Kotova O, Möbius ME, Bell AP, McCabe T, Boland JJ, Gunnlaugsson T (2015) J Am Chem Soc 137:1983–1992
201. Sandmann B, Happ B, Kupfer S, Schacher FH, Hager MD, Schubert US (2015) Macromol Rapid Commun 36:604–609
202. Terech P, Yan M, Marechal M, Royal G, Galvez J, Velu SKP (2013) Phys Chem Chem Phys 15:7338–7344
203. Bode S, Zedler L, Schacher FH, Dietzek B, Schmitt M, Popp J, Hager MD, Schubert US (2013) Adv Mater 25:1634–1638
204. Kupfer S, Zedler L, Guthmuller J, Bode S, Hager MD, Schubert US, Popp J, Grafe S, Dietzek B (2014) Phys Chem Chem Phys 16:12422–12432
205. Bode S, Bose RK, Matthes S, Ehrhardt M, Seifert A, Schacher FH, Paulus RM, Stumpf S, Sandmann B, Vitz J, Winter A, Hoeppener S, Garcia SJ, Spange S, van der Zwaag S, Hager MD, Schubert US (2013) Polym Chem 4:4966–4973
206. Basak S, Nanda J, Banerjee A (2014) Chem Commun 50:2356–2359
207. Saha S, Bachl J, Kundu T, Diaz Diaz D, Banerjee R (2014) Chem Commun 50:3004–3006
208. Varghese S, Lele A, Mashelkar R (2006) J Polym Sci A Polym Chem 44:666–670
209. Wang Z, Fan W, Tong R, Lu X, Xia H (2014) RSC Adv 4:25486–25493
210. Bode S, Enke M, Bose RK, Schacher FH, Garcia SJ, van der Zwaag S, Hager MD, Schubert US (2015) J Mater Chem A. doi:10.1039/C5TA05545H
211. Hager MD, Greil P, Leyens C, van der Zwaag S, Schubert US (2010) Adv Mater 22:5424–5430
212. Garcia SJ (2014) Eur Polym J 53:118–125
213. Zedler L, Hager MD, Schubert US, Harrington MJ, Schmitt M, Popp J, Dietzek B (2014) Mater Today 17:57–69
214. Harrington MJ, Gupta HS, Fratzl P, Waite JH (2009) J Struct Biol 167:47–54
215. Waite JH, Qin X-X, Coyne KJ (1998) Matrix Biol 17:93–106
216. Waite JH, Vaccaro E, Sun C, Lucas JM (2002) Philos Trans R Soc Lond B 357:143–153
217. Harrington MJ, Waite JH (2007) J Exp Biol 210:4307–4318
218. Harrington MJ, Waite JH (2008) Biomacromolecules 9:1480–1486
219. Harrington MJ, Waite JH (2009) Adv Mater 21:440–444
220. Schmidt S, Reinecke A, Wojcik F, Pussak D, Hartmann L, Harrington MJ (2014) Biomacromolecules 15:1644–1652
221. Harrington MJ, Masic A, Holten-Andersen N, Waite JH, Fratzl P (2010) Science 328:216–220
222. Vaccaro E, Waite JH (2001) Biomacromolecules 2:906–911
223. Degtyar E, Harrington MJ, Politi Y, Fratzl P (2014) Angew Chem Int Ed 53:12026–12044
224. Krogsgaard M, Behrens MA, Pedersen JS, Birkedal H (2013) Biomacromolecules 14:297–301
225. Liu S, Gong W, Yang X (2014) Curr Org Chem 18:2010–2015
226. Houk KN, Leach AG, Kim SP, Zhang X (2003) Angew Chem Int Ed 42:4872–4897
227. Nakahata M, Takashima Y, Yamaguchi H, Harada A (2011) Nat Commun 2:511
228. Saenger W, Steiner T (1998) Acta Cryst A54:798–805
229. Harada A, Takashima Y (2013) Chem Rec 13:420–431
230. Schmidt BVKJ, Hetzer M, Ritter H, Barner-Kowollik C (2014) Prog Polym Sci 39:235–249
231. Yang X, Yu H, Wang L, Tong R, Akram M, Chen Y, Zhai X (2015) Soft Matter 11:1242–1252
232. Moozyckine AU, Bookham JL, Deary ME, Davies DM (2001) J Chem Soc Perkin Trans 2 2001(9):1858–1862

233. Yan Q, Feng A, Zhang H, Yin Y, Yuan J (2013) Polym Chem 4:1216–1220
234. Chuo T-W, Wei T-C, Liu Y-L (2013) J Polym Sci A Polym Chem 51:3395–3403
235. Wang Y-F, Zhang D-L, Zhou T, Zhang H-S, Zhang W-Z, Luo L, Zhang A-M, Li B-J, Zhang S (2014) Polym Chem 5:2922–2927
236. Peng L, Zhang H, Feng A, Huo M, Wang Z, Hu J, Gao W, Yuan J (2015) Polym Chem 6:3652–3659
237. Kakuta T, Takashima Y, Nakahata M, Otsubo M, Yamaguchi H, Harada A (2013) Adv Mater 25:2849–2853
238. Kakuta T, Takashima Y, Sano T, Nakamura T, Kobayashi Y, Yamaguchi H, Harada A (2015) Macromolecules 48:732–738
239. Himmelein S, Lewe V, Stuart MCA, Ravoo BJ (2014) Chem Sci 5:1054–1058
240. Zhang D-L, Ju X, Li L-H, Kang Y, Gong X-L, Li B-J, Zhang S (2015) Chem Commun 51:6377–6380
241. Rodell CB, Wade RJ, Purcell BP, Dusaj NN, Burdick JA (2015) ACS Biomater Sci Eng 1:277–286
242. Dong R, Liu Y, Zhou Y, Yan D, Zhu X (2011) Polym Chem 2:2771–2774
243. Chen H, Ma X, Wu S, Tian H (2014) Angew Chem Int Ed 53:14149–14152
244. Yu C, Wang C-F, Chen S (2014) Adv Funct Mater 24:1235–1242
245. Dong S, Zheng B, Wang F, Huang F (2014) Acc Chem Res 47:1982–1994
246. Pedersen CJ (1967) J Am Chem Soc 89:7017–7036
247. Zhang M, Xu D, Yan X, Chen J, Dong S, Zheng B, Huang F (2012) Angew Chem Int Ed 51:7011–7015, S7011/7011–S7011/7019
248. Zeng F, Han Y, Yan Z-C, Liu C-Y, Chen C-F (2013) Polymer 54:6929–6935
249. Li S, Lu H-Y, Shen Y, Chen C-F (2013) Macromol Chem Phys 214:1596–1601
250. Liu D, Wang D, Wang M, Zheng Y, Koynov K, Auernhammer GK, Butt H-J, Ikeda T (2013) Macromolecules 46:4617–4625
251. Yan X, Xu D, Chen J, Zhang M, Hu B, Yu Y, Huang F (2013) Polym Chem 4:3312–3322
252. Zhan J, Zhang M, Zhou M, Liu B, Chen D, Liu Y, Chen Q, Qiu H, Yin S (2014) Macromol Rapid Commun 35:1424–1429
253. Appel EA, Biedermann F, Rauwald U, Jones ST, Zayed JM, Scherman OA (2010) J Am Chem Soc 132:14251–14260
254. McKee JR, Appel EA, Seitsonen J, Kontturi E, Scherman OA, Ikkala O (2014) Adv Funct Mater 24:2706–2713
255. Guo D-S, Liu Y (2012) Chem Soc Rev 41:5907–5921
256. Yan H, Pan X, Chua MH, Wang X, Song J, Ye Q, Zhou H, Xuan ATY, Liu Y, Xu J (2014) RSC Adv 4:10708–10717
257. Li Z-Y, Zhang Y, Zhang C-W, Chen L-J, Wang C, Tan H, Yu Y, Li X, Yang H-B (2014) J Am Chem Soc 136:8577–8589
258. Ji X, Chen J, Chi X, Huang F (2014) ACS Macro Lett 3:110–113
259. De Gans B-J, Duineveld PC, Schubert US (2004) Adv Mater 16:203–213
260. Janoschka T, Teichler A, Häupler B, Jähnert T, Hager MD, Schubert US (2013) Adv Energy Mater 3:1025–1028
261. Wild A, Teichler A, Ho C-L, Wang X-Z, Zhan H, Schlutter F, Winter A, Hager MD, Wong W-Y, Schubert US (2013) J Mater Chem C 1:1812–1822
262. Chen Y, Kushner AM, Williams GA, Guan Z (2012) Nat Chem 4:467–472

Adv Polym Sci (2016) 273: 113–142
DOI: 10.1007/12_2015_341

Published online: 16 December 2015

Characterization of Self-Healing Polymers: From Macroscopic Healing Tests to the Molecular Mechanism

Stefan Bode, Marcel Enke, Marianella Hernandez, Ranjita K. Bose, Antonio M. Grande, Sybrand van der Zwaag, Ulrich S. Schubert, Santiago J. Garcia, and Martin D. Hager

Abstract Over the last few years, several testing methods have been introduced for the detection and quantification of autonomous and thermally stimulated healing in polymers. This review summarizes some of the most prominent state-of-the-art techniques for the characterization of polymer healing occurring at the microscopic and macroscopic levels during the repair of damage such as scratches, cracks, or ballistic perforations. In addition to phenomenological investigation of the self-healing process, a range of physical characterization techniques have been explored for elucidation of the underlying healing mechanism at the molecular or polymer network level. The present state of visual methods, spectroscopic techniques, scattering techniques, and dynamic methods is described. A short outlook is provided, discussing the future challenges and expected new trends in the characterization of self-healing polymers.

Stefan Bode and Marcel Enke are equally contributed.

S. Bode, M. Enke, U.S. Schubert (✉), and M.D. Hager (✉)
Laboratory of Organic and Macromolecular Chemistry (IOMC), Friedrich Schiller University Jena, Humboldtstrasse 10, 07743 Jena, Germany

Jena Center for Soft Matter (JCSM), Friedrich Schiller University Jena, Philosophenweg 7, 07743 Jena, Germany
e-mail: ulrich.schubert@uni-jena.de; martin.hager@uni-jena.de

M. Hernandez, R.K. Bose, A.M. Grande, S. van der Zwaag, and S.J. Garcia (✉)
Novel Aerospace Materials (NovAM), Faculty of Aerospace Engineering, Delft University of Technology, Kluyverweg 1, 2629HS Delft, The Netherlands
e-mail: S.J.GarciaEspallargas@tudelft.nl

Keywords Ballistic impact • Dielectric spectroscopy • Fracture testing • Raman spectroscopy • Rheology • Scratch healing • Self-healing polymers • Tapered double-cantilever beam • Tensile testing

Contents

1 Introduction

As demonstrated in other chapters of this special edition of Advances in Polymer Science, over the last few years, a number of promising strategies and approaches for the development of man-made materials with self-healing behavior have been proposed. In particular, efficient self-healing polymers and polymer-based fiber-reinforced composites are of high significance because these materials are utilized in numerous engineering fields, such as transport vehicles (cars, ships, aircrafts, and spacecrafts), electronics, and biomedicine [1, 2]. In contrast to metallic materials, polymers offer light weight, good processability, and chemical stability [3]. The lifetime of conventional materials, however, is reduced by intentional or accidental exposure to mechanical, chemical, or thermal stresses. These conditions can lead to the formation of scratches, surface and internal cracks, or even to holes as in the case of ballistic impact [1]. Over time, these cracks grow under the influence of mechanical stresses until catastrophic failure of the entire product or system occurs. Self-healing reactions in the material itself, which reduce this early stage damage to such a state that catastrophic damage does not occur, provide polymers and polymer composites featuring longer lifetimes and a higher reliability under real life, non-steady state loading conditions [4].

The pioneering work on self-healing polymers by Dry et al. [5] in 1992 and White et al. [6] in 2001 demonstrated the basic phenomena of autonomous restoration of mechanical properties after a damage event. During the last 15 years many new strategies for the design of novel self-healing materials have been presented. In

general, self-healing can be autonomous or non-autonomous. Autonomous self-healing materials do not require any additional external stimulus because the damage itself triggers the healing process. In contrast, non-autonomous self-healing materials require an external energetic input such as heat or light to enable the healing process.

In self-healing polymers, classification into extrinsic and intrinsic self-healing polymers is more common and more relevant. Extrinsic self-healing is based on the presence of intentionally added discrete micro- or nano-encapsulated healing agents. Intrinsic healing is related to chemical modification of the base polymer such that the polymer itself is capable of restoring chemical bonds across a damage site. In the companion chapters of this special edition of Advances in Polymer Science the various routes are described in great detail. Whatever the mechanism, all self-healing polymers have in common that the damage (defined as the presence of newly created free surfaces within the material or at its surface) is reduced ("healed") sometime after the occurrence of damage, without manual intervention. This reduction in damage results in partial or complete recovery of the mechanical or functional performance of the material.

This chapter does not focus on the polymer architecture but on the suitability of test methods currently under development for quantification of the healing action and unraveling the link to the underlying molecular processes. Each of the (micro- or macroscopic) test methods is designed for a special application. For instance, scratch healing tests are suitable for the investigation of self-healing coatings and for the early characterization of the healing behavior of experimental polymers available only in small quantities; however, such tests are not useful for determining the restoration of mechanical properties. Tensile or double cantilever beam tests are better suited methods for this particular case, but they are limited to relatively brittle polymers. Fracture mechanical tests are more suitable for characterization of healing in ductile polymers or elastomers. Therefore, functional relations exist between the type of polymer, the desired application, and the testing method. Additionally, an understanding of the underlying mechanism at the molecular level is essential for the design of novel self-healing materials and to optimize existing routes towards self-healing polymers more rapidly than via a trial-and-error approach (Fig. 1). Furthermore, this information can enable the preparation of functional self-healing systems that combine various self-healing principles for various forms of structural and functional damage.

This review summarizes the characterization of self-healing polymers with different methods and describes investigations aimed at understanding the healing mechanism. Only mechanical damage and the related testing methods are discussed. The healing of additional functions, such as electrical and thermal conduction and electrochemical protection, is discussed in another chapter and the interested reader is referred to that review [7].

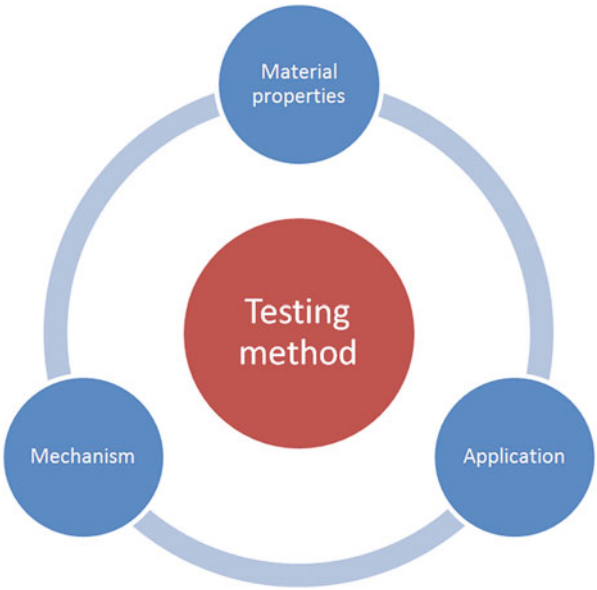

Fig. 1 Interactions between the material properties, underlying healing mechanisms, testing, and application necessary for the development of self-healing materials

2 Characterization of Self-Healing Polymers: Material Properties

2.1 Tensile Testing

Tensile testing is a standard technique for determination of the quasi-static mechanical properties of a material. It offers the possibility to determine different parameters such as tensile strength, tensile stress, elongation, or Young´s modulus as a function of temperature, time, and strain rate [8]. It requires standardized rectangular or dog-bone shaped specimens. This method can also be applied for the determination of self-healing efficiency. For this purpose, the original sample and the healed sample are measured under the same testing conditions and the resulting load-crosshead displacement curves are used for determination of the healing efficiency. The healing efficiency is generally defined as the quotient of the property value after healing and the property value of the pristine material. Despite it being widely used, tensile testing is not the ideal measurement method for quantification of the self-healing process although it offers a fast first-order approximation. To determine self-healing efficiency, different material properties are suitable, for example, elongation at break [9], the recovery of yield point stress [10], or force-displacement curves [11]. The most commonly used parameter is the maximum load at failure of the specimen [12, 13]. However, as we know from fracture mechanics, simple comparison of the failure load after damage and healing with that of the virgin material is incomplete and often misleading, even more so if the damage itself is not quantified and perfectly reproducible, as described recently

by Bose et al. [14] and Grande et al. [15]. However, the analysis of self-healing polymers via tensile testing offers the possibility to crudely assess the time-dependence of the healing process. For example, Binder and coworkers studied tensile failure of polymers with reversible hydrogen bonding groups and demonstrated the progress of the healing process at 30°C as a function of time (Fig. 2) [16].

Stress or stain recovery using tensile testing can also be a measure of network recovery, as proposed in studies of damage healing in strained mussel byssal threads [17]. In this case, the sample was elongated above the yield point and, subsequently, the stress was released. Over time, recovery of the original mechanical performance could be detected (Fig. 3), suggesting regeneration of the original structure and properties [18]. Given the simple linear geometry of the thread and the fact that the damage is at a nanoscopic level (at which fracture mechanical considerations do not apply) tensile testing is an acceptable form of testing [19].

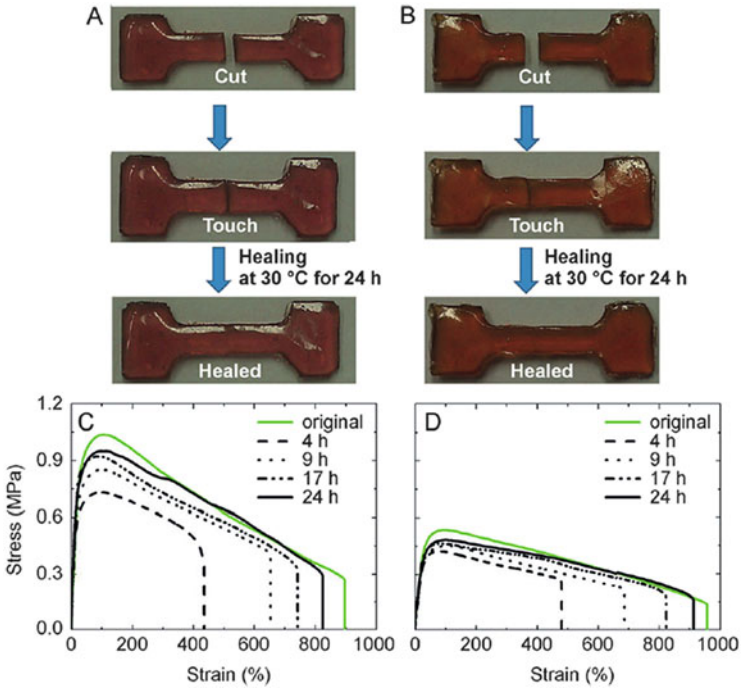

Fig. 2 Two self-healing block polymers based on hydrogen bonds: V-shaped polystyrene-*block*-poly(*n*-butyl acrylate) (*left*) and H-shaped polystyrene-*block*-poly(*n*-butyl acrylate) (*right*). (**a**, **b**) Self-healing behavior of the polymer in tensile testing specimen. (**c**, **d**) Recovery of the stress–strain behavior of the polymers (reprinted with permission from [16])

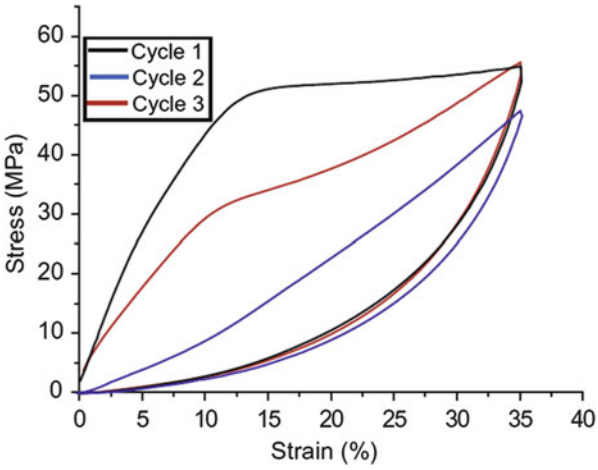

Fig. 3 Healing process of mussel byssal threads: *Cycle 1* represents the mechanical properties of the distal region, *cycle 2* shows the loss of stiffness, and *cycle 3* represents the self-repair of mussel byssus threads after 1 h and partial regeneration of the mechanical properties (reprinted with permission from [18])

2.2 Tapered Double Cantilever Beam

The most appropriate method for study of the self-healing process in brittle polymers is the tapered double cantilever beam (TDCB) [20–22]. A schematic representation of the test specimen is depicted in Fig. 4. Provided that fracture surfaces are more or less mirror-smooth and that the crack surfaces are accurately repositioned, this test geometry allows a more realistic quantification of the healing process than tensile testing as the fracture toughness is independent of the crack length (whereas the crack width is fixed by the plate thickness) [23]. The healing efficiency is the quotient of the healed and the original fracture toughness [23]. Theoretical calculations revealed a good correlation with the measured results, but small changes in the geometry and the applied load can lead to different values in the load–displacement curve [20].

Extrinsic self-healing materials have been tested intensively using this sample geometry. Kessler et al. were able to utilize this method to study one of the earliest autonomous self-healing epoxy systems, which incorporated microcapsules containing a liquid healing agent [24]. Another example has been described by Liberata et al., who utilized microcapsules filled with a norbornene derivate as healing agent and studied the healing efficiency as a function of time and temperature [25].

2.3 Fracture Mechanics

Following the initial works with stiff systems, most researchers to date have used the recovery of tensile strength of broken samples as the measure of healing in "soft polymers." However, this testing method, based on continuum mechanics, fails to

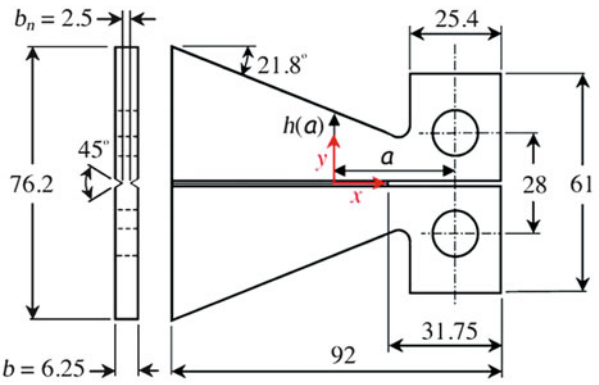

Fig. 4 Scheme of the tapered double cantilever geometry (all sizes in mm) (reprinted with permission from [23])

capture the relevant processes at the healing surfaces and the effective restoration of mechanical properties. The healing behavior across the interface between two former fracture surfaces should be treated as an interfacial phenomenon. More quantitative information on the healing process can be potentially obtained from test protocols based on fracture mechanics (e.g., the TDCB protocol for "stiff polymers"). Crack propagation represents an instructive case for investigation of the interplay between polymer structure and mechanical properties, allowing quantification of the material resistance to fracture in the presence of flaws or defects [26].

Early fracture mechanics studies on elastomers were performed by Rivlin and Thomas, demonstrating that tear energy is strictly a materials property independent of the sample geometry [27]. Over the past two decades, several approaches have been developed and applied to the characterization of the fracture properties of soft polymers, obtaining information on both the resistance to crack initiation and resistance to crack propagation [28–31]. Nevertheless, fracture mechanics-based tests are rarely considered for study of the performance of healable polymers and have been employed in only a limited number of research works [11, 15, 32, 33]. Grande et al. [15] investigated the self-healing behavior of a healable supramolecular elastomer by adapting a fracture mechanics testing procedure based on the J-integral parameter [34, 35] (Fig. 5a). In their work [33], the researchers presented a clarifying comparison between the healing efficiency measured by means of standard tensile experiments and that determined by fracture mechanical testing (Fig. 5b and c). From these results it became clear that the selection of a proper test configurations in combination with phenomenologically different experiments and healing conditions is a required step for the development of new self-healing polymers with improved properties. Moreover, it has become clear that fracture experiments are more crucial for assessment of the mechanical properties of a healed interface. The drawback of the fracture mechanical evaluation of healing efficiency is that relatively large material volumes are required, which are not always available when testing experimental polymers.

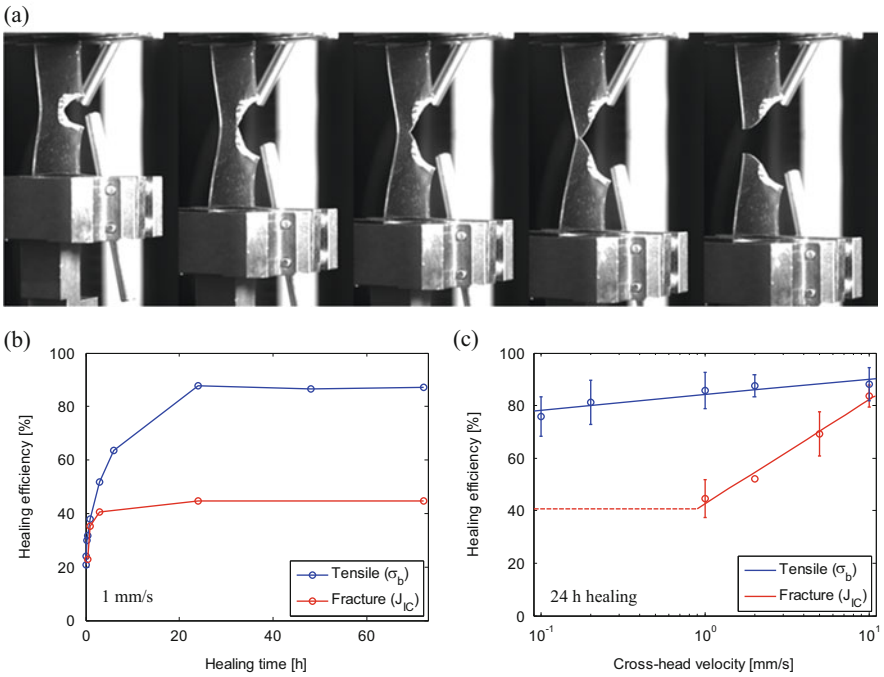

Fig. 5 (**a**) Single edge notched tensile (SENT) specimen during fracture test. (**b**, **c**) Comparison of healing efficiencies obtained in tensile (stress at break, σ_b, recovery) and fracture (fracture toughness, J_{IC}, recovery) experiments. (**b**) Effect of the healing time: maximum healing efficiencies of around 80% and 40% after 24 h healing in tensile and fracture mode, respectively. (**c**) Effect of the deformation rate: convergence of tensile and fracture healing efficiencies at the highest cross-head velocity (same failure mechanism) (adapted with permission from [15])

2.4 Scratch Healing

A widely utilized, indicative self-healing test for polymers is scratch healing. Self-healing coatings require this kind of test procedure to evaluate the damage healing potential (mostly scratch closing) and the subsequent restoration of functions such as aesthetics and corrosion protection. For extrinsic healing systems, scratching leads to local opening of the capsules, thereby releasing the healing agents, which results in polymerization and subsequent scratch closure [36, 37].

Given their natural ability to heal local damage multiple times, intrinsic healing polymers have a much higher market potential for applications (such automotive coatings, optical coatings, decorative surfaces), where autonomous or minimally stimulated scratch healing would be beneficial. Therefore, scratch healing in intrinsic healing polymers has been studied extensively by many polymer development groups.

Most studies still use scratches manually created with poorly specified sharp objects for preliminary assessment of self-healing polymers, despite the low

reproducibility and comparability [3, 38–44]. To overcome these limitations, Garcia and coworkers established a procedure to fabricate defined scratches [45]. The authors developed a microscratch tester with a 100 μm radius sphere-conical diamond indenter tip. First, a pre-scan at 0.03 N load is performed to correct for sample tilting or topology variations along the polymer surface during controlled scratching. Subsequently, the actual scratch is made at fixed load (dependent on the system and thickness) causing a maximum penetration depth (P_d). The test is completed by a post-scan at 0.03 N to determine the scratch depth after rapid viscoelastic recovery (R_d). After measuring the residual volume of the scratch with a confocal microscope, the samples are allowed to heal as a function of time, temperature, and/or relative humidity and the after-healing residual volume measured at fixed intervals. In this manner the healing efficiency can be calculated from changes in the value of the filled volume (Fig. 6) [45].

Other techniques have also been applied to investigate healing of scratches smaller than those created with a microscratch tester. For instance, several studies have utilized optical microscopy [38, 40, 42, 43], atomic force microscopy (AFM) [3], scanning electron microscopy (SEM) [44], or an optical profilometer [41]. Although these methods offer qualitative results in terms of presence or absence of healing, they offer rather poor quantitative information. More recently some works have combined controlled macroscale healing of scratches with other techniques to correlate molecular healing with macroscale healing [46–48].

Using a combination of scratching and electrochemical techniques (e.g., electrochemical impedance spectroscopy and the scanning vibrating electrode technique), the time dependence of the degree of healing of the corrosion protective power under a range of conditions can also be determined [36, 37, 49–51].

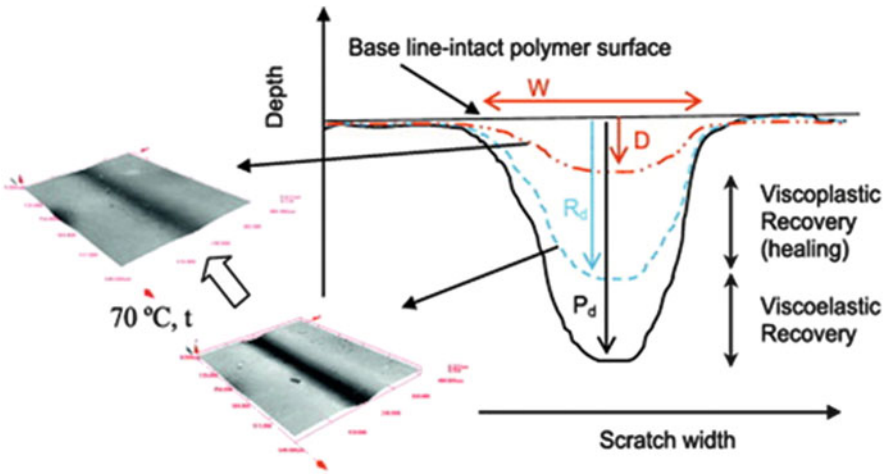

Fig. 6 Quantification of scratch healing in term of the changes in scratch size (reprinted with permission from [45])

2.5 Ballistic Impact

Given the accidental discovery by Kalista et al. [52, 53] of the phenomenon of self-healing after ballistic impact in ionomers during the early stages of development of the field of self-healing materials, ballistic healing has received a relatively large amount of attention in the literature, notwithstanding the uncontrolled conditions during damage formation itself.

Kalista and coworkers used a projectile test station, in which thick ionomer films are punctured by sharp projectiles as a function of the sample temperature [53, 54]. In self-healing polymer grades, the hole created by the projectile is fully filled by a reflow of the polymer, but the sample surface still shows clear sign of impact damage (Fig. 7). During ballistic impact there is local heating of the polymer near the impact site to temperatures approaching the melting temperature, but the extent of heating is hard to quantify. The heating effect is particularly important for pointed projectiles (causing complete hole closure) and is less relevant for blunt projectiles that do not result in hole closure.

A pressurized burst test (PBT) can be used to determine the degree of healing of samples showing more or less complete hole closure. The burst pressure of healed samples in relation to the burst pressure of pristine samples is taken as a measure of healing efficiency [54].

In an attempt to further understand the phenomena behind ionomer healing under ballistic impact, Varley and van der Zwaag developed a quasi-static test method that mimics low speed but temperature-controlled ballistic impacts [55]. For this purpose, a stainless steel cylindrical rod with a disk (heated to different temperatures and with different diameters) at the end is pulled through the sample by a standard tensile testing machine (Fig. 8). By controlling the penetration speed and environmental temperature, the contributions of elastic and viscoelastic processes can be separated. The degree of hole closure is evaluated by

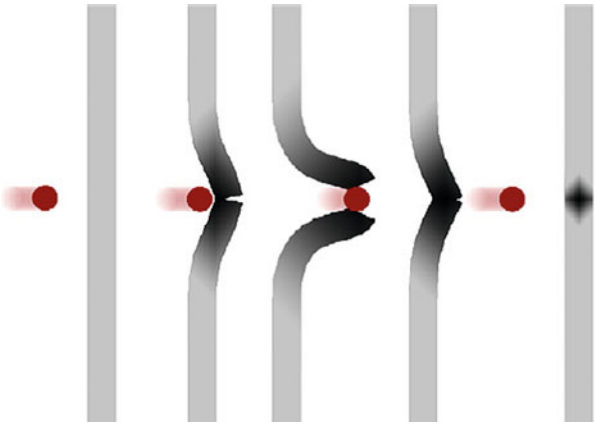

Fig. 7 Bullet penetration of thin ionomeric polymer films (reprinted with permission from [55])

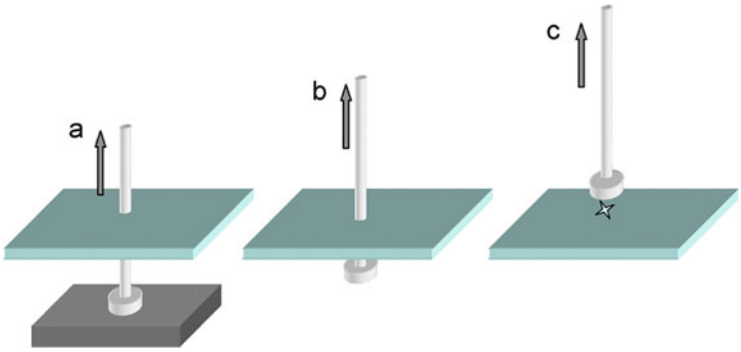

Fig. 8 Quasi-static test: (**a**) Start position of the setup where the rod is through the sample and the disk is heated. (**b**) Rod is pulled with a certain velocity through the sample. (**c**) Disk leaves the sample, resulting in an impact zone in the material (reprinted with permission from [55])

SEM and compared with hole closure data for the same polymers but after ballistic impact using pistol-fired projectiles.

The ballistic tests show that the local temperature at the impact zone plays a crucial role, whereas the ionic character of ionomeric ethylene methacrylic acid (EMAA) copolymers plays a secondary role with respect to the self-healing behavior. Also, EMAA copolymers not having any ionic content reveal some self-healing capacity [56]. For proper self-healing in these ionomers, a combination of an elastic response (i.e., shape memory or rebound of the surfaces) and a viscous response (i.e., secondary polymer flow and chain entanglement) is required [55]. To further investigate the interplay between elastic and viscous response, blends of ionomers with elastomers or thermoplastics were developed to create materials with desirable mechanical properties and some healing ability [57, 58]; the coupling between ballistic and rheology experiments clarified the effects of blend composition and blend morphology on the healing mechanism [59]. Indeed, playing with the blend mechanical properties significantly modified the healing behavior after high energy impact.

In a more recent study, healing of ionomers over a wider projectile velocity range (from 180 to 4,000 m s^{-1}) was demonstrated and a relationship between critical sample thickness (t) and bullet diameter (d) was rationalized as a critical geometrical parameter [60]. Healing clearly not only depends on the impact energy and the material, but also on the dimensions (and hence mechanical response) of the impacted structure. This complicates analysis of the molecular mechanisms involved in ballistic healing. Ballistic tests therefore only have an engineering relevance.

3 Revealing the Underlying Mechanism of Self-Healing Polymers

A better understanding of the underlying damage-restoring mechanism at the polymer network or molecular level offers the opportunity to fabricate novel polymers with improved and tailored self-healing behavior. In particular, intrinsic self-healing polymers should be investigated in detail in order to understand the origin of the dynamics and the resulting self-healing process. Molecular insight into healing in extrinsic self-healing systems is much easier to obtain, because in such systems the healing action is directly attributable to the intentionally added healing agent and the chemical reactions it can undergo or cause.

3.1 Imaging Techniques

3.1.1 Optical Microscopy and Scanning Electron Microscopy

Optical microscopy covers length scales higher than that for intrinsic (molecular scale) healing and therefore does not provide much direct information on the active molecular mechanism. In the case of extrinsic healing, the length scale of optical microscopy is the same as that of the healing entities and the encapsulation. Thus, the release of healing agent from the capsules can be studied optically [6, 61]. The effects of size distribution of the (micro)particles in extrinsic healing systems can easily be investigated using optical microscopy [6, 62, 63]. Furthermore, the encapsulated solution can be mixed with a (fluorescent) dye, which can be monitored after crack formation (Fig. 9) [6, 64, 65].

SEM gives the opportunity to observe the healing reactions in extrinsic healing systems at higher resolutions [6, 66–70]. As in optical microscopy, the distribution of the healing agent within the healed material can be analyzed in detail. To prove polymerization of the released monomer, Raman, IR, or NMR spectroscopy must be utilized [71–74]. A new trend in this context is the detection of local stress within the material [75–79]. This method allows visualization of those parts of the sample that feature the highest stresses, and leads to more quantitative information about the formation and propagation of cracks.

3.1.2 Micro-Computed Tomography Scanning

Given the fact that most polymers are not transparent (certainly not to electrons), optical and SEM microscopy only give information on healing at or near the sample surface and cannot be utilized to study the healing of internal damage. X-ray computed tomography (CT) can be utilized to obtain a more complete three-dimensional (3D) representation of the damage and healing processes. A stack of

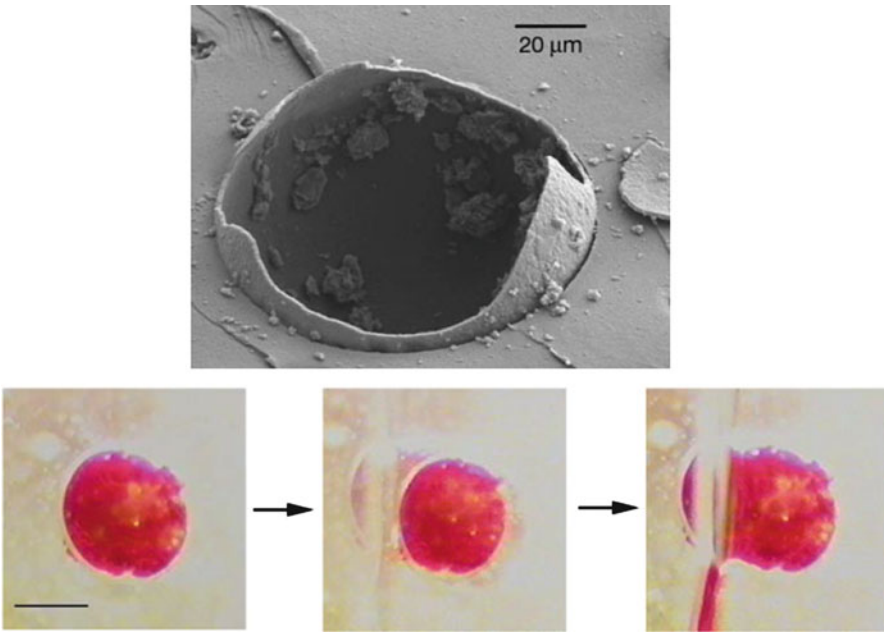

Fig. 9 Investigation of the self-healing mechanism of extrinsic self-healing polymers: capsules after disruption and release of healing agent (*above*) and process of rupture of the capsules and release of the stained healing agent (*below*) (reprinted with permission from [6])

2D X-ray micrographs can be obtained by rotating the sample. These 2D images are then processed to generate a 3D visualization of the sample. The very first micro-CT study demonstrating the release of healing agent from fractured microcapsules embedded in an epoxy matrix was that of Mookhoek et al., who used a special micro-CT set-up in an SEM system [80]. Because the method uses a coherent X-ray microbeam, spreading of the healing liquid in the matrix could be determined with great accuracy, in spite of the chemical similarity between the healing agent and the matrix.

More conventional micro-CT scanning using an incoherent X-ray beam has been used to observe the crack opening in fiber–polymer composites and subsequent release of healing agent into the surrounding polymer matrix [81]. As a result of the difference in densities of the fibers, healing agent, and surrounding polymer matrix, the release of healing agent could also be visualized for this system. A tomographic image of alginate fibers containing healing agent in an unloaded unidirectional pre-impregnated (UD prepreg)-like sample is shown in Fig. 10. Most of the vacuoles seem to be intact as no sign of release of healing agent can be observed. After loading up to 4% strain, clear distinctive "cauliflower-like" features related to the release of the healing agent can be seen in the top-right corner of the image. Tomographic observations show that the compartmented fiber responds to the

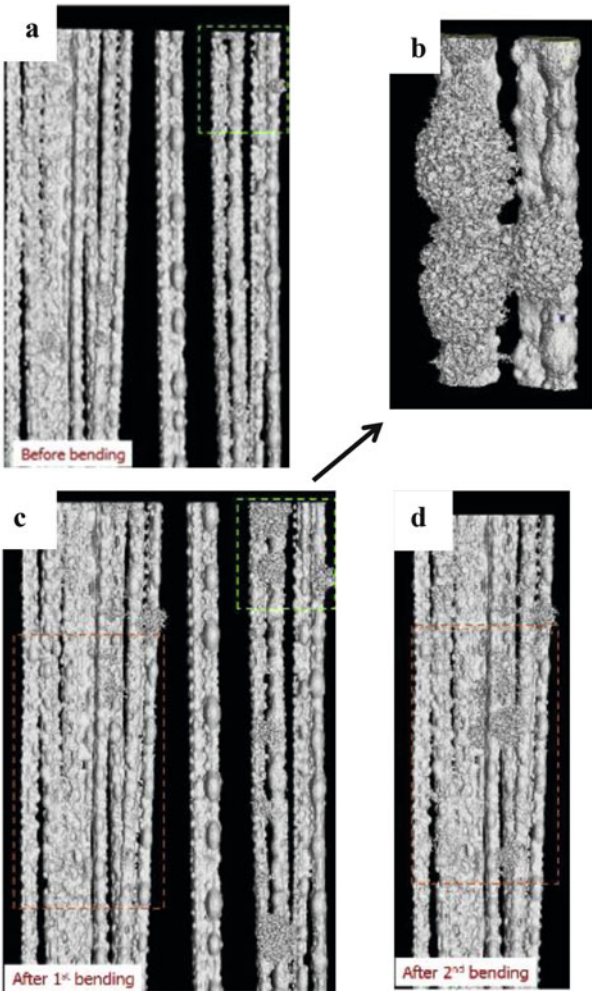

Fig. 10 Tomographic images of a set of embedded filaments: (**a**) before bending, (**c**) after 1st bending to 4% strain, and (**d**) after 2nd bending to 6% strain. (**b**) Magnified image showing compartment opening and healing agent release into the damaged matrix after the flexural test. *Rectangles* marked by *green* and *red dashed lines* represent the two areas of interest before and after first and second loading respectively. The opening of the compartments and release of healing agent can be observed in these zones by the appearance of cauliflower-like features after bending (reprinted with permission from [81])

damage progressively; that is, it is able to release the embedded liquid healing agent to the damaged sites during re-loading after a previous healing event.

Micro-CT scanning has also recently been used to analyze the healing efficiency of extrinsic healing of anticorrosion coatings [82]. In this research, the healing (or corrosion protection efficiency) was measured in terms of delamination and pitting growth onset and kinetics reduction in an epoxy coating containing capsules filled with silyl ester healing agent applied on aluminum alloy 2024-T3.

3.2 Spectroscopic Techniques

In intrinsic self-healing polymers, the most relevant processes occur at the molecular level and they are responsible for the flow and network restoration crucial to the healing process. For such materials, spectroscopic methods in combination with rheological tests are of high importance. The preferred spectroscopic methods are Raman and IR spectroscopy, NMR spectroscopy, X-ray or neutron scattering [83], and, more recently, dielectric spectroscopy. All these methods have been utilized for the investigation of self-healing materials and are explained in the following paragraphs.

3.2.1 Infrared and Raman Spectroscopy

Raman and IR spectroscopy are powerful methods for detecting and following chemical reactions [84]. The recorded spectra can be utilized to detect the presence of a chemical substance and to follow a reaction (e.g., consumption of an azide during a click reaction) [83, 85–87]. Raman and IR spectroscopy can also be employed to follow the polymerization of encapsulated monomers in extrinsic healing polymers [64, 67, 70, 74, 88–91]. The mechanism of thermally activated self-healing in metallopolymers has been investigated by the combination of temperature-dependent Raman measurements and quantum mechanical calculations [43]. The polymer was a copolymer crosslinked by terpyridine-iron(II) metal complexes [92]. The authors observed a shift of the terpyridine signals during heating (Fig. 11). The quantum mechanical calculations indicated that the shift is a result of partial opening of the metal complexes (decomplexation).

AbdolahZadeh et al. also used Raman spectroscopy to evaluate a hybrid organic–inorganic dual network containing disulfide bonds as the reversible groups [93]. The authors correlated the excellent macroscale healing capabilities of the

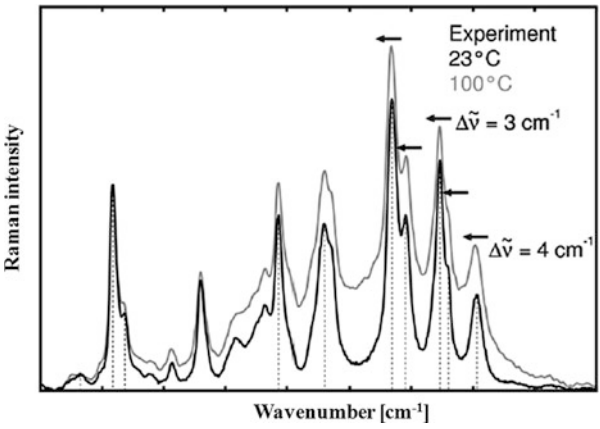

Fig. 11 Raman spectrum of a metallopolymer crosslinked by iron(II)-*bis*-terpyridine metal complexes at 23°C and 100°C (reprinted with permission from [92])

dual network with the reversibility of the disulfide links observed in cyclic heating and cooling tests, as followed by Raman spectroscopy. The signal intensity of the disulfide decreases during heating and increases to original values during cooling, suggesting the temporary opening of bonds at higher temperatures, which is crucial for the required increase in local mobility of the network.

Other reversible chemical reactions yielding intrinsic self-healing behavior can also be monitored via spectroscopic methods in the IR regime. In particular, the change in molecular structure during a Diels–Alder (DA) reaction can be monitored by IR as well as Raman spectroscopy [94–96]. Thus, Bose et al. investigated the relation between self-healing behavior and the reversible DA reaction in a copolymer of lauryl methacrylate and two monomers containing the DA moieties (i.e., furan and maleimide) [46]. The authors heated the polymer above the retro-Diels–Alder (rDA) temperature and observed that the intensity of the furan signal increased with temperature. Upon cooling, the signal intensity decreased again, indicating formation of the DA adduct. Furthermore, the reversibility of this process could be proven by repeating the heating cycle. Additionally, the polymer was heated to three different temperatures above the rDA temperature and the isothermal kinetics of the rDA chemistry in bulk could be obtained. Another possibility for investigating the DA chemistry is by making use of Raman spectroscopy, in particular Raman spectroscopic 2D correlation analysis [97]. In this case, the change in signal intensity is correlated with the change in intensity of the other Raman signals, and a clear assignment of local changes in molecular structure can be made.

3.2.2 Nuclear Magnetic Resonance Spectroscopy

Another powerful method for analysis of self-healing polymers is (solid-state) NMR spectroscopy. This technique offers the possibility to analyze the molecular structure and its changes at the atomic level. Thus, Wudl and coworkers were able to study their DA-based self-healing polymers with temperature-dependent ^{13}C-solid state NMR and showed the reversible opening of the DA units during heating [13, 98]. Bode et al. utilized ^{113}Cd-solid state NMR to show the different complexation modes of cadmium(II) acetate and cadmium(II) bromide with terpyridine moieties [42]. They were able to connect the difference in coordination between cadmium(II) acetate and terpyridine ligand to an improved self-healing behavior. In general, solid-state NMR investigations can also be utilized to study the flexibility of polymer chains [99, 100] and, hence, to deepen understanding of the relationship between molecular behavior and self-healing.

3.2.3 Broadband Dielectric Spectroscopy

Broadband dielectric spectroscopy (BDS) measures the dielectric properties of a medium by following the interactions of an external electrical field with the electric

dipole moments of the studied material and has been used extensively to study polymer dynamics [101–104]. In BDS, a broad dynamic frequency range between 10^{-2} and 10^{9} Hz can be applied under isothermal or isochronal conditions to follow motional processes occurring at different time scales (i.e., relaxation times). Such processes depend on the molecular mobility of groups, segments, or whole polymer chains (i.e., on the morphology and microstructure of the system under investigation). In polymers, information about the polymer architecture or structural state of the material can be extracted directly by taking the molecular mobility as a probe for the structure. Realizing that BDS has the unique ability to describe mobility as a function of polymer architecture and, hence, might be a powerful tool for assessing polymer healing processes, Hernández et al. recently explored the potential of the technique [105, 106]. One of the most important parameters obtained from BDS measurements is the so-called dielectric loss (ε'') [107]. The normalized evolution of this parameter with temperature has traditionally been related to polymer dynamics. In their study of the relation between self-healing and dielectric behavior, Hernández and colleagues [105, 106] monitored the healing process of a disk of self-healing rubber at a constant temperature under controlled conditions. The BDS data of the pristine and healed samples are plotted in Fig. 12. Two important conclusions can be drawn: (i) The possibility of measuring the dielectric signal is an indication that healing is occurring (damaged samples give no reliable signals). (ii) The variation in ε'' is connected to the presence of (nanoscopic) heterogeneities at the healed interface, despite the fact that optical observations suggest that the crack is fully healed. Further tests and deeper analysis of the obtained data is necessary to confirm the broader applicability and potential implementation of BDS as a relevant technique for the development and understanding of self-healing polymers.

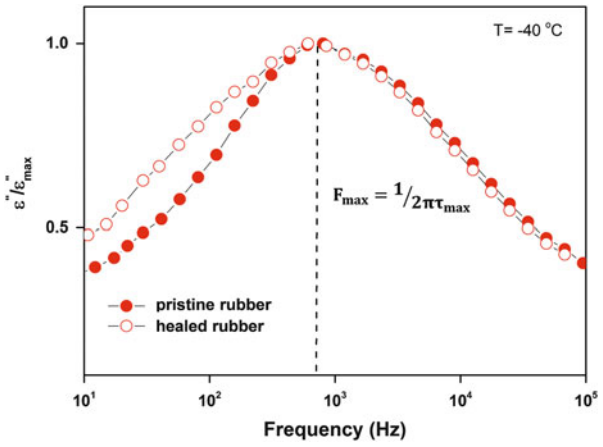

Fig. 12 Normalized dielectric loss ε'' versus frequency for pristine and healed rubber samples at −40°C [105, 106]

3.3 Scattering Techniques

Scattering methods offer the possibility to investigate ordered molecular structures in the bulk of the material in more detail. It is an appropriate method for monitoring structural changes as a function of temperature and time. The standard scattering methods utilize either X-ray or neutron radiation. No reports on the use of muon scattering to monitor self-healing behavior have been published yet.

3.3.1 X-Ray Scattering

Small and wide angle X-ray scattering (SAXS and WAXS) can reveal the presence of ordered structures of relevance for the study of certain self-healing polymers. X-ray scattering has been used extensively to correlate the appearance–disappearance of the clusters/secondary crystals in ionomers and their connection to the self-healing process [108–110]. As a result of the large difference in polarity, ionomers tend to form ionic clusters [111, 112]. The volume around the clusters has a restricted mobility, which is beneficial for mechanical properties but detrimental for self-healing. During heating, a phase transition take place (order–disorder transition), but the ionic aggregates can still be present in the melt, as shown in a very early SAXS analysis [113, 114]. This observation clearly contradicts the assumed relation between the cluster behavior and healing ability of ionomers. Another example of cluster formation in relation to self-healing was described by Binder and coworkers, who utilized polymers with hydrogen bonds [115]. The hydrogen bonding motifs form clusters/aggregates within the polymer, which can be analyzed by SAXS measurements [116, 117]. Bode and colleagues observed clustering for crosslinked self-healing metallopolymers [42, 43], using a synthesized a terpyridine-containing copolymer crosslinked by the addition of different metal salts. Ordered structures could be observed via SAXS measurements, which were assigned to the formation of ionic clusters. All these observations have increased the detailed knowledge of changes in molecular arrangement in self-healing polymers, but have not yet yielded a fully satisfying explanation for the intrinsic self-healing ability of ionomers.

3.3.2 Neutron Scattering

It is also possible to utilize neutron radiation for the investigation of molecular structures. The limiting factor is the availability of measurement techniques. Probably as a consequence of its limited availability, this technique has not yet been utilized for the investigation of self-healing polymers, although it has great potential because molecular dynamic processes can be analyzed in even more detail than with X-rays [118, 119].

3.4 Rheology

Investigation of the mechanical properties of self-healing polymers and their temperature dependency via rheology offers a powerful tool for visualizing dynamic processes [120, 121]. The recovery of G' (storage modulus) is an indicator of the self-healing process and can also be used for the quantification of self-healing behavior [122].

Scheltjens et al. showed the complete reversibility of their DA network polymers when the loss angle of the polymer reached 90° at the rDA temperature, but made no connection with the effect this could have on mechanical or self-healing behavior [123]. Bose et al. used rheology in combination with FTIR to follow the effects and occurrence of reversible DA covalent reactions [46].

Rheology measurements can also follow dynamic processes for non-covalent supramolecular systems [116, 124, 125]. For such polymers, the crossover of G' and G'' (loss modulus) can be utilized to estimate the representative supramolecular bond life time (τ), being the reciprocal of the crossover frequency. The time range contains information about the dynamics of the supramolecular unit and was found to be correlated with the self-healing ability [16, 126]. The relationship was demonstrated by Bose et al. for a set of poly(*n*-butyl acrylate)-*co*-(acrylic acids) ionomers with different amounts of acid [48]. The self-healing behavior and rheological properties were measured at different temperatures and it could be demonstrated that the self-healing ability correlates with the bond lifetime (Fig. 13). A combination of adequate mechanical properties and good ability to

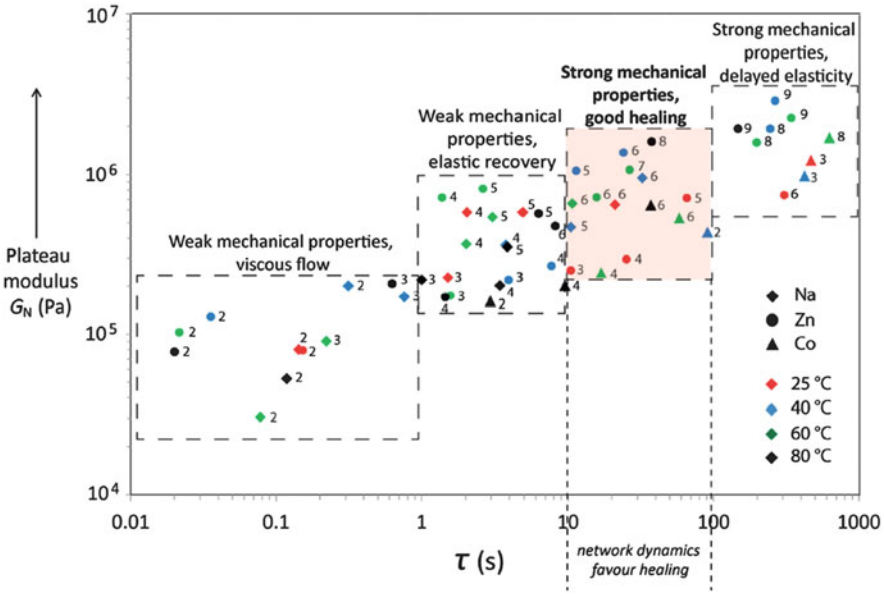

Fig. 13 Correlation of the mechanical properties and supramolecular bond lifetime (τ) for poly(*n*-butyl acrylate)-*co*-(acrylic acid) neutralized with different cations at different temperatures (reprinted with permission from [48])

close cracks was obtained when the representative supramolecular bond lifetime was between 10 and 100 s. The supramolecular bond lifetime itself depends on the amount of ionic groups, the nature of the cation, and the temperature [127]. Using this approach, the activation energy of the healing process could be determined, and it was proposed that activation of the ionic clusters rather than the chain dynamics is the rate-limiting step in the self-healing process.

Rossow et al. synthesized a model set of regular star-shaped poly(ethylene glycol) polymers end-capped with terpyridine groups that can transiently coordinate to different metal ions to form transient supramolecular polymer networks with different homogeneous architectures and different binding strengths [121]. The authors utilized dynamic temperature-dependent rheology investigations to study the network mechanics, dynamics, and relaxation from both macroscopic and microscopic perspectives. This work revealed that, for a self-healing system network, relaxation occurred on the time scale of tens or hundreds of seconds (corresponding to data in Fig. 13), depending on the strength of transient polymer building-block association and the metal-to-terpyridine stoichiometric ratio. Lewis et al. used rheology to compare the effect of increasing binding energies of hydrogen bonding side groups on the same polymer backbone [128]. The authors reported that polymers containing weak hydrogen bonding groups behaved as unentangled melts, showing higher storage and loss modulus with increasing amounts of binding group. In contrast, polymers containing strong hydrogen bonding groups behaved like entangled networks. Callies et al. showed that, below a critical molar mass, the viscosity increased with decreasing molar mass (M_n) and that the strength of the association between hydrogen bonding groups ("stickers") controls the size of molecular aggregates [129]. Above the critical molar mass, the viscosity increases with M_n and the rheology is controlled by the polymer dynamics. The stickers simply increase the terminal relaxation time relative to the unfunctionalized polymer of the same M_n. To further clarify the intrinsic dynamic behavior of a disulfide-based thermoresponsive elastomer, a correlation between its rheological and fracture measurements has been proposed recently by Grande et al. [130]. Small amplitude oscillatory shear (SAOS) rheometry coupled with the time–temperature superposition principle, allowed identification of the main relaxation processes in the polymeric network. A fracture mechanical testing procedure based on evaluation of the critical J-integral (J_{IC}) was used to investigate and quantify recovery of the mechanical properties at the repaired interface as a function of time and temperature. Activation energies for the two studied phenomena (relaxation and healing) were calculated and a comparable temperature dependence was found, highlighting the direct link between rheology and crack healing. The above examples suggest that rheology could be a more powerful tool for investigating the mechanism and dynamics of self-healing and reversible processes than is generally realized.

3.5 Thermal Characterization

Differential scanning calorimetry (DSC) measurements provide information on molecular behavior during heating, which can be linked to self-healing behavior. Any DSC measurements should be combined with thermogravimetric analysis (TGA) to verify the thermal stability of the polymer during the DSC measurement conditions [131]. In DSC measurements, the opening of reversible bonds can easily (but not irrefutably) be demonstrated because the process requires energy [1]. Several studies have been performed to evaluate the thermal behavior of ionomers, which feature an order–disorder transition during heating [53, 54, 132, 133]. Furthermore, DA systems and the rDA reaction have been monitored via DSC [134, 135]. The rDA reaction is an endothermic process, which requires energy to break the reversible covalent bond. The temperature at which the reaction takes place strongly depends on the molecular structure (i.e., the DA moiety) as well as the surrounding and the general polymer structure [3, 136]. A system based on the rDA reaction can only feature self-healing behavior above the rDA temperature [13, 98, 137]. The rDA temperature can be determined via DSC, and this temperature has been correlated with the temperature dependence of the self-healing ability [3]. The reversibility of the reaction and, hence, the intrinsic character of the healing behavior of the polymer can easily be proven by DSC because of the possibility to reheat the sample after cooling to the DA temperature [3, 136]. A basic schematic showing the thermal effects during heating and cooling of a polymer containing rDA moieties is given in Fig. 14.

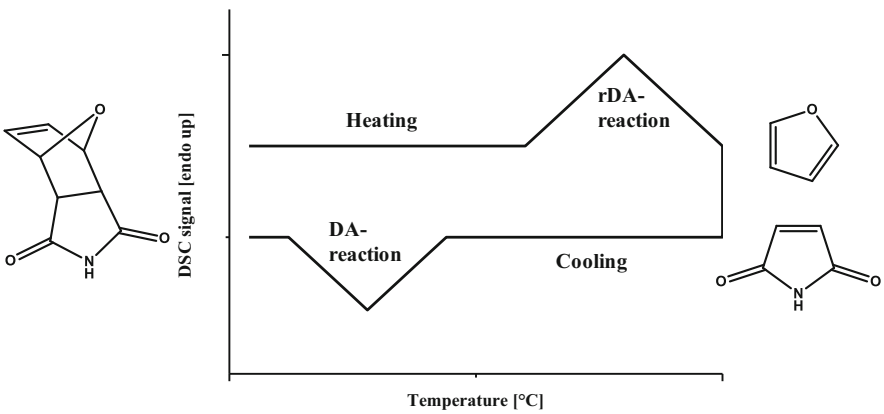

Fig. 14 Reversible opening of furan–maleimide Diels–Alder system during DSC measurements

4 Summary and Outlook

The development of self-healing materials requires techniques to characterize and preferentially quantify the healing behavior. During the last 15 years, several methods have been developed and utilized to investigate self-healing behavior and determine healing efficiency. Yet, to date, no standard technique is available that can be utilized for the universal characterization of all self-healing (polymeric) materials. Table 1 summarizes the, so far, most important techniques for characterizing self-healing materials, with specific focus on polymeric systems. Information is also included on the range and the minimal sample mass for proper characterization.

The most appropriate test method must also fit the desired application. Although scratch healing is adequate for coatings, tensile or TDCB testing may be more appropriate for applications involving mechanical loading of bulk samples. As argued above, the healing efficiency not only depends on the healing process but also on the nature and extent of damage (and the conditions creating that damage) as demonstrated elsewhere [15].

Healing of mechanical properties has attracted most of the attention in this field, and various physical characterization techniques have been used to link the macroscopic mechanical healing to underlying molecular processes. Visual methods such as optical microscopy and SEM allow visualization of the healing process, but do not provide insight into the prevailing mechanisms. Spectroscopic techniques (IR, Raman, NMR, BDS) provide potentially crucial information on the determining molecular processes (e.g., reversible bond formation and disruption) and network characteristics. Scattering techniques allow the investigation of larger aggregates and clusters as well as changes within the morphology. Dynamic methods such as rheology allow the direct correlation of molecular processes and mechanical properties.

Future developments in the field should focus on the development of a range of standardized tests and test protocols that enable the quantitative determination of the healing performance of polymers under well-defined conditions, irrespective of the molecular healing mechanisms. Such an approach would also enable fair and objective comparison of the healing ability of different materials.

Another important challenge in this context is the testing of “real-life damage.” In most reported polymer healing studies, both the damage and the healing conditions are idealized and different from (and less complex than in) real-life situations. Further challenges are the design of high-throughput testing and the testing of self-healing ability in materials only available in small quantities. Furthermore, the self-healing behavior and its stability over time should be analyzed in detail. Several authors have shown that the healing efficiency of extrinsic self-healing systems decreases over time, and the effect may also occur in intrinsic self-healing systems as a result of natural ageing although this aspect is generally overlooked [142]. To study the influence of time, it is possible to adopt the kind of testing used for photovoltaics or the accelerated testing used in coatings technology. In these

Table 1 Summary of characterization techniques for self-healing materials, their scope, and the required material amount

Characterization method	Measured parameter			Required material amount				Destructive method/measurement parameter	Reference
	Properties	Healing efficiency	Mechanism of self-healing	≤100 mg	1 g	10 g	≥10 g		
Tensile testing	☑	☑				☑	☑	Destructive; temperature dependence possible; validity of test results questionable; testing for application as bulk material	[9–13, 15–19]
TDCB	☑	☑				☑	☑	Destructive; temperature dependence possible; quantification of self-healing possible; testing for application as bulk material	[6, 20–25, 61]
Fracture testing	☑	☑	☑			☑	☑	Destructive; temperature dependence possible; quantification of self-healing possible; supports understanding of molecular process at the interface	[11, 15, 30–33]
Scratch healing		☑	☑	☑	☑	☑	☑	Non-destructive; temperature dependence possible; quantification of self-healing; testing for application as coating	[3, 36–48, 93]
Ballistic impact		☑				☑	☑	Destructive; quantification of self-healing difficult; testing for application as bulk material in very specific environments	[53–55, 57–60, 108, 109, 138–141]
SEM		☑	☑	☑	☑	☑	☑	Non-destructive; temperature dependence possible; quantification of self-healing; testing for application as coating	[3, 6, 44]

(continued)

Table 1 (continued)

Characterization method	Measured parameter			Required material amount				Destructive method/measurement parameter	Reference
	Properties	Healing efficiency	Mechanism of self-healing	≤100 mg	1 g	10 g	≥10 g		
3D CT scan		☑	☑	☑	☑	☑	☑	Non-destructive; quantification of self-healing; testing for bulk, coating, composites, and interface possible	[80–82]
Raman spectroscopy	☑		☑	☑	☑	☑	☑	Non-destructive; temperature dependence possible; understanding of molecular process; for both intrinsic and extrinsic systems	[43, 86, 87, 91, 92, 94–97]
IR spectroscopy	☑		☑	☑	☑	☑	☑	Non-destructive; temperature dependence possible; understanding of molecular process; for both intrinsic and extrinsic systems	[46, 93]
Solid-state NMR spectroscopy	☑		☑		☑	☑	☑	Non-destructive; temperature dependence possible; understanding of molecular process; for both intrinsic and extrinsic systems	[13, 42, 99]
X-ray scattering	☑		☑	☑	☑	☑	☑	Non-destructive; temperature dependence possible; understanding of molecular arrangements	[42, 43, 115, 117]

Rheology	☑	☑	☑		☑	☑	☑	Non-destructive; temperature dependence possible; determination of mechanical properties; understanding of dynamic molecular processes	[16, 46, 48, 116, 120–128]
Broadband dielectric spectroscopy	☑	☑	☑	☑	☑	☑		Non-destructive; temperature dependence possible; understanding of molecular processes; in particular for intrinsic systems	[101–107]
DSC	☑		☑	☑	☑	☑	☑	Non-destructive; determination of thermal properties; analysis of thermoreversible processes	[3, 13, 53, 54, 136]
TGA	☑			☑	☑	☑	☑	Destructive; determination of thermal stability	

Dark grey very suitable; *grey* suitable; *light grey* partially suitable or analysis of parts of the sample; *white* not suitable

systems, UV light is utilized to mimic aging of the polymer and to induce degradation, sometimes combined with humidity-induced ageing [143–148]. Induced aging of the sample can help in studies of the long-term stability and long-term healing ability.

In conclusion, a large number of testing techniques for characterization and quantification of the self-healing behavior of polymers have been explored over the past years. Some techniques are known to give an incomplete impression of the degree of healing, so accurate and reliable methods as well as measurement protocols are still required. Although there has been some progress in linking the results of test methods that measure processes at the molecular scale to the self-healing behavior, there is no truly discriminating technique available at the moment (if ever). It is increasingly clear that the combined information from a range of macroscopic and molecular measuring techniques is required to obtain a good impression of the self-healing behavior of polymers. Encouragingly, there are no indications that the acquisition of a full understanding of the critical processes in the self-healing of local mechanical damage in polymers is physically impossible.

Acknowledgements The authors thank the Deutsche Forschungsgemeinschaft (DFG, SPP 1568), the European Union (PIEF-GA-2013-623379) and the Dutch IOP-SHM program for financial support.

References

1. Wu DY, Meure S, Solomon D (2008) Prog Polym Sci 33:479–522
2. Liu Y-L, Chuo T-W (2013) Polym Chem 4:2194–2205
3. Kötteritzsch J, Stumpf S, Hoeppener S, Vitz J, Hager MD, Schubert US (2013) Macromol Chem Phys 214:1636–1649
4. Chen Y, Kushner AM, Williams GA, Guan Z (2012) Nat Chem 4:467–472
5. Dry CM, Sottos NR (1993) In: Proceedings North American conference on smart structures and materials. Albuquerque, pp 438–444
6. White SR, Sottos NR, Geubelle PH, Moore JS, Kessler MR, Sriram SR, Brown EN, Viswanathan S (2001) Nature 409:794–797
7. Ahner J, Micheel M, Bode S, Dietzek B, Hager MD (2015) Self-healing functional polymeric materials. Adv Polym Sci. doi:10.1007/12_2015_343
8. Tieke B (2005) Makromolekulare Chemie, 2nd edn. Wiley-VCH, Weinheim
9. Tuncaboylu DC, Sahin M, Argun A, Oppermann W, Okay O (2012) Macromolecules 45:1991–2000
10. Murphy EB (2011) J Mater Chem 21:1438–1446
11. Maes F, Montarnal D, Cantournet S, Tournilhac F, Corte L, Leibler L (2012) Soft Matter 8:1681–1687
12. Peterson AM, Jensen RE, Palmese GR (2010) ACS Appl Mater Interfaces 2:1141–1149
13. Chen X, Dam MA, Ono K, Mal A, Shen H, Nutt SR, Sheran K, Wudl F (2002) Science 295:1698–1702
14. Bose RK, Lafont U, Vega JM, Garcia SJ, Van der Zwaag S (2013) In: Binder WH (ed) Self-healing polymers, vol 1. Wiley -VCH, Weinheim, pp 337–359
15. Grande AM, Garcia SJ, van der Zwaag S (2015) Polymer 56:435–442
16. Chen S, Mahmood N, Beiner M, Binder WH (2015) Angew Chem Int Ed 54:10188–10192

17. Brazee SL, Carrington E (2006) Biol Bull 211:263–274
18. Harrington MJ, Gupta HS, Fratzl P, Waite JH (2009) J Struct Biol 167:47–54
19. Schmidt S, Reinecke A, Wojcik F, Pussak D, Hartmann L, Harrington MJ (2014) Biomacromolecules 15:1644–1652
20. Garoz Gómez D, Gilabert FA, Tsangouri E, Van Hemelrijck D, Hillewaere XKD, Du Prez FE, Van Paepegem W (2015) Int J Solids Struct 64–65:145–154
21. Brown EN, Sottos NR, White SR (2002) Exp Mech 42:372–379
22. Tsangouri E, Aggelis D, Van Hemelrijck D (2015) Prog Polym Sci 49–50:154–174
23. Brown EN (2011) J Strain Anal Eng Des 46:167–186
24. Kessler MR, Sottos NR, White SR (2003) Compos Part A 34:743–753
25. Guadagno L, Raimondo M, Naddeo C, Longo P, Mariconda A, Binder WH (2014) Smart Mater Struct 23:045001
26. Gent AN, Mars WV (2013) In: Mark JE, Erman B, Roland CM (eds) The science and technology of rubber, 4th edn. Academic, Boston, pp 473–516
27. Rivlin RS, Thomas AG (1953) J Polym Sci 10:291–318
28. Joe CR, Kim BH (1990) Int J Fract 44:15–26
29. Thomas AG (1994) Rubber Chem Technol 67:G50–G60
30. Hamdi A, Naït Abdelaziz M, Aït Hocine N, Heuillet P, Benseddiq N (2006) Polym Test 25:994–1005
31. Agnelli S, Baldi F, Riccò T (2012) Eng Fract Mech 90:76–88
32. Keller MW, White SR, Sottos NR (2007) Adv Funct Mater 17:2399–2404
33. Rahman MA, Sartore L, Bignotti F, Di Landro L (2013) ACS Appl Mater Interfaces 5:1494–1502
34. Rice JR (1968) J Appl Mech 35:379–386
35. Cherepanov GP (1967) J Appl Math Mech 31:503–512
36. Samadzadeh M, Boura SH, Peikari M, Ashrafi A, Kasiriha M (2011) Prog Org Coat 70:383–387
37. Cho SH, White SR, Braun PV (2009) Adv Mater 21:645–649
38. Enke M, Bode S, Vitz J, Schacher FH, Harrington MJ, Hager MD, Schubert US (2015) Polymer 69:274–282
39. Engel T, Kickelbick G (2014) Polym Int 63:915–923
40. Nguyen L-TT, Truong TT, Nguyen HT, Le L, Nguyen VQ, Van Le T, Luu AT (2015) Polym Chem 6:3143–3154
41. Barthel MJ, Rudolph T, Teichler A, Paulus RM, Vitz J, Hoeppener S, Hager MD, Schacher FH, Schubert US (2013) Adv Funct Mater 23:4921–4932
42. Bode S, Bose RK, Matthes S, Ehrhardt M, Seifert A, Schacher FH, Paulus RM, Stumpf S, Sandmann B, Vitz J, Winter A, Hoeppener S, Garcia SJ, Spange S, van der Zwaag S, Hager MD, Schubert US (2013) Polym Chem 4:4966–4973
43. Bode S, Zedler L, Schacher FH, Dietzek B, Schmitt M, Popp J, Hager MD, Schubert US (2013) Adv Mater 25:1634–1638
44. Kashif M, Chang Y-W (2015) Eur Polym J 66:273–281
45. Vega JM, Grande AM, van der Zwaag S, Garcia SJ (2014) Eur Polym J 57:121–126
46. Bose RK, Kötteritzsch J, Garcia SJ, Hager MD, Schubert US, van der Zwaag S (2014) J Polym Sci A Polym Chem 52:1669–1675
47. Kuhl N, Bode S, Bose RK, Vitz J, Seifert A, Hoeppener S, Garcia SJ, Spange S, van der Zwaag S, Hager MD, Schubert US (2015) Adv Funct Mater 25:3295–3301
48. Bose RK, Hohlbein N, Garcia SJ, Schmidt AM, van der Zwaag S (2015) Phys Chem Chem Phys 17:1697–1704
49. González-García Y, Mol JMC, Muselle T, De Graeve I, Van Assche G, Scheltjens G, Van Mele B, Terryn H (2011) Electrochem Commun 13:169–173
50. Lutz A, van den Berg O, Van Damme J, Verheyen K, Bauters E, De Graeve I, Du Prez FE, Terryn H (2015) ACS Appl Mater Interfaces 7:175–183

51. García SJ, Fischer HR, White PA, Mardel J, González-García Y, Mol JMC, Hughes AE (2011) Prog Org Coat 70:142–149
52. Kalista SJ Jr, Ward TC, Oyetunji Z (2003) In: Anderson GL (ed) Proceedings of the 26th annual meeting of the adhesion society. Adhesion Society, Blacksburg, VA, pp 176–178
53. Kalista SJ, Ward TC, Oyetunji Z (2007) Mech Adv Mater Struct 14:391–397
54. Kalista SJ Jr, Ward TC (2007) J R Soc Interface 4:405–411
55. Varley RJ, van der Zwaag S (2008) Polym Test 27:11–19
56. Fall R (2001) Puncture reversal of ethylene ionomers—mechanistic studies. MSc dissertation. Virginia Polytechnic Institute and State University, Blacksburg
57. Rahman MA, Penco M, Peroni I, Ramorino G, Grande AM, Di Landro L (2011) ACS Appl Mater Interfaces 3:4865–4874
58. Rhaman MA, Penco M, Spagnoli G, Grande AM, Di Landro L (2011) Macromol Mater Eng 296:1119–1127
59. Rahman MA, Spagnoli G, Grande AM, Di Landro L (2013) Macromol Mater Eng 298:1350–1364
60. Grande AM, Castelnovo L, Di Landro L, Giacomuzzo C, Francesconi A, Rahman MA (2013) J Appl Polym Sci 130:1949–1958
61. Billiet S, Hillewaere XKD, Teixeira RFA, Du Prez FE (2013) Macromol Rapid Commun 34:290–309
62. Yang J, Keller MW, Moore JS, White SR, Sottos NR (2008) Macromolecules 41:9650–9655
63. McIlroy DA, Blaiszik BJ, Caruso MM, White SR, Moore JS, Sottos NR (2010) Macromolecules 43:1855–1859
64. Gragert M, Schunack M, Binder WH (2011) Macromol Rapid Commun 32:419–425
65. White SR, Moore JS, Sottos NR, Krull BP, Santa Cruz WA, Gergely RCR (2014) Science 344:620–623
66. Fickert J, Makowski M, Kappl M, Landfester K, Crespy D (2012) Macromolecules 45:6324–6332
67. Xiao DS, Yuan YC, Rong MZ, Zhang MQ (2009) Polymer 50:2967–2975
68. Yin T, Rong MZ, Zhang MQ, Yang GC (2007) Compos Sci Technol 67:201–212
69. Zhu DY, Rong MZ, Zhang MQ (2013) Polymer 54:4227–4236
70. Yuan YC, Rong MZ, Zhang MQ, Chen J, Yang GC, Li XM (2008) Macromolecules 41:5197–5202
71. Fickert J, Rupper P, Graf R, Landfester K, Crespy D (2012) J Mater Chem 22:2286–2291
72. Schaubroeck D, Brughmans S, Vercaemst C, Schaubroeck J, Verpoort F (2006) J Mol Catal A Chem 254:180–185
73. Barnes SE, Brown EC, Corrigan N, Coates PD, Harkin-Jones E, Edwards HGM (2005) Spectrochim Acta A Mol Biomol Spectrosc 61:2946–2952
74. Chipara MD, Chipara M, Shansky E, Zaleski JM (2009) Polym Adv Technol 20:427–431
75. Celestine A-DN, Beiermann BA, May PA, Moore JS, Sottos NR, White SR (2014) Polymer 55:4164–4171
76. Davis DA, Hamilton A, Yang J, Cremar LD, Van Gough D, Potisek SL, Ong MT, Braun PV, Martinez TJ, White SR, Moore JS, Sottos NR (2009) Nature 459:68–72
77. Caruso MM, Davis DA, Shen Q, Odom SA, Sottos NR, White SR, Moore JS (2009) Chem Rev 109:5755–5798
78. Black AL, Lenhardt JM, Craig SL (2011) J Mater Chem 21:1655–1663
79. May PA, Moore JS (2013) Chem Soc Rev 42:7497–7506
80. Mookhoek SD, Mayo SC, Hughes AE, Furman SA, Fischer HR, van der Zwaag S (2010) Adv Eng Mater 12:228–234
81. Prajer M, Wu X, Garcia SJ, van der Zwaag S (2015) Compos Sci Technol 106:127–133
82. Garcia SJ, Wu X, Zwaag SVD (2014) Corrosion 70:475–482
83. Zedler L, Hager MD, Schubert US, Harrington MJ, Schmitt M, Popp J, Dietzek B (2014) Mater Today 17:57–69

84. Colthup NB, Daly LH, Wiberley SE (1975) Introduction to infrared and raman spectroscopy, 2nd edn. Academic, New York
85. Sandmann B, Happ B, Hager MD, Vitz J, Rettler E, Burtscher P, Moszner N, Schubert US (2014) J Polym Sci A PolymChem 52:239–247
86. Harrington MJ, Masic A, Holten-Andersen N, Waite JH, Fratzl P (2010) Science 328:216–220
87. Holten-Andersen N, Harrington MJ, Birkedal H, Lee BP, Messersmith PB, Lee KYC, Waite JH (2011) Proc Natl Acad Sci USA 108:2651–2655
88. Zhu DY, Cao GS, Qiu WL, Rong MZ, Zhang MQ (2015) Polymer 69:1–9
89. Hart KR, Sottos NR, White SR (2015) Polymer 67:174–184
90. Xiao DS, Yuan YC, Rong MZ, Zhang MQ (2009) Adv Funct Mater 19:2289–2296
91. Vasiliu S, Kampe B, Theil F, Dietzek B, Döhler D, Michael P, Binder WH, Popp J (2014) Appl Spectrosc 68:541–548
92. Kupfer S, Zedler L, Guthmuller J, Bode S, Hager MD, Schubert US, Popp J, Grafe S, Dietzek B (2014) Phys Chem Chem Phys 16:12422–12432
93. AbdolahZadeh M, Esteves ACC, van der Zwaag S, Garcia SJ (2014) J Polym Sci A Polym Chem 52:1953–1961
94. Zeng C, Seino H, Ren J, Hatanaka K, Yoshie N (2013) Macromolecules 46:1794–1802
95. Toncelli C, De Reus DC, Picchioni F, Broekhuis AA (2012) Macromol Chem Phys 213:157–165
96. Scheltjens G, Brancart J, De Graeve I, Van Mele B, Terryn H, Van Assche G (2011) J Therm Anal Calorim 105:805–809
97. Geitner R, Kotteritzsch J, Siegmann M, Bocklitz TW, Hager MD, Schubert US, Grafe S, Dietzek B, Schmitt M, Popp J (2015) Phys Chem Chem Phys 17:22587–22595
98. Chen X, Wudl F, Mal AK, Shen H, Nutt SR (2003) Macromolecules 36:1802–1807
99. Malmierca MA, González-Jiménez A, Mora-Barrantes I, Posadas P, Rodríguez A, Ibarra L, Nogales A, Saalwächter K, Valentín JL (2014) Macromolecules 47:5655–5667
100. Brown SP, Spiess HW (2001) Chem Rev 101:4125–4156
101. Mijović J, Lee H, Kenny J, Mays J (2006) Macromolecules 39:2172–2182
102. Hernández M, Carretero-González J, Verdejo R, Ezquerra TA, López-Manchado MA (2010) Macromolecules 43:643–651
103. Hernández M, Ezquerra TA, Verdejo R, López-Manchado MA (2012) Macromolecules 45:1070–1075
104. Linares A, Nogales A, Sanz A, Ezquerra TA, Pieruccini M (2010) Phys Rev E 82:031802
105. Hernández M, García SJ, van der Zwaag S (2015) In: Proceedings of the fifth international conference on self-healing materials ICSHM, Durham, NC, USA, p 85
106. Hernández M, García SJ, van der Zwaag S (2015) In: Proceedings of the European materials research society 2015 fall meeting E-MRS, Warsaw, Poland, p E I–6
107. Kremer F, Schönhals A (2003) Broadband dielectric spectroscopy. Springer, New York, p 721
108. Varley RJ, van der Zwaag S (2008) Acta Mater 56:5737–5750
109. Varley RJ, Shen S, van der Zwaag S (2010) Polymer 51:679–686
110. Varley RJ, van der Zwaag S (2010) Polym Int 59:1031–1038
111. Eisenberg A, Hird B, Moore RB (1990) Macromolecules 23:4098–4107
112. Moffitt M, Eisenberg A (1995) Chem Mater 7:1178–1184
113. Yarusso DJ, Cooper SL (1985) Polymer 26:371–378
114. Register R, Yu X-h, Cooper S (1989) Polym Bull 22:565–571
115. Herbst F, Seiffert S, Binder WH (2012) Polym Chem 3:3084–3092
116. Herbst F, Schröter K, Gunkel I, Gröger S, Thurn-Albrecht T, Balbach J, Binder WH (2010) Macromolecules 43:10006–10016
117. Yan T, Schröter K, Herbst F, Binder WH, Thurn-Albrecht T (2014) Macromolecules 47:2122–2130

118. Brás AR, Hövelmann CH, Antonius W, Teixeira J, Radulescu A, Allgaier J, Pyckhout-Hintzen W, Wischnewski A, Richter D (2013) Macromolecules 46:9446–9454
119. Ruocco N, Dahbi L, Driva P, Hadjichristidis N, Allgaier J, Radulescu A, Sharp M, Lindner P, Straube E, Pyckhout-Hintzen W, Richter D (2013) Macromolecules 46:9122–9133
120. Hackelbusch S, Rossow T, van Assenbergh P, Seiffert S (2013) Macromolecules 46:6273–6286
121. Rossow T, Habicht A, Seiffert S (2014) Macromolecules 47:6473–6482
122. Hart LR, Nguyen NA, Harries JL, Mackay ME, Colquhoun HM, Hayes W (2015) Polymer 69:293–300
123. Scheltjens G, Diaz MM, Brancart J, Van Assche G, Van Mele B (2013) React Funct Polym 73:413–420
124. Feldman KE, Kade MJ, Meijer EW, Hawker CJ, Kramer EJ (2009) Macromolecules 42:9072–9081
125. Aida T, Meijer EW, Stupp SI (2012) Science 335:813–817
126. Stukalin EB, Cai L-H, Kumar NA, Leibler L, Rubinstein M (2013) Macromolecules 46:7525–7541
127. Bose RK, Hohlbein N, Garcia SJ, Schmidt AM, van der Zwaag S (2015) Polymer 69:228–232
128. Lewis CL, Stewart K, Anthamatten M (2014) Macromolecules 47:729–740
129. Callies X, Fonteneau C, Véchambre C, Pensec S, Chenal JM, Chazeau L, Bouteiller L, Ducouret G, Creton C (2015) Polymer 69:233–240
130. Grande AM, Martin R, Bijleveld J, Odriozola I, Garcia SJ, van der Zwaag S (2015) In: Proceedings of the European materials research society E-MRS fall meeting, Warsaw, Poland, p E I–5
131. Höhne GWH, Hemminger WF, Flammersheim H-J (2003) Differential scanning calorimetry, 2nd edn. Springer, Heidelberg
132. Tadano K, Hirasawa E, Yamamoto H, Yano S (1989) Macromolecules 22:226–233
133. Tachino H, Hara H, Hirasawa E, Kutsumizu S, Tadano K, Yano S (1993) Macromolecules 26:752–757
134. Liu Y-L, Hsieh C-Y, Chen Y-W (2006) Polymer 47:2581–2586
135. Canary SA, Stevens MP (1992) J Polym Sci A Polym Chem 30:1755–1760
136. Kötteritzsch J, Hager MD, Schubert US (2015) Polymer 69:321–329
137. Murphy EB, Bolanos E, Schaffner-Hamann C, Wudl F, Nutt SR, Auad ML (2008) Macromolecules 41:5203–5209
138. Kalista SJ, Pflug JR, Varley RJ (2013) Polym Chem 4:4910–4926
139. Pestka KA, Kalista SJ, Ricci A (2013) AIP Adv 3:082113
140. Francesconi A, Giacomuzzo C, Grande AM, Mudric T, Zaccariotto M, Etemadi E, Di Landro L, Galvanetto U (2013) Adv Space Res 51:930–940
141. Sundaresan VB, Morgan A, Castellucci M (2013) Smart Mater Res 2013:271546
142. Neuser S, Michaud V (2013) Polym Chem 4:4993–4999
143. Manceau M, Rivaton A, Gardette J-L, Guillerez S, Lemaître N (2011) Sol Energ Mat Sol C 95:1315–1325
144. Manceau M, Chambon S, Rivaton A, Gardette J-L, Guillerez S, Lemaître N (2010) Sol Energ Mat Sol C 94:1572–1577
145. Sommeling PM, Späth M, Smit HJP, Bakker NJ, Kroon JM (2004) J Photochem Photobiol A Chem 164:137–144
146. Rivaton A, Chambon S, Manceau M, Gardette J-L, Lemaître N, Guillerez S (2010) Polym Degrad Stabil 95:278–284
147. Hinsch A, Kroon JM, Kern R, Uhlendorf I, Holzbock J, Meyer A, Ferber J (2001) Prog Photovolt Res Appl 9:425–438
148. McIntosh KR, Powell NE, Norris AW, Cotsell JN, Ketola BM (2011) Prog Photovolt Res Appl 19:294–300

Adv Polym Sci (2016) 273: 143–184
DOI: 10.1007/12_2015_338

Published online: 6 November 2015

Continuum Mechanical Description of an Extrinsic and Autonomous Self-Healing Material Based on the Theory of Porous Media

Steffen Specht, Joachim Bluhm, and Jörg Schröder

Abstract Polymers and polymeric composites are used in many engineering applications, but these materials can spontaneously lose structural integrity as a result of microdamage caused by stress peaks during service. This internal microdamage is hard to detect and nearly impossible to repair. To extend the lifetime of such materials and save maintenance costs, self-healing mechanisms can be applied that are able to repair internal microdamage during the usual service load. This can be realized, for example, by incorporating microcapsules filled with monomer and dispersed catalysts into the polymeric matrix material. If a crack occurs, the monomer flows into the crack, reacts with the catalysts, and closes the crack.

This contribution focuses on the development of a thermodynamically consistent constitutive model that is able to describe the damage and healing behavior of a microcapsule-based self-healing material. The material under investigation is an epoxy matrix with microencapsulated dicyclopentadiene healing agents and dispersed Grubbs' catalysts. The simulation of such a multiphase material is numerically very expensive if the microstructure is to be completely resolved. To overcome this, a homogenization technique can be applied to decrease the computational costs of the simulation. Here, the theoretical framework is based on the theory of porous media, which is a macroscopic continuum mechanical homogenization approach. The developed five-phase model consists of solid matrix material with dispersed catalysts, liquid healing agents, solidified healed material, and gas phase. A discontinuous damage model is used for the description of the damage

S. Specht (✉), J. Bluhm, and J. Schröder
Institute of Mechanics, University of Duisburg-Essen, Universitätsstrasse 15, 45141 Essen, Germany
e-mail: steffen.specht@uni-due.de; joachim.bluhm@uni-due.de; j.schroeder@uni-due.de

behavior, and healing is simulated by a phase transition between the liquid-like healing agents and the solidified healed material. Applicability of the developed model is shown by means of numerical simulations of the global damage and healing behavior of a tapered double cantilever beam, as well as simulations of the flow behavior of the healing agents at the microscale.

Keywords Multiphase system • Phase transition • Self-healing • Theory of porous media

Contents

1 Introduction

Engineering materials are designed to resist the formation, or at least the growth, of cracks. This principle is termed the "damage prevention" paradigm [1]. Nevertheless, these materials can also fail as a result of external influences (e.g., load peaks or corrosion). If damage occurs, the amount of it increases or, in the best case, stays constant [2, 3]. In polymers and polymeric composites, even microdamage can lead to degradation in stiffness and durability and sometimes also to spontaneous loss of structural integrity. Furthermore, internal microdamage is difficult to detect and nearly impossible to repair. Therefore, the damaged structural part must be replaced, which can be very difficult and expensive, for example, in aerospace applications.

To extend the structural lifetime and save maintenance costs, materials can be designed according to the "damage management" principle [1]. Here, the material can sustain a certain amount of microdamage (i.e., caused by load peaks) without a collapse in structural integrity. During the usual working load, the material is able to repair its internal microdamage via self-healing.

In general, self-healing can be divided into autonomous and non-autonomous healing [4, 5]. Non-autonomous healing implies the usage of an external trigger

such as heat or UV radiation, whereas in autonomous healing, the damage itself triggers the onset of the healing mechanism. Furthermore, it is possible to divide the healing mechanism into intrinsic and extrinsic [5, 6]. If the material is able to heal itself (e.g., by diffusion or reversible bonds), it is termed intrinsic healing. In contrast, extrinsic healing means that the healing mechanism is incorporated into the material (e.g., with embedded healing agents). An overview of the different self-healing materials and principles is given by Grigoleit [7].

We consider an extrinsic and autonomous self-healing system consisting of a polymeric matrix material containing dispersed catalysts and embedded monomer-filled microcapsules. If a crack propagates through the structure, the capsules rupture and the monomer flows out into the crack and comes into contact with the catalysts. This leads to polymerization of the monomer and, thus, the structural integrity can be recovered to a certain amount [8].

The geometry used in this contribution to investigate the damage and healing behavior of the aforementioned self healing material, is a so-called tapered double cantilever beam (TDCB) [9]. This specific geometry provides a crack length independent measurement of the stress intensity factor. Further results of experimental investigation of TDCB specimens used for consideration of microencapsulation-based self-healing polymeric materials can be found in the literature [10–14]. Several publications can also be found on the numerical simulation of self-healing polymeric materials. The following examples are not a complete list.

Global damage and healing behavior is mainly described within the framework of continuum damage mechanics, where the focus lies on the global loss and recovery of stiffness [15–19]. The work of Henson [20], for example, is based on mixture theory. Fatigue crack retardation has been studied by Maiti et al. [21], who describe fatigue crack propagation by a cohesive zone model, and the cure process on the atomistic scale by a coarse-grain molecular dynamics model. The prediction of microcapsule–matrix debonding has been analyzed [22] and an analytic model developed for computation of the probability that a crack hits a capsule [23]. A parameter identification study within a small deformation-based thermodynamically consistent model was carried out by Yagimli and Lion [24].

The focus of this contribution is the description of the global damage and healing behavior of the aforementioned multiphase material within the framework of the theory of porous media. With this approach, one can describe interactions (e.g., exchange of mass, momentum, and energy) between the different constituents. Furthermore, relative velocities between the solid skeleton and the liquid can be described, which allows simulation of flow inside the structure.

2 Theoretical Framework

To describe a material consisting of a compound of heterogeneous continua, in this case a porous medium, usage of the usual continuum mechanics is not a good choice, because this approach assumes a continuous distribution of a homogeneous

material over the whole control space. For many applications it is not sufficient to assume a simplified model with these properties. In porous media, where a porous rigid body is saturated with gas and/or liquid, the distinct components or constituents interact at the microscale. To describe such internal effects macroscopically it is necessary to use a different continuum mechanical approach: the theory of porous media (the TPM).

The TPM is able to describe internal interactions (e.g., relative velocities, interaction forces, and mass exchange) between the different constituents, without knowledge of the real microscopic structure. The theory is based on the "mixture theory" combined with the "concept of volume fractions". For the historical development of the mixture theory and the TPM, the interested reader is referred to de Boer [25].

In this article, the control space in the reference configuration (time $t = t_0$) is denoted by $\mathscr{B}_{0S,}$ with its surface $\partial \mathscr{B}_{0S}$ related to the solid phase. The control space in the actual configuration (time t) is denoted by $\mathscr{B}_{S,}$ with its surface $\partial \mathscr{B}_{S}$ also related to the solid phase. For the derivation of the equations we restrict ourselves to the actual configuration.

In Sect. 2.1 an overview of the basics of the TPM is given. Here, the basic concepts of the mixture theory and the concept of volume fractions are explained [26–30]. Within the TPM, the motion of every constituent can be described independently. Therefore, an introduction to the kinematics is given in Sect. 2.2. The balance equations of the individual constituents and the entropy inequality for the overall mixture are presented in Sect. 2.3. In Sect. 2.4 there is a brief introduction to the discontinuous damage model, which is used to describe the propagation of damage in the model. With the theoretical basics of these sections in hand and in consideration of appropriate Helmholtz free energy functions, the constitutive equations, thermodynamic restrictions, and evolution equations are derived in Sect. 2.5. These are used to develop the thermodynamically consistent material model of the considered multiphase self-healing material.

2.1 Basics

The idea of the TPM is to describe a saturated porous body, which consists of m different constituents (a solid phase, and $m-1$ pore fluids), without knowledge of the real microscopic structure. Therefore, the mixture theory is considered. Here, it is assumed that all constituents are statistically distributed over the whole control space and that all constituents φ^{α} (here $\alpha = \mathrm{S}$, H, L, G, and C for solid, healed material, liquid healing agents, gas, and catalysts, respectively; see Fig. 1) appear in every spatial point $\mathbf{x}$ of the control space $\mathscr{B}_{S}$ simultaneously. Furthermore, all quantities, both geometrical and physical (e.g., motion or deformation), are defined as statistical averages of the real quantities in the considered control space $\mathscr{B}_{S}$.

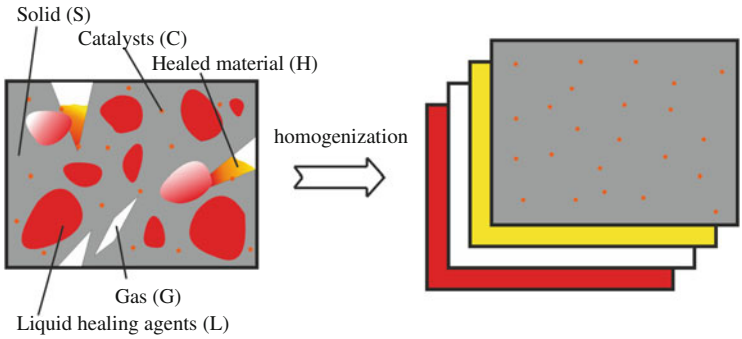

Fig. 1 Homogenization of the constituents: from the real structure (*left*) to the smeared model (*right*)

Moreover, it is assumed that every constituent φ^α has its own motion function χ_α (see Sect. 2.2). Figure 1 illustrates the homogenized "smeared" model.

With respect to the concept of volume fractions, the volume fraction $n^\alpha = n^\alpha(\mathbf{x}, t)$ is introduced, which is defined as the ratio of the infinitesimal partial volume element $\mathrm{d}v^\alpha$ to the infinitesimal total volume element $\mathrm{d}v$:

$$n^\alpha = \frac{\mathrm{d}v^\alpha}{\mathrm{d}v}\,. \tag{1}$$

This leads to the relation $\mathrm{d}v^\alpha = n^\alpha \mathrm{d}v$ between the partial volume element and the bulk volume element, which can be used to describe the total volume V in terms of the volume fractions n^α:

$$V = \int_{\mathscr{B}_S} \mathrm{d}v = \sum_{\alpha=1}^{m} V^\alpha = \int_{\mathscr{B}_S} \sum_{\alpha=1}^{m} \mathrm{d}v^\alpha = \int_{\mathscr{B}_S} \sum_{\alpha=1}^{m} n^\alpha \mathrm{d}v. \tag{2}$$

With help of the concept of volume fractions it is possible to identify the different constituents in a spatial point (see Fig. 2). We obtain the restriction:

$$\sum_{\alpha=1}^{m} n^\alpha = 1, \tag{3}$$

which is known as the "saturation condition". This condition states that in one spatial point, the sum over all constituents must be equal to one.

Additionally, the concept of volume fractions requires the introduction of two different density functions:

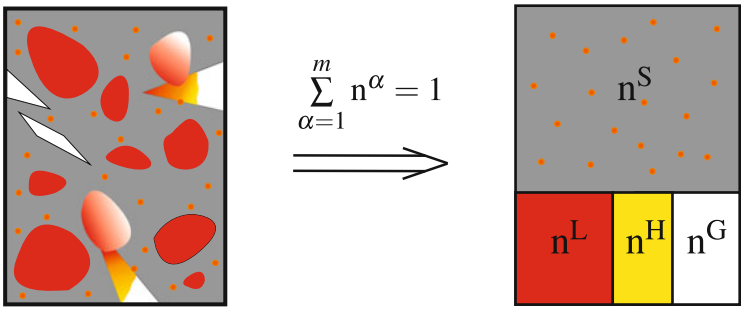

Fig. 2 Representation of the concept of volume fractions

$$\rho^{\alpha} = \rho^{\alpha}(\mathbf{x}, t), \quad \rho^{\alpha \mathrm{R}} = \rho^{\alpha \mathrm{R}}(\mathbf{x}, t), \tag{4}$$

which are the partial and real densities of a constituent φ^{α}. The two different densities are connected by the volume fraction n^{α}:

$$\rho^{\alpha} = n^{\alpha} \rho^{\alpha \mathrm{R}}. \tag{5}$$

With (5), the total mass of the observed body can be expressed as follows:

$$M = \sum_{\alpha=1}^{m} M^{\alpha} = \int_{\mathscr{B}_S} \sum_{\alpha=1}^{m} \rho^{\alpha} \mathrm{d}v = \int_{\mathscr{B}_S} \sum_{\alpha=1}^{m} n^{\alpha} \rho^{\alpha \mathrm{R}} \mathrm{d}v, \tag{6}$$

where $M^{\alpha} = \int_{\mathscr{B}_S} \rho^{\alpha} \mathrm{d}v$ is the partial mass of the constituent φ^{α}.

With respect to the catalysts, the partial mass of an infinitesimal volume element d_m^{C} of the constituent φ^{C} can be expresses in terms of its molar mass and the amount of catalysts. Therefore, the amount of catalyst is defined as:

$$n_m^{\mathrm{C}} = \frac{d_m^{\mathrm{C}}}{m_m^{\mathrm{C}}}, \tag{7}$$

where n_m^{C} [mol] is the amount of catalysts and m_m^{C} [kg/mol] denotes their molar mass. The partial mass in an infinitesimal volume element is then given by:

$$d_m^{\mathrm{C}} = \rho^{\mathrm{C}} \mathrm{d}v = n^{\mathrm{C}} \rho^{\mathrm{CR}} \mathrm{d}v = n_m^{\mathrm{C}} m_m^{\mathrm{C}}, \quad m_m^{\mathrm{C}} = \mathrm{const.} \tag{8}$$

The mass concentration of the catalysts is defined as the ratio of its partial mass and the volume of solid:

$$c^{\mathrm{C}} = \frac{d_m^{\mathrm{C}}}{\mathrm{d}v^{\mathrm{S}}} = \frac{d_m^{\mathrm{C}}}{n^{\mathrm{S}}\,\mathrm{d}v} = \frac{n_m^{\mathrm{C}} m_m^{\mathrm{C}}}{n^{\mathrm{S}}\mathrm{d}v} = c_m^{\mathrm{C}} m_m^{\mathrm{C}}, \tag{9}$$

where $c_m^{\mathrm{C}} = n_m^{\mathrm{C}}/(n^{\mathrm{S}}\mathrm{d}v)$ is the amount of catalyst concentration referred to an infinitesimal volume element of solid. Thus, the partial mass of the catalysts in the solid phase is given by the following expression:

$$d_m^{\mathrm{C}} = \rho^{\mathrm{C}}\mathrm{d}v = n^{\mathrm{C}}\rho^{\mathrm{CR}}\mathrm{d}v = n_m^{\mathrm{C}} m_m^{\mathrm{C}} = c_m^{\mathrm{C}} m_m^{\mathrm{C}}\mathrm{d}v^{\mathrm{S}} = n^{\mathrm{S}} c_m^{\mathrm{C}} m_m^{\mathrm{C}}\mathrm{d}v. \tag{10}$$

The partial density and the real density of the catalysts are given by:

$$\rho^{\mathrm{C}} = n^{\mathrm{S}} c_m^{\mathrm{C}} m_m^{\mathrm{C}}, \quad \rho^{\mathrm{CR}} = \frac{n^{\mathrm{S}}}{n^{\mathrm{C}}} c_m^{\mathrm{C}} m_m^{\mathrm{C}} = \frac{1}{s_{\mathrm{S}}^{\mathrm{C}}} c_m^{\mathrm{C}} m_m^{\mathrm{C}}, \tag{11}$$

and the saturation referring to the solid phase is denoted by:

$$s_{\mathrm{S}}^{\mathrm{C}} = \frac{n^{\mathrm{C}}}{n^{\mathrm{S}}}. \tag{12}$$

2.2 Kinematics

For the description of a saturated porous body, the principle of superposition is used. At a specific time t a spatial point $\mathbf{x}$ is simultaneously occupied by all m constituents φ^{α}. Furthermore, independent motions for each constituent are assumed, which leads to the fact that the material points $\mathbf{X}_{\alpha}$ are located in different reference positions at time $t = t_0$ (see Fig. 3). Thus, each constituent φ^{α} is described by its own independent motion function (in Lagrangian form):

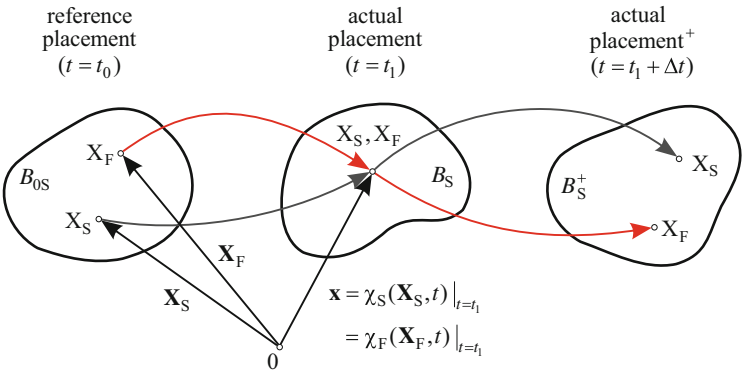

Fig. 3 Motion of solid and fluid particles in a fluid-saturated porous body [26], with kind permission from Springer Science + Business Media

$$\mathbf{x} = \chi_\alpha(\mathbf{X}_\alpha, t), \tag{13}$$

which is postulated to be unique and uniquely invertible at any time t. The Eulerian representation is the inverse of the motion function (13) and is denoted:

$$\mathbf{X}_\alpha = \chi_\alpha^{-1}(\mathbf{x}, t). \tag{14}$$

With the Lagrangian form of the motion function (13) the velocity and acceleration are defined as:

$$\mathbf{x}_\alpha^{'} = \frac{\partial \chi_\alpha(\mathbf{X}_\alpha, t)}{\partial t}, \quad \mathbf{x}_\alpha^{''} = \frac{\partial^2 \chi_\alpha(\mathbf{X}_\alpha, t)}{\partial t^2}. \tag{15}$$

In the Eulerian form they read:

$$\begin{array}{rcccl} \mathbf{x}_\alpha^{'} & = & \mathbf{x}_\alpha^{'}(\mathbf{x}, t) & = & \mathbf{x}_\alpha^{'}\left[\chi_\alpha^{-1}(\mathbf{x}, t), t\right], \\ \mathbf{x}_\alpha^{''} & = & \mathbf{x}_\alpha^{''}(\mathbf{x}, t) & = & \mathbf{x}_\alpha^{''}\left[\chi_\alpha^{-1}(\mathbf{x}, t), t\right]. \end{array} \tag{16}$$

The Jacobian is defined as:

$$\mathrm{J}_\alpha = \det \mathbf{F}_\alpha, \tag{17}$$

and $\mathrm{J}_\alpha \neq 0$ must hold, which is a mathematically sufficient condition for the existence of (14). $\mathbf{F}_\alpha$ denotes the deformation gradient of the constituent φ^α and is given by:

$$\mathbf{F}_\alpha = \frac{\partial \chi_\alpha(\mathbf{X}_\alpha, t)}{\partial \mathbf{X}_\alpha} = \frac{\partial \mathbf{x}}{\partial \mathbf{X}_\alpha} = \mathrm{Grad}_\alpha \mathbf{x}. \tag{18}$$

The inverse of the deformation gradient (18) reads:

$$\mathbf{F}_\alpha^{-1} = \frac{\partial \chi_\alpha^{-1}(\mathbf{x}, t)}{\partial \mathbf{x}} = \frac{\partial \mathbf{X}_\alpha}{\partial \mathbf{x}} = \mathrm{grad}\, \mathbf{X}_\alpha. \tag{19}$$

Considering $(15)_1$ and $(16)_1$, the material and spatial velocity gradient of the deformation gradient $\mathbf{F}_\alpha$ can be written as:

$$\left(\mathbf{F}_\alpha\right)_\alpha^{'} = \frac{\partial \mathbf{x}_\alpha^{'}}{\partial \mathbf{X}_\alpha} = \mathrm{Grad}_\alpha\, \mathbf{x}_\alpha^{'}, \quad \mathbf{L}_\alpha = \left(\mathrm{Grad}_\alpha \mathbf{x}_\alpha^{'}\right)\mathbf{F}_\alpha^{-1} = \mathrm{grad}\, \mathbf{x}_\alpha^{'}. \tag{20}$$

The spatial velocity gradient $\mathbf{L}_\alpha$ can be additively split into a symmetric part $\mathbf{D}_\alpha$ and a skew-symmetric part $\mathbf{W}_\alpha$, such that:

$$\mathbf{L}_\alpha = \mathbf{D}_\alpha + \mathbf{W}_\alpha, \tag{21}$$

The symmetric and skew-symmetric parts are given by:

$$\mathbf{D}_\alpha = \frac{1}{2}\left(\mathbf{L}_\alpha + \mathbf{L}_\alpha^T\right), \quad \mathbf{W}_\alpha = \frac{1}{2}\left(\mathbf{L}_\alpha - \mathbf{L}_\alpha^T\right). \tag{22}$$

Because the individual constituents perform different motions, different material time derivatives have to be taken into account. As an example, the material time derivative of an arbitrary scalar valued function $\Gamma(\mathbf{x}, t)$ reads:

$$\Gamma'_\alpha = \frac{\partial \Gamma}{\partial t} + \operatorname{grad}\Gamma \cdot \mathbf{x}'_\alpha. \tag{23}$$

2.3 Balance Equations and Entropy Inequality

Here, the underlying balance equations of mass, momentum, moment of momentum and energy, and the entropy inequality are discussed. As a result of the homogenization, some information about the interactions between the constituents at the inner structure is lost. To overcome this problem, the so-called total production terms [28, 31] for mass ($\hat{\rho}^\alpha$), linear momentum ($\hat{\mathbf{s}}^\alpha$), moment of momentum ($\hat{\mathbf{h}}^\alpha$), and energy ($\hat{\mathrm{e}}^\alpha$) are introduced. These production terms are used to describe interactions between different constituents such as mass exchange or heat transfer. The individual balance equations, in consideration of the total production terms, have to be derived in such a way that the sum over all m constituents for every balance equation is equivalent to the conservation laws of a one-component material. This condition is known as the third metaphysical principle of Truesdell [32], which states that "the motion of the mixture is governed by the same equation as is a single body". Therefore, the total production terms have to fulfill the following restrictions:

$$\begin{aligned}
&\text{Mass :} && \sum_{\alpha=1}^{m} \hat{\rho}^\alpha &&= 0,\\
&\text{Momentum :} && \sum_{\alpha=1}^{m} \hat{\mathbf{s}}^\alpha &&= \mathbf{0},\\
&\text{Moment of momentum :} && \sum_{\alpha=1}^{m} \hat{\mathbf{h}}^\alpha &&= \mathbf{0},\\
&\text{Energy :} && \sum_{\alpha=1}^{m} \hat{\mathrm{e}}^\alpha &&= 0.
\end{aligned} \tag{24}$$

A detailed derivation of the restrictions is given in the literature [29, 30, 33, 34].

2.3.1 Balance of Mass

The balance equation of mass states that for every constituent φ^α the rate of mass is equal to the corresponding mass production:

$$(M^\alpha)'_\alpha = \int_{\mathscr{B}_\alpha} \hat{\rho}^{\,\alpha} \mathrm{d}v, \tag{25}$$

where the mass of the constituent φ^α is defined as:

$$M^\alpha = \int_{\mathscr{B}_\alpha} \rho^\alpha \mathrm{d}v. \tag{26}$$

The material time derivative of the mass implies not only a change in density with time but also a change in volume:

$$(M^\alpha)'_\alpha = \int_{\mathscr{B}_\alpha} \left[(\rho^\alpha)'_\alpha + \rho^\alpha \mathrm{div}\ \mathbf{x}'_\alpha \right] \mathrm{d}v. \tag{27}$$

Thus, the global statement of the balance of mass reads:

$$\int_{\mathscr{B}_\alpha} \left[(\rho^\alpha)'_\alpha + \rho^\alpha \mathrm{div}\ \mathbf{x}'_\alpha \right] \mathrm{d}v = \int_{\mathscr{B}_\alpha} \hat{\rho}^{\,\alpha} \mathrm{d}v \tag{28}$$

with its local form:

$$(\rho^\alpha)'_\alpha + \rho^\alpha \mathrm{div}\ \mathbf{x}'_\alpha = \hat{\rho}^{\,\alpha}. \tag{29}$$

Considering the relation between the partial and real densities (5) leads to:

$$(n^\alpha)'_\alpha + n^\alpha \mathrm{div}\ \mathbf{x}'_\alpha + n^\alpha \frac{(\rho^{\alpha\mathrm{R}})'_\alpha}{\rho^{\alpha\mathrm{R}}} = \frac{\hat{\rho}^{\,\alpha}}{\rho^{\alpha\mathrm{R}}}. \tag{30}$$

For incompressible materials, where $\rho^{\alpha\mathrm{R}} = \text{const.}$ and $(\rho^{\alpha\mathrm{R}})'_\alpha = 0$, this reduces to:

$$(n^\alpha)'_\alpha + n^\alpha \mathrm{div}\ \mathbf{x}'_\alpha = \frac{\hat{\rho}^{\,\alpha}}{\rho^{\alpha\mathrm{R}}}. \tag{31}$$

Furthermore, if the total mass production term is also excluded (i.e., $\hat{\rho}^{\,\alpha} = 0$), the balance equation of mass can be expressed in terms of the volume fractions:

$$\left(n^{\alpha}\right)_{\alpha}^{'} + n^{\alpha}\mathrm{div}\ \mathbf{x}_{\alpha}^{'} = 0. \tag{32}$$

With respect to the catalysts, instead of the balance equation of mass, the so-called balance equation of concentration is used. Starting from the balance equation of mass of the catalysts $\left(\rho^{\mathrm{C}}\right)_{\mathrm{C}}^{'} + \rho^{\mathrm{C}}\mathrm{div}\ \mathbf{x}_{\mathrm{S}}^{'} = \hat{\rho}^{\mathrm{C}}$ and considering Eqs. (9) and $(11)_1$, the balance of mass can be written in terms of the mass concentration:

$$\left(n^{\mathrm{S}}c^{\mathrm{C}}\right)_{\mathrm{C}}^{'} + n^{\mathrm{S}}c^{\mathrm{C}}\mathrm{div}\ \mathbf{x}_{\mathrm{S}}^{'} = \hat{\rho}^{\mathrm{C}}. \tag{33}$$

Reformulation of the material time derivative with respect to the solid phase gives $\left(n^{\mathrm{S}}c^{\mathrm{C}}\right)_{\mathrm{C}}^{'} = \left(n^{\mathrm{S}}c^{\mathrm{C}}\right)_{\mathrm{S}}^{'} + \mathrm{grad}\left(n^{\mathrm{S}}c^{\mathrm{C}}\right)\cdot\mathbf{w}_{\mathrm{CS}}$, where $\mathbf{w}_{\mathrm{CS}} = \mathbf{x}_{\mathrm{C}}^{'} - \mathbf{x}_{\mathrm{S}}^{'}$ is the difference velocity of the catalysts with respect to the velocity of the solid (cf. Eq. (23) regarding the material time derivative of scalar quantities). Considering the relation $\mathrm{div}\ \mathbf{x}_{\mathrm{C}}^{'} = \mathrm{div}\ \mathbf{w}_{\mathrm{CS}} + \mathrm{div}\ \mathbf{x}_{\mathrm{S}}^{'}$ leads to the following expression:

$$c^{\mathrm{C}}\left[\left(n^{\mathrm{S}}\right)_{\mathrm{S}}^{'} + n^{\mathrm{S}}\mathrm{div}\ \mathbf{x}_{\mathrm{S}}^{'}\right] + n^{\mathrm{S}}\left(c^{\mathrm{C}}\right)_{\mathrm{S}}^{'} + \mathrm{div}\left(n^{\mathrm{S}}c^{\mathrm{C}}\mathbf{w}_{\mathrm{CS}}\right) = \hat{\rho}^{\mathrm{C}}. \tag{34}$$

Inserting the balance equation of mass of the solid:

$$\left(n^{\mathrm{S}}\right)_{\mathrm{S}}^{'} + n^{\mathrm{S}}\mathrm{div}\ \mathbf{x}_{\mathrm{S}}^{'} = \frac{1}{\rho^{\mathrm{SR}}}\left[\hat{\rho}^{\mathrm{S}} - n^{\mathrm{S}}\left(\rho^{\mathrm{SR}}\right)_{\mathrm{S}}^{'}\right] \tag{35}$$

yields:

$$c^{\mathrm{C}}\left\{\frac{1}{\rho^{\mathrm{SR}}}\left[\hat{\rho}^{\mathrm{S}} - n^{\mathrm{S}}\left(\rho^{\mathrm{SR}}\right)_{\mathrm{S}}^{'}\right]\right\} + n^{\mathrm{S}}\left(c^{\mathrm{C}}\right)_{\mathrm{S}}^{'} + \mathrm{div}\left(n^{\mathrm{S}}c^{\mathrm{C}}\mathbf{w}_{\mathrm{CS}}\right) = \hat{\rho}^{\mathrm{C}}. \tag{36}$$

For an incompressible solid phase without mass production, such that $\rho^{\mathrm{SR}} = \mathrm{const.}$, $\left(\rho^{\mathrm{SR}}\right)_{\mathrm{S}}^{'} = 0$, and $\hat{\rho}^{\mathrm{S}} = 0$, and assuming that the catalysts move with the solid ($\mathbf{w}_{\mathrm{CS}} = \mathbf{0}$), the balance equation of concentration simplifies to:

$$n^{\mathrm{S}}\left(c^{\mathrm{C}}\right)_{\mathrm{S}}^{'} = \hat{\rho}^{\mathrm{C}}. \tag{37}$$

2.3.2 Balance of Momentum

The balance of momentum states that the material time derivative of the momentum $\mathbf{l}^{\alpha}$ is equal to the sum of external forces and the total production term of momentum:

$$\left(\mathbf{l}^{\alpha}\right)_{\alpha}^{'} = \mathbf{k}^{\alpha} + \int\limits_{\mathscr{B}_{\alpha}} \hat{\mathbf{s}}^{\,\alpha} \mathrm{d}v. \tag{38}$$

The momentum and the vector of external forces are given by:

$$\mathbf{l}^{\alpha} = \int\limits_{\mathscr{B}_{\alpha}} \rho^{\alpha} \mathbf{x}_{\alpha}^{'} \mathrm{d}v, \quad \mathbf{k}^{\alpha} = \int\limits_{\mathscr{B}_{\alpha}} \rho^{\alpha} \mathbf{b}^{\alpha} \mathrm{d}v + \int\limits_{\partial \mathscr{B}_{\alpha}} \mathbf{t}^{\alpha} \mathrm{d}a\,. \tag{39}$$

Using the material time derivative of $(39)_1$:

$$\left(\mathbf{l}^{\alpha}\right)_{\alpha}^{'} = \int\limits_{\mathscr{B}_{\alpha}} \left(\hat{\rho}^{\,\alpha} \mathbf{x}_{\alpha}^{'} + \rho^{\alpha} \mathbf{x}_{\alpha}^{''}\right) \mathrm{d}v, \tag{40}$$

and reformulating the second term of the vector of external forces $(39)_2$ with help of Cauchy's theorem in combination with the divergence theorem:

$$\int\limits_{\partial \mathscr{B}_{\alpha}} \mathbf{t}^{\alpha} \mathrm{d}a = \int\limits_{\partial \mathscr{B}_{\alpha}} \mathbf{T}^{\alpha} \mathbf{n} \mathrm{d}a = \int\limits_{\mathscr{B}_{\alpha}} \mathrm{div} \mathbf{T}^{\alpha} \mathrm{d}v, \tag{41}$$

the whole expression for the balance equation of momentum reads:

$$\int\limits_{\mathscr{B}_{\alpha}} \left[\mathrm{div}\ \mathbf{T}^{\alpha} + \rho^{\alpha} \left(\mathbf{b}^{\alpha} - \mathbf{x}_{\alpha}^{''}\right)\right] \mathrm{d}v = \int\limits_{\mathscr{B}_{\alpha}} \left(\hat{\rho}^{\,\alpha} \mathbf{x}_{\alpha}^{'} - \hat{\mathbf{s}}^{\,\alpha}\right) \mathrm{d}v. \tag{42}$$

This leads to the local form of the balance equation of momentum:

$$\mathrm{div}\ \mathbf{T}^{\alpha} + \rho^{\alpha} \left(\mathbf{b}^{\alpha} - \mathbf{x}_{\alpha}^{''}\right) = -\hat{\mathbf{p}}^{\,\alpha}. \tag{43}$$

The so-called direct production term of momentum is denoted by:

$$\hat{\mathbf{p}}^{\,\alpha} = -\hat{\rho}^{\,\alpha} \mathbf{x}_{\alpha}^{'} + \hat{\mathbf{s}}^{\,\alpha}. \tag{44}$$

With the direct production term of momentum, the restriction $(24)_2$ becomes:

$$\sum_{\alpha=1}^{m} \hat{\mathbf{s}}^{\,\alpha} = \sum_{\alpha=1}^{m} \left(\hat{\mathbf{p}}^{\,\alpha} + \hat{\rho}^{\,\alpha} \mathbf{x}_{\alpha}^{'}\right) \stackrel{!}{=} \mathbf{0}. \tag{45}$$

2.3.3 Balance of Moment of Momentum

For polar materials, the balance equation of moment of momentum states that the material time derivative of the moment of momentum of the constituent φ^α along its trajectory is equal to the moment of external forces and the moment of the total production term of momentum. All moments are related to a fixed point in the reference configuration. Because nonpolar materials, as discussed in this contribution, have no rotational degrees of freedom for the spatial point $\mathbf{x}$, there are no direct production terms that have to be considered ($\hat{\mathbf{m}}^\alpha = \hat{\mathbf{h}}^\alpha - \mathbf{x} \times \hat{\mathbf{s}}^\alpha = \mathbf{0}$). Thus, the evaluation yields the local statement that the partial Cauchy stress tensor is symmetric. The equation for the change in the moment of momentum with time is given by:

$$(\mathbf{h}^\alpha)'_\alpha = \mathbf{m}^\alpha + \hat{\mathbf{h}}^\alpha \tag{46}$$

with the moment of momentum:

$$\mathbf{h}^\alpha = \int_{\mathscr{B}_\alpha} \mathbf{x} \times \rho^\alpha \mathbf{x}'_\alpha \mathrm{d}v, \tag{47}$$

and the moment of external forces:

$$\begin{aligned} \mathbf{m}^\alpha &= \int_{\mathscr{B}_\alpha} \mathbf{x} \times \rho^\alpha \mathbf{b}^\alpha \mathrm{d}v + \int_{\partial \mathscr{B}_\alpha} \mathbf{x} \times \mathbf{t}^\alpha \mathrm{d}a \\ &= \int_{\mathscr{B}_\alpha} \mathbf{x} \times \rho^\alpha \mathbf{b}^\alpha \mathrm{d}v + \int_{\mathscr{B}_\alpha} (\mathbf{x} \times \operatorname{div} \mathbf{T}^\alpha + \mathbf{I} \times \mathbf{T}^\alpha) \mathrm{d}v, \end{aligned} \tag{48}$$

where Cauchy's theorem and the divergence theorem have been taken into account. The moment resulting from the total production terms of momentum (internal interaction forces) is given by:

$$\hat{\mathbf{h}}^\alpha = \int_{\mathscr{B}_\alpha} \mathbf{x} \times \hat{\mathbf{s}}^\alpha \mathrm{d}v. \tag{49}$$

Furthermore, the material time derivative of the moment of momentum $\mathbf{h}^\alpha$ is given by:

$$(\mathbf{h}^\alpha)'_\alpha = \int_{\mathscr{B}_\alpha} \mathbf{x} \times \left(\hat{\rho}^\alpha \mathbf{x}'_\alpha + \rho^\alpha \mathbf{x}''_\alpha \right) \mathrm{d}v. \tag{50}$$

Thus, the whole balance equation of moment of momentum in its local form reads as follows:

$$\int_{\mathscr{B}_\alpha} \mathbf{x} \times \left(\hat{\rho}^{\,\alpha} \mathbf{x}_\alpha^{'} + \rho^\alpha \mathbf{x}_\alpha^{''} \right) \mathrm{d}v = \int_{\mathscr{B}_\alpha} (\mathbf{x} \times \operatorname{div} \mathbf{T}^\alpha + \mathbf{I} \times \mathbf{T}^\alpha) \mathrm{d}v + \int_{\mathscr{B}_\alpha} \mathbf{x} \times \rho^\alpha \mathbf{b}^\alpha \mathrm{d}v + \int_{\mathscr{B}_\alpha} \mathbf{x} \times \hat{\mathbf{s}}^{\,\alpha} \mathrm{d}v. \tag{51}$$

This equation can be reformulated and expressed in the local form as:

$$\mathbf{x} \times \left[\operatorname{div} \mathbf{T}^\alpha + \rho^\alpha \left(\mathbf{b}^\alpha - \mathbf{x}_\alpha^{''} \right) + \hat{\mathbf{s}}^{\,\alpha} - \hat{\rho}^{\,\alpha} \mathbf{x}_\alpha^{'} \right] + \mathbf{I} \times \mathbf{T}^\alpha = \mathbf{0}. \tag{52}$$

Considering the balance of momentum (43) and taking Eq. (44) into account, Eq. (52) reduces to:

$$\mathbf{I} \times \mathbf{T}^\alpha = \mathbf{0}. \tag{53}$$

This finally leads to the statement:

$$\mathbf{T}^\alpha = (\mathbf{T}^\alpha)^{\mathbf{T}}, \tag{54}$$

that is, the partial Cauchy stress tensor $\mathbf{T}^\alpha$ is symmetric.

2.3.4 Balance of Energy (First Principle of Thermodynamics)

Within the balance of energy we have a coupling between thermal and mechanical fields, which enables us to describe thermomechanical effects (e.g. caused by phase transitions between the individual constituents of the observed body). The balance of energy states that the sum of the material time derivatives of the internal energy $\mathcal{E}^\alpha$ and the kinetic energy $\mathcal{K}^\alpha$ is equal to the sum of the increment of mechanical work $\mathcal{W}^\alpha$, the increment of non-mechanical work $\mathcal{Q}^\alpha$, and the total production terms of energy $\hat{\mathrm{e}}^\alpha$ integrated over the corresponding volume. The balance of energy for one constituent is given by:

$$(\mathcal{E}^\alpha)_\alpha^{'} + (\mathcal{K}^\alpha)_\alpha^{'} = \mathcal{W}^\alpha + \mathcal{Q}^\alpha + \int_{\mathscr{B}_\alpha} \hat{\mathrm{e}}^{\,\alpha} \mathrm{d}v. \tag{55}$$

The internal energy and the kinetic energy are defined as:

$$\mathcal{E}^\alpha = \int_{\mathscr{B}_\alpha} \rho^\alpha \varepsilon^\alpha \mathrm{d}v, \quad \mathcal{K}^\alpha = \int_{\mathscr{B}_\alpha} \frac{1}{2} \rho^\alpha \mathbf{x}_\alpha^{'} \cdot \mathbf{x}_\alpha^{'} \mathrm{d}v, \tag{56}$$

where ε^α is the specific internal energy. The increment of mechanical and non-mechanical work are given by:

$$\begin{aligned} \mathcal{W}^{\alpha} &= \int\limits_{\mathscr{B}_{\alpha}} \mathbf{x}_{\alpha}^{'} \cdot \rho^{\alpha} \mathbf{b}^{\alpha} \mathrm{d}v + \int\limits_{\partial \mathscr{B}_{\alpha}} \mathbf{x}_{\alpha}^{'} \cdot \mathbf{T}^{\alpha} \mathrm{d}\mathbf{a}, \\ \mathcal{Q}^{\alpha} &= \int\limits_{\mathscr{B}_{\alpha}} \rho^{\alpha} r^{\alpha} \mathrm{d}v - \int\limits_{\partial \mathscr{B}_{\alpha}} \mathbf{q}^{\alpha} \cdot \mathrm{d}\mathbf{a}, \end{aligned} \tag{57}$$

where r^{α} is the partial energy source and $\mathbf{q}^{\alpha}$ is the partial heat flux vector. Furthermore, the material time derivative of the internal energy $\mathcal{E}^{\alpha}$ reads:

$$\left(\mathcal{E}^{\alpha}\right)_{\alpha}^{'} = \left(\int\limits_{\mathscr{B}_{\alpha}} \rho^{\alpha} \varepsilon^{\alpha} \mathrm{d}v \right)_{\alpha}^{'} = \int\limits_{\mathscr{B}_{\alpha}} \left[\hat{\rho}^{\,\alpha} \varepsilon^{\alpha} + \rho^{\alpha} \left(\varepsilon^{\alpha}\right)_{\alpha}^{'} \right] \mathrm{d}v. \tag{58}$$

The material time derivative of the kinetic energy $\mathcal{K}^{\alpha}$ is given by:

$$\left(\mathcal{K}^{\alpha}\right)_{\alpha}^{'} = \left(\int\limits_{\mathscr{B}_{\alpha}} \frac{1}{2} \rho^{\alpha} \mathbf{x}_{\alpha}^{'} \cdot \mathbf{x}_{\alpha}^{'} \mathrm{d}v \right)_{\alpha}^{'} = \int\limits_{\mathscr{B}_{\alpha}} \left(\frac{1}{2} \hat{\rho}^{\,\alpha} \mathbf{x}_{\alpha}^{'} + \rho^{\alpha} \mathbf{x}_{\alpha}^{''} \right) \cdot \mathbf{x}_{\alpha}^{'} \mathrm{d}v. \tag{59}$$

With the equations:

$$\int\limits_{\partial \mathscr{B}_{\alpha}} \mathbf{x}_{\alpha}^{'} \cdot \mathbf{T}^{\alpha} \mathbf{n} \mathrm{d}a = \int\limits_{\mathscr{B}_{\alpha}} \left(\mathrm{div}\ \ \mathbf{T}^{\alpha} \cdot \mathbf{x}_{\alpha}^{'} + \mathbf{T}^{\alpha} \cdot \mathbf{L}_{\alpha} \right) \mathrm{d}v \tag{60}$$

and

$$\int\limits_{\partial \mathscr{B}_{\alpha}} \mathbf{q}^{\alpha} \cdot \mathbf{n} \mathrm{d}a = \int\limits_{\mathscr{B}_{\alpha}} \mathrm{div}\ \ \mathbf{q}^{\alpha} \mathrm{d}v \tag{61}$$

the whole equation of the balance of energy can be expressed by:

$$\begin{aligned} &\int\limits_{\mathscr{B}_{\alpha}} \left[\hat{\rho}^{\,\alpha} \varepsilon^{\alpha} + \rho^{\alpha} \left(\varepsilon^{\alpha}\right)_{\alpha}^{'} \right] \mathrm{d}v + \int\limits_{\mathscr{B}_{\alpha}} \left(\frac{1}{2} \hat{\rho}^{\,\alpha} \mathbf{x}_{\alpha}^{'} + \rho^{\alpha} \mathbf{x}_{\alpha}^{''} \right) \cdot \mathbf{x}_{\alpha}^{'} \mathrm{d}v \\ &= \int\limits_{\mathscr{B}_{\alpha}} \mathbf{x}_{\alpha}^{'} \cdot \rho^{\alpha} \mathbf{b}^{\alpha} \mathrm{d}v + \int\limits_{\mathscr{B}_{\alpha}} \left(\mathrm{div}\ \ T^{\alpha} \cdot \mathbf{x}_{\alpha}^{'} + \mathbf{T}^{\alpha} \cdot \mathbf{L}_{\alpha} \right) \mathrm{d}v \\ &+ \int\limits_{\mathscr{B}_{\alpha}} \rho^{\alpha} r^{\alpha} \mathrm{d}v - \int\limits_{\mathscr{B}_{\alpha}} \mathrm{div}\ \ \mathbf{q}^{\alpha} \mathrm{d}v + \int\limits_{\mathscr{B}_{\alpha}} \hat{\mathrm{e}}^{\,\alpha} \mathrm{d}v. \end{aligned} \tag{62}$$

Because the partial Cauchy stress tensors $\mathbf{T}^\alpha$ are symmetric (see Sect. 2.3.3), the scalar product $\mathbf{T}^\alpha \cdot \mathbf{L}_\alpha$ can be replaced by $\mathbf{T}^\alpha \cdot \mathbf{D}_\alpha$ and the local form of the balance of energy can be written as:

$$\begin{aligned}\rho^\alpha (\varepsilon^\alpha)'_\alpha + \hat{\rho}^\alpha \left(\varepsilon^\alpha + \frac{1}{2}\mathbf{x}'_\alpha \cdot \mathbf{x}'_\alpha\right) = \left[\operatorname{div} \mathbf{T}^\alpha + \rho^\alpha \left(\mathbf{b}^\alpha - \mathbf{x}''_\alpha\right)\right] \cdot \mathbf{x}'_\alpha \\ + \mathbf{T}^\alpha \cdot \mathbf{D}_\alpha + \rho^\alpha r^\alpha - \operatorname{div} \mathbf{q}^\alpha + \hat{e}^\alpha.\end{aligned} \tag{63}$$

Considering the balance of momentum (43), Eq. (63) becomes:

$$\begin{aligned}\rho^\alpha (\varepsilon^\alpha)'_\alpha = \mathbf{T}^\alpha \cdot \mathbf{D}_\alpha + \rho^\alpha r^\alpha - \operatorname{div} \mathbf{q}^\alpha \\ + \hat{e}^\alpha - \hat{\mathbf{p}}^\alpha \cdot \mathbf{x}'_\alpha - \hat{\rho}^\alpha \left(\varepsilon^\alpha + \frac{1}{2}\mathbf{x}'_\alpha \cdot \mathbf{x}'_\alpha\right).\end{aligned} \tag{64}$$

Introducing the direct production term of energy:

$$\hat{\varepsilon}^\alpha = \hat{e}^\alpha - \hat{\mathbf{p}}^\alpha \cdot \mathbf{x}'_\alpha - \hat{\rho}^\alpha \left(\varepsilon^\alpha + \frac{1}{2}\mathbf{x}'_\alpha \cdot \mathbf{x}'_\alpha\right), \tag{65}$$

the local statement of the balance of energy for the constituent φ^α simplifies to:

$$\rho^\alpha (\varepsilon^\alpha)'_\alpha - \mathbf{T}^\alpha \cdot \mathbf{D}_\alpha - \rho^\alpha r^\alpha + \operatorname{div} \mathbf{q}^\alpha = \hat{\varepsilon}^\alpha. \tag{66}$$

Using the definition of the direct production terms of energy, the restriction $(24)_4$ becomes:

$$\sum_{\alpha=1}^{m} \hat{e}^\alpha = \sum_{\alpha=1}^{m} \left[\hat{\varepsilon}^\alpha + \hat{\mathbf{p}}^\alpha \cdot \mathbf{x}'_\alpha + \hat{\rho}^\alpha \left(\varepsilon^\alpha + \frac{1}{2}\mathbf{x}'_\alpha \cdot \mathbf{x}'_\alpha\right)\right] \stackrel{!}{=} 0. \tag{67}$$

2.3.5 Entropy Inequality (Second Principle of Thermodynamics)

To obtain restrictions for the constitutive and evolution equations (see Sect. 2.5.2) the entropy inequality, or Clausius–Duhem inequality, must be satisfied. For the mixture with different local absolute temperatures Θ^α it is defined as:

$$\sum_{\alpha=1}^{m} (\mathrm{H}^\alpha)'_\alpha \geq \sum_{\alpha=1}^{m} \int_{\mathcal{B}_\alpha} \frac{1}{\Theta^\alpha} \rho^\alpha r^\alpha \mathrm{d}v - \sum_{\alpha=1}^{m} \int_{\partial \mathcal{B}_\alpha} \frac{1}{\Theta^\alpha} \mathbf{q}^\alpha \cdot \mathrm{d}\mathbf{a} \tag{68}$$

with the entropy of the constituent φ^α and its material time derivative given by:

$$\mathrm{H}^{\alpha} = \int\limits_{\mathscr{B}_{\alpha}} \rho^{\alpha}\eta^{\alpha}\mathrm{d}v, \quad \left(\mathrm{H}^{\alpha}\right)_{\alpha}^{'} = \int\limits_{\mathscr{B}_{\alpha}} \left[\hat{\rho}^{\,\alpha}\eta^{\alpha} + \rho^{\alpha}\left(\eta^{\alpha}\right)_{\alpha}^{'}\right]\mathrm{d}v. \tag{69}$$

Here, η^{α} denotes the specific entropy of the corresponding constituent. Considering the relation:

$$\int\limits_{\partial\mathscr{B}_{\alpha}} \frac{1}{\Theta^{\alpha}}\mathbf{q}^{\alpha}\cdot\mathbf{n}\mathrm{d}a = \int\limits_{\mathscr{B}_{\alpha}} \left[\frac{1}{\Theta^{\alpha}}\mathrm{div}\ \mathbf{q}^{\alpha} - \frac{1}{\left(\Theta^{\alpha}\right)^{2}}\mathrm{grad}\,\Theta^{\alpha}\cdot\mathbf{q}^{\alpha}\right]\mathrm{d}v, \tag{70}$$

the reformulated local form of the balance of energy:

$$\begin{aligned}\rho^{\alpha}r^{\alpha} = {} & \rho^{\alpha}\left(\varepsilon^{\alpha}\right)_{\alpha}^{'} - \mathbf{T}^{\alpha}\cdot\mathbf{D}_{\alpha} + \mathrm{div}\ \mathbf{q}^{\alpha} - \hat{\mathrm{e}}^{\,\alpha} \\ & + \hat{\mathbf{p}}^{\,\alpha}\cdot\mathbf{x}_{\alpha}^{'} + \hat{\rho}^{\,\alpha}\left(\varepsilon^{\alpha} + \frac{1}{2}\mathbf{x}_{\alpha}^{'}\cdot\mathbf{x}_{\alpha}^{'}\right),\end{aligned} \tag{71}$$

the Helmholtz free energy $\psi^{\alpha} = \varepsilon^{\alpha} - \Theta^{\alpha}\eta^{\alpha}$, and its derivative $\left(\psi^{\alpha}\right)_{\alpha}^{'} = \left(\varepsilon^{\alpha}\right)_{\alpha}^{'} - \left(\Theta^{\alpha}\right)_{\alpha}^{'}\eta^{\alpha} - \Theta^{\alpha}\left(\eta^{\alpha}\right)_{\alpha}^{'}$, the local form of the entropy inequality can be reformulated to:

$$\begin{aligned}\sum_{\alpha=1}^{m}\frac{1}{\Theta^{\alpha}}\Bigg\{ & -\rho^{\alpha}\left[\left(\psi^{\alpha}\right)_{\alpha}^{'} + \left(\Theta^{\alpha}\right)_{\alpha}^{'}\eta^{\alpha}\right] - \hat{\rho}^{\,\alpha}\left(\psi^{\alpha} + \frac{1}{2}\mathbf{x}_{\alpha}^{'}\cdot\mathbf{x}_{\alpha}^{'}\right) \\ & + \mathbf{T}^{\alpha}\cdot\mathbf{D}_{\alpha} - \hat{\mathbf{p}}^{\,\alpha}\cdot\mathbf{x}_{\alpha}^{'} - \frac{1}{\Theta^{\alpha}}\mathbf{q}^{\alpha}\cdot\mathrm{grad}\,\Theta^{\alpha} + \hat{\mathrm{e}}^{\,\alpha}\Bigg\} \geq 0.\end{aligned} \tag{72}$$

Within the framework of the TPM, the saturation condition is understood as constrained (i.e., considered with respect to the evaluation of the entropy inequality). Therefore, the inequality (72) gets an additional term by means of the concept of Lagrange multipliers, that is, the additional term consists of the material time derivative of the saturation condition following the motion of the solid connected with the Lagrange multiplier λ. Thus, the entropy inequality is given by:

$$\begin{aligned}\sum_{\alpha=1}^{m}\frac{1}{\Theta^{\alpha}}\Bigg\{ & -\rho^{\alpha}\left[\left(\psi^{\alpha}\right)_{\alpha}^{'} + \left(\Theta^{\alpha}\right)_{\alpha}^{'}\eta^{\alpha}\right] - \hat{\rho}^{\,\alpha}\left(\psi^{\alpha} + \frac{1}{2}\mathbf{x}_{\alpha}^{'}\cdot\mathbf{x}_{\alpha}^{'}\right) \\ & + \mathbf{T}^{\alpha}\cdot\mathbf{D}_{\alpha} - \hat{\mathbf{p}}^{\,\alpha}\cdot\mathbf{x}_{\alpha}^{'} - \frac{1}{\Theta^{\alpha}}\mathbf{q}^{\alpha}\cdot\mathrm{grad}\,\Theta^{\alpha} + \hat{\mathrm{e}}^{\,\alpha}\Bigg\} \\ & + \lambda\left(1 - \sum_{\alpha=1}^{m}n^{\alpha}\right)_{\mathrm{S}}^{'} \geq 0.\end{aligned} \tag{73}$$

The Lagrange multiplier λ describes the reaction force assigned to the saturation condition. For subsequent selection of process variables, needed for the evaluation of the entropy inequality, it is important to consider different cases. If all phases are

incompressible, then the saturation condition is an excess equation and λ is indeterminate. In the case of one compressible phase, the saturation condition is needed and λ is a constitutive quantity. If more than one phase is compressible, additional constitutive or evolution equations are needed for the compressible phases.

2.4 Discontinuous Damage Model

Continuous damage is characterized by a continuous increase in damage during loading. In contrast, damage is termed discontinuous if it only increases in a strain regime that is reached for the first time. A graphical interpretation of both continuous and discontinuous damage can be seen in Fig. 4.

In Sect. 2.5.3, the $(1-d)$ approach [35] in terms of a discontinuous damage formulation is used for both the solid and healed materials. As an easy example, the discontinuous damage function for the solid phase is derived below. The free energy function ψ^{S} is introduced as:

$$\psi^{\mathrm{S}} = \psi^{\mathrm{S}}\left(\mathbf{C}_{\mathrm{S}}, d^{\mathrm{S}}\right) = \left(1 - d^{\mathrm{S}}\right)\psi_0^{\mathrm{S}}(\mathbf{C}_{\mathrm{S}}), \tag{74}$$

where $d^{\mathrm{S}} \in [0,1]$ is a scalar valued damage variable and ψ_0^{S} is the free energy of the undamaged solid material. Here, isothermal processes are assumed ($\Theta^{\mathrm{S}} = \Theta =$ const. and $\left(\Theta^{\mathrm{S}}\right)'_{\mathrm{S}} = 0$). No volume-distributed heat supply or heat fluxes are

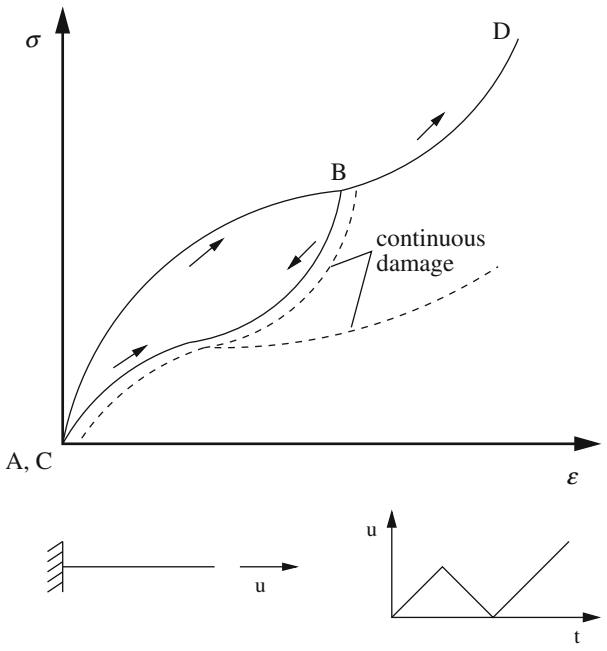

Fig. 4 Continuous and discontinuous damage

considered ($r^{\mathrm{S}} = 0$ and div $\mathbf{q}^{\mathrm{S}} = 0$). Internal interactions (production terms) are excluded. Thus, the entropy inequality (72) with respect to a one-component solid phase ($n^{\mathrm{S}} = 1$) becomes:

$$\mathbf{T}^{\mathrm{S}} \cdot \mathbf{D}_{\mathrm{S}} - \rho^{\mathrm{S}} \left(\psi^{\mathrm{S}}\right)_{\mathrm{S}}^{'} \geq 0. \tag{75}$$

Inserting the material time derivative:

$$\left(\psi^{\mathrm{S}}\right)_{\mathrm{S}}^{'} = 2\mathbf{F}_{\mathrm{S}} \frac{\partial \psi^{\mathrm{S}}}{\partial \mathbf{C}_{\mathrm{S}}} \mathbf{F}_{\mathrm{S}}^{\mathrm{T}} \cdot \mathbf{D}_{\mathrm{S}} + \frac{\partial \psi^{\mathrm{S}}}{\partial d^{\mathrm{S}}} \left(d^{\mathrm{S}}\right)_{\mathrm{S}}^{'}, \tag{76}$$

the entropy inequality reads:

$$\left(\mathbf{T}^{\mathrm{S}} - 2\rho^{\mathrm{S}} \mathbf{F}_{\mathrm{S}} \frac{\partial \psi^{\mathrm{S}}}{\partial \mathbf{C}_{\mathrm{S}}} \mathbf{F}_{\mathrm{S}}^{\mathrm{T}}\right) \cdot \mathbf{D}_{\mathrm{S}} - \frac{\partial \psi^{\mathrm{S}}}{\partial d^{\mathrm{S}}} \left(d^{\mathrm{S}}\right)_{\mathrm{S}}^{'} \geq 0. \tag{77}$$

This leads to the constitutive relation for the Cauchy stresses:

$$\mathbf{T}^{\mathrm{S}} = 2\rho^{\mathrm{S}} \mathbf{F}_{\mathrm{S}} \frac{\partial \psi^{\mathrm{S}}}{\partial \mathbf{C}_{\mathrm{S}}} \mathbf{F}_{\mathrm{S}}^{\mathrm{T}} = 2\rho^{\mathrm{S}} \mathbf{F}_{\mathrm{S}} \frac{\partial \left[\left(1 - d^{\mathrm{S}}\right) \psi_0^{\mathrm{S}}(\mathbf{C}_{\mathrm{S}})\right]}{\partial \mathbf{C}_{\mathrm{S}}} = \left(1 - d^{\mathrm{S}}\right) \mathbf{T}_{\mathrm{e}}^{\mathrm{S}} \tag{78}$$

and the reduced entropy inequality:

$$f^{\mathrm{S}} \left(d^{\mathrm{S}}\right)_{\mathrm{S}}^{'} \geq 0, \quad f^{\mathrm{S}} = -\frac{\partial \psi^{\mathrm{S}}}{\partial d^{\mathrm{S}}}. \tag{79}$$

Here, $\mathbf{T}_{\mathrm{e}}^{\mathrm{S}}$ is called the effective Cauchy stress tensor and f^{S} is the thermodynamic force that is work conjugated to the damage variable d^{S}. It turns out that:

$$f^{\mathrm{S}} = -\frac{\partial \psi^{\mathrm{S}}}{\partial d^{\mathrm{S}}} = \psi_0^{\mathrm{S}}. \tag{80}$$

To guarantee that $f^{\mathrm{S}} \left(d^{\mathrm{S}}\right)_{\mathrm{S}}^{'} = \psi_0^{\mathrm{S}} \left(d^{\mathrm{S}}\right)_{\mathrm{S}}^{'} \geq 0$, and recognizing that ψ_0^{S} is always greater than zero, $\left(d^{\mathrm{S}}\right)_{\mathrm{S}}^{'} \geq 0$ has to be fulfilled. In other words, d^{S} is only allowed to increase or stay constant. For the description of damage evolution, a damage function:

$$d^{\mathrm{S}} = d^{\mathrm{S}}\left(\alpha^{\mathrm{S}}\right) \quad \text{with} \quad \begin{pmatrix} d^{\mathrm{S}}(0) = 0 \\ d^{\mathrm{S}}(\infty) \in [0, 1] \end{pmatrix} \tag{81}$$

is introduced, which is a function of the internal variable α^{S}. To restrict damage evolution only to strain regimes that have not been reached before, α^{S} is connected to the maximum amount of already reached energy. Thus, it is postulated that:

$$\alpha^{\mathrm{S}}(t) = \max_{s\in[0,t]} f^{\mathrm{S}}(s). \tag{82}$$

Because $f^{\mathrm{S}} = \psi_0^{\mathrm{S}}(\mathbf{C}_{\mathrm{S}})$, α^{S} is always equal to the maximum amount of energy that has been reached during the loading process.

By means of the internal variable α^{S}, we are able to compare the actual effective energy ψ_0^{S} with the amount of effective energy that has been achieved before. Thus, we can introduce the damage criterion:

$$\phi^{\mathrm{S}} = f^{\mathrm{S}} - \alpha^{\mathrm{S}} \leq 0. \tag{83}$$

If $\phi^{\mathrm{S}} < 0$, no damage occurs, but if $\phi^{\mathrm{S}} = 0$, damage increases.

2.5 Multiphase Model

A five-phase model for the description of self-healing processes is developed in this section. As mentioned, the investigated body consists of the following different phases: solid matrix material (S) with dispersed catalysts (C), solid healed material (H), liquid healing agents (L), and gas phase (G), which in this context is the air inside the cracks. To develop the five-phase model, some assumptions and simplifications have been made:

- Neglecting dynamic effects
  - $$\mathbf{x}_{\alpha}^{''} = 0,$$
- Isothermal processes, no heat fluxes
  - $$\Theta^{\alpha} = \Theta = \text{const.}, \quad (\Theta^{\alpha})_{\alpha}^{'} = 0, \quad \text{div } \mathbf{q}^{\alpha} = 0,$$
- No consideration of the volume-distributed heat supply
  - $$r^{\alpha} = 0,$$
- Mass exchange only between the healing agents and the healed material, constant decrease in the amount of catalysts
  - $$\hat{\rho}^{\,\mathrm{S}} = \hat{\rho}^{\,\mathrm{G}} = 0, \quad \hat{\rho}^{\,\mathrm{H}} = -\hat{\rho}^{\,\mathrm{L}} - \hat{\rho}^{\,\mathrm{C}}$$
- Solid, healed material, healing agents, and catalysts are incompressible

–
$$\rho^{\beta \mathrm{R}} = \text{const.}, \quad \beta = \mathrm{S}, \mathrm{H}, \mathrm{L}, \mathrm{C},$$

- Gas phase is compressible

  –
  $$\rho^{\mathrm{GR}} \neq \text{const.},$$

- Neglecting the volume fraction of the catalyst phase

  –
  $$n^{\mathrm{C}} = 0,$$

- Catalysts move with the solid

  –
  $$\mathbf{x}_{\mathrm{C}}^{'} - \mathbf{x}_{\mathrm{S}}^{'} = \mathbf{0},$$

- Same velocities of the motions of the solid phases

  –
  $$(\chi_{\mathrm{S}})_{\mathrm{S}}^{'} = (\chi_{\mathrm{H}})_{\mathrm{H}}^{'} = (\chi_{\mathrm{H}})_{\mathrm{S}}^{'},$$

- Motions of solid and healed material are identical except at an initial solid motion

  –
  $$\chi_{\mathrm{H}} = \chi_{\mathrm{S}} - \chi_{\mathrm{S0}},$$

  where the initial solid motion χ_{S0} is the accrued motion of the solid before the onset of the phase transition: $\chi_{\mathrm{S0}} = \chi_{\mathrm{S}}$ for $n^{\mathrm{H}} = 0$ and $\chi_{\mathrm{S0}} = \text{const.}$ for $n^{\mathrm{H}} > 0$,

- Neglecting the stress state (osmotic pressure) of the catalysts

  –
  $$\mathbf{T}^{\mathrm{C}} = 0.$$

  For the assumption of the initial solid motion χ_{S0} it is necessary to consider a multiplicative decomposition of the deformation gradient of the solid phase:

$$\mathbf{F}_{\mathrm{S}} = \mathbf{F}_{\mathrm{H}} \mathbf{F}_{\mathrm{S0}} \quad \mathbf{F}_{\mathrm{S0}} = \mathrm{Grad} \chi_{\mathrm{S0}}. \tag{84}$$

This was originally introduced within the context of growth modeling in biological tissues (see for example [36–38]). A schematic interpretation of the multiplicative decomposition of the deformation gradient can be seen in Fig. 5. As a result of the decomposition, three different right Cauchy–Green deformation tensors (for the solid, the initial part of solid motion, and the healed material) are gained, which are given by:

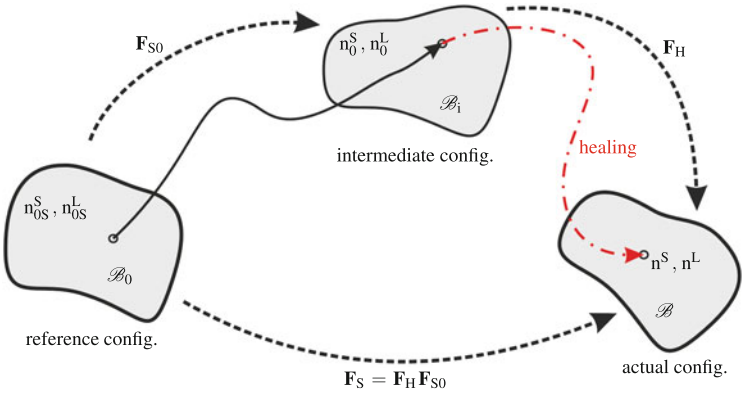

Fig. 5 Multiplicative decomposition of the deformation gradient [39], with kind permission from Springer Science + Business Media

$$\mathbf{C}_S = \mathbf{F}_S^T \mathbf{F}_S, \quad \mathbf{C}_{S0} = \mathbf{F}_{S0}^T \mathbf{F}_{S0}, \quad \widetilde{\mathbf{C}}_H = \mathbf{F}_H^T \mathbf{F}_H. \tag{85}$$

The symbol $\widetilde{(\bullet)}$ denotes the relation of the tensor to the intermediate configuration resulting from decomposition of $\mathbf{F}_S$. Furthermore, together with $(84)_1$ there exists the Jacobian of the solid:

$$J_S = J_H J_{S0} \tag{86}$$

and its material time derivative:

$$(J_S)'_S = J_S(\mathbf{D}_S \cdot \mathbf{I}) = (J_H)'_S J_{S0}. \tag{87}$$

With the relation (87), the material time derivative of the healed material with respect to the solid phase can be expressed as follows:

$$(J_H)'_S = J_S J_{S0}^{-1}(\mathbf{D}_S \cdot \mathbf{I}). \tag{88}$$

2.5.1 Field Equations

The field equations consist of the balance equations of the constituents, taken from the mixture theory, and the saturation condition. Furthermore, the aforementioned assumptions have been considered. The coupled field equations for the five-phase model are given by the local statements of the balance equations of mass (32):

$$
\begin{aligned}
&\left(n^{\mathrm{S}}\right)_{\mathrm{S}}^{'}+n^{\mathrm{S}}\mathrm{div}\ \mathbf{x}_{\mathrm{S}}^{'}=0, \quad \left(n^{\mathrm{H}}\right)_{\mathrm{S}}^{'}+n^{\mathrm{H}}\mathrm{div}\ \mathbf{x}_{\mathrm{S}}^{'}=\frac{\hat{\rho}^{\mathrm{H}}}{\rho^{\mathrm{HR}}},\\
&\left(n^{\mathrm{L}}\right)_{\mathrm{L}}^{'}+n^{\mathrm{L}}\mathrm{div}\ \mathbf{x}_{\mathrm{L}}^{'}=-\frac{\hat{\rho}^{\mathrm{H}}}{\rho^{\mathrm{LR}}}, \quad n^{\mathrm{S}}\left(c^{\mathrm{C}}\right)_{\mathrm{S}}^{'}=\hat{\rho}^{\mathrm{C}},\\
&\left(n^{\mathrm{G}}\right)_{\mathrm{G}}^{'}+n^{\mathrm{G}}\mathrm{div}\ \mathbf{x}_{\mathrm{G}}^{'}+\frac{n^{\mathrm{G}}}{\rho^{\mathrm{GR}}}\left(\rho^{\mathrm{GR}}\right)_{\mathrm{G}}^{'}=0,
\end{aligned}
\tag{89}
$$

the balance equations of momentum (43) for the mixture, liquid, and gas:

$$
\begin{aligned}
&\mathrm{div}\ \mathbf{T}^{\mathrm{SHLG}}+\rho^{\mathrm{SHLG}}\mathbf{b}=-\hat{\rho}^{\mathrm{H}}\mathbf{w}_{\mathrm{LS}}, \quad \mathrm{div}\ \mathbf{T}^{\mathrm{L}}+\rho^{\mathrm{L}}\mathbf{b}=-\hat{\mathbf{p}}^{\mathrm{L}},\\
&\mathrm{div}\ \mathbf{T}^{\mathrm{G}}+\rho^{\mathrm{G}}\mathbf{b}=-\hat{\mathbf{p}}^{\mathrm{G}},
\end{aligned}
\tag{90}
$$

and the material time derivative of the saturation condition (3) with respect to the solid phase:

$$
\left(n^{\mathrm{S}}\right)_{\mathrm{S}}^{'}+\left(n^{\mathrm{H}}\right)_{\mathrm{S}}^{'}+\left(n^{\mathrm{L}}\right)_{\mathrm{S}}^{'}+\left(n^{\mathrm{G}}\right)_{\mathrm{S}}^{'}=0. \tag{91}
$$

The form of (91) can be further reformulated assuming that the motions of the solid and healed material are equal ($\chi_{\mathrm{S}}=\chi_{\mathrm{H}}$). Considering the formula for the material time derivatives of scalar quantities (23), the material time derivative of $(n^{\beta})_{\mathrm{S}}^{'}$ ($\beta=\mathrm{H},\mathrm{L},\mathrm{G}$) can be expressed as:

$$
\left(n^{\beta}\right)_{\mathrm{S}}^{'}=\left(n^{\beta}\right)_{\beta}^{'}-\mathrm{grad}\, n^{\beta}\cdot\mathbf{w}_{\beta\mathrm{S}}, \quad \mathbf{w}_{\beta\mathrm{S}}=\mathbf{x}_{\beta}^{'}-\mathbf{x}_{\mathrm{S}}^{'}. \tag{92}
$$

This leads to the following form of the saturation condition:

$$
\left(n^{\mathrm{S}}\right)_{\mathrm{S}}^{'}+\left(n^{\mathrm{H}}\right)_{\mathrm{S}}^{'}+\left(n^{\mathrm{L}}\right)_{\mathrm{L}}^{'}+\left(n^{\mathrm{G}}\right)_{\mathrm{G}}^{'}-\mathrm{grad}\, n^{\mathrm{L}}\cdot\mathbf{w}_{\mathrm{LS}}-\mathrm{grad}\, n^{\mathrm{G}}\cdot\mathbf{w}_{\mathrm{GS}}=0. \tag{93}
$$

Inserting the given balance equations of mass for the particular phases, see (89), yields:

$$
\begin{aligned}
&-n^{\mathrm{S}}\mathrm{div}\ \mathbf{x}_{\mathrm{S}}^{'}+\frac{\hat{\rho}^{\mathrm{H}}}{\rho^{\mathrm{HR}}}-n^{\mathrm{H}}\mathrm{div}\ \mathbf{x}_{\mathrm{S}}^{'}-\frac{\hat{\rho}^{\mathrm{H}}}{\rho^{\mathrm{LR}}}-n^{\mathrm{L}}\mathrm{div}\ \mathbf{x}_{\mathrm{L}}^{'}-n^{\mathrm{G}}\mathrm{div}\ \mathbf{x}_{\mathrm{G}}^{'}\\
&-\frac{n^{\mathrm{G}}}{\rho^{\mathrm{GR}}}\left(\rho^{\mathrm{GR}}\right)_{\mathrm{G}}^{'}-\mathrm{grad}\, n^{\mathrm{L}}\cdot\mathbf{w}_{\mathrm{LS}}-\mathrm{grad}\, n^{\mathrm{G}}\cdot\mathbf{w}_{\mathrm{GS}}=0.
\end{aligned}
\tag{94}
$$

Expansion of this equation with $n^{\alpha}\mathrm{div}\ \mathbf{x}_{\mathrm{S}}^{'}-n^{\alpha}\mathrm{div}\ \mathbf{x}_{\mathrm{S}}^{'}=0$ and in consideration of $n^{\mathrm{S}}+n^{\mathrm{H}}+n^{\mathrm{L}}+n^{\mathrm{G}}=1$, the equation simplifies to:

$$\operatorname{div}\ \mathbf{x}_{\mathrm{S}}^{'} + n^{\mathrm{L}}\operatorname{div}\ \mathbf{w}_{\mathrm{LS}} + n^{\mathrm{G}}\operatorname{div}\ \mathbf{w}_{\mathrm{GS}} + \operatorname{grad} n^{\mathrm{G}} \cdot \mathbf{w}_{\mathrm{GS}} + \frac{n^{\mathrm{G}}}{\rho^{\mathrm{GR}}}(\rho^{\mathrm{GR}})_{\mathrm{G}}^{'} + \frac{\hat{\rho}^{\mathrm{H}}}{\rho^{\mathrm{HR}}} - \frac{\hat{\rho}^{\mathrm{H}}}{\rho^{\mathrm{LR}}} = 0. \tag{95}$$

Considering the calculation rule $\operatorname{div}(\gamma\mathbf{v}) = \gamma\operatorname{div}\ \mathbf{v} + \operatorname{grad}\gamma \cdot \mathbf{v}$, the final form of the material time derivative of the saturation condition is given by:

$$\operatorname{div}\left(\mathbf{x}_{\mathrm{S}}^{'} + n^{\mathrm{L}}\mathbf{w}_{\mathrm{LS}} + n^{\mathrm{G}}\mathbf{w}_{\mathrm{GS}}\right) + \frac{n^{\mathrm{G}}}{\rho^{\mathrm{GR}}}\left(\rho^{\mathrm{GR}}\right)_{\mathrm{G}}^{'} + \hat{\rho}^{\mathrm{H}}\left(\frac{1}{\rho^{\mathrm{HR}}} - \frac{1}{\rho^{\mathrm{LR}}}\right) = 0. \tag{96}$$

As mentioned in Sect. 2.3, Truesdell's third metaphysical principle has to be satisfied. Thus, the balance equation of momentum for the mixture $(90)_1$ has to be equal to the balance equation of momentum for a single phase body. Therefore, a so-called barycentric velocity must be defined (see [29, 30]) as follows:

$$\dot{\mathbf{x}} = \frac{1}{\rho}\sum_{\alpha=1}^{m}\rho^{\alpha}\mathbf{x}_{\alpha}^{'}, \quad \ddot{\mathbf{x}} = \frac{1}{\rho}\sum_{\alpha=1}^{m}\left[\rho^{\alpha}\mathbf{x}_{\alpha}^{''} - \operatorname{div}(\rho^{\alpha}\mathbf{u}_{\alpha}\otimes\mathbf{u}_{\alpha}) + \hat{\rho}^{\alpha}\mathbf{x}_{\alpha}^{'}\right], \tag{97}$$

where the mixture density and the diffusion velocity are denoted by:

$$\rho = \sum_{\alpha=1}^{m}\rho^{\alpha}, \quad \mathbf{u}_{\alpha} = \mathbf{x}_{\alpha}^{'} - \dot{\mathbf{x}}. \tag{98}$$

Neglecting dynamic effects concerning the mixture and the constituents (i.e., $\ddot{\mathbf{x}} = \mathbf{0}$ and $\mathbf{x}_{\alpha}^{''} = \mathbf{0}$), it follows from $(97)_2$ that:

$$\hat{\rho}^{\alpha}\mathbf{x}_{\alpha}^{'} = \operatorname{div}(\rho^{\alpha}\mathbf{u}_{\alpha}\otimes\mathbf{u}_{\alpha}). \tag{99}$$

Thus, the balance of momentum for the mixture $(90)_1$ becomes:

$$\operatorname{div}\left(\mathbf{T}^{\mathrm{SHLG}} - \rho^{\mathrm{H}}\mathbf{u}_{\mathrm{S}}\otimes\mathbf{u}_{\mathrm{S}} - \rho^{\mathrm{L}}\mathbf{u}_{\mathrm{L}}\otimes\mathbf{u}_{\mathrm{L}}\right) + \rho^{\mathrm{SHLG}}\mathbf{b} = \mathbf{0}. \tag{100}$$

With the definitions:

$$\mathbf{T} = \mathbf{T}^{\mathrm{SHLG}} - \rho^{\mathrm{H}}\mathbf{u}_{\mathrm{S}}\otimes\mathbf{u}_{\mathrm{S}} - \rho^{\mathrm{L}}\mathbf{u}_{\mathrm{L}}\otimes\mathbf{u}_{\mathrm{L}}, \quad \rho = \rho^{\mathrm{SHLG}} \tag{101}$$

Eq. (100) is equal to the corresponding balance law of one-component materials.

2.5.2 Constitutive Theory

The initial equation used to derive restrictions for the simplified five-phase model is the entropy inequality (73). Considering the aforementioned assumptions, the entropy inequality can be written as:

$$\begin{aligned}
&-\rho^{\mathrm{S}}(\psi^{\mathrm{S}})_{\mathrm{S}}^{'} - \rho^{\mathrm{H}}(\psi^{\mathrm{H}})_{\mathrm{S}}^{'} - \rho^{\mathrm{L}}(\psi^{\mathrm{L}})_{\mathrm{L}}^{'} - \rho^{\mathrm{C}}(\psi^{\mathrm{C}})_{\mathrm{C}}^{'} - \rho^{\mathrm{G}}(\psi^{\mathrm{G}})_{\mathrm{G}}^{'} \\
&+\mathbf{T}^{\mathrm{SH}} \cdot \mathbf{D}_{\mathrm{S}} + \mathbf{T}^{\mathrm{L}} \cdot \mathbf{D}_{\mathrm{L}} + \mathbf{T}^{\mathrm{G}} \cdot \mathbf{D}_{\mathrm{G}} - \hat{\mathbf{p}}^{\,\mathrm{L}} \cdot \mathbf{w}_{\mathrm{LS}} - \hat{\mathbf{p}}^{\,\mathrm{G}} \cdot \mathbf{w}_{\mathrm{GS}} \\
&-\hat{\rho}^{\,\mathrm{H}}\left(\psi^{\mathrm{H}} - \psi^{\mathrm{L}} + \frac{1}{2}\mathbf{x}_{\mathrm{S}}^{'} \cdot \mathbf{x}_{\mathrm{S}}^{'} - \frac{1}{2}\mathbf{x}_{\mathrm{L}}^{'} \cdot \mathbf{x}_{\mathrm{L}}^{'}\right) - \hat{\rho}^{\,\mathrm{C}}\left(\psi^{\mathrm{C}} + \frac{1}{2}\mathbf{x}_{\mathrm{S}}^{'} \cdot \mathbf{x}_{\mathrm{S}}^{'}\right) \\
&-\lambda\left[(n^{\mathrm{S}})_{\mathrm{S}}^{'} + (n^{\mathrm{H}})_{\mathrm{S}}^{'} + (n^{\mathrm{L}})_{\mathrm{L}}^{'} + (n^{\mathrm{G}})_{\mathrm{G}}^{'} - \operatorname{grad} n^{\mathrm{L}} \cdot \mathbf{w}_{\mathrm{LS}} - \operatorname{grad} n^{\mathrm{G}} \cdot \mathbf{w}_{\mathrm{GS}}\right] \geq 0.
\end{aligned} \tag{102}$$

Here, the concept of Lagrange multipliers is used in connection with the rate of the saturation condition. As described in Sect. 2.3.5, the Lagrange multiplier λ can be physically interpreted as an internal pressure.

Referring to, for example, [40] and with respect to the damage variables d^{S} and d^{H} of the solid and healed material phases, respectively (see Sect. 2.4), it is postulated that the free Helmholtz energies for the different phases depend on the following quantities:

$$\begin{aligned}
&\psi^{\mathrm{S}} = \psi^{\mathrm{S}}\left(\mathbf{C}_{\mathrm{S}}, d^{\mathrm{S}}\right), \quad \psi^{\mathrm{H}} = \psi^{\mathrm{H}}\left(\widetilde{\mathbf{C}}_{\mathrm{H}}, n^{\mathrm{H}}, d^{\mathrm{H}}\right), \quad \psi^{\mathrm{C}} = \psi^{\mathrm{C}}(c^{\mathrm{C}}) \\
&\psi^{\mathrm{L}} = \psi^{\mathrm{L}}(\mathrm{J}_{\mathrm{L}}, n^{\mathrm{L}}, n^{\mathrm{G}}, \rho^{\mathrm{GR}}), \quad \psi^{\mathrm{G}} = \psi^{\mathrm{G}}(n^{\mathrm{L}}, n^{\mathrm{G}}, \rho^{\mathrm{GR}}).
\end{aligned} \tag{103}$$

Considering the material time derivatives of the free Helmholtz energy functions:

$$\begin{aligned}
(\psi^{\mathrm{S}})_{\mathrm{S}}^{'} &= 2\mathbf{F}_{\mathrm{S}} \frac{\partial \psi^{\mathrm{S}}}{\partial \mathbf{C}_{\mathrm{S}}} \mathbf{F}_{\mathrm{S}}^{\mathrm{T}} \cdot \mathbf{D}_{\mathrm{S}} + \frac{\partial \psi^{\mathrm{S}}}{\partial d^{\mathrm{S}}} (d^{\mathrm{S}})_{\mathrm{S}}^{'}, \quad (\psi^{\mathrm{C}})_{\mathrm{S}}^{'} = \frac{\partial \psi^{\mathrm{C}}}{\partial c^{\mathrm{C}}} (c^{\mathrm{C}})_{\mathrm{S}}^{'} \\
(\psi^{\mathrm{H}})_{\mathrm{S}}^{'} &= 2\mathbf{F}_{\mathrm{H}} \frac{\partial \psi^{\mathrm{H}}}{\partial \widetilde{\mathbf{C}}_{\mathrm{H}}} \mathbf{F}_{\mathrm{H}}^{\mathrm{T}} \cdot \mathbf{D}_{\mathrm{S}} + \frac{\partial \psi^{\mathrm{H}}}{\partial n^{\mathrm{H}}} (n^{\mathrm{H}})_{\mathrm{S}}^{'} + \frac{\partial \psi^{\mathrm{H}}}{\partial d^{\mathrm{H}}} (d^{\mathrm{H}})_{\mathrm{S}}^{'}, \\
(\psi^{\mathrm{L}})_{\mathrm{L}}^{'} &= \mathrm{J}_{\mathrm{L}} \frac{\partial \psi^{\mathrm{L}}}{\partial \mathrm{J}_{\mathrm{L}}} \mathbf{I} \cdot \mathbf{D}_{\mathrm{L}} + \frac{\partial \psi^{\mathrm{L}}}{\partial n^{\mathrm{L}}} (n^{\mathrm{L}})_{\mathrm{L}}^{'} \\
&+ \frac{\partial \psi^{\mathrm{L}}}{\partial n^{\mathrm{G}}} \left[(n^{\mathrm{G}})_{\mathrm{G}}^{'} + \operatorname{grad} n^{\mathrm{G}} \cdot (\mathbf{w}_{\mathrm{LS}} - \mathbf{w}_{\mathrm{GS}})\right] \\
&+ \frac{\partial \psi^{\mathrm{L}}}{\partial \rho^{\mathrm{GR}}} \left[(\rho^{\mathrm{GR}})_{\mathrm{G}}^{'} + \operatorname{grad} \rho^{\mathrm{GR}} \cdot (\mathbf{w}_{\mathrm{LS}} - \mathbf{w}_{\mathrm{GS}})\right], \\
(\psi^{\mathrm{G}})_{\mathrm{G}}^{'} &= \frac{\partial \psi^{\mathrm{G}}}{\partial n^{\mathrm{G}}} (n^{\mathrm{G}})_{\mathrm{G}}^{'} + \frac{\partial \psi^{\mathrm{G}}}{\partial \rho^{\mathrm{GR}}} (\rho^{\mathrm{GR}})_{\mathrm{G}}^{'} \\
&+ \frac{\partial \psi^{\mathrm{G}}}{\partial n^{\mathrm{L}}} \left[(n^{\mathrm{L}})_{\mathrm{L}}^{'} - \operatorname{grad} n^{\mathrm{L}} \cdot (\mathbf{w}_{\mathrm{LS}} - \mathbf{w}_{\mathrm{GS}})\right],
\end{aligned} \tag{104}$$

and expanding the entropy inequality by the balance equations of mass in connection with the concept of Lagrange multipliers:

$$\begin{aligned}
&\lambda^{\mathrm{S}}_{\mathrm{BM}}\left[(n^{\mathrm{S}})'_{\mathrm{S}} + n^{\mathrm{S}}(\mathbf{D}_{\mathrm{S}}\cdot\mathbf{I})\right] = 0,\\
&\lambda^{\mathrm{H}}_{\mathrm{BM}}\left[(n^{\mathrm{H}})'_{\mathrm{S}} + n^{\mathrm{H}}(\mathbf{D}_{\mathrm{S}}\cdot\mathbf{I}) - \frac{\hat{\rho}^{\,\mathrm{H}}}{\rho^{\mathrm{HR}}}\right] = 0,\\
&\lambda^{\mathrm{L}}_{\mathrm{BM}}\left[(n^{\mathrm{L}})'_{\mathrm{L}} + n^{\mathrm{L}}(\mathbf{D}_{\mathrm{L}}\cdot\mathbf{I}) + \frac{\hat{\rho}^{\,\mathrm{H}}}{\rho^{\mathrm{LR}}}\right] = 0,\\
&\lambda^{\mathrm{G}}_{\mathrm{BM}}\left[(n^{\mathrm{G}})'_{\mathrm{G}} + n^{\mathrm{G}}(\mathbf{D}_{\mathrm{G}}\cdot\mathbf{I}) + n^{\mathrm{G}}\frac{(\rho^{\mathrm{GR}})'_{\mathrm{G}}}{\rho^{\mathrm{GR}}}\right] = 0,
\end{aligned} \tag{105}$$

the entropy inequality (102) becomes:

$$\begin{aligned}
&\mathbf{D}_{\mathrm{S}}\cdot\left\{\mathbf{T}^{\mathrm{SH}} - 2\rho^{\mathrm{S}}\mathbf{F}_{\mathrm{S}}\frac{\partial\psi^{\mathrm{S}}}{\partial\mathbf{C}_{\mathrm{S}}}\mathbf{F}_{\mathrm{S}}^{\mathrm{T}} - 2\rho^{\mathrm{H}}\mathbf{F}_{\mathrm{H}}\frac{\partial\psi^{\mathrm{H}}}{\partial\widetilde{\mathbf{C}}_{\mathrm{H}}}\mathbf{F}_{\mathrm{H}}^{\mathrm{T}}\right.\\
&\qquad\left. + n^{\mathrm{S}}\lambda^{\mathrm{S}}_{\mathrm{BM}}\mathbf{I} + n^{\mathrm{H}}\lambda^{\mathrm{H}}_{\mathrm{BM}}\mathbf{I}\right\}\\
&+\mathbf{D}_{\mathrm{L}}\cdot\left\{\mathbf{T}^{\mathrm{L}} - \rho^{\mathrm{L}}\mathbf{J}_{\mathrm{L}}\frac{\partial\psi^{\mathrm{L}}}{\partial\mathbf{J}_{\mathrm{L}}}\mathbf{I} + n^{\mathrm{L}}\lambda^{\mathrm{L}}_{\mathrm{BM}}\mathbf{I}\right\}\\
&+\mathbf{D}_{\mathrm{G}}\cdot\left\{\mathbf{T}^{\mathrm{G}} + n^{\mathrm{G}}\lambda^{\mathrm{G}}_{\mathrm{BM}}\mathbf{I}\right\}\\
&-\left(d^{\mathrm{S}}\right)'_{\mathrm{S}}\left\{\frac{\partial\psi^{\mathrm{S}}}{\partial d^{\mathrm{S}}}\right\} - \left(d^{\mathrm{H}}\right)'_{\mathrm{S}}\left\{\frac{\partial\psi^{\mathrm{H}}}{\partial d^{\mathrm{H}}}\right\}\\
&-(n^{\mathrm{S}})'_{\mathrm{S}}\left\{\lambda - \lambda^{\mathrm{S}}_{\mathrm{BM}}\right\}\\
&-(n^{\mathrm{H}})'_{\mathrm{S}}\left\{\lambda - \lambda^{\mathrm{H}}_{\mathrm{BM}} + \rho^{\mathrm{H}}\frac{\partial\psi^{\mathrm{H}}}{\partial n^{\mathrm{H}}}\right\}\\
&-(n^{\mathrm{L}})'_{\mathrm{L}}\left\{\lambda - \lambda^{\mathrm{L}}_{\mathrm{BM}} + \rho^{\mathrm{L}}\frac{\partial\psi^{\mathrm{L}}}{\partial n^{\mathrm{L}}} + \rho^{\mathrm{G}}\frac{\partial\psi^{\mathrm{G}}}{\partial n^{\mathrm{L}}}\right\}\\
&-(n^{\mathrm{G}})'_{\mathrm{G}}\left\{\lambda - \lambda^{\mathrm{G}}_{\mathrm{BM}} + \rho^{\mathrm{L}}\frac{\partial\psi^{\mathrm{L}}}{\partial n^{\mathrm{G}}} + \rho^{\mathrm{G}}\frac{\partial\psi^{\mathrm{G}}}{\partial n^{\mathrm{G}}}\right\}\\
&-(\rho^{\mathrm{GR}})'_{\mathrm{G}}\left\{\rho^{\mathrm{L}}\frac{\partial\psi^{\mathrm{L}}}{\partial\rho^{\mathrm{GR}}} + \rho^{\mathrm{G}}\frac{\partial\psi^{\mathrm{G}}}{\partial\rho^{\mathrm{GR}}} - \lambda^{\mathrm{G}}_{\mathrm{BM}}\frac{n^{\mathrm{G}}}{\rho^{\mathrm{GR}}}\right\}\\
&-\mathbf{w}_{\mathrm{LS}}\cdot\left\{\hat{\mathbf{p}}^{\,\mathrm{L}} - \lambda\mathrm{grad}\,n^{\mathrm{L}} + \rho^{\mathrm{L}}\frac{\partial\psi^{\mathrm{L}}}{\partial n^{\mathrm{G}}}\mathrm{grad}\,n^{\mathrm{G}}\right.\\
&\qquad\left. + \rho^{\mathrm{L}}\frac{\partial\psi^{\mathrm{L}}}{\partial\rho^{\mathrm{GR}}}\mathrm{grad}\,\rho^{\mathrm{GR}} - \rho^{\mathrm{G}}\frac{\partial\psi^{\mathrm{G}}}{\partial n^{\mathrm{L}}}\mathrm{grad}\,n^{\mathrm{L}}\right\}\\
&-\mathbf{w}_{\mathrm{GS}}\cdot\left\{\hat{\mathbf{p}}^{\,\mathrm{G}} - \lambda\mathrm{grad}\,n^{\mathrm{G}} - \rho^{\mathrm{L}}\frac{\partial\psi^{\mathrm{L}}}{\partial n^{\mathrm{G}}}\mathrm{grad}\,n^{\mathrm{G}}\right.\\
&\qquad\left. - \rho^{\mathrm{L}}\frac{\partial\psi^{\mathrm{L}}}{\partial\rho^{\mathrm{GR}}}\mathrm{grad}\,\rho^{\mathrm{GR}} + \rho^{\mathrm{G}}\frac{\partial\psi^{\mathrm{G}}}{\partial n^{\mathrm{L}}}\mathrm{grad}\,n^{\mathrm{L}}\right\}\\
&-\hat{\rho}^{\,\mathrm{H}}\left\{\psi^{\mathrm{H}} - \psi^{\mathrm{L}} + \frac{1}{2}\mathbf{x}'_{\mathrm{S}}\cdot\mathbf{x}'_{\mathrm{S}} - \frac{1}{2}\mathbf{x}'_{\mathrm{L}}\cdot\mathbf{x}'_{\mathrm{L}} + \frac{\lambda^{\mathrm{L}}_{\mathrm{BM}}}{\rho^{\mathrm{LR}}} - \frac{\lambda^{\mathrm{H}}_{\mathrm{BM}}}{\rho^{\mathrm{HR}}}\right\}\\
&-\hat{\rho}^{\,\mathrm{C}}\left\{\psi^{\mathrm{C}} + \frac{1}{2}\mathbf{x}'_{\mathrm{S}}\cdot\mathbf{x}'_{\mathrm{S}}\right\} \geq 0,
\end{aligned} \tag{106}$$

This leads to the following restrictions concerning the stresses:

$$\begin{aligned}\mathbf{T}^{\mathrm{SH}} &= 2\rho^{\mathrm{S}}\mathbf{F}_{\mathrm{S}}\frac{\partial\psi^{\mathrm{S}}}{\partial\mathbf{C}_{\mathrm{S}}}\mathbf{F}_{\mathrm{S}}^{\mathrm{T}} + 2\rho^{\mathrm{H}}\mathbf{F}_{\mathrm{H}}\frac{\partial\psi^{\mathrm{H}}}{\partial\hat{\mathbf{C}}_{\mathrm{H}}} - n^{\mathrm{S}}\lambda_{\mathrm{BM}}^{\mathrm{S}}\mathbf{I} - n^{\mathrm{H}}\lambda_{\mathrm{BM}}^{\mathrm{H}}\mathbf{I},\\ \mathbf{T}^{\mathrm{L}} &= \rho^{\mathrm{L}}\mathrm{J}_{\mathrm{L}}\frac{\partial\psi^{\mathrm{L}}}{\partial\mathrm{J}_{\mathrm{L}}}\mathbf{I} - n^{\mathrm{L}}\lambda_{\mathrm{BM}}^{\mathrm{L}}\mathbf{I}, \quad \mathbf{T}^{\mathrm{G}} = -n^{\mathrm{G}}\lambda_{\mathrm{BM}}^{\mathrm{G}}\mathbf{I}.\end{aligned} \tag{107}$$

Considering the relations for the Lagrange multipliers connected with the balance equations of mass:

$$\begin{aligned}\lambda_{\mathrm{BM}}^{\mathrm{S}} &= \lambda, \qquad \lambda_{\mathrm{BM}}^{\mathrm{H}} = \lambda + \rho^{\mathrm{H}}\frac{\partial\psi^{\mathrm{H}}}{\partial n^{\mathrm{H}}},\\ \lambda_{\mathrm{BM}}^{\mathrm{L}} &= \lambda + \rho^{\mathrm{L}}\frac{\partial\psi^{\mathrm{L}}}{\partial n^{\mathrm{L}}} + \rho^{\mathrm{G}}\frac{\partial\psi^{\mathrm{G}}}{\partial n^{\mathrm{L}}},\\ \lambda_{\mathrm{BM}}^{\mathrm{G}} &= \lambda + (\rho^{\mathrm{GR}})^2\frac{\partial\psi^{\mathrm{G}}}{\partial\rho^{\mathrm{GR}}} + \frac{\rho^{\mathrm{L}}\rho^{\mathrm{G}}}{(n^{\mathrm{G}})^2}\frac{\partial\psi^{\mathrm{L}}}{\partial\rho^{\mathrm{GR}}},\end{aligned} \tag{108}$$

as well as the expression for the Lagrange multiplier connected with the saturation condition:

$$\lambda = \lambda_{\mathrm{BM}}^{\mathrm{G}} - \rho^{\mathrm{L}}\frac{\partial\psi^{\mathrm{G}}}{\partial n^{\mathrm{G}}} - \rho^{\mathrm{L}}\frac{\partial\psi^{\mathrm{L}}}{\partial n^{\mathrm{G}}}, \tag{109}$$

the constitutive relations for the Cauchy stress tensors are then given by:

$$\begin{aligned}&\mathbf{T}^{\mathrm{SH}} = -n^{\mathrm{SH}}\lambda\mathbf{I} + \mathbf{T}_{\mathrm{e}}^{\mathrm{SH}}, \quad \mathbf{T}^{\mathrm{L}} = -n^{\mathrm{L}}\lambda\mathbf{I} + \mathbf{T}_{\mathrm{e}}^{\mathrm{L}},\\ &\mathbf{T}^{\mathrm{G}} = -n^{\mathrm{G}}\lambda\mathbf{I} + \mathbf{T}_{\mathrm{e}}^{\mathrm{G}}.\end{aligned} \tag{110}$$

The effective stress tensors are:

$$\begin{aligned}\mathbf{T}_{\mathrm{e}}^{\mathrm{SH}} &= 2\rho^{\mathrm{S}}\mathbf{F}_{\mathrm{S}}\frac{\partial\psi^{\mathrm{S}}}{\partial\mathbf{C}_{\mathrm{S}}}\mathbf{F}_{\mathrm{S}}^{\mathrm{T}} + 2\rho^{\mathrm{H}}\mathbf{F}_{\mathrm{H}}\frac{\partial\psi^{\mathrm{H}}}{\partial\hat{\mathbf{C}}_{\mathrm{H}}}\mathbf{F}_{\mathrm{H}}^{\mathrm{T}} - n^{\mathrm{H}}\rho^{\mathrm{H}}\frac{\partial\psi^{\mathrm{H}}}{\partial n^{\mathrm{H}}}\mathbf{I},\\ \mathbf{T}_{\mathrm{e}}^{\mathrm{L}} &= -n^{\mathrm{L}}\rho^{\mathrm{L}}\frac{\partial\psi^{\mathrm{L}}}{\partial n^{\mathrm{L}}}\mathbf{I} - n^{\mathrm{L}}\rho^{\mathrm{G}}\frac{\partial\psi^{\mathrm{G}}}{\partial n^{\mathrm{L}}}\mathbf{I} + \rho^{\mathrm{L}}\mathrm{J}_{\mathrm{L}}\frac{\partial\psi^{\mathrm{L}}}{\partial\mathrm{J}^{\mathrm{L}}}\mathbf{I},\\ \mathbf{T}_{\mathrm{e}}^{\mathrm{G}} &= -n^{\mathrm{G}}(\rho^{\mathrm{GR}})^2\frac{\partial\psi^{\mathrm{G}}}{\partial\rho^{\mathrm{GR}}}\mathbf{I} - n^{\mathrm{G}}\frac{\rho^{\mathrm{L}}\rho^{\mathrm{G}}}{(n^{\mathrm{G}})^2}\frac{\partial\psi^{\mathrm{L}}}{\partial\rho^{\mathrm{GR}}}\mathbf{I}.\end{aligned} \tag{111}$$

Evaluation of the entropy inequality also leads to dissipative terms. These dissipation terms are used to obtain the evolution equations for the direct production terms of mass for the healed material and for the catalysts:

$$\hat{\rho}^{\,\mathrm{H}} = -\beta^{\mathrm{H}}\left(\Psi^{\mathrm{H}} - \Psi^{\mathrm{L}}\right), \quad \hat{\rho}^{\,\mathrm{C}} = -\beta^{\mathrm{C}}\left(\psi^{\mathrm{C}} + \frac{1}{2}\mathbf{x}_{\mathrm{S}}^{'}\cdot\mathbf{x}_{\mathrm{S}}^{'}\right). \tag{112}$$

The total production terms of momentum for the liquid and gas phases are given by:

$$\begin{aligned}\hat{\mathbf{p}}^{\,\mathrm{L}} &= \left(\lambda + \rho^{\mathrm{G}}\frac{\partial \psi^{\mathrm{G}}}{\partial n^{\mathrm{L}}}\right)\mathrm{grad}\, n^{\mathrm{L}} - \rho^{\mathrm{L}}\frac{\partial \psi^{\mathrm{L}}}{\partial n^{\mathrm{G}}}\mathrm{grad}\, n^{\mathrm{G}} \\ &\quad -\rho^{\mathrm{L}}\frac{\partial \psi^{\mathrm{L}}}{\partial \rho^{\mathrm{GR}}}\mathrm{grad}\,\rho^{\mathrm{GR}} + \hat{\mathbf{p}}_{\,\mathrm{e}}^{\,\mathrm{L}}, \\ \hat{\mathbf{p}}^{\,\mathrm{G}} &= \left(\lambda + \rho^{\mathrm{L}}\frac{\partial \psi^{\mathrm{L}}}{\partial n^{\mathrm{G}}}\right)\mathrm{grad}\, n^{\mathrm{G}} - \rho^{\mathrm{G}}\frac{\partial \psi^{\mathrm{G}}}{\partial n^{\mathrm{L}}}\mathrm{grad}\, n^{\mathrm{L}} \\ &\quad +\rho^{\mathrm{L}}\frac{\partial \psi^{\mathrm{L}}}{\partial \rho^{\mathrm{GR}}}\mathrm{grad}\,\rho^{\mathrm{GR}} + \hat{\mathbf{p}}_{\,\mathrm{e}}^{\,\mathrm{G}}.\end{aligned} \tag{113}$$

In Eq. (112) the chemical potentials are given by:

$$\Psi^{\mathrm{H}} = \psi^{\mathrm{H}} + \frac{1}{2}\mathbf{x}_{\mathrm{S}}^{'}\cdot\mathbf{x}_{\mathrm{S}}^{'} - \frac{\lambda_{\mathrm{BM}}^{\mathrm{H}}}{\rho^{\mathrm{HR}}}, \quad \Psi^{\mathrm{L}} = \psi^{\mathrm{L}} + \frac{1}{2}\mathbf{x}_{\mathrm{L}}^{'}\cdot\mathbf{x}_{\mathrm{L}}^{'} - \frac{\lambda_{\mathrm{BM}}^{\mathrm{L}}}{\rho^{\mathrm{LR}}}. \tag{114}$$

In Eq. (113) the effective production terms of momentum of the liquid and gas phase are denoted by:

$$\hat{\mathbf{p}}_{\,\mathrm{e}}^{\,\mathrm{L}} = -\gamma_{\mathbf{w}_{\mathrm{LS}}}^{\mathrm{L}}\mathbf{w}_{\mathrm{LS}} - \gamma_{\mathbf{w}_{\mathrm{GS}}}^{\mathrm{L}}\mathbf{w}_{\mathrm{GS}}, \quad \hat{\mathbf{p}}_{\,\mathrm{e}}^{\,\mathrm{G}} = -\gamma_{\mathbf{w}_{\mathrm{GS}}}^{\mathrm{G}}\mathbf{w}_{\mathrm{GS}} - \gamma_{\mathbf{w}_{\mathrm{LS}}}^{\mathrm{G}}\mathbf{w}_{\mathrm{LS}}. \tag{115}$$

The occurring material parameters are restricted by:

$$\beta^{\mathrm{H}} \geq 0, \quad \beta^{\mathrm{C}} \geq 0, \quad \gamma_{\mathbf{w}_{\mathrm{LS}}}^{\mathrm{L}} \geq 0, \quad \gamma_{\mathbf{w}_{\mathrm{GS}}}^{\mathrm{G}} \geq 0, \quad \gamma_{\mathbf{w}_{\mathrm{GS}}}^{\mathrm{L}} + \gamma_{\mathbf{w}_{\mathrm{LS}}}^{\mathrm{G}} = 0. \tag{116}$$

Furthermore, the inequalities:

$$f^{\mathrm{S}}\left(d^{\mathrm{S}}\right)_{\mathrm{S}}^{'} \geq 0, \quad f^{\mathrm{S}} = -\frac{\partial \psi^{\mathrm{S}}}{\partial d^{\mathrm{S}}} \tag{117}$$

and

$$f^{\mathrm{H}}\left(d^{\mathrm{H}}\right)_{\mathrm{S}}^{'} \geq 0, \quad f^{\mathrm{H}} = -\frac{\partial \psi^{\mathrm{H}}}{\partial d^{\mathrm{H}}} \tag{118}$$

in Eq. (106) have to be fulfilled. For the derivation of the evolution equations of the damage parameters and their restrictions, please refer to Sect. 2.4.

2.5.3 Constitutive Relations

To describe the mechanical behavior of the solid and healed phases, a material model of neo-Hookean type in combination with the ansatz of Simo and Pister [41]

is used (cf. [42]). The Helmholtz free energy functions for the solid and healed material are then given by:

$$\begin{aligned}\psi^{\mathrm{S}} &= \frac{1}{\rho_{0\mathrm{S}}^{\mathrm{SR}}}\left(1-d^{\mathrm{S}}\right)\left[\frac{1}{2}\lambda^{\mathrm{S}}(\log \mathrm{J_S})^2-\mu^{\mathrm{S}}\log \mathrm{J_S}+\frac{1}{2}\mu^{\mathrm{S}}(\mathrm{tr}\ \mathbf{C}_{\mathrm{S}}-3)\right],\\ \psi^{\mathrm{H}} &= \frac{1}{\rho_{0\mathrm{H}}^{\mathrm{HR}}}\varepsilon^{\mathrm{H}}\left(1-d^{\mathrm{H}}\right)\left[\frac{1}{2}\lambda^{\mathrm{H}}(\log \mathrm{J_H})^2-\mu^{\mathrm{H}}\log \mathrm{J_H}+\frac{1}{2}\mu^{\mathrm{H}}\left(\mathrm{tr}\ \widetilde{\mathbf{C}}_{\mathrm{H}}-3\right)\right],\end{aligned} \tag{119}$$

where μ^{S}, μ^{H}, λ^{S}, and λ^{H} are the Lamé constants of the corresponding phases. The variables $\rho_{0\mathrm{S}}^{\mathrm{SR}}$ and $\rho_{0\mathrm{H}}^{\mathrm{HR}}$ describe the real initial densities of the solid and healed material, and ε^{H} is a parameter to fit the healing behavior. The tensors $\mathbf{C}_{\mathrm{S}}=\mathbf{F}_{\mathrm{S}}^{\mathrm{T}}\mathbf{F}_{\mathrm{S}}$ and $\widetilde{\mathbf{C}}_{\mathrm{H}}=\mathbf{F}_{\mathrm{H}}^{\mathrm{T}}\mathbf{F}_{\mathrm{H}}$ are the right Cauchy–Green strain tensors of the solid and healed material, respectively. The $(1-d)$ terms are used to incorporate discontinuous damage behavior (introduced in Sect. 2.4) for the solid as well as for the healed material independently.

To describe the mechanical behavior of the liquid and gas phases, as well as of the catalysts, the following free energies are postulated:

$$\begin{aligned}\psi^{\mathrm{L}} &= \frac{1}{\rho_{0\mathrm{L}}^{\mathrm{LR}}}\Bigg\{k_{\mathrm{h}}^{\mathrm{L}}\Bigg[-\mathrm{dilog}\frac{1}{s^{\mathrm{L}}}-\log\left(\frac{s_0^{\mathrm{L}}}{s^{\mathrm{L}}}-\mathrm{s}_0^{\mathrm{L}}\right)\log\frac{1}{s^{\mathrm{L}}}+\log\left(1-s_0^{\mathrm{L}}\right)\log\frac{s_0^{\mathrm{L}}}{s^{\mathrm{L}}}\\ &\qquad +\mathrm{dilog}\frac{1}{s_0^{\mathrm{L}}}+\log\left(1-s_0^{\mathrm{L}}\right)\log\frac{1}{s_0^{\mathrm{L}}}\Bigg]\Bigg\},\\ \psi^{\mathrm{G}} &= -\Theta R^{\mathrm{G}}\rho_{0\mathrm{G}}^{\mathrm{GR}}\rho^{\mathrm{GR}}\left(\log\frac{\rho_{0\mathrm{G}}^{\mathrm{GR}}}{\rho^{\mathrm{GR}}}-\frac{\rho_{0\mathrm{G}}^{\mathrm{GR}}}{\rho^{\mathrm{GR}}}+1\right)+p_0^{\mathrm{GR}}\rho^{\mathrm{GR}},\\ \psi^{\mathrm{C}} &= \frac{1}{\rho_{0\mathrm{C}}^{\mathrm{CR}}}\left[\frac{1}{2}k^{\mathrm{C}}\log\frac{1}{c^{\mathrm{C}}}-p_0^{\mathrm{CR}}\log\frac{1}{c^{\mathrm{C}}}\right],\end{aligned} \tag{120}$$

where the dependency of ψ^{L} on $\mathrm{J_L}$ has not been taken into consideration. Here, $s^{\mathrm{L}}=n^{\mathrm{L}}/(n^{\mathrm{L}}+n^{\mathrm{G}})$ represents the liquid saturation, which is defined as the fraction of liquid in the whole hollow space, and the variable s_0^{L} denotes the initial liquid saturation. The dilog function belongs to the polylogarithmic functions and is defined as the integral of a special logarithmic function ($\mathrm{dilog}(x)=\int_1^x\frac{\ln(t)}{1-t}\mathrm{d}t$), which is used to retain the logarithmic behavior of its first derivative. The factor $k_{\mathrm{h}}^{\mathrm{L}}$ is a material parameter and $\rho_{0\mathrm{L}}^{\mathrm{LR}}$ is the initial real liquid density. The Helmholtz free energy function ψ^{G} yields a gas pressure behavior described by the nonlinear gas law. Herein, Θ is the absolute temperature, R^{G} denotes the specific gas constant, $\rho_{0\mathrm{G}}^{\mathrm{GR}}$ and ρ^{GR} are the initial real gas density and the actual real gas density, respectively, and p_0^{GR} is the initial real gas pressure. In Eq. $(120)_3$, k^{C} is a material parameter, $c^{\mathrm{C}}\in[0,1]$ is the local mass concentration of catalysts, and p_0^{CR} is the initial pressure acting on the catalysts.

Considering $(111)_1$ and the insertion of the proposed free energies, (119) leads to:

$$\begin{aligned}\mathbf{T}_{\mathrm{e}}^{\mathrm{SH}} &= 2\rho^{\mathrm{S}}\mathbf{F}_{\mathrm{S}}\frac{\partial\psi^{\mathrm{S}}}{\partial\mathbf{C}_{\mathrm{S}}}\mathbf{F}_{\mathrm{S}}^{\mathrm{T}} + 2\rho^{\mathrm{H}}\mathbf{F}_{\mathrm{H}}\frac{\partial\psi^{\mathrm{H}}}{\partial\hat{\mathbf{C}}_{\mathrm{H}}}\mathbf{F}_{\mathrm{H}}^{\mathrm{T}} \\ &= \frac{1}{\mathrm{J}_{\mathrm{S}}}\left(1-d^{\mathrm{S}}\right)\left\{2\mu^{\mathrm{S}}\mathbf{K}_{\mathrm{S}} + \lambda^{\mathrm{S}}(\log\mathrm{J}_{\mathrm{S}})\mathbf{I}\right. \\ &\left. + n^{\mathrm{H}}\mathrm{J}_{\mathrm{S}}\varepsilon^{\mathrm{H}}\left(1-d^{\mathrm{H}}\right)\left[2\mu^{\mathrm{H}}\mathbf{K}_{\mathrm{H}} + \lambda^{\mathrm{H}}(\log\mathrm{J}_{\mathrm{H}})\mathbf{I}\right]\right\}\end{aligned} \tag{121}$$

for the effective stress tensor of the solid and healed material.

$$\mathbf{K}_{\mathrm{S}} = \frac{1}{2}(\mathbf{B}_{\mathrm{S}} - \mathbf{I}), \quad \mathbf{K}_{\mathrm{H}} = \frac{1}{2}(\mathbf{B}_{\mathrm{H}} - \mathbf{I}) \tag{122}$$

denote the Karni–Reiner strain tensors referred to the actual configuration, with the left Cauchy–Green deformation tensors:

$$\mathbf{B}_{\mathrm{S}} = \mathbf{F}_{\mathrm{S}}\mathbf{F}_{\mathrm{S}}^{\mathrm{T}}, \quad \mathbf{B}_{\mathrm{H}} = \mathbf{F}_{\mathrm{H}}\mathbf{F}_{\mathrm{H}}^{\mathrm{T}}. \tag{123}$$

For calculation of the total stresses of the solid and healed material, the Lagrange multiplier λ is needed, which is achieved by the derivation of the stresses for the liquid and gas phases as follows: The stresses of liquid and gas are hydrostatic, which is a result of the evaluation of the entropy inequality. Therefore, it can be postulated that the stresses depend proportionally on the macroscopic realistic pressures of the corresponding phases, such that:

$$\mathbf{T}^{\mathrm{L}} = -n^{\mathrm{L}}p^{\mathrm{LR}}\mathbf{I}, \quad \mathbf{T}^{\mathrm{G}} = -n^{\mathrm{G}}p^{\mathrm{GR}}\mathbf{I}. \tag{124}$$

The insertion of (109), $(110)_{2,3}$, and $(111)_{2,3}$ into Eq. (124) and solving this equation with respect to the realistic pressures yields:

$$\begin{aligned}p^{\mathrm{GR}} &= (\rho^{\mathrm{GR}})^2\frac{\partial\psi^{\mathrm{G}}}{\partial\rho^{\mathrm{GR}}} + \frac{\rho^{\mathrm{L}}\rho^{\mathrm{G}}}{(n^{\mathrm{G}})^2}\frac{\partial\psi^{\mathrm{L}}}{\partial\rho^{\mathrm{GR}}}, \\ p^{\mathrm{LR}} &= p^{\mathrm{GR}} + \widetilde{p}_{\mathrm{e}}^{\mathrm{L}}\end{aligned} \tag{125}$$

with the effective liquid pressure:

$$\begin{aligned}\widetilde{p}_{\mathrm{e}}^{\mathrm{L}} &= \rho^{\mathrm{L}}\frac{\partial\psi^{\mathrm{L}}}{\partial n^{\mathrm{L}}} - \rho^{\mathrm{L}}\frac{\partial\psi^{\mathrm{L}}}{\partial n^{\mathrm{G}}} - \frac{1}{n^{\mathrm{L}}}\rho^{\mathrm{L}}\mathrm{J}_{\mathrm{L}}\frac{\partial\psi^{\mathrm{L}}}{\partial\mathrm{J}_{\mathrm{L}}} + \rho^{\mathrm{G}}\frac{\partial\psi^{\mathrm{G}}}{\partial n^{\mathrm{L}}} - \rho^{\mathrm{G}}\frac{\partial\psi^{\mathrm{G}}}{\partial n^{\mathrm{G}}} \\ &= \rho^{\mathrm{L}}\frac{\partial\psi^{\mathrm{L}}}{\partial n^{\mathrm{L}}} - \rho^{\mathrm{L}}\frac{\partial\psi^{\mathrm{L}}}{\partial n^{\mathrm{G}}} - \rho^{\mathrm{LR}}\mathrm{J}_{\mathrm{L}}\frac{\partial\psi^{\mathrm{L}}}{\partial\mathrm{J}_{\mathrm{L}}} + \rho^{\mathrm{G}}\frac{\partial\psi^{\mathrm{G}}}{\partial n^{\mathrm{L}}} - \rho^{\mathrm{G}}\frac{\partial\psi^{\mathrm{G}}}{\partial n^{\mathrm{G}}}.\end{aligned} \tag{126}$$

Considering now the Helmholtz free energy functions $(120)_{1,2}$, the following partial derivatives are equal to zero:

$$\frac{\partial \psi^{\mathrm{G}}}{\partial n^{\mathrm{L}}} = 0, \quad \frac{\partial \psi^{\mathrm{G}}}{\partial n^{\mathrm{G}}} = 0, \quad \frac{\partial \psi^{\mathrm{L}}}{\partial \rho^{\mathrm{GR}}} = 0, \quad \frac{\partial \psi^{\mathrm{L}}}{\partial \mathrm{J_L}} = 0. \tag{127}$$

Furthermore, the realistic gas pressure $(125)_1$ now reads:

$$\begin{aligned} p^{\mathrm{GR}} &= (\rho^{\mathrm{GR}})^2 \frac{\partial \psi^{\mathrm{G}}}{\partial \rho^{\mathrm{GR}}} + \frac{\rho^{\mathrm{L}} \rho^{\mathrm{G}}}{(n^{\mathrm{G}})^2} \frac{\partial \psi^{\mathrm{L}}}{\partial \rho^{\mathrm{GR}}}, \\ &= \Theta R^{\mathrm{G}} \rho_{0\mathrm{G}}^{\mathrm{GR}} \log\left(\frac{\rho_{0\mathrm{G}}^{\mathrm{GR}}}{\rho^{\mathrm{GR}}}\right) + p_0^{GR} \end{aligned} \tag{128}$$

and the effective part of the liquid pressure (126) is given by:

$$\begin{aligned} \widetilde{p}_{\mathrm{e}}^{\mathrm{L}} &= \rho^{\mathrm{L}} \frac{\partial \psi^{\mathrm{L}}}{\partial n^{\mathrm{L}}} - \rho^{\mathrm{L}} \frac{\partial \psi^{\mathrm{L}}}{\partial n^{\mathrm{G}}} - \rho^{\mathrm{LR}} \mathrm{J_L} \frac{\partial \psi^{\mathrm{L}}}{\partial \mathrm{J_L}} + \rho^{\mathrm{G}} \frac{\partial \psi^{\mathrm{G}}}{\partial n^{\mathrm{L}}} - \rho^{\mathrm{G}} \frac{\partial \psi^{\mathrm{G}}}{\partial n^{\mathrm{G}}} \\ &= k_{\mathrm{h}}^{\mathrm{L}} s^{\mathrm{L}} \frac{n^{\mathrm{G}}}{n^{\mathrm{L}}} \left[\log\left(\frac{s_0^{\mathrm{L}}}{s^{\mathrm{L}}} - s_0^{\mathrm{L}}\right) - \log\left(1 - s_0^{\mathrm{L}}\right) \right] \\ &\quad + k_{\mathrm{h}}^{\mathrm{L}} s^{\mathrm{L}} \left[\log\left(\frac{s_0^{\mathrm{L}}}{s^{\mathrm{L}}} - s_0^{\mathrm{L}}\right) - \log\left(1 - s_0^{\mathrm{L}}\right) \right]. \end{aligned} \tag{129}$$

Thus, the realistic liquid pressure $(125)_2$ and the Lagrange multiplier (109) are as follows:

$$\begin{aligned} p^{\mathrm{LR}} &= p^{\mathrm{GR}} + \widetilde{p}_{\mathrm{e}}^{\mathrm{L}} \\ &= \Theta R^{\mathrm{G}} \rho_{0\mathrm{G}}^{\mathrm{GR}} \log\left(\frac{\rho_{0\mathrm{G}}^{\mathrm{GR}}}{\rho^{\mathrm{GR}}}\right) + k_{\mathrm{h}}^{\mathrm{L}} s^{\mathrm{L}} \frac{n^{\mathrm{G}}}{n^{\mathrm{L}}} \left[\log\left(\frac{s_0^{\mathrm{L}}}{s^{\mathrm{L}}} - s_0^{\mathrm{L}}\right) - \log\left(1 - s_0^{\mathrm{L}}\right) \right] \\ &\quad + k_{\mathrm{h}}^{\mathrm{L}} s^{\mathrm{L}} \left[\log\left(\frac{s_0^{\mathrm{L}}}{s^{\mathrm{L}}} - s_0^{\mathrm{L}}\right) - \log\left(1 - s_0^{\mathrm{L}}\right) \right] \end{aligned} \tag{130}$$

and

$$\begin{aligned} \lambda &= p^{\mathrm{GR}} - \rho^{\mathrm{G}} \frac{\partial \psi^{\mathrm{G}}}{\partial n^{\mathrm{G}}} - \rho^{\mathrm{L}} \frac{\partial \psi^{\mathrm{L}}}{\partial n^{\mathrm{G}}} \\ &= p^{\mathrm{GR}} - k_{\mathrm{h}}^{\mathrm{L}} s^{\mathrm{L}} \left[\log\left(\frac{s_0^{\mathrm{L}}}{s^{\mathrm{L}}} - s_0^{\mathrm{L}}\right) - \log\left(1 - s_0^{\mathrm{L}}\right) \right] \\ &= p^{\mathrm{GR}} - p^{\mathrm{h}}. \end{aligned} \tag{131}$$

Table 1 Parameters of the healing-pressure-liquid-saturation relation

Parameter	Plot 1	Plot 2	Plot 3	Plot 4
k_h^{L} [N/m^2]	0.75	1.5	1.25	1.0
s_0^{L}	0.99	0.99	0.99	0.99

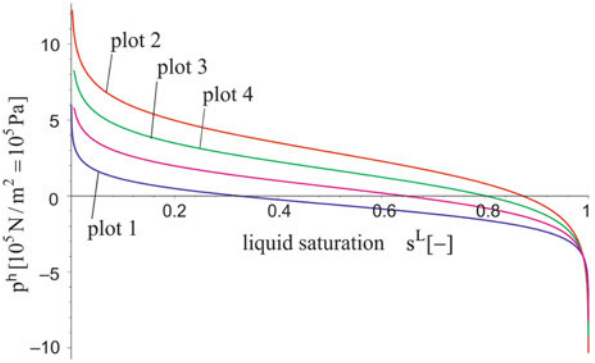

Fig. 6 Diagram of the healing-pressure-liquid-saturation with different parameters. The parameters for *plots 1–4* are given in Table 1

The pressure p^{h} is referred to here as healing pressure and denotes a driving force introduced to describe the internal pressure of the fluid-like healing agents in such a way that they flow into the damaged zones. The healing pressure is postulated as:

$$p^{\mathrm{h}} = k_{\mathrm{h}}^{\mathrm{L}} s^{\mathrm{L}} \left[\log\left(\frac{s_0^{\mathrm{L}}}{s^{\mathrm{L}}} - s_0^{\mathrm{L}} \right) - \log\left(1 - s_0^{\mathrm{L}}\right) \right], \tag{132}$$

which is aligned to the capillary pressure presented in [43]. A graphical representation of the healing-pressure-liquid-saturation relations with different parameters (cf. Table 1) can be seen in Fig. 6.

Considering Eq. (127), the direct production terms of momentum (113) for the liquid and gas phase simplify to:

$$\begin{aligned} \hat{\mathbf{p}}^{\,\mathrm{L}} &= \lambda \operatorname{grad} n^{\mathrm{L}} - p^{\mathrm{h}} \operatorname{grad} n^{\mathrm{G}} + \hat{\mathbf{p}}_{\mathrm{e}}^{\,\mathrm{L}}, \\ \hat{\mathbf{p}}^{\,\mathrm{G}} &= \left(\lambda + p^{\mathrm{h}}\right) \operatorname{grad} n^{\mathrm{G}} + \hat{\mathbf{p}}_{\mathrm{e}}^{\,\mathrm{G}}. \end{aligned} \tag{133}$$

In Sect. 2.5, one assumption was that $\hat{\rho}^{\,\mathrm{H}} = -\hat{\rho}^{\,\mathrm{L}} - \hat{\rho}^{\,\mathrm{C}}$, but because the volume fractions of the catalysts are neglected, the influence of $\hat{\rho}^{\,\mathrm{C}}$ on this relation can also be neglected. To describe the phase transition between the liquid-like healing agents and the solid-like healed material, the total production of mass for the healing phase has to be defined. Therefore, Eq. (112) is substituted by a production function, taken from [44], which is modified such that it depends on the local concentration of catalysts. The mass production function is given by:

$$\hat{\rho}^{\,\mathrm{H}} = \hat{\rho}_m^{\,\mathrm{H}} \left(\frac{c^{\mathrm{C}} - c_0^{\mathrm{C}}}{\overline{c}^{\mathrm{C}}} \right)^2 \exp\left[1 - \left(\frac{c^{\mathrm{C}} - c_0^{\mathrm{C}}}{\overline{c}^{\mathrm{C}}} \right)^2 \right]. \tag{134}$$

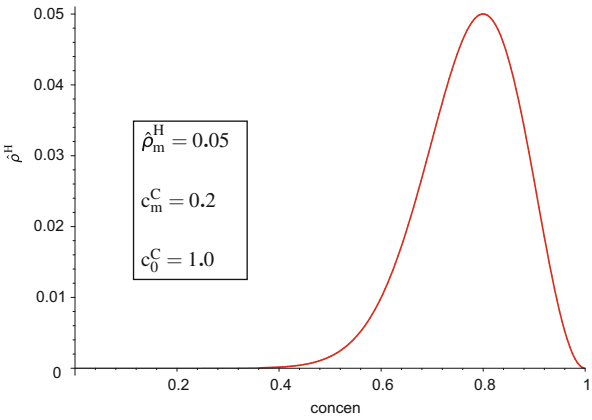

Fig. 7 Plot of the production function for a given set of parameters

Therein, $\hat{\rho}_{m}^{H}$ is the maximum value of the total production term $\hat{\rho}^{H}$ and c_0^C is the maximum value of the concentration. The value $\overline{c}^{C}$ denotes the change in concentration where $\hat{\rho}^{H}$ is maximal. A graphical interpretation of the production function for a given set of parameters is depicted in Fig. 7.

Because the concentration of catalysts decreases in the areas where healing occurs, the total production term of mass for the catalysts $\hat{\rho}^{C}$ is negative and set as constant ($\hat{\rho}^{C} = -0.001$).

3 Numerical Examples

Two different numerical examples are presented in this section. The first is a macroscopic example of a self-healing tapered double cantilever beam (TDCB). Here, the main ability of the developed model is shown in order to simulate the global damage and healing behavior of the considered specimen. Furthermore, the influences of the healing time and of the amount of liquid healing agents with respect to the healing efficiency are shown. The second example acts on the microscale and is an academic example. Here, the ability of the model to simulate the flow of healing agents from the capsule into the damaged area is presented.

3.1 Tapered Double Cantilever Beam

For the numerical example given in this section, the damage and healing behavior of an epoxy matrix material with encapsulated healing agents are demonstrated and compared with real experimental results taken from Brown et al. [10]. The real specimen consists of an EPON828 epoxy matrix material with dispersed Grubbs'

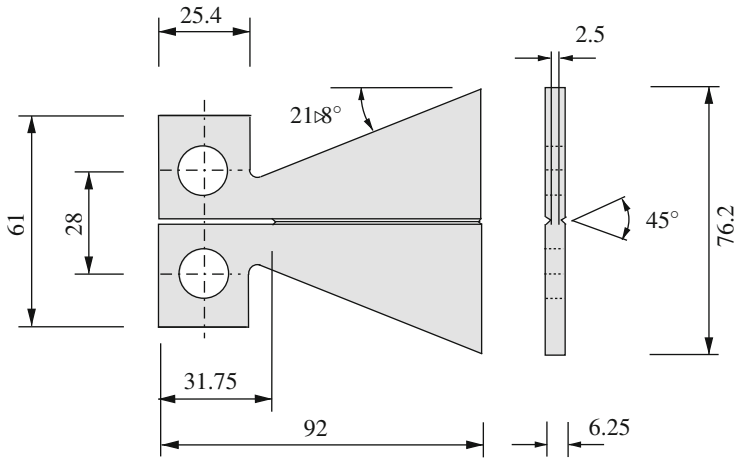

Fig. 8 Geometry of the tapered double cantilever beam (TDCB) [9]; dimensions in millimeters

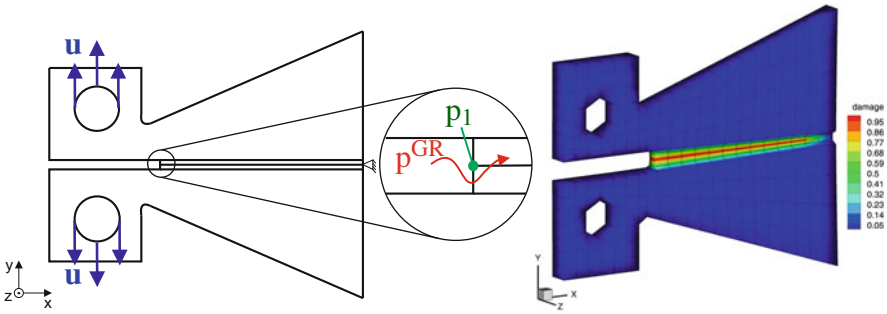

Fig. 9 *Left*: Applied boundary conditions. *Right*: Virtual damaged specimen

catalysts (2.5 wt%) and microencapsulated healing agents (5.0 wt%). Dicyclopentadiene (DCPD) is used as healing agent and the capsules are made of urea formaldehyde. The considered geometry of the TDCB specimen is shown in Fig. 8 and ensures measurement of fracture toughness independently of the crack length [9].

The numerical three-dimensional simulation is carried out within a finite element framework using the FE program FEAP [45]. The virtual model is meshed with 252 linear brick elements. The time step width during the loading and unloading is $\Delta t = 0.1$ s and $\Delta t = 10$ s during the healing period. The applied boundary conditions are depicted in Fig. 9 and the applied loading curve can be seen in Fig. 10.

The displacements of the upper half of the upper hole, as well as of the lower half of the lower hole are fixed in the x- and z-directions. A displacement of 0.6 mm is applied in the y-direction. Additionally, the middle nodes of the right edge are fixed for the displacements in y- and z-directions to retain symmetry during deformation.

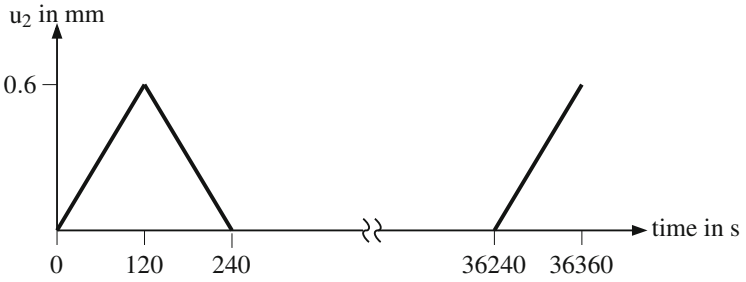

Fig. 10 The loading–unloading cycle

Table 2 Initial parameters for the different constituents

Parameter	Solid	Healed material	Liquid healing agents	Gas	Catalysts
Material parameters					
Young's modulus E^{α} [Pa]	3.0e + 9 [46]	3.4e + 9 [47]	–	–	–
Poisson's ratio ν^{α}	0.3	0.3	–	–	–
Real density $\rho_{0\alpha}^{\alpha R}$ [kg/m^3]	1.2e + 3	1.03e + 3	0.98e + 3	1.2	–
Darcy parameter $k_{\text{Darcy}}^{\alpha}$ [m^4/(N s)]	–	–	9.0e-9	5.0e-2	–
Healing pressure parameters					
Limit of saturation s_0^{L}	–	–	0.9	–	–
Saturation-dependent compression modulus k_h^{L} [Pa]	–	–	5.0	–	–
Initial values					
Initial volume fraction n^{α}	0.79	0.0	0.2	0.01	–
Initial mass concentration c_0^{C} [kg/m^3]	–	–	–	–	1.0

Furthermore, the boundaries at the end of the notch are open for the gas phase (i.e., air can flow in and out during the testing procedure). Table 2 lists the initial material parameters.

Following the experimental procedure described by Brown et al. [10], the specimen is first loaded until it is completely ruptured. After that, the crack faces are brought into contact to enable the healing agents to close the crack and heal the damage. After 10 h of rest time, the specimen is reloaded until it is ruptured for a second time. The specific geometry of the TDCB ensures that the second damage event takes place in the healed area. It should be mentioned that a second healing period in the already healed area is not possible because the local microcapsules are broken and the healing agents are already polymerized.

As in the real experiment, the virtual specimen is loaded, which results after some time in a complete rupture of the TDCB (i.e., the measured load on the flanks

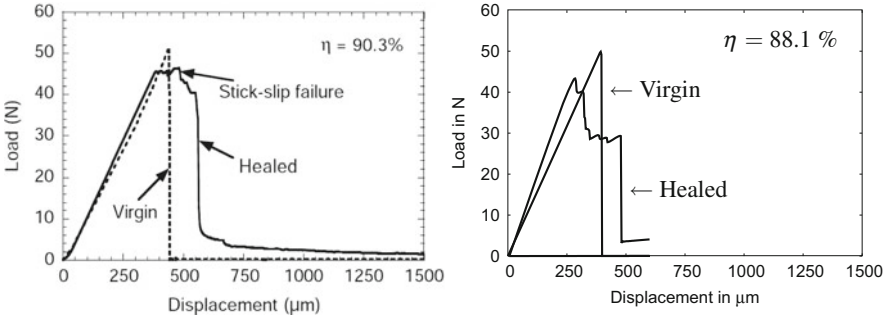

Fig. 11 Results of the real and virtual experiments. *Left*: Experimental results [10] with kind permission from Springer Science + Business Media (*left*). *Right*: Results of our virtual experiment

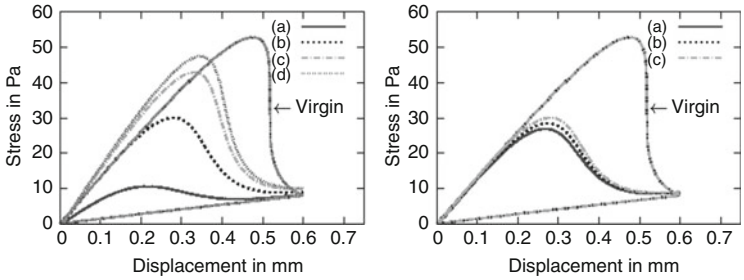

Fig. 12 *Left*: Influence of different healing times: (*a*) 14,400 s, (*b*) 25,200 s, (*c*) 32,400 s, (*d*) 36,000 s. *Right*: Influence of liquid volume fraction n^{L} for a healing time of 25,200 s: (*a*) 0.1, (*b*) 0.15, (*c*) 0.2

is equal to zero). The crack is not really modeled, but where damage takes place the stiffness of the elements is reduced according to the amount of damage. After that, the specimen is unloaded and returns to the initial placement, as in the experiment (contact of crack faces). Subsequently, the healing process starts and the specimen is allowed to heal for 10 h. During the healing time, a phase transition from liquid-like healing agents to solid-like healed material occurs. In the area where the solid matrix material is damaged and cannot bear any stress, the new solid material replaces it, leading to partial recovery of the structural integrity. After the healing time, the specimen is loaded for a second time and damage of the healed material can also be observed. As can be seen in Fig. 11, the results of both the real experiment and the numerical simulation are qualitatively in good agreement, especially with respect to the healing efficiency.

Figure 12 shows the influence of healing time and the amount of liquid healing agent. Here, the stress of one particular node at the end of the notch (see Fig. 9, point p_1) is measured over the applied displacement on the flank. As can be observed, both variables have an influence on the healing efficiency. Regarding

the healing time, the increase in amount of healed material is described by the total mass production term $\hat{\rho}^{\mathrm{H}}$, which leads to a time-dependent behavior of the healing process. The influence of the volume fraction of healing agents can be explained by the available amount of material that can polymerize in the damaged area. If the volume fraction decreases, the amount of solid-like healed material after the healing process is lower and the healing efficiency decreases.

3.2 Microstructure

In this academic example, the ability of the model to simulate the flow of healing agents from the capsule into the crack is demonstrated. The specimen under investigation is a representative volume element with an initial notch and a single inclusion, which represents the microcapsule. It has an edge length of 10×10 mm and the capsule has a diameter of 1.4 mm. The meshed geometry is depicted in Fig. 13. A displacement of 0.03 mm is applied on the upper and lower edges of the specimen, and at the end of the notch the boundary is open for the gas phase. Because the microstructure is resolved, the volume fractions of the constituents are completely different to those at the macroscopic scale. Here, the model is build with two materials: the matrix and the liquid inclusion (the capsule shell is neglected in this simplified example). The matrix material consists of 80% solid ($n^{\mathrm{S}} = 0.8$), 10% liquid healing agents ($n^{\mathrm{L}} = 0.1$), and 10% gas ($n^{\mathrm{G}} = 0.1$). The volume fractions of

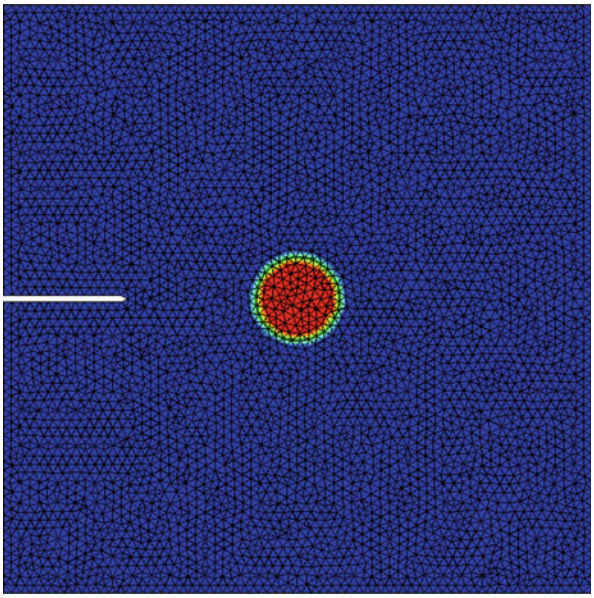

Fig. 13 Meshed microstructure with 9,395 triangular elements

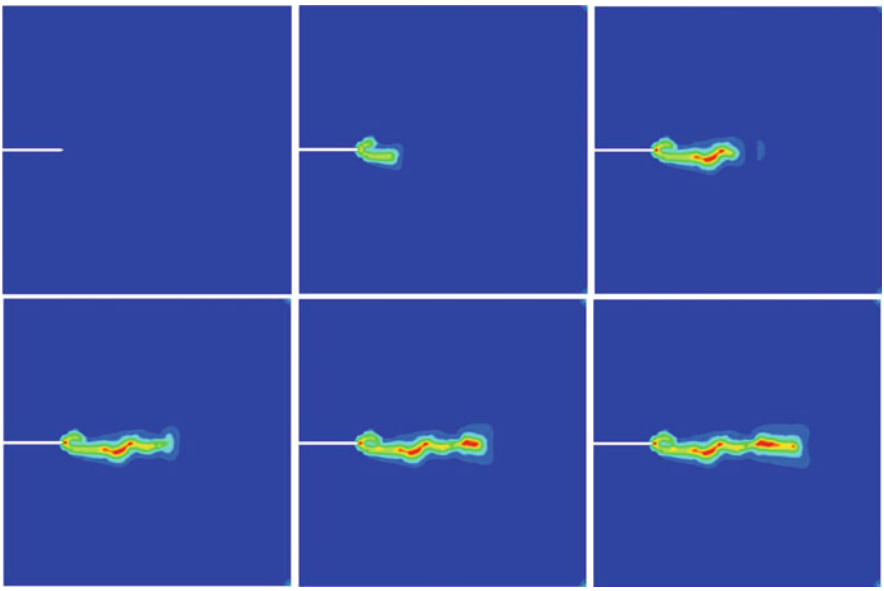

Fig. 14 Evolution of damage in the microstructure (*upper left* to *lower right*)

the inclusion are given by $n^{\mathrm{L}} = 0.8$ for the liquid, $n^{\mathrm{S}} = 0.1$ for the solid, and $n^{\mathrm{G}} = 0.1$ for the gas. The catalysts are neglected because healing is not considered here.

Figure 14 shows evolution of the damage. Because the Young's modulus of the inclusion is set to be three times lower than that of the solid, the crack propagates through the capsule. Thus, the liquid healing agents can flow into the crack (as shown in Fig. 15). Here, no change in the volume fraction inside the capsule can be observed, because small deformations are applied on the microstructure and, hence, only a very small amount of liquid can flow into the damaged area. It has also to be mentioned that the liquid flow is very slow. It is driven by the healing pressure and the permeability, which in this example is dependent on the damage variable. If the damage increases, the permeability also increases. The velocity of the liquid in this example is between 10^{-8} and 10^{-4} m/s, depending on the amount of damage.

In Fig. 16, the change in the volume fractions of liquid and gas are depicted for two points in the damaged region (see lower right picture in Fig. 15). The graphs can be interpreted as follows: the capsule ruptures, which leads to very quick initial change in the volume fractions. After that, a linear increase in the amount of liquid can be observed. The linear behavior is a result of small deformations in this example. If liquid flows into the damaged region, the gas is pushed out. The difference between the increase in the liquid volume fraction and the decrease in the gas volume fraction can be explained by the compressibility of the gas phase.

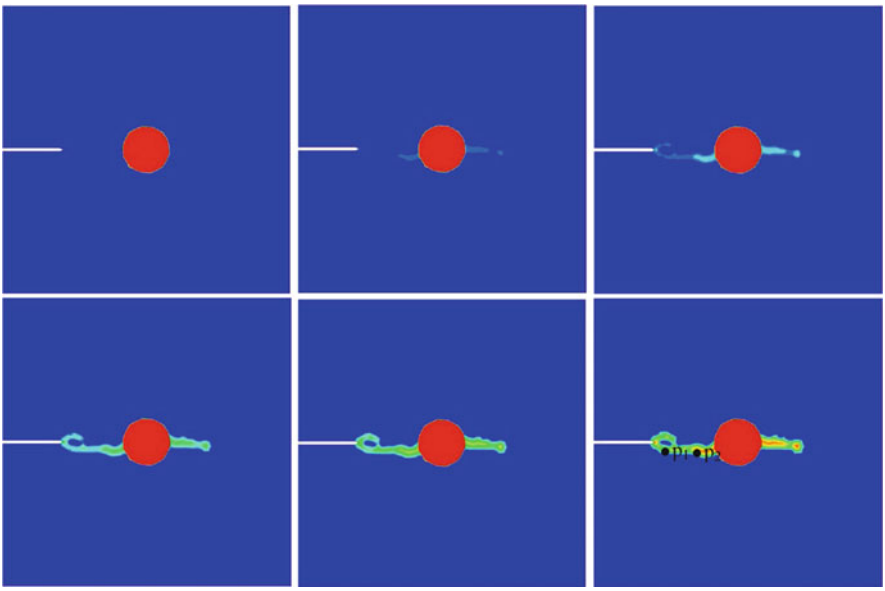

Fig. 15 Outflow of liquid healing agents from capsule into crack; increase of liquid volume fraction in the damaged area (*upper left* to *lower right*)

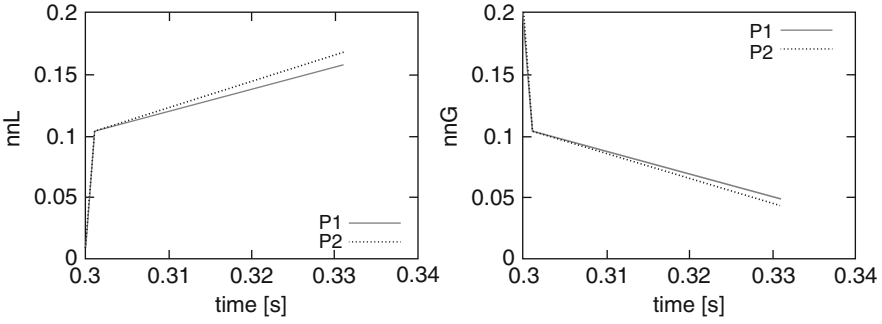

Fig. 16 Change in the volume fractions of the liquid phase (*left*) and gas phase (*right*) measured at points p_1 and p_2 (see *lower right* picture of Fig. 15)

4 Conclusion

This work numerically investigates the damage and healing behavior of a polymeric self-healing material consisting of an epoxy matrix with microencapsulated DCPD healing agents and dispersed Grubbs' catalysts. The considered multiphase material (solid matrix material with dispersed catalysts, fluid healing agents, healed material, and air) was modeled within the framework of the theory of porous media. To show the global damage and healing behavior, the geometry of the specimen was a

tapered double cantilever beam. To demonstrate the advantages of the used theoretical framework, the flow behavior of the healing agents was shown by means of an example acting at the microscale. To consider the damage effects of both the solid matrix material and the healed material, a discontinuous damage model was incorporated, using two independent damage variables (for the two different phases). The numerical results of the macroscopic example are compared with real experimental results to show the applicability of the developed model for simulation of the damage and healing behavior of self-healing materials. The simulation was in qualitatively good agreement with the experiment. Furthermore, the influence of the healing time and the volume fraction of liquid-like healing agents on the healing efficiency were demonstrated. In the microscopic example, it was shown that the flow of healing agents from the capsule into the damaged area can be simulated. Further investigations should take into account the healing process and reloading of the specimen. Furthermore, larger representative volume elements should be considered in order to investigate the behavior of liquid healing agents under larger deformations, such that more liquid flows out of the capsule.

Acknowledgement This work was supported by the German Research Society (DFG) within the Priority Program SPP 1568 "Design and Generic Principles of Self-healing Materials" under the grant number BL 417/7-2.

References

1. van der Zwaag S (2007) Self healing materials: an alternative approach to 20 centuries of materials science. Springer, Dordrecht
2. Blaiszik BJ, Kramer SLB, Olugebefola SC, Moore JS, Sottos NR, White SR (2010) Self-healing polymers and composites. Annu Rev Mater Res 40:179–211
3. van der Zwaag S (2010) Routes and mechanisms towards self healing behaviour in engineering materials. Bull Polish Acad Sci 58:227–236
4. Gosh SK (2009) Self-healing materials: fundamentals, design strategies, and applications. In: Gosh SK (ed) Self-healing materials. Wiley-VCH, Weinheim, pp 1–28
5. Hager MD, Greil P, Leyens C, van der Zwaag S, Schubert US (2010) Self-healing materials. Adv Mater 22:5424–5430
6. Yuan YC, Yin T, Rong MZ, Zhang MQ (2008) Self healing in polymers and polymer composites. concept, realization and outlook: a review. Express Polym Lett 2:238–250
7. Grigoleit S (2010) Überblick über Selbstheilende Materialien. Technical report, Frauenhofer-Institut für Naturwissenschaftlich-Technische Trendanalysen (INT)
8. White SR, Sottos NR, Geubelle PH, Moore JS, Kessler MR, Sriram SR, Brown EN, Viswanathan S (2001) Autonomic healing of polymer composites. Nature 409:794–797
9. Beres W, Koul AK, Thamburaj R (1997) A tapered double-cantilever-beam specimen designed for constant-K testing at elevated temperatures. J Test Eval 25:536–542
10. Brown EN, Sottos NR, White SR (2002) Fracture testing of a self-healing polymer composite. Exp Mech 42:372–379
11. Brown EN (2011) Use of the tapered double-cantilever beam geometry for fracture toughness measurements and its applictaion to the quantification of self-healing. J Strain Anal Eng Des 46:167–186

12. Caruso MM, Blaiszik BJ, White SR, Sottos NR, Moore JS (2008) Full recovery of fracture toughness using a nontoxic solvent based self-healing systems. Adv Funct Mater 18:1898–1904
13. Guadagno L, Raimondo M, Naddeo C, Longo P, Mariconda A, Binder WH (2014) Healing efficiency and dynamic mechanical properties of self-healing epoxy systems. Smart Mater Struct 23:045001
14. Raimondo M, Guadagno L (2013) Healing efficiency of epoxy-based materials for structural applications. Polym Compos 34:1525–1532
15. Barbero EJ, Ford KJ (2007) Characterization of self-healing fiber-reinforced polymer-matrix composite with distributed damage. J Adv Mater 39:20–27
16. Mergheim J, Steinmann P (2013) Phenomenological modelling of self-healing polymers based on integrated healing agents. Comput Mech. doi:10.1007/s00466-013-0840-0
17. Schimmel EC, Remmers JJC (2006) Development of a constitutive model for self-healing materials. Technical report, Delft Aerospace Computational Science
18. Voyiadjis GZ, Shojaei A, Li G, Kattan PI (2012) A theory of anisotropic healing and damage mechanics of materials. Proc R Soc Lond A 468:163–183
19. Voyiadjis GZ, Shojaei A, Li G (2011) A thermodynamic consistent damage and healing model for self healing materials. Int J Plast 27:1025–1044
20. Henson GM (2012) Continuum modeling of synthetic microvascular materials. In: Proceedings of the 53rd AIAA structures, dynamics and materials conference, Honolulu, Hawaii. doi: 10.2514/6.2012-2001
21. Maiti S, Shankar C, Geubelle PH, Kieffer J (2006) Continuum and molecular-level modeling of fatigue crack retardation in self-healing polymers. J Eng Mater Technol 128:595–602
22. Sanada K, Itaya N, Shindo Y (2008) Self-healing of interfacial debonding in fiber-reinforced polymers and effect of microstructure on strength recovery. Open Mech Eng J 2:97–103
23. Zemskov SV, Jonkers HM, Vermolen FJ (2011) Two analytical models for the probability characteristics of a crack hitting encapsulated particles: application to self-healing materials. Comput Mater Sci 50:3323–3333
24. Yagimli B, Lion A (2011) Experimental investigations and material modelling of curing processes under small deformations. Z Angew Math Mech 91:342–359
25. de Boer R (2000) Theory of porous media. Springer, Berlin
26. Bluhm J (2002) Modelling of saturated thermo-elastic porous solids with different phase temperatures. In: Ehlers W, Bluhm J (eds) Porous media. Springer, Berlin, pp 87–118
27. de Boer R, Ehlers W (1986) Theorie der Mehrkomponentenkontinua mit Anwendung auf bodenmechanische Probleme. Technical report, Universität - Gesamthochschule Essen
28. Ehlers W (1996) Grundlegende Konzepte in der Theorie Poröser Medien. Tech Mech 16:63–76
29. Ehlers W (2002) Foundations of multiphasic and porous materials. In: Ehlers W, Bluhm J (eds) Porous media. Springer, Berlin, pp 3–86
30. Ehlers W (2012) Poröse Medien - ein kontinuummechanisches Modell auf der Basis der Mischungstheorie. Nachdruck der Habilitationsschrift aus dem Jahr 1989, Universität - Gesamthochschule Essen
31. Acartürk AY (2009) Simulation of charged hydrated porous materials. PhD thesis, Universität Stuttgart
32. Truesdell C (1984) Rational thermodynamics, 2nd edn. Springer, New York
33. Bowen RM (1980) Incompressible porous media models by use of the theory of mixtures. Int J Eng Sci 18:1129–1148
34. Bowen RM (1982) Compressible porous media models by use of the theory of mixtures. Int J Eng Sci 20:697–735
35. Kachanov LM (1958) Time of the rupture process under creep conditions. Izvestija Akademii Nauk Sojuza Sovetskich Socialisticeskich Republiki (SSSR) Otdelenie Techniceskich Nauk (Moskra) 8:26–31

36. Ateshian GA, Ricken T (2010) Multigenerational interstitial growth of biological tissues. Biomech Model Mechanobiol 9:689–702
37. Humphrey J, Rajagopal K (2002) A constrained mixture model for growth and remodelling of soft tissues. Math Models Methods Appl Sci 12:407–430
38. Rodriguez E, Hoger A, McCulloch A (1994) Stress-dependent finite growth in soft elastic tissues. J Biomech 27:455–467
39. Bluhm J, Specht S, Schröder J (2014) Modeling of self-healing effects in polymeric composites. Arch Appl Mech 85:1469–1481. doi:10.1007/s00419-014-0946-7
40. Ehlers W (1989) On the thermodynamics of elasto-plastic porous media. Arch Mech 41:73–93
41. Simo JC, Pister KS (1984) Remarks on rate constitutive equations for finite deformation problems: computational implications. Comput Methods Appl Mech Eng 46:201–215
42. Miehe C (1988) Zur numerischen behandlung thermomechanischer Prozesse. PhD thesis, Universität Hannover
43. Bluhm J, Ricken T, Bloßfeld M (2011) Ice formation in porous media. In: Markert B (ed) Advances in extended & multifield theories for continua, vol 59, Lecture notes in applied and computational mechanics. Springer, Berlin, pp 153–174
44. Michalowski RL, Zhu M (2006) Frost heave modelling using porosity rate function. Int J Numer Anal Methods Geomech 30:703–722
45. Taylor RL (2008) FEAP – a finite element analysis program, Version 8.2. Department of Civil and Environmental Engineering, University of California at Berkeley, Berkeley, CA
46. Blaiszik BJ, Sottos NR, White SR (2008) Nanocapsules for self healing materials. Compos Sci Technol 68:978–986
47. Alzari V, Nuvoli D, Sanna D, Ruiu A, Mariani A (2015) Effect of limonene on the frontal ring opening metathesis polymerization of dicyclopentadiene. J Polym Sci A Polym Chem. doi:10.1002/pola.27776

Adv Polym Sci (2016) 273: 185–218
DOI: 10.1007/12_2015_339

Published online: 25 February 2016

Self-Healing Corrosion-Protective Sol–Gel Coatings Based on Extrinsic and Intrinsic Healing Approaches

M. AbdolahZadeh, S. van der Zwaag, and S.J. Garcia

Abstract Sol–gel pretreatments and coatings are an important class of passive coatings primarily used to increase adhesion of subsequent layers to metallic substrates herby improving the protection against corrosion. Sol–gel chemistry has been broadly used as an appropriate method for versatile implementation of extrinsic self-healing in coatings. Nevertheless, it is only recently that such a chemical approach to the development of intrinsic healing coatings has been proposed. In this review, we analyse existing literature describing the introduction of extrinsic and intrinsic self-healing routes into sol–gel coatings. The development of active sol–gel coatings capable of recovering their protective functionality is based on the broad chemical diversity of precursors and the low processing temperatures required for this type of chemistry.

Keywords Coatings • Corrosion inhibitors • Dual network • Healable • Hybrid sol–gel • Self-healing

Contents

M. AbdolahZadeh, S. van der Zwaag, and S.J. Garcia (✉)
Novel Aerospace Materials Group, Department of Aerospace Materials and Manufacturing, Delft University of Technology, Kluyverweg 1, 2629 HS Delft, The Netherlands
e-mail: s.j.garciaespallargas@tudelft.nl

1 Introduction

Synthetic coatings are of great scientific and technological importance [1]. Coatings can be defined as thin planar solid structures that are chemically attached to a thicker underlying substrate. They provide a certain functionality, such as colour, gloss, roughness, light reflectance, electrical or thermal conductivity/isolation or hydrophobicity/hydrophilicity to the ensemble as a whole and mechanical (e.g. wear and scratch resistance) and chemical (corrosion) protection to the substrate in particular [2].

Corrosion is one of the main processes leading to material destruction and economic loss, estimated at about 3% of the global GNP. Although corrosion processes are unavoidable, the cost related to premature product degradation and failure can be significantly reduced using appropriate protection methods such as protective coatings. Protective coatings minimize or control corrosion of the underlying substrate through one or a combination of three main mechanisms: (1) barrier protection, whereby the coating prevents or reduces ingress of corrosive agents to the metal–coating interface; (2) cathodic protection, whereby the coating acts as a sacrificial anode; and (3) active protection as a result of inclusion of inhibitors that offer anodic or/and cathodic protection of the underlying substrate [3–8].

Various coating technologies, including solvent and waterborne liquid paints, cataphoretic paints and powder coatings, have been around for a relatively long time. Apart from these well-established technologies, sol–gel coatings have recently attracted considerable interest because of their attractive features, such as low processing temperature, high chemical versatility, ease of application, strong bonding to a wide range of metallic substrates and an environmentally friendly mode of deposition. Originally used for the production of glass-like structures such as particles, the sol–gel process is now a well-established method for preparation of organic–inorganic hybrid (OIH) films and coatings with a broad application spectrum.

Generally, the sol–gel process can be described as the evolution of an oxide network by continuous condensation reactions of molecular precursors in a liquid medium via hydrolytic or non-hydrolytic procedures [9, 10]. The non-hydrolytic approaches are based on the formation of a colloidal suspension followed by its gelation through condensation of precursor molecules via alkyl halide elimination, ether elimination, ester elimination etc., depending on the precursor and solvent molecules [11–13]. The more common hydrolytic approaches are mainly based on the hydrolysis and condensation reactions of metal or metalloid alkoxides, $M(OR)_n$, in which M and R represent a network-forming element and an alkyl or allyl group, respectively. Although the range of precursor molecules is extremely wide, silicone alkoxides are the most studied because of their stability and moderate reaction rates, which facilitate controlled hydrolysis and condensation reactions [11, 14, 15].

Hydrolysis and condensation are equilibrium reactions and can proceed simultaneously once the hydrolysis reaction is initiated. The structure and properties of the final film or coating depend on the sequence of these steps, which themselves

are strongly affected by the precursor molecules and reaction conditions (e.g. pH, molar ratio of reactants, solvent, temperature). Prepared sol–gel systems can be applied on metallic substrates using different techniques such as dip-coating, spin-coating, spray-coating and electrodeposition, followed by a drying or curing step [9–11, 14, 15].

The potential application of sol–gel coatings as protection against corrosion was first reviewed by Guglielmi in 1997 [16]. Since then, numerous papers have been published, revealing promising results regarding improvements in adhesion of organic coatings to substrates and in protection of various metallic substrates against corrosion.

Ideally, the coatings prevent corrosion of the underlying substrate during its entire intended service life. Yet, despite substantial advances in coating performance, even the best protective coatings can fail to fulfil their function because of damage resulting from (local or global) mechanical and chemical attacks as well as thermal cycles. Damage to coatings can occur at three different dimensional levels: macro- (e.g. scratches), micro- (e.g. formation of microcracks and crazing) and nanoscale (affecting the interfaces, networks and even molecular structure of the coating by dissociation or bond breakage) [2, 17].

Incorporation of self-healing functionality into protective coatings can guarantee longer service life and reduced maintenance costs by autonomous or non-autonomous healing of local damage at different scales. However, self-healing in coatings designed to protect against corrosion is slightly different from self-healing of bulk/structural polymers or decorative coatings. In the latter cases, healing is referred to as the restoration of mechanical or aesthetic properties by providing enough material to repair or fill the defect volume. However, for corrosion protection, the most crucial form of healing is the restoration of the lost barrier and chemical protective properties. Both extrinsic and intrinsic healing approaches can be applied to development of such protective coatings. The extrinsic approach involves incorporation of discrete active healing agents such as corrosion inhibitors and binders into the coating system to enable surface protection against damage. The intrinsic approach involves introduction of reversible chemistries that enable damage closure and sealing. Extrinsic and intrinsic self-healing coatings can be further subcategorized into several groups according to their architecture, healing mechanism and the size scale of healable damage [2, 18–26]. As depicted in Fig. 1, depending on the chosen strategy, the healing process (i.e. leakage of the active agents to the damage site or flow of the coating network) can be activated using different stimuli, which is addressed in following sections.

2 Passive Protection

Sol–gel coatings, in particular silane-based coatings, have been successfully applied as anti-corrosion pretreatments (thickness <1 μm) and coatings (thickness >5 μm) on a range of metallic substrates such as aluminium alloys, steel, copper,

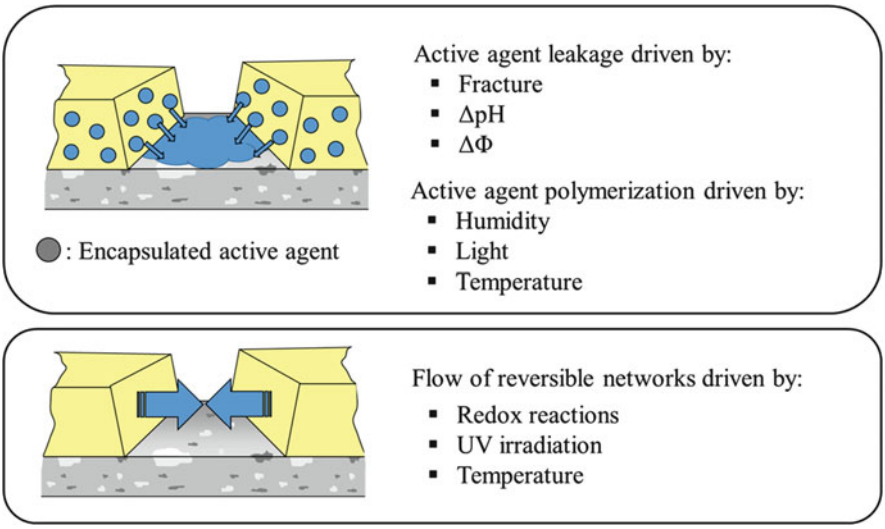

Fig. 1 Extrinsic (*top*) and intrinsic (*bottom*) healing approaches in corrosion-protective coatings

magnesium, titanium, galvanized and stainless steel and tin. However, efficient corrosion protection can only be achieved by (1) proper surface preparation of the substrate, leading to the formation of a high density of covalent bonds between the sol–gel coating and the metal surface and (2) a fine balance between the application conditions and the employed ingredients [27].

The final properties of sol–gel coatings depend on the starting materials and the processing conditions (e.g. pH and temperature) [11, 14, 28, 29]. Introduction of organic groups into inorganic sol–gel networks can facilitate preparation of thick and crack-free hybrid coatings, eliminating the drawbacks associated with conventional inorganic sol–gel coatings. In such OIH sol–gel coatings, the inorganic component of the coatings contributes to enhanced mechanical properties, whereas the organic component imparts increased flexibility and other desired functionalities such as hydrophobicity [8, 9, 30–32].

In spite of their high potential for corrosion protection, silanes are electrochemically inactive unless they carry electrochemically active functional groups. As a consequence, silane-based OIH sol–gel coatings do not provide active protection. The protection they offer is generally based on passive protection through formation of an adherent barrier layer. Depending on the nature of the precursor molecules, the OIH coatings can be hydrophobic. Hydrophobic OIH coatings can reduce the kinetics of the corrosion processes by delaying penetration of water and other electrolytes towards the metal–coating interface. However, prolonged exposure of the OIH coatings to water or electrolytes eventually results in moisture penetrating to the metal–coating interface. Considering the reversible nature of the hydrolysis and condensation reactions involved in creation of the coating, water penetration can promote hydrolysis of the bonds formed during the condensation reaction.

Unless the condensation reactions are promoted via a drying step, water or moisture ingress can result in coating failure and/or delamination [9, 22, 32, 33]. Modification of formulation parameters can lead to an improvement in general passive protective properties. The effect of different parameters such as the nature of organic components, ratio of organic to inorganic components, etc. are analysed in the following sections.

2.1 Critical Formulation Parameters

2.1.1 Organic–Inorganic Components

The OIH sol–gel coatings can be prepared over a wide compositional range. Based on the type of organic component to be added to the inorganic network and the interactions between organic and inorganic counterparts, the sol–gel OIH materials can be classified into five groups (types I–V, as shown in Fig. 2).

As Fig. 2 shows, the OIH sol–gel coatings can be prepared by addition of either organic oligomers/polymers (types I and II) or monomers (type III) to inorganic sols. In the absence of covalent bonds, the organic and inorganic counterparts of the OIHs are connected to each other through physical bonds (types I and III). Despite

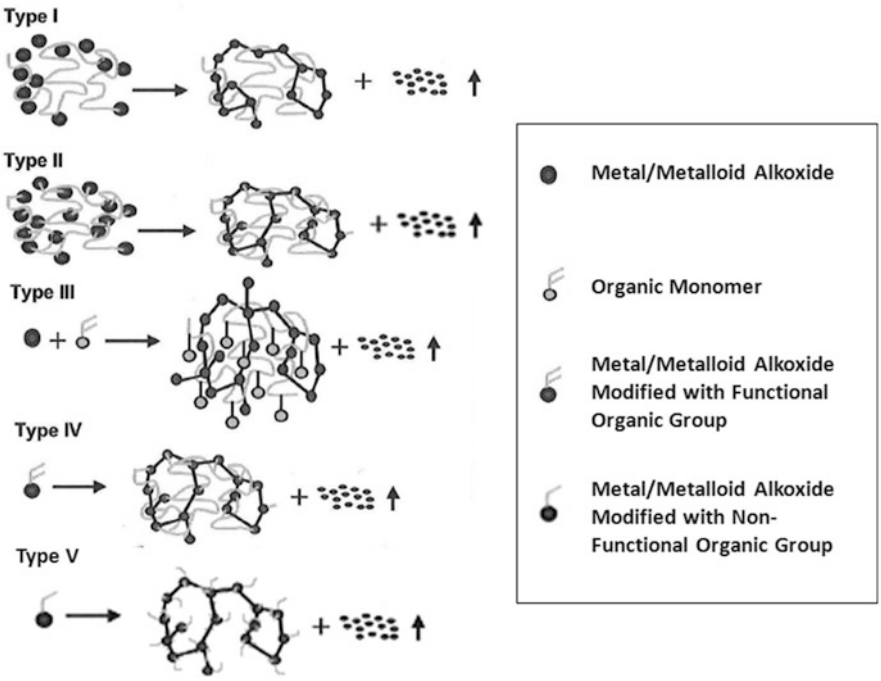

Fig. 2 Different classes (types *I–V*) of OIH materials [34]

the presence of weak dispersion forces and van der Waals interactions between organic and inorganic components of such OIHs, the physical bonds are not stable enough for long-term applications involving weathering. Formation of strong covalent bonds between organic and inorganic components can significantly improve the corrosion-protective properties of OIH coatings. This can be achieved by end-capping of oligomers or polymers with functional groups capable of reacting with the inorganic network (type II) or by application of organically modified metal/metalloid alkoxides with the general formula R'_x-$M(OR)_{n-x}$ as starting material (types IV and V). R′ can be either a non-functional group such as methyl or ethyl [8] (type V) or a functional group such as epoxy, vinyl, methacrylic, isocyanate, mercaptane or furan [8] (type IV), which can undergo further polymerization. The OIH sol–gel coatings containing functional groups outperform pure sol–gel or polymeric coatings as a result of higher crosslink density and better mechanical properties [9, 22, 30, 35].

Different functional groups impart different corrosion-protective properties to OIH coatings [35]. (3-Glycidoxyproyl)trimethoxysilane (GPTMS) has attracted considerably more interest than other organically modified precursors. It has been used in the formulation of about 70% and 30% of the OIH sol–gel coatings applied on aluminium alloys and steel substrates, respectively [8]. Yet, the corrosion-protective properties of GPTMS-derived OIH coatings dramatically depend on the absence or presence of curing/crosslinking agents. Addition of primary aliphatic amines as crosslinking agents into the formulation for a GPTMS-based OIH coating resulted in well-adherent coatings with a significantly reduced curing time [36], although the properties of the resulting coatings varied according on the number of reactive groups of the adopted crosslinker [37]. A schematic representation of the generic steps involved in the preparation of such OIHs is presented in Fig. 3 [38]. Croes et al. [39] used three different isomers of phenylenediamine (PDA) to show the superior corrosion-protective properties of a GPTMS-based OIH coating that had been crosslinked using aromatic amines rather than aliphatic amines. This could be attributed to oxidative polymerization of PDA crosslinking agents to form electro-active oligomers and polymers of PDA that were similar to polyaniline in structure.

GPTMS-based OIH coatings crosslinked using mono-, di- and tri-amino-alkoxy silanes outperformed those cured using conventional crosslinkers because amino silanes have the ability to react with epoxy hybrid coatings through both amino and alkoxy functionalities [40]. However, OIH coatings solely crosslinked using amino silanes are prone to brittle fracture. This challenge can be overcome by mixing amino silanes with organic crosslinkers in an optimum ratio [41] or by addition of flexible organic groups such as urethane moieties to the OIH coating formulation [42].

The corrosion-protective properties of OIH coatings can be improved by implementation of hyperbranched crosslinking agents with several reactive sites (e.g. polyethylene imine (PEI) [43] and lignin [44]) independently of the nature of the employed organically modified silicone alkoxide (OMSA) precursors.

Both the nature of organic components and their content in the hybrid sol–gel play significant roles in the final properties of the hybrid system. Hybrid sol–gel

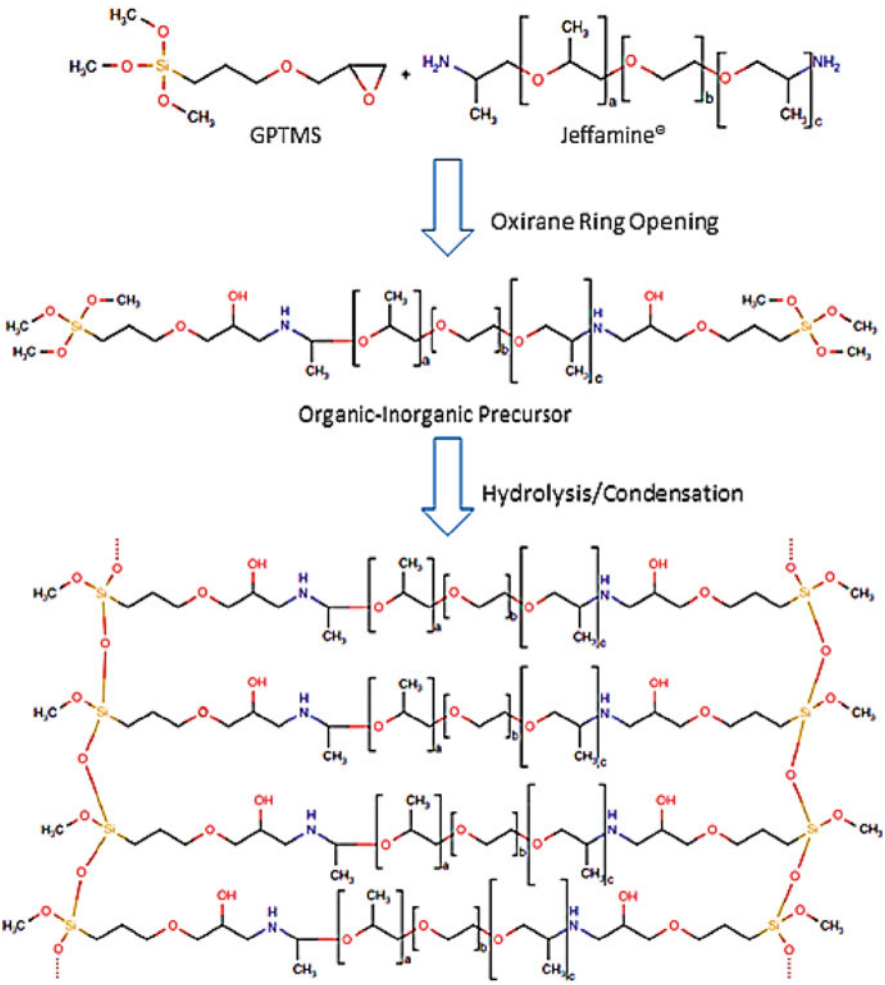

Fig. 3 Generic steps involved in preparation of GPTMS-derived OIH crosslinked (OIH type IV) coating using a conventional aliphatic amine (Jeffamine®) [38]

coatings can be prepared over a continuous compositional range, from almost organic to almost inorganic. An increase in organic content of the hybrid coatings leads to formation of less porous and thicker films, appropriate for barrier protection of metals. However, a high concentration of organic component can lower the adhesion and the mechanical properties of the final coating. In other words, although hybrid coatings potentially exhibit higher corrosion resistance than their inorganic or organic counterparts, there is an optimum inorganic to organic ratio (OOIR) that delivers maximum corrosion resistance. The OOIR varies according to the precursors employed and the coating application technique [32, 45–

54]. Moreover, the coating application method not only affects the OOIR but also the maximum achievable thickness of the hybrid sol–gel coatings [32, 33, 55, 56].

2.1.2 Curing Temperature

Drying or curing of sol–gel coatings is an important stage in the sol–gel process and dramatically affects the final properties of the coating. Measurement of linear shrinkage and weight loss of sol–gel-derived materials as a function of temperature provides valuable information on the effect of the curing treatment. A plot of these parameters versus temperature yields a curve with three distinct regions (Fig. 4, regions I–III) for high temperature curing of sol–gels [13]. Region I ($T < 200$ C) is associated with a sharp decrease in material weight as a result of solvent evaporation or desorption. Region II shows a linear shrinkage and weight loss at intermediate temperatures (200–500°C), which can be attributed to further condensation reactions and decomposition of organic components, respectively. Finally, region III shows the collapse of pores formed as a result of solvent evaporation, and loss of organic compounds leading to fast shrinkage. Therefore, an increase in the curing temperature to 500–700°C can result in lower corrosion resistance of the sol–gel coating unless the heating rate is small enough to avoid crack formation [9, 15].

Sol–gel coatings can also be cured at or near room temperature. Low temperature drying is normally employed for curing of hybrid sol–gel coatings entrapping organic compounds [9, 15]. Although compact crack-free films can be obtained, sol–gel coatings cured at room temperature exhibit higher water sensitivity than those cured at higher temperatures [57]. Higher cure temperatures (up to 200°C) promoting condensation reactions and formation of a dense OIH coating improve the barrier properties [52, 58–61]. Recently, a relatively new approach has been

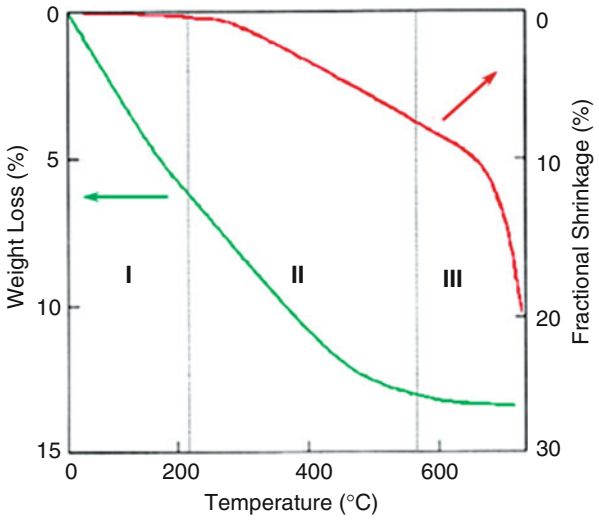

Fig. 4 Stages *I–III* of the curing process [34]

proposed for curing of sol–gel coatings using UV radiation, reporting a 2.5-fold increase in the corrosion resistance of sol–gel films treated by UV radiation at room temperature in comparison with conventional films dried at 300°C [9]. This new methodology for curing of sol–gel coatings further facilitates the implementation of this technology on temperature-sensitive substrates.

Aging of the prepared sol prior to application of the OIH on a metallic substrate has also been reported to strongly affect the corrosion-protective properties of the resulting coatings. Aging of the sol can promote condensation reactions of the precursors, increasing the viscosity of the sol and thus eventually leading to formation of a thick coating with high defect density [52, 62, 63]

2.1.3 Micro- and NanoParticles

In order to improve the mechanical and barrier properties of sol–gel coatings, micro- and nanoparticles can be added to the coating formulation, facilitating preparation of thick and defect-free coatings. The degree of improvement in physical and mechanical properties varies as function of the particle size and shape. However, the critical pigment volume concentration (CPVC), beyond which the physical and mechanical properties of the coating start to degrade, must always be taken into account. However, even for concentrations below the CPVC, a strong interaction between particle and matrix interfaces is required [22, 32]. Furthermore, the sol–gel process can be beneficially employed for modification of a particle surface with desired functional groups to enhance or impart the necessary chemical or physical interactions between particles and the coating matrix for good particulate composite formulations [64–71]. Micro- or nanoparticles can be added or can be formed in situ in the OIH coatings, eliminating some of the challenges associated with CPVC and the strong interfacial forces between matrix and particles.

3 Active Corrosion Protection

3.1 Extrinsic Self-Healing OIH Sol–Gel Coatings

Despite the effective barrier protection of metallic substrates by OIH sol–gel coatings, these systems are prone to mechanical and chemical damage as well as time-dependent water ingress. Incorporation of active species such as binding agents and corrosion inhibitors, which add active protection mechanisms to the system, can improve the protective properties of OIH sol–gel coatings. Controlled leakage of active species to the damaged sites can passivate the underlying substrate or seal it from the surrounding corrosive media through chemical or physical interactions that form thin and dense layers on the substrate. OIH sol–gel coatings

containing discrete active species can be classified as extrinsic self-healing coatings [2, 18, 22, 23, 25, 72, 73].

Bare or organically modified metal/metal oxides (i.e. precursors of the OIHs) can be employed in the preparation of robust micro- and nanocontainers such as polyurea/silica microcapsules [74], mesoporous silica [75, 76], zirconia [77] and titania nanoparticles [78] that entrap active species. Moreover, they can be utilized as humidity-sensitive [79, 80] and photosensitive [81] binding agents. The use of encapsulated binding agents based on OMSAs has already been explored in corrosion-protective organic coatings and it is only a matter of time before the concept is also implemented in OIH sol–gel coatings.

In contrast, the implementation of corrosion inhibitors in OIH sol–gel coatings has been studied extensively. Corrosion inhibitors can either be added directly to the coating formulation or immobilized in carriers to reduce possible interactions with the matrix and to control release of the inhibitor. Despite the advantages and disadvantages associated with both approaches, the second approach is the one that is leading to major developments, as addressed later in Sect. 3.1.2.

3.1.1 Direct Addition of Inhibitor

The most common way of including corrosion inhibitors into sol–gel systems is by mixing them with the coating formulation. The most important factor to be taken into account in such systems is the solubility of the inhibitor in the corrosive media. Low solubility of inhibitor can lead to a weak self-healing effect because of the low concentration of active agents at damaged site, whereas high solubility limits prolonged healing as a result of rapid leaching out of active agents from the coating. In addition, high solubility of the inhibitor can lead to coating degradation by blistering and delamination processes caused by increased osmotic pressure, which promotes water ingress into the coating–substrate interface. Despite the potential drawback of this class of extrinsic self-healing sol–gel coatings, they have been extensively studied for protection of different metallic substrates due to their ease of preparation. The corrosion inhibitors used can be divided according to their nature into inorganic and organic inhibitors.

1. Inorganic inhibitors
   Active ions with well-known corrosion inhibition ability such as rare earth metal (REM) ions (e.g. cerium and lanthanum) have attracted considerable interest as replacements for toxic Cr(VI)-based inhibitors. Although the inhibition mechanism of REM ions is not thoroughly understood, the processes by which REM and in particular Ce(III) and Ce(IV) ions protect the substrate are generally accepted [7, 82].

   The potential of Ce ions to impart healing functionality to corrosion-protective OIH sol–gel coatings for different metallic substrates such as aluminium alloys [63, 83–95], carbon steel [86, 96–98], stainless steel [99–102], magnesium [103] and galvanized steel [104–107] has been well documented

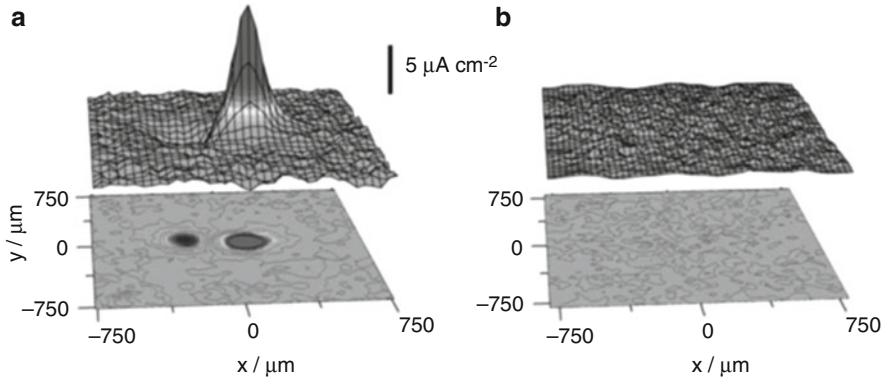

Fig. 5 Scanning vibrating electrode technique (SVET) maps over artificial defects of an OIH-coated AA2024 panel (**a**) before and (**b**) after addition of Ce(III) to 0.05 M NaCl corrosive media [108]

in the literature. Incorporation of the active Ce ions not only facilitates preparation of dense and defect-free OIH coatings [107], but also enables active protection via selective leaching of Ce ions to the damage site to (fully or partially) restore the protective properties of the coating (Fig. 5) [85, 108, 109].

In addition to the nature or type of precursor molecule [87, 92, 106] employed for synthesis of OIH sol–gel coatings and the concentration of aggressive ions (e.g. Cl^-) in the testing media, the (active) protective properties of Ce-doped OIH coatings can be significantly influenced by the salt used as the source of the Ce ions [e.g. $Ce(NO_3)_3$, $Ce(CH_3COO)_3$, $CeCl_3$ and $Ce_2(SO_4)_3$]. Earlier studies revealed that nitrate and acetate salts induce effective active corrosion protection into the OIH sol–gel coatings. However, chloride and sulfate salts can lower the corrosion resistance of the coatings as a result of release of aggressive ions (Cl^-) and reduced network stability [89, 91, 93].

Furthermore, the amount of Ce ions to be added into a sol–gel system is an important issue in modification of OIH sol–gel coatings using active species. Whereas a low concentration of active species can result in insufficient corrosion inhibition, a high concentration can promote formation of defects in OIH sol–gel coatings, lowering their barrier properties. According to several works, optimum protective properties are typically achieved by addition of 0.2–0.6 wt% active species to the OIH coating formulations, yielding a Ce ion concentration of 1×10^{-3} M in the test solution [86, 95, 102, 104, 105].

It should be noted that the inhibition mechanism of Ce ions varies according to the valence number. The different inhibition mechanisms of Ce(III) and Ce (IV) can lead to differences in their inhibition performance, as suggested by Pepe et al. [99]. In the aforementioned study, the OIH sol–gel coating loaded with Ce(IV) outperformed that loaded with Ce(III) ions as a result of plugging of the defective areas of the film by corrosion products. The insoluble corrosion products were probably produced through a chemical or electrochemical

mechanism involving a redox reaction between the substrate and Ce(IV) ions. Moreover, Ce(IV) ions can increase the crosslinking density of the OIH coatings by catalysing condensation reactions, ultimately improving the barrier properties of OIH sol–gel coatings [96, 98]

Inclusion of other REM and transition metal inhibitors such as La [106] and Zr [107] in the OIH coatings led to the improved electrochemical performance of such OIH coatings compared with unloaded coatings. However, upon prolonged immersion in aggressive electrolyte, they could not mitigate corrosion activity as effectively as the Ce-doped OIH coatings. Unlike Ce ions, VO_3^- and MoO_4^- anions had a detrimental effect on the protective properties of OIH sol–gel coatings because of a pronounced decrease in sol–gel network stability [83].

2. Organic Inhibitors

Organic inhibitors, which are usually designated as film-forming agents, mitigate corrosion by adsorption on the metal surface and formation of a hydrophobic layer. Organic inhibitors prevent corrosion by either increasing the anodic or cathodic polarization resistance of the corrosion cell or retarding diffusion of corrosive agents to the metallic surface. However, their inhibition efficiency depends on their chemical composition, molecular structure and affinity for the metal surface.

Organic inhibitors have been successfully incorporated into sol–gel systems to improve their ability to protect against corrosion by inducing active protection. In several cases, release of organic molecular species from the OIH sol–gel matrix is based on a pH-triggered release mechanism [110]. One of the advantageous features of pH-triggered desorption processes is that they can provide intelligent release of corrosion inhibitors only at damaged areas, which generally experience local pH changes originating from localized corrosion processes.

The beneficial effects of phosphonic acid on the corrosion-protective properties of OIH sol–gel coatings for Mg and Al alloys have been reported in a number of publications [55, 56, 111]. The increased corrosion resistance of such coatings can be explained by the remarkable improvement in adhesion resulting from a strong chemical interaction between the phosphonate groups and the substrate. Yet, the final active properties of such OIH coatings are dominated by the potential interactions between the inhibitor and the coating matrix (e.g. π–π interactions) as well as the general properties of the coating, such as hydrophobicity and crosslinking density [55, 56]. As mentioned before, using (hyperbranched) PEI rather than conventional crosslinking agents (e.g. DETA) results in OIH coatings with a higher crosslinking density. Additionally, PEI can undergo redox reactions in response to oxidative stress and thus act as a corrosion inhibitor, imparting an active protection mechanism (similar to polyaniline) to the coating [43, 112–114].

Inclusion of mercapto-based inhibitors such as 2-mercaptobenzothiazole (MBT), 2-mercaptobenzimidazole (MBI), benzotriazole (BTA) and tolyltriazole (TBTA) in the OIHs has been reported to improve their corrosion-protective properties. Non-ionizable inhibitors outperformed the ionizable inhibitors as a result of the strong interaction of the latter group with the sol–gel matrix, which

lowers the inhibitor release rate [114–118]. Addition of other organic inhibitors such as 8-HQ [117, 119], sodium benzoate [120] and chloranil [121] can also impart self-healing functionality to the OIH sol–gel coatings. However, in analogy to inorganic inhibitors, there is an optimum value for the amount of organic inhibitor to be added to the coating formulation.

3.1.2 Indirect Addition of Inhibitor

Although incorporation of corrosion inhibitors into sol–gel coatings is a promising route in the development of active corrosion-protective OIH coatings, there are inevitable drawbacks associated with direct mixing of active agents into coating formulations. First, it is quite difficult to control leach-out of entrapped inhibitors, especially when they are poorly soluble within the coating matrix. Second, inhibitors can chemically interact with the coating matrix, losing their own activity and lowering the barrier properties of the matrix. These drawbacks have motivated researchers to think of new ways of introducing inhibitor that enable isolation of active agents from coating components. This can be achieved either by encapsulation of active species or by complexing them with other chemicals.

1. Cyclodextrin–inhibitor complexes
   A simple approach for inhibitor entrapment or immobilization is based on the complexation of organic molecules with β-cyclodextrin. Cyclodextrins are cyclic oligosaccharides that possess a unique molecular cup-shaped structure with a hydrophilic exterior and a hydrophobic interior cavity. They are capable of forming complexes with various organic guest molecules, which fit within their cavities. Organic aromatic and heterocyclic compounds are normally the main candidates for the complexation reaction. MBT and MBI have been successfully loaded into β-cyclodextrin (Fig. 6). Although the complexation process delayed the immediate response to corrosion, a lower inhibitor release rate prolonged the self-healing potential of OIH coatings loaded with such complexes rather than with the inhibitors alone [115, 116, 122, 123].
2. Micro- and Nanocontainers
   Incorporation of ceramic particles such as silica [124–126], ceria [127–129] zirconia [127, 128], alumina [130], titania [130], zeolite [131], Na-montmorillonite [59, 132, 133] and hydrotalcite [134] as mechanical reinforcement was one of the first approaches proposed for modification of OIH sol–gel coatings. The improved mechanical properties, increased thickness and lower crack sensitivity achieved by addition of a controlled amount of particles resulted in enhanced corrosion protection of the underlying substrate. However, the particle size and surface modification proved to be crucial, because agglomeration of the embedded particles promoted by the gelation process could lead to coating rupture and deterioration of the barrier properties of the coating [124, 126–128, 131, 132, 134].

   The aforementioned ceramic particles are electrochemically inactive and therefore incapable of imparting self-healing properties to the OIH coatings.

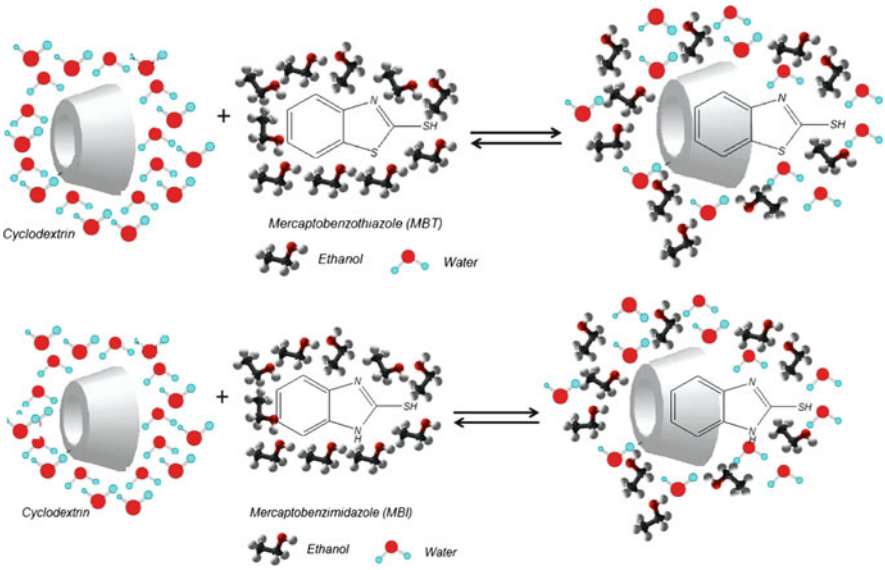

Fig. 6 Formation of α-CD/mercaptobenzimidazole (MBI) and α-CD/mercaptobenzothiazole (MBT) inclusion complexes [122]

However, they can also be employed as micro- or nanocontainers to immobilize corrosion inhibitors. Entrapment of Ce(III) ions on the surface of zirconia [72, 135] and boehmite [136] nanoparticles can be achieved through controlled hydrolysis of the relevant precursors in Ce-containing aqueous solution. The inhibiting ions can also be immobilized on the surface of commercially available particles via immersion of the particles in an inhibitor-containing solution. Activation of the nanoparticles with inhibitive species can not only bestow active anti-corrosion properties to the OIH coatings but also prevent particle agglomeration by stabilization of the particle surface charge [36, 137–140]. As in the case of cyclodextrin complexes, incorporation of the inhibitor-loaded particles into OIH coatings was more efficient than direct inhibitor loading in imparting long-term self-healing function.

Cationic active species such as Ce(III) and La(III) ions can also be entrapped within the layers or structural cages of montmorillonite clay and zeolite particles via a cation-exchange process [141–143]. The release of entrapped inhibitors from such containers is stimulated by corrosion activities involving pH changes and the presence of cationic species (M^{n+} and H^{+}). Selective leaching of the inhibitive ions to the damage site can reinforce the protective oxide layer, guaranteeing long-term protection for the metallic substrate.

In an effort to make environmentally friendly coatings that outperform those based on carcinogenic Cr(VI) addition, combinations of corrosion inhibitors have been explored following the promising results exhibited by hybrid organic–inorganic inhibitors [144]. Combination of Ce(III)- and La(III)-loaded zeolites

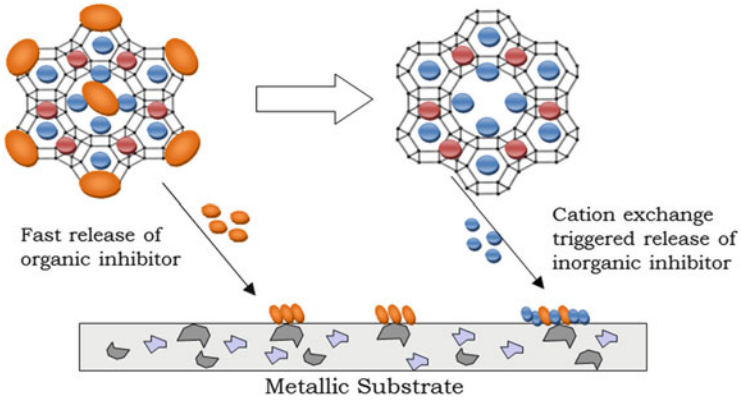

Fig. 7 Release and reaction of two corrosion inhibitors doped in a zeolite carrier acting on an idealized AA2024 metallic substrate [146]

in OIH coatings led to improved active protection as a result of synergy between the two inhibitors [145]. Successive loading of two different inhibitors, Ce(III) and DEDTC, in a single zeolite carrier has also been reported with very promising results hereby introducing a two-kinetic-release concept [146]. OIH coatings containing such carriers exhibited a noticeable improvement in active protection of AA2024 compared with zeolites loaded with single inhibitors (Fig. 7).

Mixed metal layered double hydroxides (LDHs), in particular Zn–Al LDHs, have been employed successfully for entrapment of anionic inhibitors such as vanadate, phosphate and MBT via anion-exchange [147–149]. In contrast to cation-exchange hosts, LHDs can not only release the inhibitor in response to an ion-exchange trigger, but also entrap aggressive anions such as chloride ions. A combination of LDH nanocontainers loaded with different inhibitors such as vanadate and phosphate anions, or vanadate and MBT, showed synergistic effects in suppressing corrosion of the underlying substrate in solutions containing Cl^- anions [150]. Zn–Al–Ce LDHs containing Ce(III) ions in the brucitic sheets were also prepared using a co-precipitation procedure. Depending on the concentrations of cerium salt, a two-phase mixture consisting of LDH and CeO_2 was obtained. Dispersion of the prepared nanoparticles in OIH coatings led to effective protection of the metallic substrate as a result of the synergistic inhibiting action by the dissolution of Zn–Al–Ce LDHs and CeO_2 nanoparticles [151].

Immobilization of the active Ce(III) ions in $CaCO_3$ microcarriers enabled a pH-sensitive release mechanism. Upon exposure to acidic environments the carriers dissolve and release the corrosion inhibitor, which can mitigate the corrosion activity of the bare metal [152]. Cerium has also been utilized in the preparation of MBT-loaded cerium-molybdate nanocapsules [139], imparting partial self-healing functionality to the protective coatings, as illustrated by an

increase in the charge transfer resistance of the coating system. Recently, amorphous cerium molybdate nanowires have been used as a source of Ce(III) and molybdate ions in OIH sol–gel coatings. Localized electrochemical measurements demonstrated the self-healing potential of the modified OIH by active suppression of corrosion activity in artificial defects [153].

Mesoporous silica nanoparticles with a high inhibitor loading capacity resulting from their high surface area and large pore volume [75] have been loaded successfully with benzotriazole-based inhibitors such as BTA and MBT. The OIH coatings containing inhibitor-loaded mesoporous nanoparticles outperformed both the undoped coatings and those directly loaded with the same corrosion inhibitor. The pH-triggered release mechanism is based on electrostatic repulsion between silica nanoparticles and inhibitor molecules; at pH values other than neutral, both the silica particles and the inhibitor molecules gain the same charge (positive at $pH < 6$ and negative at $pH > 6$). However, as pointed out earlier, the optimum barrier properties of sol–gel coatings are achieved at a certain dosage of embedded nanoparticles that compromises between delivering sufficient corrosion inhibitor and preserving the barrier properties of the coating [154]. To boost the release of inhibitors in acidic and alkaline media, the mesoporous silica nanoparticles can be modified using α-cyclodextrin (α-CD)/aniline supramolecular complex and cucurbit[n]uril (CB[n])/bisammonium supramolecular complex, respectively. The supramolecular nanovalves (i.e. α-CD/aniline and (CB[n])/bisammonium) can effectively tune the release of entrapped inhibitor (BTA) depending on the pH, imparting self-diagnosis and self-healing characteristics to the OIH sol–gel coatings (Fig. 8) [155]. Although not yet applied in protective coatings, different silica/polymer nanotubes have been developed with a high aspect ratio and inhibitor loading capacity that are capable of regulating the release process with various

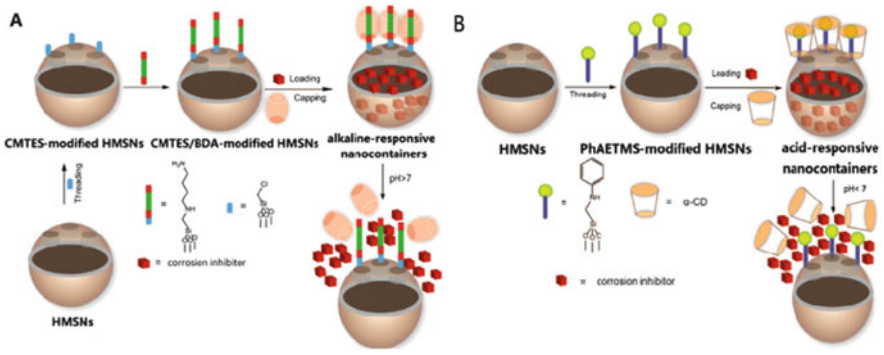

Fig. 8 Synthesis and operation of pH-responsive nanocontainers: (**a**) alkaline-responsive nanocontainers modified using cucurbit[n]uril/bisammonium supramolecular complex and (**b**) acid-responsive nanocontainers modified using α-cyclodextrin (α-CD)/aniline supramolecular complex [155]

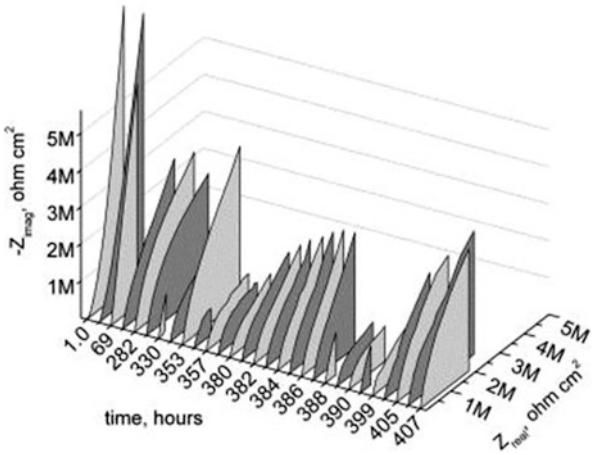

Fig. 9 Evolution of the Nyquist plots during immersion in 0.05 M NaCl obtained for AA2024-T3 treated with benzotriazole-doped TiO_x covered with sol–gel film [158]

triggering agents such as pH, temperature and redox reaction, thus opening new possibilities for feedback-active self-healing coatings [156].

Despite the improved active protection of metallic substrates achieved by inclusion of inhibitor-loaded carriers, the architectural aspects of the OIH coatings affecting the position of the embedded carriers with respect to the substrate should be taken into account. Although increasing the distance between the carriers and metal surface can lead to better barrier properties, it can delay active corrosion protection as a result of the increased diffusive path of the entrapped inhibitors [88, 150, 157].

To increase the inhibitor loading capacity of OIH coatings, a porous TiO_x layer was deposited onto the metallic substrate through controlled hydrolysis of tetra-isopropyl *ortho*-titanate in the presence of the non-ionic block copolymer Pluronic F127. Using a template-based synthesis procedure, titania nanoparticles were self-assembled on AA2024-T3 substrate, forming a cellular network capable of loading large quantities of *n*-benzotriazole. The inhibitor-loaded porous layer was subsequently coated with the OIH sol–gel coating. Electrochemical characterization of prepared samples using electrochemical impedance spectroscopy (EIS) revealed a well-defined multiple self-healing ability that resulted in effective long-term active corrosion protection of the underlying substrate (Fig. 9) [158].

3. Entrapment of inhibitors in nanocontainers in a LBL configuration
   Application of layer-by-layer (LbL) assembled shells on the surface of micro- or nanocontainers led to the development of containers with regulated storage and release of the inhibitor. The LbL method is based on the adsorption of oppositely charged layers on the surface of a template material. Entrapment of corrosion inhibitors in polyelectrolyte multilayer systems via the LbL method has several advantages. It can isolate the inhibitor, avoiding its negative effect on the integrity of the coating. Additionally, such a system can provide intelligent

release of the corrosion inhibitor, because permeability of the polyelectrolyte assemblies is regulated by changes in pH and humidity. The change in pH is the most preferable stimulus for initiating release of corrosion inhibitors. Upon restoration of neutral pH values, the polyelectrolyte shell closes, stopping inhibitor release or leakage [25].

Negatively charged SiO_2particles were coated with successive layers of PEI/poly(styrene sulfonate) (PSS)/BTA/PSS/BTA, yielding a BTA content of about 95 mg BTA/g SiO_2 nanoparticles. Electrochemical characterization of the nanocontainer-loaded OIH coating using the scanning vibrating electrode technique (SVET) revealed deactivation of cathodic sites over the artificial defect after 2 h of exposure to the test electrolyte [21].

The limited loading capacity of the nanoparticles can be overcome via the application of porous structures and nanocontainers with higher aspect ratio. Recently, self-healing OIH coatings based on MBT- or 8-hydroxyquinoline-loaded halloysite nanotubes [159–161] have been reported. Halloysites are two-layered aluminosilicate nanotubes with nominal internal diameter of 15 nm and length of 300–800 nm. In analogy to the silica nanoparticles, the LBL self-assembly method was adopted for the development of multilayer polyelectrolyte nanoshells on the surface of halloysite nanotubes and smart end-caps regulating the inhibitor release process [159]. In another work [162], OIH self-healing coatings with a high corrosion inhibitor loading were prepared through incorporation of mesoporous silica nanoparticles loaded with 2-(benzothiazol-2-ylsulfanyl)-succinic acid in the coating formulation. The spontaneous release of the corrosion inhibitor was controlled by deposition of four subsequent polyelectrolyte layers (PEI/PSS/PEI/PSS) on the inhibitor-loaded mesoporous nanoparticles. SVET characterization of AA2024 coupons coated with the developed system revealed enhanced corrosion resistance and healing performance for inhibitor-doped coatings in comparison with undoped sol–gel coatings.

LBL self-assembly of polyelectrolytes can not only regulate the inhibitor release events, but also enable loading of different inhibitors into a single container, as demonstrated by Carneiro et al. [163]. MBT and Ce(III) were loaded into LDHs via anion-exchange and LBL procedures, respectively. Although deposition of successive polyelectrolyte layers altered the inhibitor release mechanism, the OIH coatings loaded with LDH nanoparticles containing the two inhibitors exhibited an improved barrier and active protection (Fig. 10) [163].

3.2 Intrinsic Self-Healing Sol–Gel Coatings

Intrinsic self-healing coatings do not require the addition of discrete healing agents but rely on suitable generic modification of the polymer architecture to achieve complete healing, even in the case of multiple damage events at specific locations.

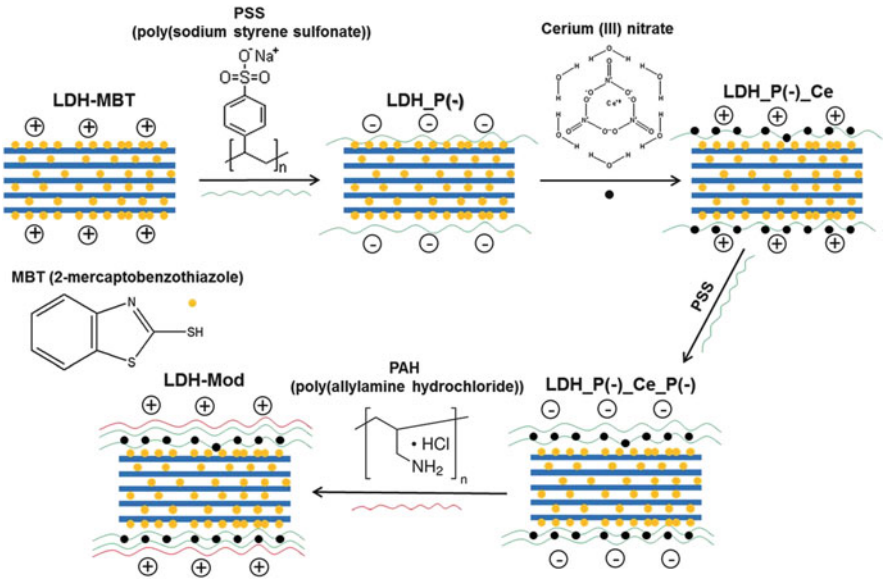

Fig. 10 Approach adopted for surface modification of LDH with PSS, PAH and cerium(III) nitrate [163]

This is true even if some controlled supply of an external stimulus is needed. Intrinsic self-healing approaches are based on local temporary mobility, leading to damage closure upon flow of the polymeric matrix (coating). Most of the intrinsic healing approaches developed to date are based on reversible physical and/or chemical bonds.

3.2.1 Deformation Recovery in Networks

In analogy to polymer coatings, OIH sol–gel coatings exhibit viscoelasto-plastic behaviour [114]. Therefore, any deformation in OIHs consists of a viscous response, plastic flow and elastic deformation. The time-independent component of the response affiliated with the stored energy can be employed for partial deformation recovery, and is referred to as elastic recovery. The plastic and the time-dependent viscous component of the deformation can also contribute to healing via the so-called shape memory effect [19].

Surface deformation of a slightly crosslinked coating using a (micro)scratch tester pushes the polymer from the scratch groove to the sides, resulting in a scratch profile (as presented in Fig. 11). In such a case, the energy applied to the system to create the scratch is generally lost in the process of viscous flow unless residual stresses are present as a result of viscoelastic (or viscoplastic) deformation. Therefore, restoration of the coating topology via flattening or levelling of the scratch profile as a result of backflow of the displaced material is generally achieved by

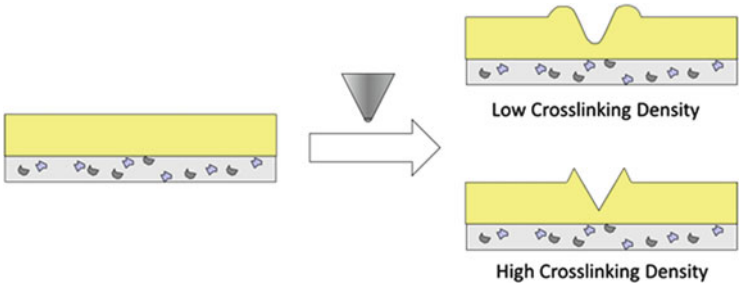

Fig. 11 Scratch profile of low and high crosslinking density coatings

temperature-assisted healing processes [164]. The temperature trigger enhances molecular mobility and allows the surface tension to drive the healing of the surface as much as possible.

In the case of a highly crosslinked coating (i.e. most OIH coatings), any scratch is also formed as a result of material transport from the indented area to the sides. In contrast to the former case, depending on whether the yield strength of the coating is exceeded, all or part of the applied energy is stored in the polymer network in the vicinity of the scratch (elastic and/or plastic response). Upon removal of the external mechanical stress, the stored elastic energy is relieved and the scratch fully or partially bounces back into a flat level surface. The timescale of such a process is determined by the mobility of the polymer network chains (i.e. the glass transition temperature, T_g). It is obvious that formation of tensile cracks along the scratch path can drastically alter the process, because fracture releases a large fraction of the stored elastic energy. Therefore, the energy is no longer available for a directed bounce-back movement.

3.2.2 Stress Relaxation in Reversible Non-covalent Networks

Self-healing polymeric systems based on reversible non-covalent bonds (e.g. hydrogen bonds) [165, 166] and ionomers [167, 168] have been extensively studied in recent years. In contrast to permanent covalent bonds, the dissociation and association of monomers and/or polymeric segments in the polymers are based on reversible non-covalent bonds, which are governed by a dynamic equilibrium ruled by thermodynamics. Reorganization of the polymeric network as a result of re-association of the reversible bonds provides these polymers with latent healing potential in the case of local structural damage. The time scale of the dynamic equilibrium plays a crucial role in the healing performance of such polymers [169]. When the dissociation/re-association time scale is larger than that of the deformation, the reversible network behaves equivalently to a covalent network; however, when the time scale is much shorter, the reversible network does not show the structural integrity of a covalently crosslinked material.

Accumulation of internal stresses as a result of physical aging is a well-known phenomenon in covalently crosslinked coatings [170, 171]. As indicated before, the residual stresses as a result of plasticity can be relieved via thermal treatment or viscoelasticity. Covalently crosslinked polymers can undergo only limited viscoelastic stress relaxation at temperatures higher than T_g, Due to the presence of physical constraints (i.e. the covalent crosslinks), polymer segments can only be stretched to a maximum extent, yielding partial relaxation. Reversible networks are not limited by such a maximal extent of relaxation and constantly creep, provided that the time scale of bond dissociation/re-association is equal to or shorter than the stress relaxation time constant (τ). The creep behaviour exhibited by the reversible network can enable (depending on the kinetics of dissociation/re-association equilibrium) relaxation of both internal stresses and imposed external stresses, preventing escalation of the damage from the microscopic to the macroscopic level and, hence, inducing an autonomous healing potential into the coating system.

Although, to date, no OIH coating capable of full stress relaxation has been reported in the literature, an OIH ionomer showing this desired behaviour was recently synthesised by Sanchez and colleagues [172] through implementation of a butyltinoxo-cluster macrocation, $[(BuSn)_{12}O_{14}(OH)_6]^{2+}$, functionalized with two 2-acrylamido-2-methyl-1-propanesulfonate anions (AMPS) as a physical crosslinking agent in poly(*n*-butyl acrylate) (pBuA). Sacrificial domains with reversible ionic bonds developed at the hybrid interface and played a double role. The interactions were strong enough to induce crosslinking and, consequently, rubber-like elastic behaviour and were labile enough to enable dynamic bond dissociation/re-association, leading to an efficient network rearrangement and healing at room temperature [172].

Although not yet studied from a stress-relaxation and self-healing point of view, heat- and corrosion-resistant urethane/urea/siloxane copolymers [69] as well as anti-fouling urea-siloxane OIH coatings [173–175] have been successfully applied on aluminium alloys. Considering the properties of the organic component in such OIHs, such as flexibility, re-flow and presence of hydrogen bonding moieties, these OIH coatings can be optimized (e.g. by variation of OOIR) for self-healing coating applications.

3.2.3 Reversible Covalent Networks

Several intrinsic self-healing approaches based on reversible covalent bonds using Diels–Alder/retro-Diels–Alder reactions [176, 177], thiol/disulfide exchange [178], disulfide bond reshuffling [179–182], radical-based thiol–ene reactions [183], alkoxyamine bonds [184], dynamic urea bonds [185], dynamic boronic esters [186] and reversible acylhydrazone formation [187] have been successfully implemented in polymers and polymer coatings.

Peng et al. [51] recently introduced an OIH coating based on mercapto- and vinyl-functionalized OMSAs for the protection of copper substrates. The increased crosslinking density of the developed OIH achieved through the in situ

condensation of silanol groups and thiol–ene click reactions led to improved protective performance of the coating compared with the coating solely crosslinked with Si–O–Si bonds. Despite the reported stress relaxation induced by heat and UV irradiation in polymeric coatings based on thiol–ene crosslinks [188, 189], the OIH coating developed has not yet been examined thermo-mechanically . The effect of the inorganic network based on Si–O–Si bridges on the thermo-mechanical properties of OIH networks containing thiol–ene moieties has been documented by Schreck and coworkers [190]. Despite the limited relaxation behaviour of the OIH network compared with a pure organic network, imposed by irreversible covalent bonds, the OIH networks exhibited reasonable stress relaxation behaviour and increased mechanical properties although they have not yet been examined as a coating.

In addition to the inclusion of reversible covalent bonds in the backbone or side chains of covalently crosslinked networks, blending of thermosets with thermoplastics of low melting point (in particular polycaprolactone, PCL) has been reported to induce shape recovery and self-healing functionality to polymeric coatings [191]. This principle has been further explored by combing it with Diels–Alder chemistry to yield thermo-re-mendable shape memory polyurethanes. PCL has also been incorporated in corrosion-protective OIH coatings. Although this leads to well-documented thick and defect-free OIH coatings having an improved potential bioactivity, the effect on scratch healing has not yet been studied [192].

Until very recently no corrosion-protective intrinsic healing sol–gel coatings have been reported in the literature. To address this issue, we recently presented a temperature-triggered intrinsic healing OIH sol–gel coating capable of healing at moderate temperatures [193–196]. Our newly developed intrinsic healing OIH sol–gel coating is a dual network consisting of epoxy precursors and bis [3-(triethoxysilyl)propyl]tetrasulfide (BS) and (3-aminopropyl)trimethoxysilane (APS) as OMSAs. BS and APS were used to incorporate reversible tetra-sulfide groups and covalent bridges, respectively, into the rigid crosslinked Epikote 828-based epoxy matrix. The chemical structure of the employed OMSAs and an idealized form of the resulting hybrid network are presented in Fig. 12.

Application of a moderate thermo-mechanical stimulus gives the developed OIH coating enough molecular mobility to close macroscopic damage such as scratches that reach the metal surface. The thermo-mechanical induced flow of the OIH polymer was quantified by examining its ability to close an artificial gap with an average width of 500 μm over a given time at different temperatures under a constant normal pressure of 30 kPa. The macroscopic flow and, hence, the healing kinetics was strongly affected by the content of reversible tetra-sulfide groups, crosslinking density and healing temperature. However, for the highest content of reversible groups employed in the study, the OIH polymer exhibited 100% gap closure efficiency for four consecutive healing cycles independently of the healing temperature and crosslinking density. The overlapping gap closure kinetic curves for four healing cycles at 70°C (presented in Fig. 13a) demonstrate the ability of the

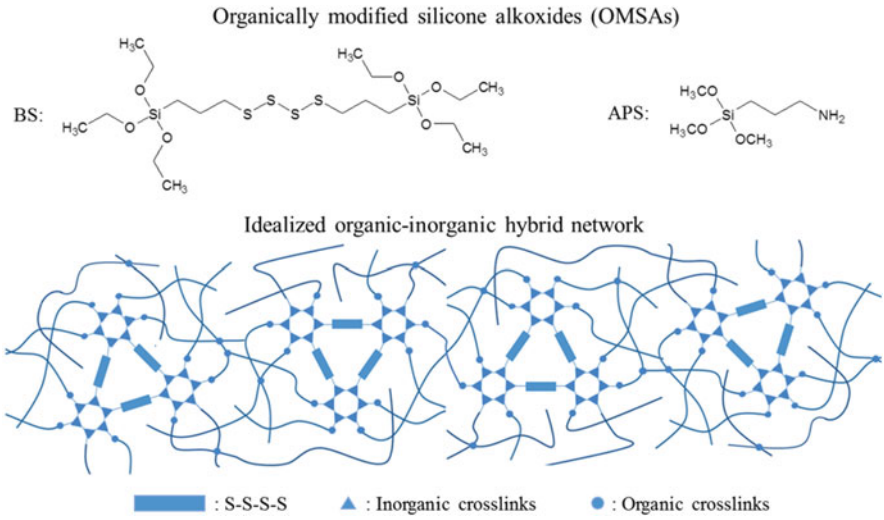

Fig. 12 Chemical structure of the OMSAs used in synthesis (*top*) and idealized structure of the resulting OIH dual network containing reversible tetra-sulfide groups (*bottom*). *BS* bis [3-(triethoxysilyl)propyl]tetrasulfide, *APS* (3-aminopropyl)trimethoxysilane [195]

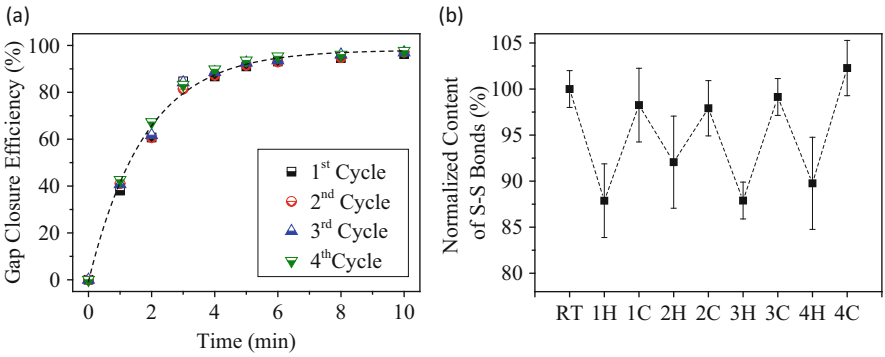

Fig. 13 (**a**) Gap closure kinetics of the OIH polymer for four consecutive healing cycles (one cycle involves one heating and one cooling step) at 70°C. (**b**) Percentage of S–S bonds in the sample after four heating and cooling cycles; *H* heating step, *C* cooling step [195]

OIH polymer to undergo multiple healing events with no decrease in its healing characteristics [195, 196].

Further evaluation of the OIH polymer during multiple healing events using hot-stage coupled Raman spectroscopy revealed a decrease in the content of the S–S bonds upon heating, followed by an increase, reaching their original content upon cooling (Fig. 13b). The amount of S–S bonds at a certain temperature is an indication of the state of those bonds at that temperature. Hence, the minimal amount of these bonds at 70°C indicates that a noticeable proportion (≈15%) of

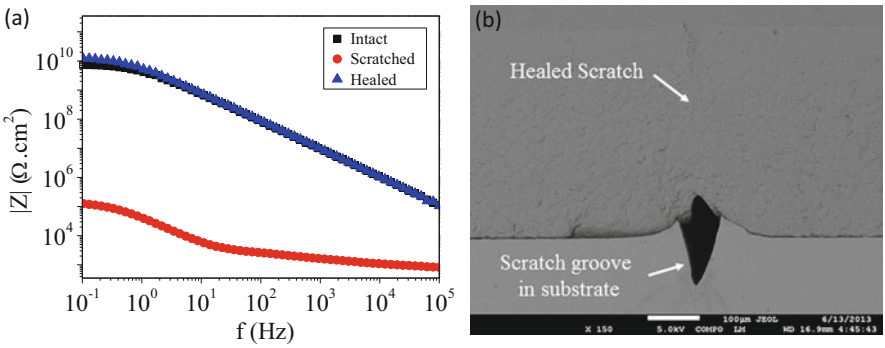

Fig. 14 (**a**) Bode modulus plots of intact (*black*), scratched (*red*) and healed (*blue*) OIH sol–gel coatings containing reversible tetra-sulfide groups in 0.5 M NaCl solution. (**b**) SEM image of cross-section of a healed coating [196]

these reversible bonds are broken, yielding a high chain mobility and enabling the macroscopic flow required to close the artificial gap. The increase in the content of S–S bonds during the cooling steps can be interpreted as joining or re-formation of the reversible bridges after the thermal trigger is removed. The results presented in Fig. 13 confirm the reversible nature of tetra-sulfide groups and correlate it with the multiple healing capability of the developed intrinsic healing OIH sol–gel polymer.

The extent of corrosion protection offered by a 300 μm thick OIH sol–gel coating on AA2024-T3 substrate was evaluated using EIS. Bode modulus plots of intact, scratched and healed coatings over the frequency range of 0.1–10^5 Hz are presented in Fig. 14. The EIS spectrum of the intact coating on AA2024-T3 showed a high Bode modulus (|Z|) at low frequency range ($|Z|_{0.1\ Hz} = 7.5E9\ \Omega\ cm^2$) and an almost pure capacitive response over the measured frequency range, characteristic of an effective barrier layer. To evaluate the healing potential of the prepared coating, a scratch with an approximate width of 300 μm and reaching the metallic substrate was created in the coating by load-controlled scratching. Upon mechanical damage, the coating lost its barrier function, as manifested by a significant drop in |Z| over the whole frequency range. Heating of the coating for 2 h at 70°C led to sealing of the fracture plane, as revealed by the scar-free SEM cross-section of the healed coating after immersion in electrolyte. Additionally, the EIS spectrum of the healed coating overlapped with that of the intact coating, confirming perfect sealing of the generated interface and full restoration of the barrier properties of the OIH sol–gel coating [196].

The thermo-mechanically triggered intrinsic healing of the developed OIH sol–gel coating can be regarded as a valuable first step towards fully autonomous intrinsic self-healing sol–gel coatings. The combination of both intrinsic and extrinsic concepts should lead to substantial lifetime extension for coated materials and a high degree of insensitivity to local mechanical damage.

4 Summary

The OIH sol–gel coatings have been successfully applied as pretreatment and protective coatings for various metallic substrates. Generally, silane-based OIH coatings are electrochemically inactive and therefore their protective function is lost when they are damaged. Yet, because of the versatility of sol–gel chemistry and the tuneable properties of the OIH materials, self-healing properties can be implemented via extrinsic and intrinsic healing approaches. Extrinsic self-healing corrosion-protective OIH sol–gel coatings can be prepared by direct or indirect (i.e. via carriers) incorporation of active species such as corrosion inhibitors into the coating formulation. Although the beneficial effects of direct inhibitor addition has been confirmed by various researchers, direct addition of these compounds can lead to network instability and loss of inhibitor efficiency as a result of chemical interaction with the sol–gel network. These challenges have been overcome through immobilization of corrosion inhibitors in nano- or microcontainers or via complexation with host structures. This approach opens up new possibilities for extrinsic self-healing OIH coatings, as it enables feedback–response mechanisms. Furthermore, the inhibitor release rate can be effectively controlled through application of supramolecular valves or polyelectrolyte multilayers, because their permeability can be tuned by several parameters (the most important being pH) or controlled by ion exchange in the case of ionic species. Although active corrosion inhibitors lead to sufficient temporary protection of the underlying metal in the case of local damage to the protective coating, to reach more extended lifetime protection or enable repeated healing at a specific location, the additional functionality of damage closure is required. Considering the chemical versatility of the OMSA-bearing moieties of reversible chemistry (sulfur chemistry, Diels–Alder, etc.), the field of intrinsic self-healing OIH materials and coatings has a high growth potential. As highlighted in this review, the development of a combined extrinsic–intrinsic self-healing sol–gel coating is feasible, leading to a multifunctional coating that could significantly extend the service lifetime of coating-protected metals.

References

1. Shchukin DG, Borisova D, Mohwal H (2013) Self-healing coatings. In: Binder WH (ed) Self-healing polymers from principles to applications. Wiley-VCH, Weinheim
2. Garcia SJ, Fischer HR, van der Zwaag S (2011) A critical appraisal of the potential of self healing polymeric coatings. Prog Org Coat 72(3):211–221
3. Fontana MG (1987) Corrosion engineering, 3rd edn. McGraw-Hill, Singapore
4. Peabody AW (2001) Peabody's control of pipeline corrosion, 2nd edn. NACE International The Corrosion Society, Houston
5. Ashirgade AA (2006) Environmentally-compliant novolac superprimers for corrosion protection of aluminum alloys. MS thesis, Materials Science and Engineering, University of Cincinnati

6. Khanna AS (2008) Nanotechnology in high performance paint coatings. Asian J Exp Sci 21:25–32
7. García SJ et al (2011) Advances in the selection and use of rare-earth based inhibitors for self-healing organic coatings. In: Fedrizzi L, Fürbeth W, Montemor MF (eds) Self-healing properties of new surface treatments, European Federation of Corrosion series. Maney, Leeds, pp 148–183
8. Figueira RB, Silva CJR, Pereira EV (2015) Organic–inorganic hybrid sol–gel coatings for metal corrosion protection: a review of recent progress. J Coat Technol Res 12(1):1–35
9. Zheludkevich ML, Salvado IM, Ferreira MGS (2005) Sol–gel coatings for corrosion protection of metals. J Mater Chem 15(48):5099–5111
10. Wang D, Bierwagen GP (2009) Sol–gel coatings on metals for corrosion protection. Prog Org Coat 64(4):327–338
11. Brinker CJ, Scherer GW (1990) Sol–gel science: the physics and chemistry of sol gel processing. Academic, Boston
12. Vioux A (1997) Nonhydrolytic sol–gel routes to oxides. Chem Mater 9:2292–2299
13. Niederberger M, Pinna N (2009) Aqueous and nonaqueous sol–gel chemistry. In: Niederberger M, Pinna N (eds) Metal oxide nanoparticles in organic solvents synthesis, formation, assembly and application. Springer, London, pp 7–18
14. Hench LL, West JK (1990) The sol–gel process. Chem Rev 90(1):33–72
15. Wright JD, Sommerdijk NAJM (2001) Sol–gel materials: chemistry and applications. Taylor & Francis, London
16. Guglielmi M (1997) Sol–gel coatings on metals. J Sol–Gel Sci Technol 8(1):443–449
17. Benthem R et al (2008) Self healing polymer coatings self healing materials. Springer, The Netherlands, pp 139–159
18. Shchukin DG, Möhwald H (2007) Self-repairing coatings containing active nanoreservoirs. Small 3(6):926–943
19. van Benthem RTM, Ming W, de With G (2007) Self healing polymer coatings. In: van der Zwaag S (ed) Self healing materials. Springer, The Netherlands, pp 139–159
20. van der Zwaag S (2007) Self-healing materials: an alternative approach to 20 centuries of materials science, vol 100, Springer series in materials science. Springer, Dordrecht
21. Zheludkevich ML et al (2007) Anticorrosion coatings with self-healing effect based on nanocontainers impregnated with corrosion inhibitor. Chem Mater 19(3):402–411
22. Ghosh SK (2009) Self-healing materials: fundamentals, design strategies, and applications. Wiley-VCH, Weinheim
23. Hughes AE et al (2010) Designing green, self-healing coatings for metal protection. NPG Asia Mater 2:143–151
24. Montemor MF, Ferreira MGS (2011) A review on the use of nanostructured and functional organosilane coatings modified with corrosion inhibitors as environmentally friendly pre-treatments for metallic substrates. In: Fedrizzi L, Fürbeth W, Montemor MF (eds) Self-healing properties of new surface treatments, European Federation of Corrosion series. Maney, Leeds, pp 39–64
25. Zheludkevich ML, Ferreira MGS (2011) Self-healing anticorrosion coatings. In: Fedrizzi L, Fürbeth W, Montemor MF (eds) Self-healing properties of new surface treatments, European Federation of Corrosion series. Maney, Leeds, pp 11–38
26. Hager MD et al (2010) Self-healing materials. Adv Mater 22(47):5424–5430
27. Kron J, Deichmann KJ, Rose K (2011) Sol–gel derived hybrid materials as functional coatings for metal surfaces. In: Fedrizzi L, Fürbeth W, Montemor MF (eds) Self-healing properties of new surface treatments, European Federation of Corrosion series. Maney, Leeds, pp 105–118
28. Schmidt H, Scholze H, Kaiser A (1984) Principles of hydrolysis and condensation reaction of alkoxysilanes. J Non Cryst Solids 63(1–2):1–11
29. Silva CR, Airoldi C (1997) Acid and base catalysts in the hybrid silica sol–gel process. J Colloid Interface Sci 195(2):381–387

30. Wen J, Wilkes GL (1996) Organic/inorganic hybrid network materials by the sol–gel approach. Chem Mater 8(8):1667–1681
31. Chou TP et al (2001) Organic–inorganic hybrid coatings for corrosion protection. J Non Cryst Solids 290(2–3):153–162
32. Zheng S, Li J (2010) Inorganic–organic sol gel hybrid coatings for corrosion protection of metals. J Sol–Gel Sci Technol 54(2):174–187
33. van Ooij WJ et al (2005) Corrosion protection properties of organofunctional silanes – an overview. Tsinghua Sci Technol 10(6):639–664
34. Abdolah Zadeh M, van der Zwaag S, Garcia SJ (2013) Routes to extrinsic and intrinsic self-healing corrosion protective sol–gel coatings: a review. Self-Healing Materials 1:1–18. doi:10.2478/shm-2013-0001
35. Liu Y et al (2005) Corrosion resistance properties of organic–inorganic hybrid coatings on 2024 aluminum alloy. Appl Surf Sci 246(1–3):82–89
36. Jeeva Jothi K, Palanivelu K (2014) Facile fabrication of core–shell Pr6O11-ZnO modified silane coatings for anti-corrosion applications. Appl Surf Sci 288:60–68
37. Vreugdenhil AJ et al (2008) The role of crosslinkers in epoxy-amine crosslinked silicon sol–gel barrier protection coatings. Thin Solid Films 517(2):538–543
38. Moreira SDFC et al (2012) Development of new high transparent hybrid organic–inorganic monoliths with surface engraved diffraction pattern. J Polym Sci B 50(7):492–499
39. Croes KJ et al (2011) An electrochemical study of corrosion protection by in situ oxidative polymerization in phenylenediamine crosslinked sol–gel hybrid coatings. Electrochim Acta 56(23):7796–7804
40. Khramov AN et al (2003) Nanostructured sol–gel derived conversion coatings based on epoxy- and amino-silanes. Prog Org Coat 47(3–4):207–213
41. Bakhshandeh E et al (2014) Anti-corrosion hybrid coatings based on epoxy–silica nano-composites: toward relationship between the morphology and EIS data. Prog Org Coat 77 (7):1169–1183
42. Suleiman R, Dafalla H, El Ali B (2015) Novel hybrid epoxy silicone materials as efficient anticorrosive coatings for mild steel. RSC Adv 5(49):39155–39167
43. Roussi E et al (2011) Novel hybrid organo-silicate corrosion resistant coatings based on hyperbranched polymers. Surf Coat Technol 205(10):3235–3244
44. Harb SV et al (2015) Siloxane–PMMA hybrid anti-corrosion coatings reinforced by lignin. Surf Coat Technol 275:9–16
45. Metroke T, Kachurina O, Knobbe E (2002) Electrochemical and salt spray analysis of multilayer ormosil/conversion coating systems for the corrosion resistance of 2024-T3 aluminum alloys. J Coat Technol 74(927):53–61
46. Juan-Díaz MJ et al (2014) Study of the degradation of hybrid sol–gel coatings in aqueous medium. Prog Org Coat 77(11):1799–1806
47. Kunst SR et al (2014) Corrosion resistance of siloxane–poly(methyl methacrylate) hybrid films modified with acetic acid on tin plate substrates: influence of tetraethoxysilane addition. Appl Surf Sci 298:1–11
48. Kunst SR et al (2014) Hybrid films with (trimethoxysilylpropyl) methacrylate (TMSM), poly (methyl methacrylate) PMMA and tetraethoxysilane (TEOS) applied on tinplate. Mater Res 17:75–81
49. Li W et al (2014) Study the factors affecting the performance of organic–inorganic hybrid coatings. J Appl Polym Sci 131(21):41010. doi:10.1002/app.41010
50. Liu J-G, Xu L, Fang Y-Q (2014) Hybrid organic–inorganic sol–gel coatings with interpenetrating network for corrosion protection of tinplate. J Sol–Gel Sci Technol 71 (2):246–253
51. Peng S et al (2014) Performance evaluation of mercapto functional hybrid silica sol–gel coating on copper surface. Surf Coat Technol 251:135–142

52. Rodič P, Iskra J, Milošev I (2014) A hybrid organic–inorganic sol–gel coating for protecting aluminium alloy 7075-T6 against corrosion in Harrison's solution. J Sol–Gel Sci Technol 70 (1):90–103
53. Rodič P, Iskra J, Milošev I (2014) Study of a sol–gel process in the preparation of hybrid coatings for corrosion protection using FTIR and ^{1}H NMR methods. J Non Cryst Solids 396–397:25–35
54. Chawada G, Dholakiya B (2015) Organic–inorganic hybrid sol–gel pretreatments for corrosion protection of mild steel in neutral and acidic solutions. Res Chem Intermed 41 (6):3659–3674
55. Sheffer M, Groysman A, Mandler D (2003) Electrodeposition of sol–gel films on Al for corrosion protection. Corros Sci 45(12):2893–2904
56. Sheffer M et al (2004) Anion embedded sol–gel films on Al for corrosion protection. Corros Sci 46(12):2975–2985
57. Du Joshua Y et al (2001) Inorganic/organic hybrid coatings for aircraft aluminum alloy substrates. Prog Org Coat 41(4):226–232
58. Kunst SR et al (2014) Effect of curing temperature and architectural (monolayer and bilayer) of hybrid films modified with polyethylene glycol for the corrosion protection on tinplate. Mater Res 17:1071–1081
59. Ansari F, Naderi R, Dehghanian C (2015) Study on the protective function of cloisite incorporated silane sol–gel coatings cured at different conditions. Appl Clay Sci 114:93–102
60. Milošev I et al (2015) Hybrid sol–gel coating agents based on zirconium(IV) propoxide and epoxysilane. J Sol–Gel Sci Technol 74(2):447–459
61. Rafiaei F, Naderi R, Dehghanian C (2015) Impact of curing on the corrosion performance of an eco-friendly silane sol–gel coating on 304L stainless steel. RSC Adv 5(54):43225–43233
62. Paussa L et al (2012) ZrO2 sol–gel pre-treatments doped with cerium nitrate for the corrosion protection of AA6060. Prog Org Coat 74(2):311–319
63. Yasakau KA et al (2014) Influence of sol–gel process parameters on the protection properties of sol–gel coatings applied on AA2024. Surf Coat Technol 246:6–16
64. Ochi M, Takahashi R (2001) Phase structure and thermomechanical properties of primary and tertiary amine-cured epoxy/silica hybrids. J Polym Sci B 39(11):1071–1084
65. Turri S et al (2010) Abrasion and nanoscratch in nanostructured epoxy coatings. J Appl Polym Sci 118(3):1720–1727
66. Nazir T et al (2011) The influence of temperature and interface strength on the microstructure and performance of sol–gel silica–epoxy nanocomposites. Polym Bull 67(8):1539–1551
67. Kim D et al (2012) Preparation and characterization of UV-cured polyurethane acrylate/ZnO nanocomposite films based on surface modified ZnO. Prog Org Coat 74(3):435–442
68. Luo Z et al (2012) One-step synthesis of functional silica nanoparticles for reinforcement of polyurethane coatings. Powder Technol 218:23–30
69. Mishra AK et al (2012) Hyperbranched polyurethane-urea-imide/o-clay-silica hybrids: synthesis and characterization. J Appl Polym Sci 125(S1):E67–E75
70. Yan X, Xu G (2012) Influence of silane coupling agent on corrosion-resistant property in low infrared emissivity Cu/polyurethane coating. Prog Org Coat 73(2–3):232–238
71. Carcouët CCMC et al (2014) Fine-tuning of superhydrophobicity based on monolayers of well-defined raspberry nanoparticles with variable dual-roughness size and ratio. Adv Funct Mater 24(36):5745–5752
72. Zheludkevich ML et al (2005) Nanostructured sol–gel coatings doped with cerium nitrate as pre-treatments for AA2024-T3: corrosion protection performance. Electrochim Acta 51 (2):208–217
73. Zheludkevich ML, Tedim J, Ferreira MGS (2012) "Smart" coatings for active corrosion protection based on multi-functional micro and nanocontainers. Electrochim Acta 82:314–323
74. Wu G et al (2014) Robust microcapsules with polyurea/silica hybrid shell for one-part self-healing anticorrosion coatings. J Mater Chem A 2(30):11614–11620

75. Borisova D, Mohwal H, Shchukin DG (2011) Mesoporous silica nanoparticles for active corrosion protection. ACS Nano 5(3):1939–1946
76. Maia F et al (2012) Silica nanocontainers for active corrosion protection. Nanoscale 4 (4):1287–1298
77. Wang M, Liu M, Fu J (2015) An intelligent anticorrosion coating based on pH-responsive smart nanocontainers fabricated via a facile method for protection of carbon steel. J Mater Chem A 3(12):6423–6431
78. Kluson P et al (2001) Preparation of titania mesoporous materials using a surfactant-mediated sol–gel method. J Mater Chem 11(2):644–651
79. Garcia SJ, Fischer HR, White PA, Mardel J, González-García Y, Mol JMC, Hughes AE (2011) Self-healing anticorrosive organic coating based on an encapsulated water reactive silyl ester: synthesis and proof of concept. Prog Org Coat 70(2–3):142–149
80. Latnikova A et al (2011) Polyfunctional active coatings with damage-triggered water-repelling effect. Soft Matter 7(2):369–372
81. Song Y-K et al (2013) Sunlight-induced self-healing of a microcapsule-type protective coating. ACS Appl Mater Interfaces 5(4):1378–1384
82. Yasakau KA et al (2006) Mechanism of corrosion inhibition of AA2024 by rare-earth compounds. J Phys Chem B 110(11):5515–5528
83. Voevodin NN et al (2001) Potentiodynamic evaluation of sol–gel coatings with inorganic inhibitors. Surf Coat Technol 140(1):24–28
84. Cabral A et al (2005) Analytical characterisation and corrosion behaviour of bis-[triethoxysilylpropyl]tetrasulphide pre-treated AA2024-T3. Corros Sci 47(3):869–881
85. Palanivel V, Huang Y, van Ooij WJ (2005) Effects of addition of corrosion inhibitors to silane films on the performance of AA2024-T3 in a 0.5 M NaCl solution. Prog Org Coat 53 (2):153–168
86. Sugama T (2005) Cerium acetate-modified aminopropylsilane triol: a precursor of corrosion-preventing coating for aluminum-finned condensers. J Coat Technol Res 2(8):649–659
87. Andreatta F et al (2010) Corrosion behaviour of sol–gel treated and painted AA2024 aluminium alloy. Prog Org Coat 69(2):133–142
88. Rosero-Navarro NC et al (2010) Optimization of hybrid sol–gel coatings by combination of layers with complementary properties for corrosion protection of AA2024. Prog Org Coat 69 (2):167–174
89. Shi H, Liu F, Han E (2010) Corrosion behaviour of sol–gel coatings doped with cerium salts on 2024-T3 aluminum alloy. Mater Chem Phys 124(1):291–297
90. Aparicio M et al (2011) Hybrid Ce-containing silica-methacrylate sol–gel coatings for corrosion protection of aluminium alloys. In: Fedrizzi L, Fürbeth W, Montemor MF (eds) Self-healing properties of new surface treatments, European Federation of Corrosion series. Maney, Leeds, pp 202–219
91. Kozhukharov S et al (2012) Protective ability of hybrid nano-composite coatings with cerium sulphate as inhibitor against corrosion of AA2024 aluminium alloy. Prog Org Coat 73 (1):95–103
92. Paussa L et al (2012) Study of the effect of cerium nitrate on AA2024-T3 by means of electrochemical micro-cell technique. Electrochim Acta 70:25–33
93. Yu M et al (2015) Effects of cerium salts on corrosion behaviors of Si–Zr hybrid sol–gel coatings. Chin J Aeronaut 28(2):600–608
94. Lakshmi RV et al (2013) Effective corrosion inhibition performance of Ce3+ doped sol–gel nanocomposite coating on aluminum alloy. Prog Org Coat 76:367–374
95. Fu C et al (2015) Effect of cerium acetate doping on corrosion behavior of solgel coatings on 2A12 aluminium alloy. Int J Electrochem Sci 10:2014–2025
96. Harb SV et al (2015) Structural properties of cerium doped siloxane-PMMA hybrid coatings with high anticorrosive performance. RSC Adv 5(20):15414–15424
97. Santana I et al (2015) Corrosion protection of carbon steel by silica-based hybrid coatings containing cerium salts: effect of silica nanoparticle content. Surf Coat Technol 265:106–116

98. Suegama PH et al (2009) Influence of cerium (IV) ions on the mechanism of organosilane polymerization and on the improvement of its barrier properties. Electrochim Acta 54:2655–2662
99. Pepe A et al (2006) Cerium hybrid silica coatings on stainless steel AISI 304 substrate. J Sol–Gel Sci Technol 39(2):131–138
100. Zandi Zand R, Verbeken K, Adriaens A (2012) Corrosion resistance performance of cerium doped silica sol–gel coatings on 304L stainless steel. Prog Org Coat 75(4):463–473
101. Certhoux E et al (2013) New sol–gel formulations to increase the barrier effect of a protective coating against the corrosion of steels. Prog Org Coat 76(1):165–172
102. Cambon J-B et al (2012) Effect of cerium concentration on corrosion resistance and polymerization of hybrid sol–gel coating on martensitic stainless steel. Prog Org Coat 75 (4):486–493
103. Montemor MF, Ferreira MGS (2007) Electrochemical study of modified bis-[triethoxysilylpropyl] tetrasulfide silane films applied on the AZ31 Mg alloy. Electrochim Acta 52(27):7486–7495
104. Garcia-Heras M et al (2004) Preparation and electrochemical study of cerium-silica sol–gel thin films. J Alloys Compd 380(1–2):219–224
105. Trabelsi W et al (2005) Electrochemical assessment of the self-healing properties of Ce-doped silane solutions for the pre-treatment of galvanised steel substrates. Prog Org Coat 54(4):276–284
106. Montemor MF et al (2006) Modification of bis-silane solutions with rare-earth cations for improved corrosion protection of galvanized steel substrates. Prog Org Coat 57(1):67–77
107. Trabelsi W et al (2006) The use of pre-treatments based on doped silane solutions for improved corrosion resistance of galvanised steel substrates. Surf Coat Technol 200 (14–15):4240–4250
108. Bastos AC et al (2010) Localised measurements of pH and dissolved oxygen as complements to SVET in the investigation of corrosion at defects in coated aluminum alloy. Electroanalysis 22(17–18):2009–2016
109. Pirhady Tavandashti N, Sanjabi S, Shahrabi T (2011) Evolution of corrosion protection performance of hybrid silica based sol–gel nanocoatings by doping inorganic inhibitor. Mater Corros 62:411–415
110. Vreugdenhil AJ, Woods ME (2005) Triggered release of molecular additives from epoxy-amine sol–gel coatings. Prog Org Coat 53(2):119–125
111. Dalmoro V, dos Santos J, Azambuja D (2012) Corrosion behavior of AA2024-T3 alloy treated with phosphonate-containing TEOS. J Solid State Electrochem 16(1):403–414
112. Akid R, Gobara M, Wang H (2011) Corrosion protection performance of novel hybrid polyaniline/sol–gel coatings on an aluminium 2024 alloy in neutral, alkaline and acidic solutions. Electrochim Acta 56(5):2483–2492
113. Akid R, Gobara M, Wang H (2011) Hybrid sol–gel/conducting polymer coatings: self-healing coatings for the corrosion protection of aerospace alloys. In: Fedrizzi L, Fürbeth W, Montemor MF (eds) Self-healing properties of new surface treatments, European Federation of Corrosion series. Maney, Leeds, pp 119–133
114. Roussi E et al (2013) Anticorrosion and nanomechanical performance of hybrid organo-silicate coatings integrating corrosion inhibitors. Surf Coat Technol 232:131–141
115. Khramov AN et al (2004) Hybrid organo-ceramic corrosion protection coatings with encapsulated organic corrosion inhibitors. Thin Solid Films 447–448:549–557
116. Khramov AN et al (2005) Sol–gel-derived corrosion-protective coatings with controllable release of incorporated organic corrosion inhibitors. Thin Solid Films 483(1–2):191–196
117. Rani A et al (2014) Scratch cell test: a simple, cost effective screening tool to evaluate self-healing in anti-corrosion coatings. J Mater Eng Perform 23(9):3328–3335
118. Ramya S, Arunchandran C, George RP (2015) Studies on hybrid sol–gel silica/PVP coatings on modified 9Cr–1Mo steel. Trans Indian Inst Metals 68(4):513–519

119. Tian Z et al (2015) Inhibiting effect of 8-hydroxyquinoline on the corrosion of silane-based sol–gel coatings on AA 2024-T3. Prog Org Coat 82:81–90
120. O'Neill H et al (2012) Characterization of morphology and active agent mobility within hybrid silica sol–gel composites. J Phys Chem C 116(26):13972–13979
121. Quinet M et al (2007) Corrosion protection of sol–gel coatings doped with an organic corrosion inhibitor: chloranil. Prog Org Coat 58(1):46–53
122. Rahimi A, Amiri S (2014) Self-healing hybrid nanocomposite coatings with encapsulated organic corrosion inhibitors. J Polym Res 22(1):1–8
123. Rahimi A, Amiri S (2015) Anticorrosion hybrid nanocomposite coatings with encapsulated organic corrosion inhibitors. J Coat Technol Res 12(3):587–593
124. Palanivel V, Zhu D, van Ooij WJ (2003) Nanoparticle-filled silane films as chromate replacements for aluminum alloys. Prog Org Coat 47(3–4):384–392
125. Rosero-Navarro NC et al (2008) Effects of Ce-containing sol–gel coatings reinforced with SiO2 nanoparticles on the protection of AA2024. Corros Sci 50(5):1283–1291
126. Suegama PH et al (2008) Corrosion behavior of carbon steel protected with single and bi-layer of silane films filled with silica nanoparticles. Surf Coat Technol 202(13):2850–2858
127. Gonzalez E et al (2011) A silanol-based nanocomposite coating for protection of AA-2024 aluminium alloy. Electrochim Acta 56(22):7586–7595
128. Ershad-Langroudi A, Rahimi A (2014) Effect of ceria and zirconia nanoparticles on corrosion protection and viscoelastic behavior of hybrid coatings. Iran Polym J 23(4):267–276
129. Zandi Zand R et al (2014) Effects of ceria nanoparticle concentrations on the morphology and corrosion resistance of cerium–silane hybrid coatings on electro-galvanized steel substrates. Mater Chem Phys 145(3):450–460
130. Abdollahi H et al (2014) Anticorrosive coatings prepared using epoxy–silica hybrid nanocomposite materials. Ind Eng Chem Res 53(27):10858–10869
131. Calabrese L et al (2014) Electrochemical behavior of hydrophobic silane–zeolite coatings for corrosion protection of aluminum substrate. J Coat Technol Res 11(6):883–898
132. Dalmoro V et al (2014) Sol–gel hybrid films based on organosilane and montmorillonite for corrosion inhibition of AA2024. J Colloid Interface Sci 426:308–313
133. Fedel M et al (2014) Effect of Na-Montmorillonite sonication on the protective properties of hybrid silica coatings. Electrochim Acta 124:90–99
134. Álvarez D et al (2010) Characterization of hybrid sol–gel coatings doped with hydrotalcite-like compounds to improve corrosion resistance of AA2024-T3 alloys. Prog Org Coat 68 (1–2):91–99
135. Zheludkevich ML et al (2006) Corrosion protective properties of nanostructured sol–gel hybrid coatings to AA2024-T3. Surf Coat Technol 200(9):3084–3094
136. Pirhady Tavandashti N, Sanjabi S (2010) Corrosion study of hybrid sol–gel coatings containing boehmite nanoparticles loaded with cerium nitrate corrosion inhibitor. Prog Org Coat 69(4):384–391
137. Montemor MF, Ferreira MGS (2008) Analytical characterization of silane films modified with cerium activated nanoparticles and its relation with the corrosion protection of galvanised steel substrates. Prog Org Coat 63(3):330–337
138. Montemor MF, Ferreira MGS (2007) Cerium salt activated nanoparticles as fillers for silane films: evaluation of the corrosion inhibition performance on galvanised steel substrates. Electrochim Acta 52(24):6976–6987
139. Montemor MF et al (2012) Evaluation of self-healing ability in protective coatings modified with combinations of layered double hydroxides and cerium molibdate nanocontainers filled with corrosion inhibitors. Electrochim Acta 60:31–40
140. Omar S et al (2015) Sol–gel hybrid coatings with strontium-doped 45S5 glass particles for enhancing the performance of stainless steel implants: electrochemical, bioactive and in vivo response. J Non Cryst Solids 425:1–10
141. Motte C et al (2012) Improvement of corrosion protection offered to galvanized steel by incorporation of lanthanide modified nanoclays in silane layer. Prog Org Coat 74(2):326–333

142. Dias SAS et al (2013) The role of Ce(III)-enriched zeolites on the corrosion protection of AA2024-T3. Electrochim Acta 112:549–556
143. Dias SAS et al (2012) Sol–gel coatings modified with zeolite fillers for active corrosion protection of AA2024. Corros Sci 62:153–162
144. Garcia SJ, Markley TA, Mol JMC, Hughes AE (2013) Unravelling the corrosion inhibition mechanisms of bi-functional inhibitors by EIS and SEM–EDS. Corros Sci 69:346–358
145. Diasa SAS et al (2014) Synergistic protection against corrosion of AA2024-T3 by sol–gel coating modified with La and Mo-enriched zeolites. J Electrochem Soc 161(4):C215–C222
146. Ferrer EL, Rollon AP, Mendoza HD, Lafont U, Garcia SJ (2014) Double-doped zeolites for corrosion protection of aluminium alloys. Microporous Mesoporous Mater 188:8–15
147. Poznyak SK et al (2009) Novel inorganic host layered double hydroxides intercalated with guest organic inhibitors for anticorrosion applications. ACS Appl Mater Interfaces 1 (10):2353–2362
148. Zheludkevich ML et al (2010) Active protection coatings with layered double hydroxide nanocontainers of corrosion inhibitor. Corros Sci 52:602–611
149. Tedim J et al (2012) Zn–Al layered double hydroxides as chloride nanotraps in active protective coatings. Corros Sci 55:1–4
150. Tedim J et al (2010) Enhancement of active corrosion protection via combination of inhibitor-loaded nanocontainers. ACS Appl Mater Interfaces 2(5):1528–1535
151. Liu J et al (2015) Influence of embedded ZnAlCe-NO3− layered double hydroxides on the anticorrosion properties of sol–gel coatings for aluminum alloy. Prog Org Coat 81:93–100
152. Snihirova D, Lamaka SV, Montemor MF (2012) "SMART" protective ability of water based epoxy coatings loaded with $CaCO_3$ microbeads impregnated with corrosion inhibitors applied on AA2024 substrates. Electrochim Acta 83:439–447
153. Yasakau KA et al (2013) Active corrosion protection of AA2024 by sol–gel coatings with cerium molybdate nanowires. Electrochim Acta 112:236–246
154. Borisova D, Möhwald H, Shchukin DG (2012) Influence of embedded nanocontainers on the efficiency of active anticorrosive coatings for aluminium alloys. Part I: influence of nanocontainer concentration. ACS Appl Mater Interfaces 4(6):2931–2939
155. Tao C, JiaJun F (2012) An intelligent anticorrosion coating based on pH-responsive supramolecular nanocontainers. Nanotechnology 23(50):505705
156. Li GL et al (2013) Silica/polymer double-walled hybrid nanotubes: synthesis and application as stimuli-responsive nanocontainers in self-healing coatings. ACS Nano 7(3):2470–2478
157. Borisova D, Möhwald H, Shchukin DG (2013) Influence of embedded nanocontainers on the efficiency of active anticorrosive coatings for aluminum alloys. Part II: influence of nanocontainer position. ACS Appl Mater Interfaces 5(1):80–87
158. Lamaka SV et al (2006) TiOx self-assembled networks prepared by templating approach as nanostructured reservoirs for self-healing anticorrosion pre-treatments. Electrochem Commun 8(3):421–428
159. Lvov YM, Shchukin DG, Mohwald H, Price RR (2008) Halloysite clay nanotubes for controlled release of protective agents. ACS Nano 2(5):814–820
160. Shchukin DG et al (2008) Active anticorrosion coatings with halloysite nanocontainers. J Phys Chem C 112(4):958–964
161. Fix D et al (2009) Application of inhibitor-loaded halloysite nanotubes in active anticorrosive coatings. Adv Funct Mater 19(11):1720–1727
162. Skorb EV et al (2009) Surface-modified mesoporous SiO2 containers for corrosion protection. Adv Funct Mater 19(15):2373–2379
163. Carneiro J et al (2015) Polyelectrolyte-modified layered double hydroxide nanocontainers as vehicles for combined inhibitors. RSC Adv 5(50):39916–39929
164. Vega J, Grande AM, van der Zwaag S, Garcia SJ (2014) On the role of free carboxylic groups and cluster conformation on the surface scratch healing behaviour of ionomers. Eur Polym J 57:121–126

165. Sijbesma RP et al (1997) Reversible polymers formed from self-complementary monomers using quadruple hydrogen bonding. Science 278(5343):1601–1604
166. Cordier P et al (2008) Self-healing and thermoreversible rubber from supramolecular assembly. Nature 451(7181):977–980
167. Varley RJ, van der Zwaag S (2008) Towards an understanding of thermally activated self-healing of an ionomer system during ballistic penetration. Acta Mater 56(19):5737–5750
168. Grande AM, Garcia SJ, van der Zwaag S (2013) Rate-dependent self-healing behavior of an ethylene-co-methacrylic acid ionomer under high-energy impact conditions. J Appl Polym Sci 130(3):1949–1958
169. Bose RK, Hohlbein N, Garcia SJ, Schmidt A, van der Zwaag S (2015) Connecting supramolecular bond lifetime and network mobility for scratch healing in poly(butyl acrylate) ionomers containing sodium, zinc and cobalt. Phys Chem Chem Phys 17(3):1697–1704
170. Perera DY, Schutyser P (1994) Effect of physical aging on thermal stress development in powder coatings. Prog Org Coat 24(1–4):299–307
171. Perera DY (2003) Physical ageing of organic coatings. Prog Org Coat 47(1):61–76
172. Potier F et al (2014) Nano-building block based-hybrid organic–inorganic copolymers with self-healing properties. Polym Chem 5(15):4474–4479
173. Holberg S, Bischoff C (2014) Application of a repellent urea–siloxane hybrid coating in the oil industry. Prog Org Coat 77(10):1591–1595
174. Figueira RB, Silva CJR, Pereira EV (2015) Hybrid sol–gel coatings for corrosion protection of hot-dip galvanized steel in alkaline medium. Surf Coat Technol 265:191–204
175. Tamboura M, Mikhailova A, Jia M (2014) A comparative study of anticorrosion paints based on silicone-urethane binders: a multilayer primer. Silicon 6(1):45–56
176. Scheltjens G et al (2011) Self-healing property characterization of reversible thermoset coatings. J Therm Anal Calorim 105(3):805–809
177. Postiglione G, Turri S, Levi M (2015) Effect of the plasticizer on the self-healing properties of a polymer coating based on the thermoreversible Diels–Alder reaction. Prog Org Coat 78:526–531
178. Pepels M et al (2013) Self-healing systems based on disulfide-thiol exchange reactions. Polym Chem 4(18):4955–4965
179. Tobolsky AV, MacKnight WJ, Takahashi M (1964) Relaxation of disulfide and tetrasulfide polymers. J Phys Chem 68(4):787–790
180. Tobolsky AV, MacKnight WJ, Takahashi M (1966) Relaxation of disulfide and tetrasulfide polymers. Rubber Chem Technol 39(3):524–529
181. Canadell J, Goossens H, Klumperman B (2011) Self-healing materials based on disulfide links. Macromolecules 44(8):2536–2541
182. Lafont U, van Zeijl H, van der Zwaag S (2012) Influence of cross-linkers on the cohesive and adhesive self-healing ability of polysulfide-based thermosets. ACS Appl Mater Interfaces 4 (11):6280–6288
183. Scott TF et al (2005) Photoinduced plasticity in cross-linked polymers. Science 308 (5728):1615–1617
184. Ono T, Nobori T, Lehn J-M (2005) Dynamic polymer blends-component recombination between neat dynamic covalent polymers at room temperature. Chem Commun 12:1522–1524
185. Ying H, Zhang Y, Cheng J (2014) Dynamic urea bond for the design of reversible and self-healing polymers. Nat Commun 5
186. Cash JJ et al (2015) Room-temperature self-healing polymers based on dynamic-covalent boronic esters. Macromolecules 48(7):2098–2106
187. Skene WG, Lehn J-MP (2004) Dynamers: polyacylhydrazone reversible covalent polymers, component exchange, and constitutional diversity. Proc Natl Acad Sci USA 101 (22):8270–8275
188. Kloxin CJ, Scott TF, Bowman CN (2009) Stress relaxation via addition – fragmentation chain transfer in a thiol-ene photopolymerization. Macromolecules 42(7):2551–2556

189. Shin J, Nazarenko S, Hoyle CE (2009) Effects of chemical modification of thiol – ene networks on enthalpy relaxation. Macromolecules 42(17):6549–6557
190. Schreck KM, Leung D, Bowman CN (2011) Hybrid organic/inorganic thiol–ene-based photopolymerized networks. Macromolecules 44(19):7520–7529
191. Lutz A et al (2015) A shape-recovery polymer coating for the corrosion protection of metallic surfaces. ACS Appl Mater Interfaces 7(1):175–183
192. Catauro M et al (2014) Corrosion behavior and mechanical properties of bioactive sol–gel coatings on titanium implants. Mater Sci Eng C 43:375–382
193. Abolah Zadeh M, van der Zwaag S, Garcia SJ (2012) Sol–gel based intrinsic self-healing polymers. In: Proceedings 8th coatings science international, Noordwijk, The Netherlands, p 52
194. Abdolah Zadeh M, van der Zwaag S, Garcia SJ (2013) Intrinsic self-healing sol–gel coatings based on epoxy alkoxysilanes containing dynamic di-sulfide bonds. In: Proceedings 9th coatings science international, Noordwijk, The Netherlands, p 123
195. Abdolah Zadeh M, Esteves ACC, van der Zwaag S, Garcia SJ (2014) Healable dual organic–inorganic crosslinked sol–gel based polymers: crosslinking density and tetrasulfide content effect. J Polym Sci A Polym Chem 52(14):1953–1961
196. Abdolah Zadeh M, van der Zwaag S, Garcia SJ (2015) Corrosion protective sol–gel coatings containing reversible tetra-sulphide groups showing intrinsic healing behaviour. In: Van der Zwaag S, Brinkman E (eds) Self healing materials – pioneering research in The Netherlands. Delft University Press, Delft

Adv Polym Sci (2016) 273: 219–246
DOI: 10.1007/12_2015_342

Published online: 2 February 2016

Self-Healing for Anticorrosion Based on Encapsulated Healing Agents

Daniel Crespy, Katharina Landfester, Johannes Fickert, and Michael Rohwerder

Abstract Although the protection of metals from corrosion appears to be a Sisyphean work, promising developments have recently been proposed in the literature. We present here some new strategies, in which traditional methodologies employed for corrosion protection are married with the concept of self-healing. Efficient anticorrosion properties can be achieved by the encapsulation of corrosion inhibitors and/or monomers and catalysts for self-healing reactions. Nanocontainers for anticorrosion comprise a shell that is responsive to stimuli induced by corrosion and a core containing the healing substance. We present here the requirements for their design, synthesis, and application in coatings for metal substrates. The important factors to be taken into account and future directions are also discussed.

Keywords Capsules • Corrosion protection • Nanocontainers • Redox-responsive • Self-healing

D. Crespy (✉)
Max Planck Institute for Polymer Research, Ackermannweg 10, 55128 Mainz, Germany

Vidyasirimedhi Institute of Science and Technology (VISTEC), School of Molecular Science and Engineering, Department of Material Science and Engineering, Rayong, Thailand
e-mail: crespy@mpip-mainz.mpg.de

K. Landfester and J. Fickert
Max Planck Institute for Polymer Research, Ackermannweg 10, 55128 Mainz, Germany

M. Rohwerder (✉)
Max Planck Institut für Eisenforschung GmbH, Max-Planck-Strasse 1, 40237 Düsseldorf, Germany
e-mail: rohwerder@mpie.de

Contents

1 Introduction

Corrosion is defined as the physicochemical interaction between a material and its environment that results in a change in properties of the material, which is often detrimental to the system it is part of. Corrosion of metals plays a crucial role in lifetime, reliability, and safety issues in microelectronics, construction, automotive, and aerospace applications, and is thus of significant economic and ecological importance [1–3]. Corrosion protection by coatings is a widespread and very effective way to prolong the lifetime of components. Such coatings can be metallic (e.g., zinc, nickel, or chromium coatings), organic (technically termed as primers or paints), or inorganic passivation coatings. Very often combinations are used.

The performance of organic coatings is often enhanced by inactive and/or active pigments. Inactive pigments mainly serve to enhance the barrier properties of the coatings, whereas active pigments can release corrosion inhibitors. This release of inhibitors from the standard pigments used in commercial paints usually occurs via leaching. However, leaching always occurs if the amount of water in the coating is high enough, regardless of whether there is a defect in the coating and corrosion takes place. Hence, the amount of pigment that has to be added to the coating matrix has to be quite high to ensure that enough inhibitor is stored inside the coating during the full targeted lifetime of the active corrosion protection. This is a serious problem, as can be seen by considering hexavalent chromium, which is probably the best corrosion inhibitor known so far. However, because of environmental concerns and its carcinogenic nature, the use of Cr^{6+} has been restricted and is already completely banned as corrosion inhibitor in several industrial sectors [4, 5]. Furthermore, many other inhibitors that are still in use might also be banned

in the future [4]. Hence, even when no corrosion is present, uncontrolled leaching of inhibitor into the environment, leading to pollution of the environment and a shortened lifespan for active corrosion protection, may become a serious problem for currently existing coatings containing active pigments.

This problem is the main incentive for the intense research on so-called smart self-healing coatings that is currently being carried out on a worldwide scale by a steadily increasing number of scientists. Ideally, such smart self-healing coatings should provide targeted delivery of corrosion inhibitors to the corrosion site only when active corrosion starts. In this review, the focus is solely on coatings that store the active agents in encapsulated form. The requirements for such coatings are:

1. Safe storage of the active agents for self-healing
2. Intelligent release
3. Inhibition of corrosion and, ideally, formation of a new organic coating at the defect
4. No further release when the corrosion has been successfully stopped

2 Requirements for Intelligent Self-Healing Coatings and Possible Triggers

Safe storage of inhibitors or self-healing agents by encapsulation can be achieved inside polymer capsules and, to some extent, inside the pores of microporous particles. These particles can be further encapsulated directly (e.g., by layer-by-layer modification with pH-sensitive polyelectrolyte multilayers) or indirectly without closing the pores by incorporation of the loaded microporous particles into either an inorganic sol–gel-based coating or an organic coating (see Sects. 4 and 5). For reported cases of storage inside microporous particles it is, however, questionable how long the loaded agents are really held inside the particles. We focus only on self-healing systems where the active agents are safely stored by encapsulation inside a polymer shell. Possibilities for encapsulation are discussed in more detail in Sect. 4. So far, for intelligent release of self-healing agents, mainly two different trigger systems are investigated, namely mechanical triggers and triggering by corrosion-induced pH change. Other possibilities will be also discussed in the following.

2.1 Mechanical Triggers

A mechanical trigger only activates capsules or other containers that are in the direct vicinity of a mechanical defect in the coating, such as a scratch. The capsules are opened by the mechanical rupture. Hence, very large capsules usually have to be used to ensure delivery of sufficient amounts of inhibitors or self-healing agents to the defect site. Usually capsules in the range of 100 μm are used, which is too large for most applications. This is discussed in more detail in Sect. 5.

2.2 pH change as Trigger

Triggering by a change in pH as a consequence of corrosion can, with time, spread from the corroding defect deeper into the coating and can thus activate capsules or other containers in a much larger volume of coating than a mechanical trigger could. Corrosion-induced release via pH, for instance, was reported for microporous particles, either through an increase in permeability of the pH-sensitive polyelectrolyte shells applied on the surface of the particles or through pH-induced degradation of the inorganic particle itself. For reliable long-term storage, pH-sensitive polymer capsules are of considerable interest.

However, a change in pH as trigger signal, although it can lead to release of a much higher amount of active agents than a mechanical trigger, is not perfect. The reason for this is that the change in pH strongly depends on the kind of metal (alloy) and on the environmental conditions under which the corrosive attack occurs. For instance, the change in pH is sensitively affected by whether the corrosive medium in the defect is continuously exchanged (e.g., by rain) or not. If the renewal rate of the corrosive medium is high, no significant pH change is expected. The change in pH also depends very crucially on the metal. In the defect sites, the pH is determined by the oxygen reduction reaction, the acidity of the dissolved metal cations, and access of CO_2 to the defect site. For iron and steel, the acidity of the iron cations means that only mildly alkaline values are to be expected (below pH 10), whereas zinc corrosion can lead to higher pH levels (pH 10 and higher [6]).

More important for triggering the release, however, is not the pH at the defect site, but the pH at the interface of the delaminating coating. Significant differences are observed, as shown schematically in Fig. 1 for different directly painted metals. On steel, corrosion-driven delamination of the organic coating proceeds as cathodic delamination (i.e., only oxygen reduction takes place at the interface between coating and metal), enabled by electrons supplied from the corroding defect site. This leads to an increase in pH at the interface. Because iron is passive at high pH, no buffering by metal cations released by an anodic counter-reaction occurs. Hence, the increase in pH can be significant, with values reaching pH 14 and more [7, 8]. This is different for galvanized steel. Zinc is not passive at high alkaline pH and hence zinc corrosion also occurs at the interface, releasing (mildly) acidic zinc cations. This buffers the increase in pH to maximum levels of around pH 12 [9]. On aluminum alloys on the other hand, as a result of the electronically non-conducting oxide layer, cathodic delamination is not possible and only anodic coating delamination occurs, as so-called Filiform corrosion (see, e.g., [10]). Here, alkaline pH levels are reached only on the intermetallic particles and generally in the Filiform tail, whereas acidic pH levels prevail in the active head of the filaments [10].

These aspects have to be considered if pH-sensitive polymer capsules are to be applied, and dedicated tests need to be carried out to ensure a sufficiently robust performance.

One interesting application field where pH-responsive capsules are probably the best choice is their incorporation into metallic coatings. Co-deposition of capsules

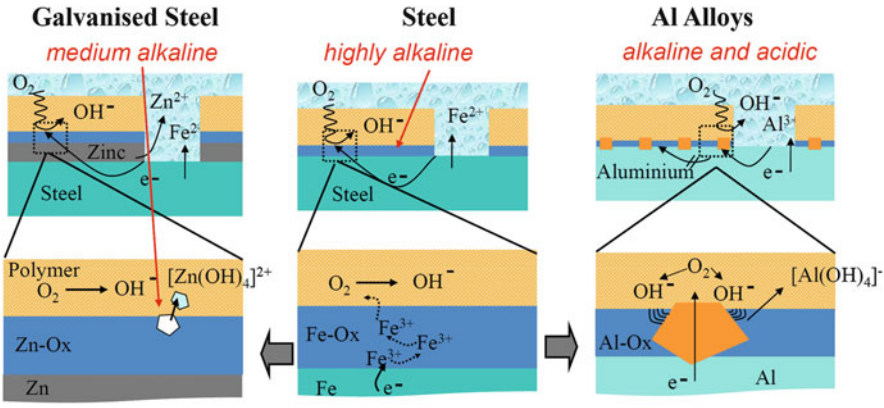

Fig. 1 Change in pH during delamination of organic coatings from different metals: *left*: zinc or galvanized steel, *middle*: steel, *right*: aluminum alloys. The oxides formed at the surface of zinc and iron are conductive and oxygen reduction can take place at the interface with the organic coating. The oxide on aluminum is insulating. In that case, Filiform corrosion occurs with acidic pH in the head and alkaline pH on the intermetallic particles (schematically sketched in dark orange).

together with the zinc coating during electrogalvanizing is of special interest. Electrogalvanizing baths in the steel industry normally have an acidic pH (usually pH ~2). Hence, capsules that are stable in this pH range and open at higher pH (ideally at neutral pH to ensure a robust and reliable performance) would be ideal. Strategies for co-deposition are discussed in the literature [11, 12]. A big advantage of choosing to store active agents inside the metallic coating is that the metallic coating is impermeable to air and water and, hence, even reactive substances can survive for a very long time.

2.3 Change of Potential: Redox-Active Capsules

While the change in pH as a consequence of corrosion is significantly different for different metals and can either increase or decrease, in all cases the corrosive attack leads to a substantial decrease in potential [7–10]. At the intact interface, the metal is passive and hence the corresponding potential more positive than at the actively corroding defect. Hence, a decrease in potential in response to the onset and spreading of corrosion in and from a defect site is the most reliable and most accurate trigger signal imaginable.

The first coating systems for self-healing that were investigated for smart release by a change in potential were conducting polymers. The main idea behind the use of conducting polymers in smart self-healing coatings is as follows: If an inhibitor anion is used as counter-ion for compensating the positive charges in the polymeric backbone, this inhibitor anion is safely stored inside the polymer as long as it is not reduced. If the potential decreases as a result of onset of corrosion, the conducting

polymer is reduced. As a consequence, stored anions are released. This idea was first proposed by Barisci et al. [13]. Kinlen and coworkers [14, 15] and Kendig et al. [16] were the first to show that anionic inhibitors can indeed be released from polyaniline-containing coatings applied on steel or aluminum when corrosion occurs. However, polyaniline can also release the anions as a consequence of pH increase and, in most cases, this was probably the main trigger. The first definitely pH-triggered release by conducting polymers was presented by Paliwoda-Porebska et al. with polypyrrole [17]. However, only anions can be stored in the bulk of the conducting polymers and the overall amount is quite low. Furthermore, release of anions can be inhibited by incorporation of cations [18–20]. Hence, other concepts are required, such as redox-active capsules, where the active agents are stored inside the capsules and the capsule wall changes permeability as a consequence of reduction. This is discussed further in Sect. 5.

2.4 Change in Ionic Strength

For completeness it should be mentioned here that another possible trigger signal being investigated is the change in ionic strength that might be induced as a consequence of corrosion. However, even more so than for a change in pH, a change in ionic strength is not a very reliable trigger because it is very dependent on the environmental conditions of the corrosion attack.

3 The Main Challenge: Release and Transport of Sufficient Amounts of Active Agents

The main challenge, besides safe storage and reliable release, is to be able to heal large defect sites and not just pinholes. If the defects are larger than pinholes, the growth of a new polymer coating at the defect requires significant amounts of self-healing agents to be released and transported to the defect site.

This is a non-trivial problem, but is usually completely neglected in research on smart coatings. In most (if not in all) publications that can be found in the literature on smart coatings for corrosion protection, the release occurs globally throughout the whole surface of the coating, and transport of the active species occurs through the electrolyte (see Fig. 2).

This is, however, not a very realistic scenario for later application. First, technical paints as they are used, for example, in the automotive industry, normally consist not just of one, but of several different coatings. Usually, special coatings are also applied on the top (e.g., to provide color and high scratch resistance). Second, in most cases it is very unlikely that the whole surface is immersed in electrolyte. It is more realistic to assume that only the defect site is covered by

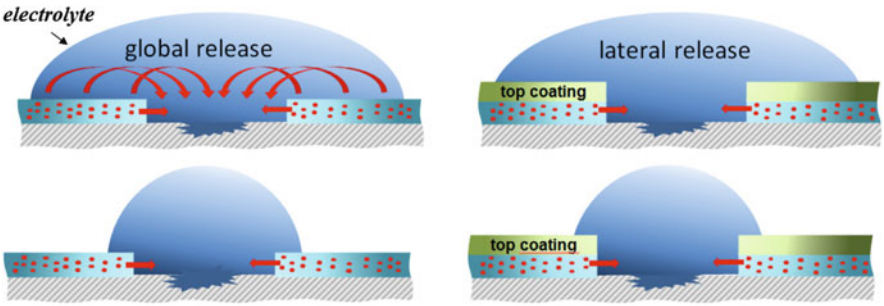

Fig. 2 Release of active agents from smart coatings to a defect site: four possible cases. *Top row* shows the situation for the case of full immersion. If there is no further coating on top of the smart coating, release can occur through the whole surface, otherwise only at the edges bordering to the defect. *Bottom row* shows the situation for the case that electrolyte is only in the defect. Here release is only at the edges, regardless of whether there is an additional top coat or not

electrolyte, because sites such as scratches generally remain wet for longer, as they take longer to dry. Additionally, defect sites have a high ionic strength once corrosion has started. Hence, the surface of the smart coating in contact with electrolyte is much smaller than usually investigated and might even be much smaller than the surface of the defect itself (see Fig. 2). This is a significant challenge that has to be taken more seriously than is currently the case.

To meet this challenge, systematic research on smart coating systems has to be carried out, involving investigation of trigger signal spreading, release kinetics, and the chemistry and kinetics of the self-healing reaction itself. The focus of current research is mainly on the encapsulation of suitable active agents, and so this is the emphasis of the following section. However, in the future more research on the transport of species is certainly very important.

4 Encapsulation Techniques

Capsules are obtained from emulsions when certain conditions are fulfilled. The interactions in a three-phase system are described in a simple theoretical model by Torza and Mason [21]. When two immiscible organic liquids 1 and 3 are mixed in an immiscible phase 2, several morphologies can be observed at equilibrium depending on the spreading coefficients S_i of the different liquids. The spreading coefficients are calculated with the interfacial tensions γ_{ij} between the different phases of the systems i, j, and k:

$$S_i = \gamma_{jk} - (\gamma_{ij} + \gamma_{ik}).$$

If $\gamma_{12} > \gamma_{23}$, three types of morphologies are possible: non-engulfing, partially

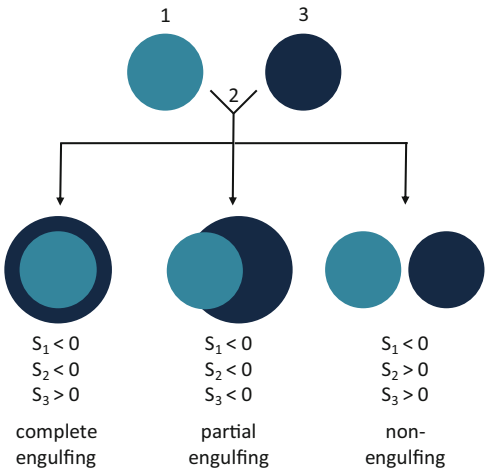

Fig. 3 Three equilibrium morphologies obtained by mixing three immiscible phases, as described by Torza and Mason [21]

engulfing, and completely engulfing, the latter being suitable for the creation of capsules (Fig. 3).

In practical cases, the surfactant and the nature of the liquids have predominant influences on the colloidal morphology [22]. Other important factors are the mobility of the polymer chains [23], the nature and amount of initiator and surfactant [24, 25], and the temperature [26, 27].

Because the thickness of the coatings for anticorrosion is usually in the micrometer range, large microcapsules are not suitable for such an application. Therefore, we focus a large part of our discussion on nanocapsules with sizes ranging from 50 to 500 nm.

4.1 Emulsion-Solvent Evaporation

Emulsion-solvent evaporation is a process that is used for preparing micro- and nanoparticles. It does not belong to the family of dispersion polymerizations because the polymer is not synthesized after emulsification, but before it. The process can be used for the preparation of nanoparticles from stable polymeric emulsions containing a solvent with a low boiling point in the dispersed phase [28]. Therefore, the system consists of a polymer solution that is emulsified in another immiscible liquid phase. The solvent of the polymer is evaporated from the droplets, and polymer nanoparticles are produced. The method is very versatile and can be applied to produce unconventional nanoparticles such as semiconducting polymer nanoparticles [29] or nanoparticles with very crystalline polymers [30]. The method allows fabrication of Janus nanoparticles [31–33], patchy particles [34], and so-called tricompartment particles (i.e., nanoparticles with two separated polymer domains and one inorganic domain) [33]. The requirement for

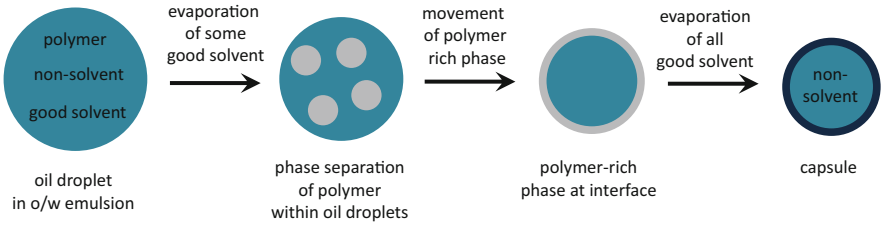

Fig. 4 Steps occurring inside droplets for the formation of capsules by emulsion-solvent evaporation [38]

preparation of nanoparticles with a controlled size is to prevent Ostwald ripening and coalescence between droplets during evaporation of the solvent. This can be realized by stabilizing miniemulsion droplets with a surfactant and an osmotic pressure agent [35, 36].

Other types of colloidal morphologies such as core–shell particles, which are of interest for the encapsulation of self-healing agents, can be also obtained by the emulsion-solvent evaporation method. The main difference with the formation of monolithic particles is that another high boiling point solvent is introduced to form the liquid core of the capsules. The low and high boiling point solvents are mixed and emulsified in the continuous phase with the help of a surfactant or stabilizers. Formation of the polymer shell is induced by phase separation inside the droplets (see Fig. 4). After evaporation of some solvent, polymer-rich droplets are created and move to the droplet surface, where they coalesce. After complete evaporation of the low boiling point solvent, a polymer shell is left [37, 38].

The formation of microcapsules by the emulsion-solvent evaporation method was first demonstrated by Vincent and colleagues [37, 38]. Large (>500 nm) capsules have been prepared with hexadecane or perfluorocarbons as liquid core [39–41]. Our group reported the preparation of aqueous dispersions of nanocapsules from many types of polymers and liquid cores. The general principle is shown in Fig. 5. The polymers used to build the shell of the nanocapsules were simple homopolymers such as poyl(methyl methacrylate) [42], polyvinyl formal [43, 44], poly(L-lactide), poly(vinyl cinnamate), polyphenylene oxide, and poly (vinyl acetate) [45]. The introduction of hydrophilic groups in random copolymers mainly composed of hydrophobic moieties was found to be favorable for the formation of nanocapsules because of the lowering of the interfacial tension between the aqueous continuous phase and the copolymer [46]. When block copolymers were employed, peculiar morphologies such as Janus particles [47], onion-like structures [47], and patchy nanoparticles [47–49] were formed. Note that the emulsion-solvent evaporation method can be also applied in nonaqueous inverse emulsions, that is, in emulsions with a polar dispersed phase (formic acid [50] or hexafluoroisopropanol [51]) dispersed in an apolar continuous phase (cyclohexane [50] or decalin [51]). The encapsulated liquid cores were alkanes [42, 45–48], halogenoalkanes [45], tertiary amines [44], silicones [45, 49], or fluorinated substances [45]. Payloads such as dyes can be dissolved in these liquid cores

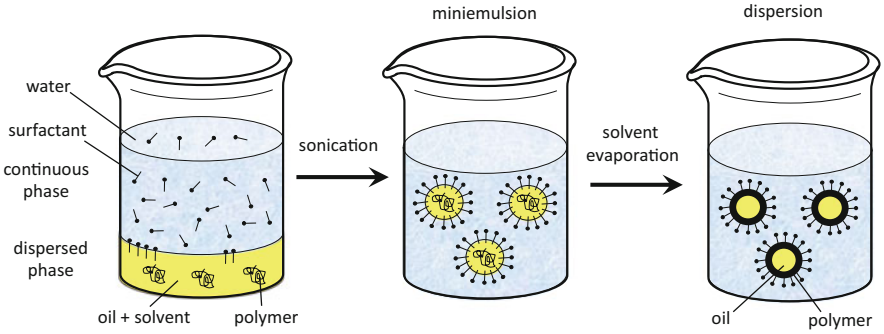

Fig. 5 Formation of nanocapsules by miniemulsion solvent evaporation technique

[42, 46, 48]. The method was employed to encapsulate low molecular weight monomers and catalytic self-healing agents [46], oligomers for step-growth polymerizations [45, 49], and polymers for self-healing reactions based on click chemistry [43].

4.2 Interfacial Polymerization

The surface of emulsion droplets can be also used as a template for the reaction between monomers dissolved in the dispersed phase and monomers dissolved in the continuous phase. Core–shell nanoparticles were obtained by alternating copolymerization of hydrophilic vinylethers with hydrophobic maleate in emulsions [52, 53]. The alternating copolymerization was the only polymerization occurring, because homopolymerization of the monomers was not possible. Polyadditions and polycondensations were also possible by employing monomers of different polarity. Hydrophilic monomers with hydroxyl and amine groups were polymerized with hydrophobic monomers containing isocyanate and thioisocyanate groups to yield polyurethane [54–57], polyurea [57], and polythioura nanocapsules [57]. The same method can be used to crosslink polymers such as dextran [57], poly (ethylene imine) [57], starch [57], or chitosan [58] at the interface of the droplets. For example, the monomer triethylene glycol dimethacrylate could be successfully encapsulated via this method [56]. Microemulsions can also be used as templates for the formation of nanocapsules, as demonstrated by the polymerization of dopamine to encapsulate octadecylamine in direct microemulsions [59].

4.3 *Internal Phase Separation Induced by Polymerization*

Instead of phase separation inside droplets triggered by evaporation of a solvent (see Sect. 4.1), the formation of nanocapsules can be triggered by a polymerization reaction. Indeed, if the monomer is miscible with the solvent that builds the liquid core but the formed polymer is not soluble in this solvent, a capsular structure can be obtained provided that it is the thermodynamically favorable morphology. One prerequisite for this method is that the yield of the polymerization should be very high to avoid the presence of unreacted monomer in the capsules. Most of the examples found in the literature are produced by miniemulsion polymerization because it is a process that can be used at high temperature [60, 61] and in the absence of water [62, 63], and yields stable nanodroplets with controlled size [64]. In aqueous miniemulsions, the dispersed phase is usually composed of a hydrophobic nonpolymerizable oil and a monomer. During the polymerization, the polymer precipitates at the droplet interface (see Fig. 6). Free-radical polymerization in oil-in-water miniemulsions were used to fabricate nanocapsules with alkanes [65–67] or monomers as liquid core for ring-opening metathesis polymerization (ROMP) [68, 69]. The formation of the polymer shell was facilitated by copolymerization with hydrophilic comonomers to reduce the interfacial tension between the polymer shell and the aqueous phase [69]. The droplet interface also served as template for oxidative polymerization. In this case, the oxidizing agent that triggers the polymerization is added to the continuous phase. Polyaniline [70, 71] and polypyrrole [70] nanocapsules could be synthesized by this method and were used to encapsulate silicones terminated with amine and carboxylic acid groups for self-healing.

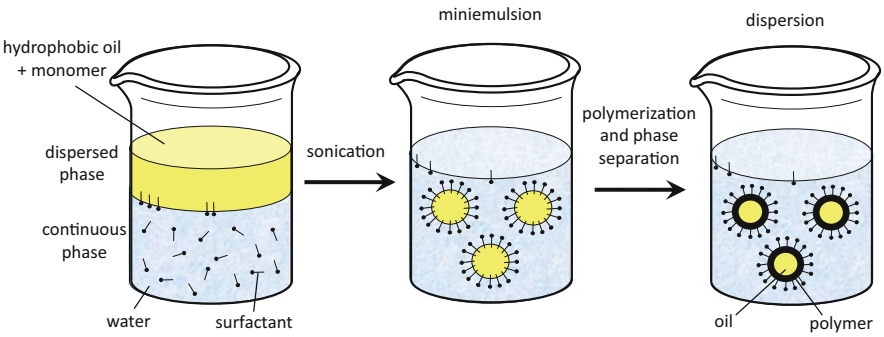

Fig. 6 Formation of nanocapsules by polymerization in oil-in-water miniemulsions

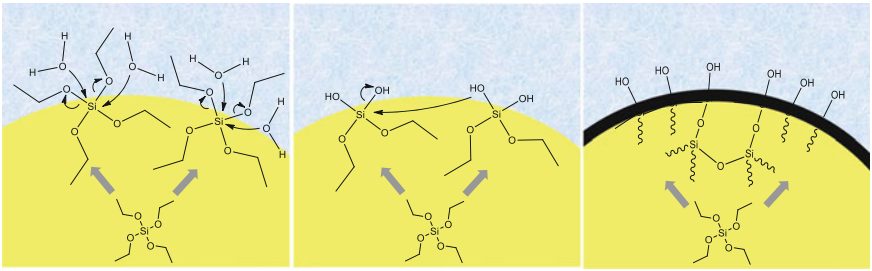

Fig. 7 Sol–gel process occurring at the interface of emulsion droplets. Tetraethoxysilane (TEOS) is emulsified and reacts with water present in the continuous phase

4.4 Sol–Gel Processes

Inorganic capsules can be easily synthesized by hydrolysis and condensation of emulsified alkoxysilanes. They are of interest because their mechanical properties are better than those of the polymer nanocapsules [72]. The reaction proceeds via a classical sol–gel process, whereby the hydroxysilane, $Si(OH)_4$, is first generated by hydrolysis of the alkoxysilane, followed by reaction between the silanol groups and elimination of water (see Fig. 7). The system was first demonstrated to be successful for the encapsulation of alkanes in nanocontainers [73]. Monomers and catalysts for self-healing reactions based on ROMP were encapsulated by this method [74, 75]. The catalysts was found to be active after formation of the silica shell and could be encapsulated as a solution in the liquid core, rendering it mobile for further self-healing reactions after rupture of the shell [74]. Microemulsions were also used to encapsulate the corrosion inhibitor 2-mercaptobenzothiazole (MBT) in silica nanocontainers [76]. The sol–gel process was used to synthesize cerium molybdate nanocontainers of ~150 nm that were subsequently loaded with corrosion inhibitors such as 8-hydroxyquinoline and 1-*H*-benzotriazole-4-sulfonic acid [77].

4.5 Layer-by-Layer Technique

Core–shell nanocapsules with a polyelectrolyte shell can be synthesized by the layer-by-layer technique [78, 79]. Polyelectrolytes of opposite charges are alternately deposited on spherical substrates such as polystyrene [80], melamine formaldehyde [81], or silica particles [79]. Afterwards, the core is dissolved and capsules are formed (see Fig. 8). The layer-by-layer method was used successfully to encapsulate the corrosion inhibitors benzotriazole [82], 2-methylbenzothiazole [83], and MBT [83].

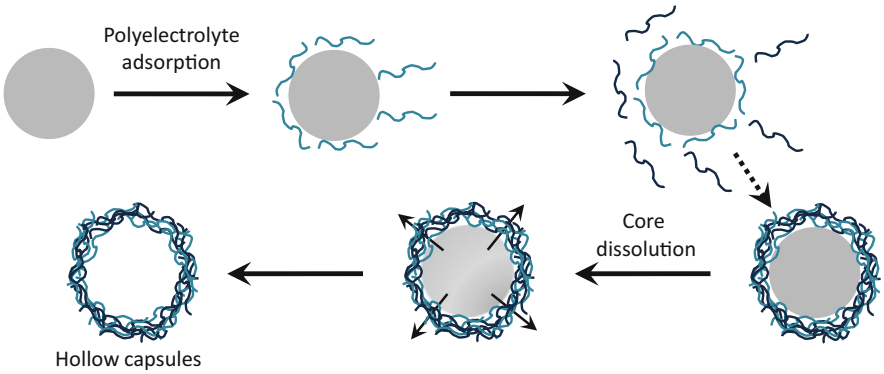

Fig. 8 Formation of capsules by the layer-by-layer technique

4.6 Functionalized Nanocapsules

Because nanocapsules for anticorrosion and self-healing are only useful when they are embedded in coatings, it is mostly necessary to functionalize their surfaces to allow their dispersion in the coating. Functionalized polymer nanocapsules can be synthesized by the polymerization of functional monomers or by post-functionalization of the nanocapsules. Various hydrophilic functionalities were introduced via free-radical copolymerization in oil-in-water miniemulsions [64, 69]. Functional comonomers, bearing carboxylic acid, amine, sulfonate, phosphate, hydroxyl, oligoethylene glycol, or phosphonate groups, acted as structure-directing agents for the formation of capsules. Similar nanocapsules can be achieved by first copolymerizing a hydrophobic monomer with a functional hydrophilic comonomer and then using the purified copolymer in the emulsion-solvent evaporation process, as described in Sect. 4.1 [46]. The surfactant can be also used as a comonomer when bearing vinyl bonds and functional molecules with, for instance, phosphate groups [65]. Interfacial step-growth polymerizations lead automatically to functional nanocapsules because the end groups of the polymers correspond to the functional group of the monomer in excess. Indeed, nanocapsules with amine or hydroxyl functional groups were produced [57]. An alternative is to use monomers bearing other functionalities that do not react in the polymerization reaction, for instance, L-arginine with two amino groups for polyaddition and one carboxylic acid for functionalization of the shell [57]. Functionalized silica nanocapsules can be synthesized by emulsifying functionalized alkoxysilanes bearing thiol [74] or tetrasulfide groups that do not interact with the sol–gel reaction [75].

Post-functionalization of nanocapsules is an alternative to in-situ formation of functionalized nanocapsules (see Table 1). Post-modification of silica nanocapsules is suitable for introducing amino groups because they catalyze the condensation of hydrolyzed alkoxysilanes and can therefore destabilize the colloidal system [74, 84]. Similarly, silica/titania nanocapsules can be functionalized with

Table 1 Different examples of post-functionalization of functional nanocapsules

Functionality	Functional molecules	Shell material	Post-functionalization	Reference
Thiol	3-Mercaptopropyl trialkoxysilane	SiO_2	Addition of functional comonomer	[74]
Amine	3-Aminopropyl trialkoxysilane	SiO_2	Addition of functional comonomer	[74, 84, 85]
Carboxyl	Carboxylethylsilanetriol sodium salt	SiO_2	Addition of functional comonomer	[85]
Vinyl	3-(Trimethoxysilyl)propyl methacrylate	SiO_2	Addition of functional comonomer	[85]
Carboxyl/amine	Monochloroacetic acid/tolylene 2,4-diisocyanate	Polyurethane/polyurea	Hydrolysis followed by carboxymethylation	[86]
Carboxylic/disulfide	Methacrylic acid/cystamine	Crosslinked poly(methyl methacrylate-*co*-methacrylic acid)	Crosslinking by addition of functional monomer	[87]
Carboxylic/vinyl	Methacrylic acid/2-aminoethyl methacrylate	Poly(methyl methacrylate-*co*-methacrylic acid)	Esterification	[88]

3-aminopropyl triethoxy silane, carboxylethylsilanetriol sodium salt, and 3-(trimethoxysilyl)propyl methacrylate to yield nanocapsules with amine, carboxyl, and vinyl groups, respectively [85]. Polyurethane/urea nanocapsules were hydrolyzed and subsequently functionalized with carboxylic acid by carboxymethylation [86]. Poly(methyl methacrylate-*co*-methacrylic acid) nanoparticles were decorated with vinyl groups after coupling reactions with 2-aminoethylmethacrylate [87]. When these nanoparticles were crosslinked with cystamine, disulfide bonds could be introduced inside the shell [88].

5 Stimuli-Responsive Capsules

The capsules produced by the processes described in Sect. 4 are all potentially subjected to mechanical rupture when the coatings into which they are embedded are damaged. Blaiszik et al. reported four different types of healing mechanisms for self-healing materials based on capsules (see Fig. 9) [89]. The caspule/catalyst approach (Fig. 9a) was first popularized in a landmark paper published by White et al. [90]. Urea-formaldehyde microcapsules were used to encapsulate dicyclopentadiene and then embedded in an epoxy matrix. Because a Grubbs catalyst was dispersed in the matrix, ROMP could occur after mechanical rupture of the microcapsules. The newly formed polymer partially filled the fractured matrix to restore its mechanical properties (Fig. 10). The ROMP reaction has the

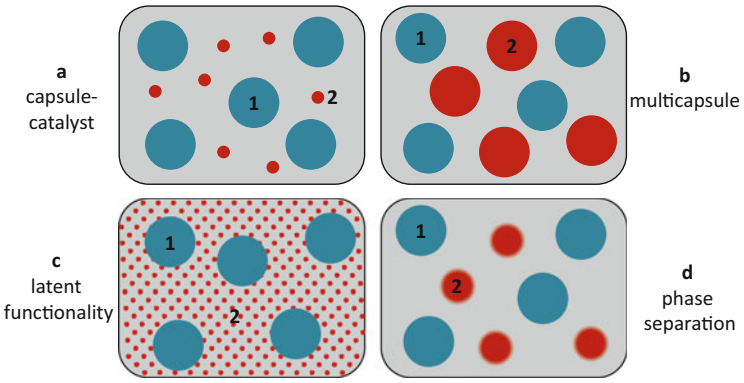

Fig. 9 Capsule-based self-healing materials with two components, **1** (*blue*) and **2** (*red*), can be divided into four categories. (**a**) Capsules/catalyst: The healing agent **1** is encapsulated and the catalyst **2** is dispersed in the matrix. (**b**) Multicapsule: Both healing components **1** and **2** are encapsulated. (**c**) Latent functionality: The healing reaction occurs through reaction between the encapsulated healing agent **1** and reactive groups **2** within the matrix. (**d**) Phase separation: The healing agent **1** is encapsulated and **2** is phase separated within the matrix phase [88]

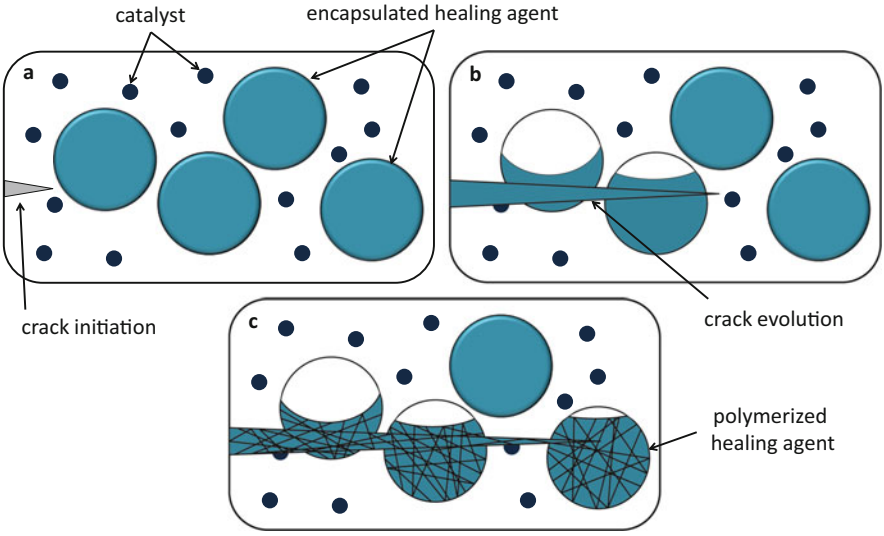

Fig. 10 Self-healing based on the capsule/catalyst concept. (**a**) The catalyst and the capsules containing the healing agent are dispersed in a matrix, which is subjected to mechanical damage. (**b**) The matrix and therefore the capsules are ruptured. (**c**) The healing agent is released from the capsules, reacts with the catalyst, and partially fills the crack [90]

advantages of yielding polymers at room temperature in a quantitative and very fast manner. However, any type of polymerization reaction (i.e., ionic, free radical, controlled radical, and step-growth) can be used as a self-healing reaction, as shown in Table 2.

Table 2 Selected self-healing reactions and reagents employed for capsule-based self-healing materials

Self-healing reaction	Self-healing agent 1	Self-healing agent 2	Catalyst	Reference
ROMP	Dicyclopentadiene 5-ethylidene-2-norbonene		Grubbs' catalysts tungsten(VI) chloride	[46, 68, 69, 74, 90, 91]
Anionic polymerization	Epoxy		$CuBr_2$(2-methylimidazole)$_4$	[92, 93]
Cationic polymerization	Epoxy		Boron trifluoride diethyl etherate $(C_2H_5)_2O{\cdot}BF_3$	[94, 95]
Polyaddition	Epoxy	Mercaptan	Amine	[96]
Polyaddition	Epoxy	Amine		[97–101]
Polyaddition	Thiol	Isocyanate	Amine	[102]
Polyaddition	Thiol	Epoxy/ene	2,4,6-Tris(dimethylaminomethyl) phenol	[103]
Polyaddition	Isocyanates	H_2O		[104]
Polycondensation	Silanol-terminated polydimethylsiloxane	Polydiethoxysilane	Di-*n*-butyltin dilaurate	[105, 106]
			Dimethyl dineodecanoate tin	
Polycycloaddition click-reaction	Polymeric azide	Alkyne	Bromo-tris(triphenylphosphine)-copper(I)-catalyst $Cu^{I}Br(PPh_3)_3$	[107]
Hydrosilylation	Hydrosiloxane copolymer	Vinyl-terminated polydimethylsiloxane	Pt catalyst	[108, 109]
Michael polyaddition	Bismaleimide	Amine		[110]
		Thiol		
Controlled radical polymerization	Glycidyl methacrylate	Living PMMA (ATRP)		[111, 112]
		Living PS (RAFT)		

Note that the table is not meant to be comprehensive

Another type of healing, occurring in the presence of water or moisture, was proposed by Garcia and coworkers [113, 114]. A silyl ester was encapsulated in microcapsules embedded in coatings and could be released by damage to the coating. The produced silanol and oleic acid adhered to the metal surface and passivated it by forming a hydrophobic barrier. Because a change in pH value and variation in electrochemical potential occur at the onset of corrosion, in the next sections we mainly discuss materials that can respond to these variations. Other types of stimuli-responsive nanocapsules have been described elsewhere [115, 116].

5.1 pH-Responsive Capsules

pH-responsive capsules are synthesized either with polymer or inorganic materials that degrade or dissolve upon pH change or with polymers containing pH-responsive units. The encapsulated substances are either reagents for self-healing polymerization reactions or corrosion inhibitors. The latter category is by far the most reported strategy in the literature. One advantage is that a monocomponent system (i.e., with one type of container to encapsulate the inhibitor) is sufficient to provide self-healing properties.

Ce(III) was loaded into zeolite particles and released at low pH during corrosion of an aluminum substrate [117]. The cerium then precipitated in the cathodic areas and hindered further corrosion. Silica nanocapsules loaded with the corrosion inhibitor MBT displayed salt concentration- and pH-dependent release kinetics [76]. Nanocontainers embedded in a coating were found to be suitable for hindering corrosion of aluminum to a larger extent than coatings containing the same non-encapsulated inhibitor. Bistable pseudorotaxanes were used as nanovalves to regulate the pH-dependent release of inhibitors from mesoporous silica nanocapsules. Payloads could be released from the nanocapsules either by lowering or increasing the pH value of the surrounding medium (see Fig. 11) [118].

Layer-by-layer assemblies of weak polyelectrolytes are automatically pH-responsive and, therefore, represent a suitable class of materials for release of payloads triggered by pH change. Such layers are coated onto inorganic spherical substrates that can be loaded with inhibitors [119–123]. Release of the corrosion inhibitor benzotriazole was triggered by the change in pH value induced by corrosion of an aluminum alloy [119].

Inorganic and organic nanocontainers can also be designed to dissolve in response to an increase or decrease in pH. Hydroxyapatite microparticles were impregnated with different corrosion inhibitors [salicylaldoxime, 8-hydroxyquinone, cerium(III), and lanthanum(III)]. The particles were dispersed in a silica–zirconia sol–gel film on an aluminum alloy substrate. The authors reported that local acidification ($pH < 4$) at the aluminum anode could trigger

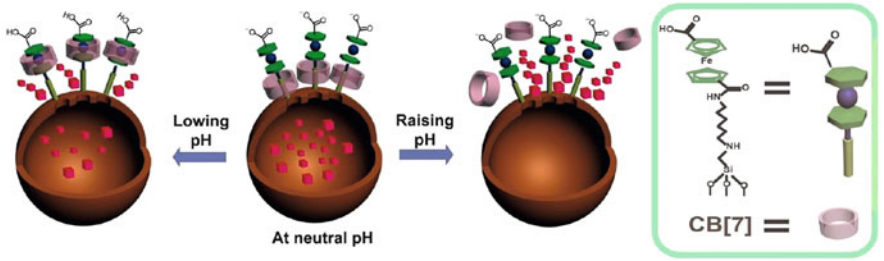

Fig. 11 Pseudorotaxane formed by curcubit[7]uril (*CB[7]*) and ferrocene carboxylic acid serves as a gate to regulate the pH-responsive release of payloads from mesoporous silica nanocapsules [118]

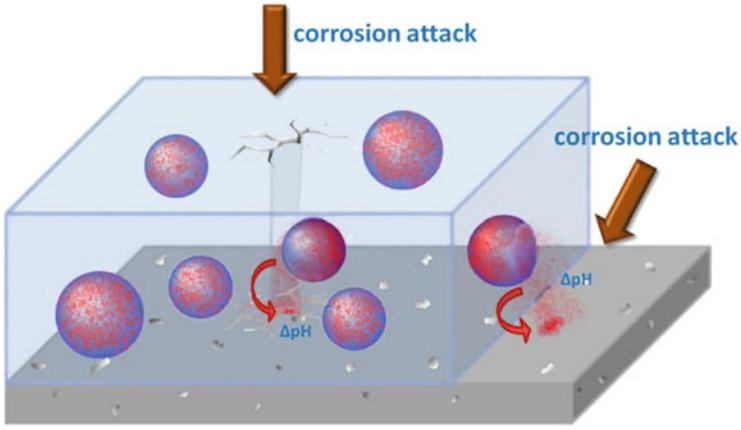

Fig. 12 Epoxy coating containing pH-responsive nanocapsules on a metal substrate. Upon corrosion, the pH decreases locally and the nanocapsule shells dissolve, releasing the encapsulated corrosion inhibitor [129]

release of the inhibitor because of dissolution of the hydroxyapatite crystals [124]. The corrosion was significantly hindered in the presence of loaded microparticles, as measured by electrochemical impedance spectroscopy. Similar systems were created using layered double hydroxides [125–127] or calcium carbonate containers [128], which also decompose after acidification. The nanocontainer shell was composed of a copolymer of uncharged methacrylates and dimethylaminoethylmethacrylate and could be also dissolved at lower pH to release the inhibitor 8-hydroxyquinoline (Fig. 12) [129].

An alternative to these systems is the use of containers that can swell in response to a change in pH. Such containers could be synthesized by in situ desilylation of a polymer in miniemulsion [130]. The shell could be swollen by an increase in pH and was efficiently used in coatings for the release of monomers for ROMP during corrosion of zinc.

5.2 *Redox-Responsive Capsules*

Redox-responsive nanocontainers for anticorrosion were designed by forming the shells of the containers from a polymer that changes its chemical properties or by introduction of chemical units into the shell that can be cleaved by a change in redox potential. Because reduction occurs at the onset of corrosion, the material chosen should be reactive upon electrochemical reduction. Polyaniline and polypyrrole were synthesized by oxidative polymerization in miniemulsion (see Sect. 4.3) and displayed a permeability for payloads that was dependent on the oxidation state of the polymer shell [70]. In another approach, the corrosion inhibitor MBT was bound to a methacrylate via a disulfide bond to yield a monomer that can be cleaved by reduction of the disulfide linkage [49, 131]. When the monomer was copolymerized randomly with the hydrophilic *N*-vinylpyrrolidone, nanocontainers could be created by self-assembly in water [131]. The obtained containers could encapsulate a dye that was released by reduction of the disulfide bond. The same monomer was copolymerized with methyl methacrylate by reversible addition fragmentation transfer (RAFT) polymerization to yield hydrophobic block copolymers that were used to build a shell by the emulsion-solvent evaporation method described in Sect. 4.1. Reduction of the disulfide bonds of the shell resulted in release of the corrosion inhibitor MBT, together with a reactive oligomer used as self-healing agent that was encapsulated in the core of the nanocontainers [49].

6 Recent Breakthroughs

In this section, we discuss two recent breakthroughs in the field of smart coatings for corrosion protection in which some of the above-discussed capsule systems have been successfully applied.

In the discussion on possible triggers for release (Sect. 2), it was mentioned that the best trigger might be the decrease in potential at the onset of corrosion. One possibility for achieving smart release triggered by this potential change is encapsulation of active agents in capsules of conducting polymer. In Sect. 5, the preparation of polyaniline (PANI) capsules is described. These have recently been successfully applied for the smart corrosion protection of zinc [132], which is relevant for the technically very important protection of galvanized steel. For this, a corrosion inhibitor for zinc, 3-nitrosalicylic acid (3-NisA), was encapsulated into PANI capsules [70]. These inhibitor-loaded capsules were incorporated into a coating matrix of poly[(vinyl butyral)-*co*-(vinyl alcohol)-*co*-(vinyl acetate)] (PVB), a widespread model coating matrix used for fundamental corrosion investigation. The corrosion performance of this coating was investigated by means of a scanning Kelvin probe, which allows measurement of the electrode potential, even through an organic coating, and thus is able to monitor the corrosion-driven delamination of

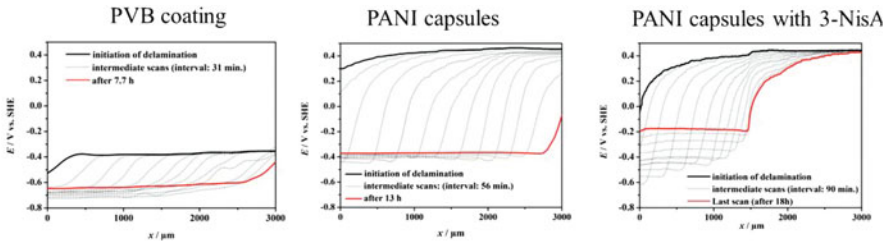

Fig. 13 *Left* to *right*: Delamination profiles, starting at the border to the defect, for pure PVB coating, PVB coating with PANI capsules, and PVB coating with inhibitor 3-nitrosalycilate (*3-NisA*)-loaded PANI capsules. Note the higher potential in the intact coatings with incorporated PANI capsules compared with the plain PVB coating. This is a result of the high redox potential that is correctly measured due to the conducting spacer particles used. Note also the increase with time of the potential in the delaminated area for PVB with inhibitor-filled PANI capsules. This indicates passivation in the defect site and leads to the observed inhibition of further delamination [132]

an organic coating in situ. Site scans into the initially still intact coating area were made from an artificially prepared corroding defect. The results were compared with the delamination performance of two reference coatings, a pure PVB coating and a PVB coating containing PANI capsules without the inhibitor.

As can be seen in Fig. 13, delamination of the pure PVB coating, which is characterized by polarization of the high potential of the intact (passive) interface towards the corrosion potential of the zinc, proceeds very fast (about 3 mm in 7 h) and shows no tendency to stop. For the PVB coating containing PANI capsules without the inhibitor, a similar process, although slightly slower, is clearly visible. The higher potential in the intact area is a result of the high potential of the polyaniline capsules. It has to be noted here that the capsules were specially modified to ensure the necessary electronic contact with zinc [132], because conducting polymers tend to form an insulating interfacial layer with conducting polymers [133, 134]. The performance of the coating containing the inhibitor-loaded PANI capsules, however, shows a strikingly different behavior. Initially, delamination sets in as usual, but then the potential in the already delaminated area quickly increases again and the delamination progress slows down until it nearly stops. Measurements of the corrosion potential in the defect site similarly show that the corrosion potential increases into the passive range of zinc, demonstrating the successful potential-triggered release from the capsules into the defect.

Not only successful release was demonstrated in the paper by Rohwerder and colleagues [132], but also that the PANI capsules are switchable (i.e., the PANI capsule wall becomes impermeable again when the potential increases again). Thus, no further release occurs when corrosion is successfully stopped, in agreement with the requirements defined in Sect. 1.

This was a major success, but the main target is not only to passivate the defect site, but also to form a new coating there. As discussed in Sect. 3, the main challenge is to activate a sufficient amount of self-healing agents such that

sufficient amounts reach the defect site. Such a coating system capable of self-healing relatively large defect sites was successfully prepared using pH-responsive capsules [130]. For the self-healing reaction, ROMP was chosen for achieving a real self-healing performance. The catalyst was stored in pH-responsive capsules incorporated into the zinc coating (see Sect. 2), and the monomer was stored inside pH-responsive capsules incorporated in a PVB coating. By corrosion-induced release of catalyst from capsules stored in the zinc coating and, likewise, corrosion-triggered release of monomer from capsules stored in the organic coating, a new polymer film was targeted to form in the defect site [130].

Successful self-healing of coatings by ROMP has already been reported [89, 90]. However, in these works the trigger is simply mechanical rupture of the large capsules by mechanical damage. Furthermore, only the self-healing agent was encapsulated and the solid catalyst was dispersed in the coating matrix (i.e., a corrosion-sensitive trigger was not used nor storage suitable for extended long-term performance). Although in a later work the catalyst was also encapsulated [105], this was only inside the organic coating where there is no reliable protection from air and water. Furthermore, the capsules were in the 100 μm size range (i.e., not applicable for most cases).

In the coating system presented by Tran et al. [130], both catalyst and monomer were encapsulated into poly(styrene-*stat*-methacrylic acid) (PSMAA) capsules, which were synthesized by the emulsion-solvent evaporation process (see Sect. 4.1). These capsules are stable at low pH, but disrupted at higher pH by the high negative charge density at their surface caused by deprotonization.

The catalyst-filled capsules to be co-deposited during electrogalvanization were surface-modified with cystamine. The choice for this modification was based on the experiences discussed by Khan and coworkers [11, 12]. Thus a 10 μm zinc coating with incorporated surface-modified pH-responsive nanocapsules (of about 3–4 vol %) filled with catalyst could be successfully electrodeposited.

The organic nanocomposite coating consisted of pH-responsive PSMAA nanocapsules filled with monomer embedded in PVB matrix and was applied to a total thickness of approximately 20 μm. As monomer, the norbornene derivative dicyclopentadiene (DCPD) was chosen because of its high tolerance to oxygen and water, which is why it can be stored in the organic coating, in contrast to the more sensitive catalyst [135].

Successful self-healing of a macroscopic defect by this coating system was demonstrated by the formation of a new polymer film on the exposed metal surfaces in the scratch (see Fig. 14). Most surprisingly, the newly formed polymer film seemed to be free of defects, even free of tiny pinholes. This was concluded from the fact that the corrosion potential in the defect showed a significant increase into the passive range of zinc (see also Fig. 14). If a significant number of pinholes were still active, they would dominate the corrosion potential of the defect and cause a significantly lower corrosion potential. This was not the case, which demonstrates surprisingly good performance of the self-healing.

However, although coverage of the defect was obviously very good, the thickness of the formed polymer film was quite low, about 100 nm. This draws attention

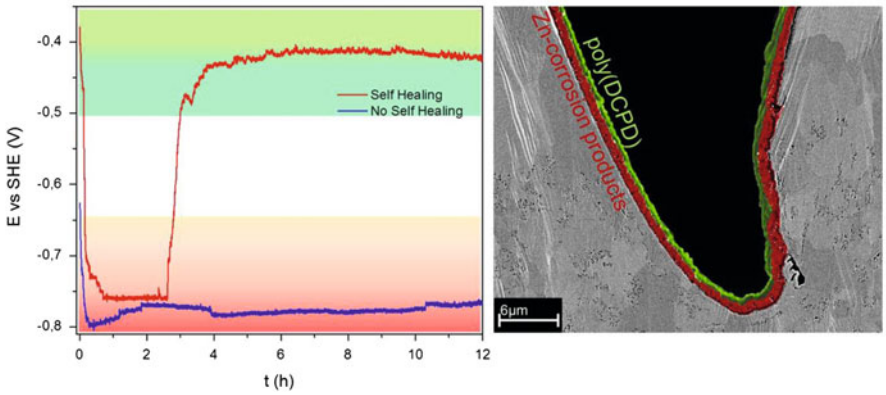

Fig. 14 *Left*: Corrosion potential of the defect site as a function of time. *Red curve* shows how, in the case of application of the self-healing system, the potential suddenly increases after about 2 h of corrosion, as a result of the onset of the self-healing reaction. *Blue curve* shows the coating reference without self-healing capability. *Right*: Cross-section of the tip region of the scratch inflicted into the coating. The surface of the scratch is covered by a thin film of zinc corrosion products (*shaded red*), covered by the thin new (DCPD) polymer film (*shaded yellow*). Identification of both the zinc corrosion product and the polymer film was carried out using micro-Raman investigations [130]

to the key problem that still needs to be solved: the limited amount of monomers released from such coatings. This is a similar problem to that found in other works, for example, where the focus is on passivation of the defect by inhibitors [17, 132]. In these two works, the trigger signal (i.e., the delamination) needed to spread quite deeply into the coating (1–2 mm) before enough inhibitor was released into the defect site to cause targeted passivation. In one case, the overall amount of inhibitor stored in the coating was relatively low, as the inhibitor was only stored as counter-anion in the polypyrrole matrix [17] and the low release rate was therefore not surprising. In the other case, the storage was inside polyaniline capsules [132] and much faster defect passivation was expected as a result of the much higher amount of inhibitor stored in the coating. However, the choice of inhibitor and other active agents for encapsulation was (and still is) limited to substances that are not too hydrophilic (in the mini- or microemulsion process the encapsulated phase is hydrophobic; see Sect. 4). This is a subject of intense current research.

Another problem that became quite obvious in the work by Tran et al. [130] is the role of self-healing at the delaminated (or delaminating) interface. The concept of fast signal spreading by delamination only has a real chance for technical application if self-healing not only occurs at the initial defect site, but also at the delaminated interface. However, if self-healing at the interface occurs too quickly, then the signal spreading by delamination is inhibited and release into the original defect site is insufficient to achieve self-healing of the defect. This was also found in the work by Tran et al. [130]. As a result of such fast healing at the interface, the defect site stays active (i.e., continues to corrode) while delamination is

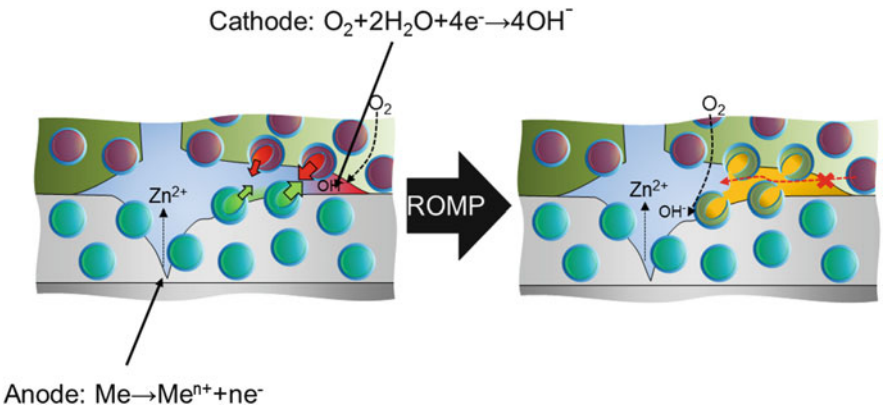

Fig. 15 If the self-healing reaction is too fast at the delaminating interface, the self-healing agents do not reach the defect site. This is shown here for the case of pH-induced release. At the delaminating interface, the main reaction is oxygen reduction, which increases the pH at the interface and leads to release of monomer from the pH-sensitive capsules in the organic coating. At these high pH levels, zinc is not stable and slowly corrodes, setting free the capsules stored in the zinc coating, which release their content (i.e., the catalyst). If the polymerization sets in too fast at the interface, the onset of this self-healing impedes further release into the defect site, which then continues to corrode and is not healed

significantly slowed (see Fig. 15). Although this inhibition of delamination by immediate self-healing at the interface is an impressive achievement, the self-healing of large defects should always be the target of research on smart self-healing coatings.

This example shows that research on self-healing coatings has to go far beyond encapsulation and triggered release. One possibility for prevention of this immediate self-healing is to look for polymerization reactions that do not take place at the high pH levels typically prevailing at a delaminating interface (see Sect. 2). Then, the self-healing agents could reach the defect site and first seal it. When the defect is healed, then the typical galvanic element between defect (anode) and delaminating interface (cathode) is stopped and, consequently, the pH at the interface drops, leading ideally to onset of self-healing there also. This still requires intense research.

As a faster solution, a delay in self-healing at the interface can be achieved by preventing release of catalyst into the interface region at the early stage of corrosion by applying an additional catalyst-free buffer layer on the catalyst-containing zinc coating [130]. Hence, initially no catalyst is released at the interface, but only at the scratch. Here, the catalyst penetrates through the organic coating and the buffer layer, leading finally to observed self-healing of the scratch (Fig. 14).

This observation shows that self-healing reactions need to be designed in such a way that at the delaminating interface they do not take place immediately, but only later when the original defect site (from where the delamination originated) is healed.

References

1. Gramberg U (1996) Werkst Korros Mater Corros 47:139
2. Lifset RJ, Eckelman E, Harper M, Hausfather Z, Urbina G (2012) Sci Total Environ 417:138
3. Markley T, Dligatch S, Trinchi A, Muster TH, Bendavid A, Martin P, Lau D, Bradbury A, Furman S, Cole IS (2010) Corros Sci 52:3847
4. Council of the European Union (2006) Regulation (EC) No 1907/2006 of the European Parliament and of the Council of 18 December 2006 concerning the Registration, Evaluation, Authorisation and Restriction of Chemicals (REACH), establishing a European Chemicals Agency. 2006R1907—EN—09.10.2012—014.001. Off J Eur Union L324:1–516
5. Sinko J (2001) Prog Org Coat 42:267
6. LeBozec N, Thierry D, Rohwerder M, Persson D, Luckeneder G, Luxem L (2013) Corros Sci 74:379
7. Leng A, Streckel H, Stratmann M (1999) Corros Sci 41:547
8. Leng A, Streckel H, Stratmann M (1999) Corros Sci 41:579
9. Fürbeth W, Stratmann M (2001) Corros Sci 43:207
10. Senöz C, Rohwerder M (2011) Electrochim Acta 56:9588
11. Khan TR, Erbe A, Auinger M, Marlow F, Rohwerder M (2011) Sci Technol Adv Mater 12:055005
12. Khan TR, Vimalanandan A, Marlow F, Erbe A, Rohwerder M (2012) ACS Appl Mater Interfaces 4:6221–6227
13. Barisci JN, Lewis TW, Spinks GM, Too CO, Wallace GG (1998) J Intell Mater Syst Struct 9:723
14. Kinlen PJ, Silverman DC, Jeffreys CR (1997) Synth Met 85:1327
15. Kinlen PJ, Menon V, Ding Y (1999) J Electrochem Soc 146:3690
16. Kendig M, Hon M, Warren L (2003) Prog Org Coat 47:183
17. Paliwoda-Porebska G, Stratmann M, Rohwerder M, Potje-Kamloth K, Lu Y, Pich AZ, Adler HJ (2005) Corros Sci 47:3216–3233
18. Rohwerder M, Michalik A (2007) Electrochim Acta 53:1300–1313
19. Michalik A, Rohwerder M (2005) Z Phys Chem 219:1547–1560
20. Rohwerder M (2009) Int J Mater Res 100:1331–1342
21. Torza S, Mason SG (1970) J Colloid Interface Sci 33:67
22. Sundberg DC, Casassa AP, Pantazopoulos J, Muscato MR, Kronberg B, Berg J (1990) J Appl Polym Sci 41:1425
23. Okubo M, Katsuta Y, Matsumoto TJ (1982) Polym Sci Polym Lett 20:45
24. Joenssmaiaon JE, Hassande H, Toernell B (1994) Macromolecules 27:1932
25. Chen YC, Dimonie V, El-Aasser MS (1992) J Appl Polym Sci 45:487
26. Karlsson LE, Karlsson OJ, Sundberg DC (2003) J Appl Polym Sci 90:905
27. Lee S, Rudin A (1992) J Polym Sci Polym Chem 30:2211
28. Staff RH, Landfester K, Crespy D (2013) Adv Polym Sci 262:329
29. Lv LP, Wu ZS, Chen L, Lu H, Zheng YR, Weidner T, Feng X, Landfester K, Crespy D (2015) RSC Adv 5:50063
30. Staff RH, Lieberwirth I, Landfester K, Crespy D (2012) Macromol Chem Phys 213:351
31. Staff RH, Willersinn J, Musyanovych A, Landfester K, Crespy D (2014) Polym Chem 5:4097
32. Urban M, Freisinger B, Ghazy O, Staff RH, Landfester K, Crespy D, Musyanovych A (2014) Macromolecules 47:7194
33. Lv LP, Zhao Y, Zhou HX, Landfester K, Crespy D (2014) Polymer 55:715
34. Zhao Y, Berger R, Landfester K, Crespy D (2014) Polym Chem 5:365
35. Staff RH, Schaeffel D, Turshatov A, Donadio D, Butt HJ, Landfester K, Koynov K, Crespy D (2013) Small 9:3154
36. Schaeffel D, Staff R, Butt HJ, Landfester K, Crespy D, Koynov K (2012) Nano Lett 12:6012
37. Loxley A, Vincent N (1998) J Colloid Interface Sci 208:49–62
38. Dowding PJ, Atkin R, Vincent B, Bouillot P (2004) Langmuir 20:11374–11379

39. Yow HN, Routh AF (2008) Soft Matter 4:2080–2085
40. Pisani E, Tsapis N, Paris J, Nicolas V, Cattel L, Fattal E (2006) Langmuir 22:4397–4402
41. Pisani E, Tsapis N, Galaz B, Santin M, Berti R, Taulier N, Kurtisovski E, Lucidarme O, Ourevitch M, Doan BT, Beloeil JC, Gillet B, Urbach W, Bridal SL, Fattal E (2008) Adv Funct Mater 18:2963–2971
42. Herrmann C, Turshatov A, Crespy D (2012) ACS Macro Lett 1:907
43. Zhao Y, Dohler D, Lv LP, Binder WH, Landfester K, Crespy D (2014) Macromol Chem Phys 215:198
44. Zhao Y, Landfester K, Crespy D (2012) Soft Matter 8:11687
45. Zhao Y, Fickert J, Landfester K, Crespy D (2012) Small 8:2954
46. Fickert J, Wohnhaas C, Turshatov A, Landfester K, Crespy D (2013) Macromolecules 46:573
47. Staff RH, Rupper P, Lieberwirth I, Landfester K, Crespy D (2011) Soft Matter 7:10219
48. Staff RH, Gallei M, Rehahn M, Berger R, Landfester K, Crespy D (2012) ACS Nano 6:9042
49. Zhao Y, Berger R, Landfester K, Crespy D (2015) Small 11:2995
50. Crespy D, Landfester K (2007) Macromol Chem Phys 208:457
51. Bohlender C, Landfester K, Crespy D, Schiller A (2013) Part Part Syst Charact 30:138
52. Scott C, Wu D, Ho CC, Co C (2005) J Am Chem Soc 127:4160
53. Wu D, Scott C, Ho CC, Co CC (2006) Macromolecules 39:5848
54. Torini L, Argillier JF, Zydowicz N (2005) Macromolecules 38:3225
55. Johnsen H, Schmid RB (2007) J Microencapsul 24:731
56. Ouyang XB, Huang XQ, Pan QH, Zuo CQ, Huang C, Yang XL, Zhao Y (2011) J Dent 39:825–853
57. Crespy D, Stark M, Hoffmann-Richter C, Ziener U, Landfester K (2007) Macromolecules 40:3122
58. He CW, Parowatkin M, Mailänder V, Flechtner-Mors M, Graf R, Best A, Koynov K, Mohr K, Ziener U, Landfester K, Crespy D (2015) Biomacromolecules 16:2282
59. Liu Y, Liu Z, Liu Y, Hu H, Li Y, Yan P, Yu B, Zhou F (2015) Small 11:426–431
60. Crespy D, Landfester K (2009) Polymer 50:1616
61. Schwab MG, Crespy D, Feng X, Landfester K, Müllen K (2011) Macromol Rapid Commun 32:1798
62. Crespy D, Landfester K (2011) Soft Matter 7:11054
63. Herrmann C, Crespy D, Landfester K (2011) Colloid Polym Sci 289:1111
64. Crespy D, Landfester K (2010) Beilstein J Org Chem 6:1132
65. Crespy D, Musyanovych A, Landfester K (2006) Colloid Polym Sci 284:780
66. Molberg M, Crespy D, Rupper P, Nüesch F, Manson JAE, Löwe C, Opris DM (2010) Adv Funct Mater 20:3280
67. Wohnhaas C, Friedemann K, Busko D, Landfester K, Balouchev S, Crespy D, Turshatov A (2013) ACS Macro Lett 2:446
68. Van den Dungen ETA, Klumpermann B (2011) J Polym Sci Polym Chem 48:5215–5230
69. Fickert J, Makowski M, Kappl M, Landfester K, Crespy D (2012) Macromolecules 45:6324
70. Lv LP, Zhao Y, Vilbrandt N, Gallei M, Vimalanandan A, Rohwerder M, Landfester K, Crespy D (2013) J Am Chem Soc 135:14198
71. Lv LP, Landfester K, Crespy D (2014) Chem Mater 26:3351
72. Galgali G, Schlangen E, van der Zwaag S (2011) Mater Res Bull 46:2445–2449
73. Peng B, Chen M, Zhou SX, Wu LM, Ma XH (2008) J Colloid Interfae Sci 321:67
74. Fickert J, Rupper P, Graf R, Landfester K, Crespy D (2012) J Mater Chem 22:2286
75. Fickert J, Schaeffel D, Koynov K, Landfester K, Crespy D (2014) Colloid Polym Sci 292:251
76. Maia F, Tedim J, Lisenkov AD, Salak AN, Zheludkevich ML, Ferreira MGS (2012) Nanoscale 4:1287–1298
77. Kartsonakis IA, Kordas G (2010) J Am Ceram Soc 93:65–73
78. Decher G (1997) Science 277:1232
79. Caruso F, Caruso RA, Mohwald H (1998) Science 282:1111
80. Caruso F (2000) Chem Eur J 6:413

81. Kato N, Schuetz P, Fery A, Caruso F (2002) Macromolecules 35:9780
82. Shchukin DG, Mohwald H (2007) Adv Funct Mater 17:1451–1458
83. Kopec M, Szczepanowicz K, Mordarski G, Podgorna K, Socha RP, Nowak P, Warszynski P, Hack T (2015) Prog Org Coat 84:97–106
84. Yang J, Lee J, Kang J, Lee K, Suh JS, Yoon HG, Huh Y, Haam S (2008) Langmuir 24:3417
85. Oh WK, Kim S, Choi M, Kim C, Jeong YS, Cho BR, Hahn JS, Jang J (2010) ACS Nano 4:5301
86. Paiphansiri U, Dausend J, Musyanovych A, Mailaender V, Landfester K (2009) Macromol Biosci 9:575
87. Bird R, Tungchaiwattana S, Freemont T, Saunders BR (2012) Soft Matter 8:3062
88. Bird R, Freemont T, Saunders BR (2012) Soft Matter 8:1047
89. Blaiszik BJ, Kramer SLB, Olugebefola SC, Moore JS, Sottos NR, White SR (2010) Annu Rev Mater Res 40:179
90. White SR, Sottos NR, Geubelle PH, Moore JS, Kessler MR, Sriram SR, Brown EN, Viswanathan S (2001) Nature 409:794
91. Rule JD, Brown EN, Sottos NR, White SR, Moore JS (2005) Adv Mater 17:205
92. Yin T, Zhou L, Rong MZ, Zhang MQ (2008) Smart Mater Struct 17:015019. doi:10.1088/0964-1726/17/01/015019
93. Yin T, Rong MZ, Zhang MQ, Zhao JQ (2009) Smart Mater Struct 18:074001. doi:10.1088/0964-1726/18/7/074001
94. Xiao DS, Yuan YC, Rong MZ, Zhang MQ (2009) Polymer 50:2967
95. Xiao DS, Yuan YC, Rong MZ, Zhang MQ (2009) Polymer 50:560
96. Yuan YC, Rong MZ, Zhang MQ, Chen J, Yang GC, Li XM (2008) Macromolecules 41:5197
97. Jin H, Mangun CL, Stradley DS, Moore JS, Sottos NR, White SR (2012) Polymer 53:581
98. Sauvant-Moynot V, Gonzalez S, Kittel J (2008) Prog Org Coat 63:307
99. Meng LM, Yuan YC, Rong MZ, Zhang MQ (2010) J Mater Chem 20:6030
100. Yuan L, Liang G, Xie J, Li L, Guo J (2006) Polymer 47:5338
101. Cosco S, Ambrogi V, Musto P, Carfagna C (2007) J Appl Polym Sci 105:1400
102. Hillewaere XKD, Teixeira RFA, Nguyen LTT, Ramos JA, Rahier H, Du Prez FE (2014) Adv Funct Mater 24:5575–5583
103. Zhu DY, Gao GS, Qiu WL, Rong MZ, Zhang MQ (2015) Polymer 69:1–9
104. Yang J, Keller MW, Moore JS, White SR, Sottos NR (2008) Macromolecules 41:9650
105. Cho SH, White SR, Braun PV (2009) Adv Mater 21:645
106. Cho SH, Andersson HM, White SR, Sottos NR, Braun PV (2006) Adv Mater 18:997
107. Gragert M, Schunack M, Binder WH (2011) Macromol Rapid Commun 32:419
108. Keller MW, White SR, Sottos NR (2007) Adv Funct Mater 17:2399
109. Keller MW, White SR, Sottos NR (2008) Polymer 49:3136
110. Billiet S, Van Camp W, Hillewaere XKD, Rahier H, Du Prez FE (2012) Polymer 53:2320
111. Wang HP, Yuan YC, Rong MZ, Zhang MQ (2010) Macromolecules 43:595
112. Yao L, Yuan YC, Rong MZ, Zhang MQ (2011) Polymer 52:3137
113. García S, Fischer H, White P, Mardel J, González-García Y, Mol J, Hughes A (2011) Prog Org Coat 70:142–149
114. García SJ, Fischer HR, van der Zwaag S (2011) Prog Org Coat 72:211–221
115. Shchukin DG, Mohwald H (2011) Chem Commun 47:8730–8739
116. Zhao Y, Lv LP, Jiang S, Landfester K, Crespy D (2015) Polym Chem 6:4197
117. Dias SAS, Lamak SV, Nogueira CA, Diamantino TC, Ferreira MGS (2012) Corros Sci 62:153–162
118. Fu JJ, Chen T, Wang MD, Yang NW, Li SN, Wang Y, Liu XD (2013) ACS Nano 7:11397–11408
119. Zheludkevich ML, Shchukin DG, Yasakau KA, Mohwald H, Ferreira MGS (2007) Chem Mater 19:402–411
120. Grigoriev DO, Köhler K, Skorb E, Shchukin DG, Möhwald H (2009) Soft Matter 5:1426–1432

121. Jafari A, Hosseini S, Jamalizadeh E (2010) Electrochim Acta 55:9004–9009
122. Shchukin DG, Zheludkevich M, Yasakau KA, Lamaka S, Ferreira MSG, Möhwald H (2006) Adv Mater 18:1672–1678
123. Sonawanec SH, Bhanvasea BA, Jamalia AA, Dubeya SK, Kalea SS, Pinjari DV, Kulkarnic RD, Gogateb PR, Pandit AB (2012) Chem Eng J 189–190:464–472
124. Snihirova D, Lamaka S, Taryba M, Salak A, Kallip S, Zheludkevich M, Ferreira M, Montemor M (2010) ACS Appl Mater Interfaces 2:3011–3022
125. Wang Y, Zhang D (2011) Mater Res Bull 46:1963–1968
126. Tedim J, Poznyak SK, Kuznetsova A, Raps D, Hack T, Zheludkevich ML, Ferreira MGS (2010) ACS Appl Mater Interfaces 2:1528–1535
127. Poznyak SK, Tedim J, Rodrigues LM, Salak AN, Zheludkevich ML, Dick LFP, Ferreira MGS (2010) ACS Appl Mater Interfaces 1:2353–2362
128. Snihirova D, Lamaka SV, Montemor MF (2012) Electrochim Acta 83:439–447
129. Snihirova D, Lamaka SV, Cardoso MM, Condeço JAD, Ferreira HECS, Montemor MF (2014) Electrochim Acta 145:123–131
130. Tran TH, Vimalanandan A, Genchev G, Fickert J, Landfester K, Crespy D, Rohwerder M (2015) Adv Mater 27:3825
131. Lv LP, Zhao Y, Landfester K, Crespy D (2015) Polym Chem 6:5596
132. Vimalanandan A, Lv LP, Tran TH, Landfester K, Crespy D, Rohwerder M (2013) Adv Mater 25:6980
133. Rohwerder M, Duc LM, Michalik A (2009) Electrochim Acta 54:6075–6081
134. Rohwerder M, Isik-Uppenkamp S, Amarnath CA (2011) Electrochim Acta 56:1889–1893
135. Lenhardt JM, Kim SH, Nelson AJ, Singhal P, Baumann TF, Satcher JH Jr (2013) Polymer 54:542

Adv Polym Sci (2016) 273: 247–284
DOI: 10.1007/12_2015_333

Published online: 7 January 2016

Self-Healing Functional Polymeric Materials

Johannes Ahner, Stefan Bode, Mathias Micheel, Benjamin Dietzek, and Martin D. Hager

Abstract Self-healing materials have been intensively investigated in recent decades, whereby the healing process was mostly based on the restoration of mechanical properties after mechanical damage. However, self-healing functional polymeric materials have now become the focus of research. In recent years, several approaches have been developed for self-healing of conductivity as well as the restoration of optical properties. In contrast to the healing of mechanical properties, such as stiffness and strength, the self-healing of functional materials focuses on the restoration of functionalities after damage caused by harmful environments (e.g., high temperatures or irradiation). The ultimate goal is the investigation or mimicking of a multifunctional self-healing system (e.g., biological material). In this review, the current state of the art in self-healing functional polymeric materials

J. Ahner, S. Bode, and M.D. Hager (✉)
Laboratory of Organic and Macromolecular Chemistry (IOMC), Friedrich Schiller University Jena, Humboldtstrasse 10, 07743 Jena, Germany

Jena Center for Soft Matter (JCSM), Friedrich Schiller University Jena, Philosophenweg 7, 07743 Jena, Germany
e-mail: martin.hager@uni-jena.de

M. Micheel
Institute of Physical Chemistry and Abbe Center of Photonics, Friedrich-Schiller-University Jena, Helmholtzweg 4, 07743 Jena, Germany

Leibniz Institute of Photonic Technology (IPHT) e.V., Albert-Einstein-Strasse 9, 07745 Jena, Germany

B. Dietzek
Jena Center for Soft Matter (JCSM), Friedrich Schiller University Jena, Philosophenweg 7, 07743 Jena, Germany

Institute of Physical Chemistry and Abbe Center of Photonics, Friedrich-Schiller-University Jena, Helmholtzweg 4, 07743 Jena, Germany

Leibniz Institute of Photonic Technology (IPHT) e.V., Albert-Einstein-Strasse 9, 07745 Jena, Germany

is summarized. In particular, we discuss self-healing conductive materials, healable optoelectronics, and functional coatings.

Keywords Conductivity · Conjugated polymers · Functional materials · Self-healing materials

Contents

1 Introduction

The design of self-healing materials is often inspired by nature. Many natural materials are able to autonomously restore their original function after damage, for example, a cut in a finger that spontaneously stops bleeding, or trees that self-heal their bark over hours to protect the underlying vascular cambium. In contrast, the design of man-made material is almost exclusively based on damage prevention. Material scientists focus on design of new materials that are resistant to mechanical and chemical damage. This strategy works very well, but ultimately cracking and other forms of damage are unavoidable over a long period of use and the original properties of virgin materials degrade over time. After accumulation of a certain amount of damage, repair or replacement of the material is required. An alternative design is the development of self-healing materials, which have become more and more important over the last few decades [1–4]. The need for materials that are reliable and durable for a long time is the driving force behind the

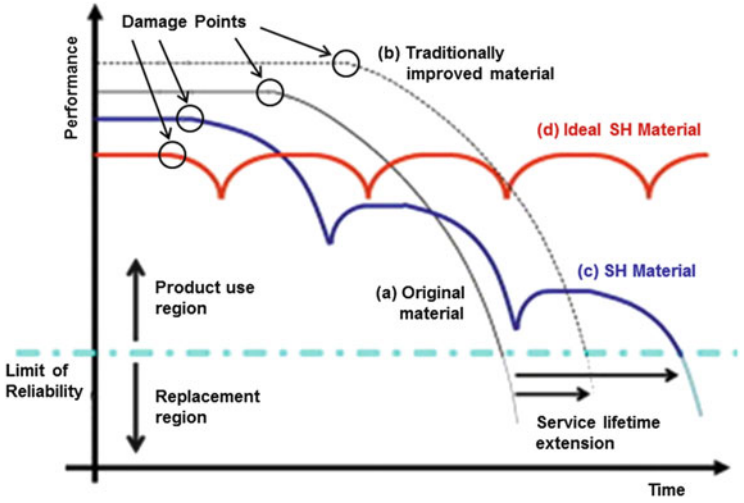

Fig. 1 Performance of conventional and various types of self-healing (*SH*) materials as a function of time [6]. Reprinted by permission of Garcia et al. [6]. Copyright (2014) Elsevier

investigation of self-healing materials. Materials that are able to heal themselves can be applied in locations that are difficult to access, such as high buildings, wind turbines, and underground piping [5]. Difficult and expensive inspections and repairs could thus be avoided. Additionally, applications for airplanes, spacecraft, and long-term storage of nuclear waste, in which safety plays an enormous role, are conceivable. Moreover, structures that must last several decades (e.g., tunnels, dams, and dikes) or products that need a damage-free surface from an aesthetic and protective point of view, are potential applications for self-healing materials.

Several self-healing materials are already commercially available, such as self-healing car body finishes that become scratch-free during exposure to solar heat. Ideally, the self-healing mechanism is a combination of damage detection and repair. A sensor, which has to be inside the material itself, must detect damage occurring somewhere in the material. Preferably, the damage itself is the sensor. After detection, the sensor must trigger the self-healing process, for example, by a chemical reaction or by guiding a mobile phase to the damage. Finally, the healed material should feature nearly the same performance as the virgin material, even after several healing cycles (Fig. 1) [6]. Traditional materials fail after a certain period of use. Consequently, their lifetime can only be improved by damage prevention. In the last few decades, the main focus for the development of self-healing systems has been on the almost complete restoration of the virgin mechanical properties after local damage in the form of cracks. In contrast, self-healable materials of other properties/functionalities have been studied less intensively. For example, in the field of self-healing conductive materials, Moore and coworkers investigated the restoration of conductivity based on the release of a conductive healing agent from microcapsules [7, 8]. Systems based on gold nanoparticles [9]

and single molecule fluorophores [10] demonstrate the first approaches in the field of self-healing of optical properties.

Conjugated polymers are still a rather blank spot on the map of self-healable systems, despite the investigations of Bielwaski [11–13]. Conjugated conductive polymers open the possibility for electrically driven self-healing processes. After a microcrack or interruption of the conjugated system is formed, the total number of conducting pathways decreases. This phenomenon leads to an increase in resistance in the material, in particular at the site of the damaged part. Provided the resistance does not become infinite and a suitable electrical current is imposed, the thermal energy resulting from the increased resistance can be large enough to trigger the induction of a mobile phase and, finally, the self-healing process [11]. Moreover, self-healing of conductivity in transparent electrodes or healable membranes in fuel cells and batteries are possible. Furthermore, layers that are included in a composite device and cannot be disassembled are conceivable options for self-healing functional materials (e.g., in OLEDs, foil displays or solar cells). In this review, we provide a short summary of the self-healing process and discuss in detail investigations of self-healing functional materials.

2 Classification of Self-Healing

Self-healing materials have been investigated intensively during the last two decades. Inspired by nature, self-healing systems have become increasingly important in the restoration of virgin material properties after local damage. The concepts for self-healing are best developed for locally damaged (i.e., scratched or cracked) structural (i.e., load bearing) materials. Healing is based on the generation of a "mobile phase," which is either triggered by an external stimulus (e.g., heat) or directly by the damage itself. The directed mass transport (e.g., swelling, patching, or simple molecular diffusion) towards the damage site and the associated local reactions and interactions lead to healing. In the best case, the original material properties are fully restored [14]. Based on different studied materials and techniques, self-healing materials can be divided into two different classes: non-autonomous and autonomous. These two classes are distinguished by the mode of triggering required. In non-autonomous systems an additional external trigger (e.g., heat, light, or electricity) is required once the damage has been formed. In contrast, no additional intentional stimulus is required to trigger the healing reaction for autonomous systems [15]. Another possible classification of self-healing systems has led to the terms "extrinsic" and "intrinsic." The self-repairing function of extrinsic materials is based on "external" (i.e., intentionally added) healing agents. Those have to be pre-embedded into the utilized matrix (e.g., in capsules, fibers, or porous networks). After the material has been damaged, the autonomous release of the healing agent initiates the desired self-healing process.

Probably the most studied extrinsic self-healing concept is based on micro- or nanocapsules, which are embedded into a (polymeric) matrix (Fig. 2). A crack

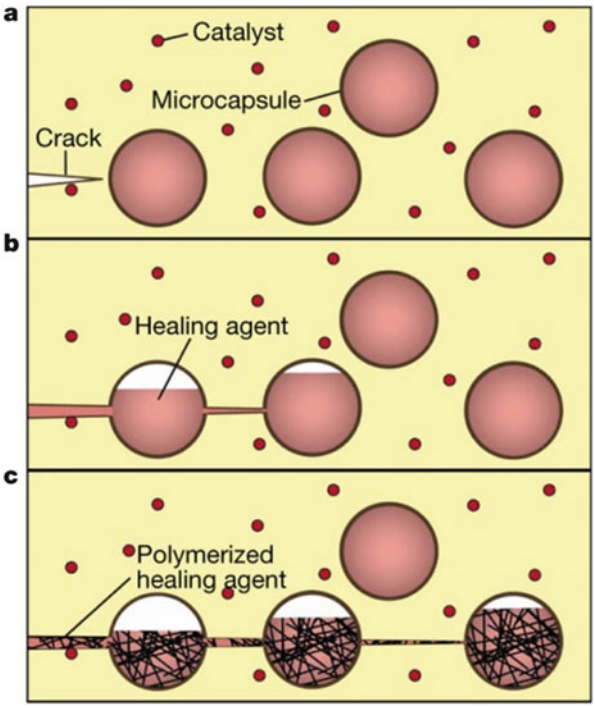

Fig. 2 Concept of extrinsic self-healing by embedded microcapsules: (**a**) crack formation, (**b**) crack formation ruptures embedded microcapsules and releases healing agent into the crack, and (**c**) healing agent contacts catalyst, which leads to polymerization and closure of the crack [16]. Reprinted by permission from Macmillan Publishers Ltd: Nature [16], copyright 2001

ruptures the embedded microcapsules and the liquid contained in the capsules is released into the crack and wets both opposing crack faces. Consequently, polymerization of the healing agent is triggered by a catalyst and, ultimately, the load-bearing capacity of the (filled) crack is restored [16]. For intrinsic healing, no additional external healing agents are required because the healing relies on the properties of the material itself. Such systems are preferable, but the implementation of a self-healing functionality can pose difficulties. Physical interactions and specific chemical bond formation are suitable examples of intrinsic self-healing. In most cases, however, the occurrence of self-healing depends not only on the material but also on the (lateral) size of the damage.

2.1 Mechanical Impetus

Self-healing materials can be distinguished according to the utilized impetus. Mechanical impetuses mostly follow a simple strategy. The healing process is generally initiated by the damage itself. Moreover, this process can be adapted to a number of different polymers and has the potential for quantitative healing. However, the required healing agent must be embedded into the polymer matrix. These requirements lead to a complicated and time-consuming fabrication and poor

atom economy. Moreover, the healing process is often impeded by different phases of the matrix and healing components [17]. White et al. investigated a microcapsule-based self-healing system, in which the healing agent and the Grubbs catalyst are embedded into the polymer matrix [16]. The different parameters of the systems, such as fiber diameter [18], healing agent [19], concentration of healing agent in the capsule and capsule size [20–22], catalyst type [23], catalyst incorporation method [19], and capsule wall thickness [24] have been optimized in the last decade. In the case of small-scale damage, nanotubes are also suitable nanoreservoirs for self-healing agents [25, 26]. The limitation of both systems is the inability to repeatedly heal at the same location of the polymer matrix. Therefore, the groups of Bond [27] and White [28] demonstrated systems consisting of refillable channels containing healing agent . Considering intrinsic self-healing polymers, only hydrogen-bonding [29] and metal–ligand complexation systems showed mechanically triggered autonomous self-healing, as a result of their high reversibility [30]. Mostly these systems are based on thermal activation (vide infra).

2.2 Photochemical Impetus

Photochemical impetuses exhibit excellent atom economy and fast time scales. Furthermore, photons can be absorbed and emitted by any molecule, which can lead to structural changes. Furthermore, precise energy delivery is possible and, therefore, specific bonds or functionalities can be targeted by a certain wavelength. The first optical self-healable materials were based on reversible cycloaddition reactions such as the [4+4] cycloaddition of anthracene-based systems [31]. The healing mechanism in this system is triggered after excitation at 340 nm, which is advantageous for applications because this wavelength overlaps with the solar spectrum at sea level. Furthermore, the [2+2] cycloadditions of cinnamoyl groups [32] and the well-known coumarin [33] are typical examples of optically triggered self-healing. Kang et al. investigated a self-healable conductor based on optical triggering [34]. The healing mechanism is based on directional diffusion along the light polarization of an azobenzene system. Green light (532 nm), even with low intensity and different polarizations, was utilized to attain multiple healing regardless of the number of cracks, light incident angles, or crack propagation directions.

Further optically triggered self-healing systems have been based on metathesis reactions. Typical examples are trithiocarbonate-based systems, which undergo reversible metathesis at ambient temperatures and light irradiation at 330 nm [35]. Additional examples are light-triggered reversible disulfide bonds [36] or allyl sulfide bonds [37]. In contrast to trithiocarbonate- and dilsufide-based systems, allyl sulfide bonds need a photoinitiator for optically triggered reversibility. Weder and coworkers investigated optically healable systems based on metal complexes [38, 39]. The metal complex absorbed light between 340 and 390 nm. The absorbed energy is transferred into heat and the metal–ligand bond is cleaved, leading to the possibility of rearrangement and, finally, to self-healing properties.

Another system of interest is based on oxetane and urea crosslinked chitosan [40]. Mechanical triggering leads to break of the urea bonds. Further optical triggering with visible light opens the oxetane rings, resulting in radical species with the ability to crosslink with the damaged chitosan network and, finally, restore the original properties. However, the healing mechanism is limited by the presence of functional oxetane groups. Urban and coworkers demonstrated a copper complex containing a healable polymer network for optical applications based on poly (dimethyl siloxane)-poly(urethane) and poly(ethylene)-poly(urethane) [41]. In that case, the copper complex induces a topology transition of the ligand sphere, resulting in a volume change and, thus, healing.

2.3 Electrochemical Impetus

Electrochemical impetuses exhibit short time scales for the healing process as a result of fast electrochemical processes. Moreover, electrons can often be easily added and removed, resulting in electronic self-protection. The improvement in atom economy and near-instantaneous control over the process are further advantages of this concept of healing. In nature, biological macromolecules undergo redox-mediated interconversions in order to change their structure and function [42]. However, electrochemically triggered self-healing is limited by the requirement of a conductive medium. For instance, Kowalski et al. investigated a self-healing coating to protect metals from corrosion [43]. The principle is based on the release of healing ions from a cation permselective membrane to the defect zone.

Further electrochemically triggered self-healing systems were investigated by Kwok et al. [44] and Bielawski and coworkers [11].

The concept is based on resistance heating for self-healing of conducting materials (Fig. 3). The existence of microcracks in conducting materials leads to partial disruption of the conjugated systems. Consequently, the conducting pathways through the material decrease, which results in an increase in resistance at the crack sites. The increasing resistance leads to an increasing temperature and the resulting thermal energy acts as trigger for the self-healing process. Another strategy for electrochemical self-healing lies in the use of a redox-responsive systems. Crespy and coworkers investigated the redox-responsive release of healing agents from polyaniline capsules, which offers the opportunity for anticorrosion applications [45]. Further investigations from Rohwerder and coworkers resulted in the first potential triggered release of healing agents from conductive polymer capsules inside an anticorrosion coating; the system successfully stopped the corrosion inside a coating defect [46].

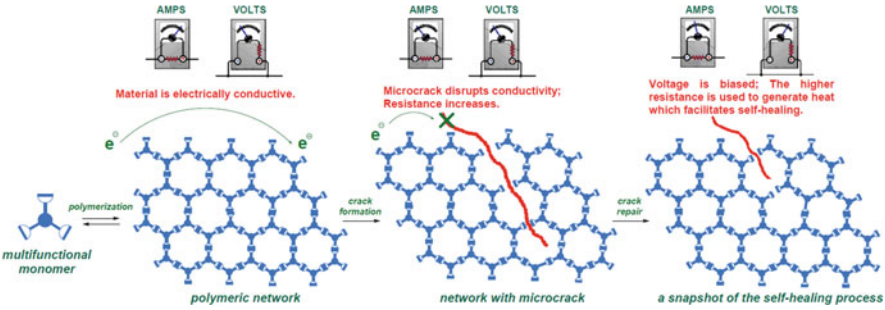

Fig. 3 Principle of resistance heating for self-healing of conducting conjugated polymers [11]. Reprinted with permission from Williams et al. [11]. Copyright (2007) The Royal Society

2.4 Chemical Impetus

Chemically triggered self-healing materials offer the advantage of total control over the chemically sensitive bonds. The drawback is that only non-autonomous healing is possible. The best-known reversible systems are based on the presence of redox agents or a change in pH value. For instance, Vogt et al. presented a triblock self-healing copolymer that is triggered by a redox agent [47]. Solutions of triblock copolymers were heated to 40°C in order to observe the gels. Aminolysis of these gels leads to thiol-terminated diblock copolymers, and further oxidation with Cu (II) catalyst or $K_3[Fe(CN)_6]$ leads to disulfide formation. In contrast, dithiothreitol was utilized as the reduction agent, resulting in an aqueous solution of the oxidized triblock copolymer. Furthermore, Chen and coworkers investigated a pH-sensitive reversible system [48]. Bisacylhydrazine-functionalized poly(ethylene oxide) and tris[(4-formylphenoxy) methyl]ethane lead to a crosslinked gel via a condensation reaction. At $pH < 4$, the acylhydrazone bonds are cleaved, consequently, self-healing can be observed. In contrast, Jay et al. demonstrated a reversible self-healing system at $pH > 7.5$ [49]. The reversibility is based on phenylboronate–salicylhydroxamate crosslinks between the polymer chains. Moreover, Liu and coworkers investigated a pH-sensitive gel consisting of a crosslinked network of a four-arm star crown ether and a two-arm dibenzylammonium-terminated poly (ε-caprolactone) [50]. Here, the reversible crown ether–ammonium complexation was triggered by trifluoroacetic acid or triethylamine.

However, many self-healable systems that are triggered by chemical, electrochemical, or photochemical impetuses are highly specialized and cannot be readily adapted for general use.

2.5 Thermal Impetus

In contrast to the aforementioned impetuses, using a thermal impetus is a suitable alternative because of the reduction in overall complexity and cost of the material. Moreover, thermal energy can be easily supplied. Chemically reactive functional groups, optical transparency, or conductive media are not required and heating can be applied to any material. In contrast, the specific reversible bonds have to be weaker than all other structural bonds in the self-healing material. Furthermore, the activation energy for undesired structural and functional changes or activation barriers for other chemical reactions have to be higher than the required energy for the reversibility of the specific bonds. Diels–Alder (DA)-based systems are the most well-known thermally triggered self-healing materials. The first thermal reversible DA system was reported by Craven and coworkers in 1969 [51] and since then different strategies have been followed to optimize DA-based self-healing systems. Wudl and coworkers demonstrated a healable DA-based system by polymerization of multifunctional monomers [52, 53]. A maleimide-based trifunctional linker (as dienophile) and a linker with four furan moieties (as diene) were utilized for the polymerization. The resulting polymer showed healing above 120°C as a result of the reversible DA system. A further strategy is the crosslinking of linear polymers that include maleimide or furan functional groups with each other or with a suitable bisfunctional linker. For instance, Picchioni and coworkers investigated crosslinked polymers consisting of furan-functionalized polyketones and bismaleimide-based linker [54]. The healing temperature was about 120°C.

Another strategy is the investigation of a one-component difunctionalized polymer. Kötteritzsch et al. demonstrated methacrylate-based furan- and maleimide-functionalized polymers, which can be thermally healed above 120°C (Fig. 4) [55, 56]. Furthermore, the concept of the reversibility of hetero-DA reactions

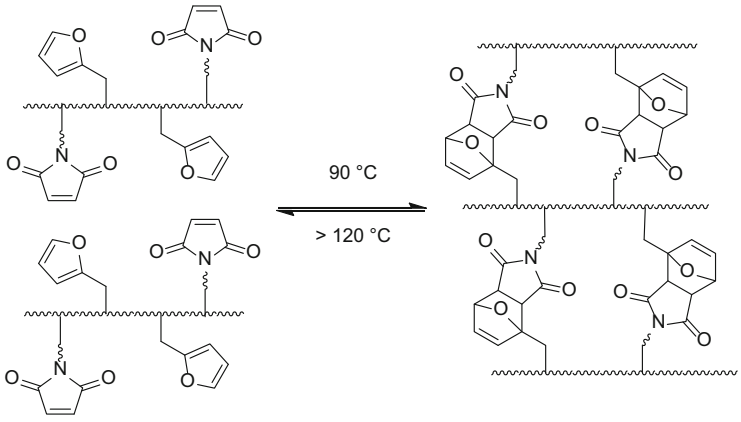

Fig. 4 Concept of self-healing via Diels–Alder-based one-component difunctionalized polymers [55]

represents a possibility for self-healing materials [57]. For example, Barner-Kowollik and coworkers demonstrated a reversible system consisting of a trifunctionalized pyridinyl dithioformate crosslinker and a bis-cyclopentadiene end-functionalized poly(methyl methacrylate) [58].

In addition to Diels–Alder chemistry, there are an enormous number of other thermally reversible linkages. For example, π-π stacking offers another class of thermally triggered self-healable materials [59–61]. For instance, Rowan and coworkers presented a mixture of a pyrene end-capped polymer and a diimide-containing polymer, which showed self-healing ability at 80°C in film [61]. Reversible disulfide bonds are another possibility for thermally induced self-healing [62]. For instance, Canadell et al. investigated a self-healable material that heals at 60°C after 1 h [63]. The system was based on the reversibility of the crosslinked disulfide bonds and the low glass-transition temperature (T_g) of the utilized epoxy resin. Moreover, Kuhl et al. demonstrated a thermally triggered self-healing polymer based on reversibly crosslinked covalent acylhydrazone bonds [64]. Another thermally triggered self-healing strategy is based on reversible metal–ligand interaction in supramolecular polymers, which have been investigated intensively by the groups of Schubert [65–69] and Guan [70].

Ballistic triggering of self-healing materials is still a peripheral field of research and a subclass of mechanically and thermally triggered systems. Kalista et al. presented poly(ethylene-*co*-methacrylic acid) copolymers that showed self-healing ability after projectile tests [71–73]. The puncture process heats the film to a viscoelastic melt state, which leads to destruction of the ionic clusters and the effective re-activation of carboxyl bonds (as shown by Varley and Van der Zwaag [74–76]) and, finally, the self-healing process.

3 Healing of Functions

Functional materials can be found in a large variety of different applications and play an important role in our life. Active layers in solar cells, electrolytes in fuel cells, porous catalysts, and the membrane in "breathing" rain coats are some typical applications of functional materials. Although the monitoring of the self-healing process of structural materials is limited to stress- and strain-resistance tests [77] as well as employing vibrational spectroscopy (i.e., infrared and Raman spectroscopy) [78], self-healing of the functionality serves as an additional metric in functional materials. Additionally, some materials are classified as coatings, because protection of the underlying material can also be considered a functionality. In contrast to structural materials, defects in functional materials do not necessarily manifest as visible cracks. These defects have to be noticed in order to extend the lifetime and to improve reliability by the initiation of a self-healing process. Moreover, damage is not only caused mechanically, but also by radiation or corrosion. Batteries, solar cells, and electronic parts require reliable, smart high-tech functional materials. The causes of malfunction in such functional materials can be divided into passive and

Table 1 Selected self-healing functionalities

Functional material	Self-healed function
Conductors	Conductivity, resistance, charge carrier mobility
Optoelectronics	Absorption, emission, reflectivity, exciton dynamics
Functional coatings	Flame resistance, superhydrophobicity, superamphiphobic properties, aesthetics, surface energy

active causes. Passive causes for the defect are comparable with structural material damage and have no influence on the functionality of the material. In contrast, active causes for failure decrease the functionality over time. For instance, blocking of active centers of a porous catalyst by side reactions and the aging of lithium ion batteries over time are typical active causes for the failure of materials. As a consequence, self-healing of functional devices is required and is a current and important issue. The healing of layers that are fully enclosed in multilayers and hard to access (e.g., in solar cells, foil displays, and OLEDs) is one example where self-healing materials could provide additional benefits. However, the development of self-healing materials in functional devices is still in its infancy. Some self-healing functionalities are presented in Table 1.

4 Self-Healing of (Electrical) Conductivity

As previously mentioned, self-healing conductors offer the possibility for introduction of electrically driven self-healing and, therefore, represent a method with excellent atom economy and instantaneous control. Moreover, fast time scales in self-healing and electronic self-protection are further advantages of electrochemical impetuses [42]. A mechanical load can potentially interrupt the chemical bonds in a conductive polymer by causing formation of microcracks. Consequently, the conductive pathways decrease, which leads to an increase in resistance on the crack side and, finally, to an increase in temperature, given an electrical current of sufficient magnitude. The resulting thermal heating can be utilized for induction of a mobile phase next to the microcrack, resulting in a healing process. Finally, the originally conducting polymer network and the associated polymer properties are almost completely restored [11]. The challenge in self-healing conductive materials is to obtain self-healing capability, while reforming the electrical properties. The state of the art for different strategies is separated into four main categories: (1) dynamic reversible bonds, (2) embedded conductive material in self-healable polymers, (3) self-healing by embedded microcapsules or microfluidic channels, and (4) additives in conductive ionic liquids. Some self-healing conductors are presented in Table 2.

Table 2 Presented self-healing conductors

Self-healing conductor	Type of damage	Electrical properties[a]	Healing conditions	Electrical properties[a] after healing	Ref.
Organometallic polymer based on NHCs and metals	Crack	10^{-3} S/cm	150°C in presence of DMSO vapor, 2 h	Not specified	[11]
Graphene	Cut	6,100 cm^2/Vs	500°C	910 cm^2/Vs	[79]
Hydrogen-bonding polymer with embedded Ni particles	Cut	40 S/cm	r. t. with pressure, 15 s	~90%	[80]
Hydrogen-bonding polymer with embedded carbon black	Crack	0.25 S/cm	r. t.	0.14 S/cm	[81]
Hydrogen-bonding polymer with embedded graphene	Cut	0.67×10^{-4} S/cm	37°C with pressure, 12 h	0.4×10^{-4} S/cm	[82]
Hydrogen-bonding polymer with embedded reduced graphene oxide	Cut	5×10^4 Ω	r. t. with pressure, 20 s	5×10^4 Ω	[83]
Poly(pyrrole) hydrogel	Crack	~0.35 S/cm	120°C (melt), 30 min	Not specified	[84]
Mesh-like silver on top of hydrogen-bonding polymer	Crack	0.38 Ω/sq	r. t. with droplet of water, 2 min	0.42 Ω/sq	[85]
Aligned CNTs scrolled onto hydrogen-bonding polymer	Cut	200 Ω	r. t. with pressure, ~ 20 s	250 Ω	[86]
Host–guest interaction between CNTs and oligomers	Crack	0.15 S/cm	r. t. with droplet of water, 5 min	~100%	[87]
Microencapsulated CNTs and graphene flakes	Crack	Not specified (gold lines)	r. t.	25% Full and 50% partial healing	[88]
Microencapsulated carbon black suspensions	Crack	1.4 to 2.0×10^{-5}/Ω (Si-anode)	r. t., 500 s	~100%	[89]
Microencapsulated eutectic gallium-indium liquid alloy	Crack	Not specified (gold lines)	r. t., 160 µs	~100%	[8, 90]

(continued)

Table 2 (continued)

Self-healing conductor	Type of damage	Electrical properties[a]	Healing conditions	Electrical properties[a] after healing	Ref.
Microencapsulated organic solvent	Crack	0.95 Ω (silver ink)	r. t., 1 week	1.45 Ω	[91]
Microencapsulated charge-transfer salt	Crack	Not specified (gold lines)	r. t.	Conductivity restoration shown	[7]
Eutectic gallium-indium into polydimethylsiloxane microchannels	Crack	3.4×10^4 S/cm	r. t.	Conductivity restoration shown	[92]
Eutectic gallium-indium into Reverlink microchannels	Cut	10^{-3} Ω	r. t., 10 min	~100%	[93]
Ionic liquid with Schmitt trigger gated transistor	Degradation of cathode	Not specified	r. t.	Onset voltage stable by varying bias range	[94]

[a]Resistance, conductivity, mobility
r.t. room temperature

4.1 Introducing Dynamic Reversible Bonds

The introduction of dynamic reversible bonds into conductive polymers is one possibility for creating a self-healing polymer. The first self-healing conductor, using a fully electrically conductive polymer network, was developed by Bielawski and coworkers (Scheme 1) [11].

Organometallic polymers, which consist of *N*-heterocyclic carbenes (NHCs) and different metal salts (M=Ni, Cu, Pt, Pd, Rh and Ag), were utilized for self-healing studies. Several NHCs were prepared by introducing different substituents (R=alkyl, aryl) for stabilization of the carbene moiety [95–98]. In combination with different metal salts, well-defined organometallic polymers were prepared featuring conductivities in the order of 10^{-3} S/cm. To investigate the self-healing behavior, a sharp razor blade was utilized for inducing microscratches. Heating the thin films at 200°C for 25 min led only to visible smoothing of the introduced edges. In contrast, the addition of dimethyl sulfoxide solvent vapor and heating to 150°C for 2 h led to significant healing of the mechanically damaged conductive film. The depth of the crack was reduced from 800 nm to nearly 0 nm. However, the electronic performance of the investigated system was rather poor. The resistivity has to be enhanced to 1 S/cm for certain applications. Moreover, conjugated imine polymers offer a possible strategy for self-healing of fully organic conductors [99–103]. Recently, the reversibility of the dynamic bonds by imine metathesis or transamination in solution was proven [104–106], which opens the possibility for self-healing conductors (i.e., bulk material) in future investigations.

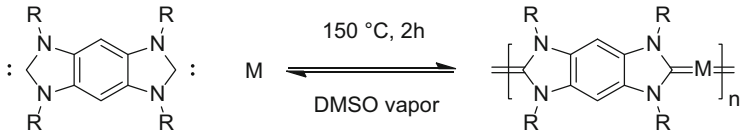

Scheme 1 Equilibrium between the dynamic reversible organometallic polymer and the corresponding monomers [11]

Graphene is an interesting conductor because of its high electrical conductivity and thermal stability. Furthermore, it can be utilized for the introduction of self-healing properties. Yu and coworkers investigated the restoration of carrier mobility in graphene conductors [79]. First, graphene was prepared on SiO_2 by mechanical exfoliation. Damage to the samples was achieved by plasma bombardment for about 5 s. X-ray photoelectron spectrum (XPS) analysis prompts material failure such as carbonyl, hydroxy, or carboxyl groups on the graphene surface. Self-healing of the defective graphene was achieved by annealing at 300–900°C. The self-healing process and its efficiency were investigated by Raman spectroscopy and high resolution transmission electron microscopy (HR-TEM). The Raman signals, which appeared after plasma treatment, disappeared almost completely as a result of the healing process. In several applications, such as microfabrication without an external carbon source, self-healing graphene would be advantageous. Further investigation of self-healable single-walled carbon nanotubes (CNTs) were reported by the groups of Yoon [107] and Kim [108].

4.2 Self-Healing Polymers by Embedded Conductive Materials

Another strategy for producing self-healing conductors is the embedding of conductive material into a matrix. However, the realization is difficult because the blend only becomes conductive if the share of conductive additive exceeds the percolation threshold. Moreover, the physical properties and self-healing ability of the material are affected by the amount of conductive fillers. Consequently, the presence of an adequate contact area and chemical compatibility between both ingredients play important roles in achieving a self-healable composite [109].

Bao and coworkers demonstrated the first bulk conductive self-healing composite, which consisted of inorganic metal particles as conductive fillers and an organic supramolecular polymer as host [80].

A reduction in phase aggregation by the usage of large spherical particles and the thin nickel oxide layer on the particle surface which allows for hydrogen bonding in the supramolecular oligomers are driving forces for efficient dispersion within the polymer matrix (Fig. 5). As a result, the T_g was increased from −20°C to 10°C and an electrical conductivity of 40 S/cm was reached by varying the content of nickel particles. Cutting the sample leads to interruption of the conductivity.

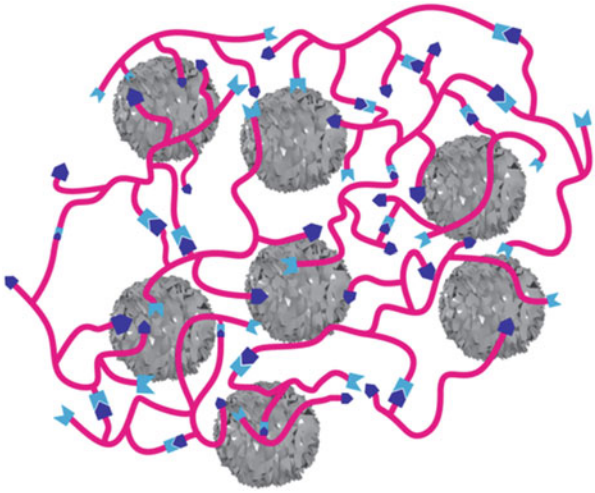

Fig. 5 Interaction of μNi particles with supramolecular polymer host [80]. Reprinted by permission from Macmillan Publishers Ltd: Nature [80], copyright 2012

Subsequently, healing was achieved by simply pressing the cut surfaces together, resulting in restored conductivity (up to 90% after 15 s). The self-healing mechanism of the supramolecular polymer is based on the dynamic hydrogen-bonding network. Suitable applications as tactile or flexible sensors have been tested.

Moreover, the utilized supramolecular polymer was investigated in further self-healing studies with incorporated silicon microparticle anodes for lithium-ion batteries [81].

Silicon as anode material in lithium-ion batteries has a ten times higher theoretical capacity than graphite anodes. However, the capacity rapidly drops after only ten cycles as a result of fracture and particle detachment. Therefore, an anode covered with a conductive self-healable material could be beneficial. Dispersing carbon black nanoparticles in a self-healing polymer leads to a conductivity of around 0.25 S/cm. The resulting capacity of the silicon-covered microparticle anode is six times higher than that of a standard graphite anode. Furthermore, because of superior mechanical stretchability and strong interactions with the silicon surface, the self-healable coating handles the volumetric changes during lithiation/delithiation better, which results in lifetime cycles ten times higher than those for virgin microparticle anodes. Li and coworkers demonstrated a self-healable hydrogel in which graphene networks are embedded [82]. The graphene-poly(*N*,*N*-dimethylacrylamide) crosslinked polymer was synthesized by a rather simple procedure. A graphene hydrogel was immersed into a *N*,*N*-dimethylacrylamide solution, followed by free-radical polymerization to obtain the desired crosslinked composite. After cutting the sample, the half-blocks were stacked together and heated to 37°C for 12 h. The proposed healing mechanism between the combined surfaces is based on the re-entanglement of the polymer chains of the freshly cut surfaces. Further interaction with neighboring graphene layers leads to healing of the scratch. Some 60% of the original conductivity was restored. Moreover, the healing procedure could also be achieved by another heating method (near-infrared laser irradiation for 2 h) in which the temperature was kept below 50°C.

Tang and coworkers reported an electrical self-healing hydrogel based on embedded reduced graphene oxide [83]. Because of the high cost of graphene, reduced graphene was utilized, which has nearly the similar electronic properties and offers the opportunity for better hydrogen bonding with functional groups of the polymer network. In combination with hyperbranched bis-2,2-bis(hydroxylmethyl)propionic acid polyester-64-hydroxyl oxide, sodium polyacrylate polymer particles, and water, a hydrogel composite was formed, which revealed electrical self-healing properties. Mechanical damage was inflicted by cutting, and self-healing was achieved by application of light pressure for only 20 s on the fractured surfaces brought in contact. The self-healing process is based on the re-association of the hydrogen bonds of the polymer. As a result of the fast and efficient self-healing, restoration of performance, and excellent water-absorption ability, the material has possible applications in soft moisture-related resistor-sensor systems. Further investigations incorporating carbon-based nanomaterials into self-healing hydrogels were carried out by Liu et al. [110], Kim et al. [111] and Banerjee and coworkers [112].

Hur et al. have demonstrated a thermoplastic polypyrrole/agarose-based hydrogel that melts during self-healing, thus representing a peripheral area of self-healing materials [84]. Gelation of agarose and polymerization of pyrrole occurred at the same time, forming the desired hydrogel with a conductivity of around 0.35 S/cm. Following the melting–flowing–fusing process initiated by heating a damaged sample to 120°C for 30 min, conductivity was nearly restored. Moreover, the same effect was achieved by heating the defect locations with a 644 nm laser.

Another approach to self-healing conductors is the deposition of electrically conductive materials on top of a self-healable system. Sun and coworkers investigated a self-healing conductor based on silver nanowires [85]. A blend of branched poly(ethyleneimine) and poly(acrylic acid)-hyaluronic acid was deposited on a silicon wafer. The resulting film was drop-cast with a conductive silver nanowire layer to achieve a mesh-like film. Finally, poly(vinylpyrrolidone) was casted on top of the silver mesh to enable strong adhesion between the polymer film and the silver nanowires by hydrogen bonds. Scratches in the conductive film were healed by addition of a droplet of deionized water (Fig. 6). The resulting swelling of the self-healing polymer blend led to re-formation of contact between the damaged areas and, consequently, to re-formation of ionic bonds. After 2 min the water was dried by nitrogen flow and the original material was obtained. As a result, an electrically

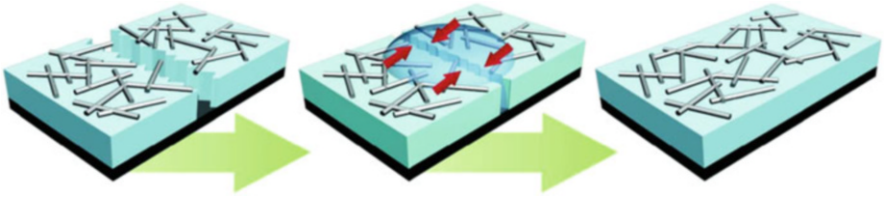

Fig. 6 Water-enabled restoration of conductivity of a silver nanowire-based composite [85]. Reprinted with permission from Li et al. [85]. Copyright (2012) John Wiley and Sons

conductive healable film was created that employed a cost-effective healing agent such as deionized water.

Energy textile woven devices are susceptible to structure fracture and, consequently, the lifetime is very low in practical applications such as wearable and portable electronics. Therefore, Peng and coworkers developed self-healing conducting wires by coating electrically conducting nanomaterials onto a polymer fiber [86]. The core of the investigated wire consisted of a self-healable polymer with hydrogen bonding and had an average diameter of 700 μm. Three different conducting materials were studied, namely CNT networks, silver nanowires, and aligned-CNT sheets. The conducting materials were spray-coated or scrolled onto the self-healable polymer fibers to form closely and uniformly attached layers with self-healing ability. The lowest resistance and best healing efficiency was achieved by scrolled aligned-CNTs as a result of strands formed along the cross-section after the broken parts were brought back into contact. The highest resistance was obtained from spray-coated CNT networks as a result of hopping-transport of the electrons over contacting points and boundaries. By introducing polyaniline as a second active phase, the electrochemical properties were improved; in particular, the specific capacitance increased from 11.1 F/g to 140.0 F/g. A self-healing efficiency of the specific capacitance of up to 92% was obtained, which offers the possibility for application as a self-healable supercapacitor.

The main disadvantage of systems based on hydrogen bonding is the rapid loss of self-healing ability as a result of absorption of moisture at ambient air conditions. In contrast, healing mechanisms based on host–guest interactions are positively affected by moisture and exhibit a quick restoration of functionality. Because of this phenomenon, Zhang et al. investigated the first self-healing conductive material based on host–guest interactions [87]. Complexes of β-cyclodextrin-decorated single-walled CNTs and adamantine acetic modified poly(ethylenimine) oligomer were utilized. The hydrogen bonds between the N–H and O–H groups play a minor role in the self-healing process. Randomly entangled single-walled nanotubes are the key factor for achieving a conductivity of 0.15 S/m. Cutting the composite leads to an interruption in conductivity, which was restored by adding a droplet of deionized water on the cut for less than 5 min. The healing efficiency of the conductivity was nearly 100%, which indicates the excellent reversible host–guest interactions of the utilized composite material.

4.3 Self-Healing by Embedded Microcapsules or Microfluidic Channels

Microencapsulated conductive core materials are typically mechanically triggered, which leads to release of the healing agent. Consequently, autonomous restoration of the electrical conductivity in a broken circuit can be achieved. Several types of conductive core materials have been encapsulated to achieve self-healing of

conductors. Moore and coworkers demonstrated the first preparation of robust, thermally stable microcapsules containing a suspension of a conductor in different solvents and offering the possibility for design of a self-healing conductor [113]. Moreover, Pastine et al. investigated several phototriggerable microcapsules with encapsulated healing agents [114]. CNTs or graphene flakes were suspended in a mixture of ethyl phenylacetate/chlorobenzene and incorporated into microcapsules, leading to partial aggregation. To improve the dispersion of CNTs or graphene, poly(3-hexylthiophene) was used as additive. Further impurities were removed by ultracentrifugation to obtain stable suspensions [88]. The resulting self-healing microcapsules were dispersed into epoxy resin and the obtained mixture was utilized for self-healing of tiny gold linear conductors. Fracture in the gold line leads to an interruption in conductivity. The simultaneous rupture of microcapsules led to release of the electrically conductive polymer-stabilized CNTs or graphene flakes. Consequently, full and partial conductivity restoration was achieved, but with wide variations in the starting time of the healing process, healing ratio, and time required for the healing process.

Sottos and coworkers further improved the maximum particle loading of conductive encapsulated healing agents by functionalization of oxidized carbon black with octadecyl groups [89]. As a result of the functionalization, the solubility in hydrophobic solvents such as *o*-dichlorobenzene was improved, resulting in better suspension stability. Furthermore, a core thickener such as poly(3-hexylthiophene) was utilized to increase the loading capacity, core viscosity, and particle stability. The resulting suspension was encapsulated in double shell microcapsules of polyurethane/poly(urea-formaldehyde), with a maximum particle loading of 0.2 mg/mL. The capsules showed good thermal stability up to 150°C. Conductivity restoration of a nanoparticle silicon anode was achieved within 500 s with efficiencies of about 95–100% using capsule diameters from 60 to 300 μm. In contrast to graphene flakes, CNTs, or carbon black-based conductive healing agents, metal particles or molten metals exhibit further possibilities for encapsulated conductive healing agents. For instance, Blaiszik et al. investigated a microencapsulated eutectic gallium-indium liquid alloy with excellent healing ability [8, 90]. The microcapsule shell consisted of the well-known poly(urea-formaldehyde) and a metal oxide passivation layer. The resulting shape of the microcapsules was ellipsoidal. For self-healing tests, gold lines were patterned on a glass substrate, followed by deposition of an epoxy layer with embedded microcapsules (diameter ca. 200 μm). Capsules with a smaller diameter of ca. 10 μm were patterned directly onto the gold lines (Fig. 7a). After crack loading, the introduced microcapsules were ruptured and the liquid metal alloy was released, which resulted in conductivity restoration of 100% after 160 μs (Fig. 7b, c). Therefore, healing is accomplished by the release and transport of the alloy as a result of its low melting point of 16°C and its high conductivity of 3.4×10^4 S/cm. The conductive self-healing performance was monitored via measurement of the normalized bridge voltage. Self-healing tests without microcapsules or with encapsulated gallium or solid glass bead microcapsules led to no healing.

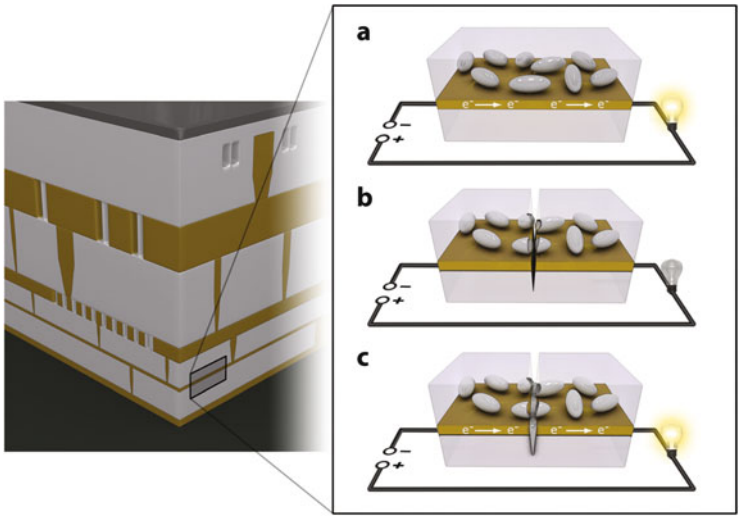

Fig. 7 Self-healing of conductivity function: (**a**) multilayer microelectronic device, (**b**) interrupted conductivity and ruptured microcapsules by crack damage, and (**c**) release of melted alloy into the crack leads to restoration of conductivity [8]. Reprinted with permission from Blaiszik et al. [8]. Copyright (2012) John Wiley and Sons

Odom et al. investigated a conductive self-healable silver ink based on an encapsulated organic solvent [91]. First, silver particle ink lines were deposited onto a plastic substrate, followed by deposition of a polyurethane layer with embedded microcapsules. Hexyl acetate as the encapsulated solvent was chosen because of its low toxicity and ability to dissolve the polymeric binder. Application of scratches on the material caused electrical failure. In the case of 30 w% hexyl acetate microcapsules, the conductivity restoration was about 80% within 10 min. The self-healing process was followed via the decrease in resistance and the increase in normalized bridge voltage. In further investigations, Odom et al. demonstrated the restoration of conductivity by encapsulation of charge-transfer salts [7]. Tetrathiafulvalene (TTF) and tetracyanaoquinodimethane (TCNQ) are soluble in a variety of organic solvents. Both components are known to form a conductive charge-transfer salt. Both substances in solutions of phenyl acetate were individually encapsulated in poly(urea-formaldehyde)-based microcapsules. By adding a polyurethane prepolymer, microcapsules with higher concentrations were achieved. In the self-healing studies, well-defined gold lines were deposited onto glass slides with gaps of 30, 50 and 100 μm. Afterwards, ruptured microcapsules, in a 1:2 ratio of TTF to TCNQ, were deposited onto the substrate over the gaps to ensure full bridging. All gap sizes showed restoration of conductivity as a result of the presence of the formed charge-transfer salt. The first conductive self-healable microfluidic channel system was investigated by Dickey and coworkers [92].

Developed dipole antennae were fabricated by injecting eutectic gallium-indium into poly(dimethylsiloxane) (PDMS) microchannels. The utilized liquid metal was

chosen for its many advantages over other conductive materials, such as low toxicity, a nearly equal conductivity to copper (3.4×10^4 S/cm), and a thin passivating oxide layer, which leads to mechanical stability. The resulting antenna was partly cut by a razor blade, and further stretching caused infinite resistance. Relaxation of the antenna led to the original conductive state. Therefore, the elasticity of the PDMS is crucial for reconnecting the broken surfaces and, consequently, the self-healing process. Because of these flexible and elastic properties, the fluidic antennae can be wrapped, rolled, folded, or stretched without any loss of electrical continuity. In further investigations, the maximum allowed strain level of the flexible antennae was raised to 600% by using poly[styrene-*b*-(ethylene-*co*-butylene)-*b*-styrene] (TPEG) as thermoplastic elastomer [115]. In further studies, Dickey and coworkers demonstrated the first self-healing conductive wire, which showed self-healing after the wire was completely severed [93]. The conductive core channel consisted again of eutectic gallium-indium, but for the self-healing polymer, Reverlink was utilized. First, the antenna was cut by scissors into two pieces and thereby the circuit was disconnected (Fig. 8). An oxide layer was rapidly

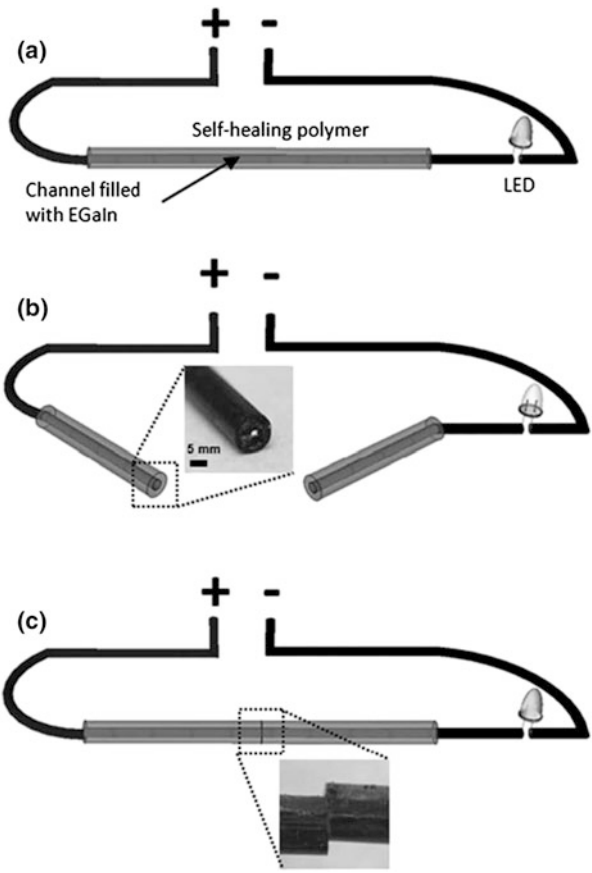

Fig. 8 Self-healing of conductive wire: (**a**) virgin conductive self-healable wire, (**b**) cut by scissors, and (**c**) rejoining of the two parts by mechanical alignment [93]. Reprinted with permission from Palleau et al. [93]. Copyright (2013) John Wiley and Sons

formed on the metal surfaces, preventing escape of the liquid eutectic metal. Mechanical and electrical healing was achieved within 10 min after rejoining and aligning the two parts. The healing mechanism is based on reversible hydrogen bonding within the polymer network sheet. The resulting conductive healing performance was nearly 100%.

4.4 Self-Healing by Additives in Conductive Ionic Liquids

Bubel et al. demonstrated for the first time a self-healable ionic liquid gated transistor [94]. The general structure of the electric double layer transistor and the chemical structure of the utilized reagents are depicted in Fig. 9.

Degradation of the utilized α-ZnO over time by cathode reduction and the production of superoxides leads to decreased transistor performance. For instance, the utilization of a pure ionic liquid (1-ethyl-3-methylimidazolium tetracyanoborate) results in an unstable onset voltage, whereby the addition of tannic acid leads to stable onset voltage as a result of the ability of the additive to form a solid electrolyte interface on the α-ZnO surface. The binding mechanism is based on reactive ester and phenolic functionalities. This layer stays intact after the first bias cycle and does not have to be re-supplied provided the concentration is high enough. All discussed self-healable conductors offer the possibility for next-generation electronic devices with desirable economic and human safety properties, as well as a remarkable lifetime.

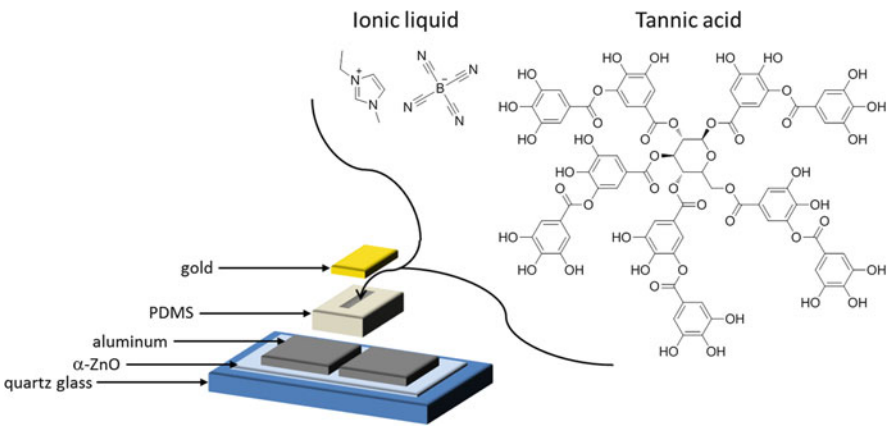

Fig. 9 Layout of electric double layer transistor and chemical structures of used ionic liquid and tannic acid additive [94]. Reprinted with permission from reference [94]. Copyright (2015) John Wiley and Sons

5 Self-Healing of Optical Properties

To achieve self-healing in optical devices, several criteria are of interest: (1) damage should be healed repeatably and at different levels of severity, (2) virgin properties and characteristics should be fully recovered after healing, (3) utilized materials should be suitable for mass production and should be economically friendly, and (4) the self-healing process should only occur on demand. In recent years, self-healable optical materials have come more and more into the focus of research.

5.1 Self-Healable Transparent Optical Coatings

All transparent optical coatings lose their main functions (i.e., transparency and protective power) after mechanical damage of the material. The most common transparent optical material is glass. Thus, Montagne and coworkers investigated an autonomous self-healable glass based on dispersed vanadium boride particles within the glass matrix [116, 117]. The healing vanadium boride particles were dispersed within an aluminosilicate glass composite and show "self-healing" ability at 700°C after damaging. The vanadium boride healing agent is oxidized at that temperature, which is below the glass transition temperature of the utilized glass matrix, and finally filled the crack. The healing mechanism was studied by ^{51}V- and ^{11}B-nuclear magnetic resonance (NMR) spectroscopy, which showed that healing was complete after 60 min. Transparent self-healing optical coatings based on dispersed microcapsules in a polymer network were also investigated by Braun and coworkers [118]. Dibutylphthalate-filled urea-formaldehyde capsules were embedded in a poly(methyl methacrylate) matrix and led to autonomic self-healing when damage occurred. The mechanism is based on solvent welding. Here, the healing efficiency correlates with the capsule size and the percentage (by weight) of healing agent within the capsules. For instance, a crack of 200 nm can be filled by 1.5 μm capsules with 15 w% of healing agent, whereas capsules of 75 μm and 5 w% healing agent content are suitable for healing 7.5 μm wide scratches. In contrast, large capsules lead to some light scattering and, consequently, reduced transmission properties. As a result of this, the healing efficiency is limited and other strategies were investigated.

Gerth et al. demonstrated a self-healable transparent nanocomposite hydrogel [119]. Terpyridine-endcapped polymers were adsorbed onto silica nanoparticles with a hydrodynamic radius of only 10 nm. Further metal coordination with Co (II) led to the desired self-healing hydrogel. The healing mechanism is based on the reversibility of the coordination and hydrogen bonds and restores the mechanical properties within several minutes. Further investigation of self-healable optical coatings based on organogelators was reported by Sureshan and coworkers [120]. Commercially available mannitol-based diols were utilized for gelation of nonpolar solvents or oils. The resulting gels show self-healing ability as a result of

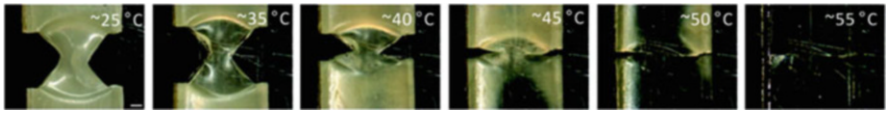

Fig. 10 Process of crack closure at different temperatures [122]. Reprinted with permission from E. D. Rodriguez et al. [122]. Copyright (2011) American Chemical Society

simple hydrogen bonding and high transmittance in the visible region as well as weak transmittance in the UV region. Therefore, application as a selective UV filter coating is possible.

Another strategy for achieving self-healing is the combination of reversibility in the chemical bonds with the shape memory effect [121]. For instance, Mather and coworkers developed a self-healing polymer system in which thermoplastic diffusion and the shape memory effect were combined [122]. This effect is called shape-memory assisted self-welding (SMASW). The rubber-like composite was deformed to 200% strain and recovered to the original shape upon heating above T_m, as shown in Fig. 10. In recent years, many other optical transparent coatings have been investigated for self-healing applications [123–125].

5.2 *Self-Healable Solar Cell Materials, Fluorophores, and Optical Limiting Nanoparticles*

Based on the efficient mechanism of self-healing in nature, Ham et al. demonstrated the first electrochemical structure that mimics this process [126]. The investigated complex consisted of CNTs, phospholipids, membrane scaffold proteins, and photosynthetic reaction centers (Fig. 11). The utilized phospholipid (1,2-dimyristoyl-*sn*-glycero-3-phosphocholine) formed lipid bilayer nanodiscs in the presence of an amphiphilic apolipoprotein that finally assembled onto single-walled CNTs.

As a result, a platform was created for attaching membrane proteins such as the photosynthetic reaction center of *Rhodobacter sphaeroides*. This reaction center consists of two bacteriopheophytins (BPHE), four bacteriochlorophylls (BCHL), as well as primary and secondary ubiquinones (Q_A and Q_B). After photoabsorption, the formed excitons are transported to the BCHL dimer, where separation into holes and electrons takes place. The self-assembled structure was confirmed by small-angle neutron scattering (SANS) and atomic force microscopy (AFM). The reversibility of this complex and therefore the ability to self-heal was achieved by adding 2 w% sodium cholate, which leads to disassembly of the system into its separate components. Subsequent removal of sodium cholate by dialysis leads to reassembly of the complex. This reversible process was monitored by changes in the emission wavelength of the CNTs. Disassembly of the complex leads to a blue emission compared with the assembled system.

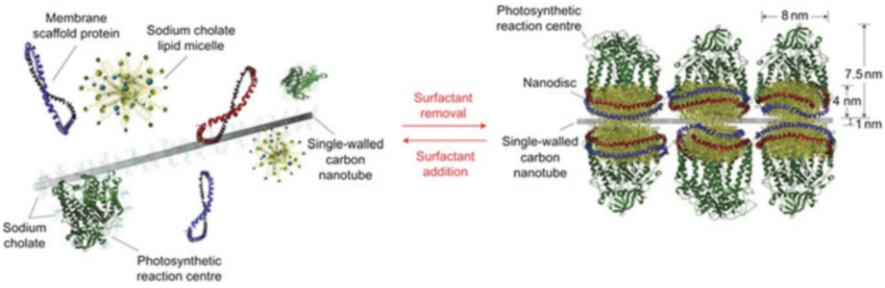

Fig. 11 Model of assembly and disassembly of bio-inspired complex by introduction and removal of sodium cholate [126]. Reprinted by permission from Macmillan Publishers Ltd: Nature [126], copyright 2010

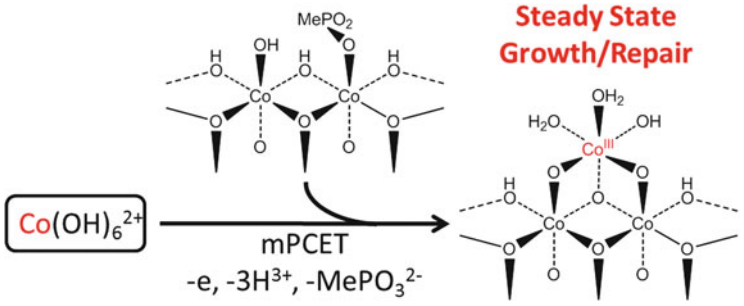

Fig. 12 Proposed self-healing mechanism for cobalt-based oxygen-evolving catalyst [127]. Reprinted with permission from Surendranath et al. [127]. Copyright (2012) American Chemical Society

In contrast to natural systems, Surendranath et al. and Lutterman et al. demonstrated an inexpensive oxygen-evolving catalyst based on cobalt oxides with a potential application in improved direct solar-to-fuel systems [127, 128]. During operation of the catalyst, Co(II) ions are released as $Co(OH_2)^{2+}$ complexes, which become oxidized in the presence of phosphate ions to re-deposit Co(III). Consequently, the cobalt oxide crystals are self-healed by spontaneous electrochemical oxidation. The proposed self-healing process depends on a specific phosphate ion concentration and the pH value (Fig. 12).

Another example of a self-healable solar cell material was investigated by Krebs and coworkers and is based on concentrated sunlight [129]. Organic solar cells were exposed to high intensity concentrated sunlight, leading to a transient decrease in performance. The desorption of oxygen by the ZnO electron transport layer leads to breakdown of the diode behavior and results in an increase in hole conductivity [130, 131]. Recovery of performance was observed when the solar cell was stored in the dark under exposure to air for 10 min. The proposed self-healing mechanism is based on the re-adsorption of oxygen by the ZnO layer.

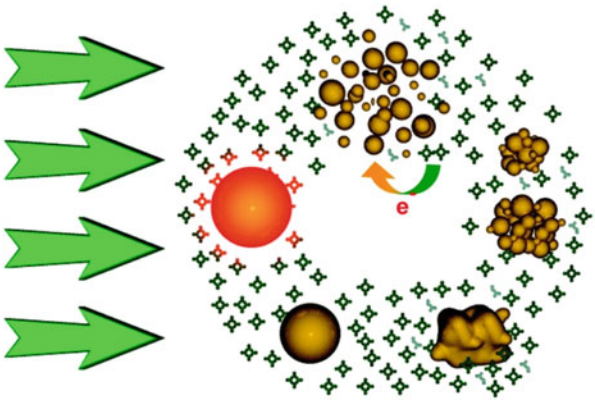

Fig. 13 Proposed self-healing process for gold nanoparticles in the presence of zinc phthalocyanines by irradiation with 532 nm laser pulses (9 ns) [132]. Reprinted with permission from Amendola et al. [132]. Copyright (2009) American Chemical Society

The first self-healing of the optoelectronic properties of nanoparticles was demonstrated by the group of Meneghetti [132]. The gold nanoparticles were synthesized by laser ablation synthesis in THF with 1,064 nm (pulse duration 9 ns) laser pulses. Further mixing with 2(3)-tetra-[2-(*tert*-butoxy)-ethyloxy]-phthalocyaninato in solution led to the desired blend. Afterwards, bare gold nanoparticles and the resulting blend were irradiated with 350 laser pulses (pulse duration 9 ns) with a wavelength of 532 nm at a constant fluence of 1,100 mJ/cm^2. Subsequently, the bare particles showed a rapid decrease in optical limiting efficiency, while the blend preserved almost the original performance as a result of self-healing ability. During laser irradiation, the gold nanoparticles absorb photons and are heated over their explosion threshold. Consequently, smaller particles with positive charges are created as a result of fragmentation of the original particles, and the optical limiting performance decreases. The presence of zinc phthalocyanines causes partial neutralization of the positive charges by oxidation of this additive. Because of the reduction in charge density, the stability of the colloidal gold nanoparticles decreases and aggregates form, which finally photomelt into the nearly original spherical gold nanoparticles with restored optical limiting properties (Fig. 13).

The fluorescence and photochromism of organic dyes is degraded by light irradiation or excessive heating, leading to a short lifetime for photonic devices. Therefore, the development of self-healable materials featuring these functions is required. The self-healing of optical functions of fluorophores at the molecular level can result in self-healable optoelectronics. For instance, Saito et al. investigated a self-healable fluorophore system based on diffusion in a swollen elastomer [133, 134]. Poly(dimethyl siloxane) was utilized as the swelling polymer matrix because of several matching properties, namely chemical stability, deformability, melting at room temperature, and high transmittance in the visible range. The swollen elastomeric dyes were prepared by simple mixing of a dye solution in toluene or 2-propanol with the polymer oil. Afterwards the mixture was solidified by adding a curing agent, and the reaction was complete after 8 h at room temperature. The fact that diffusion is required to have self-healing ability was

proven by putting a solution of dicyanomethylene in toluene on top of a toluene-swollen elastomer; after 7 days the dye was diffused throughout the whole elastomer. The self-healing mechanism was investigated using diarylethenes, which exhibit an absorption band in the visible range when exposed to a violet laser diode (405 nm, 0.15 mW/mm^2). The band disappears on exposure to a green laser diode (532 nm, 0.15 mW/mm^2). Furthermore, long-term experiments are possible because of the stable colored state of the dye. However, the transmittance of a swollen elastomeric dye with 60 vol% toluene decreases about 50% by irradiation with a violet laser diode and re-increases by irradiation with a green laser diode. This reversible process was repeated 3,000 times over 4–5 days. Degraded dye diffuses out of the operational region as a result of metabolism, and virgin dye diffuses in, which indicates the self-healing ability.

6 Self-Healing of Functional Coatings

Self-healing functional coatings are in the early stages of development. For instance, flame-retardant functional coatings were investigated by Sun and coworkers [135]. The authors utilized a trilayer composite consisting of ammonium polyphosphate, branched poly(ethylene imine), and fluorinated-decyl polyhedral oligomeric silsesquioxane. This composite was solution-dipped onto a cotton fabric. The combination of these compounds showed superhydrophobicity with an integrated self-healing function. Furthermore, the intumescent effect causes generation of a porous char layer when exposed to a flame, and cleaning can be achieved by simple water rinsing. A further self-healing of superhydrophobicity was investigated by Jia and coworkers using polystyrene/SiO_2 nanoparticles and poly(dimethyl siloxane) [136]. Treatment of the resulting superhydrophobic self-healable coatings by air plasma led to superhydrophilic properties of the surface, caused by decomposition of poly(dimethyl siloxane) and the introduction of polar groups. Restoration of the hydrophobic properties was achieved by exposure to an ambient environment for 12 h. Moreover, Wei et al. integrated a slippery effect into a superhydrophobic supramolecular self-healable polymer [137].

Further investigations on self-healing functional superhydrophobic surfaces were carried out by Liu et al. [138], Zhang et al. [139], Esteves et al. [140], and Zhou and coworkers [141]. In contrast to the previously described self-healing systems, an electrically conductive superhydrophobic surface was investigated by Lu and coworkers. 3,4-Ethylenedioxythiophene (EDOT) as a common thiophene derivative was utilized for preparing highly conductive and stable polymer films [142]. Further treatment with a hydrophobic fluoroalkylsilane (POTS) by chemical vapor deposition resulted in superhydrophobic properties. Oxygen plasma etching of the prepared coatings led to decomposition of the fluoroalkylsilane layer and, consequently, the water contact angle changed from 157° to 0°, which indicated hydrophilicity. After the damaged film was stored at 10°C and humidity of 85% for 2 h, the original superhydrophobicity was restored as a result of migration of the

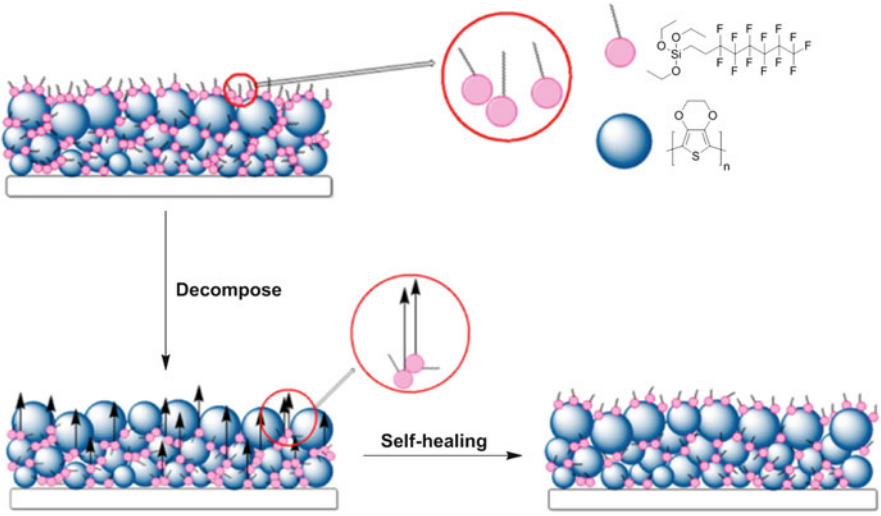

Fig. 14 Principle of a self-healable conductive superhydrophobic PEDOT coating [142]. Reprinted with permission from Zhu et al. [142]. Copyright (2014) American Chemical Society

fluoroalkylsilane out of the polymer coating onto the surface (Fig. 14). Another superhydrophobic self-healable functional coating based on the migration of small molecules in the film was investigated by Xue and coworkers [143].

Wang et al. developed an electroconductive superamphiphobic self-healing coating [144]. EDOT was vapor-phase polymerized onto fabric in the presence of fluorinated alkyl silane and oligomeric silsequioxane. The prepared coating showed contact angles of 169° and 156° against water and hexadecane, which indicated superamphiphobic properties. Furthermore, the self-healing ability was investigated by plasma treatment. The resulting plasma-treated coatings were hydrophilic and oleophilic against water and hexadecane, with a contact angle of 0°. Once the damaged samples were heated to 135°C for 5 min the original superamphiphobic properties were restored. In contrast, the self-healing process at room temperature required about 24 h. Wang et al. [145, 146] and Zou et al. [147] have made further developments on these self-healable superamphiphobic coatings.

7 Self-Healing of Other Selected Functionalities

In addition to self-healing of conductivity and optical properties, several other functionalities can be healed. However, these approaches have not been studied in detail up to now. For instance, the first self-healable supercapacitor was investigated by Chen and coworkers in 2014 [148]. Fabrication of the utilized

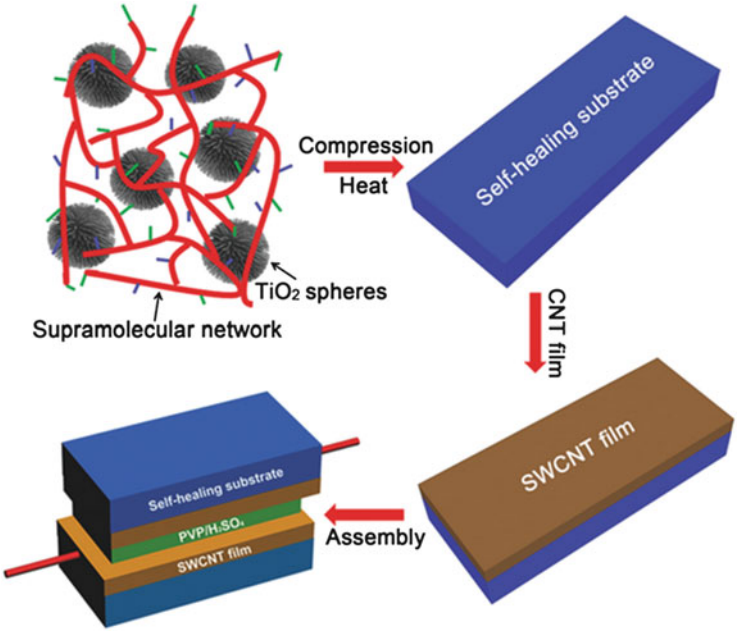

Fig. 15 Fabrication process for an electrically and mechanically self-healing supercapacitor [148]. Reprinted with permission from Wang et al. [148]. Copyright (2014) John Wiley and Sons

supercapacitors started with synthesis of the self-healing material, which consisted of reacted Empol 1016, diethylenetriamine, TiO_2 rutile nanoflowers, and urea. Subsequently, single-walled CNTs were spread onto the resulting composite. Finally, the single-walled nanotube films served as active material in the supercapacitor device, while poly(vinyl pyrrolidone) sulfuric acid gel served as a separator as well as electrolyte (Fig. 15). To investigate the self-healing ability, the prepared supercapacitor was damaged by cutting. After applying a light contact pressure to the two pieces at 50°C for 5 min, the original properties were almost fully recovered. The healing mechanism is based on reversible hydrogen bonds and self-adhering of the self-healing composite. The capacitance restoration was about 86% (30 F/g) after the fifth self-healing cycle, which indicates an efficient self-healing performance.

Katz and coworkers investigated a self-healing conductor with capacitance up to 1,440 nF/cm^2 [149]. The self-healing polymer blend consisted of poly (2-hydroxypropyl methacrylate) and poly(ethylene imine) in a mass ratio of 1:1 and was the first reported dielectric self-healable, flexible, printable and low-voltage-operable layer (with the exception of ion-gel dielectrics). Poly(ethylene imine) can interact with poly(2-hydroxypropyl methacrylate) through hydrogen bonding, which leads to increased mobility of the polymer blend at room temperature. In order to investigate the self-healing performance, the polymer surface was scratched and consequently the surface resistivity of the pure polymer increased from 4.5 to 9,000 Ω cm. Further storage at room temperature for 600 min led to

almost complete restoration of the surface resistivity (45 Ω cm), which indicates an effective self-healing ability. Moreover, the self-healing properties of the polymer blend were tested in a prepared organic field effect transistor. After cutting, the transistor was stored at room temperature for 10 h. The drain current was restored to 76% of its original value. This is the first example of a self-healing organic field effect transistor.

The first piezoelectric self-healable material was demonstrated by Groen and coworkers and was based on an ionomer matrix [150]. The self-healing material was prepared by dispersing soft doped Pb(Zr, Ti)O_3 in zinc-based ionomer Surlyn 9320 from DuPont. Piezoelectric ceramic particles embedded in a polymeric matrix exhibit several advantages compared with bare zirconium titanate ceramics, namely low acoustic impedance, mechanical flexibility, and high piezoelectric voltage constant. To investigate the self-healing properties, the resulting composites were strained at 6–8% for 15,000–50,000 cycles, which results in a decreased piezoelectric charge coefficient. Subsequent stress-free heating to 70°C for about 1 h resulted in a significant degree of recovery of the original piezoelectric properties.

Storage and capture of solar energy via conversion of water to hydrogen and oxygen, based on usage of the first self-healable photoelectrode, was investigated by Bocarsly and coworkers [151]. An efficient light absorber p-type $CuRhO_2$ electrode was demonstrated. The water reduction ability was investigated under argon- and air-saturated solutions in pH 14 electrolyte; the redox instability of the copper-containing electrode was the major limitation. Hydrogen production with 0.2 V underpotential was observed in air-saturated solutions. Argon-saturated electrolytes led to an unstable photoelectrode because of reduction to solid copper, whereas in air-saturated electrolytes the stable formation of hydrogen was observed, with a Faradaic efficiency of about 80%, by self-healing of the photoelectrode by oxygen.

The group of van der Zwaag investigated several self-healing thermally conductive adhesives based on the reversibility of disulfide bonds [152]. Loading of the matrix with fillers such as boron nitride or graphite-based materials resulted in enhancement of the adhesive and thermal conductivity properties of the composite. A mild temperature of 65°C was utilized for the desired thermally triggered self-healing process, resulting in full recovery of the adhesive strength and partial restoration of the cohesive strength. This first approach is an interesting route for production of self-healing adhesive thermal conductors for microsystem applications such as organic light-emitting diodes.

8 Conclusion and Outlook

In the early stages of research on self-healing materials, the healing process was exclusively based on the restoration of mechanical properties after mechanical damage (e.g., cracks, scratches). However, in recent years, self-healing functional materials have become the focus of research. The targeted healing of functionalities is manifold. Early self-healing polymer coatings are examples of such materials.

The healing of these coatings resulted not only in restoration of the mechanical properties; in addition, restoration of the aesthetics and electrochemical protection of the underlying material (e.g., metal) was achieved. Several other approaches have been developed, for instance the self-healing of optical properties and the restoration of conductivity. In engineering or structural materials, healing aims to restore mechanical properties such as stiffness and strength. In contrast, the healing of functional materials focuses on restoring functionalities after damage induced, for example, by irradiation, high temperature, or other harmful environments. This fact is a distinct challenge for the development of novel strategies for self-healing functional materials, because exact knowledge of the consequences of this damage (i.e., what is changed within the material of interest and what effects cause the failure) is required in order to accomplish self-healing (i.e., restoration of the original functionality). This requirement is of particular interest for self-healing materials for optical applications. The absorption or emission of such materials is primarily based on the presence of particular chromophores and luminophores. For instance, their decomposition (e.g., by photochemical processes) results in bleaching of the luminescence or loss/change in color of the materials. Consequently, healing within these materials must restore the original chromophore/luminophore. Consequently, approaches for self-healing optical materials should be based on molecular mechanisms.

Self-healing of electronic properties such as electrical conductivity was an early example of self-healing in the context of functional materials. This function allows the utilization of different healing agents and the requirements are less strict than for optical materials. The healing agent or newly generated phase "only" has to show a high charge mobility. Despite this early success in restoring the electronic properties of materials by means of self-healing, it is anticipated that future developments will result in more approaches for the restoration of conductivity. The self-healing of multifunctional materials is the ultimate goal. Biological materials/systems often fulfill different functions, which are also mimicked in artificial systems (e.g., artificial skin) [153]. Self-healing of these materials requires the independent restoration of different functionalities, which in itself requires different healing mechanisms to take place simultaneously or in close succession.

Acknowledgements The authors would like to thank the Deutsche Forschungsgemeinschaft (DFG) for financial support within the framework of the priority program SPP1568 (Design and Generic Principles of Self-healing Materials; HA6306/3-1, DI1517/9-1).

References

1. Yang Y, Urban MW (2013) Self-healing polymeric materials. Chem Soc Rev 42 (17):7446–7467
2. Zhang MQ, Rong MZ (2013) Intrinsic self-healing of covalent polymers through bond reconnection towards strength restoration. Polym Chem 4(18):4878–4884

3. Billiet S, Hillewaere XKD, Teixeira RFA, Du Prez FE (2013) Chemistry of crosslinking processes for self-healing polymers. Macromol Rapid Commun 34(4):290–309
4. van der Zwaag S (2007) An introduction to material design principles: damage prevention versus damage management. In: van der Zwaag S (ed) Self healing materials, vol 100, Springer series in materials science. Springer, Dordrecht, pp 1–18
5. Guimard NK, Oehlenschlaeger KK, Zhou JW, Hilf S, Schmidt FG, Barner-Kowollik C (2012) Current trends in the field of self-healing materials. Macromol Chem Phys 213 (2):131–143
6. Garcia SJ (2014) Effect of polymer architecture on the intrinsic self-healing character of polymers. Eur Polym J 53:118–125
7. Odom SA, Caruso MM, Finke AD, Prokup AM, Ritchey JA, Leonard JH, White SR, Sottos NR, Moore JS (2010) Restoration of conductivity with TTF-TCNQ charge-transfer salts. Adv Funct Mater 20(11):1721–1727
8. Blaiszik BJ, Kramer SLB, Grady ME, McIlroy DA, Moore JS, Sottos NR, White SR (2012) Autonomic restoration of electrical conductivity. Adv Mater 24(3):398–401
9. Amendola V, Meneghetti M (2009) Self-healing at the nanoscale. Nanoscale 1(1):74–88
10. Zheng Q, Juette MF, Jockusch S, Wasserman MR, Zhou Z, Altman RB, Blanchard SC (2014) Ultra-stable organic fluorophores for single-molecule research. Chem Soc Rev 43 (4):1044–1056
11. Williams KA, Boydston AJ, Bielawski CW (2007) Towards electrically conductive, self-healing materials. J R Soc Interface 4(13):359–362
12. Neilson BM, Tennyson AG, Bielawski CW (2012) Advances in bis(N-heterocyclic carbene) chemistry: new classes of structurally dynamic materials. J Phys Org Chem 25(7):531–543
13. Norris BC, Bielawski CW (2010) Structurally dynamic materials based on bis(N-heterocyclic carbene)s and bis(isothiocyanate)s: toward reversible, conjugated polymers. Macromolecules 43(8):3591–3593
14. Hager MD, Greil P, Leyens C, van der Zwaag S, Schubert US (2010) Self-healing materials. Adv Mater 22(47):5424–5430
15. Bergman SD, Wudl F (2008) Mendable polymers. J Mater Chem 18(1):41–62
16. White SR, Sottos NR, Geubelle PH, Moore JS, Kessler MR, Sriram SR, Brown EN, Viswanathan S (2001) Autonomic healing of polymer composites. Nature 409 (6822):794–797
17. Tennyson AG, Norris B, Bielawski CW (2010) Structurally dynamic conjugated polymers. Macromolecules 43(17):6923–6935
18. Hucker M, Bond I, Bleay S, Haq S (2003) Experimental evaluation of unidirectional hollow glass fibre/epoxy composites under compressive loading. Compos A Appl Sci Manuf 34 (10):927–932
19. Wilson GO, Moore JS, White SR, Sottos NR, Andersson HM (2008) Autonomic healing of epoxy vinyl esters via ring opening metathesis polymerization. Adv Funct Mater 18(1):44–52
20. Brown EN, White SR, Sottos NR (2004) Microcapsule induced toughening in a self-healing polymer composite. J Mater Sci 39(5):1703–1710
21. Rule JD, Sottos NR, White SR (2007) Effect of microcapsule size on the performance of self-healing polymers. Polymer 48(12):3520–3529
22. Blaiszik BJ, Sottos NR, White SR (2008) Nanocapsules for self-healing materials. Compos Sci Technol 68(3–4):978–986
23. Wilson GO, Caruso MM, Reimer NT, White SR, Sottos NR, Moore JS (2008) Evaluation of ruthenium catalysts for ring-opening metathesis polymerization-based self-healing applications. Chem Mater 20(10):3288–3297
24. Brown EN, Kessler MR, Sottos NR, White SR (2003) In situ poly(urea-formaldehyde) microencapsulation of dicyclopentadiene. J Microencapsul 20(6):719–730
25. Lanzara G, Yoon Y, Liu H, Peng S, Lee WI (2009) Carbon nanotube reservoirs for self-healing materials. Nanotechnology 20(33):335704

26. Toohey KS, Sottos NR, Lewis JA, Moore JS, White SR (2007) Self-healing materials with microvascular networks. Nat Mater 6(8):581–585
27. Williams HR, Trask RS, Knights AC, Williams ER, Bond IP (2008) Biomimetic reliability strategies for self-healing vascular networks in engineering materials. J R Soc Interface 5 (24):735–747
28. Hamilton AR, Sottos NR, White SR (2010) Self-healing of internal damage in synthetic vascular materials. Adv Mater 22(45):5159–5163
29. Cordier P, Tournilhac F, Soulie-Ziakovic C, Leibler L (2008) Self-healing and thermoreversible rubber from supramolecular assembly. Nature 451(7181):977–980
30. Kersey FR, Loveless DM, Craig SL (2007) A hybrid polymer gel with controlled rates of cross-link rupture and self-repair. J R Soc Interface 4(13):373–380
31. Chujo Y, Sada K, Nomura R, Naka A, Saegusa T (1993) Photogelation and redox properties of anthracene disulfide-modified polyoxazolines. Macromolecules 26(21):5611–5614
32. Chung CM, Roh YS, Cho SY, Kim JG (2004) Crack healing in polymeric materials via photochemical [2+2] cycloaddition. Chem Mater 16(21):3982–3984
33. Banerjee S, Tripathy R, Cozzens D, Nagy T, Keki S, Zsuga M, Faust R (2015) Photoinduced smart, self-healing polymer sealant for photovoltaics. ACS Appl Mater Interfaces 7 (3):2064–2072
34. Kang HS, Kim HT, Park JK, Lee S (2014) Light-powered healing of a wearable electrical conductor. Adv Funct Mater 24(46):7273–7283
35. Gruendling T, Kaupp M, Blinco JP, Barner-Kowollik C (2011) Photoinduced conjugation of dithioester- and trithiocarbonate-functional RAFT polymers with alkenes. Macromolecules 44(1):166–174
36. Otsuka H, Nagano S, Kobashi Y, Maeda T, Takahara A (2010) A dynamic covalent polymer driven by disulfide metathesis under photoirradiation. Chem Commun 46(7):1150–1152
37. Scott TF, Schneider AD, Cook WD, Bowman CN (2005) Photoinduced plasticity in cross-linked polymers. Science 308(5728):1615–1617
38. Burnworth M, Tang LM, Kumpfer JR, Duncan AJ, Beyer FL, Fiore GL, Rowan SJ, Weder C (2011) Optically healable supramolecular polymers. Nature 472(7343):334–338
39. Coulibaly S, Roulin A, Balog S, Biyani MV, Foster EJ, Rowan SJ, Fiore GL, Weder C (2014) Reinforcement of optically healable supramolecular polymers with cellulose nanocrystals. Macromolecules 47(1):152–160
40. Ghosh B, Urban MW (2009) Self-repairing oxetane-substituted chitosan polyurethane networks. Science 323(5920):1458–1460
41. Wang ZH, Yang Y, Burtovyy R, Luzinov I, Urban MW (2014) UV-induced self-repairing polydimethylsiloxane-polyurethane (PDMS-PUR) and polyethylene glycol-polyurethane (PEG-PUR) Cu-catalyzed networks. J Mater Chem A 2(37):15527–15534
42. Kemp M, Go YM, Jones DP (2008) Nonequilibrium thermodynamics of thiol/disulfide redox systems: a perspective on redox systems biology. Free Radic Biol Med 44(6):921–937
43. Kowalski D, Ueda M, Ohtsuka T (2010) Self-healing ion-permselective conducting polymer coating. J Mater Chem 20(36):7630–7633
44. Kwok N, Hahn HT (2007) Resistance heating for self-healing composites. J Compos Mater 41(13):1635–1654
45. Lv LP, Zhao Y, Vilbrandt N, Gallei M, Vimalanandan A, Rohwerder M, Landfester K, Crespy D (2013) Redox responsive release of hydrophobic self-healing agents from polyaniline capsules. J Am Chem Soc 135(38):14198–14205
46. Vimalanandan A, Lv LP, Tran TH, Landfester K, Crespy D, Rohwerder M (2013) Redox-responsive self-healing for corrosion protection. Adv Mater 25(48):6980–6984
47. Vogt AP, Sumerlin BS (2009) Temperature and redox responsive hydrogels from ABA triblock copolymers prepared by RAFT polymerization. Soft Matter 5(12):2347–2351
48. Deng GH, Tang CM, Li FY, Jiang HF, Chen YM (2010) Covalent cross-linked polymer gels with reversible sol-gel transition and self-healing properties. Macromolecules 43 (3):1191–1194

49. Jay JI, Langheinrich K, Hanson MC, Mahalingam A, Kiser PF (2011) Unequal stoichiometry between crosslinking moieties affects the properties of transient networks formed by dynamic covalent crosslinks. Soft Matter 7(12):5826–5835
50. Ge Z, Hu J, Huang F, Liu S (2009) Responsive supramolecular gels constructed by crown ether based molecular recognition. Angew Chem Int Ed 48(10):1798–1802
51. Craven JM (1969) US Patent 3.435.003
52. Chen XX, Dam MA, Ono K, Mal A, Shen HB, Nutt SR, Sheran K, Wudl F (2002) A thermally re-mendable cross-linked polymeric material. Science 295(5560):1698–1702
53. Chen XX, Wudl F, Mal AK, Shen HB, Nutt SR (2003) New thermally remendable highly cross-linked polymeric materials. Macromolecules 36(6):1802–1807
54. Zhang Y, Broekhuis AA, Picchioni F (2009) Thermally self-healing polymeric materials: the next step to recycling thermoset polymers? Macromolecules 42(6):1906–1912
55. Kötteritzsch J, Stumpf S, Höppener S, Vitz J, Hager MD, Schubert US (2013) One-component intrinsic self-healing coatings based on reversible crosslinking by Diels-Alder cycloadditions. Macromol Chem Phys 214(14):1636–1649
56. Kötteritzsch J, Hager MD, Schubert US (2015) Tuning the self-healing behavior of one-component intrinsic polymers. Polymer 69:321–329
57. Oehlenschlaeger KK, Mueller JO, Brandt J, Hilf S, Lederer A, Wilhelm M, Graf R, Coote ML, Schmidt FG, Barner-Kowollik C (2014) Adaptable hetero Diels-Alder networks for fast self-healing under mild conditions. Adv Mater 26(21):3561–3566
58. Inglis AJ, Nebhani L, Altintas O, Schmidt FG, Barner-Kowollik C (2010) Rapid bonding/debonding on demand: reversibly cross-linked functional polymers via Diels-Alder chemistry. Macromolecules 43(13):5515–5520
59. Burattini S, Colquhoun HM, Fox JD, Friedmann D, Greenland BW, Harris PJF, Hayes W, Mackay ME, Rowan SJ (2009) A self-repairing, supramolecular polymer system: healability as a consequence of donor-acceptor pi-pi stacking interactions. Chem Commun 44:6717–6719
60. Burattini S, Colquhoun HM, Greenland BW, Hayes W (2009) A novel self-healing supramolecular polymer system. Faraday Discuss 143:251–264
61. Burattini S, Greenland BW, Merino DH, Weng WG, Seppala J, Colquhoun HM, Hayes W, Mackay ME, Hamley IW, Rowan SJ (2010) A healable supramolecular polymer blend based on aromatic π-π stacking and hydrogen-bonding interactions. J Am Chem Soc 132 (34):12051–12058
62. Lafont U, van Zeijl H, van der Zwaag S (2012) Influence of cross-linkers on the cohesive and adhesive self-healing ability of polysulfide-based thermosets. ACS Appl Mater Interfaces 4 (11):6280–6288
63. Canadell J, Goossens H, Klumperman B (2011) Self-healing materials based on disulfide links. Macromolecules 44(8):2536–2541
64. Kuhl N, Bode S, Bose RK, Vitz J, Seifert A, Hoeppener S, Garcia SJ, Spange S, van der Zwaag S, Hager MD, Schubert US (2015) Acylhydrazones as reversible covalent crosslinkers for self-healing polymers. Adv Funct Mater 25(22):3295–3301
65. Sandmann B, Bode S, Hager M, Schubert U (2013) Metallopolymers as an emerging class of self-healing materials. In: Percec V (ed) Hierarchical macromolecular structures: 60 Years after the Staudinger Nobel Prize II, vol 262, Advances in polymer science. Springer International, Cham, pp 239–257
66. Bode S, Bose RK, Matthes S, Ehrhardt M, Seifert A, Schacher FH, Paulus RM, Stumpf S, Sandmann B, Vitz J, Winter A, Hoeppener S, Garcia SJ, Spange S, van der Zwaag S, Hager MD, Schubert US (2013) Self-healing metallopolymers based on cadmium bis(terpyridine) complex containing polymer networks. Polym Chem 4(18):4966–4973
67. Kupfer S, Zedler L, Guthmuller J, Bode S, Hager MD, Schubert US, Popp J, Grafe S, Dietzek B (2014) Self-healing mechanism of metallopolymers investigated by QM/MM simulations and Raman spectroscopy. Phys Chem Chem Phys 16(24):12422–12432

68. Enke M, Bode S, Vitz J, Schacher FH, Harrington MJ, Hager MD, Schubert US (2015) Self-healing response in supramolecular polymers based on reversible zinc–histidine interactions. Polymer 69:274–282
69. Bode S, Zedler L, Schacher FH, Dietzek B, Schmitt M, Popp J, Hager MD, Schubert US (2013) Self-healing polymer coatings based on crosslinked metallosupramolecular copolymers. Adv Mater 25(11):1634–1638
70. Mozhdehi D, Ayala S, Cromwell OR, Guan ZB (2014) Self-healing multiphase polymers via dynamic metal-ligand interactions. J Am Chem Soc 136(46):16128–16131
71. Kalista SJ, Ward TC (2007) Thermal characteristics of the self-healing response in poly (ethylene-co-methacrylic acid) copolymers. J R Soc Interface 4(13):405–411
72. Kalista SJ (2007) Self-healing of poly(ethylene-co-methacrylic acid) copolymers following projectile puncture. Mech Adv Mater Struct 14(5):391–397
73. Kalista SJ, Pflug JR, Varley RJ (2013) Effect of ionic content on ballistic self-healing in EMAA copolymers and ionomers. Polym Chem 4(18):4910–4926
74. Varley RJ, van der Zwaag S (2008) Towards an understanding of thermally activated self-healing of an ionomer system during ballistic penetration. Acta Mater 56(19):5737–5750
75. Varley RJ, van der Zwaag S (2008) Development of a quasi-static test method to investigate the origin of self-healing in ionomers under ballistic conditions. Polym Test 27(1):11–19
76. Varley RJ, van der Zwaag S (2010) Autonomous damage initiated healing in a thermo-responsive ionomer. Polym Int 59(8):1031–1038
77. Bose RK, Lafont U, Vega JM, Garcia SJ, van der Zwaag S (2013) Methods to monitor and quantify (self-) healing in polymers and polymer systems. In: Self-healing polymers. Wiley-VCH, Weinheim, pp 335–359
78. Zedler L, Hager MD, Schubert US, Harrington MJ, Schmitt M, Popp J, Dietzek B (2014) Monitoring the chemistry of self-healing by vibrational spectroscopy - current state and perspectives. Mater Today 17(2):57–69
79. Chen JH, Shi TW, Cai TC, Xu T, Sun LT, Wu XS, Yu DP (2013) Self healing of defected graphene. Appl Phys Lett 102(10):103107
80. Tee BCK, Wang C, Allen R, Bao ZN (2012) An electrically and mechanically self-healing composite with pressure- and flexion-sensitive properties for electronic skin applications. Nat Nanotechnol 7(12):825–832
81. Wang C, Wu H, Chen Z, McDowell MT, Cui Y, Bao ZA (2013) Self-healing chemistry enables the stable operation of silicon microparticle anodes for high-energy lithium-ion batteries. Nat Chem 5(12):1043–1049
82. Hou CY, Duan YR, Zhang QH, Wang HZ, Li YG (2012) Bio-applicable and electroactive near-infrared laser-triggered self-healing hydrogels based on graphene networks. J Mater Chem 22(30):14991–14996
83. Peng RG, Yu Y, Chen S, Yang YK, Tang YH (2014) Conductive nanocomposite hydrogels with self-healing property. RSC Adv 4(66):35149–35155
84. Hur J, Im K, Kim SW, Kim J, Chung DY, Kim TH, Jo KH, Hahn JH, Bao ZA, Hwang S, Park N (2014) Polypyrrole/agarose-based electronically conductive and reversibly restorable hydrogel. ACS Nano 8(10):10066–10076
85. Li Y, Chen SS, Wu MC, Sun JQ (2012) Polyelectrolyte multilayers impart healability to highly electrically conductive films. Adv Mater 24(33):4578–4582
86. Sun H, You X, Jiang YS, Guan GZ, Fang X, Deng J, Chen PN, Luo YF, Peng HS (2014) Self-healable electrically conducting wires for wearable microelectronics. Angew Chem Int Ed 53 (36):9526–9531
87. Zhang DL, Ju X, Li LH, Kang Y, Gong XL, Li BJ, Zhang S (2015) An efficient multiple healing conductive composite via host-guest inclusion. Chem Commun (Camb) 51 (29):6377–6380
88. Odom SA, Tyler TP, Caruso MM, Ritchey JA, Schulmerich MV, Robinson SJ, Bhargava R, Sottos NR, White SR, Hersam MC, Moore JS (2012) Autonomic restoration of electrical conductivity using polymer-stabilized carbon nanotube and graphene microcapsules. Appl Phys Lett 101(4):043106

89. Kang S, Jones AR, Moore JS, White SR, Sottos NR (2014) Microencapsulated carbon black suspensions for restoration of electrical conductivity. Adv Funct Mater 24(20):2947–2956
90. Blaiszik BJ, Jones AR, Sottos NR, White SR (2014) Microencapsulation of gallium-indium (Ga-In) liquid metal for self-healing applications. J Microencapsul 31(4):350–354
91. Odom SA, Chayanupatkul S, Blaiszik BJ, Zhao O, Jackson AC, Braun PV, Sottos NR, White SR, Moore JS (2012) A self-healing conductive ink. Adv Mater 24(19):2578–2581
92. So JH, Thelen J, Qusba A, Hayes GJ, Lazzi G, Dickey MD (2009) Reversibly deformable and mechanically tunable fluidic antennas. Adv Funct Mater 19(22):3632–3637
93. Palleau E, Reece S, Desai SC, Smith ME, Dickey MD (2013) Self-healing stretchable wires for reconfigurable circuit wiring and 3D microfluidics. Adv Mater 25(11):1589–1592
94. Bubel S, Menyo MS, Mates TE, Waite JH, Chabinyc ML (2015) Schmitt trigger using a self-healing ionic liquid gated transistor. Adv Mater 27(21):3331–3335
95. Boydston AJ, Williams KA, Bielawski CW (2005) A modular approach to main-chain organometallic polymers. J Am Chem Soc 127(36):12496–12497
96. Boydston AJ, Rice JD, Sanderson MD, Dykhno OL, Bielawski CW (2006) Synthesis and study of bidentate benzimidazolylidene - group 10 metal complexes and related main-chain organometallic polymers. Organometallics 25(26):6087–6098
97. Khramov DM, Boydston AJ, Bielawski CW (2006) Synthesis and study of Janus bis(carbene) s and their transition-metal complexes. Angew Chem Int Ed 45(37):6186–6189
98. Boydston AJ, Bielawski CW (2006) Bis(imidazolylidene)s as modular building blocks for monomeric and macromolecular organometallic materials. Dalton Trans 34:4073–4077
99. Meyer CD, Joiner CS, Stoddart JF (2007) Template-directed synthesis employing reversible imine bond formation. Chem Soc Rev 36(11):1705–1723
100. Fukuda K, Shimoda M, Sukegawa M, Nobori T, Lehn JM (2012) Doubly degradable dynamers: dynamic covalent polymers based on reversible imine connections and biodegradable polyester units. Green Chem 14(10):2907–2911
101. Ro S, Rowan SJ, Pease AR, Cram DJ, Stoddart JF (2000) Dynamic hemicarcerands and hemicarceplexes. Org Lett 2(16):2411–2414
102. Bozdemir OA, Barin G, Belowich ME, Basuray AN, Beuerle F, Stoddart JF (2012) Dynamic covalent templated-synthesis of [c2] daisy chains. Chem Commun 48(84):10401–10403
103. Belowich ME, Stoddart JF (2012) Dynamic imine chemistry. Chem Soc Rev 41 (6):2003–2024
104. Janeliunas D, van Rijn P, Boekhoven J, Minkenberg CB, van Esch JH, Eelkema R (2013) Aggregation-driven reversible formation of conjugated polymers in water. Angew Chem Int Ed 52(7):1998–2001
105. Zhao DH, Moore JS (2003) Folding-driven reversible polymerization of oligo(m-phenylene ethynylene) imines: solvent and starter sequence studies. Macromolecules 36(8):2712–2720
106. Kovaricek P, Lehn JM (2012) Merging constitutional and motional covalent dynamics in reversible imine formation and exchange processes. J Am Chem Soc 134(22):9446–9455
107. Kim DY, Sinha-Ray S, Park JJ, Lee JG, Cha YH, Bae SH, Ahn JH, Jung YC, Kim SM, Yarin AL, Yoon SS (2014) Self-healing reduced graphene oxide films by supersonic kinetic spraying. Adv Funct Mater 24(31):4986–4995
108. Um JE, Chung CH, Lee DC, Yoo PJ, Kim WJ (2014) Restoration of the genuine electronic properties of functionalized single-walled carbon nanotubes. RSC Adv 4(81):42930–42935
109. Benight SJ, Wang C, Tok JBH, Bao ZA (2013) Stretchable and self-healing polymers and devices for electronic skin. Prog Polym Sci 38(12):1961–1977
110. Liu JQ, Song GS, He CC, Wang HL (2013) Self-healing in tough graphene oxide composite hydrogels. Macromol Rapid Commun 34(12):1002–1007
111. Kim JT, Kim BK, Kim EY, Kwon SH, Jeong HM (2013) Synthesis and properties of near IR induced self-healable polyurethane/graphene nanocomposites. Eur Polym J 49 (12):3889–3896
112. Roy S, Baral A, Banerjee A (2013) An amino-acid-based self-healing hydrogel: modulation of the self-healing properties by incorporating carbon-based nanomaterials. Chem Eur J 19 (44):14950–14957

113. Caruso MM, Schelkopf SR, Jackson AC, Landry AM, Braun PV, Moore JS (2009) Microcapsules containing suspensions of carbon nanotubes. J Mater Chem 19(34):6093–6096
114. Pastine SJ, Okawa D, Zettl A, Frechet JMJ (2009) Chemicals on demand with phototriggerable microcapsules. J Am Chem Soc 131(38):13586–13587
115. Mineart KP, Lin YL, Desai SC, Krishnan AS, Spontak RJ, Dickey MD (2013) Ultrastretchable, cyclable and recyclable 1- and 2-dimensional conductors based on physically cross-linked thermoplastic elastomer gels. Soft Matter 9(32):7695–7700
116. Coillot D, Méar FO, Podor R, Montagne L (2010) Autonomic self-repairing glassy materials. Adv Funct Mater 20(24):4371–4374
117. Coillot D, Méar FO, Podor R, Montagne L (2011) Influence of the active particles on the self-healing efficiency in glassy matrix. Adv Eng Mater 13(5):426–435
118. Jackson AC, Bartelt JA, Braun PV (2011) Transparent self-healing polymers based on encapsulated plasticizers in a thermoplastic matrix. Adv Funct Mater 21(24):4705–4711
119. Gerth M, Bohdan M, Fokkink R, Voets IK, van der Gucht J, Sprakel J (2014) Supramolecular assembly of self-healing nanocomposite hydrogels. Macromol Rapid Commun 35 (24):2065–2070
120. Vidyasagar A, Handore K, Sureshan KM (2011) Soft optical devices from self-healing gels formed by oil and sugar-based organogelators. Angew Chem Int Ed 50(35):8021–8024
121. Hager MD, Bode S, Weber C, Schubert US (2015) Shape memory polymers: past, present and future developments. Prog Polym Sci (49–50):3–33. doi:10.1016/j.progpolymsci.2015.04.002
122. Rodriguez ED, Luo XF, Mather PT (2011) Linear/network poly(epsilon-caprolactone) blends exhibiting shape memory assisted self-healing (SMASH). ACS Appl Mater Interfaces 3(2):152–161
123. Lee MW, An S, Lee C, Liou M, Yarin AL, Yoon SS (2014) Self-healing transparent core-shell nanofiber coatings for anti-corrosive protection. J Mater Chem A 2(19):7045–7053
124. Wang X, Liu F, Zheng XW, Sun JQ (2011) Water-enabled self-healing of polyelectrolyte multilayer coatings. Angew Chem Int Ed 50(48):11378–11381
125. Lei XF, Chen Y, Zhang HP, Li XJ, Yao P, Zhang QY (2013) Space survivable polyimides with excellent optical transparency and self-healing properties derived from hyperbranched polysiloxane. ACS Appl Mater Interfaces 5(20):10207–10220
126. Ham MH, Choi JH, Boghossian AA, Jeng ES, Graff RA, Heller DA, Chang AC, Mattis A, Bayburt TH, Grinkova YV, Zeiger AS, Van Vliet KJ, Hobbie EK, Sligar SG, Wraight CA, Strano MS (2010) Photoelectrochemical complexes for solar energy conversion that chemically and autonomously regenerate. Nat Chem 2(11):929–936
127. Surendranath Y, Lutterman DA, Liu Y, Nocera DG (2012) Nucleation, growth, and repair of a cobalt-based oxygen evolving catalyst. J Am Chem Soc 134(14):6326–6336
128. Lutterman DA, Surendranath Y, Nocera DG (2009) A self-healing oxygen-evolving catalyst. J Am Chem Soc 131(11):3838–3839
129. Tromholt T, Manor A, Katz EA, Krebs FC (2011) Reversible degradation of inverted organic solar cells by concentrated sunlight. Nanotechnology 22(22):225401
130. Verbakel F, Meskers SCJ, Janssen RAJ (2006) Electronic memory effects in diodes from a zinc oxide nanoparticle-polystyrene hybrid material. Appl Phys Lett 89(10):102103
131. Verbakel F, Meskers SCJ, Janssen RAJ (2007) Electronic memory effects in diodes of zinc oxide nanoparticles in a matrix of polystyrene or poly(3-hexylthiophene). J Appl Phys 102 (8):083701
132. Amendola V, Dini D, Polizzi S, Sheng J, Kadish KM, Calvete MJF, Hanack M, Meneghetti M (2009) Self-healing of gold nanoparticles in the presence of zinc phthalocyanines and their very efficient nonlinear absorption performances. J Phys Chem C 113(20):8688–8695
133. Saito M, Nishimura T, Sakiyama K, Inagaki S (2012) Self-healing of optical functions by molecular metabolism in a swollen elastomer. AIP Adv 2(4):042118
134. Saito M, Sakiyama K (2013) Self-healable photochromic elastomer that transmits optical signals depending on the pulse frequency. J Opt 15(10):105404

135. Chen S, Li X, Li Y, Sun J (2015) Intumescent flame-retardant and self-healing superhydrophobic coatings on cotton fabric. ACS Nano 9(4):4070–4076
136. Xue CH, Zhang ZD, Zhang J, Jia ST (2014) Lasting and self-healing superhydrophobic surfaces by coating of polystyrene/SiO2 nanoparticles and polydimethylsiloxane. J Mater Chem A 2(36):15001–15007
137. Wei Q, Schlaich C, Prevost S, Schulz A, Bottcher C, Gradzielski M, Qi ZH, Haag R, Schalley CA (2014) Supramolecular polymers as surface coatings: rapid fabrication of healable superhydrophobic and slippery surfaces. Adv Mater 26(43):7358–7364
138. Liu YH, Liu YP, Hu HY, Liu ZL, Pei XW, Yu B, Yan PX, Zhou F (2015) Mechanically induced self-healing superhydrophobicity. J Phys Chem C 119(13):7109–7114
139. Zhang Y, Rocco C, Karasu F, van der Ven LGJ, van Benthem RATM, Allonas X, Croutxé-Barghorn C, Esteves ACC, de With G (2015) UV-cured self-replenishing hydrophobic polymer films. Polymer 69:384–393
140. Esteves ACC, Luo Y, van de Put MWP, Carcouët CCM, de With G (2014) Self-replenishing dual structured superhydrophobic coatings prepared by drop-casting of an all-in-one dispersion. Adv Funct Mater 24(7):986–992
141. Wang Y, Liu XW, Zhang HF, Zhou ZP (2015) Fabrication of self-healing super-hydrophobic surfaces on aluminium alloy substrates. AIP Adv 5(4):041314
142. Zhu DD, Lu XM, Lu QH (2014) Electrically conductive PEDOT coating with self-healing superhydrophobicity. Langmuir 30(16):4671–4677
143. Liu QZ, Wang XL, Yu B, Zhou F, Xue QJ (2012) Self-healing surface hydrophobicity by consecutive release of hydrophobic molecules from mesoporous silica. Langmuir 28 (13):5845–5849
144. Wang HX, Zhou H, Gestos A, Fang J, Niu HT, Ding J, Lin T (2013) Robust, electroconductive, self-healing superamphiphobic fabric prepared by one-step vapour-phase polymerisation of poly(3,4-ethylenedioxythiophene) in the presence of fluorinated decyl polyhedral oligomeric silsesquioxane and fluorinated alkyl silane. Soft Matter 9(1):277–282
145. Wang H, Xue Y, Ding J, Feng L, Wang X, Lin T (2011) Durable, self-healing superhydrophobic and superoleophobic surfaces from fluorinated-decyl polyhedral oligomeric silsesquioxane and hydrolyzed fluorinated alkyl silane. Angew Chem Int Ed 50 (48):11433–11436
146. Wang HD, Zhou H, Gestos A, Fang J, Lin T (2013) Robust, superamphiphobic fabric with multiple self-healing ability against both physical and chemical damages. ACS Appl Mater Interfaces 5(20):10221–10226
147. Zhou H, Wang HX, Niu HT, Gestos A, Lin T (2013) Robust, self-healing superamphiphobic fabrics prepared by two-step coating of fluoro-containing polymer, fluoroalkyl silane, and modified silica nanoparticles. Adv Funct Mater 23(13):1664–1670
148. Wang H, Zhu BW, Jiang WC, Yang Y, Leow WR, Wang H, Chen XD (2014) A mechanically and electrically self-healing supercapacitor. Adv Mater 26(22):3638–3643
149. Huang WG, Besar K, Zhang Y, Yang SY, Wiedman G, Liu Y, Guo WM, Song J, Hemker K, Hristova K, Kymissis IJ, Katz HE (2015) A high-capacitance salt-free dielectric for self-healable, printable, and flexible organic field effect transistors and chemical sensor. Adv Funct Mater 25(24):3745–3755
150. James NK, Lafont U, van der Zwaag S, Groen WA (2014) Piezoelectric and mechanical properties of fatigue resistant, self-healing PZT-ionomer composites. Smart Mater Struct 23 (5):055001
151. Gu J, Yan Y, Krizan JW, Gibson QD, Detweiler ZM, Cava RJ, Bocarsly AB (2014) p-Type CuRhO2 as a self-healing photoelectrode for water reduction under visible light. J Am Chem Soc 136(3):830–833
152. Lafont U, Moreno-Belle C, van Zeijl H, van der Zwaag S (2013) Self-healing thermally conductive adhesives. J Intell Mater Syst Struct 25(1):67–74
153. Ramuz M, Tee BC-K, Tok JB-H, Bao Z (2012) Transparent, optical, pressure-sensitive artificial skin for large-area stretchable electronics. Adv Mater 24(24):3223–3227

Adv Polym Sci (2016) 273: 285–306
DOI: 10.1007/12_2015_335

Published online: 3 November 2015

Self-Healing Technology for Asphalt Pavements

Amir Tabaković and Erik Schlangen

Abstract Self-healing technology is a new field within material technology. It represents a revolution in materials engineering and is changing the way that materials behave. Incorporating self-healing technology into the road design process has the potential to transform road construction and maintenance processes by increasing the lifespan of roads and eliminating the need for road maintenance. By decreasing the unnecessary premature ageing of asphalt pavements, self-healing asphalt can reduce the amount of natural resources used to maintain road networks, decrease the traffic disruption caused by road maintenance processes, decrease CO_2 emissions during the road maintenance process and increase road safety. In addition to environmental savings, self-healing materials have the potential to deliver significant cost savings for road network maintenance across the EU. There are three main self-healing technologies available for asphalt pavement design: nanoparticles, induction heating and rejuvenation. This chapter reviews all three options and outlines the future development of self-healing asphalt technology.

Keywords Asphalt pavements · Induction heating · Microcapsule · Nanoparticles · Rejuvenation · Self-healing

Contents

A. Tabaković (✉) and E. Schlangen
Materials and Environment, Faculty of Civil Engineering and Geosciences, Delft University of Technology, Delft, The Netherlands
e-mail: A.Tabakovic@tudelft.nl; Erik.Schlangen@tudelft.nl

1 Introduction

The global road network spans 16.3 million kilometres [1], of which 5 million kilometres is in the EU, 4.4 million kilometres in the USA and 3.1 million kilometres in China [2]. Road networks fulfil a major economic and social goal by facilitating the movement of goods and people. The operational health of the road network is of the utmost importance for national and regional economic and social life. As a result, governments invest heavily in the development and maintenance of national and regional road networks. In 2009, EU governments invested 42% (€4.5 billion) of the EU transport network fund (€10.74 billion) into the development and maintenance of EU road networks [2]. The development and maintenance of the EU road network is crucial for the growth and competitiveness of the EU economy.

A typical modern road system comprises double or triple asphalt layers [3] with an expected lifespan of 20–40 years [4]. Recent research highlights the importance of developing long-life or perpetual pavements and has called for innovation to prolong pavement lifespan and reduce maintenance [5, 6]. The development of self-healing asphalt and its use in road paving is an innovation that could potentially double road lifespan to between 40 and 80 years and could significantly reduce road maintenance activity. In comparison with current maintenance processes, self-healing asphalt has the potential to improve traffic flow, reduce demand for fresh aggregate, reduce CO_2 emissions and enhance road safety. The excellent durability of self-healing materials does not arise from the classical approach of minimizing damage but from the novel approach of designing materials with "self-healing" capabilities.

The objective of self-healing technology is to enable/assist material systems to heal after damage. It aims to reduce the level of damage and to extend or renew the functionality and lifetime of the damaged part [7]. Fisher defines the self-healing and self-repair of a material or system as "the ability to substantially return to an initial, proper operating state or condition prior exposure to a dynamic environment by making the necessary adjustments to restore to normality and/or the ability to resist the formation of irregularities and/or defects" [7].

The repair is, in principle, an automatic initiated response to damage or failure. To perform repair, any self-healing system must be capable of identifying and repairing damage. Fisher classifies repair into two categories:

Attributive repair: restoring the attributes of the system to its original state (i.e. to full capacity).

Table 1 Materials to which self-healing technology has been successfully applied

Material	Healing mechanism	Reference	Year
Polymer	Healing agent encapsulation	Jin et al. [9]	2012
Concrete	Bacteria	Jonkers and Schlangen [10]	2009
	Hollow fibres	Dry [11]; cited in [12]	1996
	Microencapsulation	Boh and Šumiga [13]; cited in [12]	2008
	Expansive agents and mineral admixtures	Kishi et al. [14]; cited in [12]	2007
Asphalt	Nanoparticles	Tabatabee and Shafiee [15]	2012
	Steel fibres – induction heating	Garcia et al. [16]	2011
	Rejuvenator encapsulation	Su et al. [17]	2013
Coatings	Healing agent (resin) encapsulation	Wilson and Magnus [18]	2011
Composites	Memory alloys	Kirkby et al. [19]	2008
Metals and alloys	Press and sinter powder metallurgy	Lumley [20]	2007

Functional repair: restoring the function of the system. If full functionality cannot be restored, the remaining available resources are employed/used to maximize the available functionality [7].

Attributive repair is the optimal solution. If the attempt to restore the system to its complete original condition fails, there is still significant benefit to be gained, in most instances, if the system continues to operate, even with reduced functionality. Living organisms possess intrinsic self-healing properties, enabling them to recover from damage or injuries. This repair or healing occurs with no external intervention. Some natural self-healing composite systems, such as bones, go beyond simple healing to continuous remodelling and strengthening [8]. Over the past decade, self-healing technology has entered the field of materials engineering [7]. Self-healing technology represents a revolution in materials engineering. Examples of engineering materials to which self-healing technology has been successfully applied are presented in Table 1.

1.1 Self-Healing Properties of Asphalt Pavement

Asphalt pavement is a self-healing material. When subjected to rest periods, asphalt pavement has the potential to restore its stiffness and strength by closing the micro-cracks that occur when the pavement is subjected to traffic loads. Research to date has focused on its autogenous healing properties (see Table 2).

Crack repair in an asphalt pavement system occurs as a result of the wetting and interdiffusion of material between the two faces of a micro-crack, to regain the properties of the original material [7, 33]. The three primary steps in the autonomous asphalt self-healing process are as follows:

Table 2 Factors influencing the autogenous healing properties of asphalt pavement

Factors influencing healing		Reference	Year
Bitumen properties	Bitumen type	van Gooswiligen et al. [21]	1994
	Viscoelastic properties	Kim and Little [22]	1991
	Surface free energy	Lytton et al. [23]	1993
	Ageing	Edward [24]	2006
	Diffusion	Bhasin et al. [25]	2011
	Modifiers	Lee et al. [26]	2000
Asphalt mix composition	Bitumen content	van Gooswiligen et al. [21]	1994
	Aggregate structure	Kim and Roque [27]	2006
	Gradation	ABO-Qudais and Suleiman [28]	2005
	Thickness	Theyse et al. [29]	1996
Environment	Temperature	Verstraeten [30]	1991
	Loading history	Castro and Sanchez [31]	2006
	Rest period	Bhasin et al. [25]	2007
	Water/moisture	Hefer and Little [32]	2005

1. Wetting of the two faces of a micro-crack
2. Diffusion of molecules from one face to the other
3. Randomization of the diffused molecules to reach the level of strength of the original material

Binder is key to the self-healing process in an asphalt pavement. Self-healing takes place on a molecular level, when broken (non-associated) molecules are available to form links and chains via hydrogen bonds [7]. The process is termed "reversible hydrogen bonding" [34] and is achieved by bringing together the associated molecules to form both chains and crosslinks via hydrogen bonds [7]. A repaired molecular network can be formed by linking ditopic and tritopic molecules [35], which are able to associate with each other (see Fig. 1). This system, when broken or cut, can be simply repaired by bringing two fractured surfaces into contact [34–36].

Qiu et al. [36] reported that self-healing in an asphalt pavement system is a viscosity-driven process, dependent on time (rest periods) and temperature. Qiu et al. [36] also demonstrated the self-healing time and temperature dependency of bituminous materials (see Fig. 2). A longer healing time and increased healing temperature lead to better healing [36]. Shorter time to heal results in the formation of fewer bridges across the interface and the development of a weaker bond across the break. However, if broken bonds are not healed immediately (i.e. if the fractured surfaces are not brought into contact with each other), the number of non-associated groups available for linking decreases (i.e. healing efficiency decreases) [35]. This is because, immediately after breakage, the free (non-associated) groups begin to seek other free groups within the broken part to link with [35].

Qiu et al. [36] successfully modelled the time–temperature dependence of the self- healing process in asphalt mastic using a time–temperature superposition principle, which can be expressed by the following formulation:

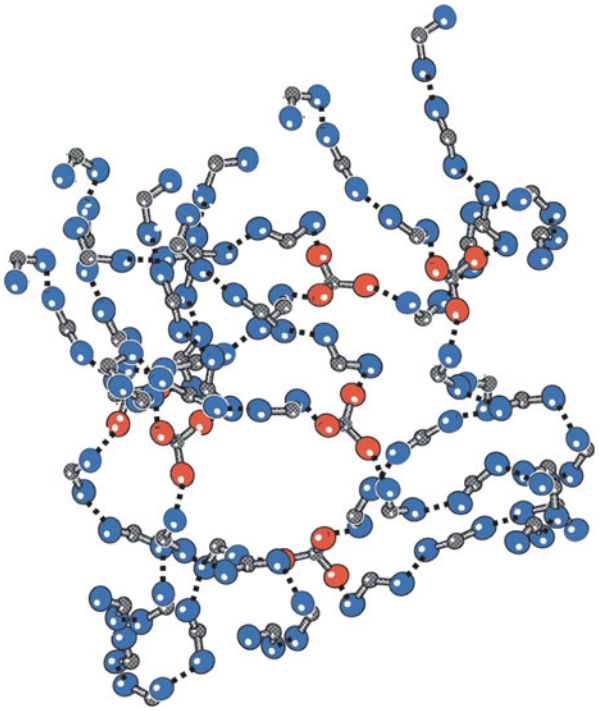

Fig. 1 Supramolecular network: Scheme of a reversible network formed by mixtures of ditopic (*blue*) and tritopic (*red*) molecules associating by directional interactions (represented by *dotted lines*) [35]

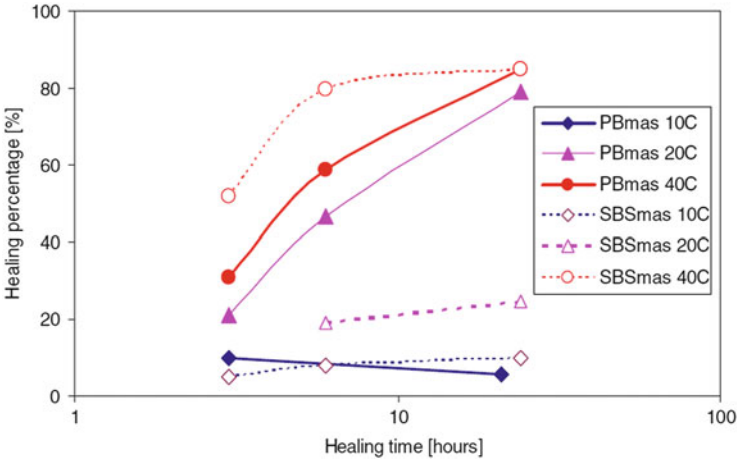

Fig. 2 Self-healing results of PBmas (asphalt mastic mix containing limestone filler and 70/100 pen bitumen) and SBSmas (asphalt mastic mix containing limestone filler and bitumen modified with styrene-butadiene-styrene polymer) [36]

$$H(t,T) = 100 \times \left[1 + \left(\frac{m}{t \times \alpha_T}\right)^{\frac{\log 2}{n}}\right]^{\frac{n}{\log 2}} \quad (1)$$

where the time–temperature superposition shift factor in Eq. (1) is based on the Arrhenius equation and is calculated using the following formulation:

$$\log\ \alpha_T(T) = \frac{\Delta E_a}{2.303R}\left(\frac{1}{T} - \frac{1}{T_0}\right) \quad (2)$$

where α_T is the time–temperature superposition shift factor; m, n are the model parameters; ΔE_a is the apparent activation energy, (J/mol) and R is the universal gas constant, 8.314 J/(mol K).

The healing of an asphalt pavement at high temperatures is governed by the so-called thixotropic effect, which describes the transformation of asphalt binder from a solid to gel state, allowing recovery from structural damage [30]. Wu reported that visible in-situ cracks within asphalt pavements disappear during periods of warm weather, only to reappear during cold weather [37]. At high temperatures, surface cracks close, but high temperatures dissipate quickly throughout the pavement depth [38], meaning that cracks 20–30 mm below the pavement surface do not heal and re-appear at lower temperatures or as a result of heavy traffic loading. Results presented in Fig. 2 show that the healing progress of two different asphalt mixtures (PBmas and SBSmas) is only 10% after healing at 10°C. The results from Qiu et al. [36] show that temperatures below 20°C are insufficient to initiate full recovery of asphalt pavements. However, the self-healing properties of asphalt can be enhanced either by heating the asphalt material or by adding modifiers or a healing agent (i.e. rejuvenator), as shown in Fig. 2.

2 Examples of Self-Healing Technology for Asphalt Pavements

The asphalt pavement design standards focus on enhancing asphalt pavement performance, that is, they aim to increase its durability and improve its load-carrying capability [39]. However, the authors consider that future of asphalt pavement design lies not with the enhancement of asphalt pavement properties, but in allowing it to repair itself to its original state.

As in nature, the self-healing performance of an asphalt pavement can be improved, for example, by introducing modifiers and additives to the asphalt mix to upgrade its self-healing properties. To function in an asphalt pavement system, the self-healing technology must have the capacity to survive the harsh conditions that prevail during asphalt pavement construction (mixing and compaction) and service life (traffic loading and environmental conditions such as rain, ice, snow,

high temperatures, etc.). Qiu et al. [34] outlined five essential conditions for self-healing agents to be included into asphalt pavement design:

1. Good compatibility with bitumen
2. High temperature stability
3. Ability to survive mixing and construction conditions
4. Healing temperature between −30°C and 40°C
5. Capable of continuous/multi-time healing

In this section, a number of existing self-healing approaches for asphalt pavement design are presented and critically analysed with respect to their functional design and performance.

Three self-healing methods for asphalt pavements have been reported to date, they are:

1. Incorporation of nanoparticles
2. Induction heating
3. Rejuvenation

2.1 Nanoparticles

2.1.1 Nanoclay

Nanoclay materials are used in asphalt pavement design to improve the ageing, rheological and thermal properties of asphalt mixtures [40]. However, they also have the potential to repair micro-cracks in asphalt [34]. The nanoparticles tend to move towards the tip of the crack, driven by the high surface energy, and thus stop crack propagation and heal damaged asphalt material [34]. Tabatabee and Shafiee [15] studied the effect of rest periods on the fatigue life of organoclay-modified asphalt mixes and found that introduced rest periods at 3% and 5% strain level increased the fatigue resistance of these mixes. This finding demonstrates that nanoclay material can be used for improving the self-healing properties of asphalt mixtures. However, the nanoclay self-healing technique has not been researched in great detail to date and there is insufficient data available on the long-term effect of nanoclay particles on the performance of self-healing asphalt mixtures. This is an interesting area for future research.

2.1.2 Nanorubber

As with nanoclay materials, polymer and rubber modifiers are used in the bitumen mix to improve the physical and mechanical properties of the binders and, as such, to improve in-situ performance of an asphalt pavement [41–43]. Rubber modifiers in the form of nanoparticles have also been used to improve the healing properties

of asphalt mastic [34]. Qiu et al. [34] studied the repair of asphalt mastic with nanorubber-modified binder (70/100 pen binder).[1] They conducted ductility self-healing tests to assess the self-healing capacity of asphalt mastics containing two different types of nanorubber modifier (NanoA and NanoB) and varying percentages of modifier (0–5%), where 0% was a control mix. The tests were performed on dog bone test specimens. The test specimens were cut at the centre, joined and left to heal for 4 h at room temperature (20–22°C). The test results showed good self-healing for non-modified asphalt mastic mixes, up to 70%. Recovery of the modified asphalt mixtures varied from 15% to 90%, depending on the type of nanorubber modifier and the amount added [34]. Unfortunately, the authors did not present the composition of the nanorubber modifier, so it is difficult to determine what type of healing mechanism activated the healing process and to understand the variability in the healing performance. Nevertheless, the study showed that nanorubber modifiers can be used to improve the self-healing properties of asphalt mixtures. Future studies should indicate the properties of the nanorubber modifiers used, that is, whether they are styrene-butadiene-rubber (SBR), styrene-isoprene-styrene (SIS) or olefinic rubber. This would enable determination of the type of healing mechanism that had occurred (i.e. whether it was reverse hydrogen bonding). The clear advantage of nanorubber as a modifier is its double role; it can improve asphalt mix durability and also act as self-healing modifier in the mix. However, the disadvantage of polymer-based modifiers is their thermodynamic incompatibility with asphalt binder as a result of the large differences in material density, polarity, molecular weight and solubility between the polymer and the asphalt [40]. This can result in delamination of the composite during thermal storage, which is not readily apparent and adversely affects the asphalt mix when it is used [40]. The thermodynamic incompatibility of nanomodifiers needs to be studied, because at high temperatures the separation of nanorubber modifier and binder could take place, resulting in deterioration of asphalt pavement performance.

The nano-effect and reverse hydrogen and ionic bonding are known for their multi-healing abilities [34], which is a benefit of this type of self-healing mechanism. However, the effect of healing time and temperature need to be further investigated to determine what effect time has on the healing of the asphalt mix. If ineffective at lower temperatures and without improvements in healing times relative to autonomous bitumen healing, the technology would be unsuitable for the self-healing of asphalt pavements.

Although nanoparticle self-healing technology has demonstrated its potential in asphalt pavement mix design, more substantial evidence of its performance must be demonstrated before it becomes acceptable as a viable self-healing technology.

[1] "pen" stands for penetration. Bitumen penetration test (EN 1426:2015) indicates the hardness of bitumen, lower penetration indicating a harder bitumen. Specifications for penetration graded bitumen normally state the penetration range for a grade, e.g. 70/100.

2.2 Induction Heating

Induction heating in asphalt pavement design was pioneered by Minsk [44, 45]. He developed and patented the first electrically conductive asphalt pavement using graphite as a conductive medium for the purpose of melting snow and ice on roadway surfaces by induction heating. More recently, induction heating has regained popularity in asphalt pavement research for to improving self-healing in asphalt pavements [46–49]. Electrically conductive fibres and fillers (carbon fibres, graphite, steel fibres, steel wool and the conductive polymer polyaniline) were added to study the electrical conductivity in asphalt pavement. Results showed that the electrical resistivity significantly varied with the type, shape and size of fibres and fillers. Wu et al. [46] studied induction heating in asphalt pavement using conductive carbon fibres, carbon black and graphite as conductive media and demonstrated that adding conductive fibres to the mixture increases conductivity more effectively than adding conductive filler. Subsequent research by Garzia et al. [47] and Liu et al. [48] initiated the development of a self-healing asphalt pavement mix by inclusion of electrically conductive steel and wool fibres into the asphalt mix and activation of self-healing by induction heating.

The induction process operates by sending an alternating current through the coil and generating an alternating electromagnetic field. When the conductive asphalt specimen is placed under the coil, the electromagnetic field induces currents flowing along the conductive loops formed by the steel fibres [50]. This method can be repeated if damage returns. A schematic diagram of induction healing is illustrated in Fig. 3.

The major healing mechanism in induction healing is the capillary flow and diffusion of the asphalt binder (bitumen) at high temperatures. García [50] verified this healing mechanism using bitumen capillary flow tests. Liu [51] studied the induction healing effect of steel fibres and steel wool and characterized asphalt healing via the following equation:

$$\mathrm{HI} = \frac{C_2}{C_1} \tag{3}$$

where HI is the healing index (%), 100% indicating complete healing of damage and 0% indicating no healing at all; C_1 is the number of loading cycles for the first loading; and C_2 is the number of loading cycles for the second loading.

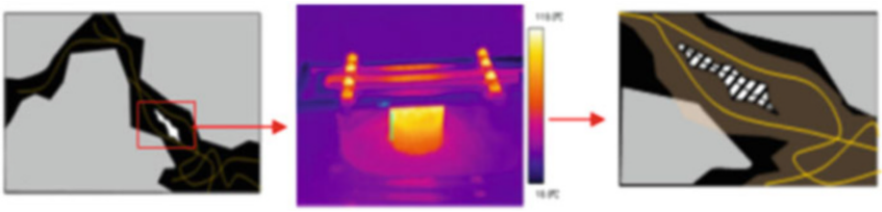

Fig. 3 Induction healing in porous asphalt [51]

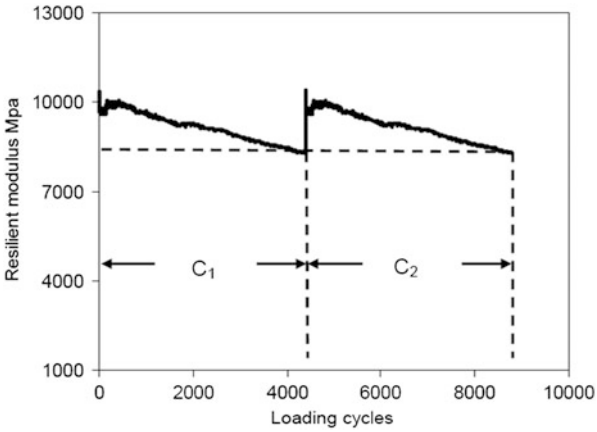

Fig. 4 Fatigue recovery of porous asphalt concrete cylinder for resilient modulus reduction to 80% [51]. C_1 and C_2 are loading cycles

Figure 4 gives the results of a fatigue test performed by Liu [51], showing values of C_1 and C_2 for two loading cycles. The loading value C_2 illustrates the effect of induction healing.

Liu et al. [48] investigated the effect of long steel wool type 000 versus short steel fibre. The results showed that long steel wool is better than short steel fibre for making porous asphalt concrete electrically conductive.

Liu et al. [48] demonstrated that the addition of steel fibres reinforces the mastic (bitumen, filler and sand) of porous asphalt concrete, which can delay the ravelling effect in asphalt pavement. Liu et al. also demonstrated that the inclusion of steel fibres into the asphalt pavement mix prevents the drainage of bitumen from the surface of the asphalt pavement. The advantage of this is that it achieves a better bond between the large aggregates (stones) in the pavement.

Although induction healing can enhance the self-healing capacity of asphalt pavement, an adverse effect is that heating the asphalt mix ages the bitumen. Furthermore, overheating ($>110°C$) the asphalt mix can cause binder swelling and drainage, which adversely affects pavement performance. Liu et al. [48] suggested that the optimal heating temperature for a porous asphalt mix is 85°C. Liu [51] demonstrated that the degree of damage incurred by overheating also affects the healing ratio, (i.e. the heating should not be applied too early or too late). If applied too early (when resilient modulus is $>80\%$ of the original asphalt pavement stiffness value), the asphalt pavement can heal itself and heating is not required. However, if the asphalt is heated too late (when resilient modulus value is $<80\%$ of the original asphalt pavement stiffness value), the healing effect is poor, because structural damage such as permanent deformation or stone aggregate cracking can occur and is beyond the healing capacity of the induction healing process. Liu [51] further concluded that the best healing results were achieved when induction heating was combined with a rest period. This study demonstrated that healing can be improved by 15% if the autogenous healing process is aided by induction heating.

In December 2010, researchers from TU Delft in cooperation with the Dutch National Roads Authority resurfaced a road (the A58 in Netherlands) using an

induction self-healing asphalt mix (i.e. an asphalt mix containing 1 cm long steel fibres) [52]. Testing of the self-healing process within the A58 motorway is ongoing at present [52].

Inductive heating is the most progressive self-healing technology for asphalt pavements reported to date. This technology has transitioned from laboratory to site in a short period of time (3 years). Although its ageing effect can be compensated for by the healing effect, a problem that has not been addressed by research is the loss of conductivity via oxidation (corrosion) of the steel wool and fibres. However, this should not be an insurmountable problem, as steel could be replaced by carbon fibres and/or conductive polymer [49, 53]. In addition, the piezoresistivity of conductive asphalt, which refers to the change in electrical resistivity with applied mechanical pressure, can be used for self-sensing of strain [54]. Self-sensing of damage for evaluating pavement distress is possible if there is a relationship between the electrical property and internal damage. Moreover, some conductive additives can improve the durability of asphalt concrete, thereby increasing the service life of the pavement system [48, 55, 56]. This aspect of self-healing induction technology needs to be further developed for the initiation of healing processes and also for self-health assessment of asphalt pavement.

2.3 Binder Healing Agent (Rejuvenation)

During the service life of a pavement, the volatile components of bitumen evaporate, and oxidation and polymerization can occur [57]. As a result, the bitumen ages and loses some of its viscoelastic properties. Asphalt binder is a combination of asphaltenes and maltenes (resins and oils). Asphaltenes are more viscous than either resins or oils and play a major role in determining asphalt viscosity [58, 59]. The oxidation of aged asphalt binder during construction and service causes the binder oils to convert to resins and the resins to convert to asphaltenes, resulting in age-hardening and a higher viscosity than for fresh binder [59, 60]. Although this process is irreversible, the viscoelastic state of the asphalt mix can be recovered through the addition of either bitumen with a high penetration value or a rejuvenating agent such as a cationic emulsion [61–63].

A rejuvenator is an engineered cationic emulsion containing maltenes and saturates. The primary purpose of a rejuvenator is to reduce the stiffness of the oxidized asphalt binder and to flux the binder to extend the pavement life by adjusting the properties of the asphalt mix [62]. Some commercially available rejuvenating agents are Reclamite, Paxole 1009, Cyclepave and ACF Iterlene 1000. A recent study by Su et al. [64] demonstrated that a by-product of waste cooking oil (WCO) can also be used as binder rejuvenator.

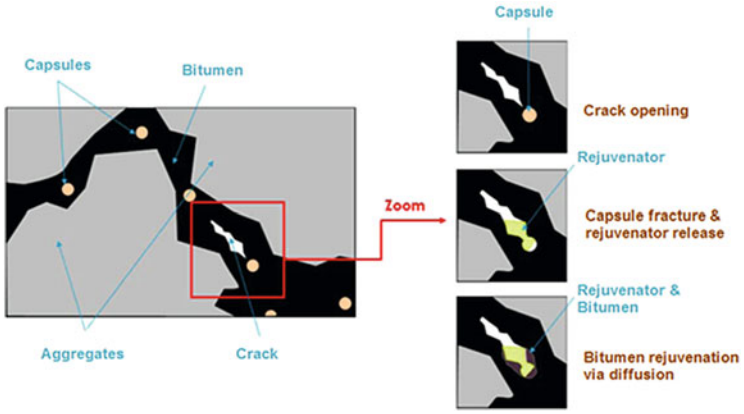

Fig. 5 Rejuvenator Encapsulation — A Self-healing Mechanism in Asphalt Mix

2.3.1 Self-Assembled Monolayers

When cracks within the surface layer of an asphalt pavement are still in an early phase, it is possible to apply a rejuvenator to the wearing course to prevent further crack propagation and pavement failure [65]. By applying the rejuvenator to the surface course, the lifespan of the asphalt pavement can be extended by several years; however, this only applies to the top few centimetres of the asphalt pavement. Shen et al. [66] reported the use of three different types of rejuvenators and found that none could penetrate further than 20 mm into asphalt concrete. A further issue encountered when applying these materials is the need for road closures for a period of time after the application. The rejuvenators can also cause significant reduction in the surface friction of the pavement and could also be harmful to the environment. Microencapsulation of the rejuvenators represents a potential means of overcoming these problems.

2.3.2 Microcapsulation Technique

The inclusion of a rejuvenator into the asphalt mix via microcapsules to restore the original binder properties is a self-healing method that has been studied by Su et al. [64, 67], Su and Schlangen [68] and García et al. [69]. The principle behind this approach is that when micro-cracks begin to form within the pavement system, they encounter a capsule in the propagation path. The fracture energy at the tip of the crack opens the capsule and releases the healing agent. The healing agent then mixes with the asphalt binder to seal the crack, thus preventing further propagation. This healing process is illustrated in Fig. 5. The process prevents the formation of micro-cracks within the pavement mix and prevents complete failure of the pavement system. Su and Schlangen [68] and García et al. [69] demonstrated that

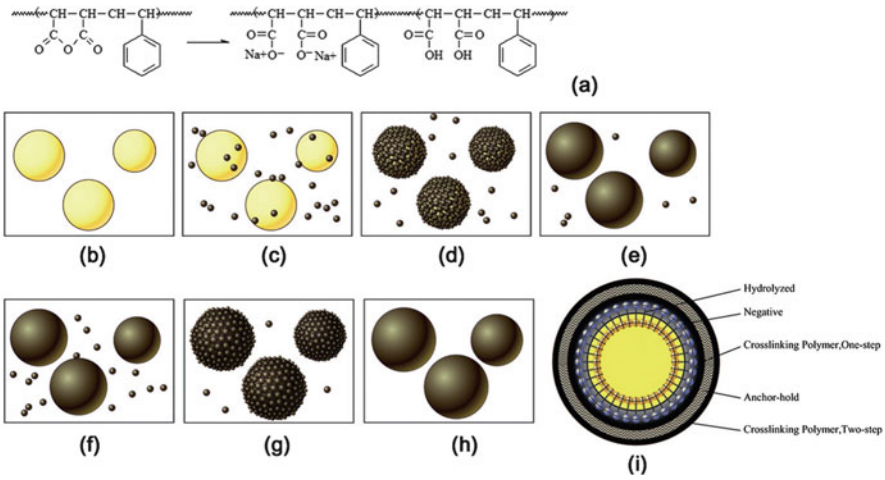

Fig. 6 Fabrication process for double-shell microcapsules containing rejuvenator by a two-step coacervation (TSC) method: (**a**) chemical structure of SMA alternating copolymer and hydrolysis polymer, (**b**–**e**) the first step coacervation, (**f**–**h**) the second step coacervation, and (**i**) microstructure of microcapsules produced by TSC method [68]

various types of capsules containing rejuvenator can be produced and that these capsules are sufficiently thermally and mechanically stable to survive the asphalt production process.

To date, the most successful microcapsule shells have been made of a prepolymer of melamine–formaldehyde modified by methanol (solid content 78.0%) and the rejuvenator was an oily product [17]. Figure 6 illustrates the fabrication process of double-shell microcapsules containing rejuvenator by two-step coacervation (TSC). The efficiency of microcapsule fabrication is measured by amount of rejuvenator retained within the microcapsule [68]. The highest efficiency achieved was 70% [67] using the following production conditions: core/shell ratio of 1:3, stirring speed 3,000 revolutions/min and 2.0–2.5% by weight styrene maleic anhydride (SMA) copolymer dispersant. Figure 7 shows the SEM morphology of dried microcapsules with a core/shell ratio of 1:3 and an average shell diameter of 25 μm.

The asphalt mortar films between aggregate particles in an asphalt pavement are found to be ≈ 50 μm thick [67]. To avoid being squeezed or pulverized during the asphalt pavement mixing and compaction processes, the size of the capsule needs to be less than 50 μm. However, Su et al. [67] stated that microcapsules of 10 μm and smaller are unsuitable for self-healing as they do not contain sufficient rejuvenator to rejuvenate the aged binder. The size of the capsule can be controlled by regulating the core/shell ratio (weight ratio between core and shell material). This can be achieved by modifying the prepolymer and the emulsion stirring rate [67]. Figure 8 shows the morphology of bitumen containing varying capsule content (10–30% of total binder volume) and capsules of varying size (10–

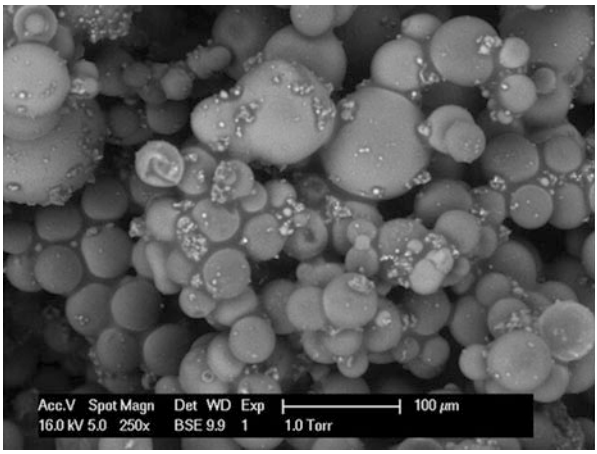

Fig. 7 SEM morphologies of microcapsules containing rejuvenator [67]

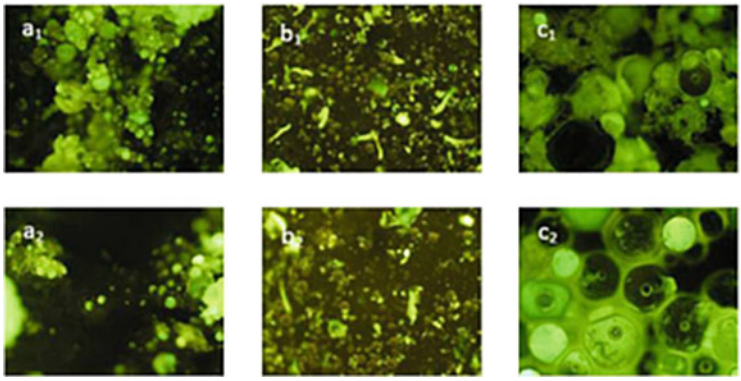

Fig. 8 Fluorescence microscope images of morphology of bitumen samples with 10% (**a**$_1$, **b**$_1$, **c**$_1$) or 30% (**a**$_2$, **b**$_2$, **c**$_2$) microcapsule content and diameters of < 10 μm (**a**$_1$, **a**$_2$), 20 μm (**b**$_1$, **b**$_2$) or 30 μm (**c**$_1$, **c**$_2$) [67]

30 μm). Figure 8a$_1$, a$_2$, shows that microcapsules with a mean size below 10 μm tend to congregate/attract as a result of the electrostatic attraction of tiny particles. In Figure 8b$_1$, b$_2$, microcapsules of 20 μm size have a homogeneously distributed, preventing from hard agglomeration of the capsules in the bitumen. Figure 8c$_1$, c$_2$ shows dispersion of larger microcapsules (30 μm size) with content of 10% and 30% in bitumen. Figure 8c$_2$ shows that large micro capsules will occupy more space, where the capsule content in the bitumen is 30%. This phenomenon may lead to the interface separation between microcapsules and binder and may result in the formation of microcracks or other structural defects [67, 70]. This could result in

Table 3 Properties of virgin bitumen, aged bitumen and aged bitumen after rejuvenation with waste cooking oil [64]

Material property	Original bitumen (80/100 pen)	Aged bitumen (40/50 pen)	Rejuvenated aged bitumen with microWCO (wt%)					
			2	4	6	8	10	12
Penetration at 25°C (mm)	86	43	52	61	74	82	84	88
Softening point (°C)	46.7	53.5	52.0	51.2	50.3	48.4	46.4	45.0
Viscocity at 135°C (mPa s)	325	578	570	520	470	390	333	310

Diffusion of microencapsulated waste cooking oil (microWCO) was carried out at 0°C. Penetration, softening point and viscosity tests were conducted following standard procedures

poor mechanical performance of the asphalt pavement and premature pavement failure. In conclusion, the optimum content of microcapsules in bitumen must be no more than 30% of overall bitumen volume within an asphalt mix [67].

More recently Su et al. [64] demonstrated that rejuvenators produced from recycled waste cooking oil (WCO) can be encapsulated and used in the asphalt self-healing technology. Capsules with high capsule shell strength of 1.0–1.52 GPa, core/shell ratio of 1:3 and good thermal stability (melting point 180°C) can survive the harsh asphalt production process. This research demonstrated that microencapsulated WCO rejuvenator can successfully penetrate and rejuvenate aged standard bitumen binder of 80/100 pen, and defuse it at low temperature (0°C) (see Table 3).

The microcapsule approach is favourable for asphalt self-healing in that it allows the rejuvenation of aged binder (i.e. returns it to its original physical and mechanical properties). However, the downside to this approach is that it works only once (i.e. once the healing material is released from the microcapsule it cannot be replenished) [34]. Nevertheless, this self-healing process is still in its early development stage and its full potential will be demonstrated in coming years. Methods for introducing a reasonable dose of microcapsules into the asphalt mix to achieve appropriate dispersion of capsules throughout the asphalt mix and enhancement of the multiphase self healing process need to be the focus of future research work in this field.

3 Towards New Generations of Self-Healing Asphalt Pavements

The key aim of research on self-healing asphalt pavements is to develop asphalt pavement material that is capable of healing itself without external intervention. Therefore, the ultimate goal for road designers is to develop an asphalt pavement material that can mimic nature itself. To achieve this, the self-healing processes

embedded within the asphalt pavement system should be capable of self-assessment. This would enable the material to assess its structural and material health and to trigger a response to initiate self-healing where necessary [7].

To develop this new generation of self-healing asphalt pavements, based on findings of currently available self-healing technologies (presented in Sect. 2), three specific working areas are identified that need particular effort:

1. *Development/design of damage sensing and repair triggering elements*. These elements are incorporated within pavement systems to give the capacity to trigger the self-healing process (i.e. signalling activation of the healing mechanism). This means that the sensory function should be enhanced and extended with an active learning functionality that is able to differentiate and detect damage, interpret the obtained information and trigger/stimulate the healing action on demand. These sensor elements should ideally be a structural component of the pavement system and not deteriorate the general functionality of the pavement system. Development of a sensory mechanism within the pavement system will allow healing-on-demand. Such an action could be triggered by a fall in current/resistivity in the pavement system or by a concentration of stress, which would initiate the repair action while activating an initiator (healing agent or heating).
2. *Development of multiple self-healing processes*. To date, only a limited number of self-healing mechanisms for asphalt pavements have been developed, such as induction heating [16, 48] and rejuvenator encapsulation [17, 64, 68]. To explore the additional potential of self-healing asphalt technology, new self-healing mechanisms must be developed to respond to a broader range of performance demands, such as healing/rest time. All three self-healing mechanisms presented in Sect. 2 require at least 4 h of rest time in order for the asphalt pavement to achieve full recovery. On roads with high traffic flow, this is difficult to achieve. Perhaps technology can improve the repair times for self-healing asphalt pavements. Another, essential, part of the self-healing mechanism in asphalt pavements is multiphase self-healing. If a self-healing mechanism is "once off", it is vulnerable to cracking after the first repair. This ultimately leads to asphalt pavement failure. This requirement of a self-healing mechanism is directly linked to the sensory/triggering mechanism. If a healing-on-demand technology can be achieved within asphalt pavements, the repair action can be re-activated and thus make self-healing asphalt more efficient.
3. *Development of self-healing assessment mechanisms*. Such mechanisms are necessary to achieve self-assessment of the asphalt pavement system and to quantify the success of the self-healing process. To date there has been only limited understanding of how to quantify the success of self-healing, mostly done by measurement of mechanical performance, such as material strength [63]. This requires in-situ pavement evaluation, or a laboratory material evaluation of test samples obtained from site. Such evaluation requires traffic control and potential traffic delays, which increases the cost and reduces the benefit of self-healing asphalt pavements. A mechanism for the autonomous self-

assessment of asphalt pavement system health and assessment of the self-healing process should be a focus for future research in this field.

If these developments in the self-healing process are accomplished, then it will be possible to create a truly smart asphalt pavement system that senses its internal state and external environment and responds in an appropriate manner to this information. The primary advantage of moving towards smart/self-healing technology is the potential cost benefit of condition-based maintenance strategies and the prospective long lifespan that can be achieved for asphalt pavement materials through in-situ health management.

The potential benefits of self-healing asphalt technology in material performance and environmental and social benefits will undoubtedly stimulate interest in the wider use of self-healing technology in asphalt pavement design and construction. However, for self-healing technology to become accepted as the industry standard, its superiority in the construction and maintenance of asphalt pavements must be demonstrated from functional, economic and environmental perspectives.

4 Cost and Environmental Benefits of Self-Healing Technology for Asphalt Pavement Design

To accurately assess the cost reductions that can accrue from self-healing materials, it would be best to compare the change (increase) in material costs with the change (decrease) in maintenance costs. Depending on the application, other costs such as operating costs, disposal costs and environmental costs could be factored in the cost–benefit analysis. It is expected that periods between road maintenance will extend when self-healing asphalt is employed, resulting in a decrease in traffic congestion and associated costs. For example, in the Netherlands the combined annual savings related to major repairs and traffic jam costs are approximately €65 million for an asphalt lifespan extension of 25%, and over €100 million for a lifespan extension of 50% for the entire porous asphalt pavement area in the Netherlands [71]. Even if the price of self-healing asphalt was double that of standard bitumen, the Netherlands would save approximately €90 million annually by investing in self-healing asphalt with a 50% extended lifespan, compared with traditional porous asphalt. The Netherlands is a fairly small country by European standards and represents only 3% of total European asphalt production, and only one third of this asphalt (1%) is used in surface layers [52]. If we extend the potential savings in the Netherlands to the EU as a whole, the potential savings could total €9 billion [52].

These figures outline the clear financial benefits to be accrued from self-healing technology in asphalt pavement design. However, the full potential benefits of self-healing technology in asphalt pavement design can only be understood when the full life cycle costs of asphalt pavements are known (financial, environmental and societal). Butt et al. [72] studied the effect of self-healing on the lifetime, energy

and environment of asphalt pavements. Using a life cycle analysis (LCA) framework, performed in conjunction with a numerical model that simulates the self-healing capacity of asphalt pavements [73], they determined that self-healing asphalt pavements increased the lifetime of the pavement by 10% (from 20 years to 22 years) compared with asphalt pavements without any self-healing capacity. This increase in lifetime would result in a reduction in energy consumption of 3% (22 GJ) and CO_2 emissions of 3% (1.5 Tonne). If the increased lifetime of an asphalt pavement is projected to 100% (from 20 years to 40 years, based on the assumption that self-healing technology can double asphalt pavement lifespan), the benefits in terms of reduced cost and reductions in energy consumption and CO_2 emission would increase accordingly.

A greater insight into the potential of self-healing technology for the asphalt pavement industry can be achieved with full scale in-situ implementation of self-healing technology in asphalt pavement design, as in the A58 road in the Netherlands [52]. However, the clear benefits of self-healing asphalt materials, in the form of an extended lifespan of the asphalt pavement and reduced maintenance costs, only become apparent over time. Steyn explains [65]: "The important point to take from reality is that for any innovation to provide real benefit in the pavement engineering field, there has to be a real positive benefit/cost ratio."

It is unlikely that decisions regarding implementation of self-healing technology in asphalt pavement design will be taken at a local level because of the high initial costs and long timeframe for savings. It requires regional (European) leadership, informed by a sound evidence base (i.e. research), to convince all that these technological advances are worth considering at a national and European level. Initial research results are positive, as shown in Sect. 2, and there is optimism that this technology has strong potential in the design of asphalt pavements.

5 Concluding Remarks

> Roads . . . [are] the most ancient of human monuments, surpassing by many tens of centuries the oldest thing of stone that man has reared to mark his passing. The tread of time. . . has beaten only to a more enduring hardness the pathways that have been made throughout the world [74].

Throughout the centuries, a civilisation's prosperity and economic development was measured and ensured by the quality of its road network, which was used for economic, social and military purposes. In its latest report *Road Infrastructure – the backbone of transport system* [75], the European Commission states: "Transport infrastructure influences both economic growth and social cohesion. A region cannot be competitive without an efficient transport network."

Today, roads designs are sophisticated engineering creations. Despite this, the materials used in asphalt mixes have remained largely unchanged for the past 100 years. The main ingredient of a modern road is the bitumen. It is a co-product of crude oil, whose production is in decline [76], meaning that the

financial and environmental costs of bitumen are on the rise [76, 77], which will result in an increase in the cost of road/asphalt pavements. Unless investment levels keep apace of increased costs, road networks of poorer standard could result.

Incorporating self-healing technology into asphalt pavement design presents a solution for some of the difficulties facing asphalt. Currently available self-healing road technologies are paving the way for the evolution of road design. Existing technologies have demonstrated their potential in repairing distressed asphalt pavements. They offer great opportunities for increased durability and reliability, reduced maintenance and lower overall cost of asphalt pavements. This includes a reduction in the material resources needed, because the usual over-design of materials is no longer required. The repair of an asphalt pavement is addressed in situ by its internal self-healing system at the very position of first appearance of damage, eliminating the need for classical in-situ maintenance processes.

However, the key objective of self-healing technology for asphalt pavement design is the development of a truly smart asphalt pavement system, capable of self-assessment and automatic response. Despite the progress made in the development of self-healing asphalt technology, further work is required to achieve truly smart asphalt pavements. Future work needs to focus on:

1. Damage sensing and repair triggering elements
2. Development of multiple self-healing processes
3. Development of self-healing assessment mechanisms

The development of such areas of self-healing technology for asphalt pavements will truly revolutionize asphalt pavement design. This will also lead to another evolutionary step in road construction and design and bring the idea of self-healing roads from science fiction to reality.

Acknowledgements This research has been conducted under the Marie Curie IEF research funding, research project Self-Healing Asphalt for Road Pavements (SHARP), project number 622863.

References

1. OECD (2013) Road traffic, vehicles and networks. In: Environment at a glance 2013: OECD indicators. OECD, Paris
2. European Union Road Federation (2012) European road statistics 2012. European Union Road Federation (ERF), Brussels
3. Sherwood PT (2001) Alternative materials in road construction, 2nd edn. Thomas Telford, London
4. Merill D (2005) Guidance on the development, assessment and maintenance of long-life flexible pavements. Transport Research Laboratory, Wokingham
5. FEHRL (2008) NR2C new road construction concepts; towards reliable, green, safe & smart and human infrastructure in Europe. Forum of European National Highway Research Laboratories (FEHRL), Brussels

6. World Road Association – PIARC (2014) Technical committees for road infrastructure. www.pirac.org
7. Fisher H (2010) Self repairing materials – dream or reality. Nat Sci 2(8):873–901
8. March DR, Li G (1999) The biology of fracture healing. Br Med Bull 55(4):856–869
9. Jin H et al (2012) Self-healing thermoset using encapsulated epoxy-amine healing chemistry. Polymer 53(2):581–587
10. Jonkers HM, Schlangen E (2009) A two components bacteria-based self-healing concrete. In: Alexander MG, Beushausen H-D, Dehn F, Moyo P (eds) Concrete repair, rehabilitation and retrofitting II. Tailor & Francis, London, pp 119–120
11. Dry C (1996) Procedure developed for self-repair of polymer matrix composite materials. Compos Struct 35(3):263–239
12. Wu M, Johnnesson B, Geiker M (2012) A review: self-healing in cementitious materials and engineered cementitious composite as a self-healing material. Constr Build Mater 28:571–583
13. Boh B, Šumiga B (2008) Microencapsulation technology and its applications in building construction materials. Mater Geoenviron 55:329–344
14. Kishi T et al. (2007) Self-healing behaviour by cementitious recrystallization of cracked concrete incorporating expansive agent. In: 1st International conference on self-healing materials, Noordwijk aan zee, The Netherlands
15. Tabatabaee N, Shafiee MH (2012) Effect of organoclay modified binders on fatigue performance. In: 7th RILEM international conference on cracking in pavements. RILEM Bookseries, Delft, The Netherlands
16. García A, Schlangen E, van de Ven M (2011) Induction heating of mastic containing conductive fibers and fillers. Mater Struct 44(2):499–508
17. Su JF, Qiu J, Schlangen E (2013) Stability investigation of self-healing microcapsules containing rejuvenator for bitumen. Polym Degrad Stab 98(6):1205–1212
18. Wilson GO, Magnus H (2011) Self-healing systems for industrial and marine protective coatings. J Protect Coat Lin 28(8):18–21
19. Kirkby EL et al (2008) Embedded shape-memory alloy wires for improvements of self-healing. Adv Funct Mater 18:2253–2260
20. Lumley R (2007) Self healing in aluminium alloys. In: 1st international conference on self healing materials, Delft, The Netherlands
21. van Gooswiligen G, de Hilster E, Robertus C (1994) Changing needs and requirements for bitumen and asphalts. In: 6th Conference on asphalt pavement for South Africa, Cape Town, South Africa
22. Kim YR, Little DN (1991) SEM analysis on fracture and healing of sand-asphalt mixtures. ASCE J Mater Civil Eng 3(2):140–153
23. Lytton RL et al. (1993) Development and validation of performance prediction models and specifications for asphalt binders and paving mixes. Strategic Highway Research Program (SHRP), National Research Council, Washington
24. Ofori-Abebresse EK (2006) Fatigue resistance of hot-mix asphalt concrete mixtures using the calibrated mechanistic with surface energy measurements approach. Master's thesis. Texas A&M University, Texas. http://oaktrust.library.tamu.edu/handle/1969.1/4136
25. Bhasin A et al (2011) Use of molecular dynamics to investigate self-healing mechanisms in asphalt binders. ASCE J Mater Civil Eng 23(4):485–492
26. Lee HJD, Daniel JS, Kim YR (2000) Laboratory performance evaluation of modified asphalt mixtures for Inchon airport pavements. Int J Pavement Eng 1(2):151–169
27. Kim B, Roque R (2006) Evaluation of healing property of asphalt mixture. In: 85th Annual meeting of the Transport Research Board, Washington, DC
28. Abo-Qudais S, Suleiman A (2005) Monitoring fatigue famage and crack healing by ultrasound wave velocity. Nondestruct Test Eva 20(2):125–145
29. Theyse HL, de Beer M, Rust FC (1996) Overview of the South African mechanistic pavement design analysis method. In: 75th Annual Transport Research Board meeting, Washington, DC

30. Verstraeten J (1991) Fatigue of bituminous mixes and bitumen thixotropy. In: 19th World road congress, AIPCR, Marrakech, Morocco
31. Castro M, Sanchez J (2006) Fatigue and healing of asphalt mixtures: discriminate analysis of fatigue curves. ASCE J Trans Eng 132(2):168–174
32. Hefer A, Little DN (2005) Adhesion in bitumen-aggregate systems and quantification of the effects of water on the adhesive bond. Ph.D. thesis, Texas A&M University, Texas
33. Kim YRL, Little DN, Lytton RL (2003) Fatigue and healing characterization of asphalt mixes. ASCE J Mater Civil Eng 15(1):75–83
34. Qiu J et al (2009) Investigation of self healing capability of bituminous binders. Road Mater Pavement Design 10(1):81–94, Special Issue on Asphalt Materials (ICAM 2009—China)
35. Cordier P et al (2008) Self-healing and thermoreversible rubber from supramolecular assembly. Nature 451:977–980
36. Qiu J et al (2012) Evaluating self healing capability of bituminous mastics. Exp Mech 52:1163–1171
37. Wu C (1998) Highway, heal thyself; cracking the code of self-healing asphalt could extend the life of roads. Sci News 153:60–63
38. Mallic RB et al (2012) Heating and its effect on hot in-place recycling of asphalt pavements with rejuvinator. Int J Pavement Res Technol 5(6):347–359
39. Newcomb DE, Buncher M, Huddleston IJ (2001) Concepts of perpetual pavements. Transport Research Circular, Transport Research Board, Washington, DC
40. Fang C et al (2013) Nanomaterials applied in asphalt modification: a review. J Mater Sci Technol 29(7):589–594
41. Manh HT, Viet AP (2013) Influence of fiber polymer reinforced asphalt concrete pavement in high temperature environment. In: Proceedings of the 2nd electronic international interdisciplinary conference (EIIC), Žilina, Slovak Republic. EICC, Žilina pp 465–468. http://www.eiic.cz/archive/?vid=1&aid=2&kid=20201-40
42. McNally T (2011) Polymer modified bitumen, PmB. In: Polymer modified bitumen properties and characteristics. Woodhead, Philadelphia
43. Abtahi SM, Sheikhzadeh M, Hejazi SM (2010) Fiber-reinforced asphalt-concrete – a review. Constr Build Mater 24:871–877
44. Minsk LD (1968) Electrically conductive asphalt for control of snow and ice accumulation. Trans Res Board 227:57–63
45. Minsk LD (1971) Electrically conductive asphaltic concrete. US patent 3,573,427
46. Wu S et al (2006) Self-monitoring electrically conductive asphalt-based composite containing carbon fillers. Trans Nonferrous Met Soc China 16:512–516
47. García A et al (2009) Electrical conductivity of asphalt mortar containing conductive fibers and fillers. Constr Build Mater 21(10):3175–3181
48. Liu Q et al (2010) Induction heating of electrically conductive porous asphalt concrete. Constr Build Mater 24:1207–1213
49. Zhang H, Wu XH, Wang XL (2011) Conductivity mechanism of asphalt concrete with the PANI/PP compound conductive fiber. Mater Sci Forum 689:69–73
50. García A (2012) Self-healing of open cracks in asphalt mastic. Fuel 93:264–272
51. Liu Q (2012) Induction healing of porous asphalt concrete. Ph.D. thesis, Faculty of Civil Engineering and Geosciences, TU Delft, The Netherlands
52. Schlangen E (2013) Other materials, applications and future developments. In: Rooij ME et al (eds) Self-healing phenomena in cement-based materials, RILEM series: state-of-the-art reports. Springer, Dordecht, pp 241–256
53. Wu S et al (2005) Investigation of the conductivity of asphalt concrete containing conductive fillers. Carbon 43(7):1358–1363
54. Liu XM, Wu SP (2009) Research on the conductive asphalt concrete's piezoresistivity effect and its mechanism. Constr Build Mater 23(8):2752–2756
55. Wu S, Zhang Y, Chen M (2010) Research on mechanical characteristics of conductive asphalt concrete by indirect tensile test. In: Proceedings of the 4th international conference on experimental mechanics. Proc. SPIE 7522: 752265. doi:10.1117/12.851473

56. Liu X, Wu S (2011) Study on the graphite and carbon fiber modified asphalt concrete. Constr Build Mater 25(4):1807–1811
57. Gerardu JJA, Hendriks CF (1985) Recycling of road pavement materials in the Netherlands. Road Engineering Division of Rijkswaterstaat, Delft
58. Airey GD (2003) Rheological properties of styrene butadiene styrene polymer modified road bitumens. Fuel 82(14):1709–1719
59. Wu S et al (2007) Investigation of temperature characteristics of recycled hot mix asphalt mixtures. Resour Conserv Recyc 51:610–620
60. Kandhal PS et al (1995) Performance of recycled hot mix asphalt mixtures. National Center for Asphalt Technology, Auburn
61. Silva HMRD, Oliveira JRM, Jesus CMG (2012) Are totally recycled hot mix asphalts a sustainable alternative for road paving? Resour Conserv Recycl 60:38–48
62. Brownridge J (2010) The role of an asphalt rejuvenator in pavement preservation: use and need for asphalt rejuvenation. In: 1st International conference on pavement preservation, Newport Beach, USA
63. Tabaković AG, Gibney A, McNally C, Gilchrist MD (2010) The influence of recycled asphalt pavement on the fatigue performance of asphalt concrete base courses. ASCE J Mater Civil Eng 22(6):643–650
64. Su JF et al (2015) Investigation the possibility of a new approach of using microcapsules containing waste cooking oil; in-situ rejuvenation. Constr Build Mater 74:83–92
65. Steyn W (2009) Potential application of nanotechnology in pavement engineering. ASCE J Trans Eng 135(10):764–772
66. Shen J, Amirkhanian S, Miller JA (2007) Effects of rejuvenating agents on superpave mixtures containing reclaimed asphalt pavement. ASCE J Mater Civil Eng 19(5):376–84
67. Su JF, Qiu J, Schlangen E, Wang Y-Y (2014) Experimental investigation of self healing behaviour of bitumen/microcapsule composites by modified beam on elastic foundation method. Materials and Structures doi:10.1617/s11527-014-0466-5
68. Su JF, Schlangen E (2012) Synthesis and physicochemical properties of high compact microcapsules containing rejuvenator applied in asphalt. Chem Eng J 198–199:289–300
69. García Á, Schlangen E, van de Ven M (2010) Two ways of closing cracks on asphalt concrete pavements: microcapsules and induction heating. Key Eng Mater 417–418:573–576
70. Su JF et al (2011) Interface stability behaviors of methanol– melamine–formaldehyde shell microPCMs/epoxy matrix composites. Polym Compos 32:810–820
71. NL Agency (2011) Self healing materials concept and application, 2nd edn. NL Agency, Dutch Ministry of Economic Affairs, Agriculture and Innovation, The Hague
72. Butt AA, Brigisson B, Kringos N (2012) Optimizing highway lifetime by improving the self-healing capacity of asphalt. Procidia – Soc Behav Sci, Transport Research Arena 48:2190–2200
73. Kringos N, Schmets A, Scarpas A, Pauli T (2011) Towards understanding of the self-healing capacity of asphalt mixtures. Heron 56(1/2):45–74. http://heron.tudelft.nl/56-12/4.pdf
74. O'Brien F (2007) The third policeman. Harper Collins, London (First published in Great Britain by MacGibbon & Kee in 1967)
75. Vita L, Marolda MC (2008) Road Infrastructure – the backbone of transport system. EU Directorate General for Research and Sustainable Surface Transport, Brussels, Belgium
76. Worth J (2014) Ending the oil age. In: New internationalist, Nov 2014, pp 12–16. http://newint.org/features/2014/11/01/extended-oil-keynote/
77. Leggett J (2014) Big oil's looming bubble. In: New internationalist, Nov 2014, pp 20–21

Adv Polym Sci (2016) 273: 307–344
DOI: 10.1007/12_2015_334

Published online: 27 October 2015

Biological Archetypes for Self-Healing Materials

Matthew J. Harrington, Olga Speck, Thomas Speck, Sarah Wagner, and Richard Weinkamer

Abstract Damage and fatigue are ever-present facts of life. Given enough time, even the most robust material, whether man-made or natural, succumbs to the deleterious effects of cracks, fissures, and defects during normal use. Traditionally, materials engineers have approached this problem by creating damage-tolerant structures, intensive quality control before use, vigilant inspection during use, and designing materials to function well below their theoretical limit. Living organisms, on the other hand, routinely produce materials that function close to their theoretical limit as a result of their remarkable ability to self-heal a range of non-catastrophic damage events. For this reason, many researchers in the last 15 years have turned to nature for inspiration for the design and development of self-healing composites and polymeric materials. However, these efforts have so far only scratched the surface of the richness of natural self-repair processes. In the present review, we provide an overview of some paradigmatic and well-studied examples of self-repair in living systems. The core of this overview takes the form of a number of case studies that provide a detailed description of the structure–function relationships defining the healing mechanism. Case studies include a number of examples dependent on cellular action in both animals (e.g., limb regeneration, antler growth, bone healing, and wound healing) and plants (e.g., latex-based healing, plant grafting, and wound closure in woody vines and succulent plants). Additionally, we examine several examples of acellular self-repair in biopolymeric materials

M.J. Harrington (✉) and R. Weinkamer
Department of Biomaterials, Max Planck Institute of Colloids and Interfaces, Potsdam 14424, Germany
e-mail: matt.harrington@mpikg.mpg.de

O. Speck and T. Speck
Plant Biomechanics Group Freiburg, Botanic Garden, Faculty of Biology, University of Freiburg and Freiburg Materials Research Center (FMF), Freiburg 79104, Germany

S. Wagner
Institute for Botany, Dresden University of Technology, Dresden 01602, Germany

(e.g., mussel byssus, caddisfly silks, and whelk egg capsules) that are already inspiring the development of a number of self-healing polymers.

Keywords Bio-inspiration • Biomimetics • Functional morphology • Regeneration • Remodeling • Self-repair • Self-sealing

Contents

1 Introduction

A major future challenge in materials engineering is the production of high-performance, damage-tolerant, and renewable materials that can be used in technical and biomedical applications. In particular, the development of self-healing materials capable of repairing damage has emerged as an important and fast-growing research focus [1]. However, successfully integrating autonomic and intrinsic self-healing behavior into polymers and composites presents numerous challenges. For biological materials, on the other hand, self-repair is business as usual. For this reason, many researchers have begun to turn to biological materials for inspiration [2–8]. The field of bio-inspired and biomimetic materials is founded on the basic premise that biology has something to teach humans about efficient and economic means of designing and building versatile high-performance materials for a wide variety of functions. Self-healing, broadly defined, is a ubiquitous feature of materials made by living organisms. Familiar examples in everyday life include healing of cuts and scrapes, as well as mending of broken bones. However, as becomes clear in this review, the complexity and diversity of healing mechanisms in living nature is expansive.

It is important at the outset to define what is meant by self-healing in a biological context. Assuming a strong evolutionary pressure on the development of self-repair functions, independent evolution of mechanisms to cope with wounds and other damage can be expected. Indeed, an enormous range and variety of self-repair

mechanisms can be observed throughout the various kingdoms of biology. Here, we define self-repair as the recovery toward native material properties following a damage event. Healing does not have to result in complete restoration of the pre-damaged structure and properties; however, at least the function of the material must be regained. Damage, in this sense, includes the formation of microcracks or macroscopic cracks, plastic deformation, and loss of mechanical function or even loss of tissue, organs, or entire limbs. For each of these categories, there are examples in nature where partial or complete self-repair occurs. In this review, a number of case studies are presented that provide an overview of the current understanding of specific model systems representing a range of different healing mechanisms. In addition, recent efforts to develop bio-inspired or biomimetic materials with self-repair functions are highlighted where relevant.

It is pertinent at this point to introduce a crucial distinction in biological healing – that between cellular and acellular healing. Typically, healing processes in living organisms are dependent on cellular metabolism to function. For example, during bone mending, wound closure, or healing of tissues such as tendon in vertebrates, the intervention of living cells is required to initiate the healing process [9, 10]. Here, the cells are active players in breaking down old tissue and rebuilding new, living tissue. On the other hand, there are several less prominent, but equally impressive examples of intrinsic and autonomic self-repair responses that occur in non-living biological materials functioning outside the confines of a living body (i.e., extracorporeally) in the absence of an active metabolism. Examples include the mussel byssus, caddisfly silk, and whelk egg capsule material [11–13], which are discussed in detail later (see Sect. 2.9). The differences between acellular and cellular biological healing are especially relevant when attempting to gain inspiration from a system, because they necessarily entail starkly different levels of inherent complexity.

In spite of the broad range of healing processes observed throughout living nature, self-repair mechanisms in many animals and plants can in general be subdivided into two phases: an initial self-sealing phase and a subsequent self-healing phase [9, 10, 14, 15]. Using "self-repair" as an umbrella term, the two phases are characterized by anatomical and biochemical modifications and changes in biomechanical properties (Table 1) [16]. Interestingly, these definitions also hold true for (most) bio-inspired technical solutions, where self-sealing and self-healing can be found either successively or individually. Self-sealing mechanisms rapidly close fissures and protect organisms against invasion of pathogenic germs and loss of precious body fluids (e.g., water, sap, blood) but, in general, the mechanical properties of the tissue are not recovered at this point. Self-sealing can be seen as an initial means of quickly stabilizing the wound following a damage event, and typically function by deposition/coagulation of healing agents that seal the wound (e.g., latex in plants [17] and blood clots in animals [9]) or by using existing surrounding tissue to create a physical barrier (e.g., *Delosperma cooperi* [14, 15, 18]). The self-healing phase, on the other hand, is characterized in general by disappearance of the fissure and at least partial recovery of the native material structure and properties. As such, this phase requires much longer time spans to

Table 1 Characteristics of self-sealing and self-healing

Self-sealing	Self-healing
Fissures . . .	Fissures . . .
. . . are still present	. . . are no longer present
. . . are repaired functionally	. . . are repaired structurally
. . . are not repaired in terms of mechanical properties	. . . are repaired (at least partially) in terms of mechanical properties
. . . are sealed rapidly	. . . are healed over a longer time span

develop and involves more complex and metabolically intensive mechanisms for replacing damaged tissue, such as cell proliferation, callus formation, synthesis of biomolecules (e.g., cellulose, lignin, or collagen) and even biomineralization [9, 10]. Further details of these processes are discussed in the individual case studies.

Before proceeding to the case studies, it is important to mention some crucial differences between biological materials and man-made materials that are vital when considering technological transfer based on a biological archetype. First, biological materials, in contrast to engineering materials, are assembled in a bottom-up process from biomolecular building blocks that are synthesized in living cells. They are often self-assembled into complex hierarchical assemblies with highly intricate architectures at the nanoscale and possess carefully crafted interfaces between components at multiple length scales [19, 20]. Thus, self-repair is typically an emergent function arising from multiple mechanisms cooperating at several length scales. Second, although it is often stated that biological materials are "optimized" for a particular function, biological materials have in fact evolved to be multifunctional. For engineering applications, there are usually one or more functions that the material is expected to perform. In the case of biological materials, a battery of selective pressures encountered over the evolutionary history of the organism influence the final product. In fact, as pointed out by Gould and Lewontin in their classic paper [21], the characteristics of biological organisms (and the materials they produce) could simply be a byproduct of evolution (i.e., evolutionary baggage) rather than being shaped by adaptive selection. For this reason, biological materials are almost always multifunctional, and some design considerations might be superfluous for the materials engineer hoping to replicate just a single function (e.g., self-healing). For example, although bone is a structural material that exhibits impressive self-healing behavior, it is also a factory for production of white blood cells and a store of calcium for the body, which might have competing design considerations.

These inherent differences between natural and man-made materials highlight the challenges of successful transfer of biological self-healing into technical applications. On one hand, although it is necessary to take a reductionist approach when faced with the complexity of natural material design, one must be cautious not to reduce too much and lose the desired emergent behavior. On the other hand, the fact that biological materials are inherently multifunctional means that a large portion of

the design features are not essential for the function of interest, in this case self-healing. Thus, it is important to elucidate the essential parameters contributing to the healing behavior, while eliminating redundant or superfluous features. This of course requires a thorough understanding of the composition–structure–function relationships defining the material. Hence, the primary goal of this review is to provide a range of case studies of well-investigated examples of biological self-healing.

2 Case Studies

The following subsections provide case studies for a range of self-repair mechanisms observed in biological archetypes. This is not meant to be an exhaustive list of self-healing in living nature, but rather an overview that highlights the inherent diversity of damage that can be healed and current understanding of the mechanisms at play. Space restrictions necessitate that the level of detail for each case study is condensed; thus, we recommend that the reader refers to the cited references for further details. The review is primarily aimed at chemical or physical material scientists, who are probably less familiar with biology and molecular biology. Hence, general terminology is used and little detail is given for the signaling pathways and molecules involved in the regulation of biological healing responses.

2.1 Limb Regrowth

Regeneration refers to the replacement of lost body parts and the restoration of both their structure and function. Regeneration occurs in simple organisms such as planarians (a type of flatworm) and Hydra (simple freshwater polyps), which are able to regenerate their whole body from only small parts, as well as in more complex organisms such as urodele amphibians (salamander, newt, and axolotl), frogs (*Xenopus* spp.), and zebrafish [22]. It is not understood why some animals are able to regenerate and others, including humans, largely lack this ability [22]; however, the general view is that regenerative capacities were lost rather than gained during evolution. In this case study, we focus on limb regrowth in salamanders as it represents a well-studied and striking example of regeneration [23].

In addition to limbs and tails, salamanders are able to regenerate the upper and lower jaw, certain parts of the eye, the intestine, and small sections of the heart [24]. Of these, the complete regrowth of a limb (including its complex tissue patterning, full vascularization, and innervation) stands out as the most remarkable. Cutting the limb of a salamander at any place along the proximodistal axis (i.e., somewhere between shoulder and wrist) initiates a regeneration process that results in regrowth of the missing part of the limb (Fig. 1). Remarkably, this procedure can

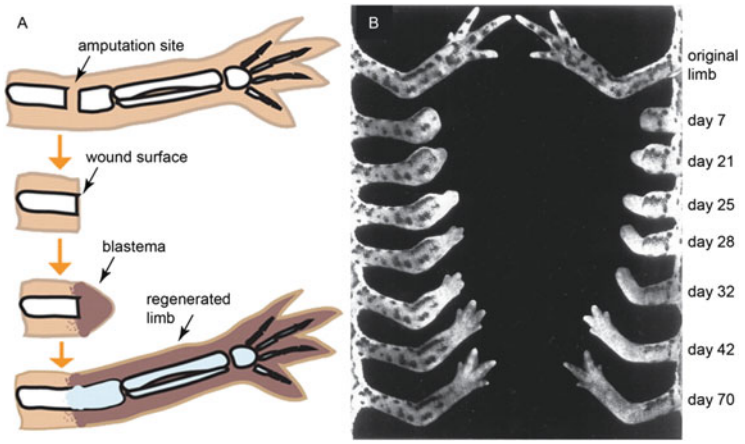

Fig. 1 Amphibian limb regeneration. (**a**) Limb regrowth in salamanders: after amputating the limb, a blastema (*in brown*) forms at the wound surface. The cells of the blastema are the source for the newly forming tissue of the regenerated limb. (**b**) Progression over time of limb regeneration following amputation of distal (*left*) and proximal (*right*) regions of the forelimb in a red spotted newt. For comparison, the original limb is shown at the *top* (Adapted from [24, 25] with permission)

be repeated a number of times with the same result. Limb regeneration can be subdivided into three phases, which are neither temporally nor spatially distinct [26]. During the initial sealing phase, the wound surface becomes covered by a specialized epithelium (the so-called wound epithelium) within a few hours after amputation. Over time, this epithelium transforms into a specialized secretory epithelia, which is thought to be the source of signals crucial in organizing the regenerative response. During the second phase, the wound epithelium prompts the cells in the underlying tissues to de-differentiate (i.e., to return to a state of less-specialized cell characteristics) and to proliferate, forming the so-called blastema at the end of the amputated limb. The blastema is a collection of cells with the potential to form specific organs or body parts (Fig. 1a). In contrast to previous theories, this blastema does not consist of a homogeneous mass of pluripotent cells, but rather of a more heterogeneous aggregation of progenitor cells with clear restrictions in their differentiation potential [23]. During the final phase, which occurs after about 2 weeks, the cells in the blastema re-differentiate and organize to build an exact replica of the amputated part of the limb (Fig. 1). At this stage, the blastema behaves similarly to a developing embryonic limb bud, such that the pathways of the two processes – limb regeneration and development – are thought to converge [26].

Diverse and creative transplantation experiments with amputated salamander limbs have clearly demonstrated the considerable autonomy of the limb blastema [23, 24] and its positional memory of its original environment (i.e., the blastema carries the information to grow the limb from which it was excised). The rule of distal transformation states that only limb elements that are more distal to its

positional memory are regenerated. As a consequence, when an upper arm blastema is transplanted onto a lower arm stump, the blastema re-forms all the distal structures starting from its position (i.e., the regenerated limb includes parts of a second lower arm). The rule of distal transformation was convincingly demonstrated by an experiment in which the orientation of the limb was inverted [27]. A salamander forelimb was amputated through the hand and the hand end was sutured to the side of the body. After successful healing, a second cut was performed through the upper limb. Because both stumps carried the positional memory of an upper limb, two complete limbs were regenerated. Blastemal autonomy extends further to limb identity. The transplantation of a forelimb blastema onto a hindlimb stump gives rise to regeneration of a forelimb. Furthermore, positional memory is not restricted just to the proximodistal axis of the limb, but extends to circumferential information in the amputation plane. For example, in a transplantation experiment in which a left upper arm blastema was transplanted to a right upper arm stump, positional discontinuities in the circumferential order of tissues was unavoidable, with the result that two extra limbs were formed [28].

Although clear parallels can be drawn between the process of limb regeneration and embryonic development of limbs from limb buds, it is still an open question how similar the underlying mechanisms actually are. Along these lines, although the cellular composition and cell signaling of the blastema and limb bud were found to be largely similar, significant differences are present regarding the starting point of each process and the relative length scales. In contrast to a developing embryo, the multiple tissues in an amputated limb of an adult salamander represent an enormously complex initial condition for regeneration [23]. Additionally, the size of a limb amputation plane is approximately tenfold larger than a limb bud. Although some have postulated that regeneration is controlled by diffusion of signaling molecules, the large length scale of the amputation plane calls this assertion into question [24]. Additional differences between regeneration and development concern the role of innervation for the regenerative response. In fact, in some cases, surgical intervention to deviate the nerve endings to a lateral wound on the limb induced the growth of a fully patterned limb out of this lateral wound in adult animals [23, 26]. Under the same experimental conditions, the regenerative outcome was significantly improved by an additional skin graft, which is thought to promote regeneration by its diverse positional information [29].

2.2 Antler Growth

In a process not dissimilar to limb regeneration, antlers grow on the skull in most species of the deer family. Antlers are branched structures made out of bone that regrow each year and should not be confused with horns, which are unbranched permanent structures that consist of keratinized tissue at their surface [30–32]. In practice, antler growth is a quite impressive feat: antler can grow to a length exceeding 1.5 m in a time span of less than 5 months, with peak growth rates of

nearly 1.75 cm/day [30]. The enormous demand for minerals to build up an antler of 30 kg is satisfied by an increase in bone turnover of the skeleton, resulting in osteoporotic conditions, particularly in non-weight-bearing bones (e.g., ribs) [32].

Notably, deer antler growth is the only example of regeneration of lost organs in mammals. The growth of antler does not start directly from the skull, but rather from bony protuberances termed pedicles, which are formed when the animal approaches puberty. The tissue from which pedicles and antlers develop is the so-called antlerogenic periosteum, which covers specific parts of the deer's frontal bone [33]. The antlerogenic potential of this early tissue was demonstrated in grafting experiments, in which the growth of antler was induced on different underlying bones and even on the skulls of nude mice [34]. The annual cycle of antler regeneration is controlled by sex hormones and begins in red deer with the casting (loss) of the old antler in spring. Sealing of the breakage plane occurs via formation of a blood clot followed by a scab. Within hours after shedding the old antler, formation of a wound epithelium over the distal ends of the pedicles begins, similar to the second stage of limb regeneration in salamander (see Sect. 2.1). It was argued that wound healing with minimal scar formation is a necessary prerequisite for successful appendage regeneration [31, 35]. In contrast to limb regeneration, full-thickness skin, including a dermis, is formed that develops later into the so-called velvet, which is a hairy surface that covers the antler during growth and is primarily responsible for the blood supply. At the distal ends of the pedicles below the skin, a mass of undifferentiated cells begins to accumulate. Unlike limb regeneration, however, this mesenchymal growth zone is based on stem cells without strong de-differentiation of cells and, therefore, is not considered a blastema [36].

Longitudinal growth of the antler occurs via endochondral ossification (i.e., ossification via a cartilage precursor). Within the growth zone, cell proliferation and differentiation into cartilage cells occurs. These chondroblasts and chondrocytes organize themselves into vertical columns with vascular space between them. At this point, remodeling occurs, by which cartilage is gradually replaced by bone (Fig. 2). Additionally, the antler grows laterally, but at a much slower rate and via a direct bone formation process termed intramembranous ossification. The final result – the mature antler – consists of a core of trabecular bone surrounded by a sleeve of compact bone. After growth has ceased and mineralization of the antler is complete, the velvet (together with the periosteum) is removed. With the bare bone exposed, the structure is then referred to as "hard antler." The general view is that the hard antler consists of dead material because velvet shedding results in interruption of the blood supply [31].

The morphology of antlers typically changes with age. In red deer, the peak in antler complexity (possessing a maximum number of tines) is reached in middle-aged adult animals. It is not known how information about previously cast antler morphology is stored in the animal's organism. Even more puzzling is the phenomenon referred to as trophic memory. An injury of the antler during growth resulting in malformation of its morphology is not restricted to the afflicted antler. Rather, the morphological abnormality can reappear in the antler of the successive

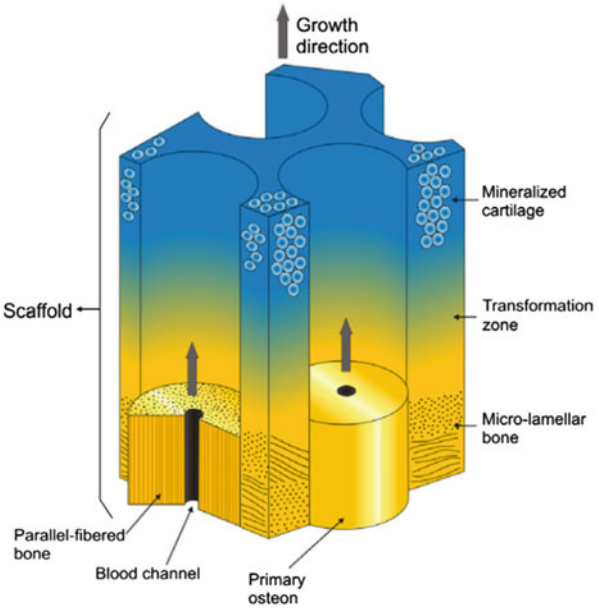

Fig. 2 Antler growth. Longitudinal antler growth proceeds via the initial construction of a tubular scaffold, which is then filled with cylindrical osteons (for a more detailed description see text) (From [37] with permission)

year and can be observed over several cycles of antler regrowth [38]. A crucial role of the nervous system was hypothesized because morphological abnormalities were not conserved when the trauma occurred with the animal under anesthesia [39]. To explain the phenomena of trophic memory, a model was proposed based on an encoded target morphology in the organism [40]; however, this is still an open question.

From a materials science perspective, with regards to the development of self-healing materials, antler provides two further notable features: (1) Antler achieves its remarkable growth rates by first constructing a porous framework. During longitudinal growth, for example, cartilage is transformed into bone with a honeycomb structure possessing cylindrical pores aligned along the antler axis (Fig. 2). In a second step, this scaffold is filled with bone with a collagen matrix that is well organized along the pores, leading to rapid assembly of a high-performance composite [37]. (2) Antlers are damage-tolerant structures with mechanical properties that are specifically adapted to withstand the high impacts occurring during combat. Compared with bone, antler is protected against fracture by high impact energy absorption [41] and high fracture toughness as a result of crack deflection mechanisms at the crack tip and bridging mechanisms in its wake [42]. Assessment of the deformation behavior showed that sliding between mineral and collagen in antler can dissipate energy on different length scales and, thereby, increase toughness [43].

2.3 Bone Healing

Bone is a complex hierarchically structured material (organ) possessing self-healing abilities on multiple length scales, ranging from repairing macroscopic fractures to nanoscale re-formation of reversible bonds [10]. Importantly, bone healing is an entirely regenerative process, resulting in the restoration of the pre-fractured state without scar tissue formation. At the micron scale, bone is constantly freed from damaged material by bone remodeling, and at the molecular scale, plastic deformation of bone is enabled by constant exchange of noncovalent molecular bonds.

Loading bones beyond their ultimate strength results not only in fracture of the bone, but is usually accompanied by significant damage to the surrounding soft tissue. In a typical situation following mechanical fixation of the fractured region, the bone fragments are able to move slightly against one another, leading to so-called secondary bone healing via the formation of extra tissue in the form of a callus. The process of secondary bone healing is subdivided into three overlapping phases [44, 45] (Fig. 3). During the initial reactive phase, a blood clot is formed and immune cells clean the site of dead material in an inflammatory response. At this point, the hematoma is infiltrated by small blood vessels and fibroblasts and is transformed into so-called granulation tissue. In the second reparative phase, mesenchymal progenitor cells migrate into the callus. Differentiation of these cells enables them to produce fibrous tissue, cartilage, fibro-cartilage, or bone. This crucial cell differentiation step is thought to be at least partly mechanically controlled, such that low mechanical stimulation results in direct bone formation, whereas cartilage is formed in locations of higher mechanical stimulation (e.g., around the fracture gap) [46]. Similarly to antler growth, bone formation during bone healing can occur directly via intramembranous ossification or by first forming cartilage in the process of endochondral ossification [47]. Also similar to antler growth, the fast bone growth required for rapid mechanical stabilization of the fracture site is obtained by first providing a scaffold of low bone quality, which is then filled by bone of improved quality [48]. In the final remodeling phase, dispensable excess bone material is removed, resulting in bone that is virtually indistinguishable in structure and function from the pre-fractured initial configuration.

Remodeling occurs not only in the final phase of healing, but continuously during the lifetime of organisms, during which bone material is constantly renewed and microdamage is removed [20]. During remodeling, specialized bone cells called osteoclasts and osteoblasts resorb and deposit small packets of bone material. In the spongy type of bone called trabecular bone, remodeling events occur at the surface. Inside the less porous cortical bone, the surface for remodeling has first to be created, which occurs when osteoclasts dig a tunnel through cortical bone with osteoblasts in their wake to close the tunnel. This results in the formation of a cylindrical structure of new bone, termed an osteon. Historically, the process of remodeling by replacing old damaged bone by new bone (bone material

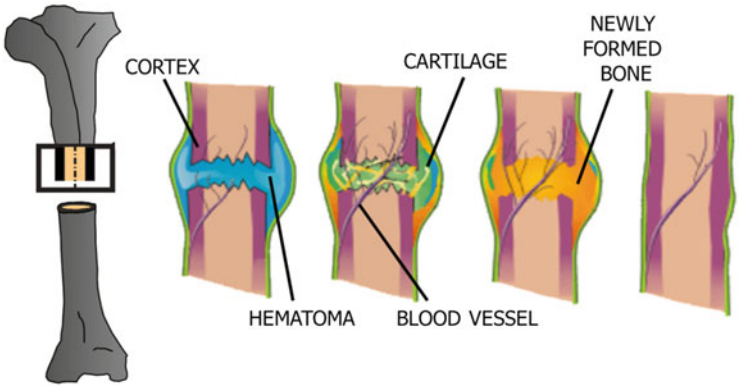

Fig. 3 The different phases of secondary bone healing of a long bone. The longitudinal sections show, from *left to right*, the broken cortex (*purple*) with the hematoma (*light blue*), followed by the succession of different soft and hard tissues within the fracture callus: fibrous tissue and cartilage (*green*) and bone (*yellow*) (Adapted from [44] with permission)

maintenance) is distinguished from modeling in which the uncoupled formation and resorption of bone allows an adaptive structural response of bone to an altered mechanical environment. Here, we use the term "remodeling" to refer to both processes [49].

To allow for such structural adaptation, it has been argued that bone remodeling must be a mechanically regulated process. Computer algorithms, with the implemented remodeling rule stating that bone is formed preferentially at sites of high mechanical load and resorbed where mechanical stimulation is low, could successfully describe the adaptive response of trabecular bone to changes in loading [50, 51]. A new experimental view on bone remodeling is offered by the possibility of obtaining multiple three-dimensional microcomputed tomography (μCT) images from the same bone, at least in small animals. Comparison of two such images taken with a time interval of about 1 week allows one to determine each remodeling event that occurs during this interval. In combination with mechanical assessment performed by finite element analysis (FEA), sites of remodeling can be correlated with the local mechanical loading, providing a quantitative description of the mechano-regulation [52] and its change with age [53]. The nature of the mechanical stimulus that triggers remodeling and the manner in which the stimulus is sensed by bone is still an open question. However, it is generally accepted that osteocytes, cells that are organized into a network-like architecture within the mineralized bone matrix, are involved in mechano-sensation [54]. One hypothesis that is gaining traction is that remodeling is stimulated when microcracks in bone result in a local interruption in the osteocyte network connecting two cells, resulting in cell death [10]. In bone, remodeling is a "housekeeping" process that protects the material against fatigue failure by using occurring microdamage as a signal for initiating the repair mechanism. From a materials science perspective, remodeling is a highly attractive mechanism that can be used in designing a material that not only responds

to potentially catastrophic damage events such as fractures, but that also preemptively addresses minor damage events before they can escalate into larger issues. Nonetheless, the frequent occurrence of stress fractures in the bones of military recruits reveals one potential drawback of a remodeling response that is too active. For example, if the microdamage caused by an intense training regime results in increased bone resorption to remove the damage [55], this can lead to further mechanical weakening of the bone, making stress fractures even more likely. This highlights the delicate balance that must be achieved between material breakdown and buildup.

At the molecular level, repair mechanisms contribute to the plastic behavior of bone and its characteristic high toughness. Similarly to antler, bone also utilizes deformation by sliding of structural elements against each other to increase material toughness. A staggered arrangement between the stiff mineralized fibrils embedded in a softer, but ductile, matrix results in tensile loading of the fibrils, while the extrafibrillar matrix is loaded under shear [20]. The matrix was previously described as a glue layer, in which a continuous breaking and re-formation of molecular bonds (so-called sacrificial bonds) [56] enables fibrils to slide against each other while dissipating energy. Mechanical tests with different strain rates and temperatures provided clues that sacrificial bonds in bone consist of calcium-mediated ionic bonds [57]. The concept of reversible sacrificial bonds is discussed extensively in the case studies of self-healing in extracorporeal biopolymers (Sect. 2.9).

2.4 Cutaneous Wound Healing

For most people, the healing of wounds to our skin (e.g., cuts and scrapes) is probably the most familiar biological repair mechanism. Even for a small cut, however, the resulting cascade of events is tremendously complex and warrants a whole review on its own [58, 59]. Consequently, we choose here to limit our focus to the classical description of the phases of cutaneous wound healing, with an additional focus on scar formation [60]. Many aspects of cutaneous wound healing are relevant to the design of self-healing materials, especially the ability to rapidly transport essential healing agents via a complex network of vasculature to the damage site in order to quickly seal the wound.

Analogous to bone healing, cutaneous wound healing in mammals has been divided into three distinct, but overlapping, phases (Fig. 4) [59, 61]: inflammation, new tissue formation, and remodeling. As with many of the other case studies presented, the first step in the repair process is to seal the wound with a temporary covering to staunch loss of blood and fluid. This is accomplished by formation of a clot consisting of aggregates of platelets embedded in a loose fibrin matrix. The clot serves as a scaffold for infiltrating cells and as a reservoir for signaling molecules. In parallel, diverse inflammatory leucocytes are recruited to the site of tissue injury to prevent infection by ridding the site of bacteria and removing dead tissue. At the

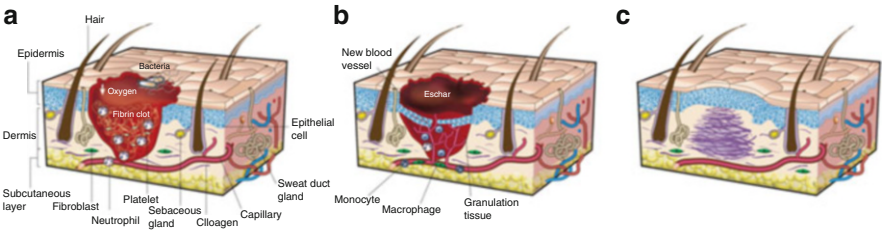

Fig. 4 Three phases of wound healing of skin: (**a**) inflammation, (**b**) new tissue formation, and (**c**) remodeling. Healing in skin with its two main layers, the upper epidermis and the lower dermis, is illustrated (for a detailed description of the process see text). Note that the region of the newly formed scar is free of the normal skin appendages (e.g., hairs, sweat glands) (From [61] with permission)

onset of the second phase, the barrier function of the epithelium is re-established. Keratinocytes migrate from the wound edge over the injured dermis separating the viable tissue from the desiccated eschar, which contains necrotic tissue as well as dried blood. As in bone healing, the formation of new small blood vessels (angiogenesis) establishes reliable blood supply to the injured tissue and transforms the fibrin matrix into granulation tissue, which consists of a dense population of cells in a mesh of collagen, fibronectin, and hyaluronic acid. At this point, some fibroblasts differentiate into myofibroblasts, which use their contractile abilities to compact the surrounding tissue and contract the wound. Extracellular matrix (ECM), mainly in the form of collagen, is generated by fibroblasts and myofibroblasts. During the final remodeling phase, most of the cells activated after the injury undergo controlled cell death (apoptosis) or leave the wound. Over a time period of roughly a year the remaining acellular collagen matrix is modestly remodeled, with a resulting scar that predominantly consists of type I collagen. The attained mechanical properties of the scar tissue are inferior to uninjured skin, with an ultimate tensile strength of only 70% of its original value [59, 61]. Although not as grave in its consequences as the life-threatening myocardial scar formed after a heart attack [61], excessive scarring of the skin, particularly after burns, is a major clinical problem [62].

Comparison between regenerative scar-free healing (as in the initial phase of limb regeneration) and non-regenerative healing with a fibrotic healing outcome reveals several important differences between the two processes that may open new possibilities for improving wound healing [60]. First, closure of the wound by a new epithelium is much more rapid in regenerative healing. For example, in axolotl (a type of salamander), wound closure occurs in less than half a day, whereas this usually requires a few days during cutaneous wound healing in mammals. Second, the composition and mechanical properties of the extracellular matrix differ for regenerative and non-regenerative healing. Myofibroblasts are also largely absent in regenerative healing and, thus, much less collagen is produced. There is general agreement that an attenuated immune response promotes scar-free healing [61, 63]. Two observations fuel hope for improving the fibrotic result of tissue

repair: (1) during early gestation most mammalian fetuses (including humans) show scarless healing outcomes [64], and (2) a mouse strain was serendipitously discovered that is able to fully regenerate ear punches as large as 2 mm [65].

2.5 Biochemical Self-Repair: Latex-Bearing Plants

We now shift focus from animal systems to plant systems for the next four case studies. Although specific details of the healing mechanisms naturally differ between these two biological kingdoms, many similarities are obvious [66]. Plants differ from many (higher) animals by their modular construction, that is, they are composed of many (self-similar) modules. This modular construction is one reason why plants can survive severe damage caused by storms, but also by pruning or mowing. In plants, self-repair can be found at all modular and hierarchical levels from the molecular scale to the entire organ, including cellular and acelluar self-repair mechanisms. In the following four case studies, we highlight specific examples of plant-based self-repair relevant to the development of self-healing materials.

Latex is found in more than 20,000 plant species coming from over 40 different plant families [67, 68]. This indicates that latex has evolved many times independently in different lineages of higher plants. One can therefore hypothesize that not only the physiological pathways of latex formation vary within these lineages, but also that the function and coagulation mechanisms differ widely regarding the biochemical structure of the latex and main selective pressures acting on latex formation. In plants, latex is typically found in cellular microtubes (laticifers), where the characteristically white to yellow milky exudate is often stored under high internal pressure (up to 15 bar). Latex contains, among other substances, phenolics, alkaloids, proteases, chitinases, and other proteins. In ca. 300 plant genera, rubber particles (*cis*-1.4-polyisoprene) are also found, often in high concentrations. As a result of the complex biochemistry, many functions for the sticky and often poisonous latex have been suggested and studied (e.g., as defense against herbivores or germs or as a transport system or reservoir for water, nutrients, and/or waste substances) [69, 70]. Surprisingly, the potential function of latex as a self-repairing substance was hardly studied in living plants [14]. This contrasts with the intensive studies of the chemistry and coagulation mechanisms of natural rubber, harvested mainly from the Pará rubber tree (*Hevea brasiliensis*), which were performed for more than 150 years, mostly for commercial reasons. Comparative analyses of latex-mediated self-repair have primarily focused on the genera *Ficus* (Moraceae, fig family), *Euphorbia* (Euphobiaceae, spurge family), and *Campanula* (Campanulaceae, bellflower family) [15, 71] (Fig. 5).

Rubber-based self-sealing is easily observed after injuring an organ of a latex-bearing plant (Fig. 5). Directly after injury, a white drop of fluid latex leaks out, typically becoming solid and translucent and sealing the wound after a time span of 20–30 min in tested *Ficus* and *Hevea* species, and after ca. 60 min in *Euphorbia* species. In contrast, the two bellflower species tested (*Campanula glomerata* and

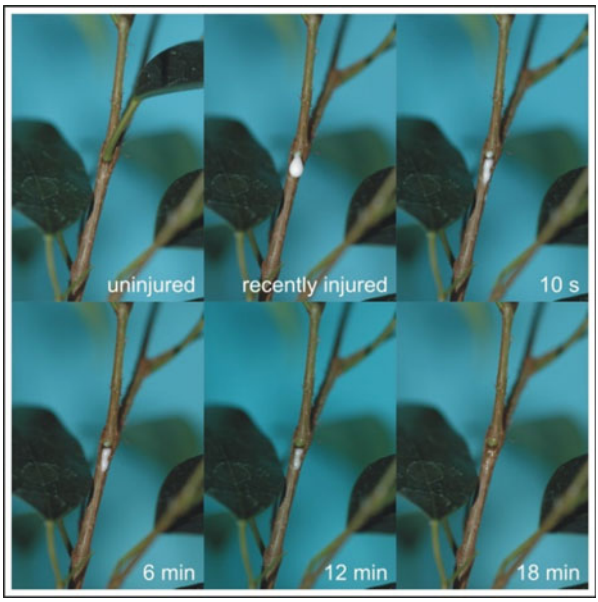

Fig. 5 Latex coagulation after injuring the bark of a weeping fig tree (*Ficus benjamina*). The fresh latex droplet directly after injury is white as a result of total light reflection by the latex emulsion. The droplet becomes more and more transparent with increasing coagulation, which mirrors the chemical alterations in the latex. From [72]

Campanula latifolia) exhibit coagulation in just a few seconds [14, 15, 72, 73]. The latex coagulation mechanism of the Pará rubber tree (*H. brasiliensis*) is one of the best understood from a chemical perspective. The latex of this species contains, among other substances, rubber particles and vacuolar structures (lutoids) that contain the protein hevein. The lutoids burst following injury as a result of the sudden pressure drop from over 7 bar in the intact laticifers to ambient pressure of 1 bar. This causes the release of hevein monomers, which form dimers in the presence of Ca^{2+} ions. Binding sites for hevein on the surface of the rubber particles induce latex coagulation, causing autonomous self-sealing via hevein-mediated crosslinking of the rubber particles [74–76]. Recent studies suggest that the latex coagulation mechanism in the weeping fig (*Ficus benjamina*) is very similar to that described for *H. brasiliensis* and is also based on protein binding between latex particles after pressure-drop-driven bursting of lutoids [15, 72]. In addition to the very efficient self-sealing of injuries, a self-healing effect of the coagulated latex has also been observed in the weeping fig. In tension experiments, it was observed that, directly after injury, the tension strength of cortex strips is reduced to 42% of that of the uninjured control sample and remains low for the next 20–25 min. After ca. 30 min (i.e., after coagulation), a significant increase in tension strength to 55% of the uninjured sample occurs. This increase is not found if the latex is removed directly after injury and confirms the self-healing function of latex. After this (mainly) physicochemical phase of self-repair, the tensile strength does not change for several hours or days until, as a result of cell proliferation and growth processes, the biological phase of self-healing begins and the tensile strength further increases [15, 17] (Fig. 6).

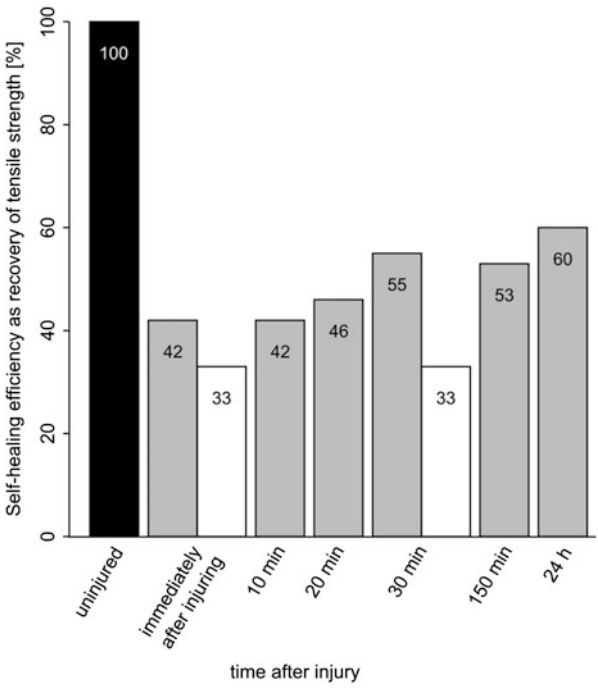

Fig. 6 Self-healing efficiency as percentage recovery of tensile strength in bark strips of the weeping fig (*Ficus benjamina*) at different time intervals after injury. *White bars* indicate barks samples in which the latex was removed directly after injury and therefore cannot contribute to self-healing. Copyright Plant Biomechanics Group Freiburg

Related studies have demonstrated that alternative mechanisms of latex coagulation and wound sealing exist in other latex-bearing plants [71, 73]. In addition to the weeping fig and Pará rubber tree, three spurge species (*Euphorbia amygdaloides, Euphorbia characias*, *Euphorbia myrsinites*) and two bellflower species (*C. glomerata*, *C. latifolia*) were studied and characterized concerning the time span between latex discharge and coagulation, size distribution of latex particles, and the rheology and wettability of latices. In addition to drastic differences in coagulation time, the latex of the two bellflowers coagulated much faster than that of the other species (see above). In addition, significant differences in the other parameters were found. In tested *Euphorbia* species, the latex particles were more densely packed and the size distribution (only one type of small latex particles) markedly differed from the bimodal particle distribution (as a result of latex particles and vacuolar structures) occurring in *F. benjamina* and *H. brasiliensis*. Additionally, the rheological behavior during latex coagulation and wettability varied between the species. These findings suggest that the coagulation mechanism in the tested *Euphorbia* species differs from the biochemically initiated mechanism found in *Ficus* and *Hevea* and is mainly caused by physical changes (i.e., simply by water evaporation). In addition to the physicochemically interesting differences, these findings suggest different evolutionary scenarios in the tested species concerning the main function of the latex. As a result of the prolonged liquid phase in *Euphorbia* spp., the anti-herbivory compounds remain dissolved longer and the main function is probably defense against herbivores,

whereas the (much) faster coagulation found in *F. benjamina, H. brasiliensis*, and the two *Campanula* species suggests that the main function of latex is self-sealing and self-healing of wounds [14, 15, 71, 73].

The wide variety of physical and chemical properties found in plant latices and the differences in coagulation mechanisms make plant latices very promising role models for the development of bio-inspired self-repairing materials. Different ideas for bio-inspired self-repair have been tested and include three basic approaches: (1) The first approach was inspired by the role of Ca^{2+} ions during latex coagulation in *Hevea* and was implemented by the development of technical ionomeric elastomers. The best results were found for carboxylated nitrile butadiene rubber (NBR). After rejoining rectangular strips (cut in half and then annealed for 24 h at 55°C), restoration of tensile strength to 50% of the undamaged strips was found for unvulcanized material, whereas in vulcanized strips the restoration dropped to 15% [14, 15, 77]. (2) The second approach was inspired by the bursting lutoid vesicles found in the latex of *Ficus* and *Hevea* and aimed for the development of technical elastomers equipped with microcapsules filled with healing agents. This approach has not been successful because of problems with the stability of the microcapsules [14, 77–79]. (3) An advancement of the idea of microcapsules was successful, in which microphase separation of the healing agent in the elastomer was used. This approach avoids a microcapsule wall by "chemically mimicking" micro-encapsulation. The concept led to the development of bio-inspired multiphase NBR blends with liquid polymers as self-sealing and self-healing agent. High internal pressure could be built up in their microphase-separated domains as a result of the different thermal expansions of NBR and polymer. Microcracks reaching such a domain are sealed and (at least partly) healed by the self-healing agent filling the microfissure. Hyperbranched polyethyleneimine (PEI) proved to be the most suitable self-healing agent for NBR and showed the best self-repairing effect. After re-joining rectangular NBR/PEI strips (cut in half, annealed in a heated sample holder for 12 h at 100°C, and then stored for another 12 h at room temperature), restoration of tensile strength to 44% of the values for undamaged strips was found [7, 14].

2.6 *Cellular Self-Repair:* Aristolochia macrophylla

In many climbing lianas (woody vines), the young axes are stiff in bending and torsion and act as searching twigs, exploring the space for new supporting structures on other branches of the current supporting tree or on new supporting trees up to several meters away. These searching twigs are anatomically characterized by a dense and stiff central wood cylinder and/or peripheral stabilizing tissue layers consisting of thick-walled collenchyma and/or sclerenchyma fibers. After being attached onto the new support, the liana stems develop a cylinder of secondary wood with large vessels and huge wood rays. This wood type is very flexible in bending and torsion. The resulting increased flexibility in bending and torsion is

advantageous because it enables attached liana stems to passively follow wind-induced movements of the supporting tree or deformations caused by climbing animals as a result of elastic deformation. It may even enable the plant to survive collapse of a supporting branch or the entire tree [80–82].

In species with closed outer cylinders of stabilizing tissues, as in twining pipevine species (*Aristolochia* spp.), these internal growth processes cause increasing radial and tangential stresses and strains in the stiff peripheral cylinders comprising collenchyma and/or sclerenchyma. As a result, the highly lignified and stiff peripheral sclerenchyma cylinders often fail and (micro)fissures occur. Although these fissures further increase the bending and torsional flexibility of the liana stems, fissures running outward to the stem are perfect entrance gates for fungus spores and bacteria that can infect the liana stem. Thus, high selective pressure for the evolution of efficient self-repair mechanisms that close the fissures quickly can be hypothesized (Fig. 7). Studies of different *Aristolochia* species showed that, following internal microfissure formation, parenchymatous cells of the outer cortex tissue swell into this fissure and seal it as a result of their internal cell pressure (turgor) of, typically, 2–3 bar. This is caused by relaxation of pressurized tissue into a newly formed opening and represents the fast self-sealing phase of wound repair. This is based (mainly) on physicochemical processes and involves neither cell wall biosynthesis nor cell division. In the further course of ontogeny, the vascular cambium produces more secondary phloem and especially secondary xylem, which causes a further increase in diameter of the central vascular tissues and provokes enlargement of the fissures in the peripheral stiffening rings. The repair cells react to this with cell divisions in tangential and radial directions (metabolic processes including significant cell wall biosynthesis) (Fig. 8). This stage of self-repair in *Aristolochia* spp. can be interpreted as the starting point of the prolonged phase of self-healing. During this self-healing phase, repair cells can even develop thickened and lignified cell walls, which (partly) restore the mechanical properties of the peripheral stiffening tissues [15, 83, 84].

Detailed and quantitative descriptions of the fast self-sealing processes for stems of the winding lianas *Aristolochia macrophylla* and *Aristolochia ringens* were used as concept generators for the production of a novel self-sealing foam. Pneumatic structures (e.g., rubber boats, tires, and airbeds) are especially "vulnerable" technical products that typically lose their functionality entirely following air loss as a result of puncturing. Joint efforts between academia and industry have resulted in the development and patenting of a self-sealing foam coating for membranes of pneumatic structures [6, 14]. Especially good results were achieved with the foam Raku-PUR 33-1024-3 (Rampf Polymer Solutions, Germany). Tensairity® technology has been utilized for applications such as ultralight bridges and roof construction. These structures consist of a combination of compression struts and tension cables, with a central stiffening pneumatic cylinder equipped with a self-repair function [85, 86]. The self-sealing phase is especially well suited for biomimetic transfer because (mainly) physicochemical processes are involved. The best results were found for closed-pore polyurethane foams cured under an overpressure of 1–2 bar, causing a pre-strained repairing layer on the inside of the membrane.

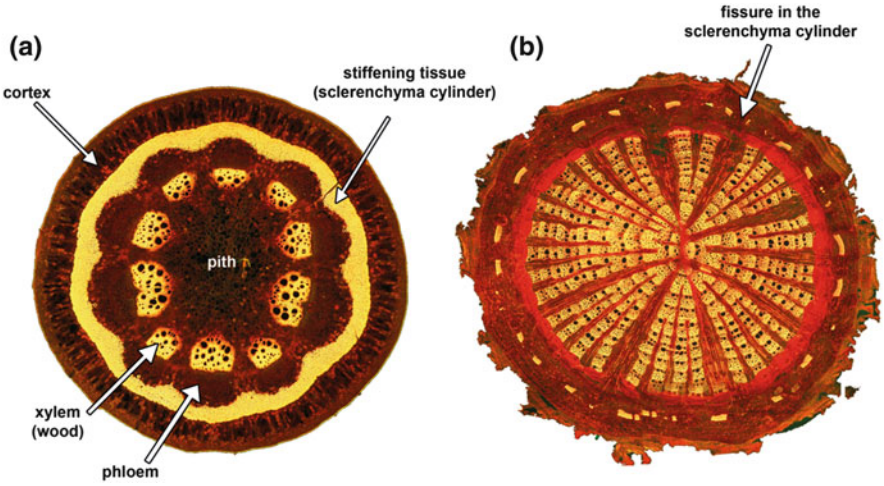

Fig. 7 Self-repair in stems of the pipe-vine (*Aristolochia macrophylla*). (**a**) Cross-section of a 1-year-old stem with closed peripheral cylinder of stiffening sclerenchymatous tissue. (**b**) Cross-section of a 10-year-old stem with repaired fissures in the peripheral cylinder of stiffening sclerenchymatous tissue. Copyright Plant Biomechanics Group Freiburg

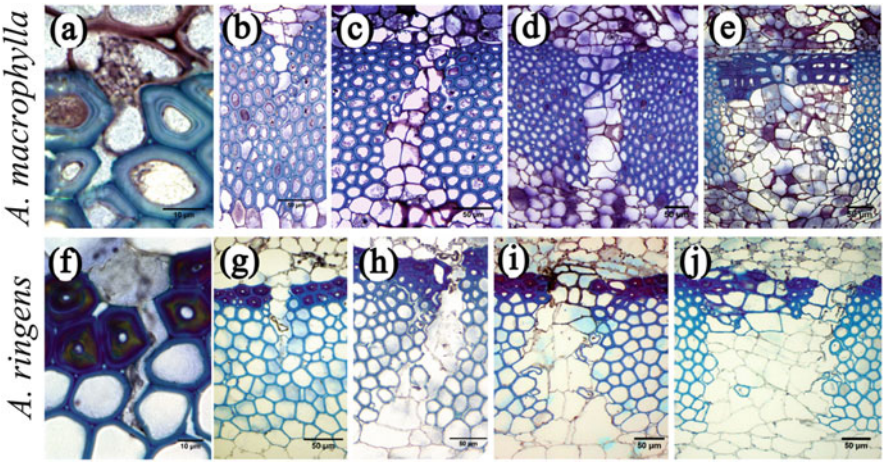

Fig. 8 Different phases of self-repair in (**a**–**e**) *Aristolochia macrophylla* and (**f**–**j**) *Aristolochia ringens*. (**a**, **f**) Initial self-sealing phase; a fissure in the sclerenchymatous cylinder (*stained in blue*) is sealed from a parenchyma cell. In subsequent phases, the fissure increases in size as a result of increasing formation of central vascular tissues. The fissure increase is compensated by cell division of thin-walled, irregularly shaped parenchymatous cells, which first occurs in the radial direction (**b**, **g**) and later – in increasingly broad lesions – also in the tangential direction (**c**, **h**), which represents the beginning of the self-healing phase of self-repair. In even later phases of repair the cell walls of the most peripheral repairing parenchyma cells become thickened and lignified (**d**, **e**, **i**, **j**). This allows, at least partly, restoration of the mechanical properties of the sclerenchymatous cylinder. From [83] with permission

The layer is only a few millimeters thick and does not add much to the weight of the membrane. As a result of pre-straining and the compression strains evoked in the foam layer on the inside of the membrane by the toroidal form typical for all pneumatic structures, the foam layer relaxes after puncturing and seals the fissure very efficiently. By this process, air leakage through a hole in the membrane can be entirely stopped or at least markedly reduced. In the case of holes of up to 5 mm diameter in foam-coated fiber-reinforced PVC membranes (as used for Tensairity® structures) the air leakage could be reduced in all tests by a factor of at least 1,000. In over 80% of the tested samples the punctured membranes were entirely sealed [6, 14, 87, 88].

2.7 Self-Sealing by Deformation

Plants growing under extreme ecological conditions are under especially high selective pressure regarding the development of effective self-repair mechanisms. Over the course of evolution, succulent plants, which evolved independently in various systematic groups, have developed the ability to store water in their tissues as an adaptation for survival in arid environments. After external damage, which can lead to exceptional drought stress, rapid self-sealing protects the plant from dehydration and is therefore of dominant selective advantage [14, 15, 18]. Highly effective self-sealing mechanisms were found in the succulent leaves of *Delosperma cooperi* belonging to the Aizoaceae family. The species is native to South Africa, where it grows in semi-arid regions with cold winters. This perennial forms dense plant stocks with striking pink flowers, responsible for the common name Pink Carpet [14, 15, 18, 89]. In cross-section, the almost cylindrical leaves reveal a centripetal arrangement of five tissue types consisting of an outer layer of epidermis with window cells, a peripheral ring of chlorenchyma, a thin net comprising vascular bundles, an inner ring of parenchyma, and a strand of vascular bundles in the leaf center (Fig. 9) [14, 15, 18, 89].

After an artificial incision, wound sealing in leaves of *D. cooperi* takes place by deformation and leaf movement. Two mechanisms are involved, the effectiveness of which are dependent on the air humidity: (1) rolling in of the wound edges within a few minutes, and (2) bending or contraction of the entire leaf within approximately 1 h. Rolling in of the fringes probably results from the different shrinkage properties of the epidermis with its huge window cells and cuticula. Occasionally, the wound edges form a hook-like structure that helps to seal the wound cavity and prevent dehydration. This feature can be found in the leaves and stems of *D. cooperi* [14, 15, 18, 89]. Depending on the wound type, the entire leaf can deform in such a way that the incision becomes closed within a maximum of 60 min. Three types of external injuries along the leaf were studied. Lateral cuts in both transversal and longitudinal directions lead to bending of the entire leaf until the wound edges are close enough together to seal the wound. Leaves with a circular cut do not bend; rather, they contract until the wound margins close the incision [14, 15, 18, 89].

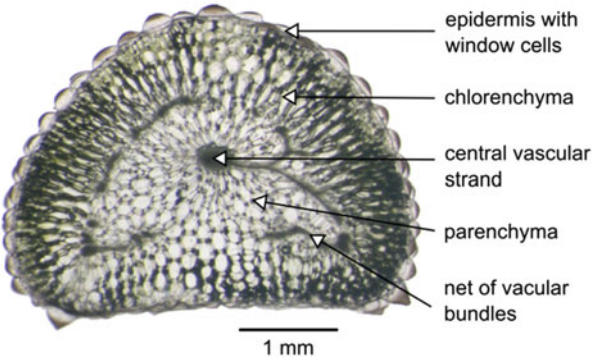

Fig. 9 Unstained cross-section of a succulent leaf of *Delosperma cooperi* with five tissue layers. Copyright Plant Biomechanics Group Freiburg

Subsequent wound healing leads to wound tissue that appears white to the naked eye, and occasionally results in permanent curvature or circular necking of the leaf.

For better understanding, the mechanical properties of the entire leaf and dissected single tissue layers were studied. Tensile tests were carried out with a microtensile tester by fixing either the entire leaf or single tissues, such as the central vascular strand or the epidermis, on two sample holders. The force-displacement diagram of an entire leaf showed a linear elastic portion of the curve (Fig. 10a, b). At maximum tensile strength the leaf seems to be fully intact (Fig. 10c). Failure occurred stepwise, showing several pre-failure events, whereby crack propagation was observed after the first visible crack (Fig. 10e) on the surface of the leaf.

On the basis of geometric data obtained from anatomic studies, combined with mechanical properties found as a result of tensile tests and pressure probe measurements, an analytical model for intact leaves and wounded leaves with regard to elastic and viscoelastic behavior was developed. The plant model was defined after considering the elastic modulus, the radius, and the Poisson's number of all five tissue layers [89, 90]. The equations are capable of describing the self-sealing process of *D. cooperi* after longitudinal, transversal, and circular damage of the leaves in terms of elastic and viscoelastic behavior. The analytical model provides a universal language in order to better understand the biological template and will help in developing a range of technical applications (e.g., multilayer materials with self-sealing function) [89].

2.8 Grafting in Plants

The seamless fusion of plant individuals or organs, known as grafting, provides another pertinent example for research on self-healing materials. Numerous descriptions of "natural grafts," the incidental fusion of plant parts, can be found in the literature [91–95]. Botanists have been understandably fascinated by this

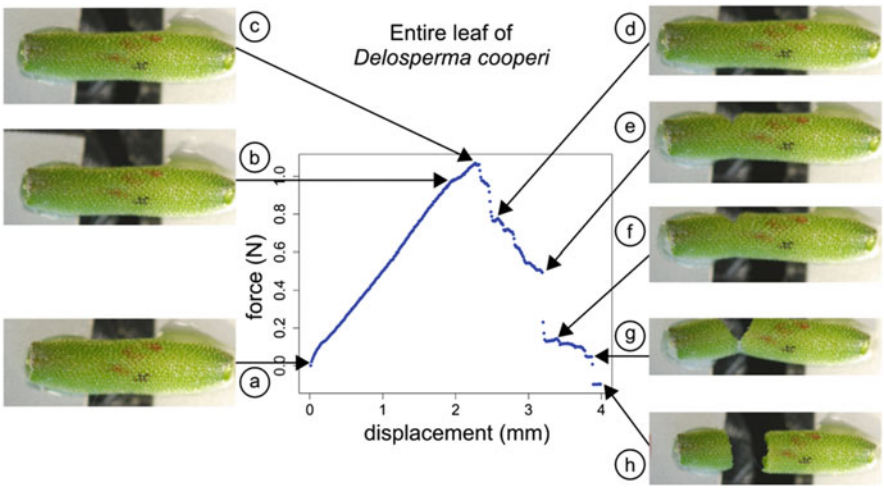

Fig. 10 Force-displacement diagram as a result of a tensile test with an entire leaf of *Delosperma cooperi*: (**a**, **b**) linear-elastic range, (**c**) maximum tensile strength, (**c**–**g**) stepwise failure with crack propagation after the first visible crack (**e**) on the surface of the leaf, and (**h**) total failure. Copyright Plant Biomechanics Group Freiburg

behavior for centuries, because a successful, compatible graft can lead to tissue fusion, vascular continuity, and a single physiologically and mechanically functioning unit [96]. Grafting is possible within an individual (autograft), between individuals of the same species (homograft), or even between different species (heterograft) [96, 97]. Natural grafting only rarely occurs above ground, whereas root fusion among forest trees seems to be a common phenomenon, probably facilitated by the dense network of roots and the surrounding soil matrix [96, 98–100]. The resulting network between roots of one individual or several individuals raises questions about the individuality of a single tree, as well as interplant relationships and communication within a whole forest [98] and, thus, about the evolutionary and ecological relevance of natural grafting.

Natural grafting (Fig. 11a) probably inspired the application of grafting in agriculture and horticulture thousands of years ago, which is currently applied for vegetative propagation and the creation of unusual growth forms in ornamental plants [100]. Several studies have shown that the tensile strength of successful autografts reaches and sometimes even exceeds the tensile strength measured for intact control plants [97, 101–105]. The connection of different tissues into one functionally united structure has clear implications for future and advanced biomimetic materials research, especially when focusing on adaptive and self-healing materials. Thus, understanding the detailed mechanisms underlying a successful graft is of utmost importance.

Grafting always requires tight contact between the partners, as well as pressure and/or injury at the points of contact [92–96, 100, 106]. Lesion formation in the closely contacting organs of both grafting partners activates wound healing

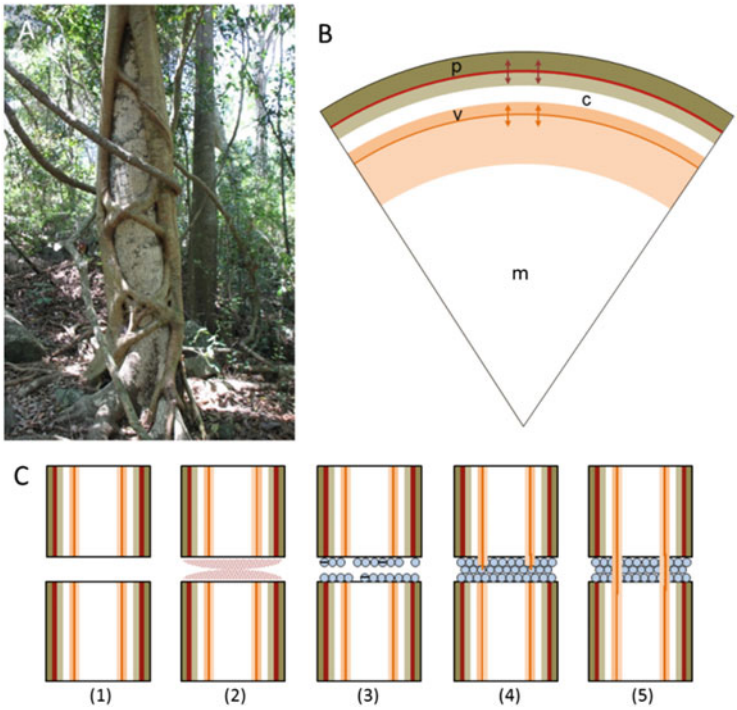

Fig. 11 Grafting behavior and mechanism in plants. (**a**) Strangler fig aerial roots fusing to a network around the host. (**b**) Diagram showing the position of meristematic tissues phellogen (*p*) and vascular cambium (*v*) in the plant stem's transverse section; *m* mark, *c* cortex. (**c**) Steps *1–5* toward the fusion of plant parts; *white* mainly parenchyma, *orange* vascular cambium and derived cells, *brown* phellogen and derived cells

processes on both sides [106, 107] by stimulating meristematic tissues (e.g., phellogen and vascular cambium) located very close beneath the stem or root surface (Fig. 11b). The vascular cambium consists of cell initials, which produce daughter cells mainly by tangential division. The descendants differentiate into the secondary conductive tissues phloem and xylem, as well as into fibers and parenchyma, taking over water and nutrient conductivity, storage, and mechanical stability [108]. The vascular cambium is a dynamic tissue and the daughter cells vary in form, function, and rate of production, which are dependent on the age of the plant or season of the year [109]. The phellogen is a secondary meristem that develops de novo in the peripheral region of the stem. Living cells convert to meristematic active cells and produce the periderm, a secondary protective tissue, also by tangential division [108, 109]. Both meristems are sensitive to internal and external signals and stimuli such as wounding or mechanical influences. Stimulation of meristematic tissues and initiation of wound-healing processes are always accompanied by the formation of a callus (i.e., a mass of uninjured, rapidly dividing parenchyma cells) [96]. However, instead of sealing each wound individually, the

activated meristematic tissues of both partners fuse to form a joint callus and coordinated healing of the wounds of each grafting partner [94].

The sequence of structural events during the grafting process (Fig. 11c) has been defined by several studies [96, 106, 110–112]. If both partners are in close contact after physical injury, deposits and residues of killed cells form a material compound between the freshly exposed surfaces, consisting of cellulosic cell wall remnants, resins, and other cell content (Fig. 11c, step 2). Adjacent parenchyma cells enlarge and extend into the interface and subsequently start to divide (i.e., callus formation), filling up the spaces between partners (Fig. 11c, step3). Formation of the callus facilitates temporary by-pass of the damaged vascular tissues. Callus cells then differentiate into wound-repair xylem and phloem, followed by formation of a new vascular cambium layer (Fig. 11c, step 4), leading to a continuous cambial connection between the two grafting partners [96, 111, 113] (Fig. 11c, step 5). Finally, the vascular connectivity between both grafting partners is established by the regular production of conductive tissue [96, 106, 113]. The early steps of grafting are supported by adhesion and cohesion between the adjacent cells, resulting from the secretion of insoluble carbohydrates and pectin polysaccharides [113]. The interactions between grafting partners during formation of a callus and the vascular connectivity are regulated and controlled by hormones such as auxin, which are released by both grafting partners and stimulate vascular tissue differentiation [107, 114–116]. Recent studies suggest that small RNA or DNA fragments and even complete chloroplast and nuclear genomes can be exchanged between the grafting partners, directing DNA methylation and allowing horizontal gene or even genome transfer between sexually incompatible species [117–120].

The fascinating subject of uniting different plant individuals or parts includes events such as cell elongation and callus formation, which are also observed elsewhere [111]. These are common plant responses and are related to a naturally much more important process, the healing of wounds. Furthermore, parallels are also seen in the response of plants to infection, such as cancer-like tissue formation in club root disease. The fusion of natural tissues and structures is fascinating and might serve as stimulation for the development of artificial adaptive and self-healing materials. In particular, the processes of sealing, gap filling, and subsequent formation of new tissue, although difficult to mimic, may open new routes for materials synthesis and functionality.

2.9 Healing in Acellular Biopolymers: Reversible Bonds

Extracorporeal biological materials such as spider and insect silks are synthesized from biomolecular building blocks (e.g., proteins) and function outside the confines of the body of the organism. Such materials are acellular and, thus, their material properties must arise from the intrinsic chemical and physical features of the building blocks themselves. For this reason, extracorporeal materials provide ideal biological archetypes for inspiration of polymeric materials. Although self-healing

is typically regarded as a cell-driven process, there are several examples in nature of self-healing extracorporeal biopolymers (e.g., mussel byssus, caddisfly silks, and egg capsules from marine snails), which achieve these behaviors through the use of reversible bonds.

2.9.1 Mussel Byssal Threads

Marine mussels of the species *Mytilus* anchor securely to wave-battered surfaces in rocky seashore habitats using protein-based holdfast fibers known as mussel byssal threads (MBTs) (Fig. 12a) [121]. The distal region of MBTs is initially stiff (500–800 MPa), but yields at a critical stress, dissipating up to 70% of applied energy in the process (Fig. 12b) [12, 122]. Yield, however, results in apparent damage in subsequent loading cycles, with stiffness and strain energy reduced by as much at 65% (Fig. 12b) [12, 122]. Initial properties are largely recovered when threads are rested for several hours in water, indicating an intrinsic and autonomic self-healing of material damage [122].

Structurally, the thread core is composed principally of a protein family known as the preCols [123], which are elongated block copolymer-like proteins with several distinctive structural domains, including a central collagen domain, flanking domains surrounding the collagen domain, and terminal histidine-rich domains (HRD) at both ends (Fig. 12c). The collagen domain forms a rigid triple helical trimer [12, 124], whereas the flanking domains of some preCol variants form a compact β-sheet structure [125, 126]. The N- and C-terminal HRDs contain at least 20 mol% of the amino acid histidine, which forms metal coordination bonds with Zn^{2+} and Cu^{2+} ions in threads [127, 128].

Recent X-ray diffraction (XRD) studies reveal that preCols are organized serially into a nano-architectured semicrystalline framework (Fig. 12c), which is highly deformable and recovers elastically immediately when relaxed through reversible unfolding of the flanking domains and HRDs [12, 124]. Slower healing of mechanical properties thus indicates a second healing stage, involving recovery of reversible bonds [124]. Histidine–metal coordination crosslinks localized in the HRDs are thought to function as load-bearing reversible bonds that provide high strength, but also high lability [123, 129]. The reduction of byssal thread stiffness and loss of healing behavior in response to low pH and metal chelation treatments aimed at disrupting metal coordination provides important support for this model [12, 129, 130]. Indeed, recent evidence from X-ray absorption spectroscopic (XAS) studies confirms the presence of mechanically active protein–Zn^{2+} crosslinks in the distal thread core, which are disrupted during the post-yield stress plateau and reorganize toward the native state during thread healing [128]. The ability of histidine–metal coordination bonds to behave as strong and reversible crosslinks was also demonstrated in vitro with micromechanical adhesion studies using HRD-mimicking peptides attached to soft-colloidal probes [127].

In addition to the protein–metal complexes in the thread core, labile crosslinks between 3,4-dihydroxyphenylalanine (DOPA) amino acid residues of mussel foot

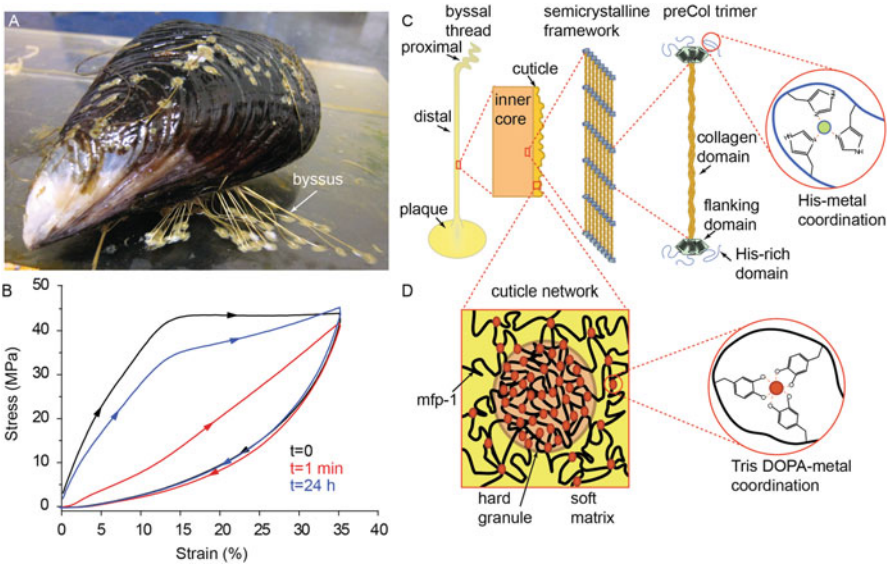

Fig. 12 Self-healing in mussel byssal threads. (**a**) Mussels anchor on hard surfaces with the byssus. (**b**) The distal region of byssal threads experiences damage following cyclic loading beyond the yield point (*red curve*); however, recovery toward native behavior is possible over time (*blue curve*). (**c**) Distal byssal threads are hierarchically structured semicrystalline fibers composed primarily of preCol protein. PreCols are collagenous protein with N- and C-terminal domains rich in histidine residues, which are believed to coordinate divalent transition metal ions. (**d**) The hard and extensible outer cuticle of byssal threads is composed of hard micron-sized granules that are centers of high DOPA–metal crosslink density surrounded by low crosslink dense matrix material

protein-1 (mfp-1) and metal ions such as Fe, V, and Al have been detected in the hard and extensible outer cuticle of MBTs (Fig. 12d) [131–133]. In this case, the coordination crosslinks are organized into submicron-sized crosslink dense regions (granules) with stiff mechanical behavior and lower crosslink density regions (matrix) that are less stiff (Fig. 12d) [134]. Microcracking in the matrix caused by rupture of DOPA–metal bonds is thought to provide extensibility in this stiff and hard biopolymer, which could facilitate resealing and healing of cracks as a result of the reversible nature of the bonds [131, 134]. Reversibility was demonstrated by metal chelation experiments in which cuticle metals could be removed with EDTA (lowering the stiffness/hardness by more than 85%) and later reintroduced by soaking in metal chloride solutions, leading to complete mechanical recovery [132]. Notably, Fe, V, and Al could all be reintegrated into the mfp-1 DOPA crosslink network without causing a pronounced difference in mechanical performance compared with the native state, underlining the inherent adaptability and versatility of this reversible crosslink network [132].

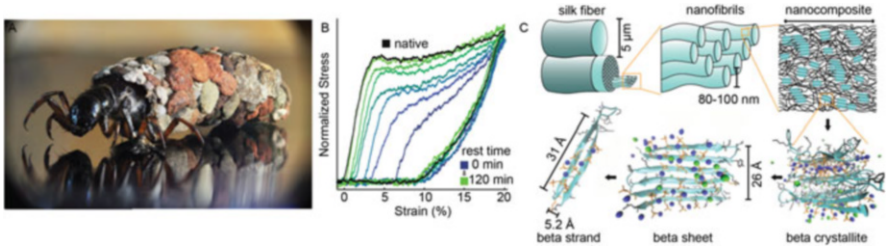

Fig. 13 Self-healing in caddisfly silk. (**a**) Caddisfly larvae build composite cases from small stones and an adhesive silk. (**b**) Silks undergo damage upon yielding, but can recover initial properties within ~2 h. (**c**) Caddisfly silk has a complex hierarchical structure in which protein β-crystallites are embedded in an amorphous protein matrix. The β-sheets are stabilized by interactions between phosphorylated serine residues and Ca^{2+} ions. Adapted with permission from [135]. Copyright (2013) American Chemical Society

2.9.2 Caddisfly Silks

Larvae of certain caddisfly species live in aqueous environments and sheath themselves in protective composite cases made of pebbles and stones that are glued together by adhesive silk fibers [135] (Fig. 13a). The silk fibers were recently discovered to exhibit tensile mechanical behaviors similar to those of byssal threads, with an initially stiff behavior, a yield event at low strain followed by a stress plateau, and a large hysteresis in cyclic loading (Fig. 13b) [11, 135]. Native material properties are similarly reduced significantly during subsequent loading, but are recovered over time to near native values [11].

Caddisfly silk is composed primarily of H-fibroin, a large protein with tandemly repeated domains [136], but also contains PEVK-like proteins that may function in material elasticity [137]. Serine residues in prevalent H-fibroin $[S\text{-}X]_n$ repeat domains are post-translationally modified to phosphoserine, a highly acidic amino acid side chain. These domains are thought to form β-crystalline nanodomains that are stabilized by inter- and intramolecular interactions between phosphate moieties and Ca/Mg ions (Fig. 13c) [11, 135, 138, 139]. Removal of ions with EDTA treatment revealed a large reduction in β-sheet structure and a marked loss of mechanical performance – an effect that was completely reversed by reintroducing calcium ions [135]. Based on these findings, a molecular model was proposed involving a multinetwork system with two different ionomeric clusters, which, like the proposed metal coordination sacrificial bonding network in the byssus, is able to reversibly rupture and re-form, leading to self-healing behavior [11].

2.9.3 Whelk Egg Capsules

Whelks (*Busycotypus canaliculatus*) are marine snails (gastropods) that lay their eggs encapsulated within a tough and compliant leathery egg case consisting of individual disk-shaped capsules linked into chains of up to meter in length(Fig. 14a)

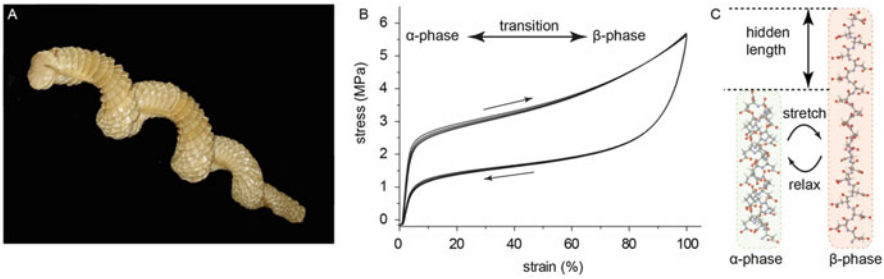

Fig. 14 Whelk egg capsule. (**a**) Whelks are marine gastropods that lay eggs in elaborate egg cases. (**b**) Whelk egg case (WEC) material exhibits yield and hysteresis behaviors similar to those of MBTs and caddisfly silk, but recovers initial behavior immediately through multiple cycles. (**c**) Shape memory behavior of WEC is attributed to reversible unfolding and refolding of α-helical protein structure into a β-sheet-like structure

[140]. Whelk egg capsule (WEC) material is a proteinaceous biopolymer that, like mussel byssus and caddisfly silk, functions to dissipate energy in aqueous environments. The WEC biopolymer is less stiff than MBTs or caddisfly silk, but similarly undergoes yield at low strain and exhibits a large hysteresis (~50%) during cyclic tensile loading (Fig. 14b) [13, 140]. However, unlike MBTs and caddisfly silk, WEC biopolymer recovers initial material properties almost instantaneously [13, 140] (Fig. 14b), which is behavior reminiscent of pseudoelastic/shape memory polymers and alloys.

XRD and vibrational spectroscopy studies clearly identify a dominant α-helical protein structure in the egg capsules aligned in orthogonal layers parallel to the capsule surface [13, 141]. Three α-helical proteins, named capsule protein (CP)-1, CP-2, and CP-3, are thought to be the primary load-bearing elements [142]. Beyond the yield point, the α-helical proteins oriented in the stretching direction undergo reversible conversion to a β-sheet-like structure, in which the hydrogen bond network stabilizing the α-helical structure is disrupted (Fig. 14c) [13, 141]. The conversion from extended β-sheet-like structure back to compact α-helical structure is associated with a notable hysteresis at the molecular level, probably arising from re-formation of the reversible hydrogen bond network along the helical axis [141, 143]. The interconversion between the two conformational protein structures was modeled successfully as a classical phase transformation, comparable to the martensitic transformation observed in shape memory metal alloys (e.g., NiTi) [141, 143].

2.9.4 Extracted Concepts and Biomimetic Materials

From these three examples of biopolymeric self-healing, several common design principles can be extracted for design of self-healing polymeric materials: (1) The use of reversible sacrificial bonds combined with folded protein lengths leads to material yield and energy dissipation, but also to molecular level damage in the

crosslinking network. Time-dependent recovery toward the native (healed) network appears to depend on transient and labile bond dissociation kinetics. The reversible bonds used in nature range from hydrogen bonds to ionic interactions and metal coordination bonds, which apparently tune material performance (e.g., stiffness and yield stress). (2) Elastic recoil of the unfolded (damaged) structure is necessary to bring ruptured reversible bonds back into register so they can re-form, somewhat analogous to the self-sealing phase observed in cellular materials. (3) Hierarchical structure at numerous length scales (e.g., protein secondary structure, higher order assemblies) localizes damage, and thus healing, to specific regions of the protein (polymer) network, probably facilitating reversible bond recovery and healing. This last point is perhaps the least well understood aspect of biological healing via reversible bonding and is being actively pursued for these materials.

Efforts to mimic these self-healing biopolymers by introducing reversible bonds into polymer networks is an active area of research that is currently based on both recombinant biopolymers [144, 145] and traditional polymers presenting metal-binding amino acid side chain moieties [4, 146–149]. In particular, a number of mussel-inspired polymers based on DOPA– and histidine–metal binding have been developed that exhibit self-healing performance as well as other industrially relevant properties such as wet adhesion and actuation [4, 146–150]. Additionally, polymeric hydrogels inspired by the phosphate-based chemistry observed in caddisfly silk have recently been produced, exhibiting similar self-recovery behavior to the natural material [151]. Efforts to mimic these materials via recombinant technology have also shown some success. For example, the rubbery insect protein resilin was recently bio-engineered to contain histidine–metal binding groups that enabled mechanical tunability with metal addition [144]. Proteins from the WEC have also been recombinantly expressed and found to self-organize into coiled-coil α-helical fibrils [145]. Although these early findings are encouraging, these materials are largely still lacking the structural and mechanical complexity of their natural counterparts (e.g., hierarchical structure and organization). Nonetheless, further progress is certainly expected in this very active area of research.

3 Conclusions

Our goal in providing these specific case studies has been, on the one hand, to bring attention to the broad range of mechanisms that living organisms employ to accomplish self-healing behavior and, on the other hand, to address the potential challenges that researchers face in hoping to emulate these behaviors in man-made systems. If the aim is to directly copy natural self-healing behaviors, such as tissue regeneration, in all their complexity, the challenge is significant [152]. However, if the goal is to abstract and integrate into materials specific features and design principles of natural healing mechanisms, such as vascularization or reversible sacrificial bonding, then the literature is already rife with examples of progress in this direction [2–8]. Several examples of successful bio-inspired design based on

latex-based healing of plants (Sect. 2.5), cell-based healing in pipe vines (Sect. 2.6), and reversible sacrificial bonding in extracorporeal biopolymers such as the mussel byssus (Sect. 2.9.4) have been discussed. The concluding remarks of this review are dedicated to highlighting and discussing the most promising design paradigms presented in the specific case studies.

For the purposes of this review, we have provided only a superficial glimpse of cell-initiated healing and regeneration in animals and plants because of the inherent underlying complexities of such processes. Deeper examination of such mechanisms reveals that biomolecular cell–cell interactions, cell–matrix interactions [153, 154], vascularization, and innervation are crucial to the self-healing response. Furthermore, there probably exists a carefully coordinated synergy of local and non-local interactions that gives rise to the memory effects observed during tissue regeneration. Faithfully emulating such a complex network of interactions and sub-processes as present in regeneration and cellular healing, even roughly, seems unlikely in our lifetime.

In spite of these clear challenges, certain concepts and design paradigms observed in cellular healing and regeneration processes (e.g., vascularization, callus (scaffold) formation, remodeling, stimuli responsive growth, and programmed growth) are interesting for technology transfer. For example, as emphasized in the introductory section, the concept of "sealing-and-healing" (Table 1) found in various forms across the plant and animal kingdoms, is already inspiring development of self-healing materials [6, 7, 14, 15]. In examples from nature, biological systems clearly follow a "first things first" approach that is aimed at avoiding further damage and stabilizing the damaged site. In latex-based healing (Sect. 2.5) and cutaneous wound healing (Sect. 2.4), the rapid mobilization of healing agents is a crucial factor in quickly shoring up the damage so that the subsequent healing stage can bring the material back toward the native state. In both cases, this is facilitated through an extensive vascular transport network. Inspired by these and other examples, there are numerous reports in the literature of self-healing composites possessing a vascular network of channels for the transport of chemical reagents [2, 3, 5, 8]. In such systems, healing agents are conveyed to impact sites within the composite through capillaries comprising one-, two-, or three-dimensional networks in the material. Once there, the various healing agents polymerize and seal/heal the damage, resulting in significant recovery of initial material properties.

Once the damaged area is sealed and the general integrity restored, many of the biological examples in the presented case studies exhibit a subsequent, slower self-healing phase to restore the initial properties and function of the damaged site. However, in general, the current generation of bio-inspired vascular composite systems combine both steps, which limits the damage volume that can be healed to microscopic cracks and defects [3, 155]. From this perspective, the examples of antler growth (Sect. 2.2), bone healing (Sect. 2.3), and plant grafting (Sect. 2.8) reveal how the use of relatively quickly synthesized, but mechanically inferior, scaffolds enables the eventual complete healing, regeneration, or fusion of tissues on the macroscopic scale. In this respect, there is at least one example of a

man-made vascular composite capable of healing larger damage volumes that employs a two-stage healing mechanism [155]. In this case, control of the polymerization reaction kinetics of the healing mixture allows highly viscous gel-like behavior at early stages of self-repair that is capable of filling holes of more than 35 mm, while still resulting in a slow polymerization over hours that recovers more than 60% of native material properties.

In addition to healing in response to specific damage events, the process of remodeling and stimuli-responsive healing/growth, as observed in bone, suggests that it is possible to be more proactive in the design of synthetic self-repair mechanisms. For example, the idea of using remodeling to preemptively heal microcracking in a material as a result of fatigue before it can develop into a more serious fracture is highly appealing and perhaps not so far from actualization. One possibility already present in the self-healing literature is the use of dynamic chemical bonds that are able to reorganize under relevant environmental conditions and timescales [156, 157]. Notably, as discussed in Sect. 2.9.4, dynamic reversible bonding in acellular biopolymers (e.g., mussel byssus) perhaps possesses the best possibility of directly transferring design principles from nature to technical and biomedical materials [148]. This stems from the fact that the protein biomolecules comprising these materials are essentially polymeric in nature and are constructed of linear chains of relatively simple amino acid building blocks. Although the concept of reversible bonding has been present in self-healing literature for some time [156, 158], the recent successes of mussel-inspired polymers based on DOPA– and histidine–metal crosslinking suggest that biological systems have something to offer in this regard [4, 148].

Additionally, as we have seen in these highly dynamic examples of biological healing, external physical stimuli can potentially be harnessed to guide healing in a "smart" way. In bone healing, mechanical loading provides information – in terms of the local strain – that dictates what material with which properties should be formed where and when. This has further implications during healing, because new tissue formation results in local stiffening of the tissue. Consequently, an intricate feedback loop between the effect of global mechanical stimulation and local mechanical properties is responsible for the control of bone healing. Inspired by bone healing, recent computer simulations of a generic self-healing material demonstrated that small changes in this local response of the material can grossly change the global healing outcome – the broken ends either reconnected by directly closing the fracture gap or the two segments were first reconnected by a material bridge at the outside of the fracture gap, as observed in bone healing [159]. Although such complex feedback mechanisms are not currently found in any man-made self-healing systems, mechanically responsive crosslinks in polymers (so-called mechanophores) could conceivably provide a pathway for the development of materials that sense mechanical loading in the damaged state and respond by localizing healing and recovery of specific structures [160]. It remains to be seen whether the potential of biological materials research to inspire development of a new generation of bio-inspired self-healing materials will be fully realized; however, current progress seems quite encouraging.

Acknowledgement The authors thank A. Miserez and R. Stewart for providing images for figures, and C. Neinhuis for helpful input. Part of the work on mussel byssal thread healing was funded by the DFG priority program 1568 on "Design and Generic Principles of Self-Healing Materials" (HA6369/1-1 and HA6369/1-2). Financial support from the DFG for research within the Cluster of Excellence: "Image Knowledge Gestaltung: An Interdisciplinary Laboratory" is acknowledged. Several of the projects on self-repair mechanisms in plants were funded by the German Federal Ministry of Education and Research in the frameworks of the funding programme BIONA (project 'Self-healing polymers "OSIRIS"') and of the Ideenwettbewerb "Bionik – Innovationen aus der Natur" (FKZ0313778A, together with Empa Dübendorf). Two other projects on self-repair mechanisms in plants are part of the European Marie Curie Initial Training Network "Self-Healing Materials: from Concepts to Market" (SHeMat).

References

1. Hager MD et al (2010) Self-healing materials. Adv Mater 22(47):5424–5430
2. Bond I et al (2008) Self healing fibre-reinforced polymer composites: an overview. In: Zwaag S (ed) Self healing materials: an alternative approach to 20 centuries of materials science. Springer, Dordrecht, pp 115–138
3. Diesendruck CE et al (2015) Biomimetic self-healing. Angew Chem Int Ed. doi:10.1002/anie.201500484
4. Holten-Andersen N et al (2011) pH-induced metal-ligand cross-links inspired by mussel yield self-healing polymer networks with near-covalent elastic moduli. Proc Natl Acad Sci USA 108(7):2651–2655
5. Norris CJ et al (2011) Self-healing fibre reinforced composites via a bioinspired vasculature. Adv Funct Mater 21(19):3624–3633
6. Rampf M et al (2013) Investigation of a fast mechanical self-repair mechanism for inflatable structures. Int J Eng Sci 63:61–70
7. Schuessele AC et al (2012) Self-healing rubbers based on NBR blends with hyperbranched polyethylenimines. Macromol Mater Eng 297(5):411–419
8. Toohey KS et al (2007) Self-healing materials with microvascular networks. Nat Mater 6 (8):581–585
9. Clark RAF (1988) Overview and general considerations of wound repair. In: Clark RAF, Henson PM (eds) The molecular and cellular biology of wound repair. Springer, New York
10. Fratzl P, Weinkamer R (2007) Hierarchical structure and repair of bone: deformation, remodelling, healing. In: Self healing materials: an alternative approach to 20 centuries of materials science, vol 100. Springer, Dordrecht, pp 323–335
11. Ashton NN, Stewart RJ (2015) Self-recovering caddisfly silk: energy dissipating, Ca2+-dependent, double dynamic network fibers. Soft Matter 11(9):1667–1676
12. Harrington MJ et al (2009) Collagen insulated from tensile damage by domains that unfold reversibly: in situ X-ray investigation of mechanical yield and damage repair in the mussel byssus. J Struct Biol 167(1):47–54
13. Miserez A et al (2009) Non-entropic and reversible long-range deformation of an encapsulating bioelastomer. Nat Mater 8(11):910–916
14. Speck T et al (2013) Bio-inspired self-healing materials. In: Fratzl P, Dunlop JWC, Weinkamer R (eds) Materials design inspired by nature: function through inner architecture. Royal Society of Chemistry, Cambridge, pp 359–389
15. Speck T, Muelhaupt R, Speck O (2013) Self-healing in plants as bio-inspiration for self-repairing polymers. In: Self-healing polymers: from principles to applications. Wiley, Weinheim, pp 61–89
16. Speck O et al (2014) Selbstreparatur in Natur und Technik. Konstruktion 9:72–75

17. Bauer G, Speck T (2012) Restoration of tensile strength in bark samples of *Ficus benjamina* due to coagulation of latex during fast self-healing of fissures. Ann Bot 109(4):807–811
18. Speck O, Speck T (2015) Selbstreparatur in Natur und Technik – Versiegeln, heilen, reparieren. Biologie in unserer Zeit 45:44–51
19. Dunlop JWC, Weinkamer R, Fratzl P (2011) Artful interfaces within biological materials. Mater Today 14(3):70–78
20. Fratzl P, Weinkamer R (2007) Nature's hierarchical materials. Prog Mater Sci 52 (8):1263–1334
21. Gould SJ, Lewontin RC (1979) Spandrels of San Marco and the Panglossian paradigm – a critique of the adaptationist program. Proc R Soc Lond B Biol Sci 205(1161):581–598
22. Alvarado AS (2000) Regeneration in the metazoans: why does it happen? Bioessays 22 (6):578–590
23. Nacu E, Tanaka EM (2011) Limb regeneration: a new development? Annu Rev Cell Dev Biol 27:409–440
24. Brockes JP, Kumar A (2005) Appendage regeneration in adult vertebrates and implications for regenerative medicine. Science 310(5756):1919–1923
25. Brockes JP (1997) Amphibian limb regeneration: rebuilding a complex structure. Science 276(5309):81–87
26. Bryant SV, Endo T, Gardiner DM (2002) Vertebrate limb regeneration and the origin of limb stem cells. Int J Dev Biol 46(7):887–896
27. Butler EG (1955) Regeneration of the urodele forelimb following after reversal of its proximo-distal axis. J Morphol 96(4):265–281
28. French V, Bryant PJ, Bryant SV (1976) Pattern regulation in epimorphic fields. Science 193 (4257):969–981
29. Maden M, Holder N (1984) Axial characteristics of nerve induced supernumerary limbs in the axolotl. Rouxs Arch Dev Biol 193(6):394–401
30. Goss RJ (2012) Deer antlers: regeneration, function and evolution. Academic, New York
31. Kierdorf U, Kierdorf H (2011) Deer antlers - a model of mammalian appendage regeneration: an extensive review. Gerontology 57(1):53–65
32. Price JS et al (2005) Deer antlers: a zoological curiosity or the key to understanding organ regeneration in mammals? J Anat 207(5):603–618
33. Li CY, Suttie JM (2001) Deer antlerogenic periosteum: a piece of postnatally retained embryonic tissue? Anat Embryol 204(5):375–388
34. Li CY, Harris AJ, Suttie JM (2001) Tissue interactions and antlerogenesis: new findings revealed by a xenograft approach. J Exp Zool 290(1):18–30
35. Goss RJ (1995) Future-directions in antler research. Anat Rec 241(3):291–302
36. Li CY, Suttie JM, Clark DE (2005) Histological examination of antler regeneration in red deer (*Cervus elaphus*). Anat Rec A Discov Mol Cell Evol Biol 282A(2):163–174
37. Krauss S et al (2011) Tubular frameworks guiding orderly bone formation in the antler of the red deer (*Cervus elaphus*). J Struct Biol 175(3):457–464
38. Bubenik AB, Pavlansk R (1965) Trophic responses to trauma in growing antlers. J Exp Zool 159(3):289–302
39. Bubenik GA (1990) The role of the nervous system in the growth of antlers. In: Bubenik GA, Bubenik AB (eds) Horns, pronghorns, and antlers. Springer, New York, pp 339–358
40. Lobo D, Solano M, Bubenik GA, Levin M (2014) A linear-encoding model explains the variability of the target morphology in regeneration. J R Soc Interface 11(92):20130918. doi:10.1098/rsif.2013.0918
41. Currey JD et al (2009) The mechanical properties of red deer antler bone when used in fighting. J Exp Biol 212(24):3985–3993
42. Launey ME et al (2010) Mechanistic aspects of the fracture toughness of elk antler bone. Acta Biomater 6(4):1505–1514

43. Gupta HS et al (2013) Intrafibrillar plasticity through mineral/collagen sliding is the dominant mechanism for the extreme toughness of antler bone. J Mech Behav Biomed Mater 28:366–382
44. Sfeir C et al (2005) Fracture repair. In: Bone regeneration and repair. Humana Press, Totowa, New Jersey, pp 21–44
45. Betts DC, Muller R (2014) Mechanical regulation of bone regeneration: theories, models, and experiments. Front Endocrinol (Lausanne) 5:211
46. Vetter A et al (2012) The spatio-temporal arrangement of different tissues during bone healing as a result of simple mechanobiological rules. Biomech Model Mechanobiol 11 (1–2):147–160
47. Gerstenfeld LC et al (2003) Fracture healing as a post-natal developmental process: molecular, spatial, and temporal aspects of its regulation. J Cell Biochem 88(5):873–884
48. Liu Y et al (2010) Size and habit of mineral particles in bone and mineralized callus during bone healing in sheep. J Bone Miner Res 25(9):2029–2038
49. Huiskes R et al (2000) Effects of mechanical forces on maintenance and adaptation of form in trabecular bone. Nature 405(6787):704–706
50. Ruimerman R et al (2005) A theoretical framework for strain-related trabecular bone maintenance and adaptation. J Biomech 38(4):931–941
51. Dunlop JWC et al (2009) New suggestions for the mechanical control of bone remodeling. Calcif Tissue Int 85(1):45–54
52. Schulte FA et al (2013) Local mechanical stimuli regulate bone formation and resorption in mice at the tissue level. PLoS One 8(4):e62172
53. Razi H et al (2015) Aging leads to a dysregulation in mechanically driven bone formation and resorption. J Bone Miner Res. doi:10.1002/jbmr.2528
54. Bonewald LF (2011) The amazing osteocyte. J Bone Miner Res 26(2):229–238
55. Evans RK et al (2008) Effects of a 4-month recruit training program on markers of bone metabolism. Med Sci Sports Exerc 40(11):S660–S670
56. Fantner GE et al (2005) Sacrificial bonds and hidden length dissipate energy as mineralized fibrils separate during bone fracture. Nat Mater 4(8):612–616
57. Gupta HS et al (2007) Evidence for an elementary process in bone plasticity with an activation enthalpy of 1 eV. J R Soc Interface 4(13):277–282
58. Martin P (1997) Wound healing--aiming for perfect skin regeneration. Science 276 (5309):75–81
59. Singer AJ, Clark RA (1999) Cutaneous wound healing. N Engl J Med 341(10):738–746
60. Murawala P, Tanaka EM, Currie JD (2012) Regeneration: the ultimate example of wound healing. Semin Cell Dev Biol 23(9):954–962
61. Gurtner GC et al (2008) Wound repair and regeneration. Nature 453(7193):314–321
62. Aarabi S, Longaker MT, Gurtner GC (2007) Hypertrophic scar formation following burns and trauma: new approaches to treatment. PLoS Med 4(9), e234
63. Harty M et al (2003) Regeneration or scarring: an immunologic perspective. Dev Dyn 226 (2):268–279
64. Larson BJ, Longaker MT, Lorenz HP (2010) Scarless fetal wound healing: a basic science review. Plast Reconstr Surg 126(4):1172–1180
65. Clark LD, Clark RK, Heber-Katz E (1998) A new murine model for mammalian wound repair and regeneration. Clin Immunol Immunopathol 88(1):35–45
66. Birnbaum KD, Alvarado AS (2008) Slicing across kingdoms: regeneration in plants and animals. Cell 132(4):697–710
67. Lewinsohn TM (1991) The geographical distribution of plant latex. Chemoecology 2:64–68
68. Metcalfe CR (1967) Distribution of latex in plant kingdom. Econ Bot 21(2):115–127
69. Agrawal AA, Konno K (2009) Latex: a model for understanding mechanisms, ecology, and evolution of plant defense against herbivory. Annu Rev Ecol Evol Syst 40:311–331
70. Hunter JR (1994) Reconsidering the functions of latex. Trees Struct Funct 9(1):1–5

71. Bauer G et al (2014) Comparative study on plant latex particles and latex coagulation in *Ficus benjamina*, *Campanula glomerata* and three Euphorbia species. PLoS One 9(11):e113336
72. Bauer G, Nellesen A, Speck T (2010) Biological lattices in fast self-repair mechanisms in plants and the development of bio-inspired self-healing polymers. In: Brebbia C, Carpi A (eds) Design and nature V: comparing design in nature with science and engineering. WIT, Southampton, pp 453–459
73. Bauer G, Freidrich C, Gillig C, Vollrath F, Speck T, Holland C (2014) Investigating the rheological properties of native plant latex. J R Soc Interface 11(90):20130847. doi:10.1098/rsif.2013.0847
74. D'Auzac J, Prevot JC, Jacob JL (1995) What's new about lutoids – a vacuolar system model from *Hevea* latex. Plant Physiol Biochem 33(6):765–777
75. Gidrol X et al (1994) Hevein, a lectin-like protein from *Hevea brasiliensis* (rubber tree) is involved in the coagulation of latex. J Biol Chem 269(12):9278–9283
76. Wititsuwannakul R et al (2008) *Hevea* latex lectin binding protein in C-serum as an anti-latex coagulating factor and its role in a proposed new model for latex coagulation. Phytochemistry 69(3):656–662
77. Nellesen A et al (2011) Self-healing in plants as a model for self-repairing elastomer materials. Int Polym Sci Technol 38:T/1–T/4
78. Binder W (2013) Self-healing polymers. Wiley, Weinheim
79. Jin H et al (2013) Self-healing epoxies and their composites. In: Self-healing polymers: from principles to applications. Wiley, Weinheim, pp 361–380
80. Rowe NP et al (2006) Diversity of mechanical architectures in climbing plants: an ecological perspective. In: Herrel A, Speck T, Rowe NP (eds) Ecology and biomechanics: a mechanical approach to the ecology of animals and plants. CRC, Boca Raton, pp 35–59
81. Rowe NP, Speck T (2004) Hydraulics and mechanics of plants: novelty, innovation and evolution. In: Hemsley AR, Poole I (eds) The evolution of plant physiology. Academic, London, pp 301–329
82. Rowe NP, Speck T (2015) Stem biomechanics, strength of attachment, and developmental plasticity of vines and lianas. In: Schnitzer S et al (eds) The ecology of lianas. Wiley-Blackwell, Chichester, pp 323–341
83. Busch S et al (2010) Morphological aspects of self-repair of lesions caused by internal growth stresses in stems of *Aristolochia macrophylla* and *Aristolochia ringens*. Proc R Soc B Biol Sci 277(1691):2113–2120
84. Speck T et al (2004) The potential of plant biomechanics in functional biology and systematics. In: Stuessey T, Hörandl F, Mayer V (eds) Deep morphology: toward a renaissance of morphology in plant systematics. Koeltz, Königstein, pp 241–271
85. Luchsinger RH, Pedretti M, Reinhard A (2004) Pressure induced stability: from pneumatic structures to Tensairity. J Bionic Eng 1:141–148
86. Speck T et al (2006) Self-healing processes in nature and engineering: self-repairing biomimetic membranes for pneumatic structures. In: Brebbia CA (ed) Design and nature III: comparing design in nature with science and engineering. WIT, Southampton, pp 105–114
87. Rampf M et al (2011) Self-repairing membranes for inflatable structures inspired by a rapid wound sealing process of climbing plants. J Bionic Eng 8(3):242–250
88. Rampf M et al (2012) Structural and mechanical properties of flexible polyurethane foams cured under pressure. J Cell Plast 48(1):53–69
89. Konrad W et al (2013) An analytic model of the self-sealing mechanism of the succulent plant *Delosperma cooperi*. J Theor Biol 336:96–109
90. Caliaro M et al (2013) Novel method for measuring tissue pressure in herbaceous plants. Int J Plant Sci 174(2):161–170
91. Beddie AD (1941) Natural root grafts in New Zealand trees. Trans R Soc New Zealand 71 (3):199–203
92. Dallimore W (1917) Natural grafting of branches and roots. Bull Misc Inf (Royal Botanical Gardens Kew) 1917:303–306

93. Küster E (1899) Über Stammverwachsungen. Jahrbücher für Wissenschaftliche Botanik 33:487–512
94. Millner ME (1932) Natural grafting in *Hedera helix*. New Phytol 31(1):2–25
95. Seidel CF (1879) Über Verwachsungen von Stämmen und Zweigen von Holzgewächsen und ihren Einfluss auf das Dickenwachsthum der betreffenden Theile. Isis Sitzber, Dresden, pp 161–168
96. Hartmann HT et al (2002) Hartmann and Kesters's plant propagation: principles and practices. Prentice-Hall, New Jersey
97. Yeoman MM, Brown R (1976) Implication of formation of graft union for organization in intact plant. Ann Bot 40(170):1265–1276
98. Graham BF, Bormann FH (1966) Natural root grafts. Bot Rev 32(3):255–292
99. La Rue CD (1934) Root grafting in trees. Am J Bot 21(3):121–126
100. Mudge K et al (2009) A history of grafting. Hortic Rev 35:437–493
101. Moore R (1982) Graft formation in *Kalanchoe blossfeldiana*. J Exp Bot 33(134):533–540
102. Moore R (1983) Studies of vegetative compatibility-incompatibility in higher plants. IV. The development of tensile strength in a compatible and an incompatible graft. Am J Bot 70 (2):226–231
103. Moore R (1984) Graft formation in *Solanum pennellii* (Solanaceae). Plant Cell Rep 3 (5):172–175
104. Moore R, Walker DB (1983) Studies of vegetative compatibility-incompatibility in higher plants. VI. Grafting of Sedum and Solanum callus tissue in vitro. Protoplasma 115 (2–3):114–121
105. Pedersen BH (2005) Development of tensile strength in compatible and incompatible sweet cherry graftings. Can J Bot 83(2):202–210
106. Pina A, Errea P (2005) A review of new advances in mechanism of graft compatibility-incompatibility. Sci Hortic 106(1):1–11
107. Yin H et al (2012) Graft-union development: a delicate process that involves cell-cell communication between scion and stock for local auxin accumulation. J Exp Bot 63 (11):4219–4232
108. Esau K, Evert RF, Eichhorn SE (2006) Esau's plant anatomy: meristems, cells, and tissues of the plant body: their structure, function, and development. Wiley, Hoboken
109. Larson PR (1994) The vascular cambium: development and structure. Springer, Berlin
110. Dormling I (1963) Anatomical and histological examination of the union of scion and stock in grafts of scots pine (*Pinus silvestris* L.) and Norway spruce (*Picea abies* (L.) Karit). Stud For Suec 13:1–136
111. McCulley ME (1983) In: Moore R (ed) Vegetative compatibility responses in plants. Baylor University Press, Waco, pp 71–88
112. Moore R (1983) In: Moore R (ed) Vegetative compatibility responses in plants. Baylor University Press, Waco, pp 89–105
113. Pina A, Errea P, Martens HJ (2012) Graft union formation and cell-to-cell communication via plasmodesmata in compatible and incompatible stem unions of *Prunus* spp. Sci Hortic 143:144–150
114. Aloni B et al (2010) Hormonal signaling in rootstock-scion interactions. Sci Hortic 127 (2):119–126
115. Aloni R (1987) Differentiation of vascular tissues. Annu Rev Plant Physiol Plant Mol Biol 38:179–204
116. Mattsson J, Ckurshumova W, Berleth T (2003) Auxin signaling in Arabidopsis leaf vascular development. Plant Physiol 131(3):1327–1339
117. Fuentes I et al (2014) Horizontal genome transfer as an asexual path to the formation of new species. Nature 511(7508):232–235
118. Molnar A et al (2010) Small silencing RNAs in plants are mobile and direct epigenetic modification in recipient cells. Science 328(5980):872–875

119. Stegemann S, Bock R (2009) Exchange of genetic material between cells in plant tissue grafts. Science 324(5927):649–651
120. Stegemann S et al (2012) Horizontal transfer of chloroplast genomes between plant species. Proc Natl Acad Sci USA 109(7):2434–2438
121. Denny MW, Gaylord B (2010) Marine ecomechanics. Ann Rev Mar Sci 2(1):89–114
122. Carrington E, Gosline JM (2004) Mechanical design of mussel byssus: load cycle and strain rate dependence. Am Malacol Bull 18(1/2):135–142
123. Waite JH, Qin X-X, Coyne KJ (1998) The peculiar collagens of mussel byssus. Matrix Biol 17(2):93–106
124. Krauss S et al (2013) Self-repair of a biological fiber guided by an ordered elastic framework. Biomacromolecules 14(5):1520–1528
125. Arnold AA et al (2013) Solid-state NMR structure determination of whole anchoring threads from the blue mussel *Mytilus edulis*. Biomacromolecules 14(1):132–141
126. Hagenau A et al (2011) Mussel collagen molecules with silk-like domains as load-bearing elements in distal byssal threads. J Struct Biol 175(3):339–347
127. Schmidt S et al (2014) Metal-mediated molecular self-healing in histidine-rich mussel peptides. Biomacromolecules 15(5):1644–1652
128. Schmitt CNZ, Politi Y, Reinecke A, Harrington MJ (2015) The role of sacrificial protein-metal bond exchange in mussel byssal thread self-healing. Biomacromolecules 16 (9):2852–2861. doi:10.1021/acs.biomac.5b00803
129. Harrington MJ, Waite JH (2007) Holdfast heroics: comparing the molecular and mechanical properties of *Mytilus californianus* byssal threads. J Exp Biol 210(24):4307–4318
130. Vaccaro E, Waite JH (2001) Yield and post-yield behavior of mussel byssal thread: a self-healing biomolecular material. Biomacromolecules 2(3):906–911
131. Harrington MJ et al (2010) Iron-clad fibers: a metal-based biological strategy for hard flexible coatings. Science 328(5975):216–220
132. Schmitt CNZ, Winter A, Bertinetti L, Masic A, Strauch P, Harrington MJ (2015) Mechanical homeostasis of a DOPA-enriched biological coating from mussels in response to metal variation. J R Soc Interface 12(110):20150466. doi:10.1098/rsif.2015.0466
133. Taylor SW et al (1996) Ferric ion complexes of a DOPA-containing adhesive protein from *Mytilus edulis*. Inorg Chem 35(26):7572–7577
134. Holten-Andersen N et al (2007) Protective coatings on extensible biofibres. Nat Mater 6 (9):669–672
135. Ashton NN et al (2013) Self-tensioning aquatic caddisfly silk: Ca2+-dependent structure, strength, and load cycle hysteresis. Biomacromolecules 14(10):3668–3681
136. Yonemura N et al (2009) Conservation of silk genes in Trichoptera and Lepidoptera. J Mol Evol 68(6):641–653
137. Wang C-S et al (2014) Peroxinectin catalyzed dityrosine crosslinking in the adhesive underwater silk of a casemaker caddisfly larvae, Hysperophylax occidentalis. Insect Biochem Mol Biol 54:69–79
138. Addison JB et al (2013) Beta-sheet nanocrystalline domains formed from phosphorylated serine-rich motifs in caddisfly larval silk: a solid state NMR and XRD study. Biomacromolecules 14(4):1140–1148
139. Addison JB et al (2014) Reversible assembly of beta-sheet nanocrystals within caddisfly silk. Biomacromolecules 15(4):1269–1275
140. Rapoport HS, Shadwick RE (2002) Mechanical characterization of an unusual elastic biomaterial from the egg capsules of marine snails (*Busycon* spp.). Biomacromolecules 3 (1):42–50
141. Harrington MJ et al (2012) Pseudoelastic behaviour of a natural material is achieved via reversible changes in protein backbone conformation. J R Soc Interface 9(76):2911–2922
142. Wasko SS et al (2014) Structural proteins from whelk egg capsule with long range elasticity associated with a solid-state phase transition. Biomacromolecules 15(1):30–42

143. Fischer FD, Harrington MJ, Fratzl P (2013) Thermodynamic modeling of a phase transformation in protein filaments with mechanical function. New J Phys 15(6):065004
144. Degtyar E et al (2015) Recombinant engineering of reversible cross-links into a resilient biopolymer. Polymer 69:255–263
145. Fu T et al (2015) Biomimetic self-assembly of recombinant marine snail egg capsule proteins into structural coiled-coil units. J Mater Chem B 3(13):2671–2684
146. Fullenkamp DE et al (2013) Mussel-inspired histidine-based transient network metal coordination hydrogels. Macromolecules 46(3):1167–1174
147. Krogsgaard M et al (2013) Self-healing mussel-inspired multi-pH-responsive hydrogels. Biomacromolecules 14(2):297–301
148. Li L, Smitthipong W, Zeng H (2015) Mussel-inspired hydrogels for biomedical and environmental applications. Polym Chem 6(3):353–358
149. Enke M et al (2015) Self-healing response in supramolecular polymers based on reversible zinc–histidine interactions. Polymer 69:274–282
150. Lee BP, Konst S (2014) Novel hydrogel actuator inspired by reversible mussel adhesive protein chemistry. Adv Mater 26(21):3415–3419
151. Lane DD et al (2015) Toughened hydrogels inspired by aquatic caddisworm silk. Soft Matter. doi:10.1039/C5SM01297J
152. van der Zwaag S et al (2009) Self-healing behaviour in man-made engineering materials: bioinspired but taking into account their intrinsic character. Philos Trans R Soc A Math Phys Eng Sci 367(1894):1689–1704
153. Discher DE, Janmey P, Wang YL (2005) Tissue cells feel and respond to the stiffness of their substrate. Science 310(5751):1139–1143
154. Kollmannsberger P et al (2011) The physics of tissue patterning and extracellular matrix organisation: how cells join forces. Soft Matter 7(20):9549–9560
155. White SR et al (2014) Restoration of large damage volumes in polymers. Science 344 (6184):620–623
156. Wojtecki RJ, Meador MA, Rowan SJ (2011) Using the dynamic bond to access macroscopically responsive structurally dynamic polymers. Nat Mater 10(1):14–27
157. Ying H, Zhang Y, Cheng J (2014) Dynamic urea bond for the design of reversible and self-healing polymers. Nat Commun 5:3218. doi: 10.1038/ncomms4218
158. Cordier P et al (2008) Self-healing and thermoreversible rubber from supramolecular assembly. Nature 451(7181):977–980
159. Vetter A et al (2013) Healing of a mechano-responsive material. Europhys Lett 104(6):68005
160. Brown CL, Craig SL (2015) Molecular engineering of mechanophore activity for stress-responsive polymeric materials. Chem Sci 6(4):2158–2165

Adv Polym Sci (2016) 273: 345–386
DOI: 10.1007/12_2015_332

Published online: 2 February 2016

Bio-Based Self-Healing Concrete: From Research to Field Application

Eirini Tziviloglou, Kim Van Tittelboom, Damian Palin, Jianyun Wang, M. Guadalupe Sierra-Beltrán, Yusuf Çagatay Erşan, Renée Mors, Virginie Wiktor, Henk M. Jonkers, Erik Schlangen, and Nele De Belie

Abstract Cracks are intrinsic concrete characteristics. However, cracking can endanger the durability of a structure, because it eases the ingress of aggressive gasses and liquids. Traditional practices tackle the problem by applying manual repair. Scientists inspired by nature have created self-healing concrete able to self-repair as a result of the metabolic activity of bacteria. Various research groups have studied bio-based self-healing concepts over the last decade. Although the metabolic pathways of different bacteria can vary, the principle is essentially the same: a bio-based healing agent is incorporated into fresh concrete and when a crack appears in hardened concrete the bacteria become active, precipitate limestone and seal the open crack. Bio-based self-healing concrete technology targets the recovery of the original performance of concrete by regaining water tightness lost by cracking. Along these lines, bio-based repair systems have also been developed to protect existing structures by applying materials that are more concrete-compatible and environmentally friendly than existing repair materials. All these innovative concepts have shown promising results in laboratory-scale tests. Steps have been taken towards the first full-scale outdoor applications, which will prove the functionality of this new technology.

Keywords Bacteria · Calcium carbonate precipitation · Concrete · Crack sealing · Repair systems

E. Tziviloglou, D. Palin, M.G. Sierra-Beltrán, R. Mors, V. Wiktor, H.M. Jonkers (✉), and E. Schlangen
Delft University of Technology, Delft, The Netherlands
e-mail: h.m.jonkers@tudelft.nl

K. Van Tittelboom, J. Wang, Y.Ç. Erşan, and N. De Belie
Ghent University, Ghent, Belgium

Contents

1 Introduction

In the past decade, several research groups worldwide have addressed the durability-related problem of micro-crack formation in traditional concrete by developing bacteria-based self-healing concrete and repair systems [1]. Early age crack formation in concrete is known to occur as a result of temperature effects and shrinkage of the setting concrete, as well as loading of steel-reinforced structures. Although micro-crack formation does not pose an immediate threat to the strength and integrity of the structure, it does typically lead to problems with water tightness and durability, particularly in wet or moist environments. Networks of micro-cracks can expose the embedded reinforcement to the outside environment with, as a consequence, premature corrosion that necessitates costly manual maintenance and repair actions.

Limestone and other types of mineral formation in concrete can be beneficial and durable, as these are concrete-compatible materials. Filling up (i.e. sealing) of cracks makes concrete water tight and at the same time protects the embedded steel reinforcement from detrimental compounds such as chlorides and other corrosion-stimulating ions that otherwise migrate rapidly through micro-cracks. One of the main targets of applying bacteria that stimulate limestone deposition is, therefore, the recovery of decreasing functional concrete properties such as water tightness and strength. Self-healing of concrete therefore relates to the regain of a certain functional property, which could be water tightness, strength, porosity or aesthetics. In order to enhance the natural, or autogenous, healing capacity of concrete, a specific ‘self-healing agent’ in the form of encapsulated bacteria and required mineral precursor compounds or chemicals is added to the concrete mixture. This enhanced ‘autonomous’ healing should not only reduce manual maintenance and repair costs but also extend the service lifetime of constructions.

Several specific species of bacteria are known to precipitate calcium carbonate and other inorganic minerals in the direct vicinity of the cells. This process, however, is strongly dependent on environmental conditions. It can therefore be stated that bacteria, by employing specific metabolic pathways, change environmental conditions in such a way that precipitation of inorganic minerals is

increased. The designation of 'limestone-producing bacteria' in relation to a functional trait is strictly speaking incorrect, because metabolically driven limestone precipitation by bacteria is always a result of a specific combination of metabolic pathway, activity and physico-chemical environmental conditions. A specific bacterium can thus be 'limestone-producing' in one environment but not in another.

The potential application of limestone deposition enhanced by bacteria for improving durability aspects of concrete has been investigated using specific types of bacteria employing different metabolic pathways. A common characteristic of the various bacterial metabolic pathways is that they result in supersaturation of calcium carbonate in solution, resulting in precipitation of calcium carbonate. Although bacteria usually only change environmental calcium ion concentration to a minor extent, several metabolic pathways strongly affect the environmental concentration of carbonate ions and thereby the saturation state of calcium carbonate in solution. Typical bacterial metabolic pathways that increase the carbonate ion concentration and related calcium carbonate saturation in solution are the hydrolysis of urea, oxidation of organic compounds using oxygen under aerobic conditions and oxidation of organic compounds using nitrate under anaerobic conditions. This chapter describes these bacterial metabolic routes and their applicability for enhancing the autogenous self-healing capacity of concrete.

2 Autogenous Healing

Concrete has a natural or autogenous ability to seal micro-cracks, regain water tightness and greatly reduce chemically driven degradation phenomena. Autogenous healing upon contact with water is primarily attributed to three processes: swelling of the cement matrix, hydration of unhydrated cement particles and precipitation of calcium carbonate [2, 3].

The most significant of these is the precipitation of calcium carbonate ($CaCO_3$), which is formed as a result of carbon dioxide (CO_2) reacting with calcium hydroxide [$Ca(OH)_2$] according to Eq. (1):

$$CO_2 + Ca(OH)_2 \rightarrow CaCO_3 + H_2O \quad (1)$$

Occurrence of precipitation depends on the solubility product of calcium carbonate, which in turn depends on the temperature, ionic strength, composition, pH and carbon dioxide partial pressure of water in the crack [2]. Primarily, the amount of precipitate and, hence, crack healing potential depends on the amount of calcium and carbonate ions available in the cracks.

The autogenous healing ability of concrete was first reported by the French Academy of Science in 1836 [8]. Numerous studies have followed since then [e.g. 2, 4–6]; however, studies quantifying this ability are still relatively few [2, 5, 7–9]. Of the techniques employed to quantify the autogenous healing capacity of cementitious materials, water permeability has received the most attention. Clear [8] was the first to quantify the autogenous healing ability of cementitious materials

through permeability measurements, demonstrating how cracks narrower than 200 μm healed even under continuous water flow. Edvardsen [2] in a later study examined the autogenous healing ability of cracked concrete specimens in freshwater through visual observation and permeability measurements. She found that approximately 50% of the specimens with crack widths of 0.2 mm (mean value) healed completely during 7 weeks of exposure. She also noted that the highest healing rate occurred within the first 3–5 days after submersion. Reinhardt and Jooss [5] investigated the relationship between the initial crack width, temperature and autogenous healing potential. They revealed that the flow rate for specimens with cracks of 50 μm wide incubated at 20°C, 50°C or 80°C was almost reduced to zero after 14 days, whereas for cracks 100 μm wide at 20°C it was ~5%, and for those of 150 μm it was ~15% of the initial flow. Van Tittelboom et al. [9] investigated the influence of blast furnace slag (BFS) and fly ash (FA) binders on the autogenous healing capacity of continuously submerged cementitious specimens. They showed that the series containing these binders had 3–400 times greater flow reduction than those containing only Portland clinker. This was attributed to the latent hydraulic properties of these binders, which caused a lower reaction rate and thus a higher availability of unhydrated material for further hydration (Fig. 1). When, however, series containing these binders were exposed to wet–dry cycles, where carbonation-driven carbonate precipitation was expected to be the main contributor to healing, the series with BFS and FA binders healed visually less than ordinary Portland cement (OPC) specimens. The latter phenomenon was attributed to calcium hydroxide consumption by the binders, resulting in less carbonation-driven calcium carbonate precipitation as a result of calcium hydroxide limitation.

In a recent study, Palin et al. [7] visually quantified the autogenous healing ability of cracked OPC (CEM I) and BFS cement (CEM III/B) specimens submerged in fresh water and seawater. After 56 days, BFS cement specimens in

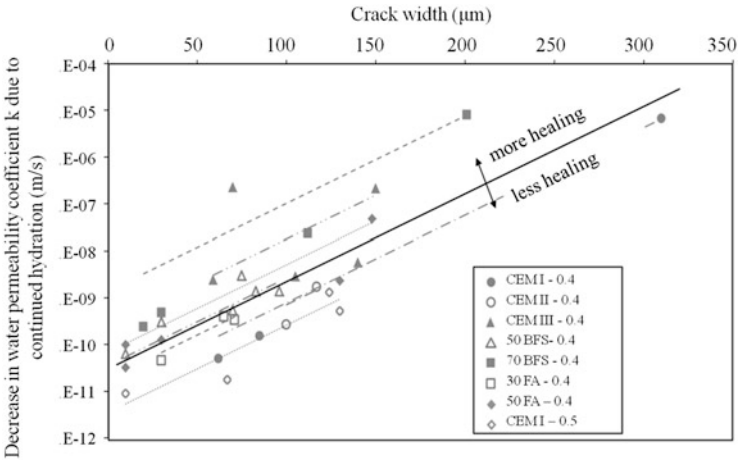

Fig. 1 Difference in water permeability as a result of autogenous crack healing for different mixes [9]. Codes *30*, *50* and *70* in the legend refer to the percentage of BFS or FA in the binder; *0.4* and *0.5* refer to the water/cement ratio of the specimens

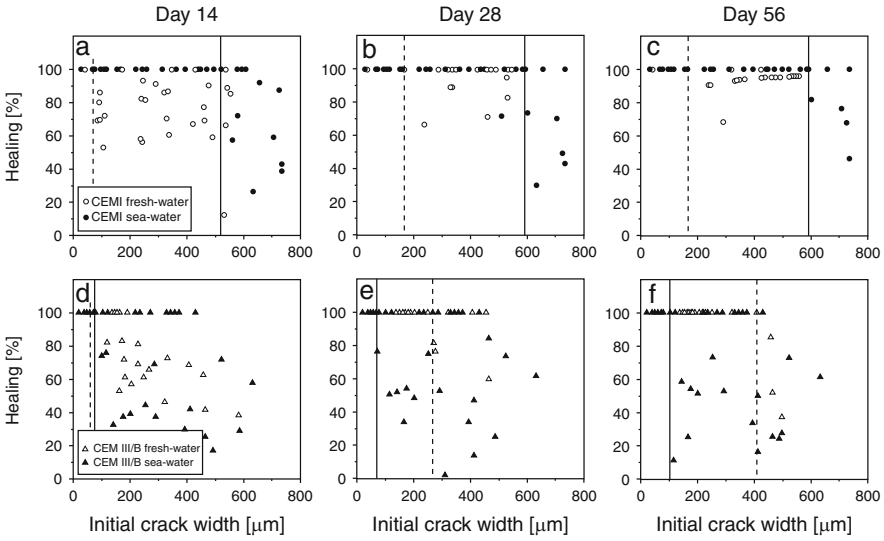

Fig. 2 Crack healing percentage as a function of the initial crack width for (**a**–**c**) CEM I-based specimens in fresh water and seawater and (**d**–**f**) CEM III/B in fresh water and seawater after (**a**, **d**) 14, (**b**, **e**) 28 and (**c**, **f**) 56 days submersion. *Unbroken* and *broken vertical lines* mark 100% visual crack closure (up to the largest crack width) for specimens submerged in seawater and fresh water, respectively [7]

seawater healed 100% of cracks up to 100 μm width, whereas for OPC specimens healing was 100% for cracks up to 600 μm. In fresh water, blast furnace slag cement specimens healed 100% of cracks up to 400 μm, whereas OPC specimens healed 100% of cracks up to 170 μm (Fig. 2). However, although OPC specimens submerged in seawater displayed the greatest autogenous healing capacity, they also developed an unacceptable loss in compressive strength. Observed differences in healing and strength loss phenomena were attributed to higher amounts of calcium hydroxide present in OPC mortars and the presence of magnesium ions in seawater, respectively. Seawater contains high concentrations of calcium and magnesium ions, which at high pH precipitate to yield hydroxide- and carbonate-based minerals, giving seawater-submerged specimens a greater healing potential. However, exchange of calcium ions for magnesium ions results in formation of magnesium-silicate hydrates, which are substantially weaker than calcium-silicate hydrates, explaining the loss of strength of seawater-incubated OPC specimens.

3 Autonomous Healing

The main healing product in bacteria-based self-healing concrete is biogenic $CaCO_3$. Under suitable conditions, most bacteria can mediate the formation of $CaCO_3$. This part reviews bacteria-based self-healing systems that have been or

are being investigated by research groups at Ghent University and Delft University of Technology.

3.1 Enzymatic Hydrolysis of Urea

3.1.1 Laboratory Work

Enzymatic hydrolysis of urea is a process that results in formation of carbonate ions, and thus increases the potential for calcium carbonate precipitation.

The biogenic, urease-driven, reaction rate of urea hydrolysis is approximately 1,014 times faster than the chemical (non-urease driven) rate [10]. Equation 2 shows the overall reaction of enzymatic urea hydrolysis:

$$CO(NH_2)_2 + 2H_2O \rightleftarrows 2NH_4^+ + CO_3^{2-} \quad (2)$$

The amount of calcium carbonate formed by the reaction of available calcium ions with produced carbonate ions is directly dependent on the amount of urea decomposed during urea hydrolysis. Urease-active bacteria can be used to increase autogenous healing rates of concrete as a result of the potentially enhanced rate of calcium carbonate formation. To obtain truly autonomous healing of concrete, both bacteria and nutrients required for bacteria-driven calcium carbonate formation should be introduced to the concrete mixture. Therefore, spore-forming bacteria instead of vegetative cells are selected, because only the former can survive direct incorporation into the concrete matrix. Spores can stay dormant inside concrete and become activated when concrete cracks if water, oxygen and nutrients are present, and other environmental conditions such as temperature and pH are at values compatible with their metabolic capacity. Wang and colleagues of Ghent University used *Bacillus sphaericus*, an alkali-resistant spore-forming ureolytic strain initially applied for consolidation of building materials [11].

Ghent University studies revealed that the concentration of bacteria should be higher than 10^6 cells/mL to obtain a considerable amount of calcium carbonate precipitation. Apart from bacterial numbers, the concentrations of urea and calcium ions (Ca^{2+}) also greatly influence the yield of $CaCO_3$ precipitation. Theoretically, ureolytic bacteria can continue to hydrolyse urea as long as the urease enzyme remains active. Recommended concentrations of both urea and calcium source are 0.5 M [12]. Wang and colleagues also found that yeast extract ($\geq$2 g/L) is an essential nutrient as it stimulates germination of spores, a requirement for urease-driven formation of calcium carbonate. Because working with pure cultures is relatively expensive, a more economical way of producing ureolytic bacterial suspensions was developed at Ghent University. A new selective process named CERUP (cyclic enriched ureolytic powder) was developed to obtain a ureolytic microbial community [13]. It was estimated that the production cost of CERUP was about 40 times less than that of pure cultures [14].

Encapsulation of bacteria is considered of crucial importance in a bacteria-based self-healing system as mechanical forces during concrete mixing can damage the bacterial spores. Sorption of bacterial cells onto diatomaceous earth (DE) provides a protective effect for bacteria in high pH cement slurry [15]. Furthermore, DE has no negative effect on the mechanical properties of mortar and may even show pozzolanic activity. The concept of impermeable microcapsules containing bacterial spores has been patented [16]. The capsules change properties from humid to dry state, allowing them to withstand forces during concrete mixing, but break when cracking occurs [17]. Another idea for encapsulation is to use hydrogels as carrier. Hydrogels act not only as protective carrier for bacterial spores during mixing and hydration, but also as water reservoir for spore germination and bacterial activity when cracking occurs. In normal humidity conditions, hydrogels can absorb moisture and retain it for bacterial use, which is beneficial for realistic self-healing. Wang et al. [18] observed substantial and fast crack closure: a crack of 0.5 mm was completely closed within 1–2 weeks (Fig. 3). However, a drastic loss in strength (as much as 50%) occurred after addition of bio-hydrogels, which indicated incompatibility between the hydrogels and concrete matrix. More compatible hydrogels have now been developed [19], as well as modified alginate- based hydrogels [20].

Besides bacteria, the nutrients and deposition agents (urea and calcium source) are also essential elements for biogenic precipitation and should also be

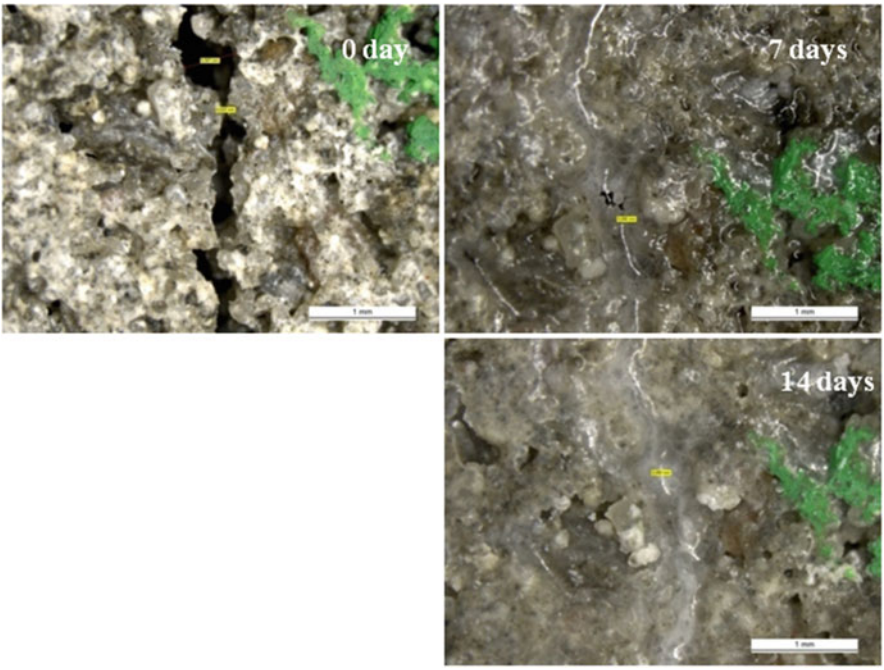

Fig. 3 Crack closure process in specimen with hydrogel-encapsulated *Bacillus sphaericus* spores (the initial widest part is 507 μm) [18]

incorporated into concrete in advance. The latter compounds, however, do not necessarily need to be encapsulated and therefore can be added directly to the concrete mixture. In subsequent studies it was found that, although urea and calcium source have no negative effect on concrete strength development, yeast extract and other organic compounds do. Encapsulation of yeast extract should therefore be considered in future studies.

In most studies, evaluation of self-healing efficiency was based on crack sealing and a decrease in water permeability. Realistic cracks in test specimens were made by three-point bending, splitting or tensile loading. The sealing of a crack can increase water tightness of the structure and possibly prevent corrosive substances from penetrating into the matrix.

Wang et al. [18] observed substantial and fast crack closure; for example, a crack of 0.5 mm was completely closed within 1–2 weeks (Fig. 3).

In addition to light microscopy, which only provides information on the surface part of the crack, X-ray computed micro-tomography (X-ray μCT) has proved to be useful in providing a three-dimensional (3D) deep view inside the crack to quantitatively establish the amount and distribution of internal precipitates. Figure 4

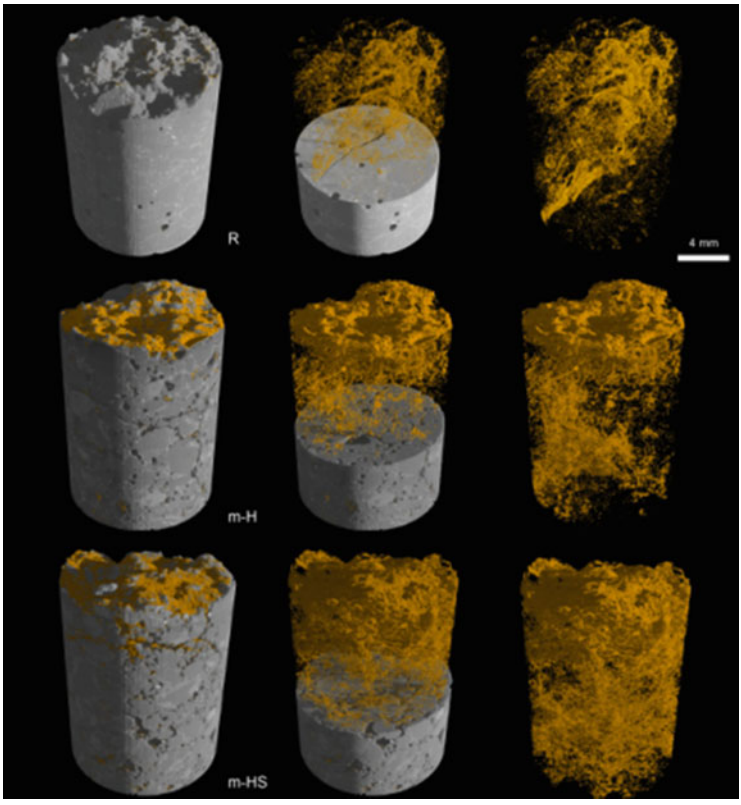

Fig. 4 3D view of the spatial distribution of healing products (in *yellow*) in reference specimens (*R*), in specimens with pure hydrogel (*m-H*) and in specimens with bacteria-loaded hydrogel (*m-HS*) [21]

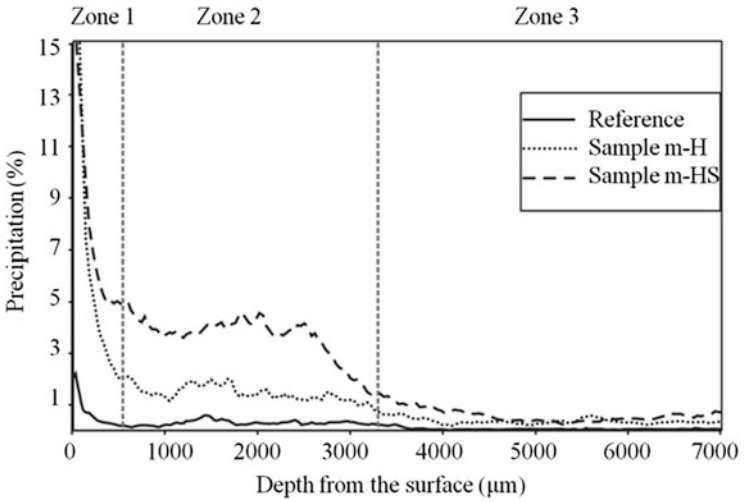

Fig. 5 Quantification of precipitation as a function of depth of the specimen. Three different zones were distinguished: surface, subsurface and internal [21]

shows a 3D view of the healing products inside reference (R) specimens and specimens with (m-HS) and without (m-H) hydrogel-encapsulated bacteria. Precipitates appeared mostly distributed in the surface layer, but not in the deeper part of the crack in the specimens containing bacteria-hydrogels. For the R specimen, the small amount of precipitate was attributed to autogenous healing. A higher amounts of precipitation was found in the specimen containing hydrogel. The amount of precipitate as a function of the depth inside the specimen was calculated and is shown in Fig. 5. For all specimens, the volume ratio of the precipitation was much higher in the surface layer (zone 1) than in the deeper zones 2 and 3. The m-HS and m-H specimens exhibited similar amounts of precipitate in the surface layer, around 8% (volume ratio). However, the former showed more precipitation in the subsurface layer than the latter (about 3% versus 1%), generated from the bacterial activity.

3.1.2 Upscale Application

Most of the laboratory-scale research was performed on small cylinders ($h = 20$ mm; $d = 80$ mm) or prisms ($40 \times 40 \times 160$ mm^3 or $30 \times 30 \times 360$ mm^3). Recently, an upscaled bacteria-based self-healing system has been developed in which ureolytic mixed self-protected bacterial cultures (CERUP) can be produced at the 50 L scale [13]. This allowed casting of a concrete beam of $150 \times 250 \times 3{,}000$ mm^3, into which was incorporated 3% (per cement weight) of CERUP. Multiple cracks were created by four-point bending. To facilitate the water permeability test (Fig. 6), the beam was loaded in the upward direction (Fig. 7) and

Fig. 6 Test setup for measuring water permeability

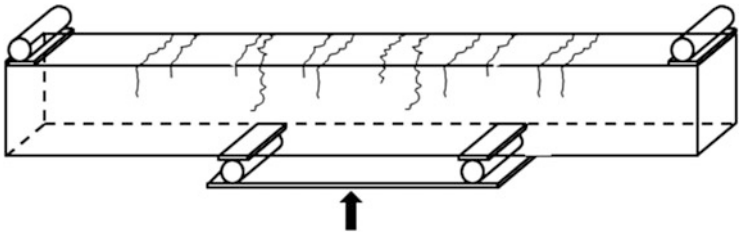

Fig. 7 Scheme of four-point loading on the beam

subjected to cyclic water supply instead of full immersion to mimic realistic conditions. An automatic water-spray system was installed above the beam, which sprayed water for 1 min four times per day over 6 weeks. It was found that less sealing was obtained in the large-scale beam than in the smaller prisms. The average crack filling ratio was only around 24% (for the R beam 20%), which was much lower than obtained in the small specimens (40%) using the same mixed culture [14]. The recovery of water permeability after healing was not significant. At this point, it can be confirmed that, in bacteria-based self-healing systems, the concrete should have good water retention properties, which can be realized by embedding functional materials such as hydrogels.

3.2 Oxidation of Organic Carbon

3.2.1 Expanded Clay Particle System

Laboratory Work

Biological calcium carbonate precipitation and carbon dioxide production can occur during the degradation of organic compounds, where bacteria act as catalysts. This biochemical reaction (via organic carbon oxidation) is the principle of bio-based healing in concrete.

Healing agents can be defined as the chemical/biochemical components that, upon crack formation, are activated to seal a crack. In the case of bio-based self-healing concrete using organic carbon oxidation (as developed in Delft University of Technology), the healing agent consists of alkaliphilic bacterial spores of the genus *Bacillus*, calcium lactate and yeast extract. For protection and immobilization of the healing agent during concrete mixing, all components are dissolved in water and are impregnated via vacuum application into lightweight aggregates (LWA). The healing agent solution contains bacteria spores (10^{11} spores/mL), calcium lactate (200 g/L) and yeast extract (4 g/L) and is incorporated into expanded clay particles (Liapor 1/4 mm; (Liapor GmbH, Germany) via impregnation under vacuum.

The $CaCO_3$ crystals that are formed during the healing process can seal open concrete cracks as a result of the biological conversion of the available organic carbon source; for example, in the case of calcium lactate, $Ca(C_3H_5O_3)_2$, the reaction producing calcium carbonate is the following [22]:

$$Ca(C_3H_5O_3)_2 + 6O_2 \rightarrow CaCO_3 + 5CO_2 + 5H_2O \quad (3)$$

According to the metabolic reaction shown in Eq. (3), one equivalent of calcium lactate is converted to one equivalent of $CaCO_3$, five equivalents CO_2 and five equivalents of H_2O. If the above reaction takes place in concrete, the produced carbon dioxide reacts further with the calcium hydroxide present, as cement hydration product, to produce another five equivalents of calcium carbonate [23]:

$$5CO_2 + 5Ca(OH)_2 \rightarrow 5CaCO_3 + 5H_2O \quad (4)$$

Presumably, Eqs. (3) and (4) result in the production of six equivalents of $CaCO_3$ from one equivalent of calcium lactate. It has been reported that biochemical $CaCO_3$ production can improve autogenous healing by efficiently sealing cracks of up to 460 μm [23].

Three significant aspects of bio-based self-healing concrete are examined and analyzed below:

- Influence of the healing agent on the compressive strength of concrete
- Crack sealing efficiency of the healing agent

Table 1 Mortar mix designs

Mixture	CEM I (kg/m^3)	Water (kg/m^3)	0.125/1 mm sand (kg/m^3)	1/4 mm sand (kg/m^3)	1/4 mm LWA (kg/m^3)
REF	463	231.5	855	825	0
CTRL	463	231.5	855	0	257
BAC	463	231.5	855	0	280[a]

[a]Includes the weight of impregnated healing agent in pores of the LWA

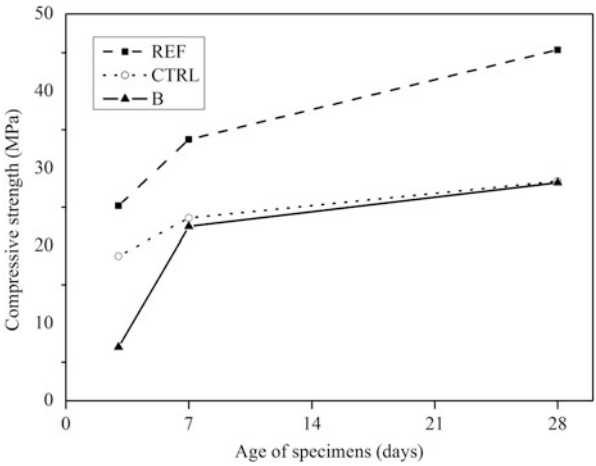

Fig. 8 Compressive strength for REF, CTRL and B specimens (see Table 1 for descriptions)

- Validation that crack sealing in bio-based concrete originates from bacterial activity

Experiments were conducted on three types of mortar mixtures: a reference mixture (REF) with normal weight aggregates (sand fraction 0.125/4.0 mm); a control mixture (CTRL) in which normal-weight sand fraction 1/4 mm was substituted by unloaded LWA; and a mixture with loaded LWA (B). Mix designs are presented in Table 1.

Investigation of the influence of the healing agent on the compressive strength of mortar was conducted on prisms ($40 \times 40 \times 160$ mm). All specimens were demoulded 24 h after casting and kept in a room with standard temperature ($20 \pm 2°C$) and $> 90\%$ relative humidity for 28 days. Compressive tests were performed on 28-day-old specimens. The results (Fig. 8) revealed that replacement of sand with LWA leads to substantial reduction in compressive strength, as expected. Furthermore, the healing agent seems to delay the development of compressive strength of mortar (at the age of 3 days), but has no significant effect after 7 days.

The crack-sealing ability of mortar is of prime importance in addition to its strength characteristics. In many studies, light microscopy images taken before and after healing treatment are used as a tool to quantify the visual sealing efficiency of

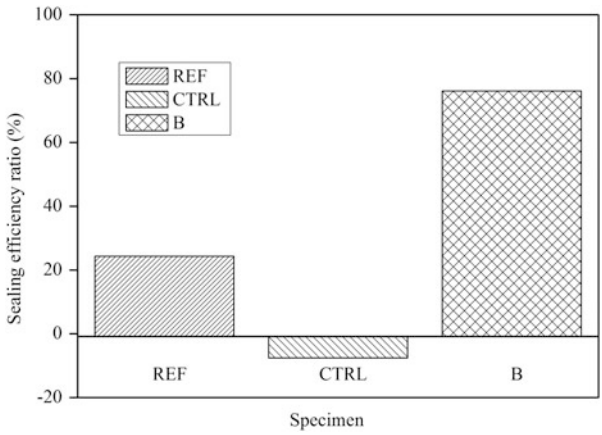

Fig. 9 Average sealing efficiency ratio for REF, CTRL and B specimens (see Table 1 for descriptions)

a certain healing agent. However, visual crack closure does not always leads to reliable conclusions about the functional effectiveness of the healing agent. Thus, a crack permeability test has been designed. The test was performed on steel-reinforced prismatic specimens ($40 \times 40 \times 160$ mm) modified with a hole (diameter 5 mm) in the middle and similar holes along their length. A crack of approximately 350 µm was introduced to the specimen via three-point bending. Following crack creation, the specimen was placed horizontally in a plastic bucket and subjected to 12-h wet–dry cycles for 28 days. The crack permeability test was performed on the specimen before and after water submersion, as described in the literature [24].

After test completion, the sealing efficiency ratio (SER) was calculated according to a reported method [24]. This ratio indicates the amount of healing that has taken place inside the crack during the 28 days of healing treatment. Figure 9 presents the average SER values calculated after completion of crack permeability tests via water flow. The graph shows that there is a noticeable difference in crack sealing between specimens with and without healing agent. Specimen B exhibited more than three times higher sealing performance than REF and CTRL specimens, as a result of the presence of the bio-based healing agent.

Additional tests were conducted to confirm that the improved sealing performance of specimens containing bacteria can be attributed to the bio-based system. The bacterial activity was traced by oxygen concentration measurements on 3-month-old specimens submerged in carbonate–bicarbonate buffer solution (0.1 M, pH 10.5, 20 ± 2°C, in a 4-L tank). For this test, the microsensor Oxy50M (Pyro-Science, Germany) was used. The microsensor measured the oxygen concentration in vertical steps of 50 µm, from 5 mm above the specimen down to the surface. Typical oxygen microprofile measurements for REF, CTRL and B samples are displayed in Fig. 10. The profiles of specimens without bacteria were similar (i.e. oxygen concentration was almost stable along the measuring height). The profile of the bacteria-containing specimen, however, differed. The oxygen concentration was constant until approximately 1 mm above the surface of the specimen, where it started to decrease. Oxygen consumption near the surface of the

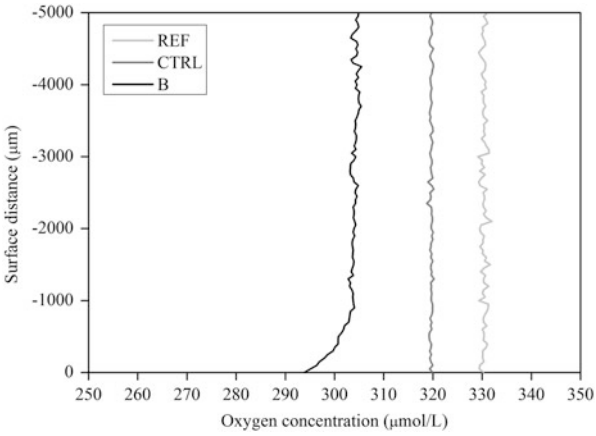

Fig. 10 Oxygen profile measurements for REF, CTRL and B specimens (see Table 1 for descriptions)

specimen provides evidence that metabolically active bacteria (germinated bacterial spores) were degrading the available organic carbon inside the mortar.

Test results revealed that the compressive strength of mortar specimens containing the bio-based system was considerably reduced (approximately 37%), caused by replacement of normal weight sand by LWA. Therefore, this material can be used where a lightweight structure is needed, or as an external layer on a structure of normal weight. Despite the lower strength performance, this self-healing material exhibited a significantly improved crack sealing performance when exposed to wet–dry cycles, compared with mortars without healing agent. Consequently, it is safe to state that bio-based self-healing concrete with LWA is suitable for preventing micro-cracking-related durability problems in structures.

Field Application

The first field application of bio-based self-healing concrete with LWA and natural fibres took place on July 2014 in the Andean highlands in Ecuador, South America. In this region the local economy is based on agriculture, for which a constant water supply is necessary. For this reason, about 100 years ago several canals were dug in the soil to transport water from melting ice and snow to the valleys. Because of infiltration of water through the walls (soil) the yield was very low. In 2011, the farmers who owned the canals and the local authorities cast concrete linings in the canals to improve this situation. Unfortunately, the concrete started cracking soon after casting, resulting in a large amount of leakage that put the sustainability of the system in danger. Bio-based self-healing concrete with LWA was proposed as a measure to improve the sustainability and performance of the irrigation system.

The concrete mix was designed taking into account the materials available in Ecuador, the strength and performance demands for the concrete linings and the building practice in the highlands in Ecuador. This mix included gravel with maximum size of 10 mm, sand, LWA with and without healing agent and natural

fibres. To ensure the sustainability of the self-healing concrete a fibre indigenous to Ecuador, Abaca, was chosen. This fibre has been successfully studied in Ecuador as reinforcement for mortar to improve the structural behaviour of houses under seismic forces [25].

In the laboratory, the mechanical properties of the concrete mix as well as the healing capacity were evaluated. The average compressive strength was 30 MPa for the mix with healing agent and 26 MPa for the mix without healing agent [26]. Specimens pre-cracked by means of three-point bending tests and placed to heal in contact with water for 6 weeks exhibited crack sealing.

In Ecuador, the concrete mix design was adjusted to the properties of the materials available at the site. A section of canal that did not have concrete lining was chosen for this field application. First, the water supply was closed. Then, the local farmers who are the owners and users of the canal cleaned the canal section of dirt and vegetation. The framework was prepared while the LWA was impregnated with bacteria and nutrients in the field.

Three linear meters of concrete linings with bacteria and 3 m without bacteria were cast. About 110 L of concrete were prepared at the time. The temperature during the casting was around 5°C. This portion of canal is located at about 2,900 m above sea level.

The framework was removed after 3 days. Two days later, the water flow through the canal was reopened. Now, a year after casting, the concrete linings show no signs of cracking or deterioration (as reported from the last inspection).

3.2.2 Condensed Powder System

Laboratory Work

Although proof of concept was shown for healing agent components contained in LWA, the application range may be limited because of incorporation of volumes of expanded clay, which influence the mixture design. In order to extend the applicability range, the volume of added healing agent was reduced by increasing the content of efficient healing agent component in particles. For this reason, scalability of production is an important factor to take into account. A way of producing scalable particles almost fully consisting of active ingredients is by roller-compacting powders to sheets, with subsequent milling to flakes that are in the size range of the sand fraction (1–4 mm) [27]. A typical property of these flakes is solubility in water, which is beneficial for matrix cracking and water ingress, dispersing the healing agent in the crack volume. It is challenging, however, to retain particle integrity during the wet mixing stage of mortar or concrete production to prevent premature incorporation of nutrients in the cementitious matrix. Partial particle dissolution can be prevented by application of a protective barrier around the soluble particle, in the form of a coating. The coating material can be inorganic (e.g. cement paste or geopolymer) or organic (e.g. calcium cross-linked polyvinyl alcohol alginate or lactic acid derivatives) (Fig. 11) [28–30]. To retain

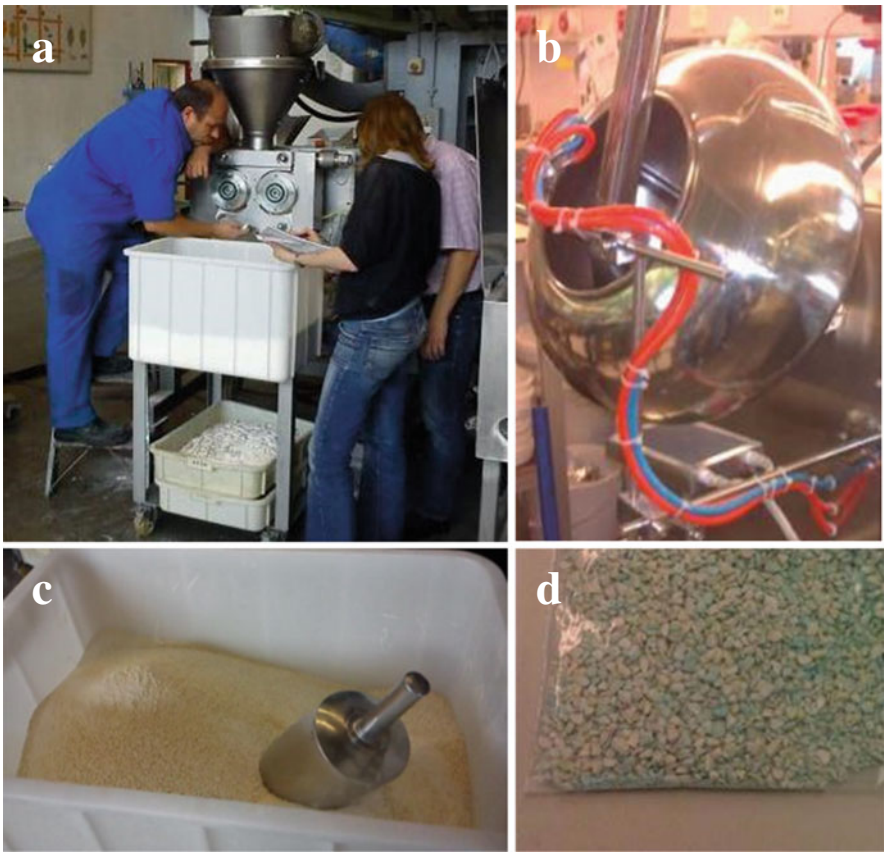

Fig. 11 (**a**) Roller compaction of powders, (**b**) coating of particles, (**c**) uncoated powders and (**d**) coated powders

equal active healing agent content in the mortar or concrete mixture, the addition of particles decreased from 30% by volume for LWA to 1% for the proposed flakes.

Important characteristics of flakes containing healing agent are survivability during the mixing stage, limited influence on mortar or concrete hardening properties, nutrient availability over time and ability to enable regain of crack water tightness [31]. Negligible influence on fresh mixture consistency was seen from flow tests, but some delay in strength development indicated interaction of healing agent particles and cementitious matrix (Fig. 12). After 7 days of hardening, the influence on strength development became negligible. The effect on strength is expected to be caused by partial loss of soluble core material near the particle surface, which could be amplified by increased surface area. Decreasing the surface area, by increasing particle size or homogeneity towards a spherical shape, should limit the superficial material loss and therefore further reduce the effect on strength development. Visual evidence of particle presence upon wet sawing of hardened

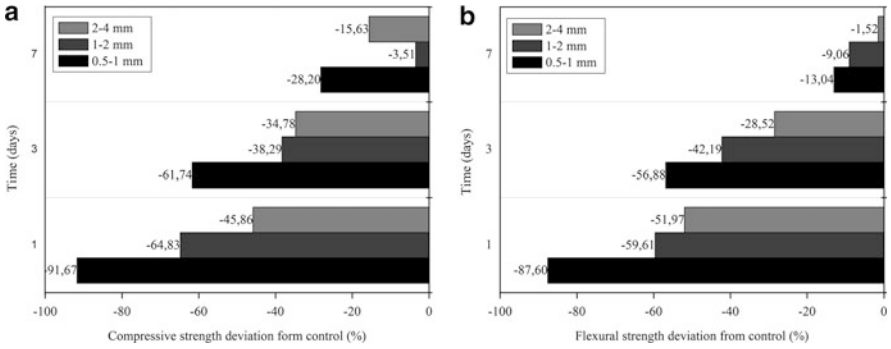

Fig. 12 (**a**) Flexural and (**b**) compressive strength deviation from control mortar after addition of healing agent flakes of various sizes

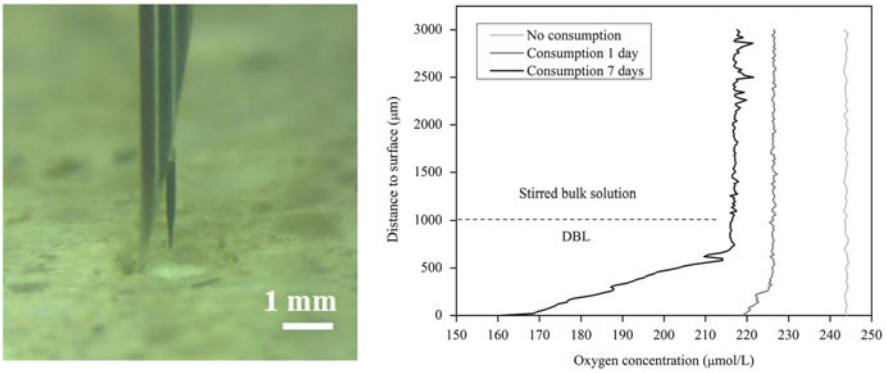

Fig. 13 *Left:* Oxygen microsensor approaching the surface of the mortar slice. *Right:* Profile measurement for surface oxygen consumption in time, showing a decrease in oxygen concentration in time towards the surface. *DBL* diffusive boundary layer

mortar specimens confirmed that particle retrieval was possible from hardened matrices and, therefore, that particles survived the mixing process.

In order to indicate bacterial activation and nutrient conversion, mortar slices with exposed healing agent flakes were immersed in water in a closed vial or stirred in an open system to measure the decrease in oxygen concentration, as evidence for bacterial metabolic activity (Fig. 13). Externally visible progressive mineral formation in a water-immersed cracked mortar specimen indicated crack closure. More important than visual mineral formation is confirmation of functionality regain, for which water tightness tests were performed. Half-cube mortar specimens were split to a crack width above the autogenous healing capacity (>400 µm). After determination of the initial water flow rate through the cracks, specimens were either stored in a 95% relative humidity room or placed under water. Water leakage was measured at intervals, until crack water tightness was restored. To indicate the possibility for multiple healing events, after drying of the specimens, the water leakage was checked and cracks were reopened and again placed in a water bath or humidity

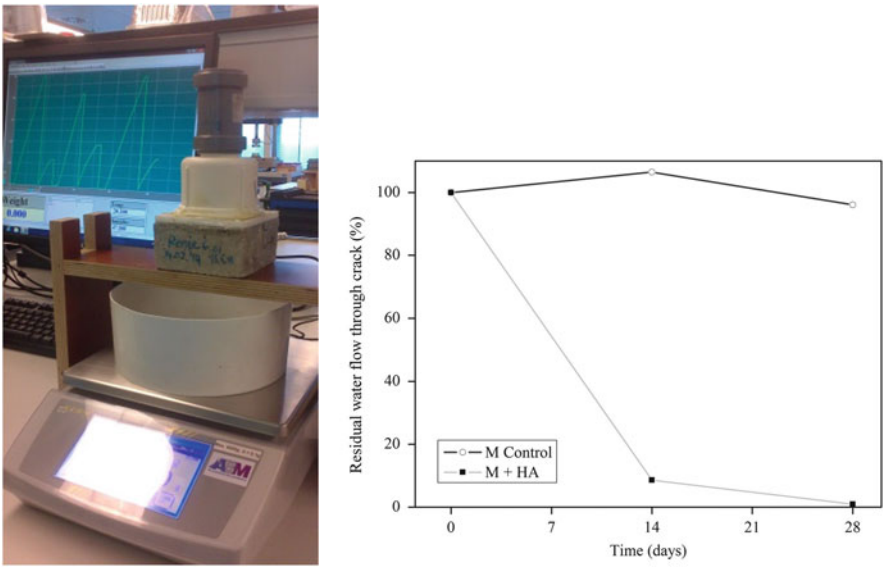

Fig. 14 *Left:* Set-up for the water leakage test. *Right:* Residual water flow through cracks at various water curing times. *M* control mortar, M+HA mortar with healing agent flakes

room. For specimens with similar crack widths, significantly higher recovery of water tightness was found in mortar containing healing agent flakes (Fig. 14).

Field Application

To check performance under outdoor conditions, flakes containing healing agent were added to a commercially available repair mortar. A 16 m^2 square part of a wall was divided into four quarters. For the top square, half the surface was removed until the reinforcement appeared; for the bottom half, the surface was removed until behind the reinforcement and the reinforcement was cleaned. Reference mortar, without healing agent, was applied on the left half of the square by spraying, whereas mortar containing healing agent was applied to the right half (Fig. 15, left). Observations were obtained on practicality, workability, consistency and visual appearance of the healing agent complemented mixture throughout application by spraying. Surface speckling indicated the locations of agent particles (Fig. 15, right); the stain intensity reduced over time. A first visual comparison of the superficial speckle pattern with laboratory cube specimens indicated homogenous spread of particles throughout the matrix. It would be interesting to visualize particle distribution over the depth of the sprayed mortar patch, as particles could have the tendency to settle predominantly at the surface as a result of rebound action at jetting. Because crack closing ability is mainly needed in the concrete covering the steel, a preferential distribution of particles towards the surface creates

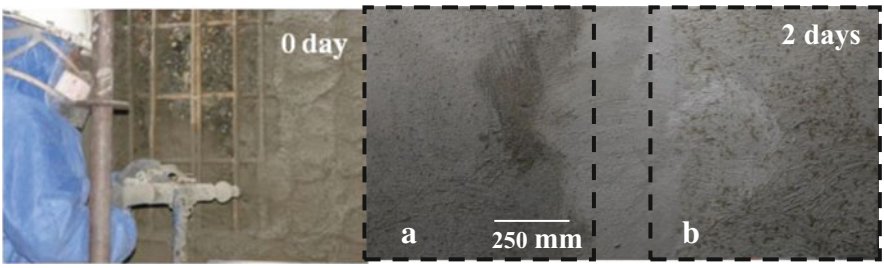

Fig. 15 *Left*: Spray application of commercial ready-mix mortar complemented with healing agent flakes. *Right*: During hardening, locations of healing agent particles are indicated by formation of speckles (**b**) compared with control (**a**)

an efficient use of healing agent particles. For an equal healing capacity, the amount of particles could therefore potentially be reduced, limiting the total cost added to that of the base mortar. Effective healing agent particle distribution and functional crack sealing capacity for regain of water tightness will be quantified in further outdoor applications.

3.3 Anoxic Oxidation of Organic Carbon

Microbial urea hydrolysis and aerobic oxidation of organic carbon require oxygen to initiate and maintain microbial activity, respectively. As a result of the poor solubility of oxygen in water (~9 mg/L) and its related deficiency in the deeper parts of the crack, healing efficiency through either of the processes is mostly inhibited with depth. Moreover, aerobic oxidation of organic carbon is known for its relatively low $CaCO_3$ yield [32], and urea hydrolysis is well known for its ammonia production, which is toxic for the environment [33, 34]. These issues have prompted study of alternative pathways in several applications of microbially induced $CaCO_3$ precipitation (MICP). Anoxic oxidation of organic carbon consumes nitrate (NO_3^-) or nitrite (NO_2^-) ions, as electron acceptor, and does not produce any toxic by-products. The process is called nitrate reduction and has been proposed for soil consolidation and Ca^{2+} removal from industrial wastewater [32, 35, 36]. Because of its highly negative standard Gibbs free energy (ΔG°) [Eq. (5)], nitrate reduction can be expected to dominate in the presence of NO_3^- and organic carbon, under oxygen-limited conditions, and generate carbonate (CO_3^{2-}) and bicarbonate (HCO_3^-) ions, which are necessary for $CaCO_3$ precipitation [Eq. (5)]:

$$5HCOO^- + 2NO_3^- \leftrightarrow N_2 + 3HCO_3^- + 2CO_3^{2-} + H_2O \quad \Delta G^\circ = -1153 \text{ kJ/mole} \tag{5}$$

MICP studies aiming at sand and soil consolidation through nitrate reduction have revealed that $CaCO_3$ precipitation rates achieved through NO_3^- reduction are not adequate for in situ application [32, 35, 37]. Indeed, under optimum conditions, MICP rates achieved through denitrification are 100–1,000 times lower than those achieved through ureolysis [36]. Yet, the concrete environment is at far from optimum conditions. Apart from its alkaline state, in concrete cracks oxygen and nutrients are limited and are the main factors affecting the germination and growth rate of the used bacteria. $CaCO_3$ precipitation rate mainly depends on the initial bacteria concentration, growth rate and specific metabolic activity of each bacterium in the relevant environment. Therefore, the condition in concrete cracks favours denitrifying bacteria rather than aerobic bacterial cultures. Bacteria that are able to grow on NO_3^- under nutrient-limited conditions could supersede the MICP rate and self-healing performance of aerobic bacteria.

Generally, concrete properties are affected by the addition of bacteria, nutrients and the protective carriers necessary to develop microbial self-healing concrete. If the appropriate bacteria are chosen to minimize the necessary modifications, application of the self-healing technology becomes more feasible. Anoxic oxidation of carbon sources as a self-healing mechanism requires three main components:

- Organic carbon source
- NOx (NO_3^- and/or NO_2^-) as electron acceptor
- Appropriate bacteria for enzymatic oxidation

There are already certain concrete admixtures, calcium formate and calcium nitrate, that can serve as carbon source and electron acceptor, respectively. Calcium formate, $Ca(HCOO)_2$, is used as an accelerator (0.5–4% w/w cement) and calcium nitrate, $Ca(NO_3)_2$, is used as set accelerator, strength enhancer or anti-freeze admixture (0.2–4% w/w cement) in concrete [38, 39]. Using this information, at Ghent University, microbial strains that can grow on these admixtures were selected and investigated for MICP [36]. Among the selected strains, *Diaphorobacter nitroreducens*, a NO_3^- reducing vegetative bacterial strain, appeared to grow on formate and nitrate salts with a higher growth rate than the NO_3^- reducing *Bacillus* species (Fig. 16).

The difference in growth performance was attributed to the absence of yeast extract, which is an essential nutrient for germination of spores. Ability to grow in the absence of trace elements and nutrients such as vitamins and yeast extract makes *D. nitroreducens* advantageous over currently studied strains. Furthermore, a $CaCO_3$ precipitation yield of 7 g $CaCO_3$/g NO_3-N per day could be achieved, which is distinctive among the reported MICP studies [36]. Moreover, by using starvation-resilient bacteria, repetitive $CaCO_3$ precipitation could be achieved. If the growth of the microbial culture is limited (due to the absence of yeast extract, oxygen, etc.) precipitation around the cell membrane kills bacterial cells and decreases the rate of precipitation [32, 40]. The resilience of *D. nitroreducens* against starvation enabled repetitive $CaCO_3$ precipitation to be achieved from a single inoculum, with a constant precipitation rate of 0.3–0.5 mM $CaCO_3$/h [36]. The bacterial strain could survive when nutrient diffusion was limited as a result of mineral formation

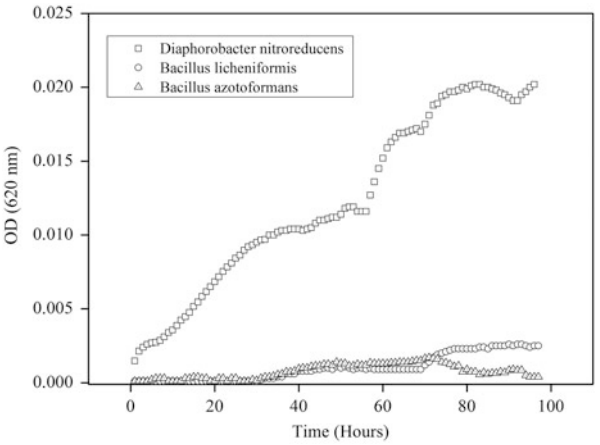

Fig. 16 Difference in growth of different NO_3^- reducing species under minimal nutrient conditions, lacking yeast extract and trace elements

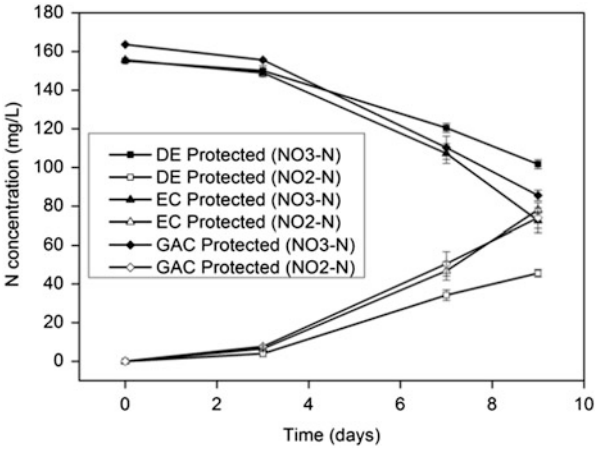

Fig. 17 Resuscitation performance of protected *Diaphorobacter nitroreducens* cells after 28 days in mortar. *DE* diatomaceous earth powder, *EC* expanded clay particles, *GAC* granular activated carbon particles ($n = 3$)

around the cell membrane, and created new cells that enabled repetitive $CaCO_3$ precipitation. Survival experiments showed that *D. nitroreducens* can survive at pH 13 with the aid of protective carriers [41]. Nitrate reduction activity of the bacteria could be recovered in 48–96 h following a pH decrease to below 10. Survival tests were further conducted in mortar environments. Prior to addition to mortar, bacterial cells (0.5% w/w cement) were incorporated into diatomaceous earth, expanded clay particles or granular activated carbon (5% w/w cement). These protective carriers enabled bacterial cells to survive in mortar environments. Bacterial cells extracted from the 28-day cured mortar specimens revealed nitrate reduction activity after 72 h of incubation (Fig. 17) in a minimal nutrient solution (pH 9.5–10) containing $Ca(HCOO)_2$ and $Ca(NO_3)_2$.

In a recent study, various types of commercially available protective carriers and nutrients were investigated for their influence on mortar setting and strength [42]. Results indicated that although diatomaceous earth provided protection for

NO_3^- reducing vegetative strains, it significantly decreased the setting time when combined with the respective nutrients, $Ca(HCOO)_2$ and $Ca(NO_3)_2$, necessary for self-healing [41, 42]. Therefore, diatomaceous earth was suggested not to be used as a protective carrier for denitrifying microorganisms in the development of self-healing concrete. By contrast, promising results were achieved when either expanded clay particles or granular activated carbon particles were used as protective carriers for vegetative bacterial strains. These porous carriers did not significantly change the setting and strength properties of mortar [42].

Recently, the self-healing performance of mortar specimens containing *D. nitroreducens* has been investigated. Bacterial cells (0.5% w/w cement) were loaded into 0.5–2 mm expanded clay particles (5% w/w cement) and added to the mortar during mixing. As nutrient source, concrete admixtures $Ca(HCOO)_2$ (2% w/w cement) and $Ca(NO_3)_2$ (3% w/w cement) were dissolved in water and added during mixing. The amounts used were in the range of suggested literature values for concrete use [38, 39]. Mortar specimens composed of sand, cement and water in the ratio 3:1:0.5 ($30 \times 30 \times 360$ mm) with embedded steel reinforcement (diameter 6 mm) were cured under temperature- and humidity-controlled conditions (20°C and relative humidity >90%) for 28 days. After the curing period, specimens were submitted to direct tensile load applied to the reinforcement, and multiple cracks (crack width range 100–500 μm) were achieved. Upon formation of cracks, mortar prisms were immersed in tap water for 28 days. Self-healing performance of the mortars was observed through visual crack analysis using a stereomicroscope (Leica S8 APO). At the end of 4 weeks treatment in wet conditions, specimens with bacteria could completely close the cracks up to 350 μm (Fig. 18).

At the end of the healing period, capillary sorption tests were conducted to check the water tightness of the healed crack (235 ± 35 μm original crack width). Mortar prisms containing healing agents absorbed 51% less water than the reference specimen in the first 24 h (Fig. 19).

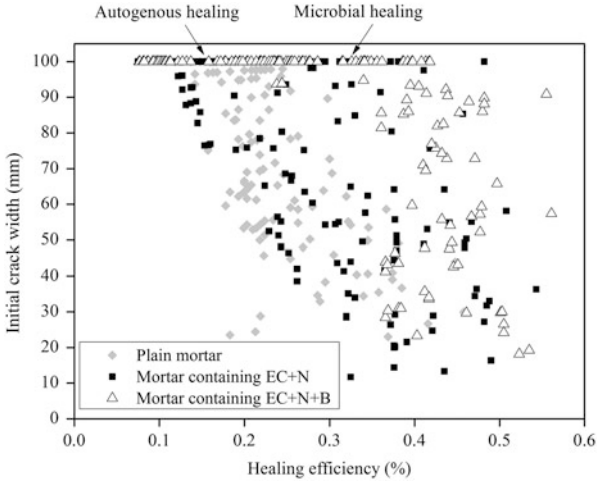

Fig. 18 Self-healing capability of mortar specimens with and without *Diaphorobacter nitroreducens*. *EC* expanded clay particles, *N* nutrients $Ca(HCOO)_2$ + $Ca(NO_3)_2$, *B* *Diaphorobacter nitroreducens*)

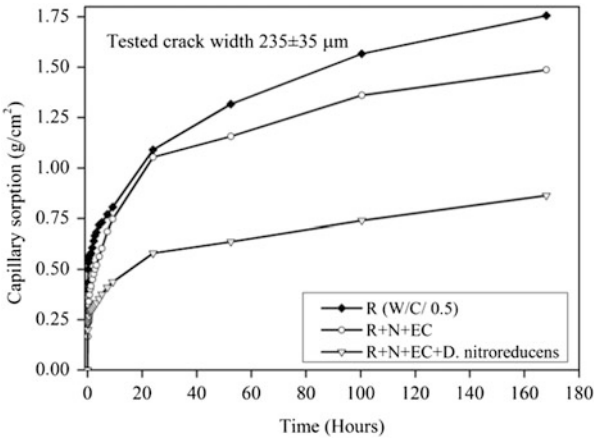

Fig. 19 Microbial self-healing through NO_3^- reduction provides higher water tightness than autogenous healing. *R* plain mortar (0.5 water-to-cement ratio), *EC* expanded clay particles, *N* nutrients Ca $(HCOO)_2$ + $Ca(NO_3)_2$

Elaborating visual quantification of the crack healing to 3D crack closure is important for clear distinction between autogenous and autonomous healing [7]. Therefore, it is necessary to investigate reported NO_3^- reducing strains in terms of their actual precipitation performance inside the crack and the stability of healing product under pressure, which is an on-going research topic.

It has been indicated that implementation of axenic bacterial cultures can be expensive for applications in situ [43]. Silva et al. [14] revealed that use of self-encapsulated non-axenic cultures decreases the cost while providing comparable performance. Therefore (following the proof of concept with denitrifying axenic cultures), non-axenic denitrifying cultures that have comparable resilience and performance to axenic cultures have been developed for microbial self-healing concrete through NO_3^- reduction.

From economic point of view, it is essential to optimize the amount of bacteria and nutrients necessary for efficient self-healing of concrete cracks. Therefore, various combinations of bacterial healing agents and nutrients should be tested in concrete and optimized according to the needs of the concrete industry.

4 Repair Systems

4.1 Repair with Ureolytic Bacteria

4.1.1 Microbial $CaCO_3$ for Surface Protection

Because many current surface protection treatments are not satisfactory, in recent years researchers have focused on the application of bacterial calcium carbonate precipitation for surface consolidation and protection.

For research on the laboratory scale, specimens were immersed in bacterial culture or/and deposition media. The immersion time varied from 3 to 30 days

depending on the bacterial activity. The formed $CaCO_3$ layer decreased the water permeability, and showed a strong cohesion and adhesion with the matrix. This was confirmed by ultrasonic measurements and drilling resistance tests on limestone. In the latter tests, the resistance the drill bit experiences while drilling a small hole is a measure of the consolidation.

For on-site use, application by immersion is not easy to perform and has to be replaced by other techniques such as brushing or spraying. The procedure generally contains the following steps:

- Removal of loose particles from the original surface
- Spraying the bacterial culture
- Spraying the deposition medium

The second and the third steps can be repeated several times depending on the matrix type, bacterial concentration, etc. The first on-site application (50 m^2) was carried out in 1993 on the limestone of the Saint Medard Church in Thouars, France. The formed biocalcin reduced water absorption (1:5 ratio), yet the stone retained its gas permeability and aesthetic surface [44]. Tiano et al. [45] and Jroundi et al. [46] also applied bio-mineralization for on-site conservation of limestone surfaces. Jroundi applied only a nutritious medium to stimulate the carbonatogenesis activity of bacteria inhabiting the decayed calcarenite stones of San Jeronimo Monastery, Lisbon. Subsequently, bio-$CaCO_3$ crystals formed in situ, resulting in significant strengthening. To apply this in-situ bio-treatment, it is necessary to have preliminary knowledge about the microbial community inhabiting the matrix, and then the culture medium should be carefully chosen. However, it is easier and faster to import external bacterial strains whose high carbonatogenesity has been testified. De Muynck et al. [47] have been able to homogeneously strengthen limestone up to depths of 30 mm with similar or better performance than traditional surface treatments (such as ethyl silicates). The bio-deposition treatment is solvent free and entails both a significant protective and consolidating effect after two spray applications within the same day. By optimizing the concentrations of the urease and carbonate precursor solutions, they were able to lower the cost of the treatment to within the range of traditional consolidants. Furthermore, the replacement of carbonate precursors with silica or calcium carbonate nanoparticles presents a promising strategy for decreasing the amount of by-products, but needs optimization prior to being used in practice. A patent application was submitted (EP12155132.9 and PCT/EP2013/052783) with respect to the modified bio-deposition procedure.

Several aspects should be highlighted when applying a bio-treatment to a surface:

- Culture medium composition, culture conditions and bacterial type should not cause further damage to the building materials. One should be able to repeat the treatment.
- The amount of nutrients and deposition medium supplied should be balanced with the amount of bacteria, because the remains of nutrients and salts could

facilitate extra growth of other microbes on the surface and cause unpredicted damage to matrix materials.

- Spore-forming bacteria were suggested not to be used on the surface by many researchers [48, 49]. The germination of spores and uncontrolled growth pose a potential risk for the environment. However, other researchers such as Le Metayer-Levrel [44] have stated that no increase in microbial activity or changes in the autochthonous microbiota were observed immediately or 4 years after the treatment with *Bacillus cereus*, a spore-forming strain. Therefore, with a carefully controlled culture and medium supply, the risk could be greatly reduced.
- Bacterial strains applied should not be pathogenic.

Until now, the on-site application of bio-treatment is mainly used on historical building materials such as porous calcareous stones, but not on cementitious materials. Nevertheless, promising results have been obtained with bio-treatment of cement-based materials at the laboratory scale and in small on-site tests [50–55]. In most studies, the specimens were immersed in bacterial culture and deposition media. Compared with porous limestones, cement/concrete specimens are denser with a lower porosity, resulting in less retention of bio-agents in the surface layer after spraying or brushing. Also for limestone, the pore structure has an influence on the penetration depth and bio-deposition treatment efficiency, as shown by De Muynck et al. [56]. It was found that the largest amount of bacterial precipitation occurred in stones with a large amount of macropores, which is because absorption of bacterial cells (1–4 μm) occurs in pores with dimensions of 4–20 μm. De Muynck et al. (Fig. 20) have shown that the surface deposition of calcium carbonate crystals on mortar decreased the water absorption by 65–90% depending on the porosity of the specimens. As a consequence, the carbonation rate and chloride migration decreased by about 25–30% and 10–40%, respectively. An increased resistance to freezing and thawing was also noticed. The results obtained

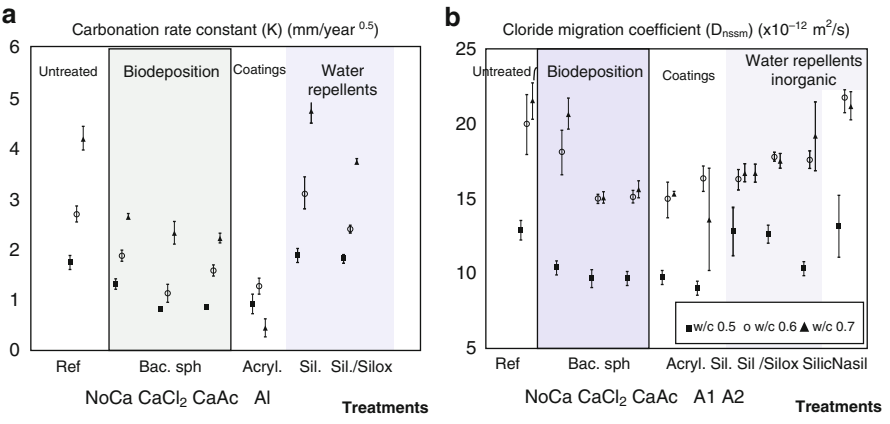

Fig. 20 (**a**) Carbonation rate constant and (**b**) chloride migration coefficient for mortar with different water-to-cement ratios, with different surface treatments [51]

with the bio-deposition treatment were similar to those obtained with conventional surface treatments (e.g. acrylate, silane, siloxane, silicone, silicate).

4.1.2 Microbial $CaCO_3$ for Crack Repair

Microbial $CaCO_3$ is also a promising material for repair of cracks in concrete. Bang et al. were among the first researchers to investigate the bacterial remediation of concrete cracks [57–59]. The bacterium they used was *Bacillus pasteurii*, a spore-forming strain with high urease activity and endurance in extreme environments. Artificial cracks with a constant width of 3.175 mm but with depths ranging from 3.175 to 25.4 mm were made on the specimens artificially by saw cutting. Pure microbial $CaCO_3$ is not able to seal such wide cracks completely. Therefore, Ramachandran et al. [58] applied a mixture of bacterial cells, nutrients and sands to the artificial cracks, followed by immersion of the specimens in urea–$CaCl_2$ medium for 28 days. The experimental results showed that specimens with cracks filled with bio-mixture demonstrated a significant increase in compressive strength compared with those without bacteria, from 10% to 27% depending on the bacterial amount added [58]. Scanning electron microscopy (SEM) showed that dense crystals embedded with bacterial cells mainly occurred close to the surface area of the crack. Because the bacterium *B. pasteurii* has higher activity in the presence of oxygen, the authors attributed this result to the limited oxygen availability in the deeper zones of the cracks. To induce precipitation throughout the cracks, Bang et al. [57] tried to repair cracks with *B. pasteurii* immobilized on polyurethane (PU) open cell foam. An obvious increase in the compressive strength was observed in the specimens with bacteria compared with those without bacteria, especially after 7 days. However, because there was no bonding between PU strips and the crack wall, PU together with MICP only functioned as filling material to seal the cracks.

De Belie et al. [60] and Van Tittelboom et al. [61] (Fig. 21) utilized silica sol–gel as filling material and as protective carrier for bacteria in the high pH environment in concrete. Bacterial cells were well mixed with silica sol and injected into the cracks manually, after which they were immersed in a solution of urea and calcium chloride, calcium nitrate or calcium acetate. The efficiency of this repair technique was compared with traditional repair techniques such as epoxy injection and application of grout mortar. Crack closure was shown by ultrasonic pulse velocity, microscopic investigation and water permeability tests. Crack sealing by means of this biological treatment resulted in a decrease in water permeability. However, the greater part of the decrease in water permeability was attributed to crack filling by the sol–gel matrix. Thermogravimetric analysis (TGA) of the crack repair material showed the presence of $CaCO_3$ crystals only in the case of active bacteria. Precipitation of these crystals inside the gel matrix could enhance the durability of this repair material.

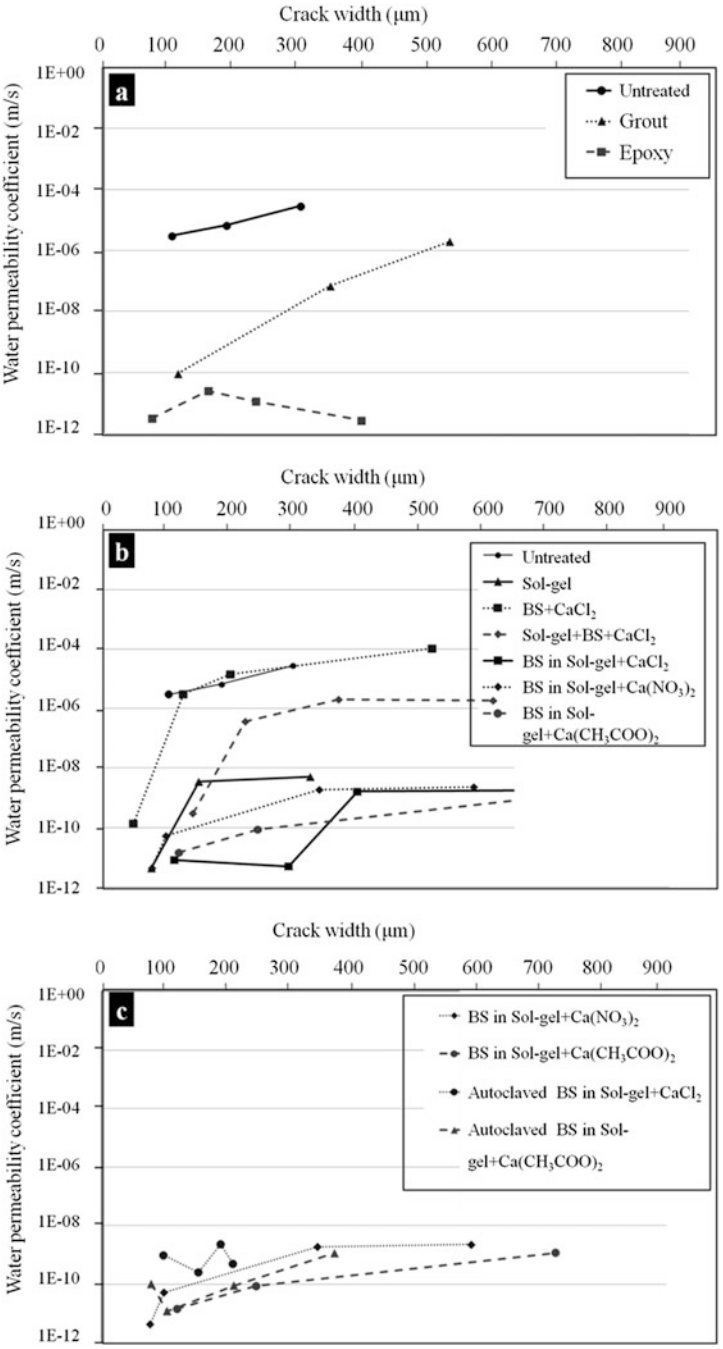

Fig. 21 Water permeability coefficient k (m/s) versus crack width (μm). (**a**) Untreated specimens and specimens treated with traditional repair techniques. (**b**) Untreated specimens and specimens treated with bacteria-based repair techniques. (**c**) Comparison of specimens treated with living and autoclaved *Bacillus sphaericus* [61]

4.1.3 Microbial $CaCO_3$ for Mechanical Strengthening

In addition to surface protection or crack healing, applying bacteria internally could also improve the mechanical properties and durability of concrete. Achal et al. [62, 63] applied *B. pasteurii* and *Bacillus megaterium* (urease +), both at a concentration of 107 cells/mL, and the 28-day compressive strength was increased by 17% and 21%, respectively. The durability of the specimens was also improved as a result of decreased water permeability. An increased pull-out strength of rebars in reinforced concrete after MICP was also reported [55]. Park et al. [64] isolated different calcite-forming bacterial strains from concrete structures and found that only one of the considered strains contributed to an increase (by 9%) in the 28-day compressive strength, whereas a decrease of 17% was observed in specimens with *B. pasteurii*. This is in contradiction to the results of Achal et al. [62]. Basaran [65] mixed vegetative *Sporosarcina pasteurii* cells in a urea–yeast extract medium with cement. An increase in calcium carbonate precipitation, reduction in porosity (24% at 28 days) and increase in compressive strength occurred when the bacterial medium was used. Viable *S. pasteurii* cells were found in hardened cement paste specimens as old as 330 days, with approximately 2% viability retention. About 50% of the viable cells detected were defined as vegetative cells, which could be metabolically active. This is the longest survival period recorded for microorganisms in cement-based materials without any encapsulation.

Overall, according to the authors of this section, two main mechanisms could be related to bacterial strengthening of concrete.

Formation of MICP as a Result of Bacterial Urease Activity

The formation of calcite inside the matrix could be related to urease activity inside both alive and dead bacterial cells. From the results of bacterial viability inside mortar specimens, it was found that the average number of viable bacteria decreased from 6×10^6 to 4.5×10^4 after 7 days, which means that most bacteria died. Bacterial growth was greatly inhibited, as shown by the similar cell numbers at 7 days and 28 days [63]. On the other hand, additional mortar strength increased slowly from 7 to 28 days. Urease remains in dead cells, but because of the high pH inside the specimens, urease activity is dramatically decreased, resulting in an extremely low calcite formation rate, which might be the reason for measurable strength increase only after 28 days. A high concentration of bacterial cells would cause extra voids inside concrete, which cannot be completely compensated for by the formation of calcite. Therefore, there would be a threshold value of bacterial cells.

New Silica Phase Introduced by Enzymes from Special Bacterial Strains

Ghosh et al. [66] investigated the interaction between bacteria and mortar matrix at the microscale. Mercury porosimetry confirmed the modification in pore size distribution resulting from the addition of microorganisms. They attributed the modification of pore properties to the newly formed silicate phase, which was induced by a silica-related enzyme excreted from bacteria. At higher cell concentrations, matrix integrity could be disrupted by excessive bacterial activity and thus result in a decrease in compressive strength of the mortar. A control experiment was carried out by adding the isolated protein (from the bacterium) to mortar specimens. An obvious increase in compressive strength was observed. The protein was characterized and found to dissociate silica from silica-rich substances and to form new silica phases. This resulted in enhanced coherence between sand particles and cement matrix at the microscale and, hence, in increased strength.

To summarize, use of calcite-forming bacteria on surfaces to improve surface properties and, hence, durability is a promising and convincing technique. However, to apply bacteria internally with the aim of increasing strength is more complex and dependent on bacterial strain. Whether bacterial cells simply remain in the matrix as organic fillers or make an active contribution still needs further exploration.

4.1.4 Microbial Repair Mortars

For the repair of (limestone) monuments, mortars made of Euville stone powder and traditional ethylsilicates, colloidal $Ca(OH)_2$ nanoparticles, amorphous silicon dioxide (SiO_2) nanoparticles, or *Bacillus sphaericus* in combination with nutrients have been investigated [67]. The procedure used by the Royal Institute for Cultural Heritage in Belgium was adopted for evaluation of the consolidation performance of loose grains of two different fractions (diameter, $d \leq 1.25$ mm and $1.5 \leq d \leq 3$ mm). According to this procedure, the consolidative action is determined from the weight of grains cemented compared with the total weight of grains present.

Overall, the cohesion of loose grains in Flacon tubes was better for the fine stone powders than for the coarse powders. The SiO_2 nanoparticles performed better than $Ca(OH)_2$ nanoparticles. Specimens treated only with bacteria absorbed water vapour after storage at 20°C and 65% relative humidity, giving rise to the loss of initial cohesion between grains. Treatment with SiO_2 nanoparticles in combination with *B. sphaericus* (Fig. 22), however, maintained cohesion and showed superiority over the traditional ethylsilicate consolidant.

The preparation of microbial repair mortars shows similarity to soil improvement techniques in that bacterial suspension and cementation media are injected from the top. Bio-$CaCO_3$ forms in situ in the pore space of the sand matrix and, hence, cements the sand particles. Using MICP from urea hydrolysis for soil improvement has been applied successfully at a scale of 1 m^3 and the first field

Fig. 22 Consolidation of Euville stone powder in Falcon tubes, using SiO_2 nanoparticles in combination with *Bacillus sphaericus*

test at a large scale (100 m^3) has also been performed, showing very promising efficiency [32]. These studies demonstrate the feasibility of in-situ soil improvement by MICP from bacterial urea hydrolysis.

4.2 Oxidation of Organic Carbon

4.2.1 Liquid Repair Systems

The repair system developed at the Technical University of Delft consists of concrete-compatible bacteria [23] and feed, which produces calcite-based minerals that decrease concrete porosity. This system is composed of two solutions:

- Solution A: Sodium-silicate (alkaline buffer), sodium-gluconate (carbon source for bacteria growth), alkaliphilic bacterial spores
- Solution B: Calcium nitrate (nitrate source for denitrification when oxygen is depleted and calcium for $CaCO_3$ precipitation), alkaliphilic bacterial spores

The silicate-based compound, sodium silicate, ensures an alkaline pH in the system and the formation of a gel inside the crack. Although not very strong, this gel allows rapid sealing of the crack (within a few hours) and an optimum environment for bacteria to precipitate $CaCO_3$. By the time the gel becomes too weak, a substantial amount of $CaCO_3$ has been precipitated to seal the crack.

Example of Application in a Parking Garage

The test location was a two-storey underground parking garage. The parking deck was suffering from cracking, resulting in leakage of the structure. Some cracks seem to have been previously injected with cementitious grout but were still leaky. For the new repair campaign, the bacteria-based liquid system developed at the Delft University of Technology was selected as repair material over other traditional repair methods such as epoxy injection. Besides lower cost, this material requires significantly shorter time for application than other methods, one day rather than several weeks. The system was hereby tested for the first time on a large scale. The surface area to be treated was around 2,000 m^2.

Figure 23 gives an overview of the pilot test, and the various treatments and tests performed. The treatment of the parking deck with the bacteria-based repair system took place on 18th October 2014. Seven weeks later (9th December 2014), a leakage test was performed on three cracks, selected randomly on the parking deck. Two cores were drilled for analysis to look for any evidence of biomineral formation. Because the tested cracks were still leaky, a second treatment was carried out on one crack on 17th December 2014. This time, as the treatment was performed in winter time, bacteria that grow at low temperatures (4–8°C) were added to the repair system. Crack impregnation was carried out manually with sprayers. Seven weeks later (10th February 2015), a second leakage test was carried out on the same cracks as previously tested on 9th December 2014. Two cores from the crack treated with cold temperature bacteria were drilled again for analysis.

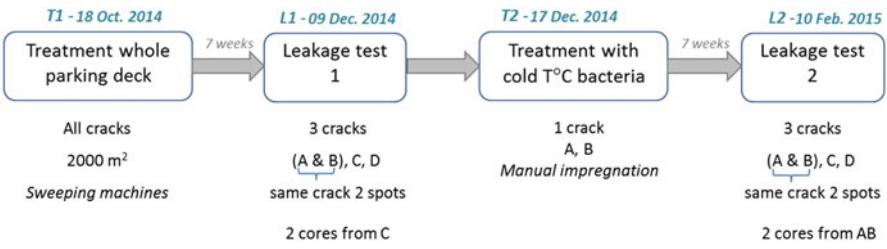

Fig. 23 Overview of treatments and leakage tests

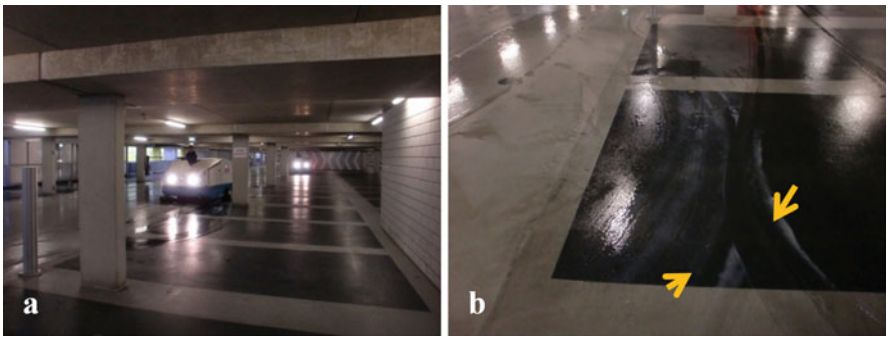

Fig. 24 (**a**) Application of solutions A and B (see text for composition) by the sweeping machines. (**b**) After the application/mixing of the two solutions. The *yellow arrows* indicate the gel that has formed at the surface of a crack

Preparation of the Bacteria-Based Repair System: 18th October 2014

The composition of the solution was calculated per bag of 25 kg of either sodium gluconate or calcium nitrate tetrahydrate for either 200 or 50 L of solution. Usually, 0.5 L of bacteria-based repair solution is used per square meter of surface to be treated. However, this amount can vary depending on the crack volume and the porosity of the substrate. Before the application, little was known about the crack volume, concrete porosity or dead volume of solution needed for the sweeping machine, so an excess quantity of powders were transported.

The buckets were first filled with 50 L warm water and the powders were added. The solutions were mixed with electric mixers until complete dissolution of the powders. pH was checked and the solutions were poured into the sweeping machines (solution A into machine A and solution B into machine B).

Sweeping machine B needed to deliver less solution than sweeping machine A in order to obtain the right mixing ratio of solution A to solution B. Because the amount of solution released by the machines could not be adapted, sweeping machine A went first and somewhat slower than sweeping machine B. The pH of the gel obtained after passage of the sweeping machines was checked to validate the mixing ratio (Fig. 24).

Leakage Test 1 (9th December 2014) and Core Analysis

Wooden frames were placed along the cracks to be tested and sealed with silicon. About 5 L of tap water was poured and left 15 min for saturation of the crack. The drops leaking through the crack were counted for 1 min; the count was performed six times to obtain an average value. Results showed that one crack was still leaking significantly, suggesting that the treatment might not have penetrated deep in the crack. However, it should be mentioned that no initial leaking test had been performed, and although the crack seemed to leak heavily, it might be less than before treatment.

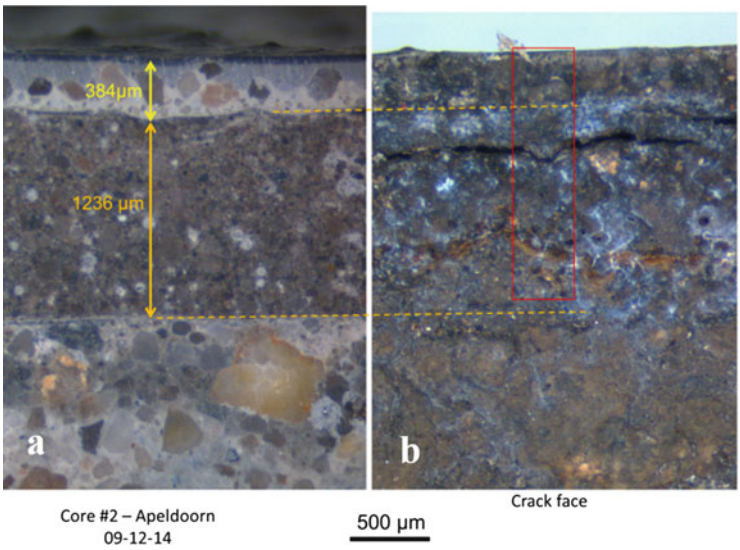

Fig. 25 Observation with stereomicroscope of the core: (**a**) outer part of the core and (**b**) crack face. The *red rectangle* indicates the area observed and analyzed with ESEM

Observation of the cores using stereomicroscopy (Fig. 25) and environmental scanning electron microscopy (ESEM) showed that the coating present on the parking deck was not well attached to the concrete, and so the repair solution might have penetrated along the delamination. Figure 25 shows a whitish colour along the crack surface, which might indicate the presence of the repair system. However, observations and elemental analysis with the ESEM did not show any significant differences in composition nor in morphology between these whitish and non-whitish areas, making it hard to draw any conclusion relating to the penetration depth of the repair system.

Second Treatment with Cold Temperature Bacteria: 17th December 2014

Based on the results from the leakage test, a second treatment with the repair system amended with bacteria adapted to cold temperatures was performed on 17th December 2014. One crack (AB) was impregnated manually with the repair system. Inspection from the level below showed that the repair solution was dripping through and thus had penetrated through the full length of the crack. The second leakage test (Fig. 26) was performed on crack AB 7 weeks after the second treatment, on 10th February 2015. Two cores were also drilled for analysis. Results of the leakage test were encouraging as the crack was leaking significantly less. Location A had 43% less leakage compared with the previous test and location B, which was dripping heavily, had 80% less leakage. Moreover, the leakage at location B only came from specific spots along the crack. Figure 27 shows ESEM observations of the core drilled after the second treatment. Calcium-based mineral (Fig. 27a) and distinctive morphologies, small rod-like imprints (Fig. 27b), were

Fig. 26 Second leakage test on crack AB

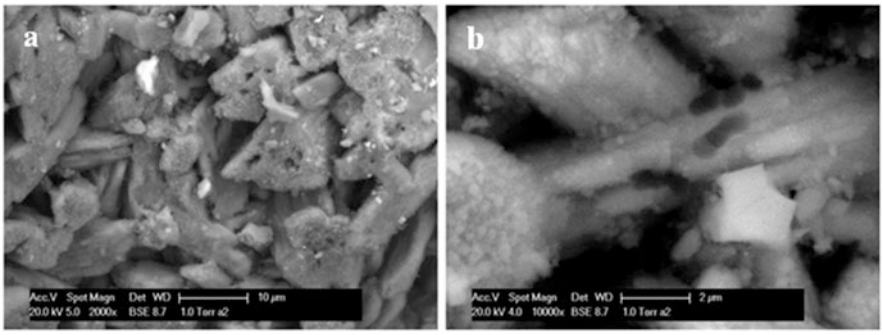

Fig. 27 ESEM observations from the core drilled along crack AB on 10th February 2015

observed along the core. The shape and size of these imprints were in good agreement with those of bacteria, suggesting that they were bacteria. This is a strong indication of the involvement of bacteria in the calcium carbonate formation, which suggests that the second treatment was successful.

4.2.2 Bio-Based Mortar for Patch Repair

Laboratory Scale Testing

Concrete patch repair systems frequently face durability-related problems because of a lack of compatibility between the repair material and the concrete substrate. The newly cast repair materials are subjected to differential shrinkage deformations, which lead to tensile stress development. Shrinkage deformations can be compensated for, but it is also possible to apply a material with a higher tensile capacity such as strain-hardening cement-based composites (SHCC). SHCC are

designed to have a large strain capacity because of the use of a low percentage of randomly distributed polymer fibres [68]. As a repair material, SHCC can carry more tensile load and accommodate larger tensile strain than other repair systems [69, 70]. The tensile strain translates into micro-cracking. To a certain extent these micro-cracks heal through autogenous healing, but to improve the healing capacity of SHCC a bacteria-based healing agent can be included into the mix design.

The healing agent consists of bacterial spores related to the species *Bacillus cohnii*, calcium lactate and yeast extract immobilized on LWA. The mortar mix includes CEM I, fly ash, limestone powder, LWA impregnated with the healing agent, poly(vinyl alcohol) fibres, water and superplasticizer.

The average compressive strength at 28 days of the SHCC with bacteria was 39.8 MPa and without bacteria 38.5 MPa, fulfilling the strength requirements for structural repair according to the EN 1504 standard. Under bending stress, both materials exhibited ductile behaviour and developed multiple cracks prior to failure [71]. When tested as a repair material, SHCC with healing agent showed reduced delamination with the concrete substrate, sufficient bond strength according to EN 1504 and improved flexural behaviour as a composite (together with the concrete substrate) compared with the mortar without healing agent [72].

To evaluate the healing capacity, specimens with and without bacteria were pre-cracked under bending stress, then unloaded and placed to cure under water. After a certain curing period the specimens were tested to failure. The results of these tests were compared with the results of tests conducted on specimens that had the same curing conditions but no pre-cracking. The healed specimens (with and without bacteria) had a higher strength than the reference specimens, which had no pre-cracking [71]. Same results were obtained even after 2 pre-cracking cycles [73]. Microscopic observation after the healing period showed calcium carbonate precipitates in the cracks in all specimens. Oxygen consumption measurements and Fourier transform infrared (FTIR) analysis of the precipitates showed bacterial activity in the SHCC with healing agent, but the lack of enhanced $CaCO_3$ precipitation could be attributed to limited amounts of feed applied [73].

In order to overcome this problem, more bacteria and food should be included in the mortar. For this purpose, particles as suggested in Sect. 3.2.2 were incorporated into the mortar mixture. The use of these particles (15 g/L of mortar) in combination with LWA are currently being tested both in the laboratory and in field applications.

Field Applications in the Netherlands

Since 2013, the mortar for concrete repair described above has been applied as patch repair in different locations in the Netherlands, under very diverse weather conditions. The first application took place during May 2013 in a garage exposed to the weather elements. In the structure to be repaired, the steel reinforcement showed signs of corrosion, which led to spalling of the concrete. During the week prior to application the temperature fluctuated around 20°C and only 1.3 mm of rainfall was registered; hence, the concrete was dry. The repair mortar was placed to

Fig. 28 Self-healing mortar applied in a tunnel in the Netherlands: (**a**) surface preparation and (**b**) monitoring for shrinkage and possible delamination

completely cover the reinforcement. After 1.5 years the patch repair is in good condition without signs of deterioration.

The repair mortar was also applied under extremely moist conditions in an underground parking garage where the retaining walls had suffered water leakage problems for months. Traces of previous repair materials were removed with a hisel prior to casting, including traces of bitumen. The mortar was cast in place and no curing compound was applied. A month after casting a very small amount of leakage was still spotted, but it has not led to spalling even after 6 months. Another indoor application took place in a tunnel that was built in the late 1930s. The concrete slab showed signs of steel bar corrosion and concrete spalling. A concrete patch of about $250 \times 500 \times 110$ mm^3 was removed and the exposed steel bars were cleaned of traces of corrosion (Fig. 28a). After casting the mortar, the patch was covered with a geotextile material for the first 7 days. The possible cracking or delamination as a result of restrained shrinkage was monitored for the following 2 months (Fig. 28b). No delamination occurred and only very small shrinkage cracks were observed.

5 Conclusions

Autogenous healing of concrete and mortar can be drastically enhanced by combining with limestone originating from bacterial activity. The bio-based self-healing agents described in this review use several bacterial strains that follow

different metabolic pathways; yet, in all systems the final healing product that fills the cracks is limestone. The selected bacterial strains are able to survive in the alkaline concrete environment. In order to obtain maximum protection during concrete mixing and to yield the highest survival potential for many years, encapsulation of the healing agent is of great importance, although it can affect the mechanical properties of the material.

The development of bio-based self-healing concrete aims to minimize durability problems related to cracking. Therefore, crack closure observations together with water permeability tests were conducted to assess the recovery of water tightness after healing treatment. The results proved to be very promising, thus upscaling processes and outdoor applications with bio-based self-healing concrete are currently being investigated.

In addition, the less innovative concept of concrete repair, but with novel technologies embracing environmentally friendly practices has been described. Repair systems with incorporated bacteria have been studied and applied in real structures suffering from cracking, spalling and other problems related to concrete ageing. Recent results revealed that there is definitely a market for these novel repair systems, which meet needs that conventional repair systems cannot.

Acknowledgments The authors acknowledge the financial support of European Union Seventh Framework Programme (FP7/2007–2013) under grant agreement no 309451 (HEALCON), the financial support of European Union Seventh Framework Programme (FP7/2007–2013) under grant agreement no 290308 (Marie Curie Program action SHeMat "Training Network for Self-Healing materials: From Concepts to Markets") and the financial support from the Netherlands Enterprise Agency (IOP grants SHM012020 and SHM01018).

References

1. 5th International conference on self-healing materials (ICSHM2015), Durham, NC, 24–24 June 2015. icshm2015.pratt.duke.edu/icshm-2015-extended-abstracts
2. Edvardsen C (1999) Water permeability and autogenous healing of cracks in concrete. ACI Mater J 96:448–454
3. Mihashi H, Nishiwaki T (2012) Development of engineered self-healing and self-repairing concrete-state-of-the-art report. J Adv Concr Technol 10:170–184
4. Li VC, Yang EH (2007) Self healing in concrete materials. In: van der Swaag S (ed) Self healing materials, vol 100. Springer, Dordrecht, pp 161–193
5. Reinhardt HW, Jooss M (2003) Permeability and self-healing of cracked concrete as a function of temperature and crack width. Cem Concr Res 33:981–985
6. Neville A (2002) Autogenous healing-a concrete miracle? Concr Int 24:76–82
7. Palin D, Wiktor V, Jonkers HM (2015) Autogenous healing of marine exposed concrete: characterization and quantification through visual crack closure. Cem Concr Res 73:17–24
8. Clear C (1985) The effects of autogenous healing upon the leakage of water through cracks in concrete. Cement and Concrete Association technical report no 559
9. Van Tittelboom K, Gruyaert E, Rahier H, De Belie N (2012) Influence of mix composition on the extent of autogenous crack healing by continued hydration or calcium carbonate formation. Construct Build Mater 37:349–359

10. Benini S, Gessa C, Ciurli S (1996) *Bacillus pasteurii* urease: a heteropolymeric enzyme with a binuclear nickel active site. Soil Biol Biochem 28:819–821
11. Wang J (2013) Self-healing concrete by means of immobilized carbonate precipitating bacteria. Ph.D. thesis, Ghent University, Ghent
12. Wang J, Van Tittelboom K, De Belie N, Verstraete W (2010) Potential of applying bacteria to heal cracks in concrete. In: Zachar J, Claisse P, Naik TR, Ganjian E (eds) Proceedings of the 2nd international conference on sustainable construction materials and technologies (SCMT2), Ancona, 28–30 June 2010, pp 1807–1819. Available at http://www.claisse.info/2010%20papers/k48.pdf
13. Silva F (2015) Up-scaling the production of bacteria for self-healing concrete application. Ph. D. thesis, Ghent University, Ghent
14. Silva F, De Belie N, Boon N, Verstraete W (2015) Production of non-axenic ureolytic spores for self-healing concrete applications. Construct Build Mater. doi:10.1016/j.conbuildmat.2015.05.049
15. Wang J, De Belie N, Verstraete W (2012) Diatomaceous earth as a protective vehicle for bacteria applied for self-healing concrete. J Ind Microbiol Biotechnol 39:567–577
16. De Belie N, Wang J, Soens H, Durka M (2013) Microcapsules and concrete containing the same. UK patent application number: 1303690.0; WO 2014131913 A1
17. Wang J, Soens H, Verstraete W, De Belie N (2014) Self-healing concrete by use of microencapsulated bacterial spores. Cem Concr Res 56:139–152
18. Wang J, Snoeck D, Van Vlierberghe S, Verstraete W, De Belie N (2014) Application of hydrogel encapsulated carbonate precipitating bacteria for approaching a realistic self-healing in concrete. Construct Build Mater 68:110–119
19. Mignon A, Graulus G, Snoeck D, Martins J, De Belie N, Dubruel P, Van Vlierberghe S (2015) pH-sensitive super absorbent polymers: a potential candidate material for self-healing concrete. J Mater Sci 50(2):970–979
20. Wang J, Mignon A, Snoeck D, Wiktor V, Boon N, De Belie N (2015) Application of modified-alginate encapsulated carbonate producing bacteria in concrete: a promising strategy for crack self-healing. Front Microbiol. doi:10.3389/fmicb.2015.01088
21. Wang J, Dewanckele J, Cnudde V, Van Vlierberghe S, Verstraete W, De Belie N (2014) X-ray computed tomography proof of bacterial based self-healing in concrete. Cem Concr Compos 53:289–304
22. Jonkers HM, Thijssen A, Muyzer G, Copuroglu O, Schlangen E (2010) Application of bacteria as self-healing agent for the development of sustainable concrete. Ecol Eng 36:230–235
23. Wiktor V, Jonkers HM (2010) Quantification of crack-healing in novel bacteria-based self-healing concrete. Cem Concr Compos 33:763–770
24. Tziviloglou E, Jonkers HM, Schlangen E (2014) Bacteria-based self-healing concrete to increase liquid tightness of cracks. In: van Breugel K, Koenders EAB (eds) Proceedings of the first conference on ageing of materials and structures (AMS14), Delft, 26–28 May 2014. Delft University of Technology, Delft, pp 650–655
25. Mera Ortiz W (2011) Comportamiento sísmico de paredes de mampostería con refuerzo artificial y natural no-metálico (in Spanish). Universidad Católica de Santiago de Guayaquil, Guayaquil
26. Sierra Beltrán MG, Jonkers HM, Mera Ortiz W (2013) Concrete with Abaca fibres and bacteria to improve sustainability and performance of irrigation Canals in Ecuador. In: Proceedings of the 1st international conference on natural fibres, Guimaraes, 9–11 June 2013
27. Jonkers HM, Mors RM (2012) Full scale application of bacteria-based self-healing concrete for repair purposes. In: Alexander MG, Beushausen H-D, Dehn F, Moyo P (eds) Concrete repair, rehabilitation and retrofitting III: Proceedings of the 3rd international conference on concrete repair, rehabilitation and retrofitting (ICCRRR-3), Cape Town, 3–5 Sept 2012. Taylor & Francis, London, pp 967–971
28. Francisconi J (2013) Bacteria-based self-healing mortar through embedded compressed particles. M.Sc. thesis, University of Bologna, Bologna and Delft University of Technology, Delft

29. de Koster SAL, Mors RM, Nugteren HW, Jonkers HM, Meesters GMH, van Ommen JR (2015) Geopolymer coating of bacteria-containing granules for use in self-healing concrete. Procedia Eng 102:475–484
30. Lawant SAG, Mors RM, Jonkers HM, Meesters GMH, Nugteren HW (2015) Developing a geopolymer based coating for use in self-healing concrete. Paper presented at geopolymers – an ECI conference, Hernnstein, 24–29 May 2015
31. Mors RM, Jonkers HM (2015) Reduction of water permeation through cracks in mortar by addition of bacteria based healing agent. In: Proceedings of the 5th international conference on self-healing materials, Durham, NC, 22–24 June 2015
32. Van Paassen LA, Daza CM, Staal M, Sorokin DY, van der Zon W, van Loosdrecht MCM (2010) Potential soil reinforcement by biological denitrification. Ecol Eng 36:168–175
33. Hammes F, Boon N, de Villiers J, Verstraete W, Siciliano SD (2003) Strain-specific ureolytic microbial calcium carbonate precipitation. Appl Environ Microbiol 69(8):4901–4909
34. Randall DJ, Tsiu TKN (2002) Ammonia toxicity in fish. Mar Pollut Bull 45(1–12):17–23
35. Karatas I (2008) Microbiological improvement of the physical properties of soil. Ph.D. thesis, Arizona State University
36. Erşan YC, De Belie N, Boon N (2015) Microbially induced $CaCO_3$ precipitation through denitrification: an optimization study in minimal nutrient environment. Biochem Eng J 101:108–118
37. Van Der Star WRL, Taher E, Harkes MP, Blauw M, Van Loosdrecht MCM, Van Paassen LA (2009) Use of waste streams and microbes for in situ transformation of sand into sandstone. In: Proceedings of international symposium on ground improvement technologies and case histories, Singapore, 9–11 Sept 2009, pp 177–182
38. Ramachandran VS (ed) (1996) Concrete admixtures handbook, 2nd edn. Elsevier, Amsterdam
39. Justnes H (1999) Calcium nitrate as a multifunctional concrete admixture. In: Proceedings of international RILEM conference on the role of admixtures in high performance concrete, Mexico, 21–26 March 1999, pp 199–212
40. Whiffin VS, van Paassen LA, Harkes MP (2007) Microbial carbonate precipitation as a soil improvement technique. Geomicrobiol J 24(5):417–423
41. Ersan YC, De Belie N, Boon N (2015) Resilient denitrifiers wink at microbial self-healing concrete. Int J Environ Eng 2(1):28–32
42. Ersan YC, Silva FB, Boon N, Verstraete W, De Belie N (2015) Screening of bacteria and concrete compatible protection materials. Construct Build Mater 88:196–203
43. Silva FB, Boon N, De Belie N, Verstraete W (2015) Industrial application of biological self-healing concrete: challenges and economical feasibility. J Commer Biotechnol 21(1):31–38
44. Le Metayer-Levrel G, Castanier S, Orialb G, Loubièrec JF, Perthuisota JP (1999) Applications of bacterial carbonatogenesis to the protection and regeneration of limestones in buildings and historic patrimony. Sediment Geol 126(1–4):25–34
45. Tiano P, Cantisani E, Sutherland I, Paget JM (2006) Biomediated reinforcement of weathered calcareous stones. J Cult Herit 7(1):49–55
46. Jroundi F, Fernandez-Vivas A, Rodriguez-Navarro C, Bedmar EJ, González-Muñoz MT (2010) Bioconservation of deteriorated monumental calcarenite stone and identification of bacteria with carbonatogenic activity. Microb Ecol 60(1):39–54
47. De Muynck W, Boon N, De Belie N (2015) From lab scale to in situ applications – the ascent of a biogenic carbonate based surface treatment. In: Quattrone M, John VM (eds) Proceedings of XIII international conference on durability of building materials and components (DBMC), São Paulo, 2–5 Sept 2014, pp 711–718. Available at http://www.rilem.org/gene/main.php?base=500218&id_publication=435
48. Rodriguez-Navarro C, Rodriguez-Gallego M, Ben Chekroun K, Gonzalez-Munoz MT (2003) Conservation of ornamental stone by *Myxococcus xanthus*-induced carbonate biomineralization. Appl Environ Microbiol 69(4):2182–2193
49. Jimenez-Lopez C, Rodriguez-Navarro C, Pinar G, Carrillo-Rosua FJ, Rodriguez-Gallego M, Gonzalez-Munoz MT (2007) Consolidation of degraded ornamental porous limestone stone by

calcium carbonate precipitation induced by the microbiota inhabiting the stone. Chemosphere 68(10):1929–1936
50. De Muynck W, Cox K, De Belie N, Verstraete W (2008) Bacterial carbonate precipitation as an alternative surface treatment for concrete. Construct Build Mater 22:875–885
51. De Muynck W, Debrouwer D, De Belie N, Verstraete W (2008) Bacterial carbonate precipitation improves the durability of cementitious materials. Cem Concr Res 38:1005–1014
52. Qian CX, Wang JY, Ruixing W, Liang C (2009) Corrosion protection of cement-based building materials by surface deposition of $CaCO_3$ by *Bacillus pasteurii*. Mater Sci Eng C Biomim Supramol Syst 29(4):1273–1280
53. Okwadha GDO, Li J (2011) Biocontainment of polychlorinated biphenyls (PCBs) on flat concrete surfaces by microbial carbonate precipitation. J Environ Manage 92(10):2860–2864
54. Achal V, Mukherjee A, Reddy MS (2011) Effect of calcifying bacteria on permeation properties of concrete structures. J Ind Microbiol Biotechnol 38(9):1229–1234
55. Achal V, Mukherjee A, Goyal S, Reddy MS (2012) Corrosion prevention of reinforced concrete with microbial calcite precipitation. ACI Mater J 109(2):157–164
56. De Muynck W, Leuridan S, Van Loo D, Verbeken K, Cnudde V, De Belie N, Verstraete W (2011) Influence of pore structure on the effectiveness of a biogenic carbonate surface treatment for limestone conservation. Appl Environ Microbiol 77(19):6808–6820
57. Bang SS, Galinat JK, Ramakrishnan V (2001) Calcite precipitation induced by polyurethane-immobilized *Bacillus pasteurii*. Enzyme Microb Technol 28(4–5):404–409
58. Ramachandran SK, Ramakrishnan V, Bang SS (2001) Remediation of concrete using micro-organisms. ACI Mater J 98(1):3–9
59. Ramakrishnan, V, Ramesh KP, Bang SS (2001) Bacterial concrete In: Wilson AR, Asanuma H (eds). Smart materials. Proc. SPIE 4234, pp 168–176. doi:10.1117/12.424404
60. De Belie N, De Muynck W (2009) Crack repair in concrete using biodeposition. In: Alexander MG, Beushausen H-D, Dehn F, Moyo P (eds) Concrete repair, rehabilitation and retrofitting II: Proceedings of 2nd international conference on concrete repair, rehabilitation, and retrofitting (ICCRRR-2), Cape Town, 24–26 Nov 2008. Taylor Frances, London, pp 291–292
61. Van Tittelboom K, De Belie N, De Muynck W, Verstraete W (2010) Use of bacteria to repair cracks in concrete. Cem Concr Res 40(1):157–166
62. Achal V, Mukherjee A, Basu PC, Reddy MS (2009) Lactose mother liquor as an alternative nutrient source for microbial concrete production by *Sporosarcina pasteurii*. J Ind Microbiol Biotechnol 36(3):433–438
63. Achal V, Pan XL, Ozyurt N (2011) Improved strength and durability of fly ash-amended concrete by microbial calcite precipitation. Ecol Eng 37(4):554–559
64. Park SJ, Park YM, Chun WY, Kim WJ, Ghim SY (2010) Calcite-forming bacteria for compressive strength improvement in mortar. J Microbiol Biotechnol 20(4):782–788
65. Bassaran Z (2013) Biomineralization in cement based materials: inoculation of vegetative cells. Ph.D. thesis, The University of Texas at Austin
66. Ghosh S, Biswas M, Chattopadhyay BD, Mandal S (2009) Microbial activity on the microstructure of bacteria modified mortar. Cem Concr Compos 31(2):93–98
67. Van Lancker B (2013) Consolidation of natural stone using microorganisms and nanoparticles. M.Sc. thesis, Civil Engineering, Ghent University
68. Li VC (1993) From micromechanics to structural engineering – the design of cementitious composites for civil engineering applications. JSCE J Struct Mech Earthq Eng 10(2):37–48
69. Li M (2009) Multi-scale design for durable repair of concrete structures. Ph.D. thesis, University of Michigan, Ann Arbor
70. Zhou J (2011) Performance of engineered cementitious composites for concrete repairs. Ph.D. thesis, Delft University of Technology
71. Sierra Beltran MG, Jonkers HM, Schlangen E (2014) Characterization of sustainable bio-based mortar for concrete repair. Construct Build Mater 67:344–352
72. Sierra Beltran MG, Jonkers HM, Schlangen E (2014) Performance of SHCC with bacteria for concrete patch repair. In: Forde MC (ed) Structural faults and repair: Proceedings of the 15th

international conference and exhibition on structural fault and repair, London, 6–8 July 2014, pp1–18. The Electrochemical Society, Pennington, NJ
73. Sierra Beltran MG, Jonkers HM, Schlangen E (2015) Self-healing capacity of a strain-hardening cement-based composites (SHCC) with bacteria. In: Proceedings of 7th RILEM workshop on high performance fibre reinforced cement composites, Stuttgart, 1–3 June 2015

Adv Polym Sci (2016) 273: 387–408
DOI: 10.1007/12_2015_337

Published online: 2 February 2016

Self-Healing Metals

Blazej Grabowski and C. Cem Tasan

Abstract Designing self-healing in metals is a challenging task. Self-healing concepts successfully applied in polymers cannot be directly transferred because of different energetics. This has detained the field of self-healing metals, as evidenced by absolute publication numbers. Yet, relative publication numbers indicate a rapidly increasing interest in recent years triggered by the potential economic impact of advanced metallic materials. This chapter reviews all currently available self-healing concepts in bulk metallic materials. We provide a classification into two conceptually distinct routes: (1) autonomous self-healing of nanovoids at the nanoscale, aiming at a prevention of large-scale damage and (2) non-autonomous self-healing of macrocracks by an external trigger such as heat. The general idea of each self-healing concept is comprehensibly introduced, relevant publications are reviewed, and the characteristics of the concepts are compared. Finally, we discuss current constraints and identify the most promising concepts.

Keywords Crack closure • Nanoparticles • Phase transformation • Precipitation • Self-healing metals • Shape-memory alloys • Solder

Contents

B. Grabowski (✉) and C.C. Tasan
Max-Planck-Institut für Eisenforschumg GmbH, 40237 Düsseldorf, Germany
e-mail: b.grabowski@mpie.de

1 Introduction: Status of Self-Healing Metals

The field of self-healing materials is dominated by polymer-based systems. This dominance has been stressed in other reviews (see, e.g., [1–6] and the accompanying reviews in this volume) and it also becomes apparent by analyzing publication numbers in the field of self-healing materials. Figure 1 shows an exponentially increasing number of polymer-based publications on self-healing (blue line) with an absolute number of 250 in 2014. A similar search for self-healing concrete and ceramics and self-healing metals reveals much smaller numbers (orange and gray lines). In fact, the gray line for metals is an overestimate. Optimization of the search keywords to rule out metallic ion-related self-healing polymers and surface oxides shows the true self-healing metal curve to be the black line.

The reason for this dominance of polymers is the fact that the self-healing concept is highly compatible with the energetic properties of polymers. Chemical reactions in polymers are very efficient, that is, they produce a significant energy

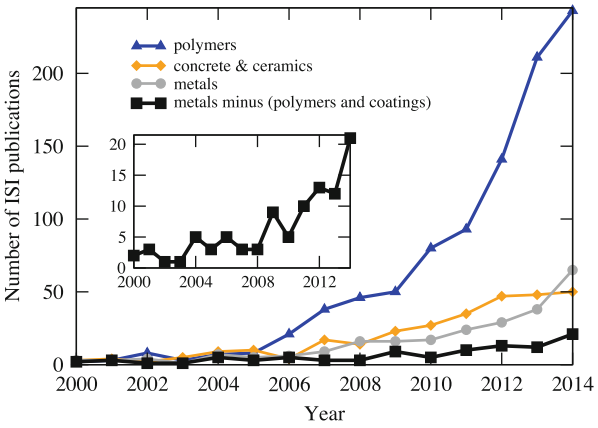

Fig. 1 Publication numbers from ISI Web of Knowledge for the last 14 years in the field of self-healing polymers, concrete and ceramics, and metals. The search term for metals (*gray line*) was TOPIC: ("self-healing") AND TOPIC: (metal). Because the search term includes polymer self-healing studies employing "metal-ions" and also polymeric or oxide self-healing coating studies, a corrected search term was employed for metals, TOPIC: ("self-healing") AND TOPIC: (metal) NOT TOPIC: (*polymer* OR *coating*). The latter results are shown by the *black line* (enlarged in the *inset*) and give a more representative publication curve for bulk metallic materials, which are the main focus of this review

release compared with the typical bonding strength. Relatively fast and massive diffusional processes are thus feasible, even at room temperature. These processes can be utilized to design self-healing agents that are autonomously activated and transported to sites of damage localization.

Atomic bonding is strong in concrete and ceramics and in metals. Diffusional processes that are needed to transport the self-healing agents to the damaged sites are therefore slow at ambient temperatures. The traditional concepts successfully applied in polymer-based self-healing materials cannot be directly transferred. The concepts must be modified or novel concepts must be developed. For that reason, the fields of self-healing concrete and ceramics and self-healing metals are less mature than that of self-healing polymers. In fact, judging by the absolute publication numbers (inset in Fig. 1), the field of self-healing in bulk metallic materials is in its infancy.

Yet, the black curve (inset of Fig. 1) shows a significant positive gradient over the last few years, indicating a rapidly increasing interest. This interest can be understood if one considers the role of metallic materials in the world today and the ecological and economic concerns associated with their production, use, and re-use. Although often well hidden, it is the discovery and employment of advanced metallic materials that undoubtedly trigger changes that revolutionize, for example, energy, transportation, health, safety, and infrastructure sectors. Examples are numerous: advanced high-strength steels enable lighter and safer cars, aluminum alloys enable larger and more fuel-efficient planes, creep-resistant nickel alloys enable more efficient power plants and long-life plane turbines, etc. All in all, metals-related industries account for $\sim$3.5 billion US$ of exports in 2013 in the world [7]. However, this high rate of industrialization is responsible for increasing natural problems, primarily regarding climate change [8]. Therefore, to avoid harmful effects the Intergovernmental Panel on Climate Change (IPCC) has recommended a challenging cut of 50–85% in global emission of greenhouse gases by 2050 [9]. Detailed investigations reveal that material efficiency options are compulsory in achieving this goal [8]. It is for this reason that, despite the inherent difficulties, successful self-healing in bulk metals would have enormously positive consequences, as such mechanisms have the potential to increase service lifetime significantly.

2 Classification of Self-Healing Metals

Schematics, features, and relevant publications for the presently available self-healing concepts in bulk metals are compiled in Fig. 2 and Tables 1 and 2, respectively. We found it useful to classify the concepts by employing the characteristic length scale of the healed damage. According to this classification there are two groups defined by (1) healing of nanoscale voids in the nanometer range (*precipitation* and *nanoSMA-dispersoids* concepts) and (2) healing of macroscale cracks in the millimeter range (*SMA-clamp&melt*, *solder tubes/capsules*, *coating*

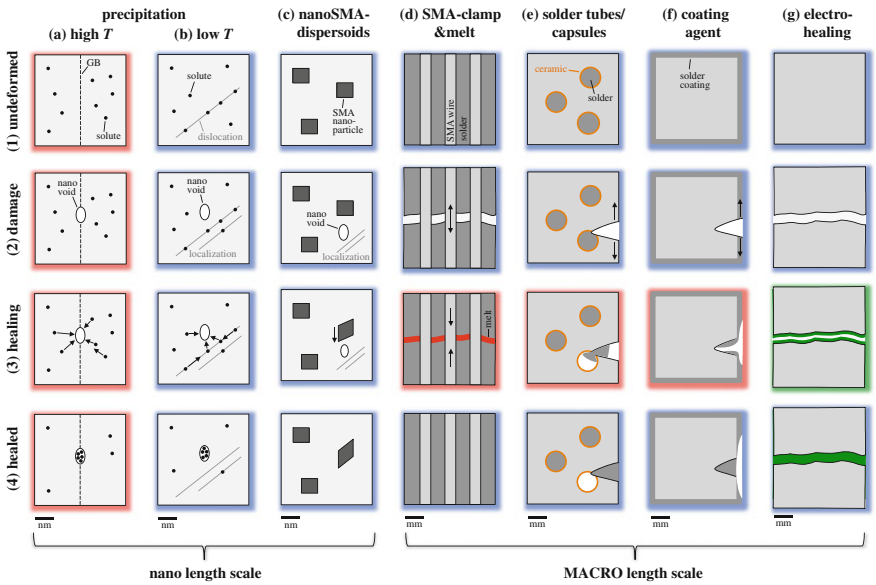

Fig. 2 (**a**–**g**) Overview of the proposed/investigated self-healing concepts in metals. Rows *1–4* indicate the requirements and processes for each concept. *Background shading* indicates the conditions required; *red* high temperature, *blue* low temperature, *green* applied voltage. See main text for details

agent, and *electro-healing* concepts). The healing within each group occurs exclusively on the respective scale. Within the first group, only the nanoscale is accessible and, thus, if macrocracks appear, they cannot be healed and lead eventually to fracture. That stated, because the crack coalescence process involves interaction of spatially dispersed cracks, it can be safely proposed that these concepts would also be effective in slowing down the overall failure process. Within the second group, only the macroscale is observable and, thus, nanovoids are not healed until they grow or coalesce to form macrocracks. This could be seen as a disadvantage for the service life because the presence of unhealed nanovoids would cause fast growth of secondary macrocracks, even if the first macrocrack is healed. It should, as a general note, be stated that the success of any self-healing strategy needs to be considered in connection with the capabilities of the base microstructure. That is, introduction of a nanoscale self-healing mechanism could be more crucial in rendering an originally brittle microstructure sufficiently tough for application, compared to its effect in a microstructure that already had plenty of microstructural hardening mechanisms.

Our classification corresponds well with the classification into damage prevention and damage management introduced by van der Zwaag [10]. The self-healing concepts in the nanoscale group pursue the management of nanoscale damage in order to prevent macroscale damage (see Table 1, rows 1–3). In contrast, the self-

Table 1 Key features of the different self-healing concepts in metals

		Precipitation		NanoSMA-dispersoids	SMA-clamp&melt	Solder tubes/capsules	Coating agent	Electro-healing
		High T precipitation	Low T precipitation					
1.	Characteristic length scale classification	Nano	Nano	Nano	MACRO	MACRO	MACRO	MACRO
2.	Nanoscale damage	Management	Management	Management	Invisible	Invisible	Invisible	Invisible
3.	Macroscale damage	Prevention	Prevention	Prevention	Management	Management	Management	Management
4.	Type according to [11]	Solid-state healing	Solid-state healing	Solid-state healing	Liquid assisted	Liquid assisted	Liquid assisted	Electrolyte assisted
5.	Matrix material	Fe–B–Ce, Fe–B–N–Ce	Al–Cu	Ti–Nb, Ti–V	Sn–Bi, Mg–Zn	Al	Ti	Ni
6.	Reinforcement solutes/material	B, N	Cu	Ti–Ni	Ti–Ni	Sn–Pb	In–Sn	Metallic ions in electrolyte
7.	Phase transition involved	Solute precipitation	Solute precipitation	Austenite ↔ martensite of nano particles	Austenite ↔ martensite of wires	Solidification of solder	Solidification of coating	Chemical reaction
8.	Target property	Creep resistance	Fatigue resistance	Fatigue resistance	All properties retained	?	Fatigue resistance	Strength
9.	Autonomous?	Yes, at service temperature	Yes	Yes	No	No	No	No
10.	Number of healing cycles (ideal case)	Ratio between solute fraction and nano-void volume	Ratio between solute fraction and nano-void volume	Number of nano-particles	Unlimited	Number of capsules	Ratio between coating volume fraction and macro-crack volume	Practically unlimited if electrolyte is provided
11.	Macroscopic anisotropy	No	No	No	Yes, along the SMA wires	Yes, along the solder capsules	No	No
12.	Main advantage	Autonomous	Autonomous	Autonomous	Limitlessly applicable in ideal case	?	Applicable to "commonly used" materials	Strong bonding after crack filling

Table 2 Timeline of relevant publications for the different self-healing concepts in metals

Precipitation		NanoSMA-dispersoids	SMA-clamp&melt	Solder capsules	Coating agent	Electro-healing	
High T precipitation	Low T precipitation						
Shinya, NIMS van der Zwaag, TU Delft	Lumley, CSIRO van der Zwaag, TU Delft	Grabowski/Tasan, MPI für Eisenforschung	Olson, Northwestern Manuel, University of Florida	Rohatgi, University of Wisconsin-Milwaukee	Leser, North Carolina University Newman et al., NASA	Zheng et al., SYNL	Reviews/books including discussion on metals
2003 Shinya et al., 347 steel +TiCe+BN [12]	2002 Lumley et al., enhanced creep performance in Al alloys [24]		1997 Files, PhD thesis Fe–Ni–Co–Ti–Al and Sn+TiNi metal matrix composite [44]				
2005 Laha et al., 347 steel+ Ce+B [13]	2005 Lumley et al., enhanced fatigue performance [26]						
2006 Shinya et al., 347 steel +TiCe+BN [14]							
2007 Laha et al., 347 steel+ Cu+Ce+B [15]	2007 Wanhill, industrially inapplicable [33]	2007 Mayer et al., transformation-induced crack closure [36]	2007 Manuel, PhD Thesis [45] and [46], SnBi+TiNi metal matrix composite and modeling				2007 Lumley [32]
	2007 Lumley, review in book (van der Zwaag) [32]						
	2008 Hautakangas et al., PAS [30]			2008 Lucci et al., Al+Al_2O_3 capsule+SnPb solder [53]			2009 van der Zwaag et al. [1]
2009 Shinya, review in book (Ghosh) [23]	2009 Shinya, review in Self-healing Materials (Ghosh) [23]		2009 Manuel, review in book (Ghosh) [11]	2009 Nosonovsky et al., theoretical framework [54]			2009 Shinya [23] and Manuel [11]
2010 He et al., PAS in FeCuBN [17]							2010 Hager et al. [2]
							2010 van der Zwaag [3]
2010 He et al., in situ SANS in FeCuBN [18]							
			2011 Fisher/Manuel, SbCu+SMA and SbZn+SMA [47]				
2012 Laha et al., 347+Cu+ Ce+changing B [16]				2012 Nosonovsky/Rohatgi, review in book [55]			2012 Nosonovsky and Rohatgi [55]
2012 Karpov et al., crack closure modeling [22]							
2013 Zhang et al., in situ SANS of FeAuBN [20]		2013 Baxevanis et al., toughness due to SMA transformation [38]	2013 Wright/Manuel, AlSi+SMA [48]			2013 Zheng et al., electro-healing cracks in Ni [58]	2013 Kötteritzsch, Schubert, Hager [4]
		2013 Xu/Demkowicz, molecular dynamics of crack closure [40]					
	2014 Shahri et al., 2024 Al alloy, different R-ratios [31]	2014 Grabowski/Tasan, nanoSMA-dispersoids idea [39]	2014 Rohatgi, comercial Al alloy+NiTi [49]		2014 Leser/Newman et al., fatigue crack healing in Ti alloy [56]		2014 Drenchev and Sobczak [5]
							2014 Ferguson, Schultz, Rohatgi [6]
2015 Zhang, PhD Thesis, self-healing in Fe based alloys [21]			2015 Fergusson et al., commercial ZnAlCu alloy+SMA [50]				

healing concepts in the macroscale group pursue management of macroscale damage.

Manuel [11] has proposed a classification based on the type of phase transformation involved during healing. Row 4 of Table 1 shows that the self-healing concepts exhibiting solid-state healing according to Manuel's classification correspond to the group of nanoscale concepts. Three of the macroscale concepts utilize liquid-assisted healing in the sense that the healing temperature must be close to the melting temperature of the solder (i.e., of the low-melting material used to "glue" the cracks together). The electro-healing concept does not fit well into Manuel's original definitions (solid-state versus liquid-assisted) and we have therefore introduced a third class of electrolyte-assisted self-healing concepts.

The next section introduces the general idea of each of the available self-healing concepts, following the schematics in Fig. 2 along with relevant publications.

3 Proposed Self-Healing Concepts in Metals

*3.1 High-*T *Precipitation*

The self-healing concept using precipitation at high temperatures (high-T precipitation) is the most intensively studied concept. Corresponding studies have been initiated and advanced by the group of Shinya from NIMS, Japan [12–16] (cf. Table 2). The group of van der Zwaag from TU Delft, The Netherlands has contributed several important investigations [17–21]. Besides these experimental studies, corresponding modeling efforts have recently been started by Karpov et al. [22]. A detailed introduction to the high-T precipitation concept can be found in Shinya's review [23]. Here we concentrate on the general idea and on results obtained in recent years.

Figure 2a (first column of Fig. 2) shows the relevant requirements and processes of the high-T precipitation concept. The original microstructure (Fig. 2a, row 1) must contain a supersaturated amount of solute atoms. The supersaturation can be achieved by conventional metallurgical treatment, given that the phase diagram of the constituent atoms shows sufficient solubility of the solute atoms at high temperatures. Quenching from these temperatures produces a metastable, supersaturated solid solution, which upon additional aging tends to precipitate secondary phases. However, for the high-T precipitation concept to work properly, precipitation should not happen spontaneously throughout the microstructure, but only in localized regions where nanovoids are present. This is illustrated in Fig. 2a, row 2, where a nanovoid forms at a grain boundary during the damage phase and acts as an attractor for the solute atoms during the healing stage (Fig. 2a, row 3) and eventually as a nucleation site for the precipitation process (Fig. 2a, row 4).

An important feature of the high-T precipitation concept is that the temperature during the service lifetime must be sufficiently high. This is reflected by the name

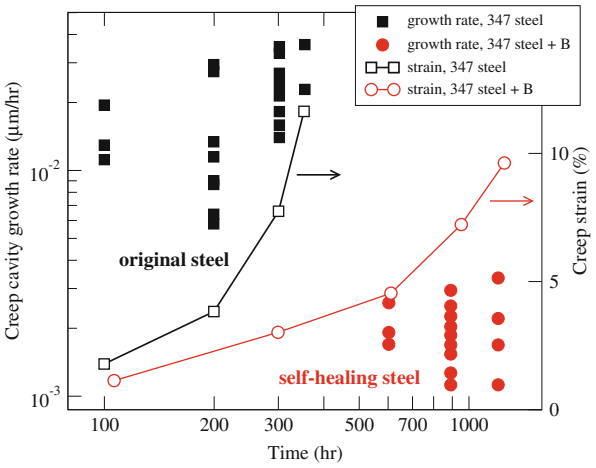

Fig. 3 Creep cavity growth rate and creep strain with creep exposure time in Ar at 750°C and 78 MPa. The growth rate in boron-modified 347 steel is slower by an order of magnitude than that of standard 347 steel. Figure based on data from Laha et al. [13]

itself and is also highlighted in Fig. 2a by the red shaded background behind all four stages. An elevated temperature is required to enable lattice diffusion of the solutes toward the nanovoids, as indicated by the arrows in the healing stage. As mentioned above, the temperature must be not too high to prevent nucleation of precipitates at sites other than the nanovoids.

The described conditions on the phase diagram and for the service temperatures give significant constraints on the materials and applications for the high-*T* precipitation concept. One successful example was provided by Laha et al. [13], who applied this concept to improve the creep resistance of heat-resisting steels. The reference material studied by the authors was a standard 347 austenitic stainless steel, which is used in high temperature applications. A second modified steel with self-healing ability was prepared by adding boron to the standard 347 steel. The B atoms act as the solute healing agent by diffusing to the nanovoids and precipitating at the void surfaces. The precipitation was confirmed by Auger spectroscopy, and a significant improvement in creep properties was demonstrated by corresponding tests [13] (cf. Fig. 3). Further successful investigations were conducted by employing B together with N as solute atoms [14] and in Cu-modified heat-resisting steel [15].

A slightly different route toward understanding and optimizing the high-*T* precipitation concept was undertaken by the group of van der Zwaag from TU Delft. Rather than investigating complex industrial steel grades, they focused on high purity model systems of FeCu + BN for analysis of the fundamental mechanisms. In addition to considering model systems, high resolution techniques were employed for that purpose. For example, He et al. [17] used positron annihilation spectroscopy (PAS) to clearly confirm that the addition of B and N significantly accelerates Cu precipitation in a Fe–Cu alloy and that most open volume defects (nanovoids) can be closed. This result was corroborated by He et al. [18] using in-situ time-resolved small-angle neutron scattering (SANS) measurements. They found that Cu precipitation occurs in the form of spherical nanoscale precipitates

inside the grains and in the form of dislocation and interface decoration. More recent investigations by the Delft group focused on replacing Cu by Au (i.e., FeAuBN) [20, 21]. The choice of Au was motivated by an atomic-scale analysis showing that homogenous nucleation can be prevented while enhancing nucleation at the damaged nanovoids sites [20]. SANS measurements indeed confirmed that Au strongly precipitates at nanovoids [20], and creep tests showed an improved creep lifetime [21].

3.2 Low-T Precipitation

The low-*T* precipitation concept is closely related to the high-*T* precipitation concept, with the main difference being that at all stages during service the temperature can be lower, as indicated by the blue background shading in Fig. 2b. The original idea was introduced by the group of Lumley from CSIRO, Australia [24–27] and further work was contributed by the TU Delft group [28–31] (Table 2). We give here a concise summary, while a detailed introduction can be found in reviews by Shinya [23] and Lumley [32].

As in the case of the high-*T* precipitation concept, the microstructure required for the low-*T* precipitation concept must contain supersaturated solute atoms. A distinctive and necessary feature for the healing process is that the solute atoms tend to segregate to dislocation cores, as indicated in Fig. 2b, row 1. In particular, the solute atoms within the dislocation cores can be considered mobile even at low temperatures, which is a consequence of pipe diffusion. When localization of dislocations in pile ups leads to stress concentration and formation of nanovoids, the mobile solute atoms are attracted and diffuse through the dislocations toward the stress region. Precipitation within the nanovoids eventually leads to void closure and healing of the damaged region.

Potential material systems with such a self-healing ability are Al alloys supersaturated with Cu solutes. A crucial requirement is that the Al alloys are prepared in an under-aged condition, that is, aging should be aborted before the peak strength of the material is reached. This condition guarantees that there are enough Cu atoms left in solution for performing the self-healing process in the form of precipitation.

Lumley studied under-aged Al alloys in detail and showed that they can posses enhanced creep behavior [24], fracture toughness [25], and fatigue resistance [26]. In particular, enhanced fatigue resistance (Fig. 4) is relevant in the present context because it can be explained in terms of the low-*T* precipitation concept, that is, Cu atoms are assumed to diffuse through dislocations by pipe diffusion toward the nanovoids and precipitate there, leading to void closure. This assumption is supported to some extent by positron annihilation spectroscopy investigations performed by Hautakangas et al. [28, 29]. Other possible mechanisms for the enhanced fatigue resistance are conceivable: (1) a general reduction in dislocation mobility caused by the Cu solutes and (2) localized matrix hardening as a result of dynamic precipitation at dislocations [27]. The actual contribution of nanovoid

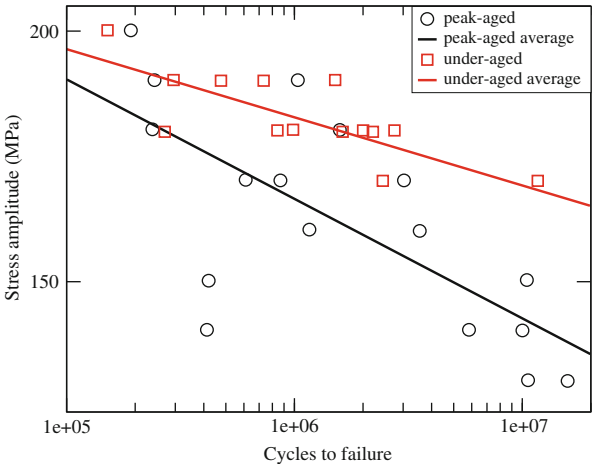

Fig. 4 Comparison between fatigue life of standard, peak-aged, and under-aged Al alloys for a stress ratio $R = -1$. Overall, the under-aged material shows a better fatigue resistance because it reaches larger cycles to failure at the same stress level. Figure based on data from Lumley et al. [26]

closure as a result of Cu precipitation to the enhanced fatigue resistance is not yet fully clarified.

Besides this uncertainty in the actual mechanism, a technologically more important issue was raised by Wanhill [33]. By comparing various fatigue studies, he concluded that self-healing in commercially used Al alloys, particularly in aerospace applications, is inapplicable. The reasons are that most damage is either too large to be healed or is located on the surface of the component, where environmental effects could potentially hinder crack healing. These statements possibly explain the rather limited interest in the low-T precipitation concept in recent years (cf. Table 2).

3.3 NanoSMA-Dispersoids

Crack closure is a well-known phenomenon under cyclic loading conditions [34], and phase transformation is often discussed as one of the mechanisms responsible for it [35, 36]. Although direct experimental verification of the microstructural processes is scarce because of experimental challenges [37], results are available for shape memory alloys (SMA) [38], where the role of the transformation is more evident, clarifying the strength of this mechanism. Motivated by these observations, the nanoSMA-dispersoids self-healing concept was only very recently proposed by the present authors [39]. This concept belongs to the group of nanometer-scale healing mechanisms and the general idea is that nanovoids are closed by phase-transforming SMA nanoparticles. Note that the concept is presently in the development stage and that the self-healing ability has yet to be confirmed.

The nanoSMA-dispersoids self-healing idea is sketched in Fig. 2c. The original microstructure consists of a host matrix with embedded coherent SMA

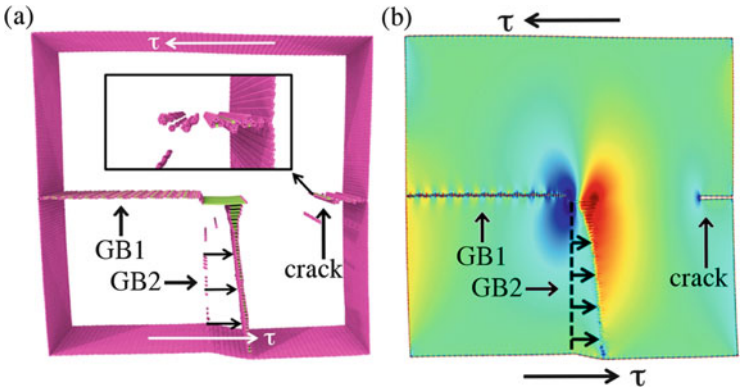

Fig. 5 Nanocrack healing by stress-driven grain boundary (GB) migration. The stress (τ) is applied such that GB1 does not move while GB2 moves toward the crack. (**a**) Atomistic picture, with the perfect bulk atoms removed for clarity. (**b**) Resulting strain fields (*blue* compressive, *red* tensile field). Figure adapted from [40] with permission

nanoparticles (Fig. 2c, row 1). The nanoparticles are stabilized by the host matrix in their austenite phase (i.e., high temperature phase). When damage is initiated in the form of dislocation localization and nanovoid formation (Fig. 2c, row 2), the nanoparticles are activated. In particular, the stress field of the nanovoid is thought to trigger phase transformation of the SMA nanoparticle from the austenite into the martensite phase. This phase transformation is accompanied by a strong change in the shape of the particle (Fig. 2c, row 3) that induces local strain fields on the host matrix and eventually leads to crack closure (Fig. 2c, row 4).

A crucial stage of the described self-healing process is crack closure by the phase-transforming nanoparticle. Recent theoretical simulations provide strong support that such a crack closure scenario is indeed realistic. Xu and Demkowicz [40] investigated the migration of a stress-driven grain boundary and found that close-by nanocracks are significantly affected. As illustrated in Fig. 5, when a stress-driven grain boundary (GB2) moves toward the crack, the size of the crack is reduced and, depending on the stress magnitude, the crack can be completely closed leaving behind only geometrically necessary dislocations [40]. Detailed analysis showed that stress fields around the grain boundaries (see blue and red fields in Fig. 5b) generated image stress fields at the crack tip, eventually leading to crack healing.

In the work of Xu and Demkowicz [40], crack closure was achieved by an externally driven (i.e., non-autonomous) grain boundary migration. In the nanoSMA-dispersoids self-healing concept, the moving grain boundary is replaced by the moving interface between host matrix and nanoparticle during its phase transformation. If similar stress fields can be achieved by the SMA nanoparticle transformation, as in the case of the moving grain boundary, autonomous nanovoid closure can be achieved.

A main challenge in implementing the nanoSMA-dispersoids concept in practice is production of the desired microstructure (Fig. 2c, row 1). For the nanoparticles, NiTi SMA is very well suited as it has been thoroughly investigated and shows significant shape changes during transformation. Present investigations focus on determining an ideal alloying addition to NiTi, with the condition that a double phase field connecting the NiTi phase with a solid solution is present in the phase diagram. Such a phase diagram would allow use of an annealing step, followed by an aging treatment to nucleate NiTi SMA nanoparticles inside the solid solution host matrix. To optimize the search for the alloying element, highly accurate finite temperature first-principles simulations are currently being developed [41–43] to provide the required phase stability dependencies.

3.4 SMA-Clamp&Melt

The SMA-clamp&melt concept (also called SMA reinforcement or SMA self-healing) is possibly the oldest self-healing concept for bulk metals. First investigations were started at the end of the 1990s by the group of Olson at the Northwestern University of Chicago, USA [44]. Manuel continued research at Northwestern [45, 46] and later at the University of Florida [47, 48] in collaboration with the Materials Science Division of NASA [48]. Recently, the group of Rohatgi at the University of Wisconsin-Milwaukee also began investigations [49, 50] (cf. Table 2). Because of the wide interest, the SMA-clamp&melt concept is currently the best-investigated macroscale concept. A detailed introduction can be found in the review by Manuel [11]. Here we discuss only the general idea of this concept.

Figure 2d illustrates the required microstructure and the self-healing process. The crucial difference from the self-healing concepts discussed so far relates to the characteristic length scale. The relevant microstructural features as well as the cracks to be healed are in the millimeter regime. In particular, a composite microstructure is required that consists of SMA reinforcement wires embedded in a solder matrix material (Fig. 2d, row 1). The solder material is the “glue”, and for that purpose it must have a melting point that is considerably lower than that of the SMA wires.

When the stress applied to a SMA–solder composite exceeds the ultimate tensile strength of the solder material, a crack is produced in the solder material (Fig. 2d, row 2). The SMA wires have a higher ultimate tensile strength and they respond to the applied stress by a transformation into the martensite phase. To achieve self-healing, the composite sample needs to be externally heated (cf. red shaded background in the healing stage; Fig. 2d, row 3) to a temperature above the austenite transition temperature. The increase in temperature leads to phase transformation of the SMA wires from the martensite to the high-temperature austenite phase. The transition is accompanied by a compressive stress that contracts the composite sample, bringing the cracked surfaces together. The temperature needs to be further increased toward the melting point of the solder. Once the cracked

surfaces have started to melt, they can rejoin and the temperature can be reduced to the original, low value.

A unique advantage of this self-healing concept is that (in the ideal case) it can be repeated limitlessly. This is indicated in Fig. 2d by the fact that the original structure (Fig. 2d, row 1) is exactly the same as the healed structure (Fig. 2d, row 4). A marked disadvantage is the strong anisotropic response. As evident from the schematics, an applied horizontal stress causes a crack, leading to catastrophic fracture of the sample. Extensions of the present concept toward a three-dimensional SMA wire network are conceivable, preventing such material failure. Whether this idea can be implemented in practice remains to be shown.

A further disadvantage, common to all macroscale approaches, is the requirement for an externally applied trigger to activate the self-healing process. In the case of the SMA-clamp&melt concept, the external trigger is the heat transfer required to transform the SMA wires and melt the solder. This renders the process non-autonomous, such that possible industrial applications would require routine service intervals.

A successful example of the SMA-clamp&melt concept has been presented by Manuel and Olson [46]. The authors used the CALPHAD method [51] to select and optimize the material system and its properties. The finally selected material was a Sn-13at%Bi alloy matrix (Sn–Bi alloy with 13 Bi atoms and 87 Sn atoms per 100 atoms) containing continuous uniaxially oriented equiatomic TiNi SMA wires. The composition of the matrix was designed for a healing temperature of 169°C, with a 20% liquid fraction. This proof-of-concept composite was subjected to a tensile test, which confirmed more than 95% recovery of the ultimate tensile strength after self-healing [46]. Images of damaged and healed samples are presented in Fig. 6.

Recent investigations have been directed toward industrially more relevant host matrix materials. For instance, Ferguson et al. [50] investigated the self-healing properties of a commercial ZnAlCu alloy enforced with TiNi SMA wires. A crucial insight was that encasing the samples in sand was necessary to maintain structural stability. However, even with this auxiliary technique, the retained ultimate tensile strength was only 30%. In another study, NASA [48] tested Al-based alloys with the focus on improving the damage tolerance of aeronautical structures. The authors [48] could show that an AlSi matrix reinforced with 2 vol% of SMA wires can retain more than 90% ultimate tensile strength after self-healing.

3.5 Solder Tubes/Capsules

The solder tubes/capsules concept is very interesting because it emulates the original self-healing concept employed in polymers [52]. It was tried by the group of Rohatgi at the University of Wisconsin-Milwaukee [53, 54] and is discussed in detail in the book by Nosonovsky and Rohatgi [55].

The central idea of the solder tubes/capsules concept is to encapsulate a solder material inside ceramic capsules or ceramic tubes, inside a host matrix of a higher

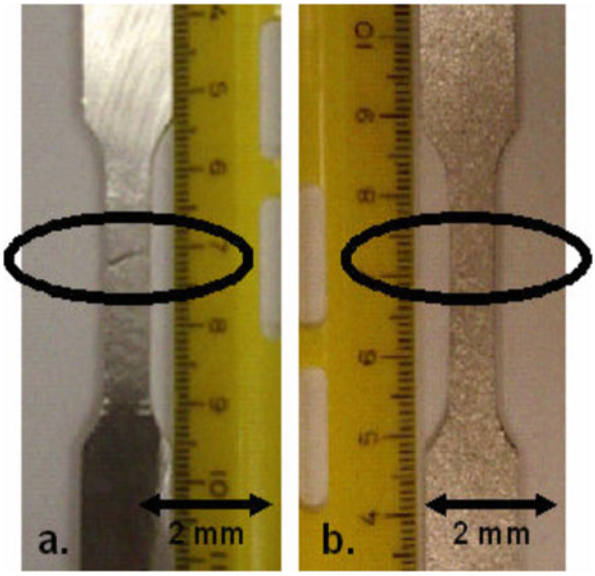

Fig. 6 Demonstration of the SMA-clamp&melt self-healing concept. (**a**) Damaged SMA-matrix composite with a through-matrix crack. (**b**) Sample after self-healing. Figure taken from [46] with permission

melting material (Fig. 2e, row 1). Compared with the SMA-clamp&melt concept discussed in the previous section, the role of the solder is critically modified in the solder tubes/capsules concept. For the SMA-clamp&melt concept, the solder constitutes the host matrix and the crack to be healed appears in the solder itself (i.e., it is the ultimate tensile strength of the solder that determines crack initiation). For the solder tubes/capsules concept, the host matrix is composed of a different, high-melting material with an ultimate tensile strength that can be significantly larger than that of the solder. The solder is activated only when a crack in the host matrix has formed (Fig. 2e, row 2). Activation of the solder is achieved by increasing the temperature above the melting temperature of the solder (Fig. 2e, row 3). After activation, the solder wets the crack surfaces, fills the crack as a result of capillary pressure and surface tension, and solidifies, thereby closing the crack.

Despite the conceptual analogy to the successful self-healing concept in polymers, the solder tubes/capsules concept applied to metals involves many complications. Designing the original microstructure (Fig. 2e, row 1) is difficult when solder capsules are used. The ceramic capsules need to contain holes so that the solder can be filled in. The filling is easier for through-thickness tubes, but these introduce an anisotropy, as in the case of SMA reinforcement wires. Three, even more critical problems with the solder tubes/capsules concept occur during the damage and healing phases. First, for the solder to have any effect, the crack must not only hit a capsule, but must also destroy the ceramic shell such that the solder can escape. This condition is not easily fulfilled because the crack can spread along the interface of the host matrix and the ceramic shell. Second, even if the first condition is fulfilled and the solder can be activated to flow into the crack, the solder must wet the crack properly and, more importantly, bind strongly to the crack

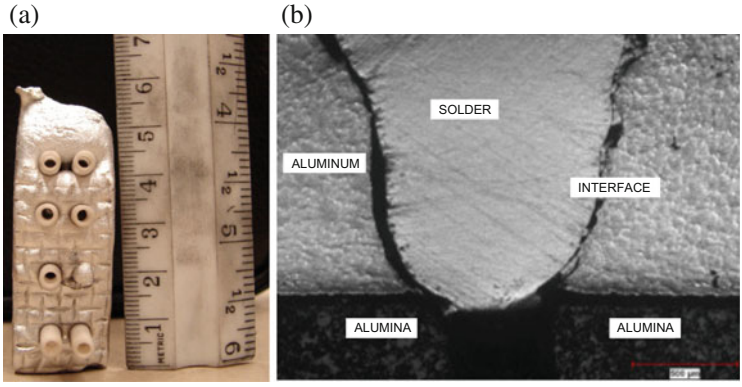

Fig. 7 (**a**) Al host matrix with embedded Al_2O_3 tubes (solder has not been filled in yet). (**b**) Solder filling a crack after the self-healing process. The interface between solder and Al matrix shows high porosity. Figure adapted from [55] with permission

surface. Third, after the healing process new voids are created inside the bulk (cf. Fig. 2e, row 4), possibly leading to additional weakening of the sample.

In practice, the described conditions appear too difficult to be fulfilled in metallic systems. This probably explains why corresponding studies are very limited (Table 2). Lucci et al. [53] have investigated the possibility of embedding Al_2O_3 ceramic tubes filled with Sn_3Pb_2 solder inside an aluminum host matrix (cf. Fig. 7a). To simulate the self-healing process, an artificial crack was intentionally created such that one of the ceramic tubes was pierced. Although crack filling was achieved after heating above the melting temperature of the solder, the interface between solder and Al matrix was found to be very weak as a result of high porosity (Fig. 7b). In fact, more detailed scanning electron microscope studies revealed that no portion of the solder is in intimate contact with the aluminum and thus the bonding would not be sufficient to stop a realistic crack from growing [53].

3.6 Coating Agent

The coating agent concept was proposed in 2014 by Leser at North Carolina State University and Newman et al. from Langley Research Center, NASA [56]. This work was an effort to bring self-healing to "commonly used" metallic materials. Because the bulk microstructure is unchanged with respect to the usual material and only a coating is applied (Fig. 2f, row 1), the concept is expected to be applicable to a wide range of materials.

The central idea of the coating agent concept (i.e., utilization of a coating for self-healing) classifies it in principle into the family of self-healing coatings, as discussed in the review "Self-healing coatings" by Abdolah Zadeh et al. in this volume [57]. However, application of a solder as the self-healing agent renders the

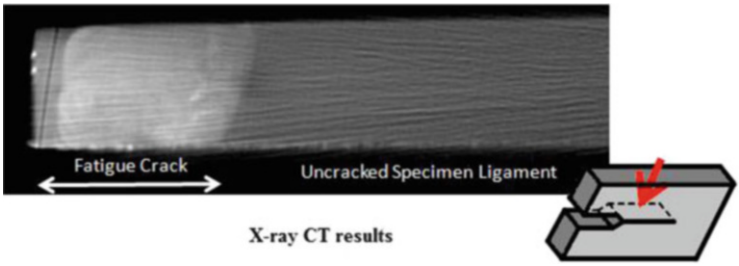

Fig. 8 X-ray microtomography image of a healed crack using the coating agent concept. Figure taken from [56] with permission

present concept similar to the previously discussed macroscale concepts and therefore it is useful to include this concept in the present discussion. To trigger self-healing with the solder, a heat treatment is required (indicated in Fig. 2f, row 3 by the red shaded background). After the application of the heat treatment, the crack should be filled with solder (Fig. 2f, row 4), as in the case of the solder tubes/capsules concept. The same crucial issue needs to be resolved, which is to guarantee good wetting of the crack surfaces and strong bonding between the host matrix and solder. An advantage of the coating agent concept over the solder tubes/capsules concept is that no voids occur after healing. It is only the solder coating that is locally reduced.

Based on the apparent applicability to aerospace components, Leser and coworkers [56] chose to carry out a proof-of-principle study of the coating agent concept on a titanium alloy with a 60% indium–40% tin (wt%) coating (near-eutectic composition). The melting temperature of this coating material is 124°C. Note that a low melting temperature is not only crucial for the healing heat treatment, but also for avoiding over-aging of the base material in the process. In this proof-of-principle case study, the thickness of the single-notch tension specimen and the coating were 2.03 mm and 0.01–0.02 mm, respectively. Fatigue crack growth testing results revealed that crack arrest is possible at lower crack-tip loads and that up to 50% reduction in crack growth rate is observed at higher crack-tip loads (where no full arrest is observed). A proof of full crack arrest was documented by X-ray tomography analysis, as shown in Fig. 8.

3.7 Electro-healing

The electro-healing concept has been recently proposed and tested by Zheng et al. [58], who were inspired by a partially successful, electropulsing-based healing of microcracks [59]. The electro-healing concept is a macroscale concept that differs quite significantly from the other macroscale concepts. In particular, no composite matrix material and no solder as healing agent are required. Instead, the cracked sample needs to be immersed in an electrolyte solution and a voltage needs

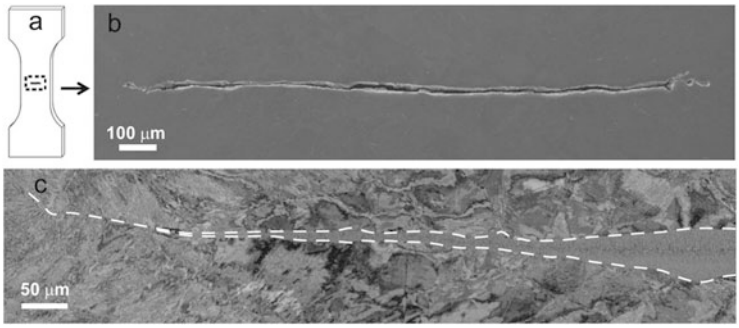

Fig. 9 (**a**) Schematic of the tension sample with a through-thickness crack in the center. (**b**) Image of a through-thickness crack. (**c**) Healed crack after electro-healing treatment. Figure taken from [58] with permission

to be applied (indicated by the green shaded background in Fig. 2g, row 3). The subsequent electrochemical reaction leads to deposition of material inside the crack, eventually closing it.

The electro-healing concept is very appealing for several reasons: (1) The original microstructure needs no modification (cf. Fig. 2g, row 1). (2) Experience from the field of electrochemical metallic coatings can be utilized for design and optimization purposes. (3) As verified by the work of Zheng et al. [58], very strong bonding between the crack surfaces and the newly deposited material can be achieved, enabling good material properties in the healed stage. A present limitation is that a through-thickness crack is required for the self-healing process to work. The authors [58] argue that healing of single-sided cracks is possible, but this remains to be verified in future studies.

Zheng et al. [58] applied the electro-healing concept to polycrystalline plates of pure nickel, with grain sizes ranging from 0.1 to 0.15 mm. Pre-cracked tensile samples were prepared by creating a hole in cylindrical samples by electrodischarge machining (EMD), compression to close the hole into a crack, and then EDM cutting of the tensile sample. Crack healing was achieved as explained above and shown in Fig. 9, and then cracked, crack-free, and healed samples were tested in tension. The results revealed that through-thickness cracks could be successfully healed by the growth of healing crystals with finer grain sizes (and higher strength) than the pristine material. Full recovery of the tensile strength and partial recovery of ductility was observed, although success also depended on sample thickness.

4 Summary

We have reviewed the available self-healing concepts in metallic bulk materials. Generally, the concepts can be subdivided into a group of nano length-scale concepts and a group of macro length-scale concepts. The first group comprises

concepts that autonomously self-heal nanovoids to prevent large-scale damage. The concepts falling into this group are the high-*T* precipitation concept, the low-*T* precipitation concept, and the nanoSMA-dispersoids concept. Of these, the most intensively studied and possibly the most promising concept is the high-*T* precipitation concept. It is applicable to heat-resisting steels and has been shown to considerably improve creep resistance.

The macroscale group comprises self-healing concepts that are designed to heal large-scale cracks (i.e., macroscopic cracks in the range of millimeters). These concepts are not autonomous because they require an external trigger to start the self-healing process, either heat treatment or an electrochemical reaction. The concepts falling into the macroscale group are the SMA-clamp&melt concept, the solder tubes/capsules concept, the coating agent concept, and the electro-healing concept. The SMA-clamp&melt concept is the most studied and possibly the most promising of the macroscale concepts. Its great advantage is that (in an ideal case) the self-healing process can be repeated limitlessly. The challenge is to design SMA reinforcement structures that avoid the strong anisotropy of currently available SMA–solder composites.

An important general characteristic of the available self-healing concepts is that they are bound by rather strict constraints. Mostly, these constraints relate to the choice of material. For example, for the precipitation concepts to work, the chosen elements must have specific phase diagrams and specific diffusion profiles. For the nanoSMA-dispersoids concept, the choice is restricted to material combinations that enable nanosized coherent particles showing the shape-memory effect. For the SMA-clamp&melt concept, an appropriate combination of an SMA and a solder is required. For the solder tubes/capsules concept and the coating agent *c*oncept, the host matrix and the solder must be carefully chosen to ensure good wetting and bonding properties at the crack surfaces. The possibly least restrictive concept with respect to material choice is the electro-healing concept, which "only" requires that the host matrix favors an electrochemical reaction with the electrolyte. However, for this latter concept, another restriction is the requirement of a through-thickness crack to enable sufficient flow of the electrolyte self-healing agent.

Given these constraints, the design of self-healing approaches in metals is challenging but, as evidenced by several successful examples, also very promising and, judging by the number of relevant publications in Fig. 1, becoming an increasingly active area of materials design research.

Acknowledgements Funding by the Deutsche Forschungsgemeinschaft (SPP 1568) and the European Research Council under the EU's 7th Framework Programme (FP7/2007-2013)/ ERC Grant Agreement No. 290998 is gratefully acknowledged.

References

1. van der Zwaag S, van Dijk NH, Jonkers HM, Mookhoek SD, Sloof WG (2009) Self-healing behaviour in man-made engineering materials: bioinspired but taking into account their intrinsic character. Philos Trans A Math Phys Eng Sci 367:1689
2. Hager MD, Greil P, Leyens C, van der Zwaag S, Schubert US (2010) Self-healing materials. Adv Mater 22:5424
3. van der Zwaag S (2010) Routes and mechanisms towards self healing behaviour in engineering materials. Bull Pol Acad Sci Tech Sci 58:227
4. Kötteritzsch J, Schubert US, Hager MD (2013) Triggered and self-healing systems using nanostructured materials. Nanotechnol Rev 2:699
5. Drenchev L, Sobczak JJ (2014) Self-healing materials as biomimetic smart structures. Instytut Odlewnictwa, Kraków
6. Ferguson JB, Schultz BF, Rohatgi PK (2014) Self-healing metals and metal matrix composites. JOM 66:866
7. World Trade Organization (2014) International trade statistics. https://www.wto.org/english/res_e/statis_e/its2014_e/its2014_e.pdf
8. Allwood JM, Cullen JM, Carruth MA, Cooper DR, McBrien M, Milford RL, Moynihan M, Patel ACH (2012) Sustainable materials: with both eyes open. UIT, Cambridge
9. Intergovernmental Panel on Climate Change (2007) Fourth assessment report. https://www.ipcc.ch/report/ar4/
10. van der Zwaag S (2007) Self-healing materials: an alternative approach to 20 centuries of materials science. Springer, Dordrecht
11. Manuel MV (2009) Principles of self-healing in metals and alloys: an introduction. In: Ghosh G (ed) Self-healing materials: fundamentals, design strategies, and applications. Wiley-VCH, Chichester
12. Shinya N, Kyono J, Laha K (2003) Improvement of creep rupture properties of heat resisting steels by the self-healing of creep cavities. Mater Sci Forum 426–432:1107
13. Laha K, Kyono J, Kishimoto S, Shinya N (2005) Beneficial effect of B segregation on creep cavitation in a type 347 austenitic stainless steel. Scr Mater 52:675
14. Shinya N, Kyono J, Laha K (2006) Self-healing effect of boron nitride precipitation on creep cavitation in austenitic stainless steel. J Intell Mater Syst Struct 17:1127
15. Laha K, Kyono J, Shinya N (2007) An advanced creep cavitation resistance Cu-containing 18Cr–12Ni–Nb austenitic stainless steel. Scr Mater 56:915
16. Laha K, Kyono J, Shinya N (2012) Copper, boron, and cerium additions in type 347 austenitic steel to improve creep rupture strength. Metall Mater Trans A 43:1187
17. He SM, van Dijk NH, Schut H, Peekstok ER, van der Zwaag S (2010) Thermally activated precipitation at deformation-induced defects in Fe-Cu and Fe-Cu-B-N alloys studied by positron annihilation spectroscopy. Phys Rev B 81:094103
18. He SM, van Dijk NH, Paladugu M, Schut H, Kohlbrecher J, Tichelaar FD, van der Zwaag S (2010) In situ determination of aging precipitation in deformed Fe-Cu and Fe-Cu-B-N alloys by time-resolved small-angle neutron scattering. Phys Rev B 82:174111
19. He SM, Brandhoff PN, Schut H, van der Zwaag S, van Dijk NH (2013) Positron annihilation study on repeated deformation/precipitation aging in Fe–Cu–B–N alloys. J Mater Sci 48:6150
20. Zhang S, Kohlbrecher J, Tichelaar FD, Langelaan G, Brück E, van der Zwaag S, van Dijk NH (2013) Defect-induced Au precipitation in Fe–Au and Fe–Au–B–N alloys studied by in situ small-angle neutron scattering. Acta Mater 61:7009
21. S. Zhang (2015) Self healing of damage in Fe-based alloys. Ph.D. thesis, TU Delft
22. Karpov EG, Grankin MV, Liu M, Ariyan M (2012) Characterization of precipitative self-healing materials by mechanokinetic modeling approach. J Mech Phys Solids 60:250
23. Shinya N (2009) Self-healing of metallic materials: self-healing of creep cavity and fatigue cavity/crack. In: Ghosh G (ed) Self-healing materials: fundamentals, design strategies, and applications. Wiley-VCH, chichester

24. Lumley RN, Morton AJ, Polmear IJ (2002) Enhanced creep performance in an Al–Cu–Mg–Ag alloy through underageing. Acta Mater 50:3597
25. Lumley RN, Polmear IJ, Morton AJ (2003) Interrupted aging and secondary precipitation in aluminium alloys. Mater Sci Technol 19:1483
26. Lumley RN, O'Donnell RG, Polmear IJ, Griffiths JR (2005) Enhanced fatigue resistance by underageing an Al-Cu-Mg-Ag alloy. Mater Forum 29:256
27. Lumley RN, Polmear IJ (2007) Advances in self-healing of metals. In: Proceedings of the first international conference on self-healing materials, Noordwijk aan Zee, The Netherlands
28. Hautakangas S, Schut H, van der Zwaag S, Rivera Diaz del Castillo PEJ, van Dijk NH (2007) Self healing kinetics in an underaged AA2024 aluminium alloy. In: Proceedings of the first international conference on self-healing materials, Noordwijk aan Zee, The Netherlands
29. Hautakangas S, Schut H, van der Zwaag S, del Rivera Diaz Castillo PEJ, van Dijk NH (2007) Positron annihilation spectroscopy as a tool to develop self healing in aluminium alloys. physica status solidi C 4:3469
30. Hautakangas S, Schut H, van Dijk NH, del Rivera Díaz Castillo PEJ, van der Zwaag S (2008) Self-healing of deformation damage in underaged Al–Cu–Mg alloys. Scr Mater 58:719
31. Mahdavi Shahri M, Alderliesten RC, van der Zwaag S, Schut H (2014) Postponing crack nucleation in 2024 aluminium alloy by dynamic precipitation from the supersaturated state. Adv Mater Res 891–892:1577
32. Lumley RN (2007) Self healing in aluminium alloys. In: van der Zwaag S (ed) Self healing materials: an alternative approach to 20 centuries of materials science. Springer, Dordrecht
33. Wanhill R (2007) Fatigue crack initiation in aerospace aluminium alloys, components and structures. In: Proceedings of the first international conference on self-healing materials, Noordwijk aan Zee, The Netherlands
34. Ritchie RO (1999) Mechanisms of fatigue-crack propagation in ductile and brittle solids. Int J Fract 100:55
35. Vasudeven AK, Sadananda K, Louat N (1994) A review of crack closure, fatigue crack threshold and related phenomena. Mat Sci Eng A Struct 188:1
36. Mayer HR, Stanzl-Tschegg SE, Sawaki Y, Hühner M, Hornbogen E (2007) Influence of transformation-induced crack closure on slow fatigue crack growth under variable amplitude loading. Fatigue Fract Eng Mater Struct 18:935
37. James MN, Knott JF (1985) Critical aspects of the characterization of crack tip closure by compliance techniques. Mater Sci Eng 72:L1
38. Baxevanis T, Parrinello AF, Lagoudas DC (2013) On the fracture toughness enhancement due to stress-induced phase transformation in shape memory alloys. Int J Plasticity 50:158
39. Grabowski B, Tasan C (2014) Towards self-healing metals by employing optimally-dispersed Ti-Ni shape-memory nano-particles. Project within DFG SPP 1568: Design and generic principles of self-healing materials. DFG, Bonn
40. Xu GQ, Demkowicz MJ (2013) Healing of nanocracks by disclinations. Phys Rev Lett 111: 145501
41. Glensk A, Grabowski B, Hickel T, Neugebauer J (2015) Understanding anharmonicity in fcc materials: from its origin toab initioStrategies beyond the quasiharmonic approximation. Phys Rev Lett 114:195901
42. Grabowski B, Wippermann S, Glensk A, Hickel T, Neugebauer J (2015) Random phase approximation up to the melting point: impact of anharmonicity and nonlocal many-body effects on the thermodynamics of Au. Phys Rev B 91:201103
43. Duff AI, Davey T, Korbmacher D, Glensk A, Grabowski B, Neugebauer J, Finnis MW (2015) Improved method of calculating ab initio high-temperature thermodynamic properties with application to ZrC. Phys Rev B 91:214311
44. Files BS (1997) Design of a biomimetic self-healing superalloy composite. Ph.D. thesis, Northwestern University, Chicago
45. Manuel MV (2007) Design of a biomimetic self -healing alloy composite. Ph.D. thesis, Northwestern University, Chicago

46. Manuel MV, Olson GB (2007) Biomimetic self-healing metals. In: Proceedings of the first international conference on self-healing materials, Noordwijk aan Zee, The Netherlands
47. Fisher CR, Manuel MV (2011) Design considerations for matrix compostions of self-healing metal-matrix composites. In: Proceedings of the third international conference on self-healing materials, Bath, UK
48. Wright MC, Manuel MV, Wallace T (2013) Fatigue resistance of liquid-assisted self- repairing aluminum alloys reinforced with shape memory alloys. NASA/TM-2013-216629. National Aeronautics and Space Administration, Hampton
49. Rohatgi PK (2014) Al-shape memory alloy self-healing metal matrix composite. Mat Sci Eng A Struct 619:73
50. Ferguson JB, Schultz BF, Rohatgi PK (2015) Zinc alloy ZA-8/shape memory alloy self-healing metal matrix composite. Mat Sci Eng A Struct 620:85
51. Kaufman L, Bernstein H (1970) Computer calculation of phase diagrams. Academic, New York
52. White SR, Sottos NR, Geubelle PH, Moore JS, Kessler MR, Sriram SR, Brown EN, Viswanathan S (2001) Autonomic healing of polymer composites. Nature 409:794
53. Lucci JM, Rohatgi PK, Schultz B (2008) Experiment and computational analysis of self-healing in an aluminum alloy. In: Proceedings of the ASME international mechanical engineering congress and exposition, Boston, USA
54. Nosonovsky M, Amano R, Lucci JM, Rohatgi PK (2009) Physical chemistry of self-organization and self-healing in metals. Phys Chem Chem Phys 11:9530
55. Nosonovsky M, Rohatgi PK (2012) Biomimetics in materials science: self-healing, self-lubricating, and self-cleaning materials. Springer, New York
56. Leser PE, Newman JA, Smith SW et al. (2014) Mitigation of crack damage in metallic materials. NASA/TM-2014-218272. National Aeronautics and Space Administration, Hampton
57. Abdolah Zadeh M, van der Zwaag Z, Garcia SJ (2015) Self-healing coatings. Adv Polym Sci. doi:10.1007/12_2015_339
58. Zheng XG, Shi YN, Lu K (2013) Electro-healing cracks in nickel. Mat Sci Eng A Struct 561:52
59. Zhou Y, Guo J, Gao M, He G (2004) Crack healing in a steel by using electropulsing technique. Mater Lett 58:1732

Index